Integrating Gravity and Magnetic Data with Remote Sensing in Structural Modelling of Benue Trough (Middle and Lower) of Nigeria

By

Yenne Yusuf Ezekiel

Submitted in accordance with the requirements for the degree of Doctor of Philosophy.

The University of Leeds
School of Earth and Environment
Institute of Applied Geosciences

April 2022

Declarations

The candiadate confirms that his work submitted is his own and that appropriate credit has been given where reference has been made to the work of others.

Acknowledgment

My sincere appreciation goes to the Petroleum Technology Development Fund (PTDF) of Nigeria for funding and supporting this study at the University of Leeds. I would like to thank the staff of the University of Jos especially the Head of the Department of Geology for their moral support throughout this research period.

I would like to express my gratitude to my supervisors; Dr. Chris Green and Dr. Taija Tovela for painstakingly reading through my thesis, giving me advice, comments, and recommendations to help improve the research and make it better. Special thanks to Dr. Stephen Grebby of the University of Nottingham, Nottingham Geospatial Institute for taking his time out of his busy schedule to give me useful suggestions on my remote sensing techniques and Dr. Kim Welford of the Department of Earth Sciences, Memorial University of Newfoundland, Canada for the useful discussions on the concepts of developing a reference model for gravity inversion.

I would like to thank the International Gravimetric Bureau (BGI) and Getech Plc. for allowing me to have access to their gravity data sets. My appreciation goes to the Nigeria Geological Survey Agency (NGSA) especially Mr. Nansak Bitrus Rimven for facilitating the acquisition of the high-resolution aeromagnetic data sets and NASA's Land Processes Distributed Active Archive Center (LP DAAC) for providing free and downloadable remote sensing data sets. Again, I want to specially thank Prof. U.A Lar, the former Chair of PTDF at the University of Jos for giving me the opportunity to gain the necessary field experience for this research during the Integrated Data Services Limited of the Nigeria National Petroleum Corporation (IDSL-NNPC) gravity and magnetic data acquisition for the Middle Benue Trough. This opportunity was the backbone for the development of the research!

I really want to thank Dr. Roman Shekhtman of the University of British Columbia (UBC), Geophysical Inversion Facility for providing the license and the codes for Grav3D and Mag3D inversion software, Dr. Jeffrey Phillips of the U.S. Geological Survey for providing USGS GX software, Dr. Mohammed Gouiza for providing VPmg software and Getech Plc. for the freedom to use GETgrid software and other of their unlicensed codes for the work.

I would like to thank the members of Basin Structural Group (BSG) of the University of Leeds, Society of Exploration Geophysicist (SEG), American Geophysical Union (AGU), Tectonic Structural Group (TSG), and the Petroleum Geology Group for their useful comments during

presentations over the past years of my research. Indeed, you have made the outcome of this work awesome! I want to also extend my appreciation to all my friends and colleagues at the Department of Geology, University of Jos for their calls and kind words, and to all my friends and church members at Holborn Church Leeds. You all made my years at the University of Leeds great and rewarding. I want to express my appreciation to a special friend and an office mate, Anthonio Fuggi for helping me navigate through Matlab codes when it was very difficult to decipher their content. Thank you so much!

ABSTRACT

The Benue trough is a rift-related basin associated with interesting geological and structural features, but these features are barely observed on the surface due to sediment and vegetation cover. An integrated approach of combining remote sensing with gravity and magnetic data sets has been presented in this research. A new geology map was constructed for the area from the existing literature map and remote sensing data sets. Surface to near-surface/shallow lineaments and other non-linear geological bodies were mapped from remote sensing, residual gravity, and magnetic data sets while deep lineaments interpreted as basement lineaments were mapped from regional gravity and magnetic data sets. The study isolated tectonic-related lineaments (faults/fractures/shear zones) from non-tectonic (dykes and lithological contacts) and non-linear geological bodies (sills, volcanic rocks, plugs, etc.). The tectonic-related lineaments were interpreted as faults and grouped into four major types based on their orientations: the NE-SW, NW-SE, ENE-WSW, and N-S trending normal faults. This study interpreted two main tectonic regimes in the area; the extensional and the compression events. The extensional regime involved the formation of the NE-SW, ENE-WSW, NW-SE, and N-S trending normal faults during the Early Aptian (142 Ma), Late Aptian (120 Ma), the Albian Age (119-101 Ma), and the Maastrichtian (65 Ma) when the regional maximum extensional stress fields acted in NNW-SSE, N-S, NE-SW, and ENE-WSW extensional directions, respectively. The compressional regimes are characterized by the reversal in the stress field which occurred mainly during the Late Santonian (84 Ma). It is interpreted as responsible for basin inversion, fault reactivation, shortening, and the deformation of pre-existing sediments which produced several sub-basin, uplifted block, folds, etc.

The basement is estimated to have a maximum depth of 9 km and a shallowest depth estimate of 4 km within the basin based on the pseudo-gravity inversion method, and its morphology revealed several areas of basement subsidence and uplift. Four 2D gravity and magnetic model profiles were generated in the NW-SE trend direction and three major subsurface depth interfaces were identified as basement, Curie, and Moho depth interfaces with an average maximum depth of 9.65 km and minimum average depths of 12.50 km and 19.02 km, respectively, measured from topography surface. The model showed deepening of the trough to a maximum depth of about 10 km and shallowing of Moho to a depth of about 19 km, which generally indicated a thinned crust and Moho doming beneath the trough. The study also modelled a 3-D variation in density and susceptibility contrasts across the basin and obtained Moho interface from gravity data sets and areas of magmatic intrusions from magnetic data

sets. The spatial distribution of the Moho interface was modelled and combined with the 3-D depth estimate from the pseudo-gravity inversion method to reveal the crustal structure for the whole trough. The crust is thinned to about 14 km in the northern part of the area while the crust thinned to about 9 km in the south especially at the centre of the trough. This has been interpreted to be because of the crustal extension during rifting. The amount of crustal extension varies between 93 km in the north and 142 km in the south giving the trough a 'scissors style' extensional opening while the rate of extension determined from stretching factor estimation increases from the Middle Benue Trough to the Lower Benue Trough. The lithosphere (the crust and upper mantle) analysed from the spectral technique has been interpreted to be stronger in the Middle Benue Trough with an average T_e value of 15 km than the Lower Benue Trough with an average T_e value of 10 km where T_e acts as a proxy for the lithosphere strength. The thermal structure predicted from power spectrum and three-dimensional magnetic inversion techniques have been interpreted to influence the long-term strength of the lithosphere as well in this study. This research has further shown that the strength of the lithosphere and the Curie depth with values ranging between 5 km and 32 km, are directly related i.e., areas with high values of $T_{e,}$ are correlated with areas of high Curie depth values even if the area is too small to map spatial variation of T_e . This study also showed that a mantle temperature of 1400 ℃ between Aptian and Albian times (125-100 Ma i.e., 25 Ma) produces about 9 km of magma melts from the lithosphere to be emplaced within the trough.

Dedication

To

God Almighty

Kaneng Ezekiel Yenne (wife) and Laubirwa, Mananyan, and Kima Ezekiel Yusuf Yenne (Children).

Yenne Yusuf Takasanne (Dad), Lawrence, and Christopher (brothers), and Emobarsa and Navonke (sisters).

and to the everlasting memories of

Asabe Yusuf Yenne (mother) and Lois Stephen Gonsur (elder sister).

TABLE OF CONTENTS

LIST OF FIGURES

LIST OF TABLES

ACKNOWLEDGEMENT

Table of Contents

List of Tables

List of Figures

List of Abbreviations

ATMDS - Adaptive Tilt Multi Directional Shading

ASTER - Advanced Space-borne Thermal Emission and Reflection Radiometer

AZ - Azimuthal Filter

CARS - Central African Rift System

CPD - Curie Point Depth

DEM - Digital Elevation Model

DN – Digital Number

DRTE - Differential Reduction to the Equator

DRTP - Differential Reduction to the Pole

EGM2008 - Earth Gravitational Model 2008

EM - Electromagnetic

ENVI: Environment for Visualizing Images

ESRI - Environmental Systems Research Institute

FFT - Fast Fourier Transform

FPCS - Feature-oriented Principal Component Selection

GMT - Generic Mapping Tools

GRACE - Gravity Recovery and Climate Experiment

IGRF - International Geomagnetic Reference Field

ITG- Institute of Theoretical Geodesy

LP DAAC - Land Processes Distributed Active Archive Centre

MBA - Mantle Bouguer Anomaly

NASA - National Aeronautics and Space Administration

NDVI - Normalized Difference Vegetation Index

NTRTP - Nonlinear Thresholding RTP

OLI - Operational Land Imager

OIF - Optimum Index Factor

PCA - Principal Component Analysis

PCs - Principal Components

σ_1 - Maximum Principal Stress Axis

σ_2 - Intermediate Principal Stress Axis

σ_3 - Minimum Principal Stress Axis

RTE - Reduction to the Equator

RTP - Reduction to the Pole

SAM - Spectral Angle Mapper

SI - Structural Index

β - Stretching Factor

SRTM - Shuttle Radar Topographic Mission

SWIR - Shortwave Infrared

T – Earth Magnetic Field

TA - Total Amplitude Anomaly

T_e - Elastic Thickness

TIRS - Thermal Infrared Sensor

TIR - Thermal Infrared

TMI - Total Magnetic Intensity

UBC - University of British Columbia

VNIR - Visible and Near-Infrared

WCARS - West and Central African Rift System

CHAPTER ONE

GENERAL INTRODUCTION

1.1 Background

Rift-related basins are usually characterized by interesting geological and structural features which may be exposed at the surface or buried in the subsurface. It is very common to find researchers applying seismic, gravity, and/or magnetic techniques for basin structural and tectonic studies (Mohriak et al., 1995; Stanton et al., 2016; Ali et al., 2017; Harkin et al., 2020). However, in situations where seismic data sets are unavailable, good gravity and magnetic data sets have successfully yielded accurate and reliable surface and subsurface basin results (Onwuemesi and Egboka, 1989; Maden et al., 2015; Spampinato et al., 2015; Welford et al., 2015). The advent of remote sensing techniques has broadened and improved understanding of basin structures and tectonics on local and regional scales. Several scientists have utilized remote sensing data for mapping surface geology and structures (Bhagat and Verma, 2006; Shi et al., 2012; Paranhos Filho et al., 2013). In the absence of seismic data, the integration of remote sensing with gravity and magnetic data sets has proven effective in the structural and tectonic modelling and evaluation of many basins e.g., the South Rewa Gondwana basin in India, the Al Hamada al Hamra, and the Sirt basins in Libya, the Pedirka Basin in Australia, the Muglad and the Melut basins of South Sudan, etc., (Boud, 1987; Saadi et al., 2008; Bishop, 2013; King et al., 2013; Azizi and Saibi, 2015; Chowdari et al., 2017).

The Benue Trough is an extensional basin filled with about 6 km of Cretaceous rocks and bordered on either side by a crystalline Basement located in the western part of Africa (Ofoegbu, 1985; Ajayi and Ajakaiye, 1981; Akande et al., 2012). Cenozoic volcanic rocks are found within and on the sediments (Fitton, 1980; Benkhelil, 1989). The trough is divided into the Lower, Middle, and Upper parts (Obaje, 2009; Akande et al., 2012; Fig. 1.1). The Upper Benue part is well studied due to the ease of finding well-exposed rock outcrops while the Lower and the Middle parts are characterized by flat undulating topography and fewer outcrops and hence are more challenging in geological and structural studies. The Lower and Middle Benue Trough has most of its stratigraphy deformed and covered within thick sediments and vegetation. The evidence of these episodes of deformation is rarely observed at the surface or mapped at the subsurface. However, this challenge presents an opportunity for this study, thus, an integrated approach of remote sensing with high resolution aeromagnetic and ground gravity data sets are used to proffer solutions to the challenges above. The remote sensing data were

used for surface lithology and lineament mapping while the magnetic and gravity data were employed in subsurface structural modelling/studies and interpretations.

1.2 Geography of Benue Trough

The Benue Trough is in the Western part of Africa located within Nigeria (Fig. 1.2). It is an elongated trough that is about 800 km long and 150 km wide, stretching out from the South to the North in an NE–SW direction (Ofoegbu, 1985; Obaje, 2009; Akande et al., 2012). It is filled with Cretaceous rocks whose ages range from 113 Ma to 65 Ma (Ajayi and Ajakaiye, 1981; Ofoegbu, 1982; Obaje, 2009) and with the intrusion of some Cenozoic volcanic rocks (Fitton, 1980; Benkhelil, 1989). The trough is bordered by four main high topographic massifs: Northern Nigeria massif, the West Africa Massif, the Adamawa Massif, and the Oban Massif (Benkhelil, 1989). These Massifs form the Precambrian Basement Complex that surrounds the low-lying sediments. The trough is to its southern and northern limits bordered by the Niger Delta and Chad basins, respectively (Abubakar, 2014). The southern and central parts of the trough are recognized by flat undulating topography with few hills making it prone to flooding while the northern part is marked by high and rugged topography due to the presence of volcanic plugs and outcrops of deformed sandstones (Benkhelil, 1989).

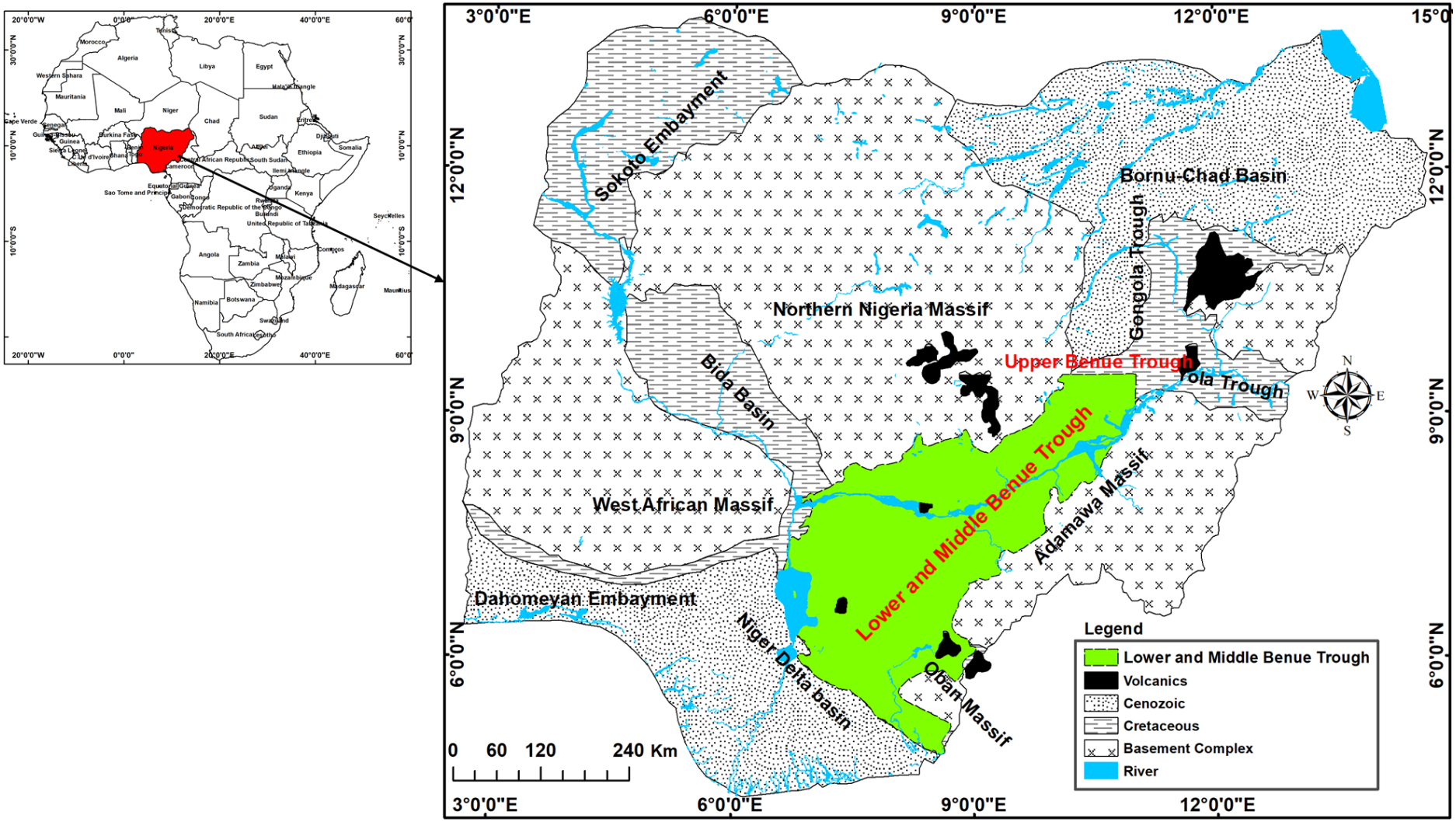

Fig. 1. 1: General geological map of Nigeria. Location of Nigeria (in red polygon-left) and Lower and Middle Benue Trough (in green polygon) (modified after Onuoha, 1999). Upper Benue Trough is composed of Gongola and Yola troughs.

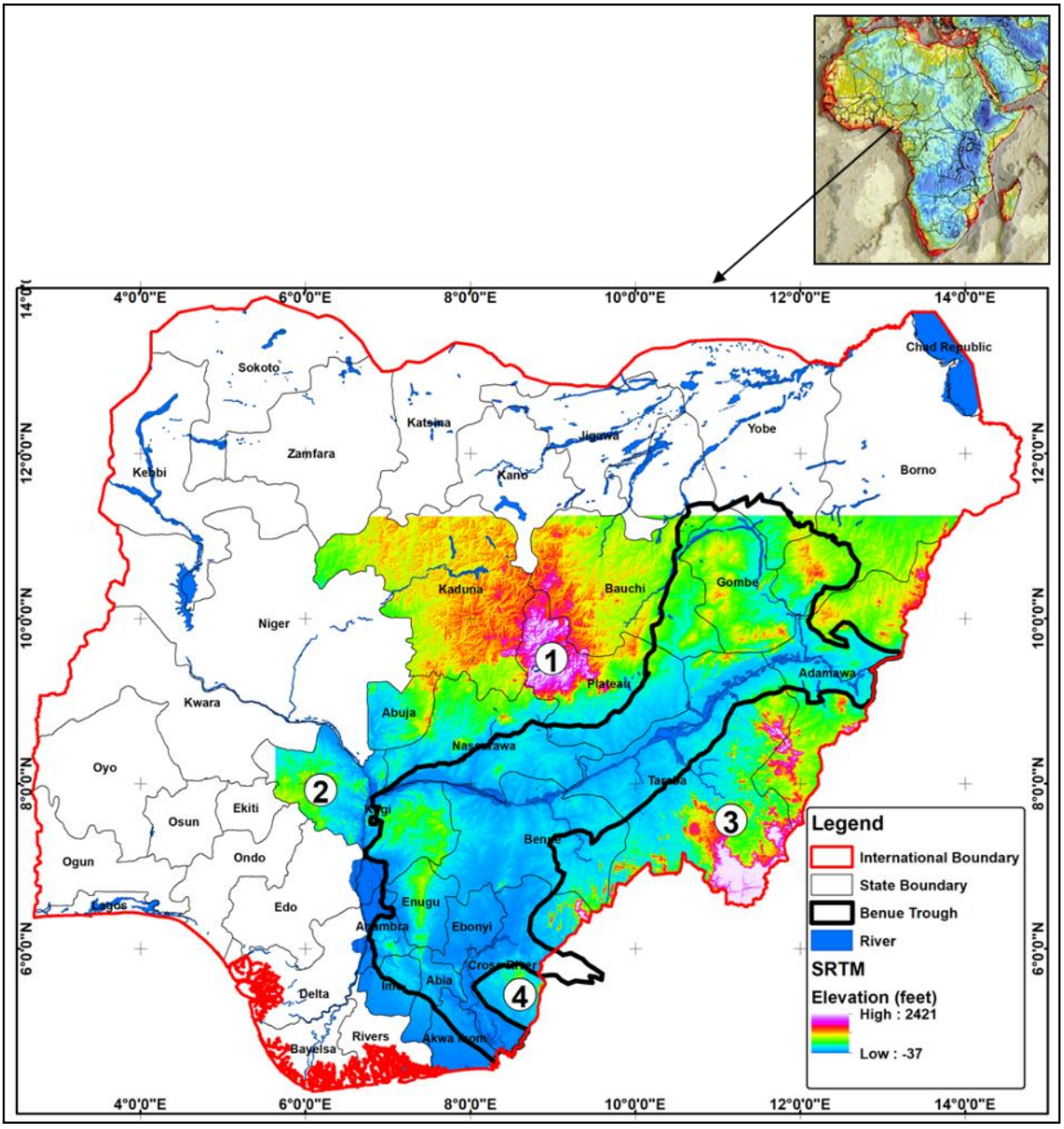

Fig. 1. 2: Political map of Nigeria showing the Benue Trough overlain on Shuttle Radar Topographic Mission (SRTM) topography. 1, 2, 3 and 4 represent the Northern Nigeria, the West Africa, the Adamawa, and the Oban Massifs.

1.3 Geological setting of the Benue Trough

The geological setting of the Benue Trough has been reviewed by several authors (Ofoegbu, 1985; Benkhelil, 1989; Obaje, 2009; Akande et al., 2012). It is generally composed of an underlying Precambrian Basement Complex and overlying Cretaceous sedimentary rocks with several intra-sedimentary intrusive rocks. The Precambrian Basement Complex is composed of two rock series; the less metamorphosed series is made up of mainly gneisses, schists, and quartzites, and the highly metamorphosed series of banded and contorted gneisses (Cratchley and Jones, 1965; Ofoegbu, 1985; Benkhelil, 1989). In each of the series are many major and minor intrusive rocks separated into younger and older rock types. The older intrusive rocks (Older Granites) are largely granites while the younger intrusive types (Younger Granites) are made up of granites, pegmatites, diorites, dolerites, and syenites with numerous associated dyke-like bodies (Wright, 1968). The Cretaceous sedimentary rocks form a major part of the trough and overlie the Precambrian basement rock with intrusive rocks embedded within them.

Tectonic stress fields control the formation and geometry of structures either by far or near fields (Min and Hou, 2019). Movements of the African sub-plates during the breakup of the continent in the Early Cretaceous have been recognized to be the main cause of regional stress field in controlling the geometry of basin structures in Africa (Lowell, 1995 and Fairhead et al., 2013; Fig. 1.3) while mantle plume uplift is the main contributor of local stress-field (Delaney and Gartner, 1997; Fossen, 2010; Min and Hou, 2019). The trans-tensional regime of Equatorial Atlantic formed as a series of large pull-apart basins bounded by rifted and transform segments leading to the creation of large intercontinental basins in West Africa such as the Benue Trough during the Aptian – Albian (Benkhelil, 1989; Fig. 1.3). In this study, however, both stress fields are believed to have influenced the structural evolution of the basin. Four different stress field orientations have been observed to be responsible for developing the basin structures at different times during the evolution of the basin (Figs. 1.4).

1.4 The structural setting and stratigraphy of the Benue Trough

1.4.1 Structural setting

The Benue Trough is a rifted basin that trends in a major NE-SW direction. Several tectonic activities have led to the development of the structural features within the trough (Nwachukwu, 1972; Agagu and Adighije, 1983) and these occurred mainly during Cenomanian, Santonian, Post Maastrichtian and Palaeocene tectonism (Olade, 1975; Ofoegbu, 1985; Fairhead *et al.*,

2013). Multiple phases of deformation have been identified (i.e., extensional and compressional phases) in carving the geometry as well as the orientation of the trough (Fairhead, 1988; Fairhead et al., 2013). Some of the structures prominent are sub-basins, uplifts, ridges, volcanic rocks, etc.

The Upper Benue Trough is characterized by structural features like the Kaltungo inlier, the Zambuk and Gombe ridge, the Yola, and Gombe sub-basins, and the Lamurde anticline (Benkhelil, 1989) while in the Lower and Middle Benue Trough, there is evidence of faulting and compressive folding in general NE-SW, N-S, NW-SE, and ENE-WSW directions with several structures observed by field work, gravity, and magnetic methods (Cratchley and Jones, 1965; Agagu and Adighije, 1983; Ofoegbu, 1985; Anudu *et al.,* 2014). Folding, some faulting and upliftment of the basement leading to the formation of structural features like the Abakaliki anticline, the Anambra Basin, Afikpo synclines, the Keana anticline, and Awe syncline, etc., occurred during the Santonian tectonism (Agagu and Adighije, 1983; Benkhelil, 1989; Akande et *al.*, 2012). Post-Santonian sediments have been shown not to be affected by these Santonian tectonic activities (Cratchley and Jones, 1965; Ofoegbu, 1985; Obaje, 2009; Fatoye and Gideon, 2013).

Intrusive rocks were emplaced within the trough from Mesozoic to Cenozoic times (Ofoegbu, 1985; Coulon et al., 1996; Fig. 1.4). There are three (3) magmatic activities recognized based on Argon age dating: Early to Middle Cretaceous (147-106 Ma), Late Cretaceous (97-81 Ma), and Palaeocene-Eocene (68-49 Ma). The northern volcanic intrusions are older than those in the south i.e., the dykes in the south are probably 68-49 Ma (Coulon et al., 1996). The igneous intrusions are predominantly basaltic composed of tholeiitic and alkaline basalts while very few are acidic (Benkhelil, 1987; Ekwueme, 1994; Coulon et al., 1996). Most of the igneous intrusions are in the form of sills, dykes, bosses, plugs, etc., and are found within or across folded/unfolded sedimentary rocks indicating that they post-date the deposition of the sediments they cut (Cratchley and Jones, 1965; Wright, 1968; Ofoegbu, 1982). The sills are mostly dolerites while the dykes trend in NE-SW and NW-SE directions (Anudu et al., 2014; Ofoegbu, 1985).

1.4.2 Stratigraphy

The trough is divided into the Lower, Middle, and Upper structural and sedimentary domains (Benkhelil et al., 1998; Obaje, 2009; Akande et al., 2012, Figs. 1.4). The stratigraphy of the

trough was established based on the continuous correlation in the stratigraphy between the Upper and the Lower Benue Trough (Cratchley and Jones, 1965), but this study, however, focuses on the Lower and the Middle parts of the trough.

1.4.2.1 Upper Benue Trough

The Upper Benue Trough is sub-divided into two parts; the Gongola and the Yola Arms trending in NNE-SSW and ENE-WSW directions, respectively (Obaje, 2009). The Bima sandstone is 113 Ma which overlies the Precambrian Basement Complex and is composed of sandstones, intercalated with carbonaceous clays, siltstones, shales, and mudstones. The Yolde formation is 100 Ma in age and lies conformably on the Bima sandstones. It was deposited within a transitional marine environment and is composed of sandstones, limestones, claystone, clays, and shales. The Pindiga formation is found overlying the Yolde formation and is composed of dark carbonaceous shales with limestones and intercalation of pale-coloured limestones, shales, and minor sandstones. Pindiga formation is marine and 86 Ma in age. The Gombe sandstone lies over the Pindiga formation and was deposited in the post-folding period. It is aged 72 Ma and composed of intercalations of coal, lignite, and shale. The youngest formation in the Upper Benue Trough is the Kerri-Kerri formation which is 66 Ma and composed of whitish-grey sandstones, siltstones, and claystone (Fig. 1.4).

1.4.2.2 Lower and Middle Benue Trough

The Lower and the Middle part of the Benue Trough is composed of mainly the Asu River Group, the Eze-Aku Formation, Makurdi sandstone, Keana-Awe, and Awgu Formations, which were deposited between 113 Ma and 90 Ma (Cratchley and Jones, 1965; Nwachukwu, 1972; Ofoegbu, 1985; Obaje, 2009; Akande et *al.*, 2012; Fig. 1.4).

Sedimentation in the area started in 113 Ma with the deposition of the Asu River Group (Middle Albian to Late Albian age) that is composed of the basal sandstones, dark shales, siltstones, fine-grained sandstones, and limestones in the southern and central part of the trough (Cratchley and Jones, 1965; Nwachukwu, 1972; Ofoegbu, 1985) while its lateral equivalent in Upper Benue Trough is the Albian Bima Formation which lies unconformably on the Precambrian Basement (Obaje, 2009). This is overlain by the 100 Ma - 93 Ma formations. In the south are the Ezeaku Formation with its lateral equivalent of the Konshisha River Group in the Gboko area, Makurdi sandstone at Makurdi-Oturkpo area, and Keana/Awe Formations in the Keana area, all within the Middle part of the trough (Nwachukwu, 1972; Offodile, 1976;

Ofoegbu, 1985; Obaje, 2009). They generally consist of hard grey and black calcareous shales, shelly limestone, and siltstone. In the northern part is the Yolde Formation composed of sandstones, limestones, shales, clays, and claystone (Benkhelil, 1989; Obaje, 2009). Overlying the formation is the Awgu Formation (94 Ma - 86 Ma) consisting of marine fossiliferous, grey bluish shales, limestones, and calcareous sandstone usually in the southern and central part of the trough while towards the north is the Pindiga formation (Ofoegbu, 1985; Obaje, 2009; Akande *et al.*, 2012). The earlier deposited sediments were folded, faulted, and uplifted to form structures like the Abakaliki anticline, the Anambra Basin, Afikpo synclines, the Keana anticline, and Awe syncline, during a period of Santonian tectonism (Agagu and Adighije, 1983; Benkhelil, 1989; Akande *et al.*, 2012). The 83 Ma - 72 Ma sediments or the post-Santonian sediments overlie the Awgu formation. They include the Lafia Formation in the Middle part of the trough (Cratchley and Jones, 1965; Ofoegbu, 1985a; Obaje, 2009) while in the south, are the Asata/Nkporo Shales consisting of a sequence of bluish to dark grey shale and mudstone locally with sandy shales, thin sandstones, and shelly limestone beds. The shaly facies grade laterally to sandstones of the Afikpo sandstones. The sandstones, shales, siltstones, and mudstones and the inter-bedded coal seams of the deltaic Mamu Formation is 72 Ma and overlies the Asata/Npkoro shales. The deltaic facies grade laterally into the overlying marginal marine sandstones of the Ajali and Nsukka Formations. The Nsukka Formation consists of carbonaceous shales, sandstones, and seams of coal (Ofoegbu, 1985; Fatoye and Gideon, 2013). A sequence of shales with sandstone intercalations forms the Imo Shale which is 66 Ma and overlying it into the Niger Delta is the Ameki formation and the Ogwashi-Asaba Formation.

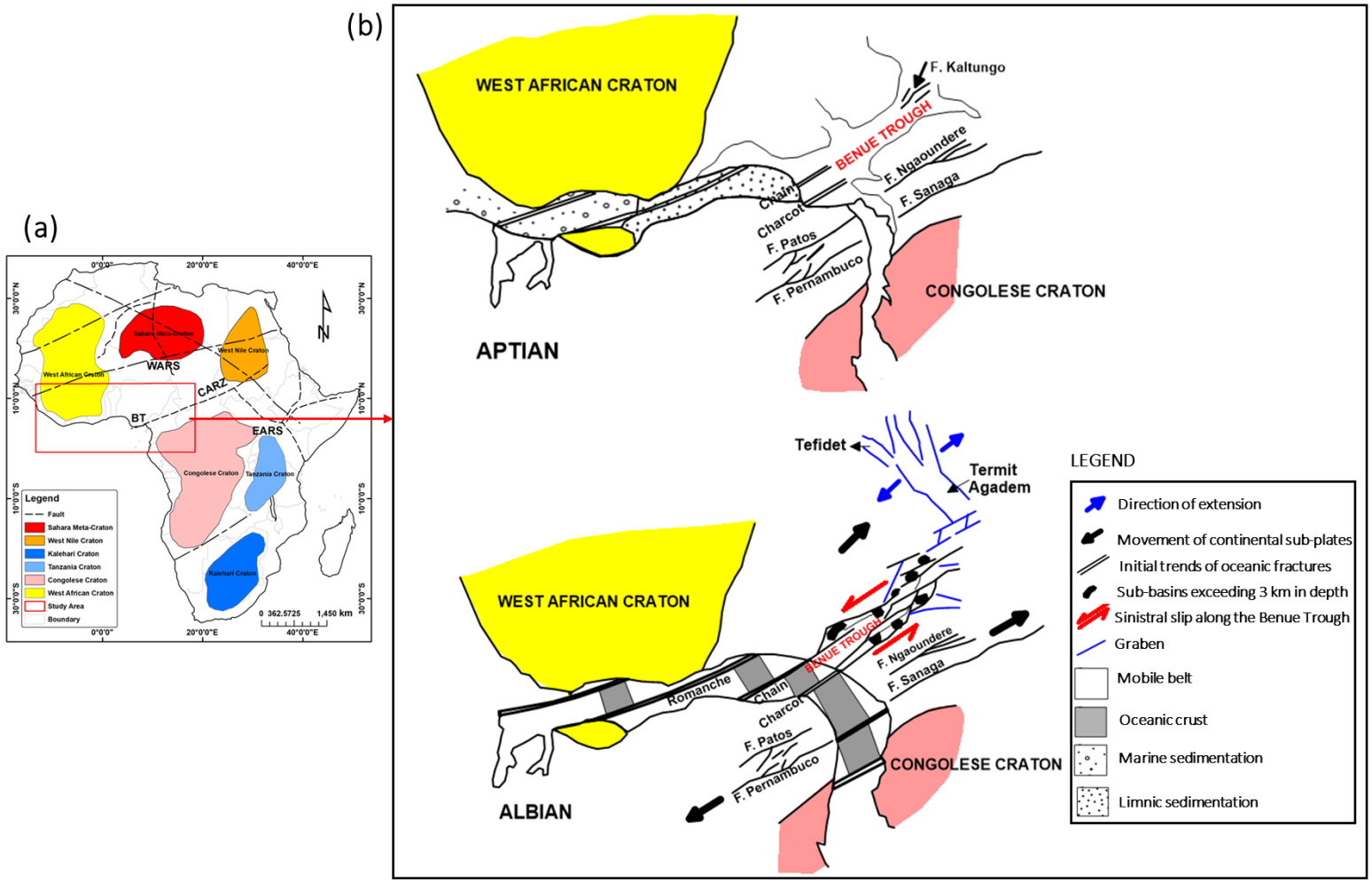

Fig. 1. 3: Structural setting and location of the study area (a) Cretaceous intracontinental deformation zones and cratons in Africa (after Pérez-Diaz and Eagles, 2014). BT: Benue Trough; CARZ: Central African Shear Zone; EARS: East African Rift System; and WARS: West African Rift System. (b) Tectonic reconstitution activities showing the position of the study area between West African and Congolese Cratons during the Aptian and Albian times (after Benkhelil, 1989).

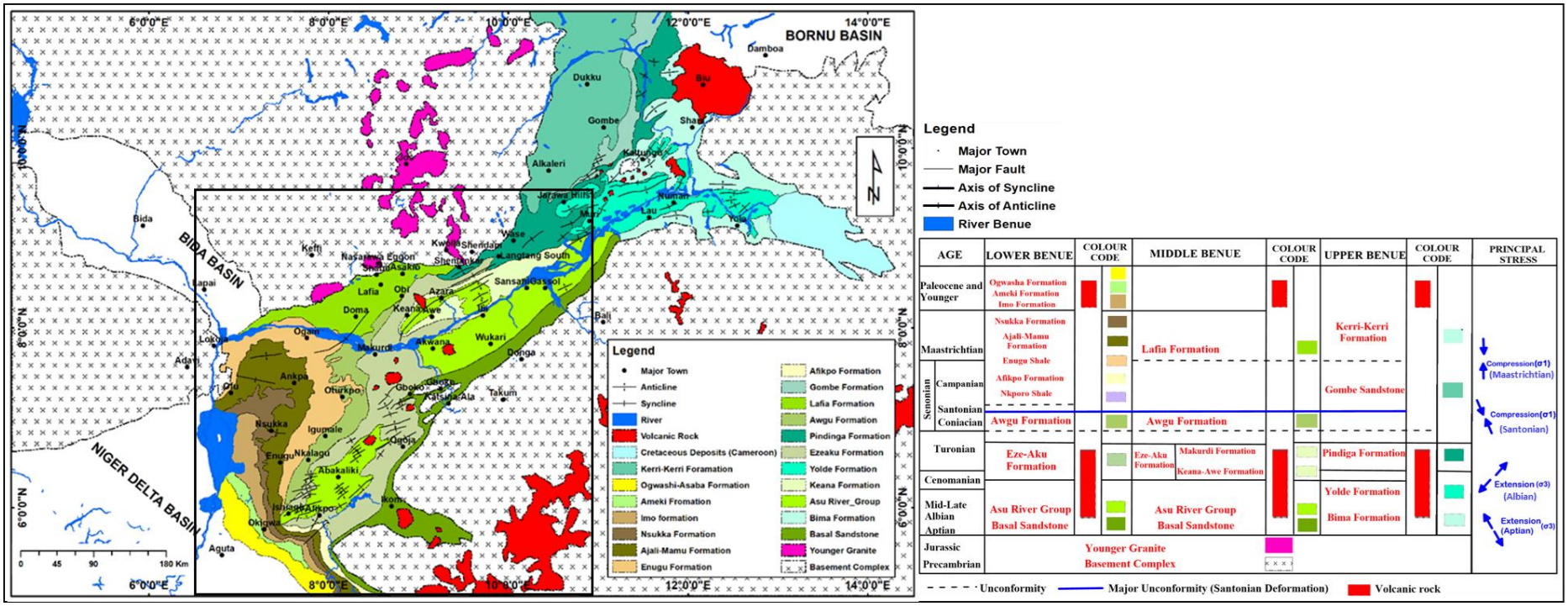

Fig. 1. 4: A generalized geology of Benue Trough with a simplified stratigraphic succession. The spatial distribution of intrusive rocks (volcanic rocks, dykes, and plugs) is also shown. The four (4) major principal stresses that affected the area over time have been identified. The Upper Benue Trough (North) is bordered by the Bornu Basin while the Lower Benue Trough is by the Niger Delta Basin (South) (modified after Olade, 1975; Guiraud et al., 1989; Najime, 2011).

1.5 Background for rifting hypotheses for the Benue Trough

The debate about the evolution of the Benue Trough due to either mantle plume-related or plate tectonic rifting hypotheses has been on for many years without definitive and tangible agreement. However, this study will apply the knowledge gained from remote sensing, gravity, and magnetic data sets analyses to attempt to highlight and give a more robust explanation to the evolution of the Benue Trough. Many authors concluded that the Benue Trough originated from a series of repeated tectonic activities (Nwachukwu, 1972; Wright, 1976; Fitton, 1980; Fairhead and Okereke, 1987; Benkhelil, 1989; Fairhead and Green, 1989; Binks and Fairhead, 1992; Fairhead *et al.*, 2013; Abubakar, 2014) but failed to agree on one best evolutionary model. Several tectonic models have been put forward over the years to explain the processes that led to the development of the trough and two models have been identified to be relevant to this study, the mantle plume related, and the plate tectonic rifting models. The mantle plume model suggests that rifting was due to the rise of a mantle plume beneath the lithosphere (Olade, 1975) while the plate tectonic rifting model believes that plate movement caused lithospheric stretching leading to rifting (McKenzie, 1978). Ofoegbu (1984) suggested that a combination of the two models has been responsible for the evolution of the basin.

The hypothesis that the mantle plumes rise from the base channel near the core-mantle boundary and discharge into the low-viscous asthenosphere with the lithosphere moving over the plume creating a hot spot track is believed to be responsible for rifting in many basins (Sleep, 1990; Bourgeois et al., 2005; Hoyer et al., 2022; Fig. 1.5). Its geometry consists of narrow vertical pipe that supplies hot mantle materials to the lithosphere. Darros de Matos (2021) posited that based on the progressive distribution of magmatic events, multiple plume systems have been recognized to have caused Cretaceous South Atlantic rifting. He gave evidence and demonstrated the trails of these plume heads on continental crust causing rifting. Wilson (1992) and Renne et al. (1992) believed that the initial stages of rifting between Africa and South America as well as the opening of the South Atlantic Ocean are related to superplume tectonic activities. In fact, they agreed that two main mantle plumes of contrasting characteristics i.e., St. Helena and Tristan da Cunha exerted a fundamental control on the process of continental break-up at those points. The Trista da Cunha plume is believe to later give rise to the Mesozoic Parana volcanism in Brazil (Renne et al., 1992) while St. Helena volcanism resulted in the formation of the Benue Trough (Coulon et al., 1996). The hypothesis that the Benue trough evolved from the mantle-plume related activities has been supported by

many workers (Olade, 1975; Fitton, 1980; Coulon et al., 1996; Shemang et al., 2001). Olade (1975) posited that the Benue Trough evolved from doming and rifting associated with the rise and cessation of a mantle plume. His model appears to be the most accepted for the mantle-plume related hypotheses as it seems to address most of the issues with this hypothesis such as the presence of magmatic material, sedimentary thickness, uplift and subsidence, and the geometry of the basin. Fitton (1980) observed a similarity in shape between the Benue trough and the volcanic Cameroon line suggesting that both are related to a common "Y"-shaped hot zone origin in the asthenosphere over which the African plate has drifted and as such could have formed from mantle-plume rising at the centre of the shape. The magmatism of the Cameroon line is believed to have replaced the Mesozoic to early Cenozoic magmatism of the Benue trough (Coulon et al., 1996). Shemang et al., (2001) recently modelled the presence of large and continuous bodies of mafic rocks within the Benue Trough and suggested that it is an old rift formed by mantle-plume related activities.

The plate tectonic rift hypothesis involves the formation of rifted sedimentary basin by plate movements, stretching, and gradual cooling of the lower part of the plate (McKenzie, 1978). The opening of the South Atlantic initiated by the separation of Africa and South America plates and/or the relative movements of African sub-plates are believed to be the major tectonic activities that led to the formation of the Benue Trough (Benkhelil, 1989; Fairhead and Green, 1989; Fairhead and Binks, 1991; Binks and Fairhead, 1992; Fairhead et al., 2013; Fig. 1.6). Benkhelil (1989) supported the plate tectonic hypothesis for evolution of the Benue Trough based on sinistral wrenching of the continental plates that occurred during the early stages of the opening of the Gulf of Guinea. Fairhead and Green (1989) noted that regional plate tectonic processes and more localized mechanical anisotropy processes within the African lithosphere have influenced rifting leading to the formation of the rift basins. The formation of this rift system was formed contemporaneously with the early opening of the South Atlantic during the period of plate motion changes (Fairhead and Binks, 1991; Binks and Fairhead, 1992). Fairhead et al. (2013) recently gave that the evolution of the Benue Trough is linked to relative movements of African plates and sub-plates and to global plate tectonic processes and plate interactions.

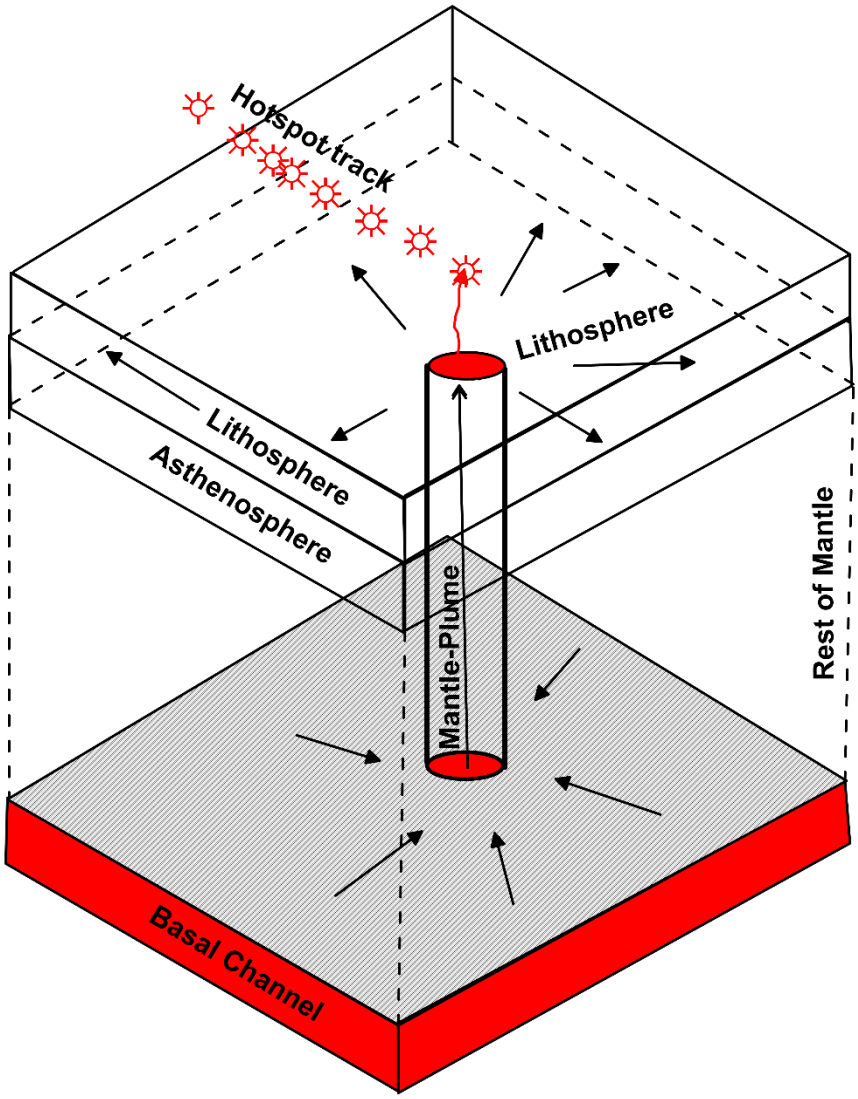

Fig. 1. 5: Mantle plumes tapping magma materials near the core-mantle boundary and discharged into the asthenosphere through the vertical pipe-like plume. The lithosphere moves over the plume creating a hotspot track (Sleep, 1990).

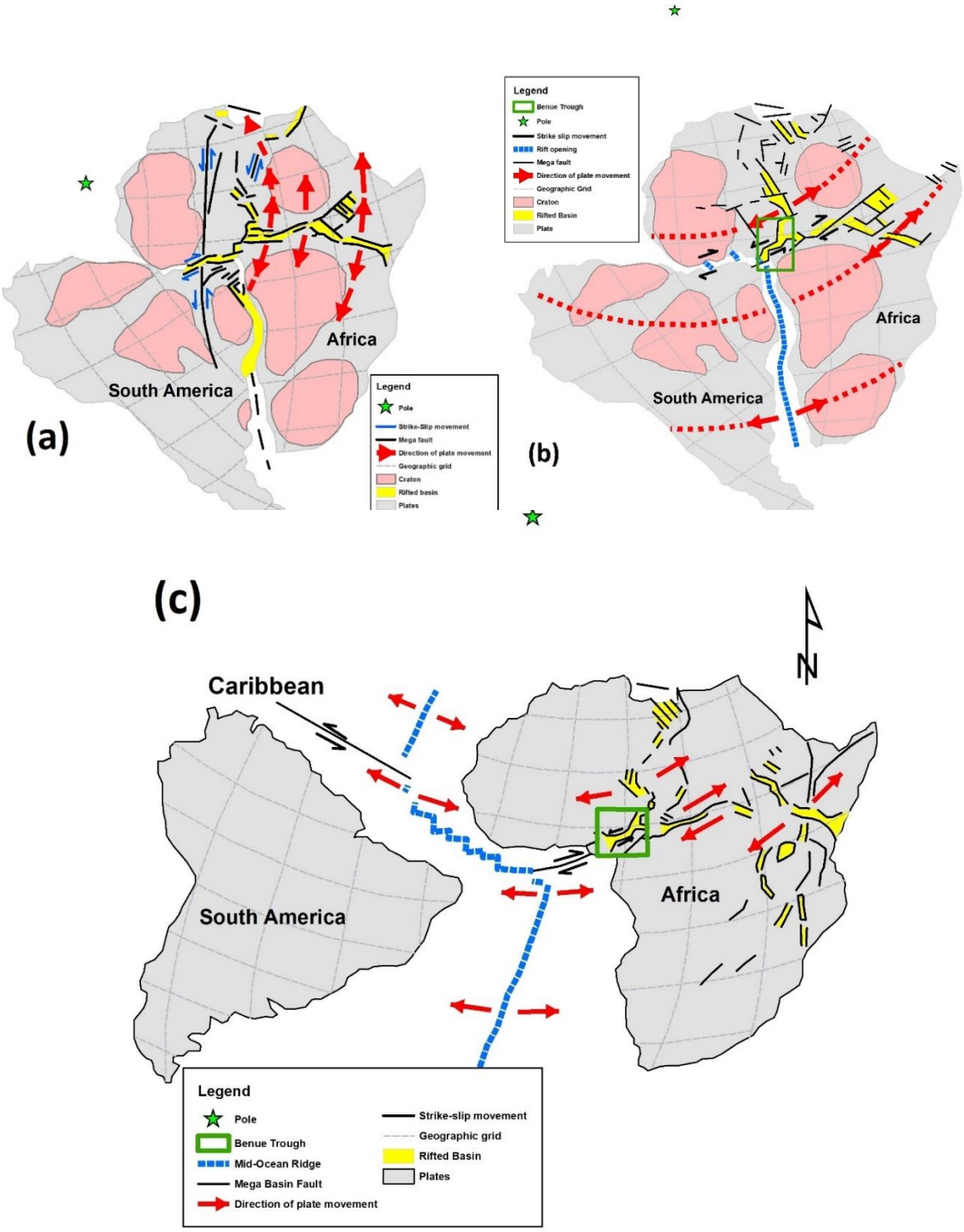

Fig. 1. 6: Plate tectonic model for the development of the Benue Trough (a) During the Barremian (127Ma) (b) During the Albian (105 Ma) (c) showing the complete formation of the Benue Trough at the end of Cretaceous time from the opening of the Central Equatorial and South Atlantic Oceans (Fairhead and Green, 1989; Fairhead et al., 2013).

1.5.1 Tectonic evolution models of the Benue Trough

1.5.1.1 Mantle plume upwelling model

Olade (1975) proposed the tectonic model involving the rising and the relaxation of mantle plumes with resulting patterns of doming, rifting, magmatism, and sedimentation. This he concluded started during the Aptian to Early Albian times when there was mantle upwelling underneath the Niger Delta resulting in doming and rifting, and the development of the rift-rift-rift (RRR) triple plate junction involving the Benue Trough, South Atlantic, and the Equatorial Atlantic (Fig. 1.7 a). There was also the emplacement of felsic and mafic magma material. Rifting continued with the deposition of sediments within the rapidly subsiding depression due to thermal relaxation to Middle Albian (Fig. 1.7 b). During Cenomanian times, there was a cessation of mantle upwelling to create crustal contraction and compressive folding of the sediments because of mantle deepening (Fig. 1.7 c). This implies that folding of the sediments was passive caused simply by the cessation of rifting. However, this may not be feasible as it is not possible for a non-geodynamic model to cause such folding as experienced within the Benue Trough. However, mantle upwelling resumed during Turonian times where earlier normal faults were reactivated and blocks uplifted (Fig. 1.7 d). But, during the Senonian (Santonian), there was a migration of the mantle plume eastwards away from the trough and this produced crustal contraction and the collapse of the trough. Also, there was widespread compressive deformation affecting all Pre-Santonian rocks to form folds, faults, sub-basins, etc. (Fig. 1.7 e). This aspect of the mantle plume model is controversial in the sense that crustal contraction has been recorded to be as a result of far-field compressional stresses causing a significant change in the poles of the opening of the North Atlantic that swept across the entire African plate leading to folding of the older sediments (Bosworth et al., 1999).

Ofoegbu (1984) agreed with the tectonic model above but added that a sequence of events above possibly occurred in a repeated cycle of activities. He also observed that the large stresses resulting from the domal uplift can only produce 200 m subsidence - far less than what is estimated for the Benue Trough. He also argued that the addition of some dyke-like bodies within the crust because of the mantle doming for the model could fully explain the evolution of the Benue Trough. However, doming of the mantle alone cannot provide sufficient energy to intrude the crust but doming is easier when the crust is stretched allowing mantle materials doming as well as igneous rock emplacement (Fairhead et al., 2013).

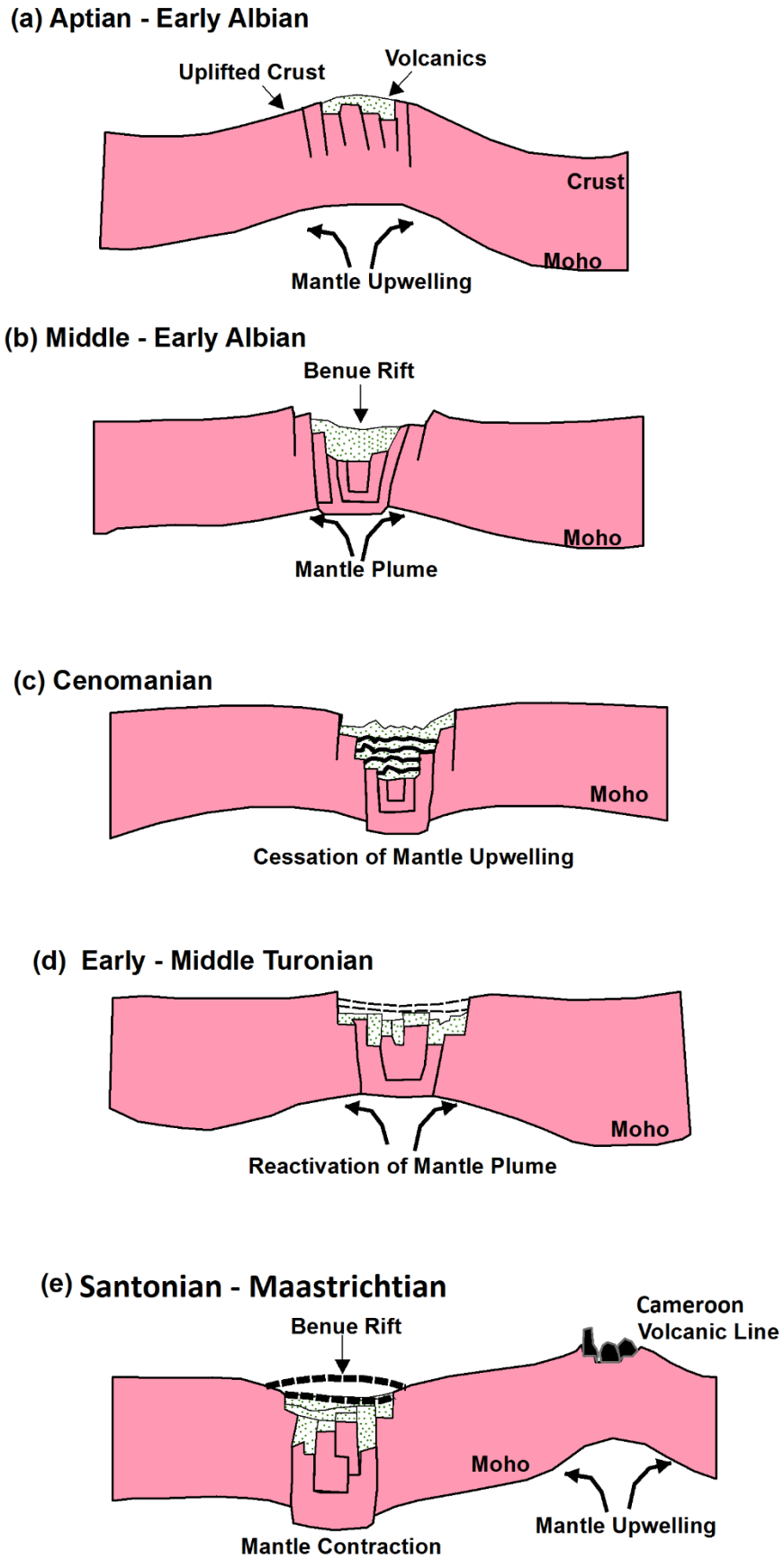

Fig. 1. 7: Tectonic evolution of the Benue Trough (Modified after Olade, 1975).

1.5.1.2 Plate tectonic rifting model

McKenzie (1978) proposed a simple plate/lithospheric extension model for the development and evolution of basins (Fig. 1.8). He stated that the process involves stretching of continental lithosphere leading to block faulting, the rise of hot mantle materials, and subsidence. This is followed by lithospheric thickening through cooling by heat conduction to the surface, which causes further continued thermal subsidence without active faulting. The basin continues to subside, and the lithosphere is not stretched although its depth still increases significantly. This thermal subsidence is due to the gradual cooling and contraction of mantle rocks over a long period of time. The downward movement of the lithosphere-asthenosphere boundary (LAB) is agreed to be partly due to subsidence (which is downward movement) and partly change of phase due to cooling. Fairhead and Green (1989) and Fairhead et al. (2013) accepted the McKenzie model in the development of the Benue Trough. They agreed that the basin evolution was initiated during the opening of the South Atlantic in the Early Cretaceous (Albian - 105 Ma) and internal African plate deformation or interaction (Barremian - 127 Ma) (Fig. 1.6). The process of rifting continued leading to the formation of the Benue Trough with a sinistral strike-slip movement. The rate of subsidence decreased, hence, there was thermal relaxation by the Cenomanian-Turonian (100 – 85 Ma) which closely followed expectations based on the McKenzie model. During the Santonian, there was a change in the regional stress field that resulted in basin inversion that involved basin uplift, folding, and subsidence through reactivation of old basin normal faults. This age marked the end of the rift basin development. However, minor rifting continued from the Eocene through to the Recent thereby shaping the basin geometry (Ofoegbu, 1985a; Fairhead et al., 2013).

1.5.1.3 Relationship between the tectonic models

Generally, it can be deduced from the two tectonic models that both elucidated the crucial fact that the evolution of the basin involved a series of events that included rifting, the rise of a mantle plume, emplacement of igneous rocks, crustal stretching, and thinning. These events can be repeated in a cyclic manner with structural deformation occurring during any two cycles. The sequence of these events that lead to the final architecture of the Benue Trough is what is debatable and controversial. The findings from this study based on the analyses and interpretations of satellite remote sensing, gravity and magnetics will attempt to elaborate on the two tectonic models discussed and propose the best model that will explain the evolution of the trough and try to give a possible sequence of events based on structural models.

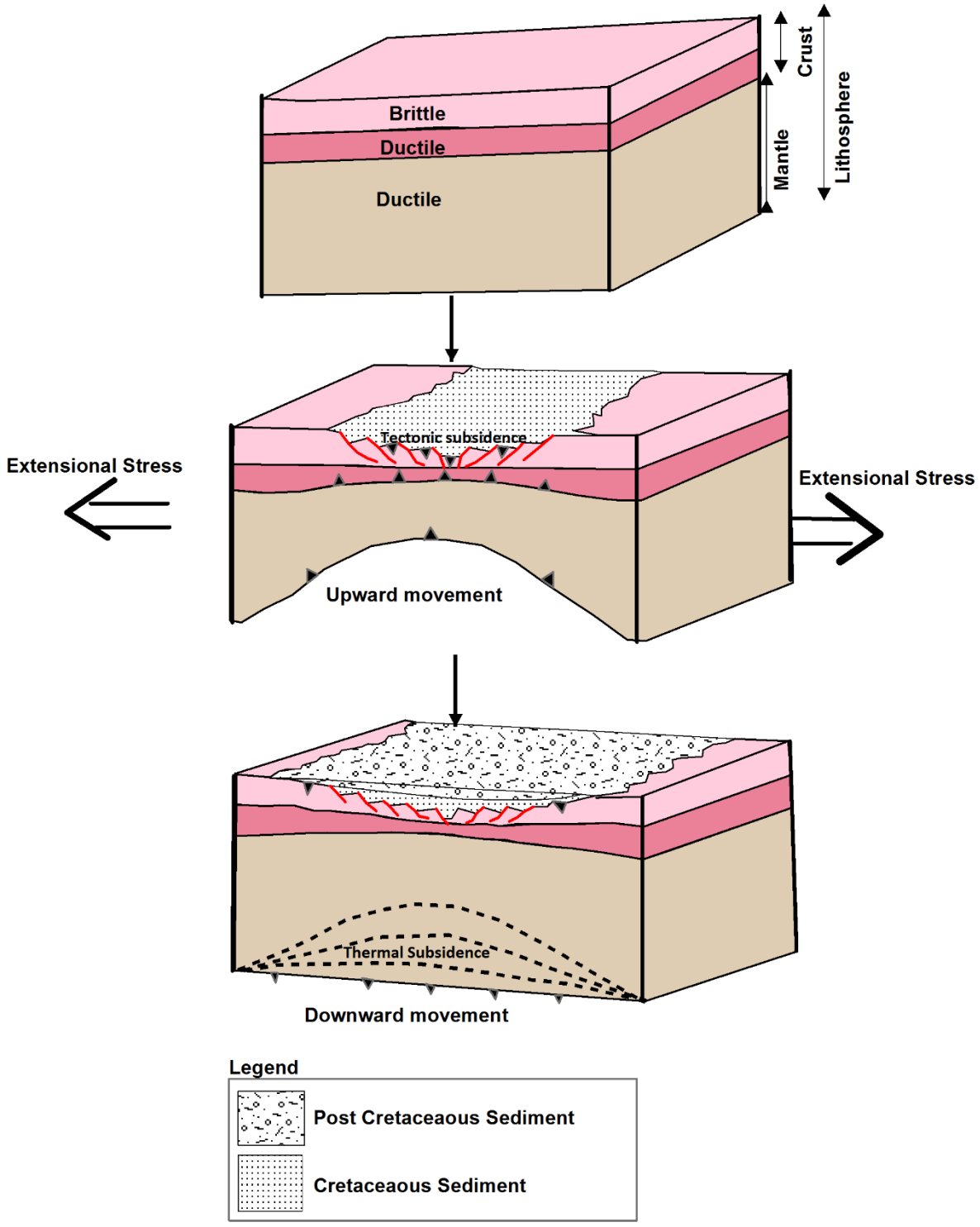

Fig. 1. 8: Simple lithospheric extension model for the development of a basin (McKenzie, 1978).

1.6 Geophysical studies of the Benue Trough

Seismic, gravity, and magnetic methods form the most used geophysical methods in basin structural analyses. Seismological investigations have few references and no available data sets within the area. Stuart et al. (1985) recorded the refractions and reflections from quarry blasts for crustal structure study of part of the Benue trough (Yola arm) and concluded that the crust is thinned to about 23 km thick. Akpan et al. (2016) used P-wave receiver functions from eleven seismological stations and estimated the thickness of the crust beneath the Benue Trough also to be 23 km. However, results obtained from the use of gravity and magnetic techniques form the main background that led to the understanding of its structural framework.

1.6.1 Gravity study

Ground gravity surveys have been carried out to investigate the Benue Trough and understand the mode of formation, evolutionary pattern, nature of geologic structures and features, etc. (Cratchley and Jones, 1965; Ajakaiye, 1975; Adighije, 1978; Okereke, 1984). A compilation of the ground gravity survey shows the good data coverage of the Benue Trough has been achieved over the years (Fig. 1.9). Many authors reported a general central positive anomaly flanked by negative anomalies at the margins of the trough (Cratchley and Jones, 1965; Ajayi, 1979; Adighije, 1981a; Adighije, 1981b; Ajayi and Ajakaiye, 1981). They attributed the positive anomalies at the centre to the shallow granitic basement and/or igneous intrusion and uplift of the Moho, while the negative anomalies were associated with thick deposits of sediments. Adighije, (1981b) observed that the broad positive gravity anomaly is due to the uplift of the Moho interface while the axial negative anomaly is due to the infill of sedimentary and post deformational sediments. Also, Fairhead and Okereke (1987) defined the positive anomaly to have a high amplitude value of 90 mGal and with a broad wavelength of 400 km correlating well with the topographic expression of the trough while the sedimentary infill is associated with short wavelength negative anomalies. An interpretation of extensional rifting is supported by gravity evidence of crustal thinning beneath the trough (Scheidegger and Ajakaiye, 1985; Fairhead and Okereke, 1987). The crustal structure and the Moho interface of the Benue Trough have been studied extensively using gravity data (Adighije, 1981b; Fairhead and Okereke, 1990; Fairhead et al., 1991; Okiwelu et al., 2009; Ugbor and Okeke, 2010; Obasi et al., 2018; Mukaila et al., 2019). However, deep structural analyses such as 3D spatial distribution of the Moho, crustal structure, and the long-term strength of the lithosphere, etc. have not been well studied and this research will attempt to study them.

1.6.2 Magnetic study

Earlier aeromagnetic data sets for the Benue Trough were acquired in 1965 surveyed along E-W profiles with about 2 km spacing, tie-line spacing of 20 km, and a mean flight elevation of 200 m above the surface (Ofoegbu, 1982; Ajakaiye et al., 1991; Ofoegbu and Onuoha, 1991). This low-resolution magnetic dataset covering the trough was usually provided in the form of a contour map of scale 1:100, 000. Another magnetic dataset was generated from digitizing contour maps of earlier surveys as part of the African Magnetic Mapping Project (AMMP) from 1989 to 1992 (Fairhead et al., 1997; Esuene, 2012). The data measures a 1 x 1-degree grid sheet (1:250, 000 scales) at 150 m mean terrain clearance, 2 km flight line spacing, with NNW-SSE survey flight line direction and varying tie line spacings between 10 km and 20 km (Esuene, 2012), in which the resolution is also low for detailed study. Fugro Airborne Surveys recently acquired high-resolution aeromagnetic data on behalf of the Nigerian Geological Survey Agency (NGSA) covering the Benue Trough between 2003 and 2009 (Fig. 1.10). The survey employed 3 x Scintrex CS3 Cesium Vapour magnetometers that were flown along a series of NW-SE (135°) flight lines perpendicular to the general regional structural trend. A tie line trend and spacing of 45 degrees and 5 000 metres were used, respectively. The data sets with 80 m mean terrain clearance was stored as 1 X 1-degree sheets making the resolution better than earlier available high-altitude data (Reford et al., 2010; Anudu et al., 2014). These are the aeromagnetic data sets used for the research in this thesis.

Many researchers studied various geologic features of the Benue Trough using aeromagnetic data at different times with different data resolutions (Ofoegbu, 1982; Scheidegger and Ajakaiye, 1985; Ofoegbu, 1984; Ofoegbu, 1986; Onwuemesi and Egboka, 1989; Ajakaiye *et al.*, 1991; Ofoegbu and Onuoha, 1991; Abbass and Mallam, 2013; Anudu *et al.*, 2014; Nwosu, 2014; Oha *et al.*, 2016; Ugwu et al., 2018; Abdullahi *et al.*, 2019; Osinowo and Taiwo, 2020) and mostly focussed on small parts of the trough. Low-resolution aeromagnetic data sets have been used to carry out 2D-modelling of intrusive rocks for depths, thickness and magnetization polarity (Ofoegbu, 1982; Ofoegbu, 1984; Ofoegbu, 1985b; Ofoegbu, 1986; Ofoegbu and Onuoha, 1991). High-resolution aeromagnetic data have also been used over the years to delineate several near-surface geologic features and structures within different parts of the trough and general NE-SW, NW-SE, and ESE-WNW with minor ENE-WSW and N-S structural trends have been observed (Anudu et al., 2014; Oha et al., 2016; Abdullahi et al., 2019). It has also been employed to estimate the depth to the magnetic basement so as to know

sedimentary thickness (Abbass and Mallam, 2013; Nwosu, 2014; Oha et al., 2016; Ugwu et al., 2018; Abdullahi, et al., 2019a; Abdullahi, et al., 2019b; Anudu et al., 2020). Osinowo and Taiwo (2020) recently analysed the high-resolution aeromagnetic data of lower Benue Trough and delineated areas with basement in more than 3 km depth to be suitable for the generation of oil and gas. In all the depth estimates above, the authors did not consider the influences of volcanic rocks, vertical limit to anomalous sources, and the effect of gridding techniques, of all which may lead to depth underestimation and basement framework misrepresentation.

Aeromagnetic data sets of the Benue Trough have not been fully utilized in understanding the subsurface structures of the area. In this research, an expanded application and interpretation of the high resolution aeromagnetic from 2- and 3-D magnetic models, finite depth and inversion estimation techniques, Curie depths, etc., will be used to obtain a more robust result and interpretation strategy for the trough.

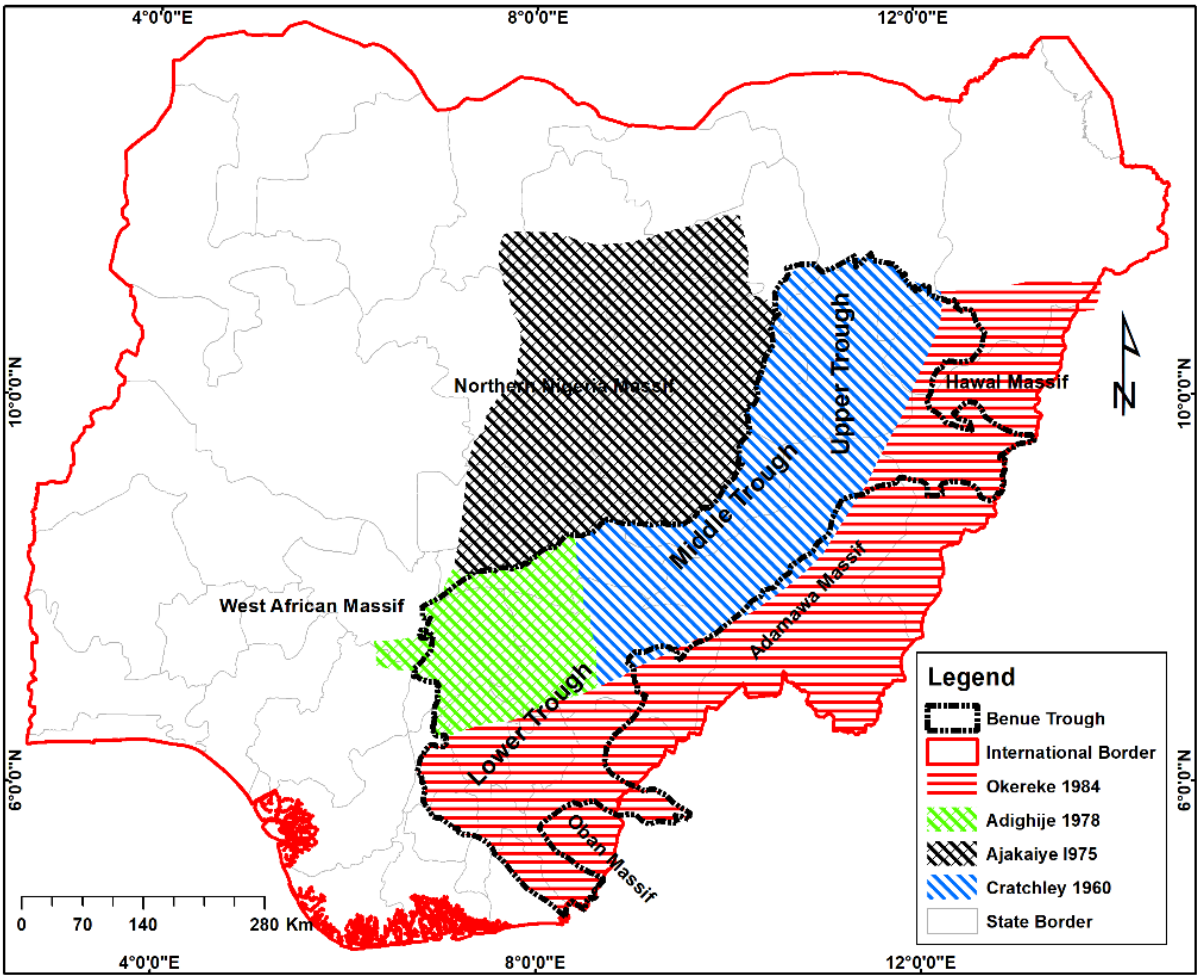

Fig. 1. 9: Gravity data covering the Benue Trough. The data collected in different years overlap to cover the area.

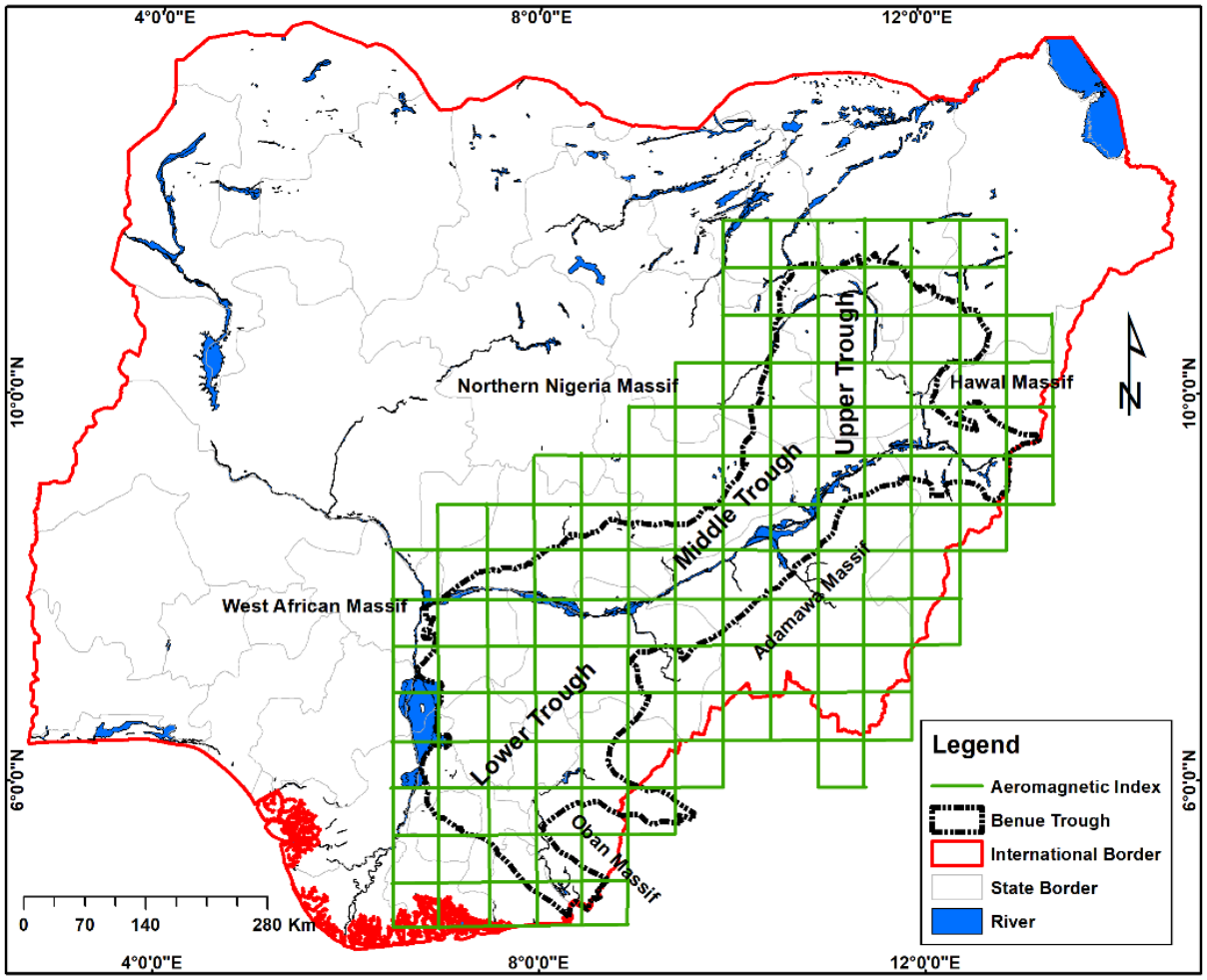

Fig. 1. 10: Aeromagnetic data covering the Benue Trough. The data coverage spans 100 km x 100 km for each square.

1.7 Remote sensing of the Benue Trough

Remote sensing techniques provide the means to map the spatial distributions of large geological features/structures on the surface of the earth, which may not be recognized by other small-scale exploration methods. There are very few detailed works involving the application of remote sensing in the Benue Trough. Chukwu-Ike (1977) used Landsat 1 and 2 images to extensively map and interpret en-echelon lineaments, shear, and fractures zones within the Benue Trough. He identified three significant structural trends (N-S, NE-SW, and NW-SE) that are associated with the basement structural fabrics. Others employed remote sensing to effectively study and interpret regional scale geology, features, and structure in the Benue Trough (Nkono et al., 2009; Jatau and Abu, 2013; Ogunmola et al., 2014; Omo-Irabor et al., 2014; Ogunmola et al., 2016). Major tectonic events interpreted from remote sensing mapping techniques have have proved to be influential in mineral and oil resource distribution (Boud, 1987). The presence of vegetation and the resolution of the data play key roles in achieving good results. Abubakar et al. (2018) employed Advanced Spaceborne Thermal Emission and Reflection Radiometer (ASTER) and Hyperion data to map hydrothermal alteration zones related to geothermal systems in the Upper part of the trough. This study combines several multispectral data sets (ASTER, Landsat 8, Shuttle Radar Topographic Mission -SRTM, etc.) for lithology and structural mapping with the aim of updating the existing geology map of the area.

1.8 Rationale for the Research

There are several motivations that prompted this research on the structural modelling. The study is of great interest to structural, geological, and resource explorations. The availability of quality remote sensing, gravity, and magnetic data sets covering the area make the research unique and suitable for building more robust structural models to understand the subsurface processes that led to the development of the trough. These subsurface processes to a very large extent control the geometry, accumulation pattern, and resource potential of the area.

The recent discovery of commercial accumulations of hydrocarbon in intracontinental rift zones in the republic of Sudan and Chad, which have comparable structural and stratigraphical characteristics with the Benue Trough, is another motivation that led to the development of this work (Obaje et al., 2004; Akande et al., 2012; Habib and Xie, 2012). The Doba basin South-West Chad, the Muglad Basin in Sudan, and the Benue Trough in Nigeria all lie within the

Central African Rift System (CARS) and West African Rift System (WARS) with related evolution history (Fig. 1.11). The discoveries of hydrocarbons in the Benue Trough's neighbouring inland basins, with their similar geological and structural settings serve as a boost to encourage this study.

Exploration for hydrocarbon in the Benue Trough is still in its early stages but three and one exploratory wells were drilled in the Upper and Lower (Anambra Basin) Parts of the Benue Trough, respectively. Nigeria Exploration and Production Company (SNEPCo) drilled the Kolmani River-1 well to a depth of 3 km in 1999 and discovered about 935 million m^3 of gas with an unspecified amount of oil (Obaje et al., 2004; Obaje, 2009) while in 1999, Elf Petroleum Nigeria Limited (TotalFinaElf) drilled the Kuzari-1 well to a depth of 1.7 km and reported dry oil and gas. Also, Chevron Nigeria Limited (ChevronTexaco) reported a dry well at Nasara-1, which was drilled to a depth of 1.5 km in 2000 (Obaje, 2009). In 2012, Orient oil petroleum resources plc. discovered commercial quantities of hydrocarbons in the Lower Benue Trough (Anambra Basin) (Habib and Xie, 2012). The Middle part of the trough has been inadequately studied due to its very difficult terrain, unknown geology, and the over-dependence on the prolific fields in the Niger Delta basin. These interesting preliminary findings prompted the need to further study the structural features that may likely be responsible for the accumulation of hydrocarbons in the Middle and Lower Benue Trough.

There is evidence of a mega structural link between oceanic fracture zones (Chain and Charcot fracture zones) and the continental West and Central African Rift System (WCARS) through the Benue Trough to the Nile Delta in North Africa (Wright, 1985). Gravity and magnetic data imaged this transcontinental megastructure entering the Benue Trough at the southwestern end, beneath the thick sediments of the Niger Delta (Fairhead et al., 2013; Figs. 1.3 and 1.12). It is agreed to have controlled significantly the deep-seated oil-bearing structures in the Niger delta and the neighbouring Benue Trough (Zbořil et al., 1986; Wu et al., 2015). This structure is covered within the Cretaceous sedimentary strata and deeply seated within the crust (Ajayi and Ajakaiye, 1981; Benkhelil, 1989; Fairhead et al., 2013). It is difficult to establish the relationship between basement fabric most especially as it might have been covered extensively by Tertiary to Recent sediments, but the architecture of the trough is observed to have been influenced by the activities of the Atlantic Ocean fractures triggering crustal deformation (Fairhead and Green, 1989). This study, therefore, seeks to find out, model, and characterize the geometry of the structures at all depths.

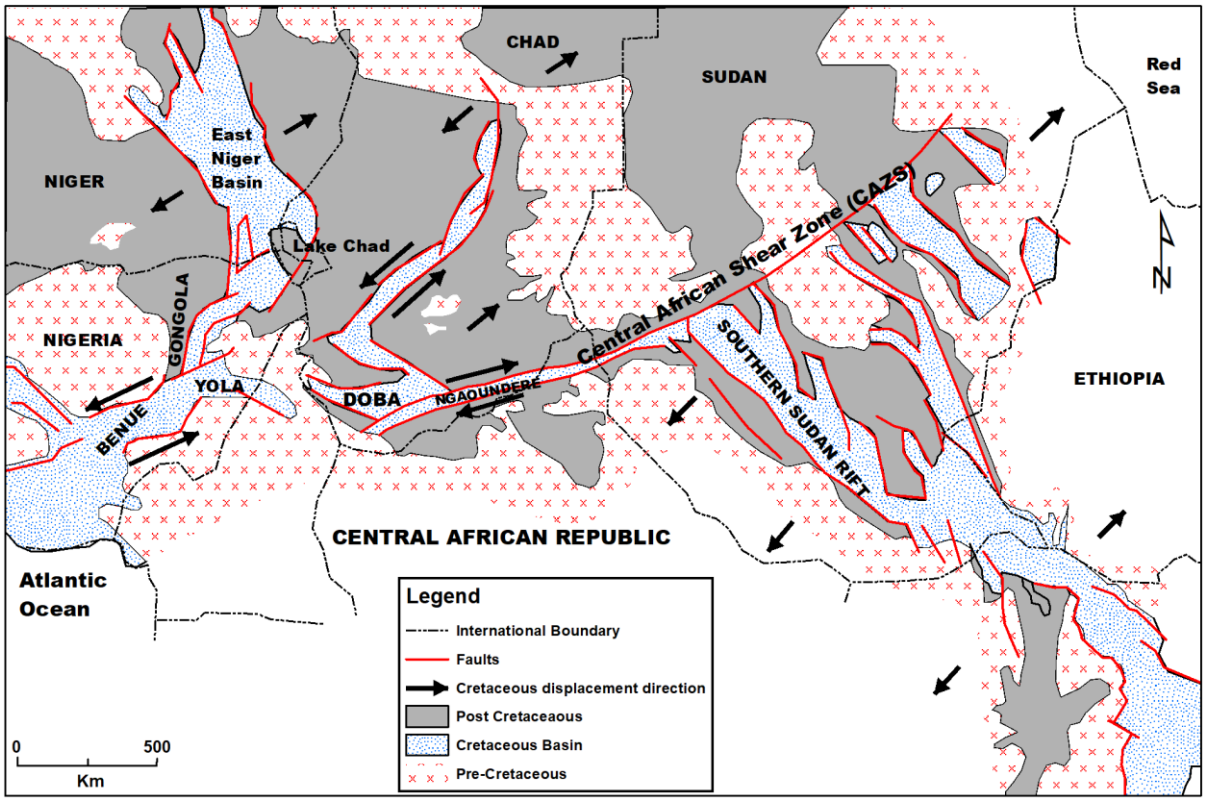

Fig. 1. 11: Regional tectonic map of the Western and Central African rift system showing the relationship of the Benue Trough with Chad and the Sudan Republic Basins (Modified after Fairhead and Binks, 1991; Obaje, 2009).

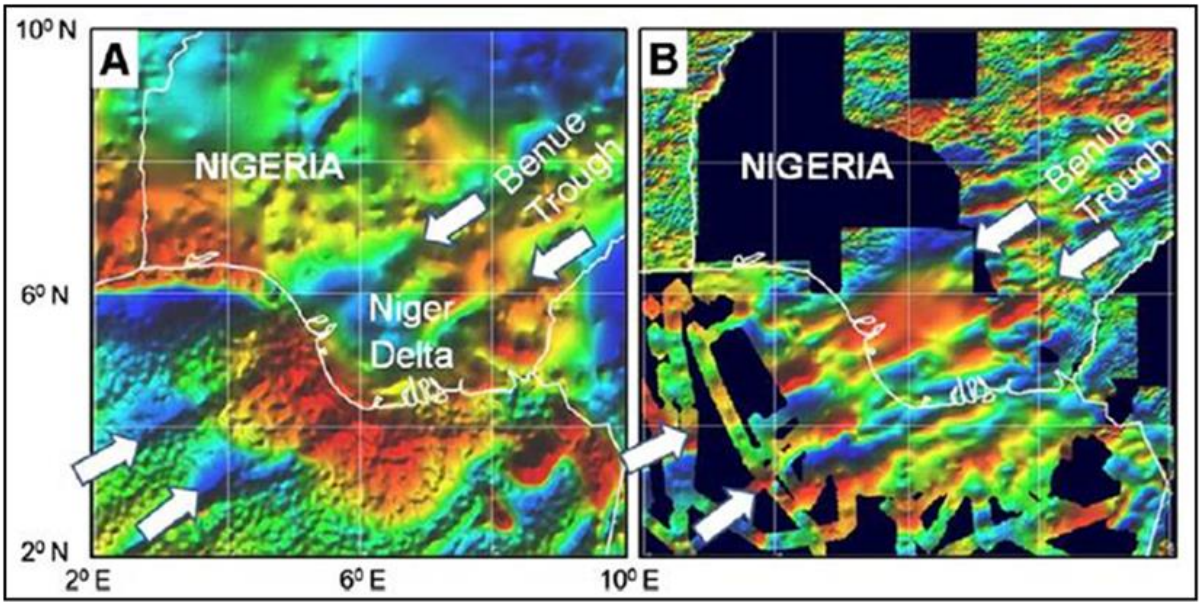

Fig. 1. 12: (a) Gravity field (b) Total magnetic intensity (TMI) field. White arrows indicate the trend of oceanic fractures i.e., the presence of Chain and Charcot fractures beneath the Niger Delta at the base of the Benue Trough (Fairhead et al., 2013).

1.9 Aim and Objectives

To date, there has been no integrated application of high-resolution aeromagnetic data, gravity, and remote sensing data for the study of Middle and Lower Benue Trough. Recent studies only show the application of low-resolution data sets and/or one geophysical data set in limited parts of the basin leading to inadequate investigation of the trough. It is a good opportunity to apply an integrated approach to obtain surface and subsurface structural information, which is significant in understanding the tectonic evolution of the basin and its relationship with resource occurrences. Therefore, the research is aimed at understanding the tectonic and non-tectonic development framework of the trough through modelling of surface and subsurface structures using combined gravity/magnetics and remote sensing techniques.

The following objectives will assist in achieving the above aim.

i. Apply multispectral analysis to construct and update a geological map and combine gravity/magnetic data sets with the multispectral images to map surface and near-surface geological bodies and lineaments.
ii. Delineate deeper structures by mapping basement lineaments and estimating the depth to the basement for basement morphology/geometry studies. Analysing tectonic lineaments for interpreting tectonic models of the area.
iii. 2- and 3-Dimensional modelling of the trough from gravity and magnetic data sets to understand the various processes involved in crustal structural architectures, rate/amount of extension, amount of heat, etc.
iv. Use spectral modelling methods to estimate the effective elastic thickness of the lithosphere as a proxy for determining the long-term strength of the lithosphere and infer the influence of thermal structure on the lithosphere strength.
v. Understand the tectonic framework and its significance in defining the evolution pattern of the trough as well as its effect.

1.10 Thesis Summary

This research is organized as follows and describes the various contents of each chapter.

Chapter one (1), which is this chapter, is the general introduction chapter that summarizes the literature background for the study, the geography, the geological settings, the stratigraphy, and structural settings as well as tectonic evolution models of the Benue Trough. Remote

sensing, gravity, and magnetic data sets available for the study and previous works done are discussed. The chapter ends with a statement for the main aim of the study and the objectives to achieve them and a summary of the structure of the thesis.

Chapter two (2) describes process of suppressing the effect of vegetation and enhancing multispectral data sets for lithology mapping. It also re-assessed published geology maps and compare with the lithology map. The techniques for processing and analysing remote sensing data sets are well discussed. The chapter discusses the processes of mapping surface lineaments from SRTM and Landsat data sets. The result at the end of the chapter are maps of geology and lineaments obtained from multispectral data sets.

Chapter three (3) describe procedures for processing both gravity and magnetic data sets especially the techniques for analysing magnetic data sets at or near the magnetic equator i.e., reduction to the equator and reduction to the pole. The chapter also discusses the processes of residual-regional separation of gravity and magnetic data sets and mapping of near-surface lineaments and geological bodies.

Chapter four (4) begins with the description of uncertainties involved in surface/shallow lineaments extraction and the processes of isolating tectonic-related lineaments from non-tectonic and non-linear geological bodies. The result at the end of the chapter is an updated geological and structural map of the Lower and Middle Benue Trough based on remote sensing, gravity, and magnetic data sets.

Chapter five (5) presents method for mapping and modelling deep structures of the trough in 2- and 3-dimensions. The techniques for basement lineament mapping and basement depth estimates are discussed. It also involves discussions on the uncertainties associated with deep lineament extraction, the nature of the lineaments and geological bodies, and the technique involved in the separation of tectonic and non-tectonic lineaments. Basement and Moho depths are calculated using 2D gravity/magnetic models across four profiles. This chapter also investigates and models 3-D density and magnetic susceptibility structures of the area. It concludes by examining the crustal structure, the amount of crustal extension, and the rate of extension estimated in terms of stretching factor.

Chapter six (6) introduces isostasy and the methods for estimating the effective elastic thickness of the lithosphere, which is a proxy for understanding the long-term strength of the lithosphere as it affects the trough. It also presents the methods involved in the calculation of

Curie depth, geothermal gradient, and heat flow. The chapter compares the results of (spectral and 3D inversion) methods for estimating Curie depth and finally relates the Curie depth points and the heat flow estimated using it with the strength of the lithosphere as it affects the trough's isostasy equilibrium.

Chapter seven (7) discusses the relationship between geologic lineaments (faults and dykes) and stress fields in understanding and predicting the evolutionary pattern of the basin and predicting the sources of magmatic intrusions. The chapter then tries to express the time span of rifting and the amount of heat energy needed to cause melting. The basin tectonic model based on fault kinematics and its relationship with magmatic emplacement is studied. The chapter then combines all results and proposes a tectonic model which is presented in plan-view and in 2D depth slices. Finally, the implication of hydrocarbons to the study is discussed.

Chapter eight (8) summarizes the main points obtained from previous chapters and give main conclusions from the study as well as recommendations suggested for future work.

CHAPTER TWO

REMOTE SENSING DATA SETS AND METHODS

2.1 Introduction

The area of study is part of the Benue Trough comprising of the Lower and Middle Benue Trough. This chapter focuses on the processes of mapping lithology and delineating surface lineaments from remote sensing data sets. The main targets are to update the knowledge of the existing geology map of the area using satellite remote sensing interpretations and map out the structures necessary to understand the tectonic processes that led to the current basin morphology. The data sets used for the study are ASTER, SRTM, Landsat 8.

The first stage presents methods of mapping lithology to infer the geology of the area. This process involved applying and finding solutions to the main problem of the vegetation cover by the application of vegetation suppression technique. Colour composite, spectral band ratio and principal component analyses (PCA) techniques were used to enhance signals of diagnostic minerals related to geology. Spectral angle mapping (SAM) was used to classify the various lithologies and their boundaries were manually traced for geological map construction. Then, a new geological map based on existing maps and remote sensing interpretation was generated.

The second step in this chapter presents the procedure for mapping surface geological lineaments. Directional and non-directional filters were applied to SRTM and Landsat 8 data sets to enhance their spectral differences for better lineament extraction and surface lineament interpretation.

Finally, an updated geo-structural map of the area is presented with the lineament orientations used in analysing and understanding the trough. This chapter gives a clearer preliminary understanding and provides a basis for deep structural mapping in subsequent chapters.

2.1.1 Remote sensing background and methods

Remote sensing is the science of acquiring, processing, and interpreting images and data sets from a distance that measure the interaction between matter and electromagnetic energy (Sabins, 1999). The principle of remote sensing depends on the measurement of EM energy. The source of EM energy at the surface of the Earth is the sun, however, all matter with a temperature above absolute zero (greater than 0 K) may radiate EM energy due to the movement of the molecules (Bakker et al., 2004). Sensors measure reflected sunlight, or the

amount of energy emitted by the earth's materials modelled in the form of either waves or particles called photons.

In the wave model, EM is characterized by the equation

$$\boldsymbol{c = v \times \lambda} \text{ ……(2. 1)}$$

c is the speed of light (3.0 x 10^8 m/s), v is the frequency (cycles per second, Hz), λ is the wavelength (m).

while the particle model is defined by the amount of energy of photon wavelength as

$$\boldsymbol{Q = h \times v} \text{ ……(2. 2)}$$

where Q is the energy of a photon (J), h is Planck's constant (6.6262 $\times 10^{-34}$ J s), and v is the frequency (Hz).

The total range of wavelengths that is radiated by a material on the earth's surface is called the electromagnetic spectrum (Fig. 2.1) whose characteristics are measured by remote sensors (Richards and Jia, 2006). Remote sensing operates in several regions of the electromagnetic spectrum.

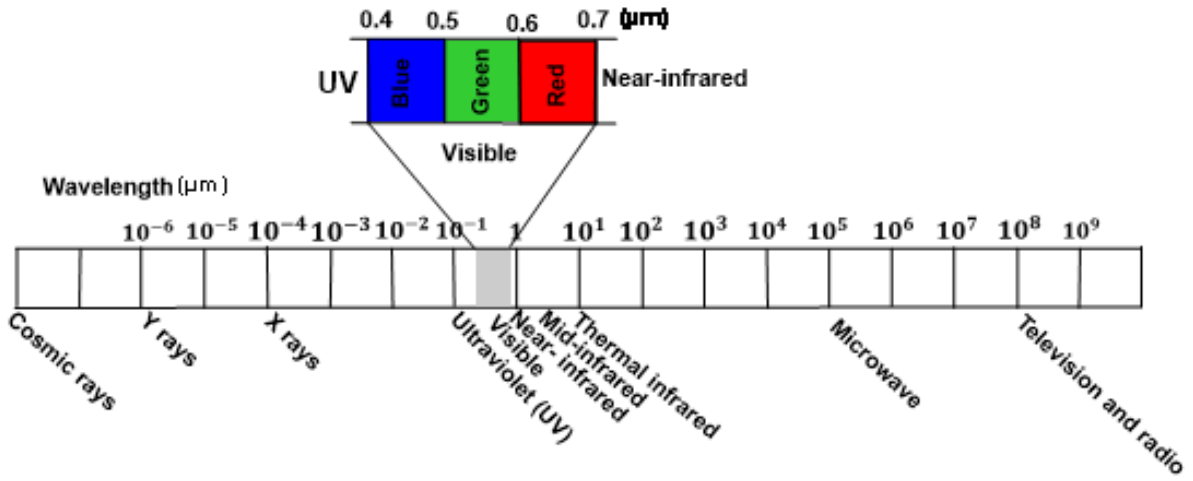

Fig. 2. 1: Electromagnetic spectrum (after Bakker et al., 2004). The visible EM range is what human eyes can capture but remote sensors see beyond this EM bands.

Energy interaction with the Earth's surface due to reflected radiation from the target earth materials gives information about the make-up and characteristics of surface materials (Bakker et al., 2004; Richards and Jia, 2006). The energy that reaches such a surface is called irradiance while the energy reflected by the surface is radiance. The radiance from any specific material is described by the reflectance curve which indicates the fraction of the incident radiation that is reflected as a function of wavelength. These reflectance curves are very specific for different materials. The reflectance curves for materials can be measured in a laboratory or in the field using a field spectrometer or by satellites sensors, and these curves can be compared with typical curves in the spectral libraries. The spectral library is a large stores collection of spectral curves (Kalinowski and Oliver, 2004). The images captured by the sensors are processed and stored in band layers. The wavelengths in these bands are represented in digital number characterized by numerical values of between 0 – 255 values (Yamaguchi and Naito, 2003).

2.2 Data processing of Landsat 8, ASTER and SRTM data sets

The Landsat 8, ASTER and SRTM DEM data sets were downloaded from NASA's LPDAAC choosing imagery with minimal cloud cover. Landsat 8 deploys OLI and TIRS for recording spectral signatures. Each scene acquired is composed of four visible spectral bands, three near/shortwave infrared channels, two thermal bands, and a panchromatic channel (U.S Geological Survey, 2015; Table 2.1). The ASTER scene is made up of three visible and one near-infrared bands, six shortwave infrared bands, and five thermal infrared bands (Table 2.1). While ASTER is downloaded pre-processed i.e. already corrected, calibrated, and registered at-sensor radiance, the Landsat data sets were subjected to atmospheric correction in ENVI software by dark pixel subtraction to remove the effects of atmospheric scattering and additive radiance represented by negative and zero digital numbers, and then pan-sharpened to increase their spatial low resolution of 30 m to high resolution of 15 m using panchromatic band 8 (Crippen and Blom, 2001; Yu et al., 2011). A total of eleven and seventy-eight scenes of Landsat 8 and ASTER data sets, respectively, were individually layer stacked. In each case, a single raster was seamlessly mosaiced, colour balanced with histogram matching, seamlessly feathered for the entire area to smoothen, and colour scale differences were eliminated using ENVI software (Yu et al., 2011) making it suitable for further image analyses. The results covering the area were displayed as colour composites (Fig. 2.2 and 2.3). The processed Landsat and ASTER data sets were employed for mapping geology of the study area. The red and green pixels on the ASTER and Landsat data respectively show the presence and distribution of vegetation cover within the area of study.

The SRTM DEM is a digital elevation model acquired by the Shuttle Radar Topographic Mission sensor with 30 m spatial resolution (1 Arc-Second) and was downloaded with voids filled and pre-processed (Rodríguez et al., 2013). In the study, the SRTM DEM shows high and low elevations with the low elevations found within the trough signifying a sedimentary environment while high elevations bound the trough in the north and east indicating basement complexes (Fig. 2.4). The Landsat 8 OLI bands were further transformed using PCA technique. PCA helped in segregating the noise components and reducing the correlation of the spectral signatures of different materials thereby providing maximum spectral information in a single colour combination image (Solomon and Ghebreab, 2006). The three best PCs (PC 1, PC 2, and PC 3), which have the greatest information for the area, were filtered for lineament extraction. A colour composite of PC 1, PC 2 and PC 3 enabled the successful extraction of lineaments (Fig. 2.5). The SRTM DEM was preferred to the ASTER DEM because its data features are more accurate in terrain mapping (Isioye and Yang, 2013; Forkuor and Maathuis, 2012; Elkhrachy, 2018). The two processed data sets (SRTM and Landsat 8 PCA) were used to map lineaments of the study area.

Table 2. 1: Sensors and spectral band characteristic for ASTER and Landsat-8 (OLI/TIRS)

ASTER			Landsat-8 (OLI/TIRS)		
Band	**Wavelength (µm)**	**Resolution (m)**	**Bands**	**Wavelength (µm)**	**Resolution (m)**
			1—Coastal/aerosol	0.435–0.451	30
			2—Visible blue	0.452–0.512	30
1—Visible green	0.520–0.600	15	3—Visible green	0.533–0.590	30
2—Visible red	0.630–0.690	15	4—Visible red	0.636–0.673	30
3N—NIR	0.760–0.860	15	5—NIR	0.851–0.879	30
3B—NIR	0.760–0.860	15			
			8—Panchromatic	0.503–0.676	15
			9—Cirrus	1.363–1.384	30
4—SWIR	1.600–1.700	30	6—SWIR	1.566–1.651	30
5—SWIR	2.145–2.185	30			
6—SWIR	2.185–2.225	30			
7—SWIR	2.235–2.285	30	7—SWIR	2.107–2.294	30
8—SWIR	2.295–2.365	30			
9—SWIR	2.360–2.430	30			
10—TIR	8.125–8.475	90			
11—TIR	8.475–8.825	90			
12—TIR	8.925–9.275	90			
13—TIR	10.250–10.950	90	10—TIR	10.60–11.19	100
14—TIR	10.40–12.50	90	11—TIR	11.50–12.51	100

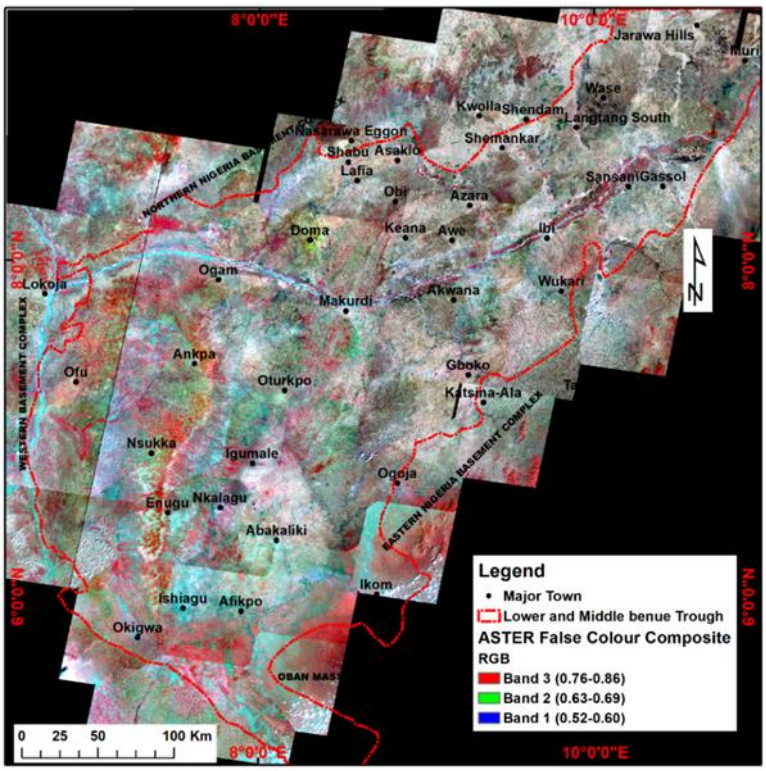

Fig. 2. 2: A total of 78 ASTER scenes processed and mosaiced into a single seamless raster to cover the area of study. A colour combination of Band 1 in blue, Band 2 in green, and Band 3 in red where the red patches represent vegetation

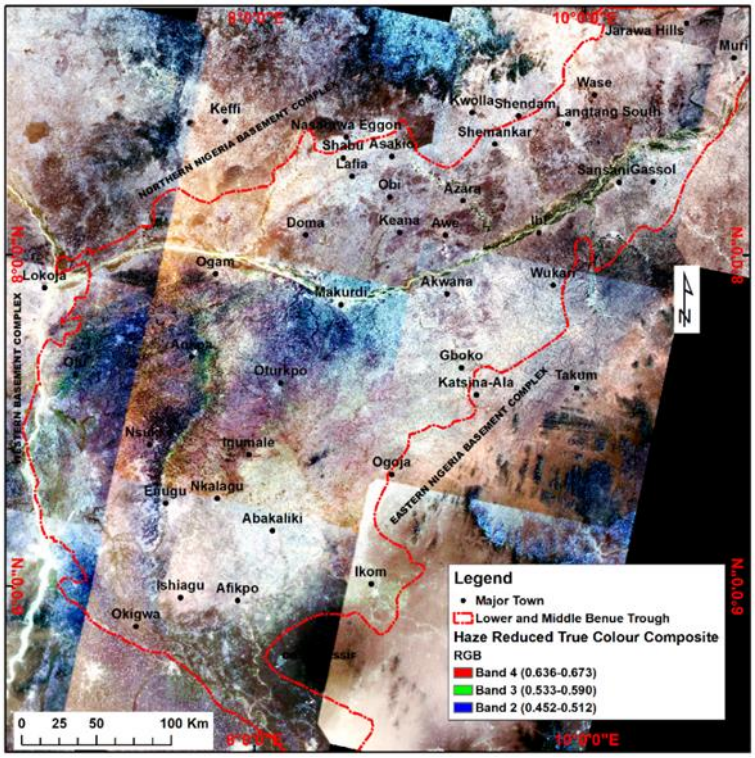

Fig. 2. 3: Eleven haze-reduced Landsat scenes mosaiced and combined into a true colour composite (TCC) with band 1 in blue, band 2 in green, and band 3 in red to cover the area of study.

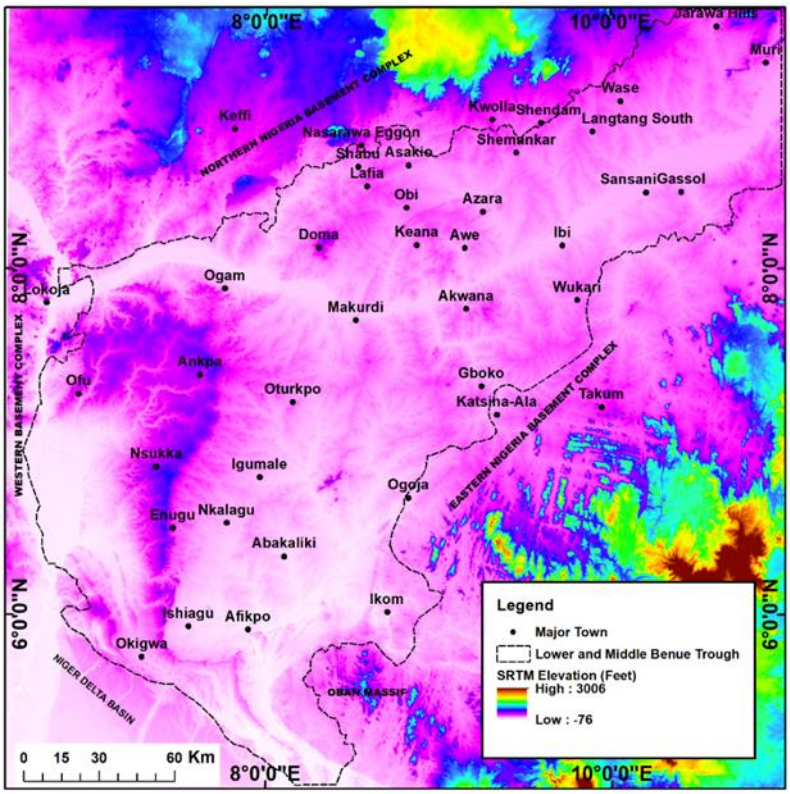

Fig. 2. 4: Shuttle Radar Topographic Mission (SRTM) of the study area showing low elevations within the basin surrounded by high elevations indicative of exposed basement.

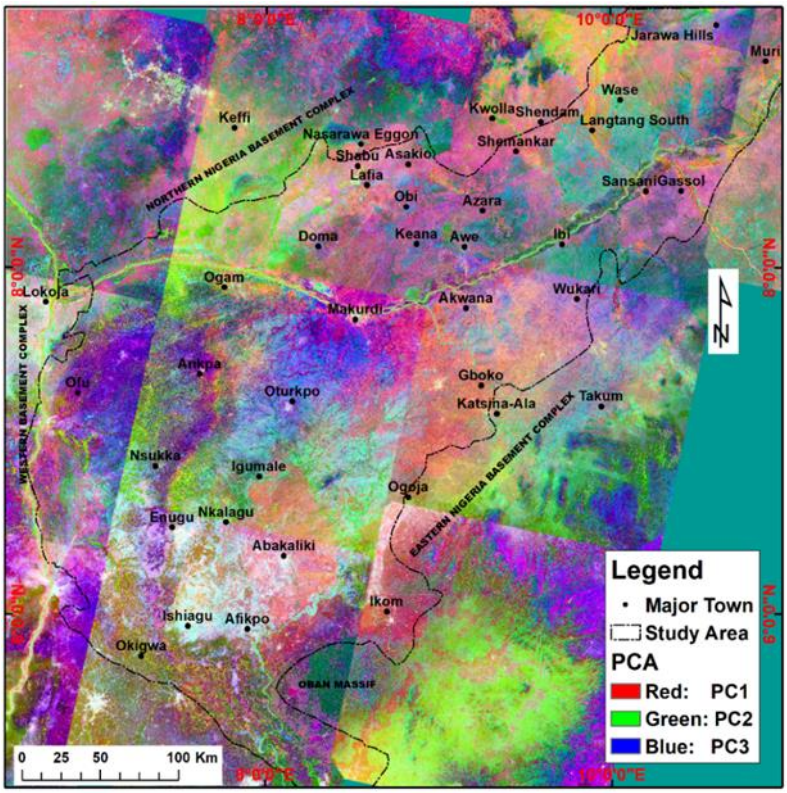

Fig. 2. 5: Landsat 8 PCA colour composite (PC 1: R, PC 2: G, PC 3: B).

2.3 Methods for geological mapping using remote sensing data sets

Geological mapping can be done using remote sensing which has the advantage of low cost, regional-scale, and speed, when compared to other mapping methods (Boud, 1987). Landsat 8 and ASTER data sets were used for mapping lithologies at the surface in the basin. These data provide suitable spectral and spatial band coverage and integrating the two data sets gives a more robust result than using either one of them (Zhang et al., 2016; Pour et al., 2017).

The methodology is designed to effectively differentiate the varying spectral information related to the geology of the area (Fig. 2.6). The approach involved first reducing the influence of vegetation cover on the data sets by masking and suppression. The result is added to the unmasked raster to form the processed raster map of the area. Colour composite, spectral band ratioing, and principal component analyses (PCA) were then used to discriminate different mineral components that act as end members for further image classification.

2.3.1 Masking and vegetation suppression

The presence of vegetation cover acts as a strong barrier, damping the effective record of radiance by remote sensors. The normalized difference vegetation index (NDVI) estimate was used to calculate and understand the spatial amount of vegetation in the area (Grebby et al., 2014). NDVI is obtained by subtracting the red reflectance (R) values from the near infra-red (NIR) and then dividing the result by the sum of the near-infrared and the red bands (Yu et al., 2011). The NDVI is given by.

$$\mathbf{NDVI} = (\mathbf{NIR} - \mathbf{R})/(\mathbf{NIR} + \mathbf{R}) \quad \textbf{(2. 3)}$$

The values of NDVI in the Landsat and ASTER data were estimated using ENVI software to fall between -1 and 0 but were linearly rescaled and presented in integer values in the range of 0 - 255. The minimum value of 0 is represented by dark patches signifying the non-vegetated part of the area while the highest value of 255 is indicated by white patches showing the presence of vegetation (Appendix A1). The NDVI results for the two data sets show an increase in vegetation in the southern part of the study area. A mask data range was built such that two threshold ranges were obtained from the vegetation index calculation after rescaling the image to values between 0 and 255, i.e., 0-244- and 245-255-pixel values for vegetation and non-vegetation covers, respectively. The threshold range values of 0-244 were applied to mask out areas lacking vegetation cover aimed at preserving the original spectral information of the area while the value range 245-255-pixel values were used to mask out areas of vegetation cover

(Crippen and Blom, 2001; Yu et al., 2011; Yao et al., 2017). The process of vegetation suppression was applied to the vegetated masked raster using the forced invariance method in ENVI that subdues the expression of vegetation and enhances the expression of underlying lithology (Crippen and Blom, 2001). This technique quantified, segregated, and suppressed the spectral contributions from the vegetation. The suppressed vegetation was then added to the unsuppressed raster for further analyses (Figs. 2.7 and 2.8).

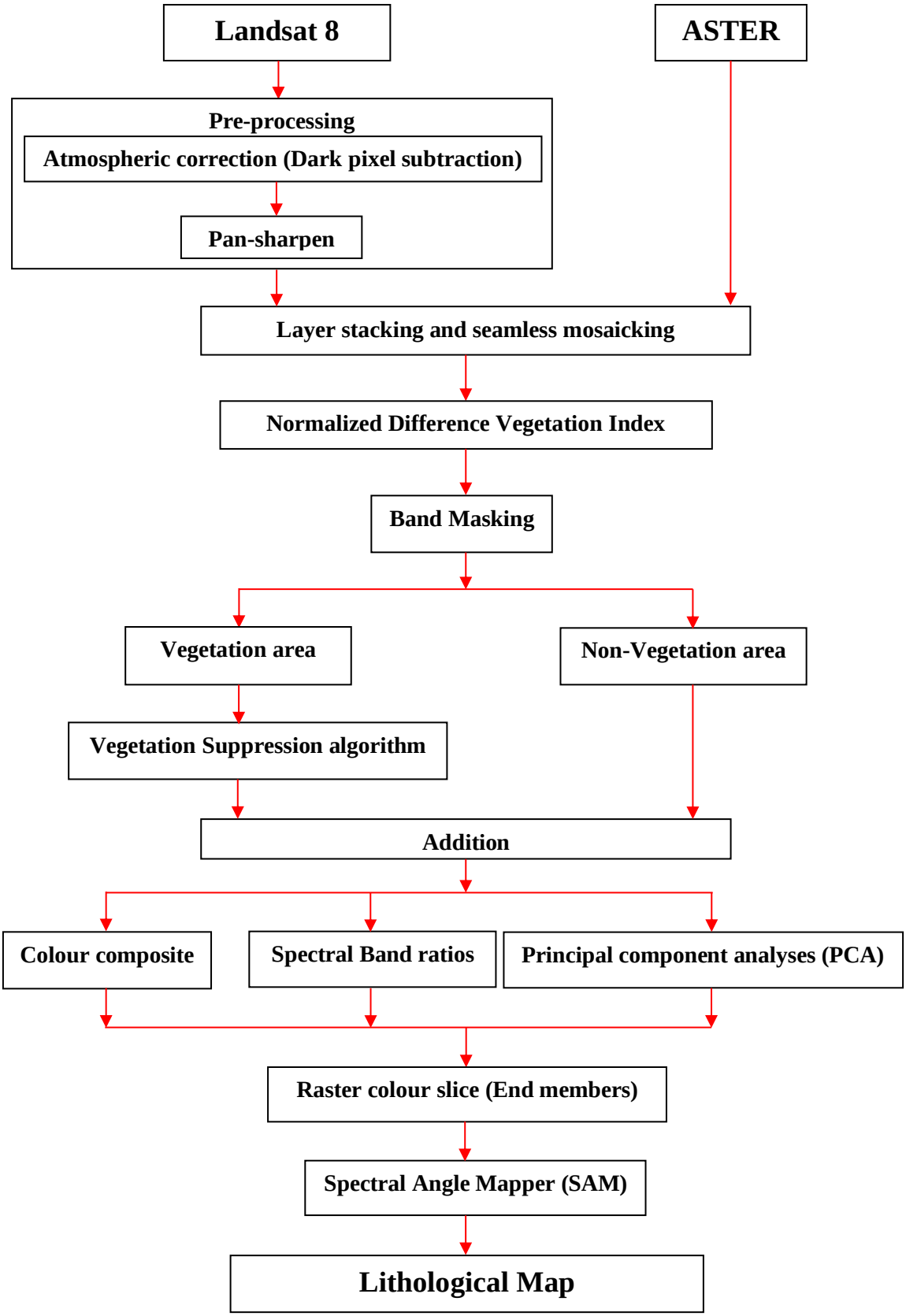

Fig. 2. 6: Methodology for mapping lithology using Landsat 8 and ASTER

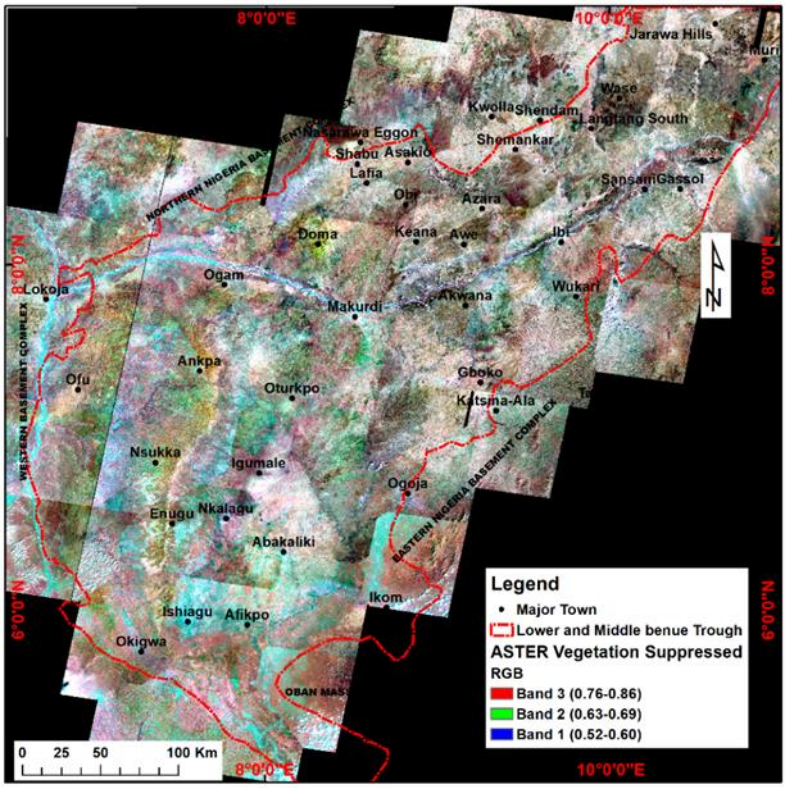

Fig. 2. 7: ASTER vegetation suppressed map where the red patches (seen in fig. 2.1) that represent vegetation have been reduced.

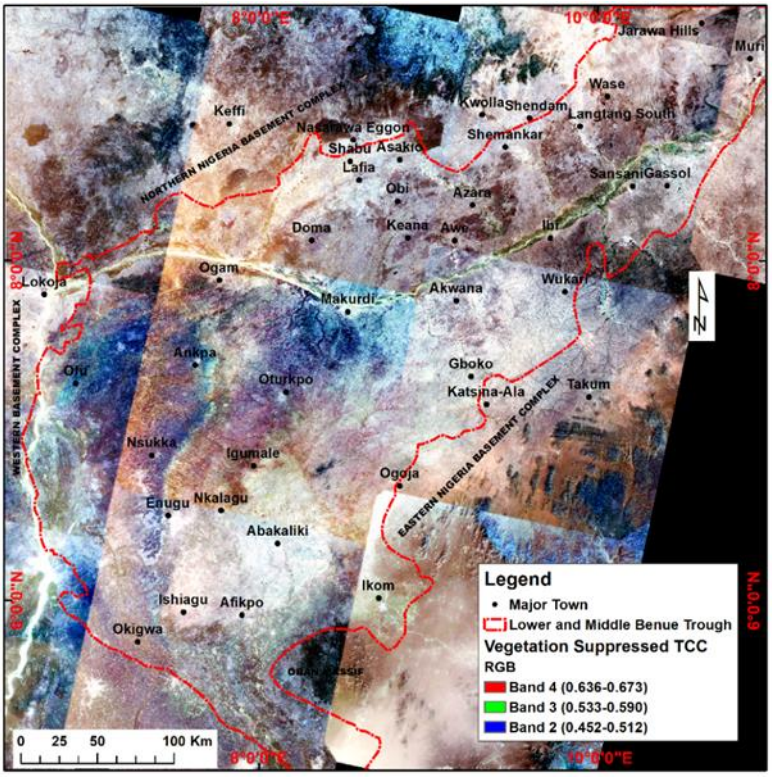

Fig. 2. 8: Vegetation suppressed true colour composite (TCC). The amount of vegetation in green (seen in fig. 2.2) has been grossly suppressed after mask addition.

2.3.2 Band composite

Band composite provides a method of detecting lithological and hydrothermal alteration units and can be obtained by combining three bands or ratio images in red, green, and blue colours (Sabins, 1999; Testa et al., 2018). ASTER and Landsat data sets usually have several bands with varying wavelengths and the processes of combining the bands to form the best possible colour composite for interpretations may be time-consuming and difficult. However, the OIF has been employed in most instances to carry out such combinations for easy lithology detection. The OIF is a statistical value that is aimed at quantitatively identifying the best three-band combinations with the highest spectral information (Chavez et al., 1982; Mokhtari et al., 2015). Normally, an expected number of combinations can be determined by using the formula.

$$\binom{\mathbf{N}}{\mathbf{3}} = \frac{\mathbf{N!}}{(\mathbf{3!}*(\mathbf{N-3})!)} \quad \text{.....(2. 4)}$$

Where N is the total number of bands in a scene and for each combination of three bands, the OIF is calculated as:

$$\mathbf{OIF} = \frac{\boldsymbol{\delta_i + \delta_j + \delta_k}}{|\boldsymbol{\gamma_{i,j}}| + |\boldsymbol{\gamma_{i,k}}| + |\boldsymbol{\gamma_{j,k}}|} \quad \text{.....(2. 5)}$$

Where δ_i, δ_j, δ_k are the standard deviations of digital numbers of bands i, j, k, respectively, and $|\gamma_{i,j}|, |\gamma_{i,k}|, |\gamma_{j,k}|$ are the correlational coefficients of bands i & j, i & k, j & k respectively.

OIF values for the ASTER and Landsat bands were estimated, and the six highest OIF index values each are presented (Table 2.2). The VNIR and SWIR were used in the OIF estimations. Landsat band 1 was not involved in the calculation due to its strong propensity to detect aerosol/cloud cover, which, would give high variance during calculations and so may result in a wrong estimation. Based on the OIF calculation, the combinations with the highest OIF values are bands 3, 4, and 8 (RGB); and 2, 5 and 7 (RGB) in the ASTER and Landsat images, respectively. However, other ranked OIF values were tested and compared with the chosen band composites. The best colour composite shows more clearly iron/water-bearing minerals (Figs. 2.9 and 2.10).

The VNIR bands will detect naturally occurring features with iron, water and OH bearing group minerals while SWIR tends to capture mostly clay minerals (Hunt, 1977). ASTER SWIR band 8 image highlights clay minerals and alunite due to distinctive mineral absorption features with

minimum reflectance while band 3 has higher reflectance for the minerals (Jain et al., 2018). The ASTER colour composite 3-8-4 (RGB) in fig. 2.9 (a) shows areas with light to deep green colours that may signify the presence of clay minerals. ASTER TIR is responsive to heat signature and can also be combined as a false colour composite in 13, 12, 10 as RGB (Appendix A2). The colour composite shows highly correlated pixels, and this can be resolved by decorrelation stretching (Kalinowski and Oliver, 2004). Fig. 2.9 (b) shows the ASTER decorrelation stretch of colour composite with quartz mineral highlighted in different parts of the map as red colour. Landsat band 7 image also shows absorption by clay minerals with minimal reflectance, while their reflectance is high on band 5 (Sultan et al., 1987; Sabins, 1999; Jain et al., 2018). The 7-5-2 (RGB) Landsat 8 colour composite in fig. 2.10 show areas as magenta colour stains that are diagnostic for clay minerals and alunite. The colour composite from the area shows the spatial variation in hydrothermally altered minerals (mostly clay minerals) in light-deep green in ASTER and Magenta colour in Landsat 8. These intensely altered minerals (dark green and magenta) are concentrated within the sedimentary area and around the fringes of basement rocks. However, this method of mapping lithology has not helped in differentiating the various types of clay minerals as well as the iron-bearing and OH group minerals.

Table 2. 2: OIF ranking

OIF Ranking	1	2	3	4	5	6
ASTER Band	**3, 4, 8**	1, 3, 8	2, 3, 8	1, 3, 4	2, 3, 4	1, 4, 8
OIF Value	**92.79**	92.57	92.06	91.09	90.84	88.99
Landsat 8 Band	**2, 5, 7**	2, 5, 6	2, 4,5	3, 5, 7	2, 6, 7	3, 5, 6
OIF Value	**107.57**	106.79	103.62	102.13	101.58	100.84

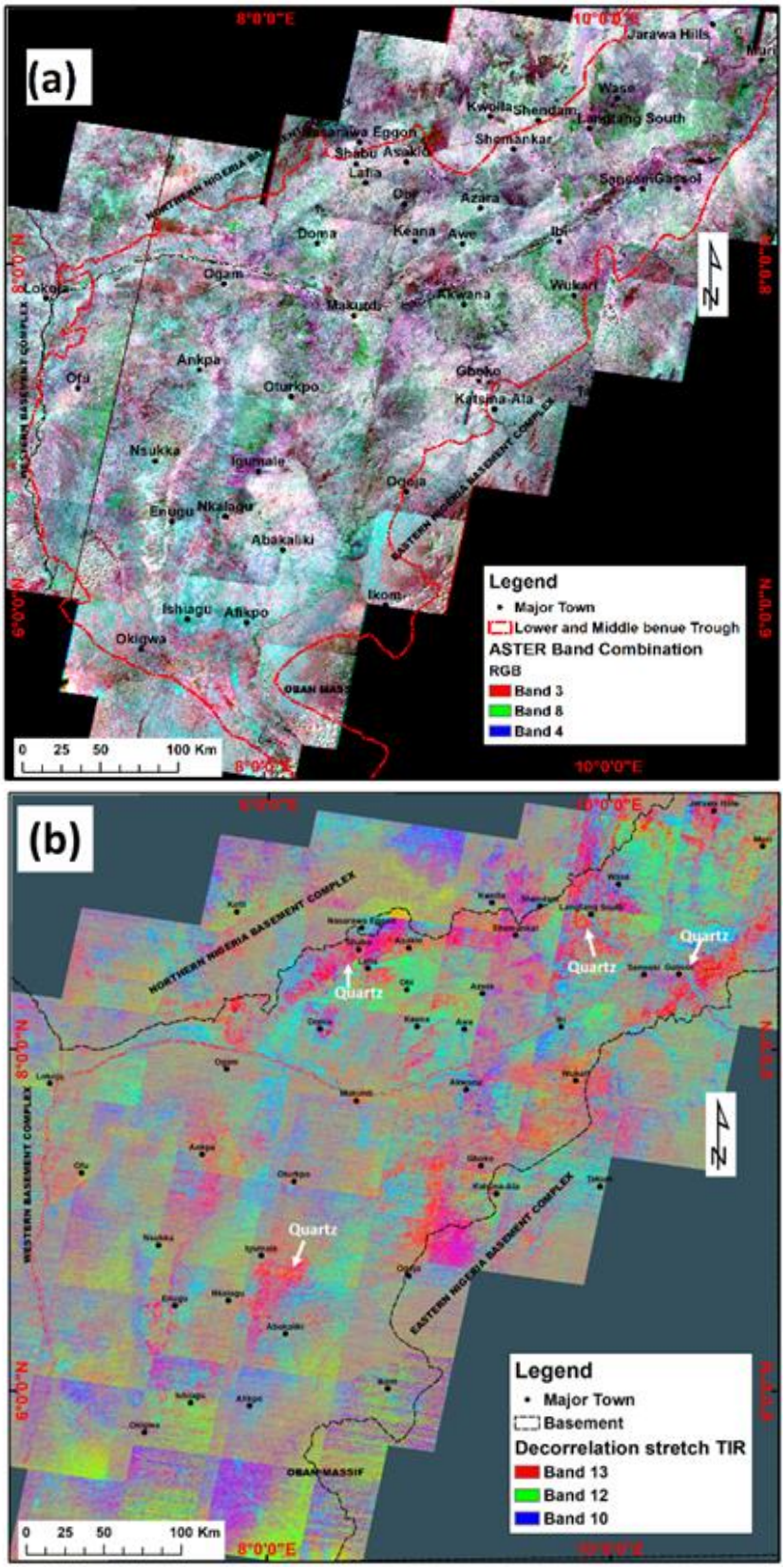

Fig. 2. 9: ASTER false colour composite (a) Best SWIR bands in 3, 8, 4 (RGB) showing main hydrothermally altered zones in dark and light green colour (b) Decorrelation stretched TIR in 13, 12, 10 (RGB) showing the presence of quartz minerals in red colour.

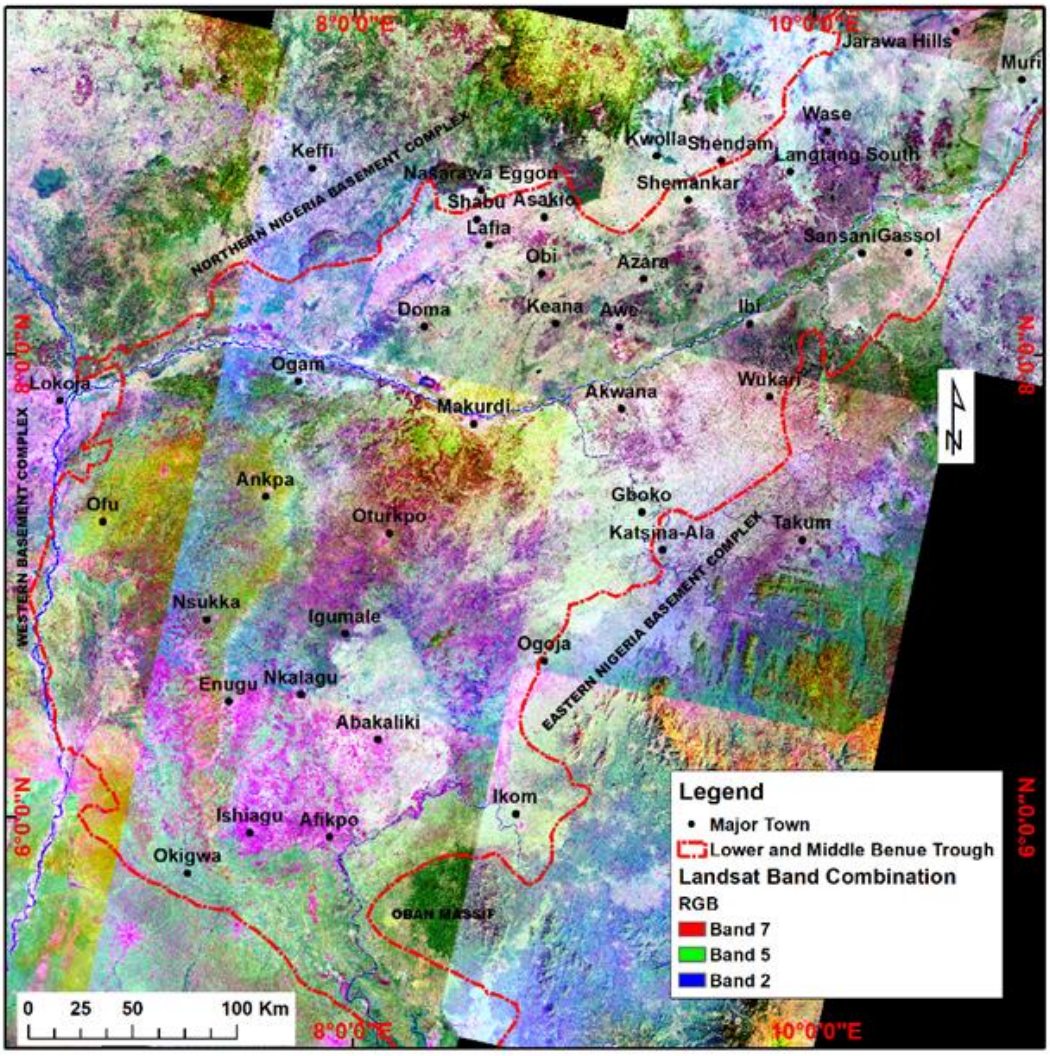

Fig. 2. 10: Best Landsat 8 colour composite in 7, 5, 2 (RGB) showing clay minerals in magenta colour stains.

2.3.3 Principal Component Analyses

The PCA is a linear transformation process that adjusts the variance in a multispectral band image into a new set of uncorrelated linear combinations (Richards and Jia, 2006). Multispectral data are normally highly correlated and the PCA transformation produces uncorrelated output bands suitable for lithological boundary mapping. This statistical method is employed to subdue the effects of irradiance dominating all bands and enhance the spectral reflectance related to surface materials such as rocks, soils, and vegetation, hence, improving the appearance of geological features (Loughlin, 1991; Testa et al., 2018). PCs are products of PCA that contain the target spectral information obtained by considering the highest eigenvector loadings from the multispectral bands, coinciding with the target's most diagnostic features (Loughlin, 1991; Cŕosta et al., 2003). This establishes the relationship between the spectral response of target materials and numeric values from the PCA eigenvector matrix and this has been used to map iron oxide and hydroxide in soils related to geology (Cŕosta et al., 2003). The technique is called FPCS or Cŕosta technique. It helps in selectively mapping hydrothermal minerals more effectively (Loughlin, 1991; Cŕosta et al., 2003; Testa et al., 2018). FPCS depends on understanding the relationship between the spectral signature from specific materials and the PC images (Cŕosta et al., 2003). In this technique and case, the PCA of four bands were analysed such that one mineral type such as iron-oxide is avoided while hydroxyl-bearing minerals are detected in the SWIR if only one input band is from the visible spectrum. Also, to detect iron-oxide minerals in the VNIR spectrum, one band from the SWIR is used while the remaining three bands are used from the VNIR spectrum (Loughlin, 1991). The FPCS technique was applied to the Landsat and ASTER data to examine the PCA eigenvector weighting to predict which of the principal component images will concentrate information directly associated with hydrothermal minerals of the area.

2.3.3.1 Landsat data

The FPCS method was applied on bands 2, 5, 6, and 7; and 2, 4, 5, and 6 to map the possible presence of hydroxyl and iron oxide minerals, respectively. Band 2 can also be substituted by bands 3 and 4 of the VNIR and bands 7, 8 and 9 for band 6 during the analyses (Loughlin, 1991). The PC transformation for detecting hydroxyl minerals with bands 2, 5, 6, and 7 show four PCs (Table 2.3). PC1 represents brightness or albedo even though it has the highest eigenvalues (98.8%), PC2 describes more of the contrast between infrared and visible bands while PC3 could have some amounts of vegetation that have not been completely suppressed. Hydroxyl-bearing minerals are detected in PC4 as represented by dark pixels negative values

(Appendix A 3a). The anomalous concentration of the image was enhanced by calculating the negative of the image to highlight hydroxyl minerals (Fig. 2.11). This shows the hydroxyl mineral concentration represented by the brightest pixel value. Three distinct areas have been density sliced with different colours to mark areas of high hydroxyl minerals concentrations with lithology boundary identified and delineated as well (Fig. 2.12). The boundaries were obtained by tracing edges of lithologies that show distinct visual differences in contact with another lithology.

The PCs transformation on Landsat 8 bands 2, 4, 5, and 6 of the area (Table 2.3) show that PC1 has the highest eigenvalue of 98.8%, dominated by brightness or albedo, while PC2 describes more components of the infrared and visible spectrum. Vegetation pixels that have not been successfully suppressed are evident in PC3. However, iron-oxide is presented in PC4 as dark pixels (Appendix A 3b). The amount of iron-oxide was observed when the negative of PC4 was calculated, so that the brightest pixels show the amount of iron-oxide (Fig. 2.13). Fig. 2.14 shows density sliced portions of the iron-oxide images that tend to describe the lithology boundary too. The red circular polygon highlighted in the figure in pink may be a volcanic rock that has been altered and contains a considerable amount of iron oxide.

Hydroxyl-containing minerals are found to spread all over the area mostly within the basin while the spread of iron oxide is mostly found around the basement areas with few deposits in the basin. The ability of Landsat 8 to map altered minerals is limited to just two SWIR wavelengths i.e., bands 6 and 7 (Zhang et al., 2016).

Table 2. 3: Principal Component Analysis for Hydroxyl-bearing and iron-oxide bearing mineral mapping

Principal component analyses for Hydroxyl mapping					
Eigenvectors	**Band 2**	**Band 5**	**Band 6**	**Band 7**	**Eigenvalues (%)**
PC1	0.999	0.002	-0.014	0.030	91.498
PC2	0.006	-0.980	0.197	-0.019	4.320
PC3	0.014	0.198	0.980	-0.014	3.880
PC4	0.029	0.016	-0.018	**-0.999**	0.302
Principal component analyses for Iron oxide mapping					
Eigenvectors	**Band 2**	**Band 4**	**Band 5**	**Band 6**	**Eigenvalues (%)**
PC1	0.999	-0.004	0.018	-0.032	91.907
PC2	-0.005	-0.998	0.068	-0.006	4.597
PC3	0.019	-0.069	-0.996	0.050	2.669
PC4	-0.031	0.002	-0.051	**-0.998**	0.828

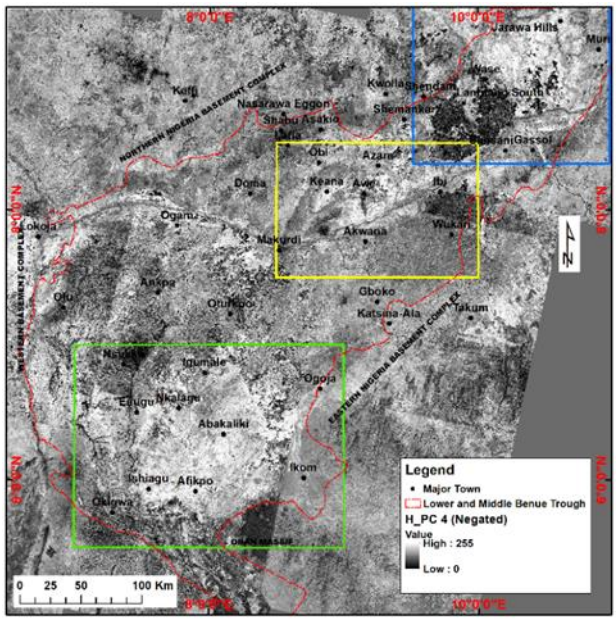

Fig. 2. 11: Negated principal component 4 for bands 2, 5, 6 and 7 (Hydroxyl image). The bright zones represent areas with anomalous concentrations of hydroxyl-bearing minerals.

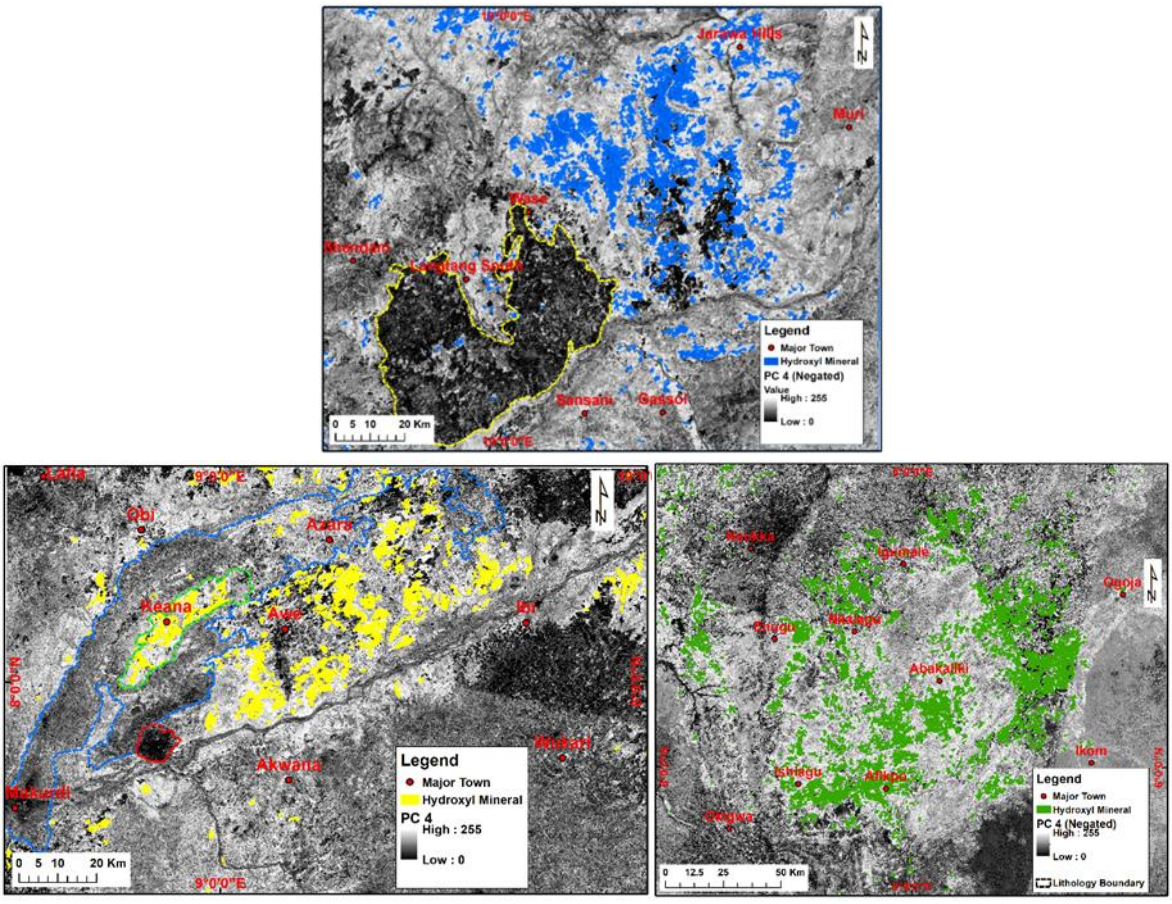

Fig. 2. 12: Brightest pixels have been colour density sliced to highlight areas of high concentration of the hydroxyl-bearing minerals with some lithology boundaries delineated

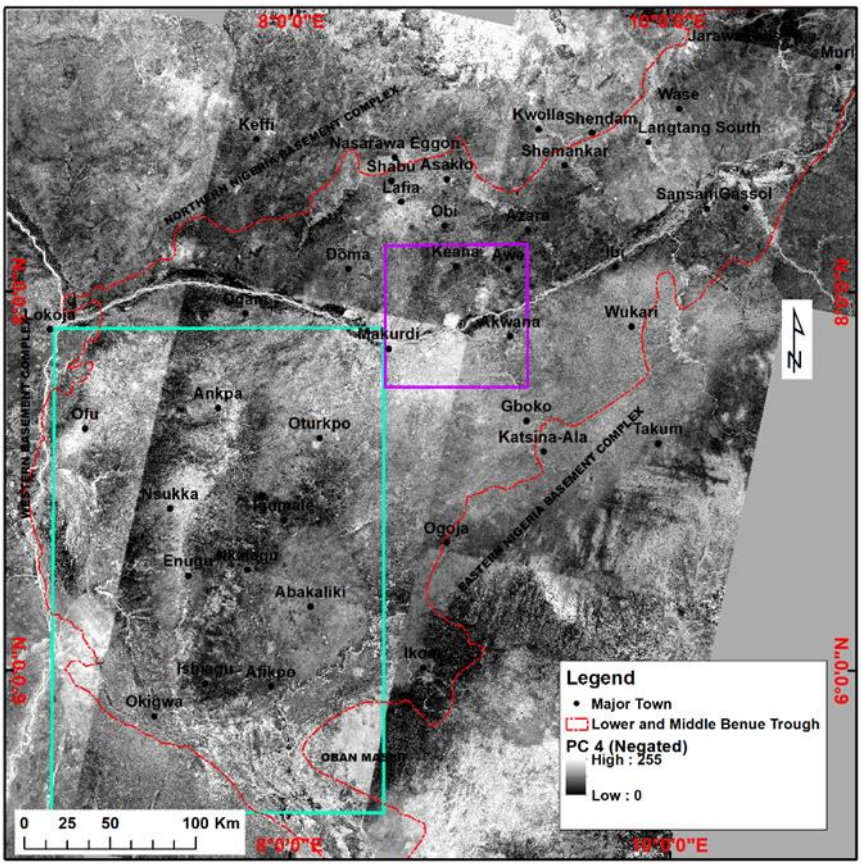

Fig. 2. 13: Iron-oxide image where the brightest pixels marks iron-oxide bearing minerals (calculated from the negation of PC4)

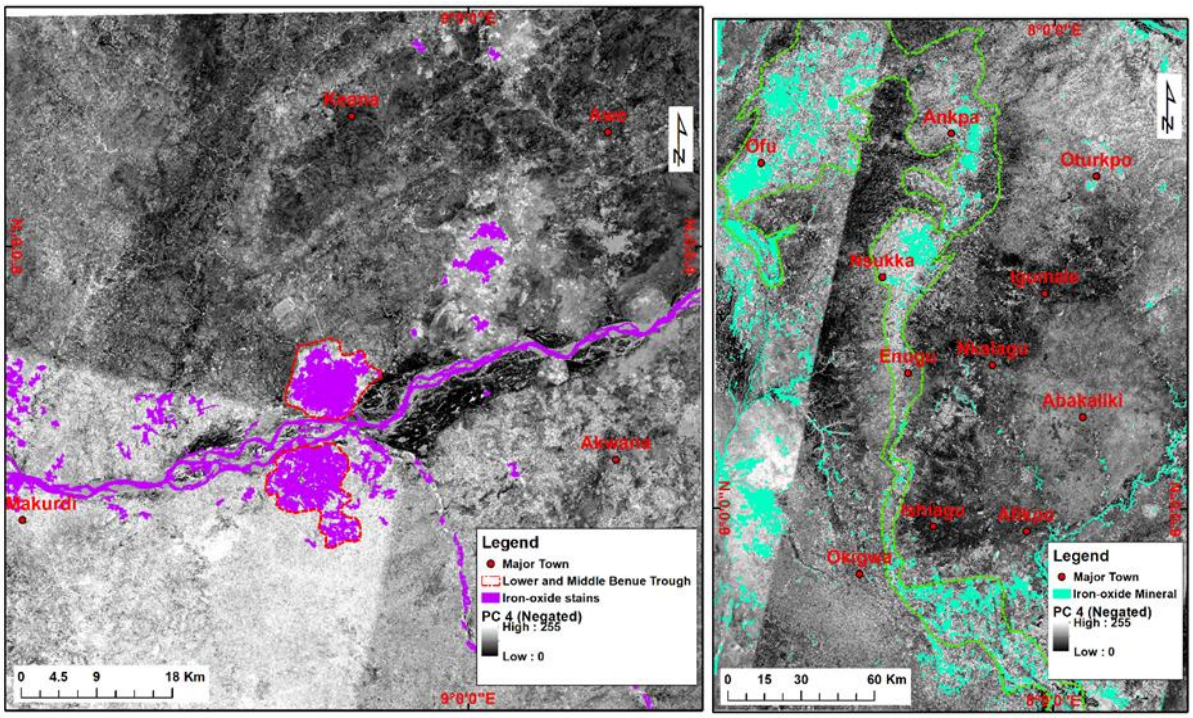

Fig. 2. 14: Iron-oxide image density slices where the brightest pixels mark iron-oxide bearing minerals. Lithology boundaries are delineated within the area.

2.3.3.2 ASTER SWIR data sets

ASTER-SWIR bands help in discriminating and identifying surface vegetation and hydrothermal alteration minerals better than Landsat due to ASTER's broad wavelength range (Ninomiya et al., 2005; Pour and Hashim, 2011; Hewson et al., 2015). This dataset is limited though by cross-talking, which is a situation where stray light from other bands leaks into nearby bands as additive noise signals making interpretation difficult (Hewson et al., 2015). The PCA transformation is designed to eradicate such problems. ASTER with six SWIR bands can discriminate and identify mineral assemblages such as phyllosilicates, sulphates, and carbonates, which have diagnostic spectral signatures or spectral curves (Cŕosta et al., 2003; Ninomiya, 2004). Bands 4 and 2 can be ratioed to enhance the display of gossan (Iron sulphide mineral deposits) formed due to the oxidation or alteration of iron sulphides (Hewson et al., 2001, 2004a; Volesky et al., 2003; Rowan and Mars, 2003) and at the same time, techniques such as FPCS can be applied to give a more robust discrimination result.

FPCS was applied to ASTER VNIR and SWIR bands by selectively analysing and examining PCA eigenvector loadings to predict which of the principal component images will concentrate information directly associated with mineral occurrence within the area (Loughlin, 1991; Testa et al., 2018). The wavelength ranges selected for the analyses are diagnostic due to the characteristics of specific alteration mineral end members such as 0.520– 0.600, 0.760–0.860, 1.600–1.700, 2.145–2.185, 2.185– 2.225, and 2.235–2.285 for bands 1, 3, 4, 5, 6, and 7 respectively (Fig. 2.15). Fig. 2.15 shows high reflectance for the VNIR band i.e., low spectral absorbance while as the wavelengths increase to the SWIR bands, the percentage of electromagnetic spectrum absorbed increases making it suitable for the measurement of alteration minerals like alunite, illite, kaolinite, smectite. Hydroxyl minerals such as kaolinite and alunite have absorption at ASTER SWIR bands 5 and 6 (Ninomiya, 2004; Testa et al., 2018). Alunite is a sulphate hydroxyl bearing mineral with a unique sharp spectral feature absorption at band 8. ASTER band combinations (1, 3, 5, 7); (1, 3, 5, 6) and (1, 4, 6, 7) have been used to identify diagnostic spectral responses for alunite, illite, and kaolinite minerals respectively (Cŕosta et al., 2003).

The PC produced from 1, 3, 5, and 7 estimation contains the expected spectral information for alunite. The eigenvector statistics show high reflectance in band 1 (0.999) and band 7 (1.00), and high absorbance in bands 3 and 5 (Table 2.4). PC 3 has a high and negative loading from band 5 (-0.999) which indicates that the pixels likely to contain alunite are represented by low

(dark) DN values (Appendix A 4a). This was visualized by multiplying all pixels with -1 (or simply negated) so that the dark pixels for alunite are displayed as bright pixels in the image (Fig. 2.16). Raster colour slice has been used to identify the areas that alunite is found.

The analyses of bands 1, 3, 5, and 6 for PCA show an eigenvector that highlighted the presence of illite. There is high reflectance in band 1 and high absorbance in bands 3, 5 and 6 (Fig. 2.15). Thus, the PCA analyses show the amount of illite from bands 5 and 6 and as such PCs 3 and 4 have high eigenvectors of 0.9996 and 0.9999, respectively (Table 2.4). PC 3 displays the most possible abundance of illite due to combined amounts of bands 5 and 6 (0.9996 and 0.0044, respectively) while PC 4 shows a reduced amount in band 5. PC 3 discriminates illite better than the other PCs (Fig. 2.17).

The calculated PCA selected bands 1, 4, 6, 7 shows high reflectance values in ASTER bands 4 and 7, and high absorbance 1 and 6 powerfully in bands 1 and 6 (Fig. 2.15); while the PCA eigenvector statistics of these bands (Table 2.4) indicate that PC3 has high and negative loading values for band 6 (-0.9987). This shows that pixels likely to contain kaolinite are observed by low and dark digital number values (Appendix A4 b), and visualized as bright pixel values, the whole image was additively inverted by multiplying with -1. The kaolinite abundance image was then displayed as bright pixels as green in colour density slice (Fig. 2.18).

A colour density slice composite shows the abundance for alunite, illite, and kaolinite and their spatial distributions within the area (Fig. 2.19). Alunite has been detected mostly along the river channels while illite is mapped in the southern part.

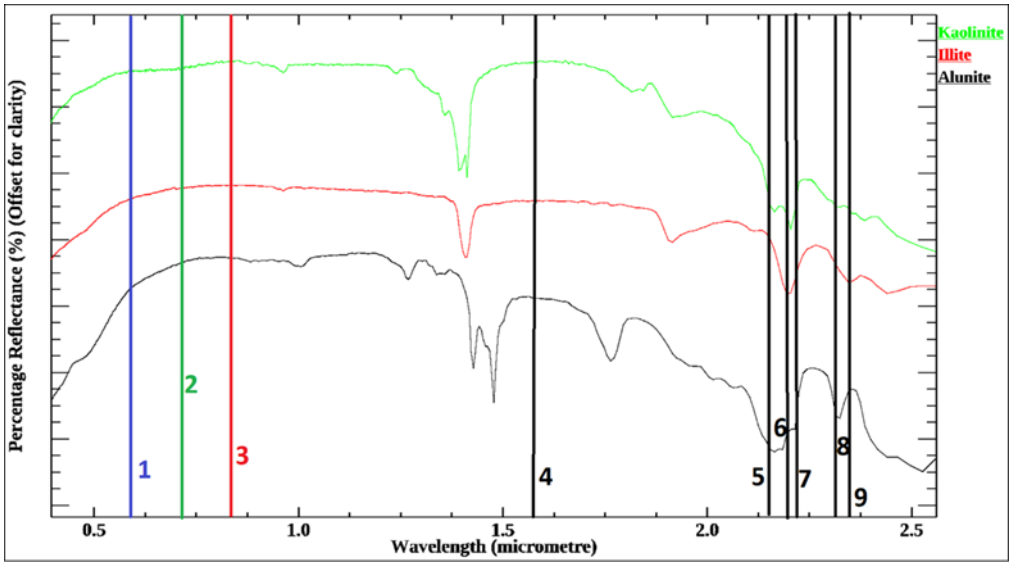

Fig. 2. 15: Spectral library showing the three diagnostic alteration minerals of Kaolinite, Illite and Alunite, and their percentage reflectance and absorbance (After Cŕosta et al., 2003).

Table 2. 4: Eigenvector statistics for ASTER bands for mapping alteration minerals. Highlighted values were used to identify spectral responses from alunite, illite and kaolinite.

Alunite					
Eigenvector	**Band 1**	**Band 3**	**Band 5**	**Band 7**	**Eigenvalue (%)**
PC 1	0.9990	-0.0393	0.0234	-0.0013	93.0250
PC 2	-0.0396	-0.9991	0.0131	-0.0023	4.1189
PC 3	0.0229	-0.0140	**-0.9996**	0.0072	2.2184
PC 4	0.0011	-0.0022	0.0072	1.0000	0.6376
Illite					
Eigenvector	**Band 1**	**Band 3**	**Band 5**	**Band 6**	**Eigenvalue (%)**
PC 1	-0.9985	0.0481	-0.0247	-0.0123	93.3876
PC 2	0.0486	0.9987	-0.0153	-0.0079	4.0008
PC 3	-0.0240	0.0165	**0.9996**	0.0044	2.2165
PC 4	-0.0118	0.0084	-0.0048	0.9999	0.3950
Kaolinite					
Eigenvector	**Band 1**	**Band 4**	**Band 6**	**Band 7**	**Eigenvalue (%)**
PC 1	-0.9982	0.0531	0.0269	-0.0047	95.9337
PC 2	0.0533	0.9985	0.0053	-0.0087	2.6858
PC 3	-0.0264	0.0063	**-0.9987**	-0.0432	0.9574
PC 4	-0.0054	0.0092	-0.0430	0.9990	0.4231

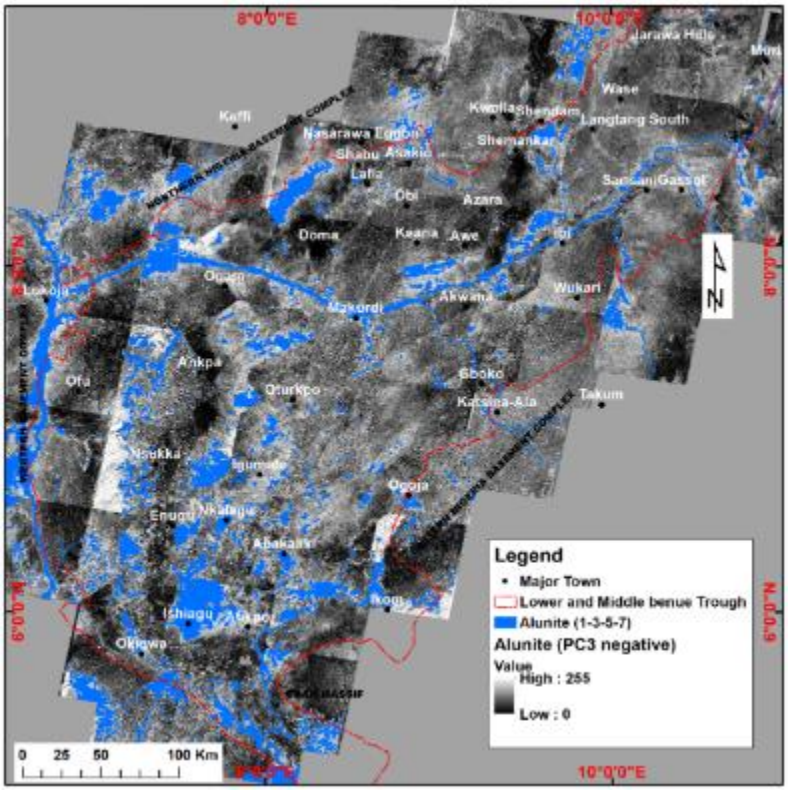

Fig. 2. 16: Alunite mineral abundance colour density sliced from ASTER bands 1, 3, 5, 7

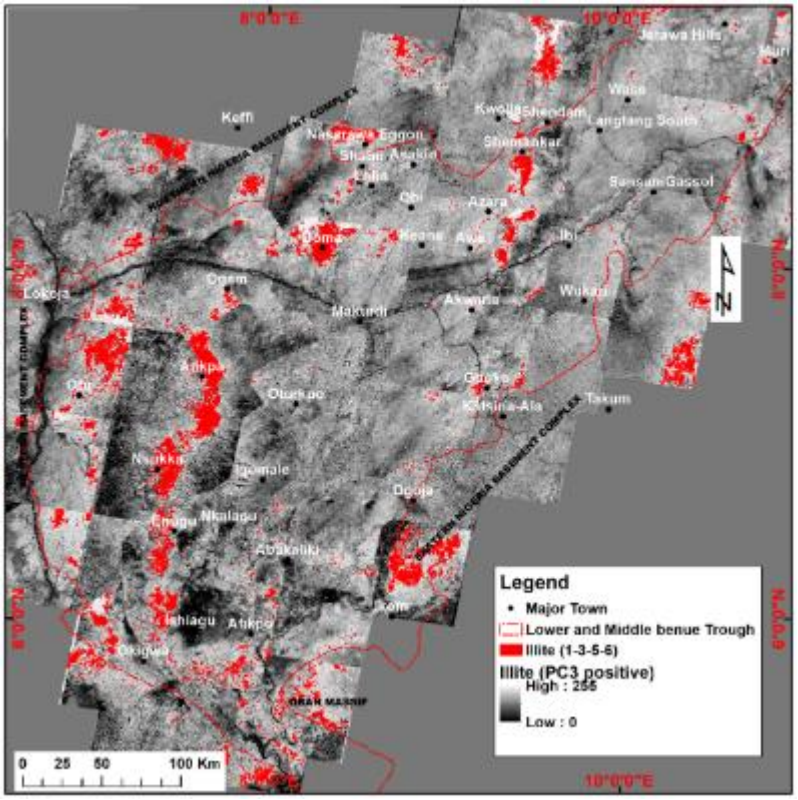

Fig. 2. 17: Raster colour slice showing illite mineral stains from ASTER bands 1, 3, 5, 6

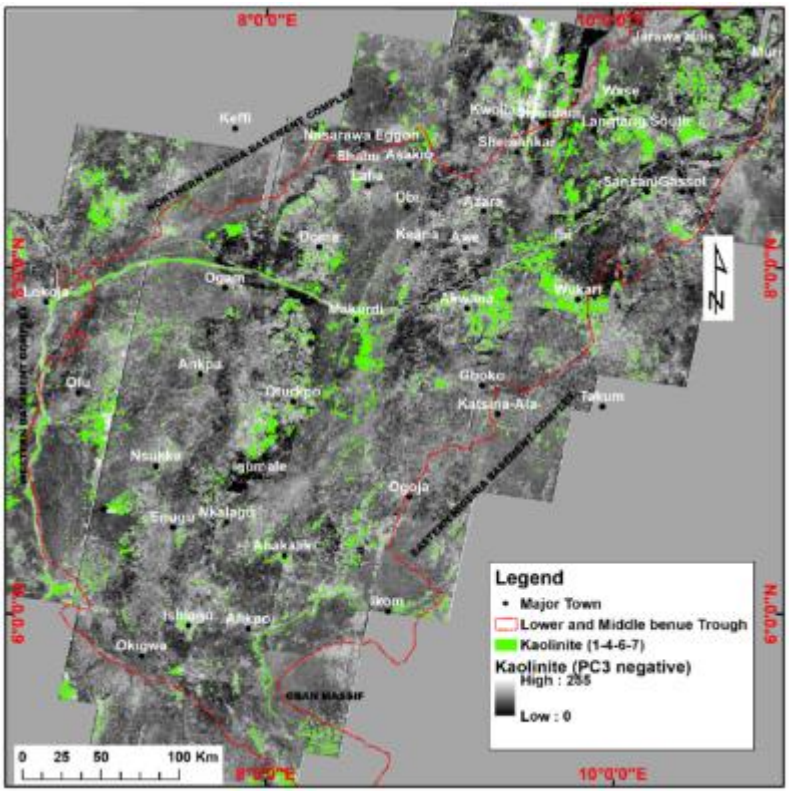

Fig. 2. 18: Raster colour slice kaolinite mineral stains from ASTER bands 1, 4, 6, 7

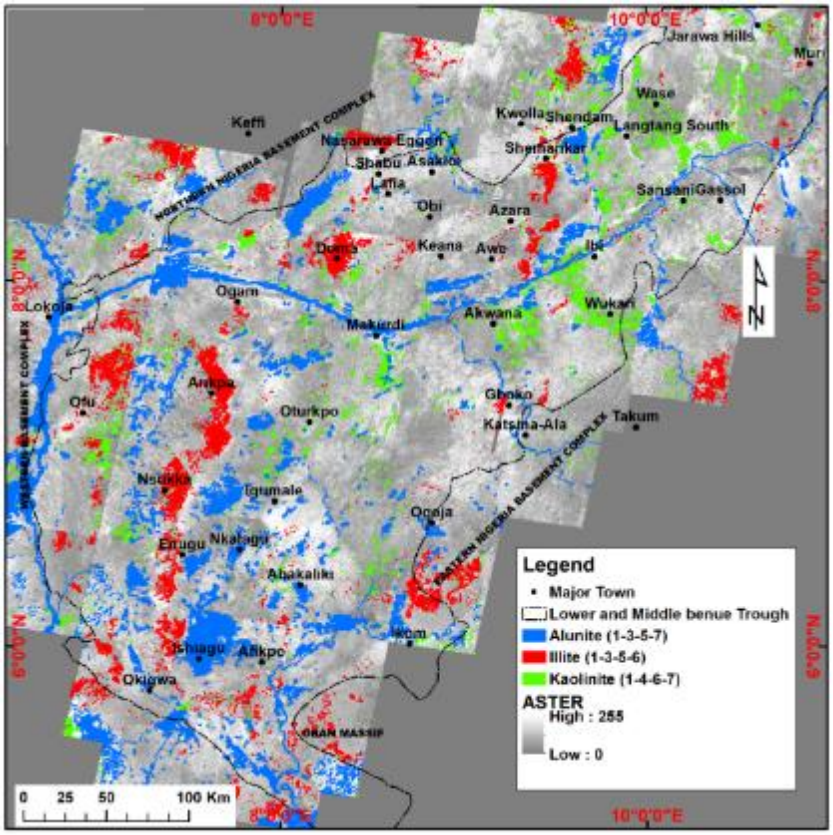

Fig. 2. 19: Combined colour density slice image showing the abundance for alunite, illite, and kaolinite draped over grey scale ASTER image

2.3.4 Spectral band ratioing

Band ratioing is a process that aims to achieve the detection of mineral groups with strong absorption bands at similar wavelengths by dividing pixels brightness values of one band by another (Khidir and Babikir, 2013; Ducart et al., 2016). Band ratios can be estimated in three-band to form a composite that can be represented in colour contrast for the mapping of geological formations. Band ratio calculations were applied to both Landsat and the ASTER data.

2.3.4.1 Landsat 8 data sets

Several Landsat band ratios were calculated and used for lithological mapping and interpretation. Band ratio 4/2 was used to detect iron-stained hydrothermally altered rocks during ferrugination (Ninomiya, 2003a; Rowan et al., 2005), as it has proven to show high spectral values for ferric iron minerals such as hematite and magnetite. (Fig. 2.20). Ferrous iron minerals were differentiated from ferric ones by using a band ratio of 5/6 (Kaufmann, 1988; Sabins, 1999; Gad & Kusky, 2006; Jain et al., 2018). Fig 2.21 indicates that the raster sliced areas contain a high amount of ferrous iron minerals. Hydroxyl bearing minerals were detected by using a band ratio of 6/7 (Sultan et al., 1987; Kaufmann, 1988; Sabins, 1999; Jain et al., 2018; Fig. 2.22), which shows the spread of these minerals particularly within the sedimentary area.

Colour composites representing mineral features were obtained using OIF analyses to obtain the best band ratio combinations (Table 2.5). Band ratios 6/2, 7/5, 6/5, and 7/2 for Fe-bearing aluminosilicates, clay minerals, ferric iron, and ferrous minerals, respectively, have been used to map different lithologies (Abrams *et al.*, 1983; Sultan et al., 1987 Kaufmann, 1988; Sabins, 1999; Carranza and Hale, 2002; Laake, 2011; Rajendran et al., 2012; Yao *et al.*, 2016). The OIF technique was applied to these ratios and the best colour composite was obtained and displayed. Fig. 2.23 shows a colour composite with cyan stains showing the presence of Fe^{3+} related clay minerals and green patches indicating other clay minerals. Landsat data, however, have limited spectral band coverage for mineral mapping i.e., two SWIR (Bands 6 and 7) and two Thermal Infrared (Bands 10 and 11). This means that minerals such as quartz and carbonates may not be easily identified, and thus Landsat data sets are mostly restricted to detecting alteration zones (Cŕosta et al., 2003). In contrast, ASTER has six SWIR bands (bands 4–9) and five TIR (bands 10-14) where diagnostic spectral features shown by clay and carbonate minerals are detected (Abrams and Hook, 2002; Cŕosta et al., 2003).

Table 2. 5: OIF Index Highest Ranking of Landsat 8

Rank	Band Ratio			OIF
1	7/5	6/2	6/5	91.01
2	7/5	6/2	7/2	88.49
3	6/2	6/5	7/2	87.74
4	7/5	6/5	7/2	86.59

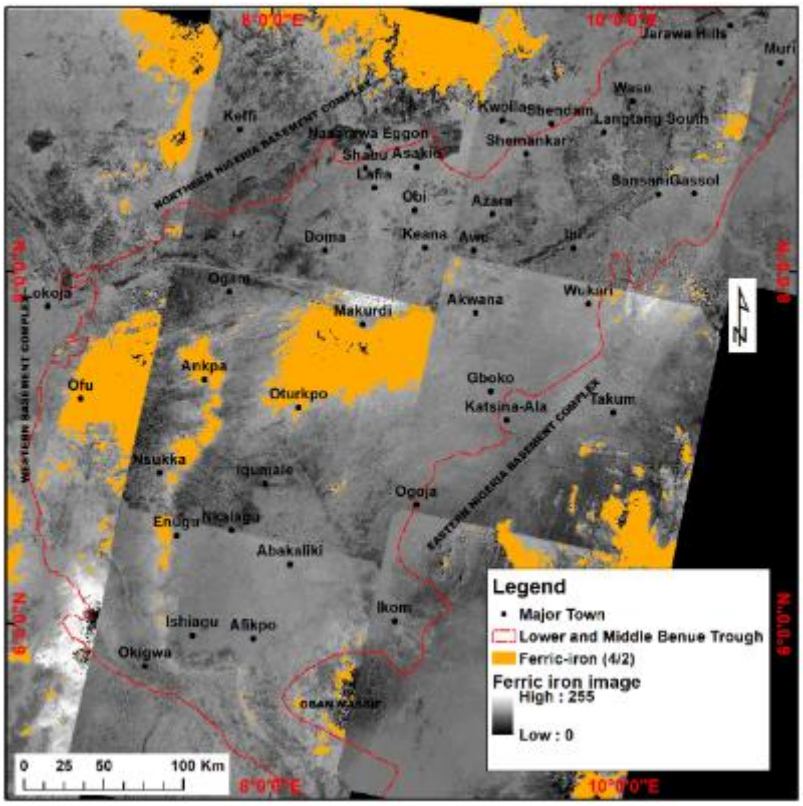

Fig. 2. 20: 4/2 ratio image with the brightest digital number colour density sliced. It shows the presence of ferric minerals

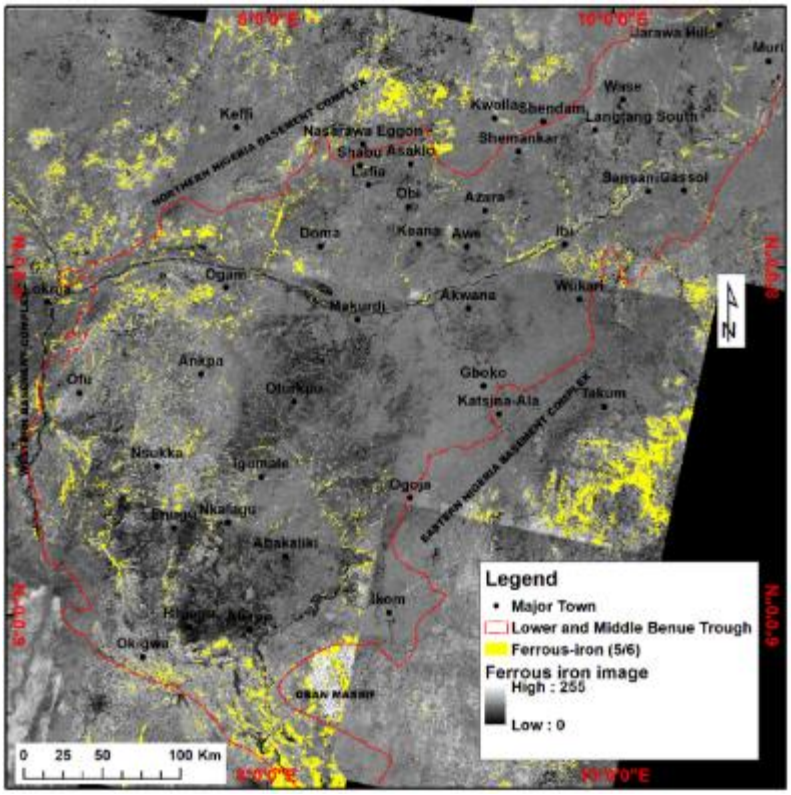

Fig. 2. 21: 5/6 ratio image. Areas with a significant amount of ferrous-iron minerals as raster colour sliced.

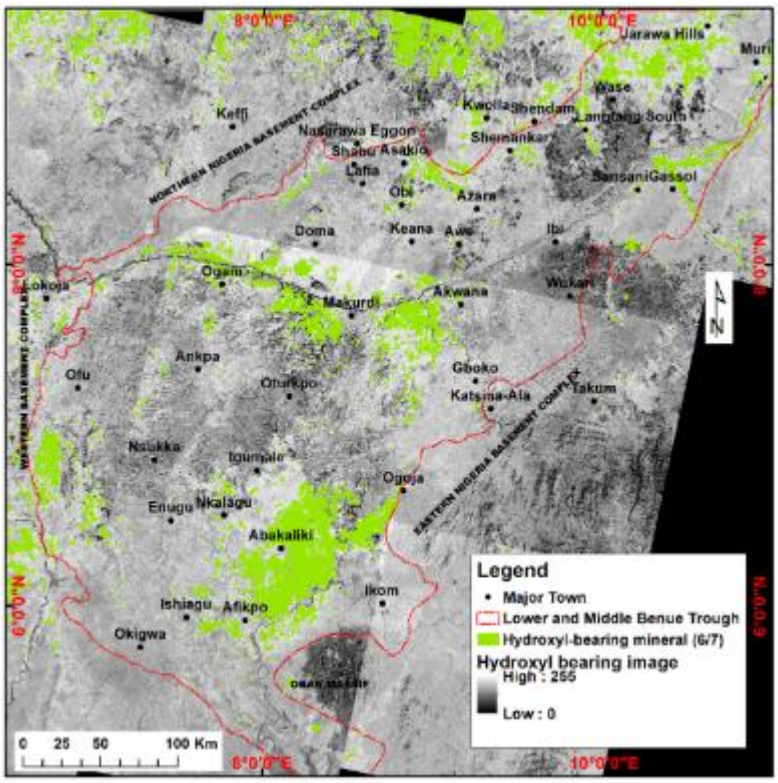

Fig. 2. 22: Raster sliced 6/7 ratio image showing the presence of hydroxyl-bearing minerals (high pixel number values).

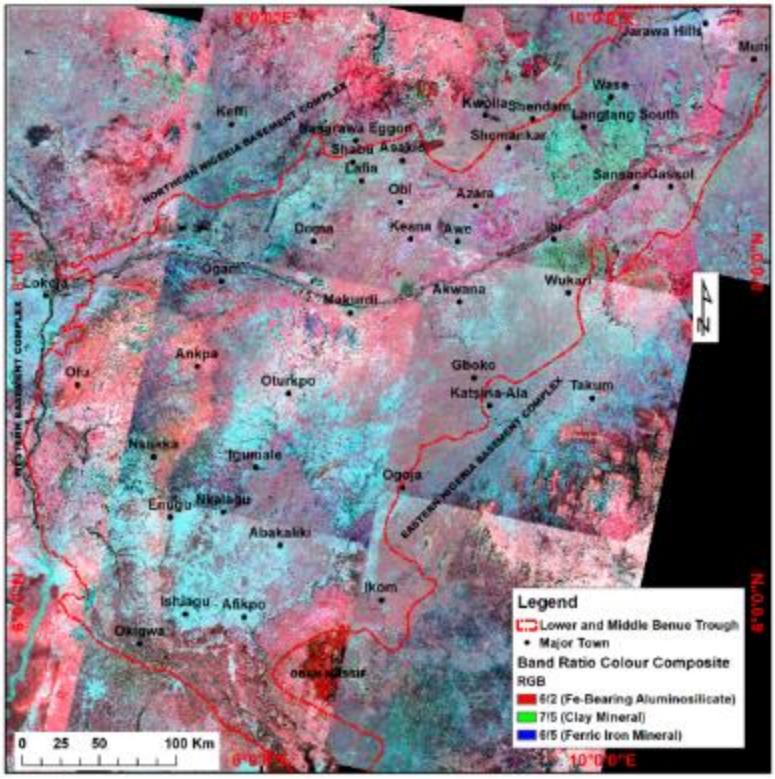

Fig. 2. 23: Band ratio colour composite in R: 6/2; G:7/5; B:6/5 with 2% linear stretching. The cyan stains show areas dominated by Fe^{3+} related clay minerals while green patches are dominated by other clay minerals.

2.3.4.2 ASTER TIR indices

Mineral indices for ASTER TIR bands can be used to detect minerals such as quartz, carbonates, and mafic rocks by considering their spectral absorption features (Ninomiya, 2004, Beiranvand Pour and Hashim, 2015; Kalinowski and Oliver, 2004; Ninomiya, 2004). The mineral ratio for ASTER TIR is diagnostic for specific mineral deposits known as mineral indices (Yamaguchi and Naito, 2003; Ninomiya and Fu, 2016). The TIR spectral bands (10, 11, 12, 13, and 14) with a spatial resolution of 90 metres were used for the calculation of mineral indices to help in the delineation of quartz-rich, carbonate, and mafic minerals (Ninomiya, 2003; Ninomiya *et al.*, 2005; Ninomiya and Fu, 2016). The VNIR and SWIR spectral bands are not suitable for effectively detecting the absorption features of these minerals (Yao et al., 2017). These minerals (quartz-rich, carbonate, and mafic minerals) have capacity for the absorption and reflection of heat energy which can easily be measured by the TIR sensors. The mineral indices of Quartz (QI), Carbonate (CI) and Mafic (MI) were calculated and applied in extracting geological information based on the formulae suggested by Ninomiya *et al.*, 2005.

$$\textbf{Carbonate Index (CI)} = \left({}^{\mathbf{B_{13}}}/_{\mathbf{B_{14}}}\right) \text{.....(2. 6)}$$

$$\boldsymbol{Quartz\ Index\ (QI)} = \left({}^{(\boldsymbol{B_{11}} \times \boldsymbol{B_{11}})}/_{(\boldsymbol{B_{10}} \times \boldsymbol{B_{14}})}\right) \text{.....(2. 7)}$$

$$\boldsymbol{Mafic\ Index\ (MI)} = \left({}^{\boldsymbol{B_{12}}}/_{(\boldsymbol{B_{13}} \times \boldsymbol{CI_n})}\right) \text{.....(2. 8)}$$

Where B_{10}, B_{11}, B_{12}, B_{13} and B_{14} are ASTER bands 10, 11, 12, 13 and 14 respectively used at "radiance-at-sensor" data with or without atmospheric corrections for B, bands.

The spatial distributions of QI, CI, and MI were raster colour sliced to show areas dominated by the mineral deposits (Appendices A5 a, b, and c respectively). The raster colour slices were merged (Fig. 2.24) and false-colour composites of QI, CI, and MI as red, green, and blue, also produced (Appendix A5 d). Lithological boundaries have been mapped from the false-colour composite that displays brown as areas contaminated by quartz-rich lithologies with subordinate carbonates while yellow shows areas containing quartz and carbonates (Fig. 2.25). The areas mapped as brown and yellow are a good indicator for the presence of marine sedimentary rocks that are rich in quartz and calcite and/or dolomite (Ninomiya and Fu, 2016). Transported quartz mineral occurrences, such as sandy alluvial cover, can be discriminated from silicate rock outcrops with shaded DEM slope map (Hewson et al., 2015).

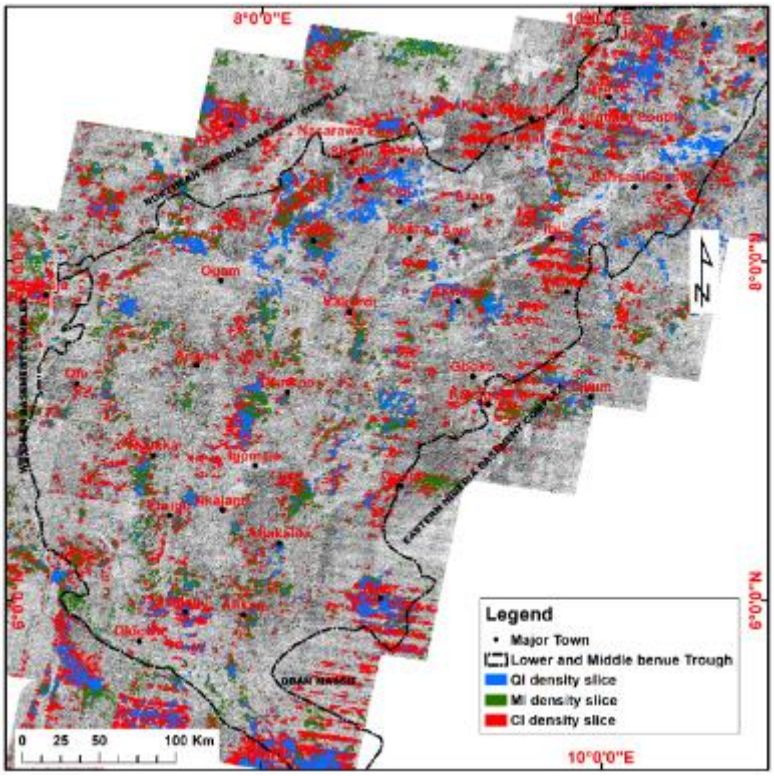

Fig. 2. 24: Merged raster colour sliced image showing QI-Quartz index in blue, CI - Carbonate index in green and MI-Mafic index in the red.

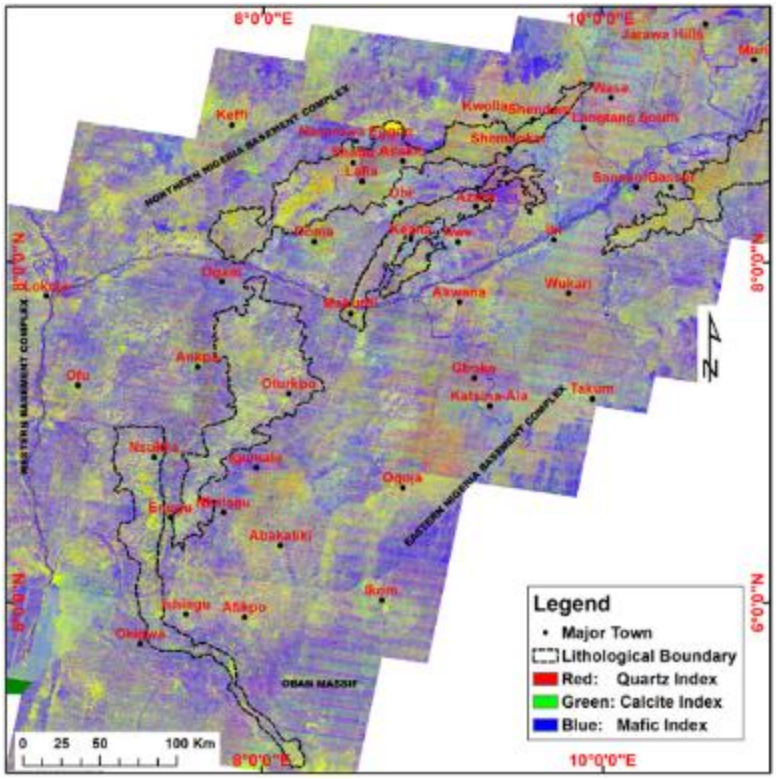

Fig. 2. 25: False-colour composite mineral indices for ASTER image where QI (Quartz index), CI (Carbonate Index) and MI (Mafic Index) are represented as red, green, and blue, respectively. Lithological boundaries were manually delineated.

2.3.5 Image classification using the spectral angle mapper

The spectral angle mapper (SAM) is a supervised and automated image classification technique that determines the angular spectral similarities between two image spectra using the number of band-dimension angles to match pixels to reference spectra (Khaleghi et al., 2014). The method is not sensitive to illumination and albedo effects as all illumination directions are accounted for in the calculation. SAM involves the angular comparison between the endmember spectrum vector and each pixel vector in space (Rowan and Mars, 2003; Rowan et al., 2005). It can be achieved by considering the relationship between two bands (i and j) and a library spectrum of 2D scatter plots or a developed end member (Fig. 2.26). When a vector line passes through the origin, it describes the position of each respective spectrum under all illumination conditions. The SAM classifier generalizes this geometric interpretation in n-dimensional space, where n is the number of bands in the image (Khaleghi et al., 2014). For each library spectrum or end member selected during the analysis, the n-dimensional spectral angle (in radians) is determined for every pixel in the input image, and output is expected for every end member.

Here, the known mineral spectral reflectance results mapped earlier from Landsat 8 were used as end members or region of interest since they represent pure mineral signature to create four lithologic classes. A SAM maximum angle of 0.7 rad (40 degrees) was used to classify the best Landsat 8 colour composite image (Fig. 2.10) into four lithological classes of clay minerals, hydroxyl-bearing minerals, ferric-iron minerals, and ferrous-iron minerals (Fig. 2.27 a). A closer look at the lithology in the southern part of the map shows unique distinctions between lithologies with sharp boundary differences (Fig. 2.27 b). As noted earlier, Landsat data sets, due to the short range of wavelength bands, cannot predict individual types of mineral assemblages but has been shown to be very efficient in mapping lithological boundaries.

The results of mineral mapping from ASTER SWIR were used to form four lithological end members. SAM classification was applied to the best false colour composite (Fig. 2. 9 a) with a maximum angle of 0.5 rad (29 degrees) and four distinct lithologic mineral classes were obtained: alunite, illite, kaolinite and gossan (Fig. 2.28 a). Fig. 2.28 b clearly shows that SAM has successfully mapped out different mineral compositions better with ASTER data sets than Landsat data sets.

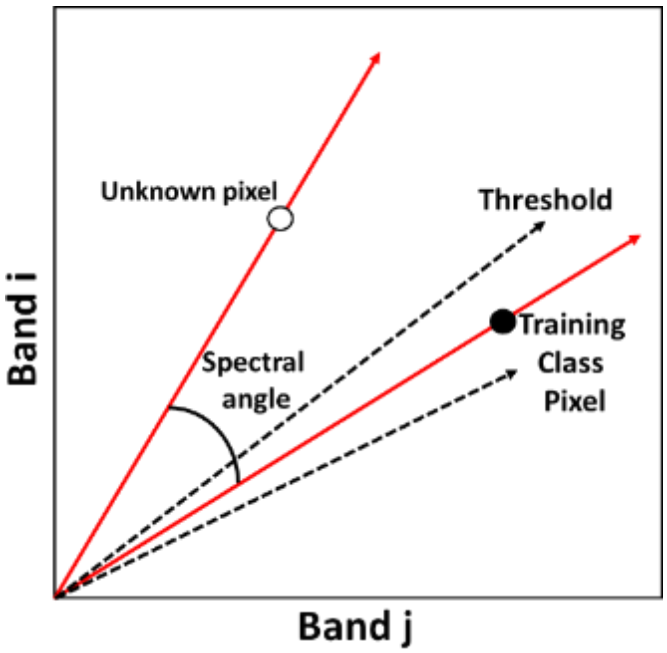

Fig. 2. 26: Principle of image classification using the spectral angle mapper (SAM). Bands i and j represent spectral intensity at digital number level.

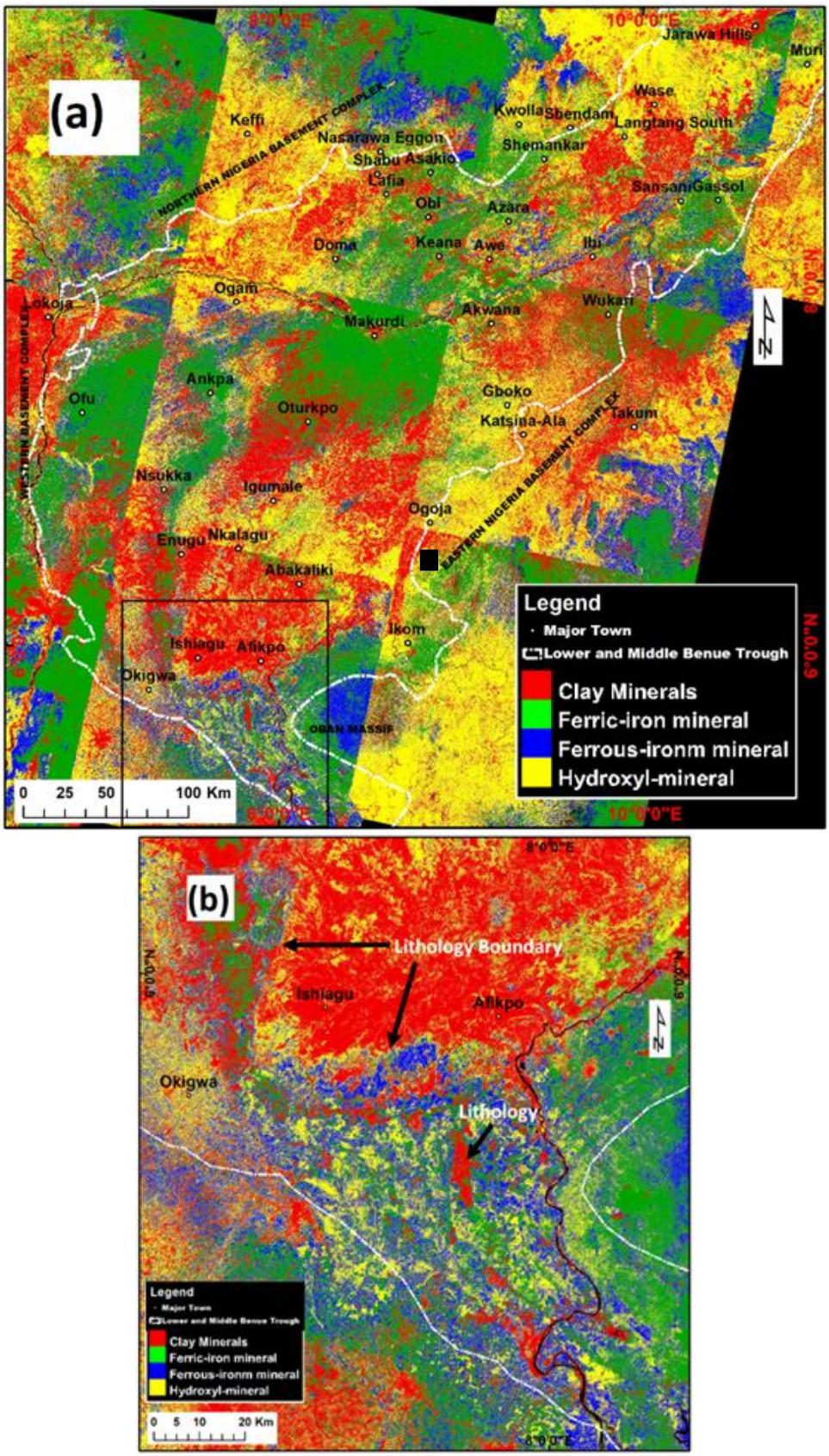

Fig. 2. 27: (a) Landsat lithology mapping using SAM. The process of mosaicking the edges of the bands are not seamless probably due to bands edge effects and noise. (b) Subset lithology map showing the lithologies and their boundaries.

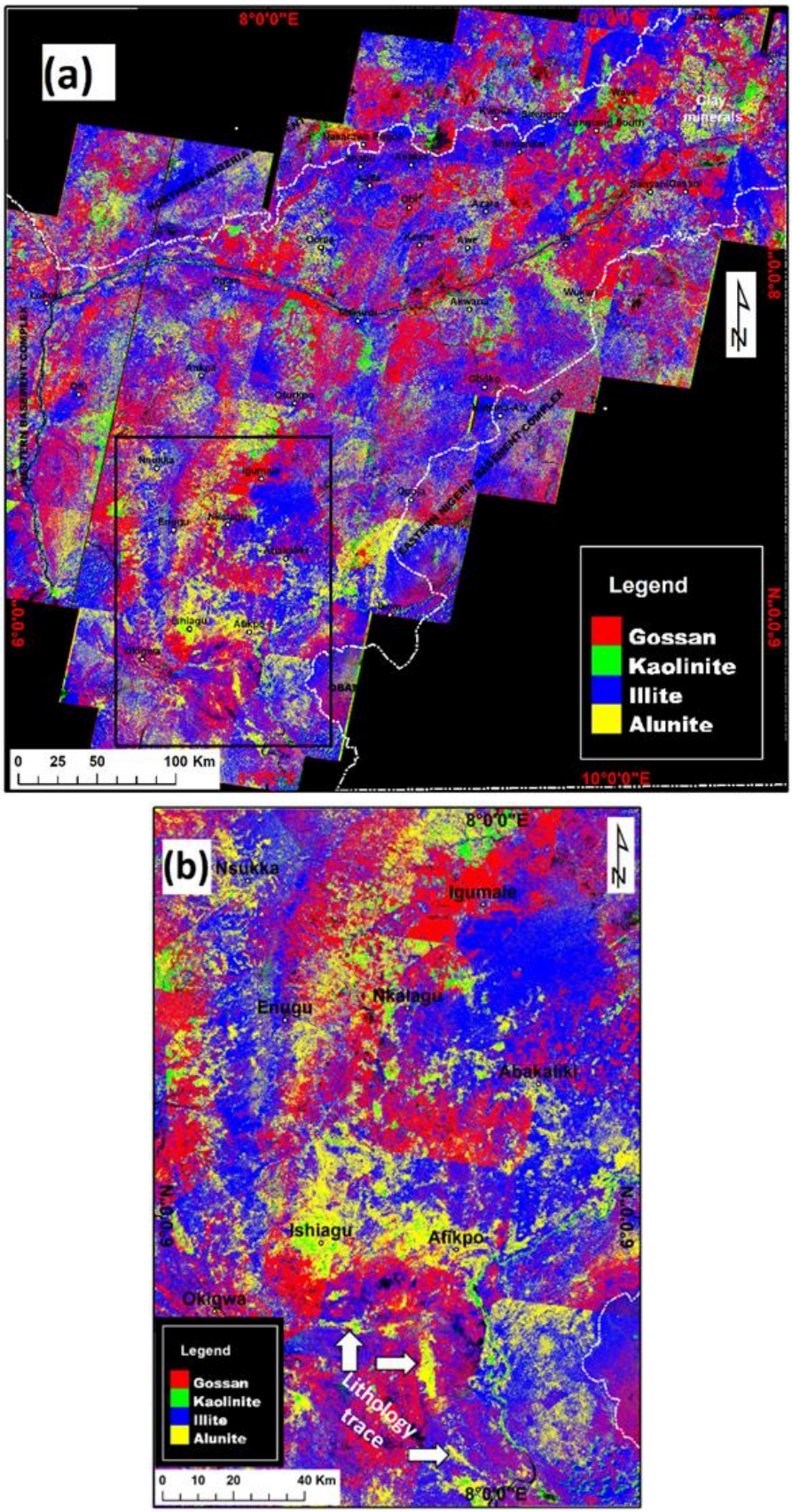

Fig. 2. 28: (a) Lithology mapping from ASTER SWIR data using SAM with a threshold of 0.7 rad. (b) Subset showing lithology trace with more mineral distinction.

2.3.6 Construction and interpretation of the lithological map

The lithology of the area was carefully mapped from the analyses of results obtained from colour composites, band ratioing, and FPCS techniques and subsequently identified and classified by SAM. The lithological boundaries detected during the analyses were compiled for all areas and tied to the lithology produced in this study to form the geological map. The process of geological map construction in this study from ASTER and Landsat involved matching the lithologies (Fig. 2.29 a) and their boundaries (Fig. 2.29 b) with descriptions of previously identified geological units taken from literature.

Lithology L1 is composed of mainly quartz and illite which has a similar composition to Bima Sandstone made up of sandstones, carbonaceous clays, shales, and mudstones (Obaje, 2009; Ogunmola *et al.*, 2014). The Asu River group comprises fine-grained sandstones, dark shales, volcanoclastics, limestones and siltstones. which can be tied to the lithology L2 consisting of mainly illite, quartz, and carbonates. L3 is composed of mafic, illite, and gossan minerals like those deposited as shales of the Odukpani formation (Nwachukwu, 1972). The Yolde Formation consists of thinly bedded sandstones, limestones, shales, clays, claystones, and sandy mudstones which have similar lithological characteristics to L4 with its prevalence composed of quartz, carbonate, illite, and alunite (Benkhelil, 1989; Obaje, 2009). Lithology L5 is rich in clay minerals such as alunite and illite, and mafic minerals that are diagnostic of alteration of the Awe-Keana formation (Ofoegbu, 1985; Obaje, 2009). L6 is characterized by the dominance of quartz, carbonates, illite, and alunite, typical of the composition of the Makurdi Formation, which comprises ferruginous micaceous sandstones, clays, mud rocks and carbonate-bearing minerals (Najime, 2011). L7 is made up of gossan, illite, and alunite minerals, similar in characteristics to Eze–Aku formation of marine shales, calcareous siltstones, limestones, and friable sandstones and marls (Olade, 1975; Obaje, 2009; Akande *et al.*, 2012). The Pindinga formation, consisting of marine fossiliferous, grey bluish shales, limestones, and calcareous sandstone (Ofoegbu, 1985; Obaje, 2009; Akande *et al.*, 2012) can be tied to L8 which is composed of quartz, kaolinite, gossan, and carbonate. The Agwu Formation consists of shales, limestones, and siltstones with similar lithological characteristics to those of L9 which is composed of alunite, illite, mafic, and gossan (Nwachukwu, 1972; Najime, 2011). Lithology L10, made up of quartz and carbonates, shows a close relationship with the Lafia formation which is characterized by ferruginized sandstones, loose sands, mudstones, and clays (Obaje, 2009). L11 is dominated by illite, alunite, gossan, and quartz-like the composition of Asata/Nkporo formation's shales, marine shales and arenaceous

sandstones (Ofoegbu, 1985, Obaje, 2009). The Ajali sandstone is like L12 consisting of major illite, quartz, and alunite. Lithology L13 has predominance of kaolinite, gossan, and alunite minerals, which are closely relatable to the marine shales of Imo formation (Fatoye and Gideon, 2013). The presence of alunite, illite, and mafic minerals infer that Lithology L14 could be relatable to the Ameki formation, since this formation has been observed to contain intercalations of sand and clay deposits as well as relics of ironstone (Oyewole and Ukaegbu, 2017). The presence of mafic and gossan minerals from L15 signifies the weathered relics of basaltic volcanic rocks (Ofoegbu, 1985).

The allocation of names to the lithological boundaries based on the described lithologies and existing associated formations enabled the production of the final geology map of the area (Fig. 2.30). Fourteen lithologies have been mapped with the Bima, Odukpani, and the Asu-river groups the oldest and Ameki formation the youngest. The basement and the basin boundary have also been mapped with this method. The geology map produced from Landsat and ASTER data sets (Fig. 2.30) is similar but more robust than the existing geology map from literature (Fig. 1.4). This study mapped fewer lithologies within the basin while existing literature showed more lithologies especially in the southern part of the basin because it is usually supported by field mapping and interpretations. However, the lithology boundaries produced from this study defines more precise lithological contacts than those of existing geology. The sedimentary-basement boundaries are better defined in this study than the existing geology map. Synclinal, anticlinal, faults, and magmatic intrusion have not been imaged by these data sets but can clearly be observed in the existing geology map even though there is a need for improvement of both geology maps. A combination of the geology map from this study and that of literature has shown great improvement and update the general understanding of the geology of the trough (Fig. 2.30).

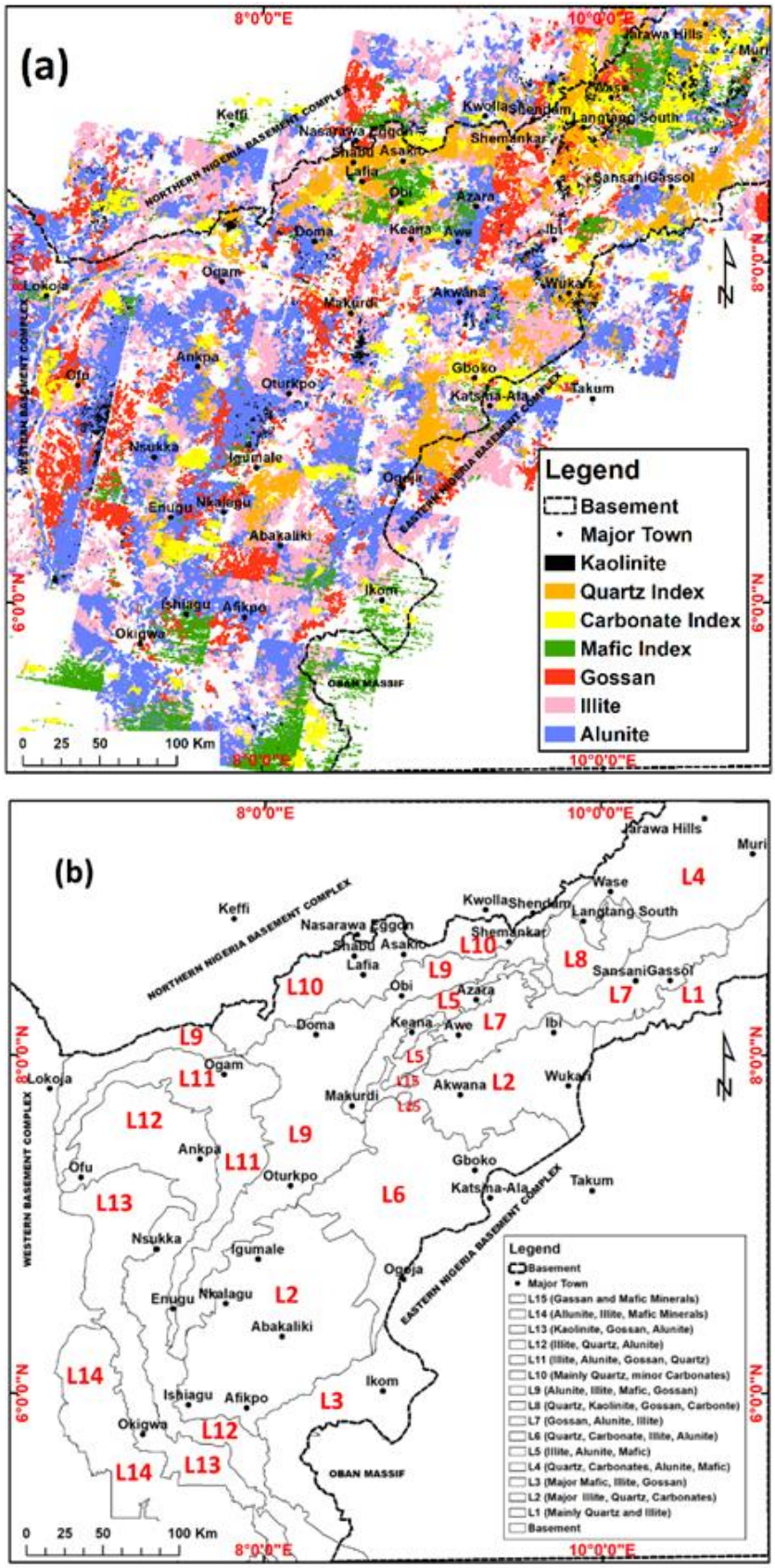

Fig. 2. 29: (a) Combined lithological map from ASTER SWIR and TIR data using spectral angle mapper (SAM) (b) Compiled lithological boundary map extracted when there is distinct spectral differences between lithologies.

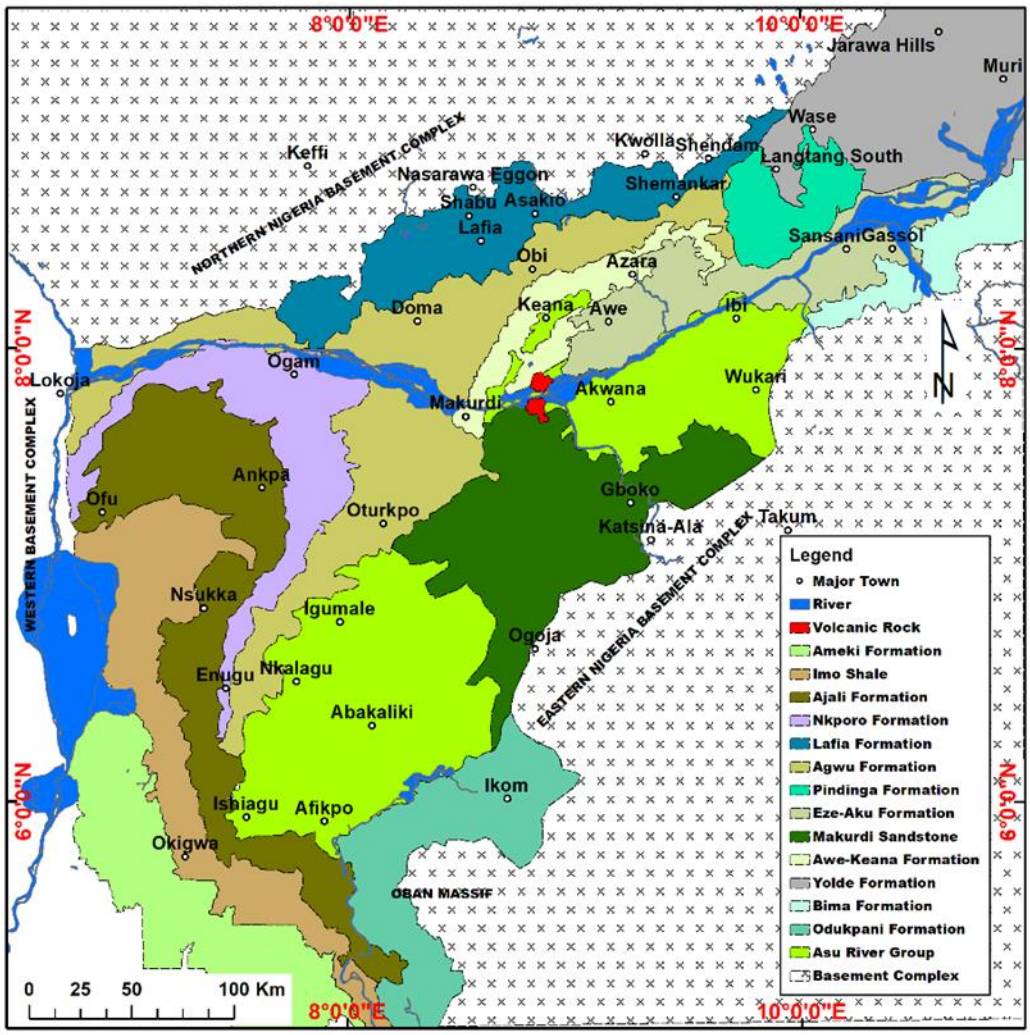

Fig. 2. 30: Interpreted geological map from remote sensing (ASTER and Landsat)

2.4 Methods for mapping surface lineaments from remote sensing data sets

2.4.1 Techniques

Several mapping techniques can be used to delineate surface lineaments from remote sensing data sets. Shaded relief, Sobel edge detection, directional and non-directional filters were applied to enhance remote sensing data for mapping geologic structures within the area.

2.4.1.1 Shaded Relief Technique

The shaded relief technique involves the use of multi-azimuth and elevation angles or tilt angles of simulated sun illumination on the topographic surface (Saadi et al., 2008). To address the problem of shading which makes a false determination of structural direction, an ATMDS technique involving illumination model of light in all directions is used to get the maximum shade intensity at each kernel size (Masoud and Koike, 2006; Masoud and Koike, 2011) as it enhances linear features.

2.4.1.2 Directional Filters

Directional filters are applied to detect edges of images by calculating their first derivatives or slopes (Papliński, 1998). It produces output images in which the brightness values at a given pixel are functions of some weighted averages of the brightness of the surrounding pixels. The first derivative edge enhancement filter selectively enhances image features in a specific direction (Haralick et al., 1987). Directional filters can be designed for *x*- and *y*-directions within a given space and areas with uniform pixel values are zeroed in the output image, while those that are variable in a particular direction are presented as bright edges defining the edges of the structures.

2.4.1.3 Sobel Edge Detection

Sobel edge detection is a non-directional filter that enhances edges in images in all directions. The Sobel operator helps in computing a discrete gradient in the horizontal and vertical directions at a pixel location within the image (Richards and Jia, 2006). This helps to detect horizontal, vertical, and diagonal slope edges (Marghany and Hashim, 2010) (Abarca, 2006) that are related to geological structures.

2.4.2 Delineating surface lineaments from remote sensing datasets

2.4.2.1 Shuttle Radar Topographic Mission (SRTM)

A shaded relief image of SRTM data was created from the topography modelling tool in ENVI software downloaded from L3Harris geospatial solutions website using a 3 x 3 kernel size varied at 15°, 30° and 45° sun elevation and azimuthal angles of 0°, 45°, 90° and 135°. A total of twelve separate shaded relief images with modelled light sources coming from three different directions were obtained (Appendices A6, A7, and A8). Lineaments were automatically extracted in PCI Geomatica software sourced from the Catalyst PCI geomatica website (Fig. 2.31). Most of the lineaments were extracted in the southern part of the area where the topography is higher and seems to be controlled by structural features (Fig. 2.32 a). Again, the lineaments are detected without any distinction between tectonic and lithological/bedding or erosional features, making it difficult to interpret faults (blue rectangle). The black rectangle at the middle of the study area shows the presence of curved lineaments which may be evidence of folding or faulting. Results show that the lineaments trend dominantly in the NE-SW direction about a mean vector of 72° (Fig. 2.32 b). Fig. 2.33 (a) focuses on the middle lineaments showing curved and curvilinear features that trend dominantly in the major NE-SW and subordinately in NW-SE directions (Fig. 2.33 b). The inability of the automatic lineament extraction technique to differentiate between tectonic and erosional structures is typified in fig. 2.34 a. Fig. 2.34 (a) shows linear structures that may not be tectonically formed, but instead due to erosion and other methods. A rose plot of the lineament indicates a slight NE-SW major trend but is masked strongly by bedding-related geometries (Fig. 2.34 b). The automatic extraction method mapped lineaments, lithological boundaries, trends of layers, and other erosional features without preference to tectonic lineaments. The processes of removing non-tectonic lineaments to produce a structural geological map are discussed in chapter 4.

A directional convolution filter of 3 x 3 kernel size in a moving window with 45-degree positive angle was applied to the SRTM to extract the lineaments. Four filtered images were obtained, and lineaments were manually extracted in the ArcGIS environment which was downloaded from ESRI website (Appendix A9). The lineaments extracted were combined to produce a lineament map and overlaid on SRTM (Fig. 2.35). The extracted lineaments show a general NE-SW trend and minor but significant NW-SE trend (Figs. 2.36 a and b). The manual method of lineament extraction resolved lineaments better but with fewer structures imaged than the shaded relief model. The minor lineament trends may be due to bedding contacts or boundaries

that interact with erosion levels and topography. Lineaments are better enhanced and mapped with the SRTM than those from Landsat due to the radar sensor that images bare earth with less vegetation, cloud, and night-time influences (Haralick et al., 1987; Hofton et al., 2013).

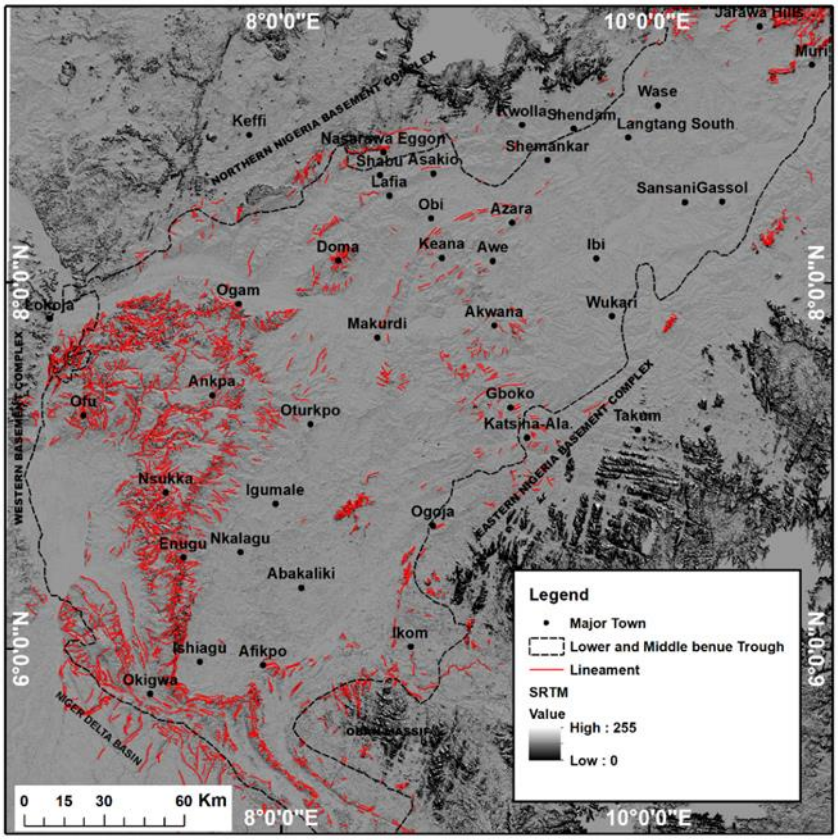

Fig. 2. 31: Lineaments delineated and draped over shadow relief model plotted with minimum values highlights.

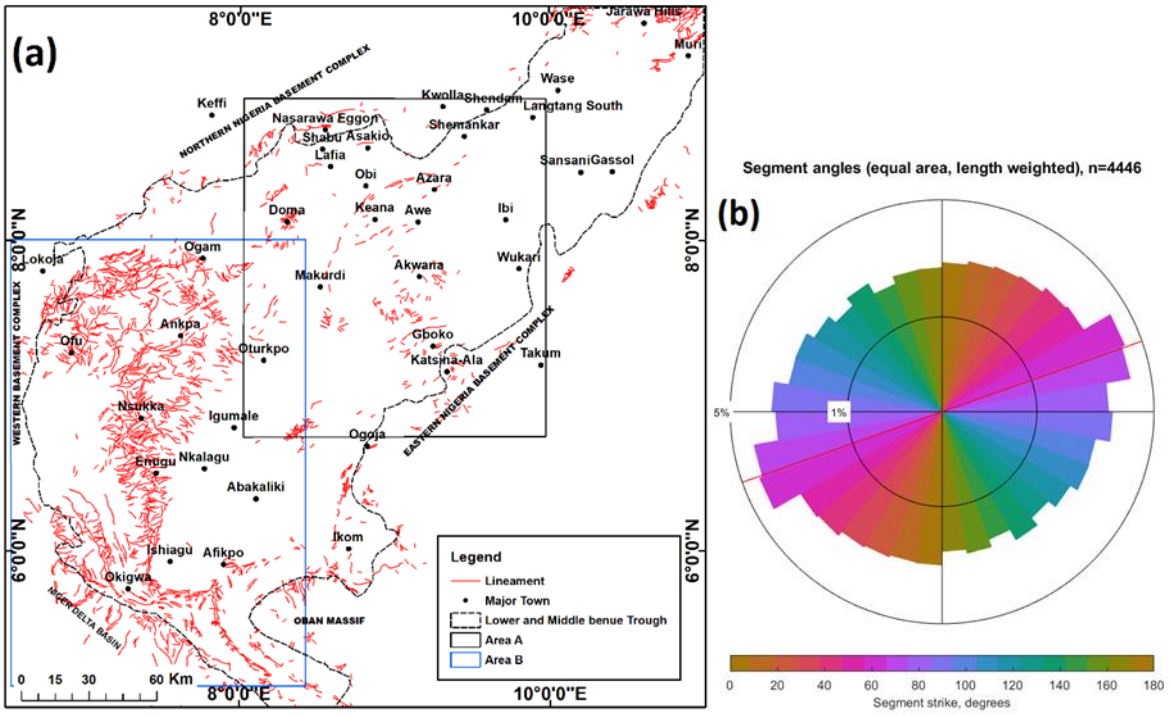

Fig. 2. 32: (a) Extracted SRTM lineaments. Two areas of interest with the upper (black rectangle) and the lower parts (blue rectangle) showing significant linear trends (b) a rose plot diagram showing the major NE-SW lineament trend.

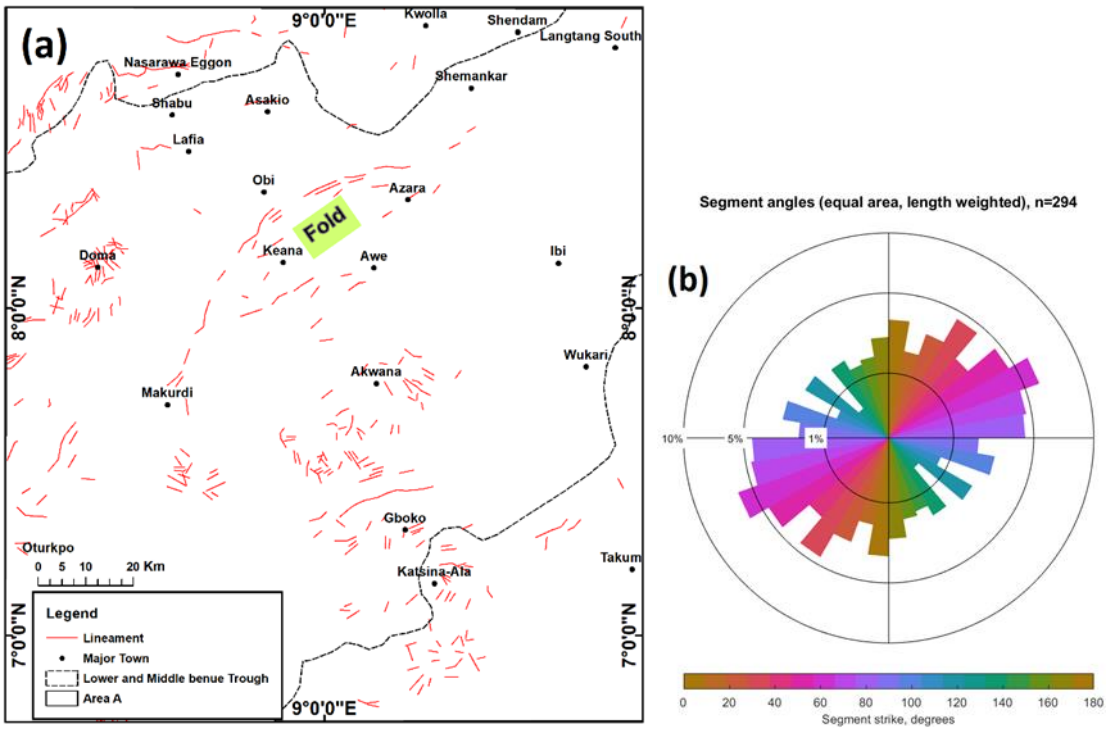

Fig. 2. 33: (a) Extracted lineaments of the middle part of the area showing possible folding of the structure around Keana (b) A rose diagram with a predominant NE-SW and minor NW-SE structural trends.

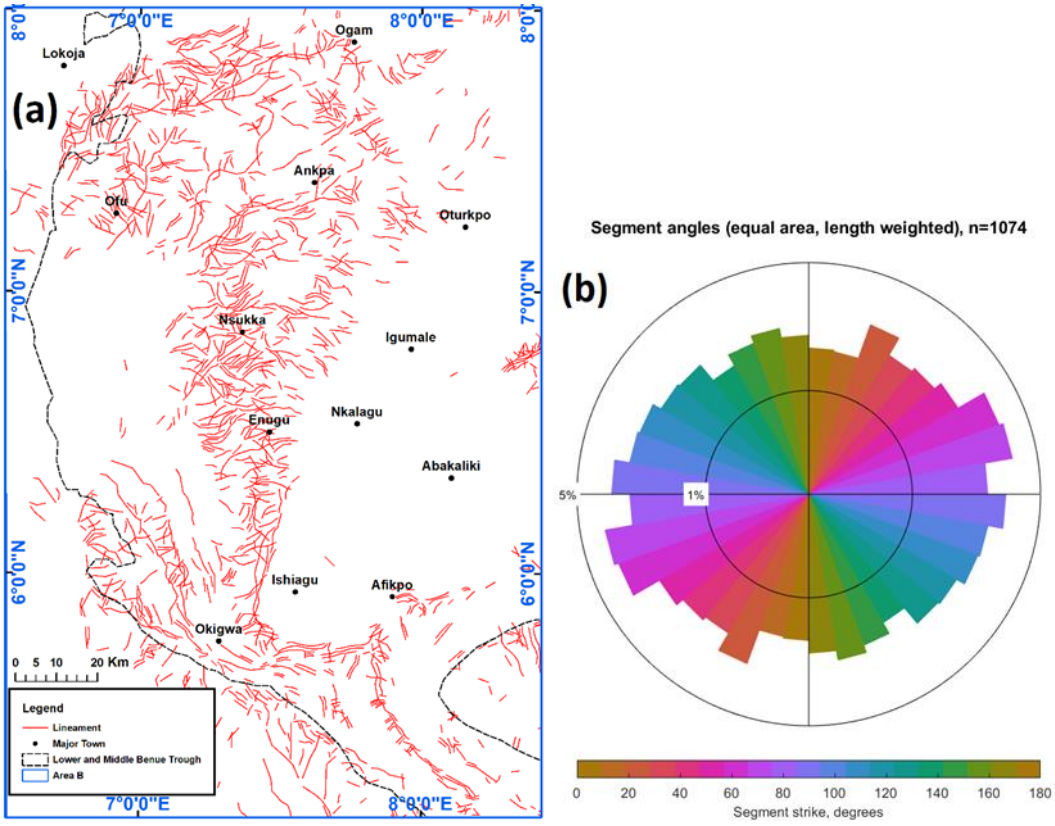

Fig. 2. 34: (a) SRTM lineaments of the southern part of the area (b) A rose diagram with a major NE-SW direction.

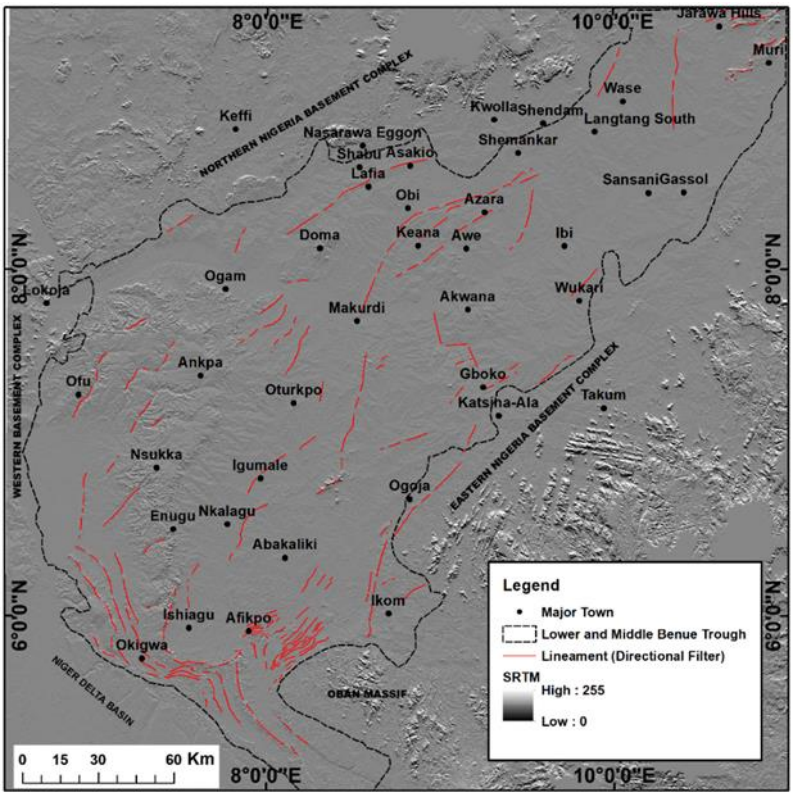

Fig. 2. 35: Lineaments draped over from SRTM using the directional filtering technique

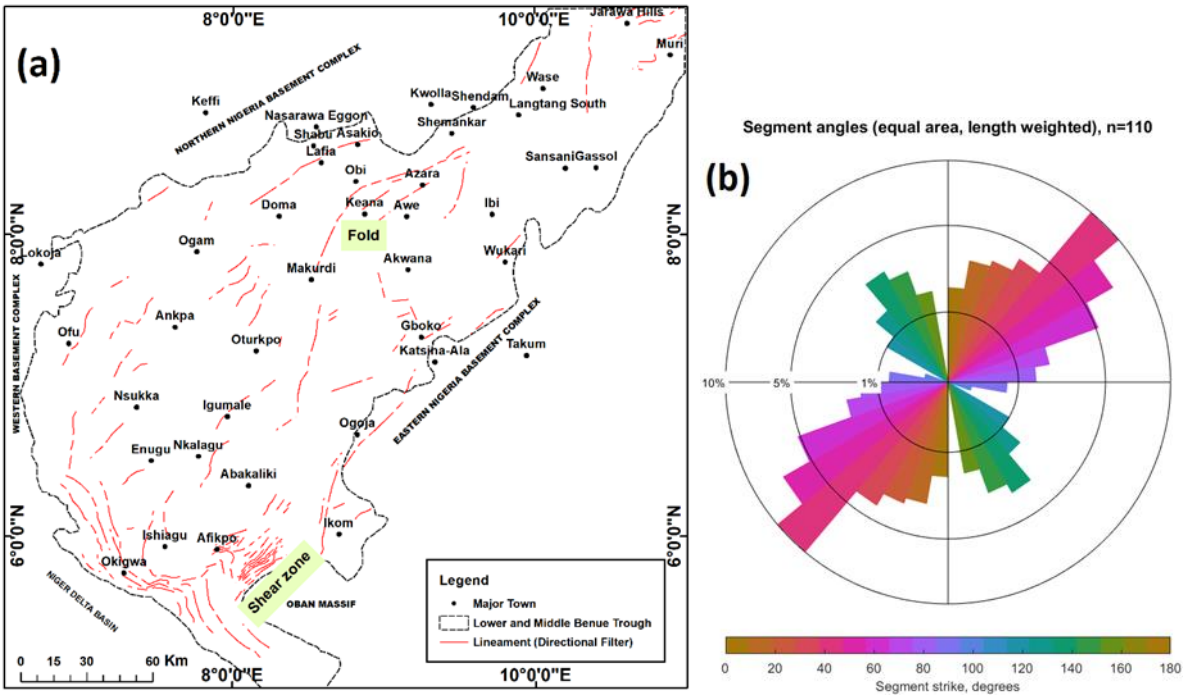

Fig. 2. 36: (a) Extracted SRTM lineaments showing areas of possible folded and sheared zones (b) a rose plot diagram showing a major NE-SW and a minor NW-SE structural trend.

2.4.2.2 Landsat 8 PCA colour composite

Structural features that may not be so obvious on SRTM data but can become clearer on Landsat due to differences in the textural cover pattern of an area. A directional filter of 3 x 3 kernel size window was used to enhance the appearance of Landsat PCA colour composite for extraction of lineaments in ENVI software. The lineaments were manually delineated and examined in ArcGIS software produced by ESRI and overlaid on the directional filter (Fig. 2.37). This image looks blurred due to the poor resolution of the Landsat image after PCA. Manual extraction was preferred in this case because the automatic extraction method does not discriminate between man-made and geological features during the analysis (Hung *et al.,* 2005; Abdullah *et al.,* 2010; Masoud and Koike, 2011). Again, the Sobel edge detector, which is a non-directional filter operator with the advantage of detecting edges of structures was tested (Richards and Jia, 2006). A filter threshold of 5 x 5 kernel size in a moving window for 45-degree positive varied angle was applied to the Landsat 8 PCA composite and several lineaments were extracted (Fig. 2.38). A road network map of the area was used as a guide to prevent mapping linear features associated with it. A general predominance of NE-SW and NW-SE lineament trends was observed from the combined lineaments of directional and Sobel filters (Fig. 2.39 a and b). The short length and poor imaging of the geologic structures are consequences of vegetation and sediment cover which impede the ability to pick continuous and extensive geologic structures.

The extracted lineaments observed from Landsat 8 and SRTM have been carefully selected based on lineament lengths greater than 4 km after removal of trends from lithological boundaries (Fig. 2.40 a). A rose diagram showing lineaments' orientations (Fig. 2.40 b). The result does not indicate any preferred lineament orientation and could be attributed to the presence of geologic and non-geologic lineaments. These trends are indications of the major tectonic activities that affected the basin over the years (Anudu et al., 2014).

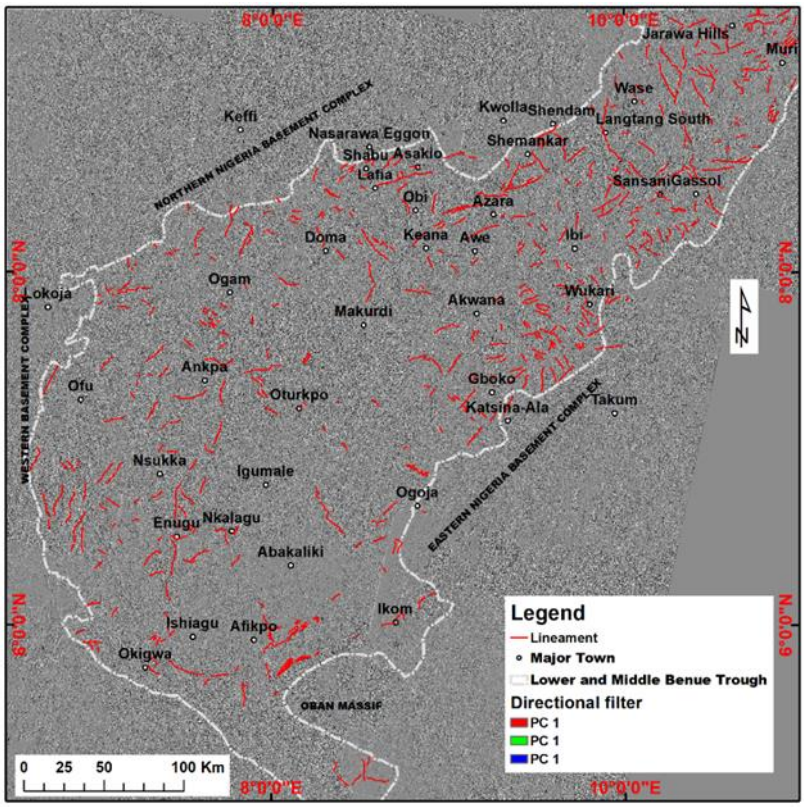

Fig. 2. 37: Lineaments extracted from directional and non-directional filters superimposed on Landsat 8 PCA image.

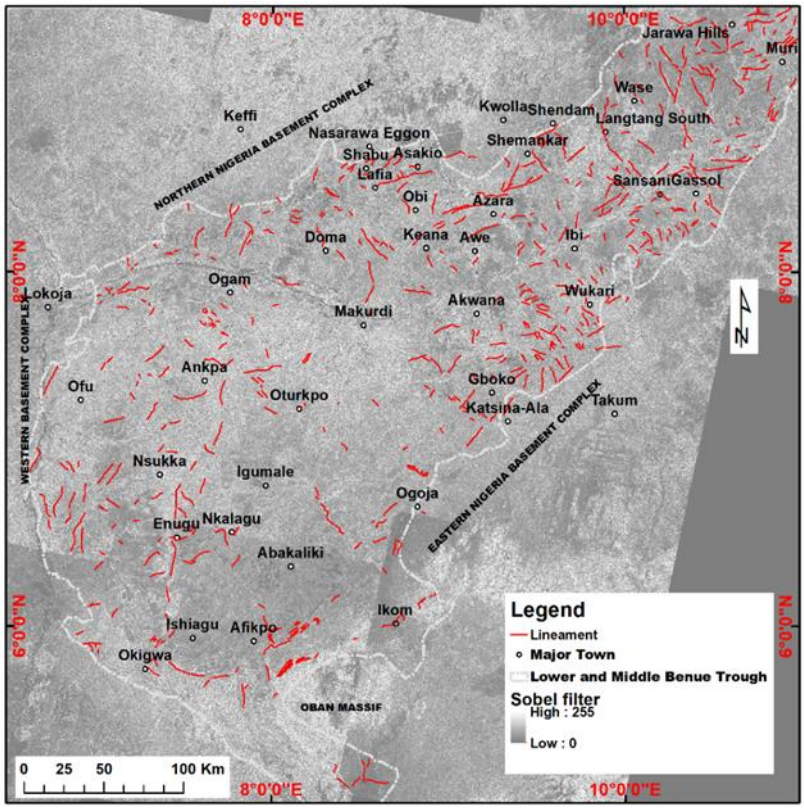

Fig. 2. 38: Sobel filter with lineaments overlaid on Landsat 8 PCA.

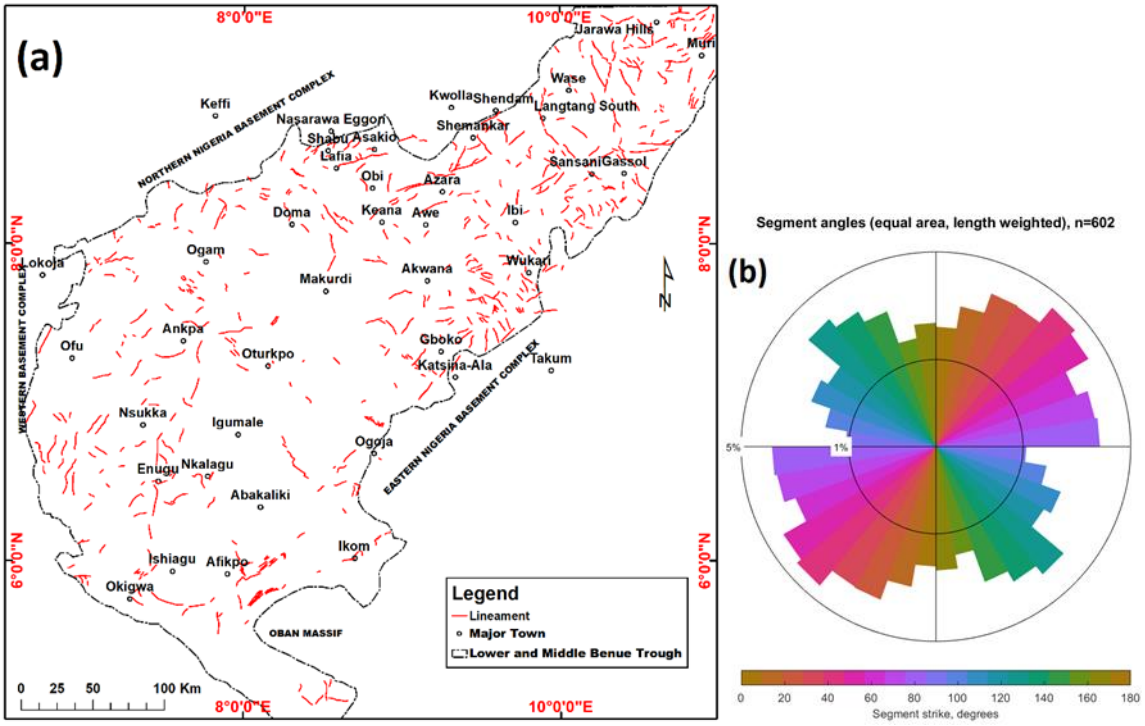

Fig. 2. 39: (a) Lineaments extracted from Landsat 8 analyses PCA (Directional and Sobel filters) (b) rose diagram showing the number of lineaments analysed and their orientations (major NE-SW and NW-SE directions).

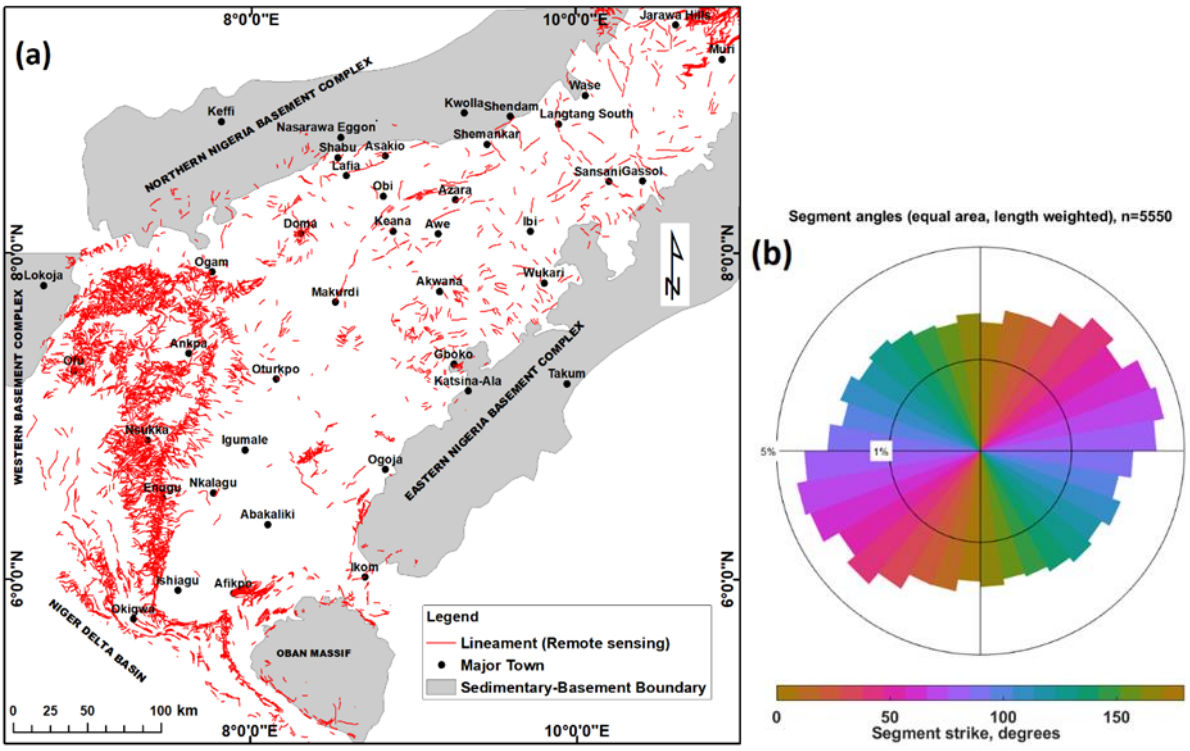

Fig. 2. 40: (a) Interpreted lineaments from remote sensing (SRTM and Landsat) (b) rose diagram with no distinct structural trends due to the presence of both geologic and non-geologic lineaments.

CHAPTER THREE

MAGNETIC AND GRAVITY DATA SETS AND METHODS

3.1 Introduction

The area of study is part of the Benue Trough comprising of the Lower and Middle Benue Trough. This chapter focuses on the techniques for processing magnetic and gravity data sets and the methods for mapping and delineating surface and near-surface lineaments as well as other geologic features. The main targets are to update knowledge of the existing geology and structures of the basin using interpretations derived from this study to understand the tectonic processes that led to the current basin morphology. The data sets used for the study are aeromagnetic and gravity data sets.

The steps and procedures for mapping surface and near-surface geological lineaments and bodies are presented. A key stage in the processing of the magnetic data sets was the transformation of the TMI map into RTE and RTP which are transforms that both help to shift anomalies directly over the source magnetizations for proper interpretation. Processed gravity and magnetic data sets were first separated into regional and residual components by depth slicing the various components through power spectrum analyses. The residual anomaly components relating mostly to shallow structures, were obtained and derivative-based techniques, Euler deconvolution, and other filters were applied to enhance the residual anomaly map and map out near-surface features and lineaments.

This chapter gives a clearer preliminary understanding of lineaments and igneous bodies and provides additional data interpretation for improving the geology map in chapter four.

3.1.1 Magnetic and gravity fields background and methods

3.1.1.1 Magnetic field background and methods

Magnetics technique determines the sub-surface spatial distribution of rock magnetization properties, J, or susceptibility, k and remanence causing changes in the Earth's magnetic (geomagnetic) field strength and direction (Fairhead, 2015).

The geomagnetic field is the space through which the influence of the centre of the Earth's magnetic field is exerted (Esuene, 2012). It comprises of three major sources as described below.

$$\mathbf{B_{obs} = B_{core} + B_{crust} + B_{external}} \text{.....(3. 1)}$$

Where B_{obs} is the observed geomagnetic field; B_{core} represents the magnetic field derived from the core; B_{crust} represents local anomalies of magnetic field because of the presence of anomalous crustal and/or lithospheric magnetic sources while, and $B_{external}$ represents atmospheric, ionospheric and magnetospheric contributions usually considered as very noisy in studies of the crust or core.

IGRF is a standard mathematical model that is employed to describe the Earth's core field (B_{core}) for the period of five years (Finlay et al., 2010). B_{crust} is earth-sourced magnetic field data acquired on the ground, aeroplanes, or ships. They are contributions from magnetisation of crustal rocks bearing ferromagnetic minerals such as magnetite, titanomagnetite, pyrrhotite, that are at temperatures below the Curie point (Esuene, 2012). It is important to note also that magnetization can be induced by an external magnetic field known as induced magnetization. Contributions to the geomagnetic field that are external to the Earth can be derived from the Earth's ionosphere and magnetosphere. The $B_{external}$ contributes short wavelength noise to marine and aeromagnetic data sets (Maus et al., 2007). It is important to subtract combined models by all the long wavelength due to core magnetic fields, as well as external fields from magnetic field observations, to obtain crustal magnetic anomalies.

Geomagnetic dipole field measurement can be sub-divided into a range of components (Fig. 3.1). The magnetic inclination, I, is the angle between the horizontal plane and the magnetic field vector while the declination, D is the angle on the horizontal plane between magnetic north and true north (the geographic North Pole) (Hinze et al., 2010; Fairhead, 2015).

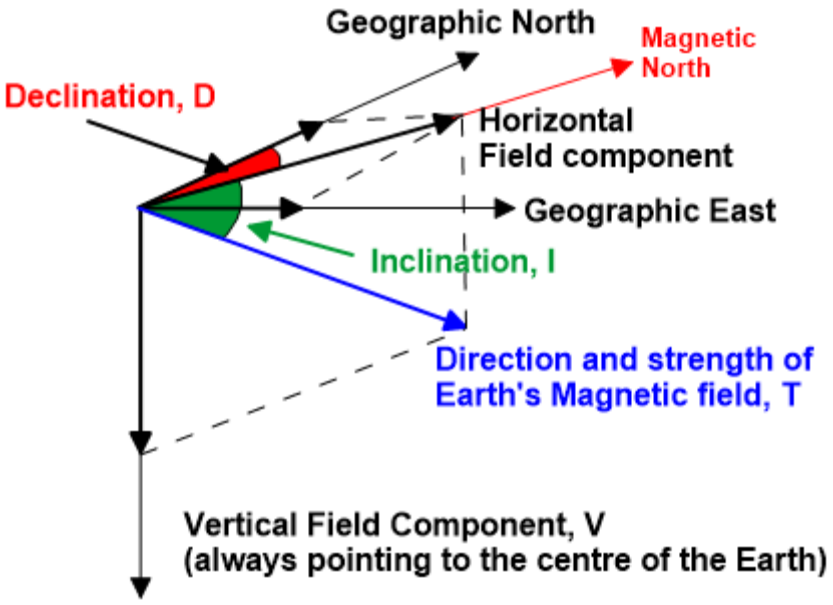

Fig. 3. 1: Measured geomagnetic field components

Blakely (1996) relates B_{obs} in equation 3.1 to the Magnetic field intensity or strength (TMI or T) which represents local magnetic field anomalies superimposed on B_{obs} where magnetite-bearing crustal media occur. B_{obs} is the sum magnetic response of microscopic and macroscopic surface magnetization currents while T is easily measured by magnetometers and represents magnetic fields strength produced in response to macroscopic magnetization currents on the surface of anomalous magnetic media in the subsurface (Blakely, 1996).

$$\mathbf{T_{obs} = T_{core} + T_{crust} + T_{external}} \text{.....(3. 2)}$$

T_{obs} is the measured T, T_{core} represents the core-derived field, T_{crust} represents local perturbations of T due to the presence of anomalous crustal magnetic sources, and Texternal represents atmospheric contributions (Noise). These variables are assumed to be parallel.

The difference between the observed and theoretical TMI values for each location assuming that external contributions have been removed is known total magnetic field intensity (TMI) anomaly, ΔT and can be estimated as

$$\Delta \boldsymbol{T} \equiv \mathbf{T_{crust} = T_{obs} - (T_{core} + T_{external})} \text{.....(3. 3)}$$

T_{core} induces secondary magnetic fields, T, in crustal magnetic minerals through its magnetization. The volume of the crustal magnetization, J_v, is the sum of the induced magnetization, J_i and remanent magnetization components, J_r. J_i is the magnetization observed in rocks that contain ferrimagnetic minerals in the presence of inducing or ambient magnetic fields while J_r observed in ferrimagnetic materials when there is permanent record of magnetizations acquired by a rock over its history (Esuene, 2012).

$$\mathbf{J_v = J_i + J_r} \text{.....(3. 4)}$$

Where, $J_v = kT$, and k is a dimensionless constant called magnetic susceptibility, which is positive when the J_r is in the same direction as J_i.

3.1.1.2 Gravity field background and methods

Gravity method determine the sub-surface spatial distribution of rock mass. The variations in the mass distribution can give changes in the Earth's gravitational field strength and are easily observed and mapped.

Sir Isaac Newton showed that the Earth's gravitational force field, F between two monopoles of strength masses, m_1 and m_2 situated at a distance, r apart as.

$$F = G\,{}^{m_1 m_2}/_{r^2} \ldots\ldots\ldots\ldots\ldots (3.5)$$

The gravitational pull on mass body close to the Earth's surface is small compared with the overall gravitational effect of the Earth (Hinze et al., 2010). The density of a body is commonly used in gravity study rather than the mass as it is defined as the mass per unit volume. The gravity response at the surface in terms of gravity difference, measure by a gravity meter, normally measures the vector (vertical component) sum of the Earth's gravity field plus the vertical component of the 3D variation in the density of the near surface geology. The density of sediments increases with depth but its density contrast decreases with depth within a sedimentary basin since the higher density crystalline basement rocks that surrounds the base already have high density and do not change with depth (Fairhead, 2015). The gravity effects of the near-surface sediments that have lower density and high-density contrast with respect to the basement gives rise to a large gravity effect.

The density of a body is usually determined using gravity data sets by estimating the value of Bouguer anomaly, BA. BA is defined as

$$\mathbf{BA = g_{obs} - g_{th} + 0.3086 - 0.04191\rho h + T_{\rho} \ldots\ldots\ldots\ldots\ldots (3.6)}$$

Where h is the elevation of the observation point in metres, ρ is the density in g/cc, g_{obs} is observed gravity, g_{th} is the theoretical gravity, T_{ρ} is terrain correction.

3.2 Magnetic data sets processing

The magnetic data set used in this study is the high-resolution aeromagnetic data acquired by Fugro Airborne Surveys on behalf of the Nigerian Geological Survey Agency (NGSA). The survey employed 3 x Scintrex CS3 Cesium Vapour magnetometers that were flown along a series of NW-SE (135°) flight lines perpendicular to the general regional geologic structural trend. This was done at 500 m line spacing and 5000 m tie-line spacing between the years 2005 and 2007 as part of the first phase of the African project. The data were recorded at 0.1-second interval with 80 m mean terrain clearance making the resolution better than earlier available high-altitude data (Reford *et al.*, 2010; Anudu *et al.*, 2014). A total of fifty-three aeromagnetic grids, each measuring about 111 km x 111 km were knitted to form one grid covering the study area (Fig. 3.2). A bi-directional gridding technique with cell size of 125 m by 125 m being one-quarter of the flight line spacing (Geosoft, 2004; Foss, 2011) was used, and a TMI map for the study area produced. The TMI ranges from -2330.6 nT to 1259.2 nT and is characterized by anomalies on short, medium, and long wavelengths. The short wavelengths (high wavenumber)

anomalies are observed mostly outside the basin and in a few places within the basin that are typified by basement highs and intrusive rocks. The long-wavelength (low wavenumber) anomalies are seen within the basin signifying deep magnetic anomalies associated with the deep basement.

The interpretation of TMI anomalies at low magnetic latitudes is very challenging compared to the same task at high latitudes (Beard, 2000). One of the difficulties encountered at low magnetic latitudes is finding a suitable process that will vertically align the magnetization direction and the direction of the measured field. Unless this is achieved, the anomaly will be shifted laterally with respect to its source, and its shape will be distorted, making magnetic and geologic interpretations very difficult (Li, 2008). Reduction to the equator or the pole techniques have been applied over the years to transform TMI anomalies so that they align over their sources (Arkani-Hamed, 1988; Swain, 2000; Li, 2008; Zhang et al., 2014) and aid in geologic interpretation.

3.2.1 Reduction to the Equator (RTE)

The RTE operator is usually employed at low magnetic latitudes to centre of magnetic anomalies lows over the disturbing source (Geosoft Inc., 2015). RTE corrects the amplitude of the TMI and suppresses N-S structures. This method produces an interpretable map by removing the effects of magnetic inclination and preserving the amplitude of the anomaly.

Assuming all magnetization in source is induced, the RTE operator in the wavenumber domain is calculated in 2D FFT and expressed as:

$$\boldsymbol{L(\theta) = \frac{-\cos^{-1}(D+\theta)}{[\sin(I)+i\cos(I)\cos(D-\theta)]^2}} \quad \textbf{.....(3. 7)}$$

Where θ, i , I, and D are the wavenumber component horizontal direction, square root of -1, inclination, and declination of both the magnetic field and the magnetization of the causative body, respectively. $\sin(I)$ is defined as the amplitude component while $i\cos(I)\cos(D-\theta)$ is the phase component.

The 2D FFT helps to transform the magnetic data which is normally expressed in the space domain in x and y directions into the wavenumber domain. This makes calculation of the operation faster (Geosoft Inc., 2015). The wavenumber domain usually samples the Fourier domain function at even increments of 1/ (grid size) (cycles/ meter) between 0 and the Nyquist wavenumber (1/ [2*cell size]). Usually, the wavenumber has both negative (imaginary) and

positive (real) parts such that the main representation is centered around zero, and the closer values to the center point are dominated by long wavelengths (Fairhead, 2015).

The 2D FFT of a function varying in the space domain as $f(x, y)$ is mathematically calculated based on:

$$\bar{f}\,(U, V) = \int_{-\infty}^{\infty}\int_{-\infty}^{\infty} f(x, y)\,.\,e^{-(ux,vy)}\,dx\,dy \ldots\ldots\ldots\ldots (3.8)$$

While the reciprocal relationship is given by:

$$f(x, y) = \frac{1}{4\pi^2}\int_{-\infty}^{\infty}\int_{-\infty}^{\infty} f(x, y)\,.\,e^{-(ux,vy)}\,dU\,dV \ldots\ldots\ldots (3.9)$$

Where U and V are wavenumbers in the x and y dimensions, respectively, measured in radian per metre and relate to spatial frequencies of $f(x)$ and $f(y)$ in cycles per metre.

The RTE transformation gives a result like the TMI without significant loss of any geophysical meaning (Esuene, 2012). The RTE transform provides a partial alternative to RTP, which becomes unstable at low geomagnetic latitude, they both help to shift anomalies directly over the source magnetizations (Foss, 2011; Anudu *et al.*, 2014; Appendices B1 and B2). The limitations of this technique are that it may cause undesirable results in practice, such as slight amplification and elongation of anomalies in East-West directions and non-imaging of N-S features.

The RTE transformation is sensitive to magnetic inclination and declination (equation 3.7). Based on the IGRF model, these parameters show significant variations across the study area (Appendices B3 a and b). The inclination ranges between -4.37°in the north and -16.43° in the south while the declination decreases from -1.07° in the north-eastern part to -2.88° in the south. These variations in the geomagnetic inclination and declination are large enough to imply that the application of average values to the RTE operator may lead to inappropriate results. Therefore, differential reduction of the TMI may be most appropriate in this case. This technique has been applied to areas at a high geomagnetic latitudes where magnetic inclinations and declinations very strongly (Arkani-Hamed, 2007; Ali et al., 2017). A comparable procedure was adopted and applied to the TMI data with the aim of reducing the effects of the variation in inclination and declination on the RTE results and, in this study, it is called the differential reduction to the equator technique. The process of DRTE involved dividing the data into eight (8) strips with a degree (1°) latitude range and a 30-minute overlap (Appendix

A4) and average values of inclination and declination are calculated for each strip. The standard RTE transform was applied multiple times to the whole area, each using the estimated mean inclinations and declinations from one of the strips. The appropriate strips for each declination/inclination pair were combined into a large scale DRTE grid to cover the entire area (Fig. 3.3). The DRTE map is very similar to the TMI map, but closer inspection reveals that the DRTE has helped in positioning the anomalies over disturbing sources (black arrows on the map). Negative DRTE magnetic anomalies are directly situated over sources of disturbance with negative magnetic susceptibility.

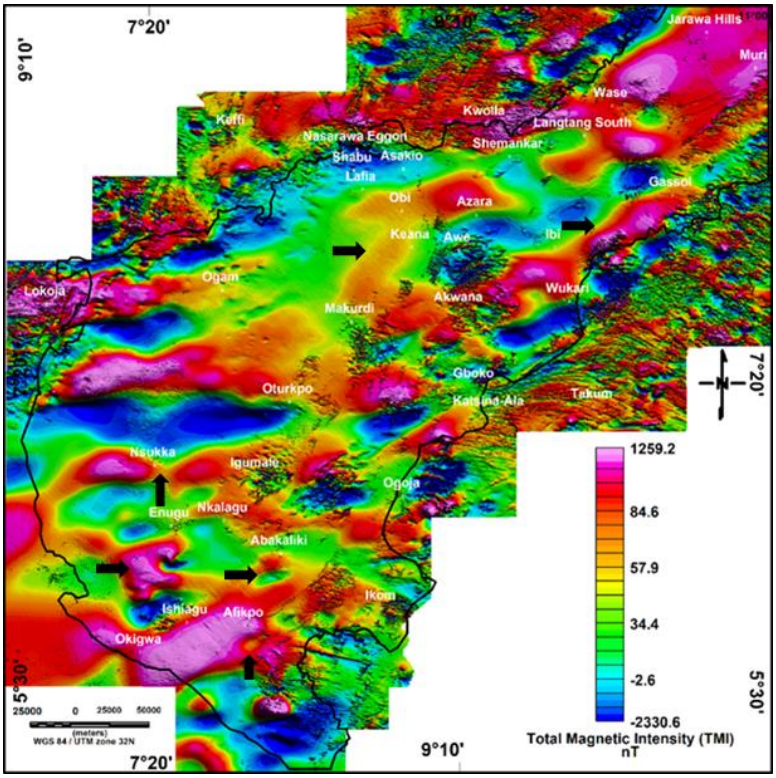

Fig. 3. 2: Total Magnetic Intensity (TMI) map that has been colour filled and histogram equalised. The purple to red colours show areas of high magnetic values while the blue colours signify areas of low magnetic values.

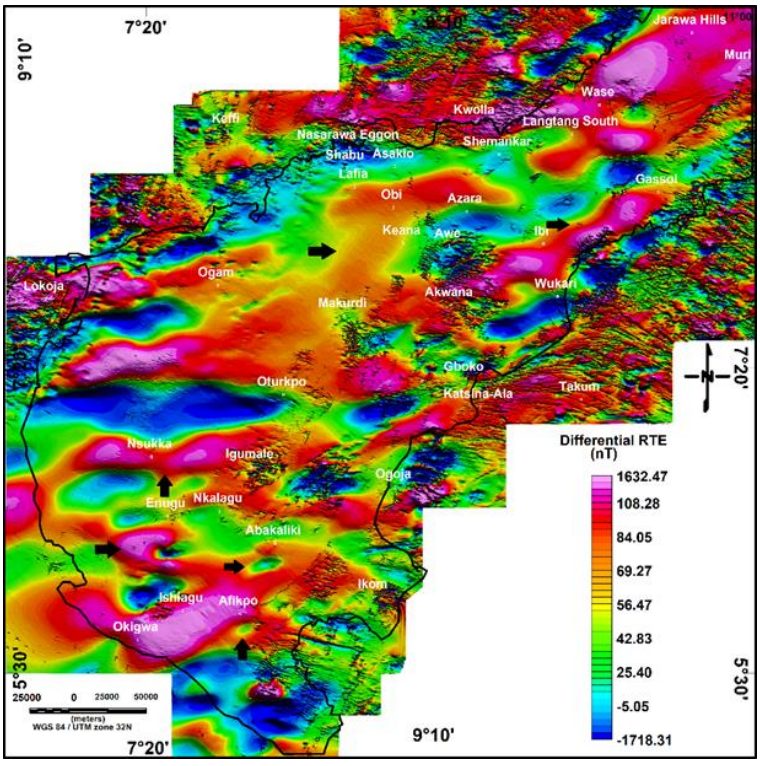

Fig. 3. 3: Results of Differential Reduction to the Equator transformation of TMI data. Black arrows show anomalies that have been significantly transformed and positioned vertically over their sources

3.2.2 Reduction to the Pole (RTP)

RTP operator transforms the TMI anomaly to the form that would have been measured at the north magnetic pole i.e., it locates the anomalies vertically above their sources of disturbance (Swain, 2000; Li, 2008). It is usually difficult to reduce magnetic anomalies to the pole at low latitudes due to instability of results from N-S structures.

The RTP operator for a single 2D FFT component can be expressed as:

$$\boldsymbol{L(\theta) = \frac{1}{[\sin(I)+i\cos(I)\cos(D-\theta)]^2}} \quad \textbf{.....(3. 10)}$$

From equation 3.10, the RTP becomes unstable when the absolute magnetic inclination, I is small (the real part is close to zero) and D–θ is near ± 90° making the imaginary part also close to zero (Li, 2008). This instability causes the transformed anomaly to align within a narrow wedge-shaped area centred on the declination direction (Fig. 3.4). The effects is to amplify and blow up anomalies that are oriented North-South, making them uninterpretable (Tulyatid and Fairhead, 1996; Beard, 2000).

The standard RTP operator was applied to the TMI anomaly map of the area. The result shows the expected extreme elongation of anomalies in the N-S direction (Fig. 3.5). This distorts the magnetic anomalies and makes the map very difficult to interpret. As a result of this distortion, techniques such as the Differential Reduction to the Pole (DRTP), Azimuthal filter (AF) and Nonlinear Thresholding RTP (NTRTP) were applied to correct for the N-S strip blow up and make it more interpretable.

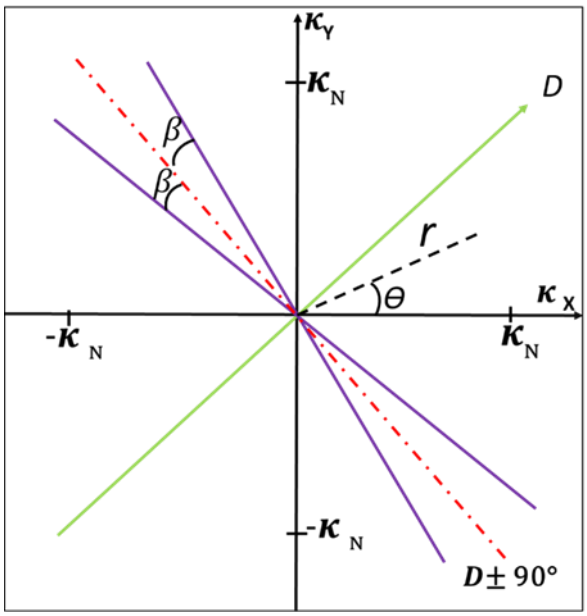

Fig. 3. 4: RTP operator in the wavenumber domain at low latitudes becomes unstable in a wedge-shaped segment (purple lines) centred along the direction of the magnetic declination. The threshold angle, β is relative to an azimuth of D±90° (Modified after Li, 2008).

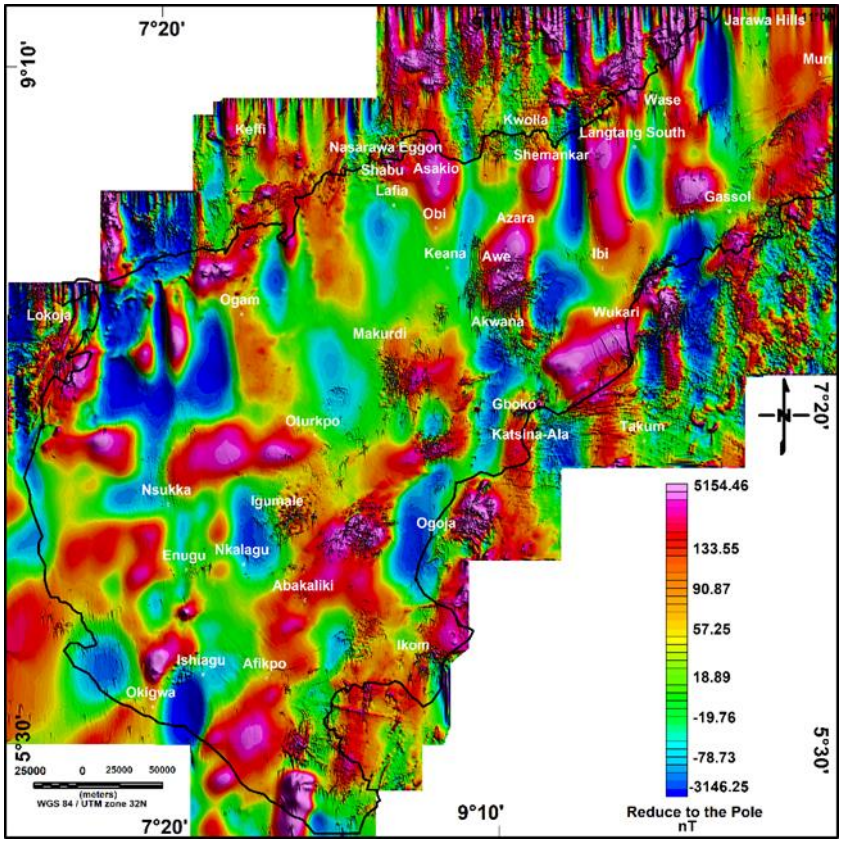

Fig. 3. 5: Reduced to the pole (RTP) magnetic anomalies showing extreme distortion in N-S direction leading to distortion of anomalies. This makes geological interpretation very difficult.

3.2.2.1 Differential Reduction to the Pole (DRTP)

This method addresses the problem of instability results observed from the amplification of features in magnetic N-S strike by introducing a second inclination (I') known as the 'phase parameter' or the pseudo-inclination to control the amplification and filter the anomaly near the equator (MacLeod et al., 1993; Li, 2008). The operator now becomes,

$$\boldsymbol{L(\theta) = \frac{1}{[\sin(I') + i\cos(I)\cos(D-\theta)]^2}} \quad \textbf{.....(3. 11)}$$

The value of (I') is set to be greater than the inclination of the magnetic field (I). The true inclination is used in the $i\cos(I)$ term and the chosen pseudo-inclination in $\sin(I')$. Li, (2008) suggested a value of I' between 20^0 and 30^0 for best results.

DRTP reduces the magnetic anomalies to the pole and corrects for the variation in inclination and declination by assuming that the geomagnetic field and the crustal magnetization have constant directions (Arkani-Hamed, 1988; Arkani-Hamed, 2007). The result is to shift positive magnetic anomalies towards the pole and suppress their negative lobes on the poleward side, thereby making positive anomalies symmetrical and position them directly over the causative body (Swain, 2000; Cooper and Cowan, 2005; Ali et al., 2017).

The TMI map of the area was divided into eight strips each with a degree (1°) latitude range and a 30-minutes overlap (Appendix A4). The mean inclination and declination of each strip were estimated from the IGRF model, and the standard RTP using the pseudo-inclination of 30° to suppress noise was applied. The strips were merged and filtered using 3X3 Hanning to smoothen and remove aliasing from the grid (Fig. 3.6). The result shows that DRTP has successfully corrected for the blown-up N-S structures and highlights many of the magnetic sources. However, amplitudes have been significantly increased during the process (e.g., the positive anomaly has increased from 1259 nT to 2008 nT and the minimum from -2330 nT to -2187 nT).

3.2.2.2 Azimuthal filter (AF) method

The azimuthal filter method uses directional or strike filters to selectively filter wavenumber components of magnetic anomalies which trend over a specific range of directions (Hinze et al., 2010). The filter is usually applied relative to the direction of the declination by using a threshold angle which smoothly tapers the RTP operator to suppress the linear artifacts that result from the N-S strip blow up (Phillips, 1997; Li, 2008; Fig. 3.7).

The azimuthal filter factor, $S(\theta)$ is given by.

$$\mathbf{S(\theta) = \sin^{p}\left[\frac{\pi|\theta - D \pm 90|}{2\beta}\right]}\ldots\ldots\ldots\mathbf{(3.\ 12)}$$

The exponential power parameter, p determines the falloff rate of the taper and has a weak effect on the RTP result while β denotes the threshold angle. Fig. 3.2 shows the orientations of various directions as it decreases from 1 at the edges of the wedge-shaped segment (the purple line) to 0 along the direction of the declination.

A threshold angle, β of 30° was applied on the RTP data (Fig. 3.5) and the N-S noise was effectively reduced by smoothly tapering it relative to the direction of declination to give a more interpretable result (Fig. 3.7). Small strips of artificial noise are introduced in the NW-SE direction during the tapering process. However, the filter has achieved its aim for it to ease the task of interpretation. A general increase in the amplitude of the result relative to TMI is observed from 1259 nT to 3328 nT for the maximum value and from -2330 nT to -1488 nT for the minimum compared to the distributed RTP grid, amplitudes are greatly reduced. though, there is a great reduction in the distorted RTP values.

3.2.2.3 Nonlinear thresholding RTP method

The NTRTP method divides the RTP operator into two parts; the real and the imaginary parts and applies a nonlinear threshold to suppress the large amplitudes associated with instability (Zhang et al., 2014; Zhang et al., 2018).

The RTP operator, Q is divided into.

$$\boldsymbol{Q = Re + i.Im}\ldots\ldots\ldots\mathbf{(3.\ 13)}$$

Where Re and Im represent the real and imaginary parts, respectively.

The main reason for the instability of RTP at low magnetic latitude is due to large amplitudes of *Re* or *Im* of the area. Therefore, a special filter is used to suppress the large amplitude responsible for the instability by application to both the real and imaginary parts.

$$\boldsymbol{Q = Re.F + i.Im.F}\ldots\ldots\ldots\ldots\mathbf{(3.\ 14)}$$

The filter, F, is obtained by using the sine function to constrain the amplitudes to between 0 and 1.

$$\boldsymbol{F = f(x) = \begin{cases} x, & \boldsymbol{abs\ (x) \leq 0.9A} \\ \sin(x).\left(0.9.A.\sin\left(\frac{\theta-\theta_1}{\theta_2-\theta_1}.\pi\right)\right), & \boldsymbol{abs\ (x) > 0.9A} \end{cases}} \quad \text{.....(3. 15)}$$

where x denotes the value of Re or Im, θ_1, and θ_2 denote the two edges of the wedge-shaped segment (Fig. 3.4). The smaller the amplitude threshold, A, the smoother the RTP result.

The NTRTP technique was employed to the TMI anomaly map of the area using the maximum amplitude threshold of 20° for the RTP operator and a low pass filter value of 0.3 times the Nyquist frequency. The transformation process was able to suppress the N-S strike strips that make the data difficult to interpret (Fig. 3.8). The transformation technique performed very poorly for shallow structures and as such, a low pass filter of 0.3 was used to suppress most of the shallow components. The NTRTP shows that it can perform better on isolated anomalies and deep magnetic sources than shallow structures with multiple sources of anomalies in a complicated area like the area of study.

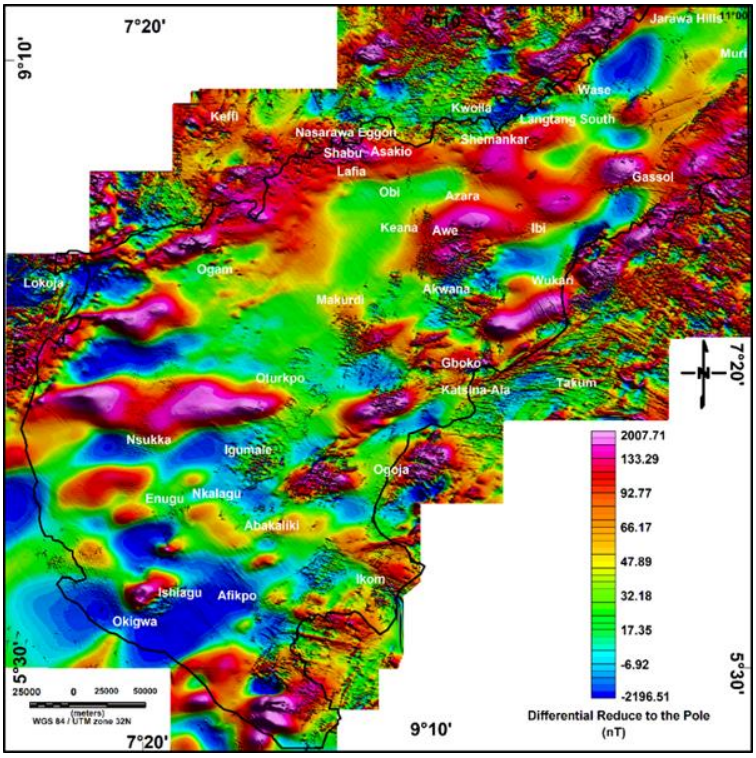

Fig. 3. 6: Differential reduction to the pole TMI. The N-S blown-up structures have been substantially reduced and many magnetic anomalies enhanced and placed vertically over their sources.

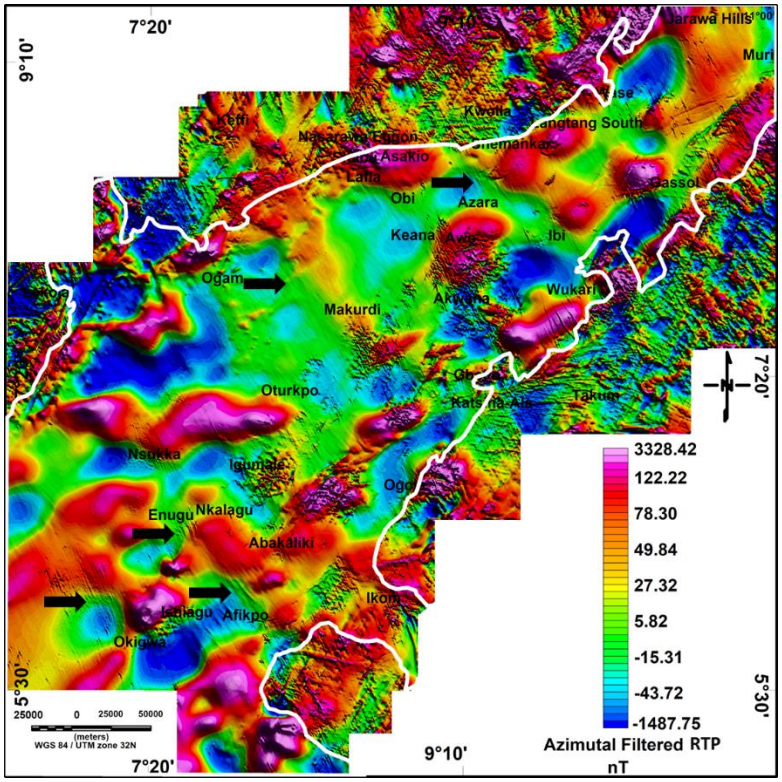

Fig. 3. 7: Azimuth filtered RTP. A threshold angle value of 30° was applied to the RTP to suppress the N-S strips that make interpretation difficult. There are small strips of distortion in the NW-SE direction (this is shown by the black arrows).

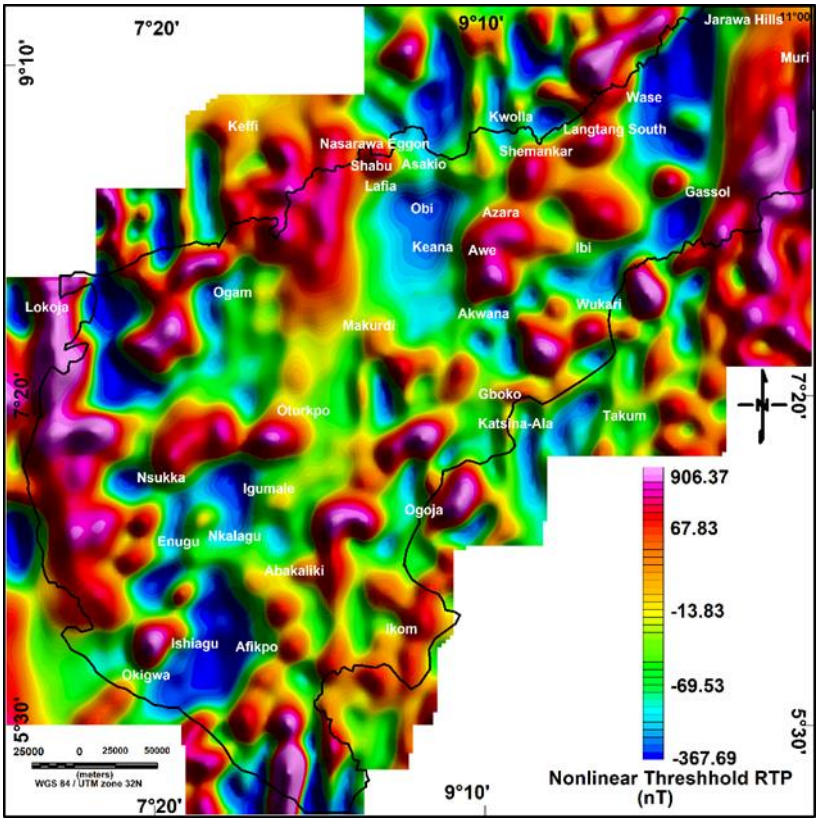

Fig. 3. 8: Nonlinear threshold RTP (NRTP) obtained using 20° maximum amplitude threshold, 0.5 exponential functions constant, and 0.3 low pass filter (the wavenumber larger than the 0.3 times the Nyquist frequencies are suppressed).

3.2.3 Regional-residual magnetic anomaly separation

The TMI anomaly dataset indicates magnetic anomalies over sedimentary basins that come from two main ranges of depths – the basement surface and variations within the crust (regional), and surface or shallow features which can be related to cultural "noise" and shallow intrusive and extrusive volcanic rocks (residual). The shallow or surface component is comprised of short-wavelength anomalies and originates from shallow depths, and the basement and crustal components are characterized by long-wavelength anomalies and are of greater depths source (Phillips, 2001; Ali *et al.*, 2017). Separation of the various components is possible because the magnetic fields have different characteristics in the TMI data (Foss, 2011). Many methods, such as the matched bandpass filter, power spectrum, upward continuation, polynomial and preferential filtering methods, have been used to separate the shallow and deep source contributions from magnetic data (Spector and Grant, 1970; Jacobsen, 1987; Phillips, 2001; Guo et al., 2013; Ali *et al.*, 2017; Koumetio et al., 2019).

3.2.3.1 Separating regional and residual DRTE anomalies using a matched bandpass filter.

The matched bandpass filter technique was initially designed to match the spectra of anomalies of a two-layer equivalent source model (Spector and Grant, 1970; Hinze *et al.*, 2010), but Phillips (2001) expanded the scope to be able to analyse multi-layer equivalent source models. This is a more robust process of matched filtering that enables the separation of the magnetic data into different wavelengths through a better overall fit to the spectrum, making it easier to process and map possible geologic structures at different depth averages.

The TMI DRTE data sets contain contributions from multiple crustal magnetization sources and as a result, the contributions can easily be individually separated out into their different anomalies for proper interpretation (Hinze *et al.*, 2010; Foss, 2011). The matched bandpass filter technique is achieved based on apparent depth slicing of the magnetic data into near-surface, shallow and deep solutions. In this study, the matched bandpass filter was applied on the TMI DRTE, and four distinct equivalent source layers were obtained by analysing the power spectrum plot using amplitude and Wiener filters (Fig. 3.9 a and b). The summary of matched bandpass wavelength filter results shows four depth slice ranges **(**Table 3.1). Layer 1 corresponds to a depth of about 60 m (Fig. 3.10 a) and is dominated by surface and/or cultural noise. Layer 2 corresponds to an equivalent dipole layer at depth of about 430 m, with wavelengths ranging between 388 m and 3109 m, and seems to be dominated by near-surface anomalies and some noise (Fig 3.10 b) while Layer 3 matches an equivalent source depth of

about 1834 m, and wavelengths of 3109 m to 15240 m (Fig. 3.10 c). Layer 4 is relatable to deep sources producing regional anomalies with a depth of about 8392 m (Fig. 3.10 d). It is important to mention that this separation method is not necessarily perfect as there could be a spill of anomaly signals across all depths. Thus, the process at best gives the average of the depths of most magnetic signals at such wavelengths rather than absolute values. Figs. 3.10 b and c depicts the two layers that may be most readily related to mapping surface or near surface geologic features and represent shallow magnetic anomalies or residual anomalies and are henceforth used for further analyses. These residual results can be utilized to map shallow structures and correlate them with surface geological structures or give more information about geology.

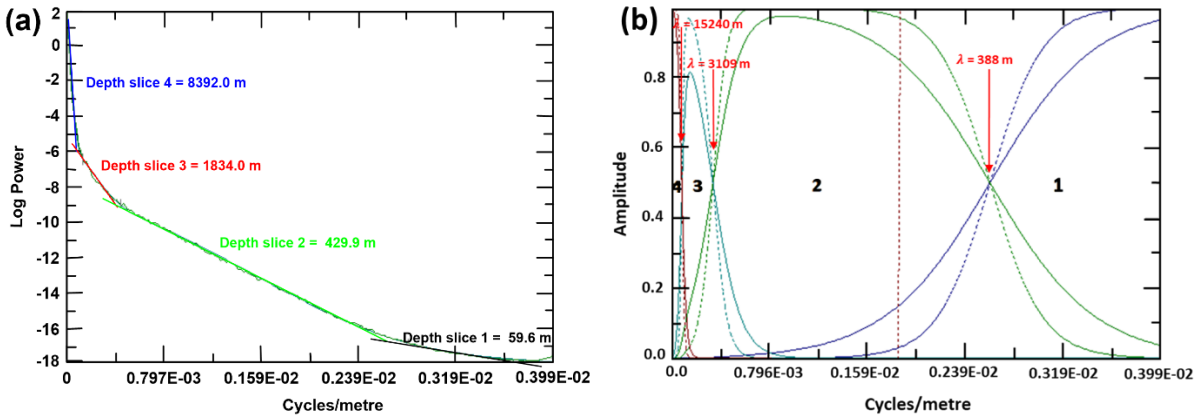

Fig. 3. 9: (a) The radially symmetric power spectrum of the DRTE data sets matching four-layer equivalent sources (b) The matched bandpass filters corresponding to the four equivalent layers. Solid and dashed lines are amplitude and Wiener filters.

Table 3. 1: Summary of the matched bandpass wavelength filter

Bandpass wavelength (m)		Av. Depth (m)	Equivalent source Layer	Terrain Height correction (80 m)	Layer/Sources
Minimum	Maximum				
251	388	59.6	1	---	Noise
388	3109	429.9	2	350 (0.4 km)	Near surface
3109	15240	1834.0	3	1754 (1.8 km)	Shallow
15240	252	8392.0	4	8312 (8.4 km)	Deep i.e., basement surface below sediments and intra-basement magnetic sources

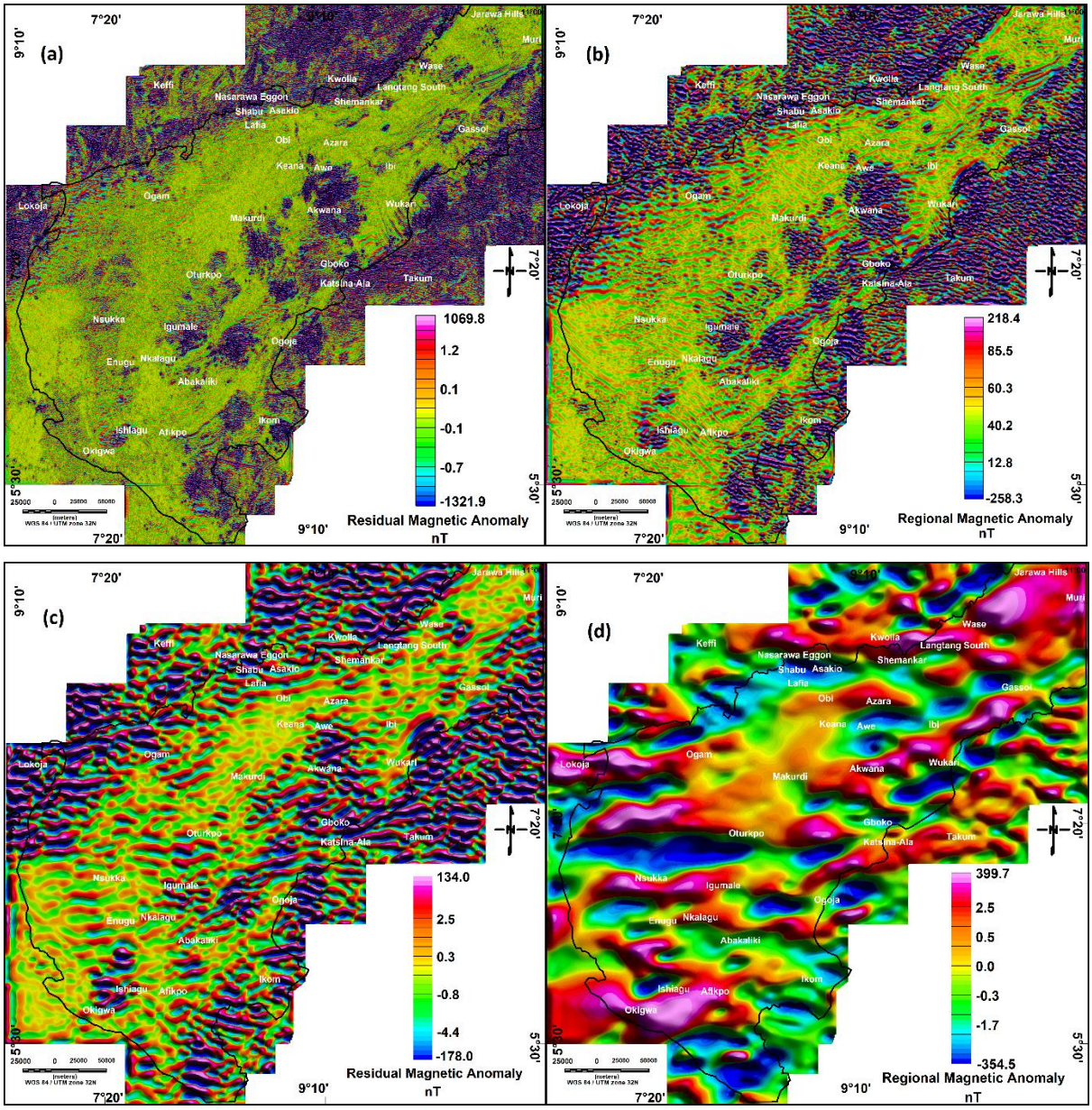

Fig. 3. 10: Filtered aeromagnetic data (a) Bandpass 1 corresponding to an equivalent dipole layer at 56.9 m containing wavelengths dominated by surface geology and cultural noise. (b) Bandpass 2 corresponds to an equivalent dipole layer at 350 m which contains the intermediate wavelengths relatable to shallow geologic and some cultural features (c) Bandpass 3 corresponds to an equivalent dipole layer at 1754 m which contains shallow geologic features with less noise. (d) Bandpass 4 corresponds to the deepest equivalent layer at magnetic half space at 8312 m which is due to basement anomaly and other deep crustal geologic features.

3.2.3.2 Separating regional-residual DRTP anomaly using power spectrum method

Power spectrum analysis can be used to determine the different wavelength contributions to any TMI data sets and attribute them to shallow and deep structures (Ali et al., 2017). The corresponding fields can be separated by filtering and evaluated separately for further analyses. A pseudo-depth slice estimate from the power spectrum method easily helps in differentiating several depth sources with the separation of shallow from deep sources (Hinze et al., 2010; Ali et al., 2017).

Spector and Grant (1970) gave the expressions for the radially averaged power spectrum of a random assemblage of narrow vertical prisms. For the ensemble of vertical sources, the azimuthally averaged power spectrum as a function of wavenumber, k is given by:

$$\boldsymbol{S^2(k) = B\left[e^{-4\pi hk}\right]\left[1 - e^{-2\pi kt}\right]^2} \text{.....(3. 16)}$$

where h is depth to top, t is thickness, and B depends on magnetic susceptibility. But for long vertical sources, t becomes very large and $S^2(k)$ tends to

$$\boldsymbol{S^2(k) = B\left[e^{-4\pi hk}\right]} \text{.....(3. 17)}$$

A plot of log power versus wavenumber gives.

$$\boldsymbol{log\ \left(S^2(k)\right) = logB - 4\pi hk} \text{.....(3. 18)}$$

A plot of log power versus wavenumber gives a straight line whose slope equals -4πh (for k = 1/λ) i.e., the slope is proportional to the depth of the source. This result gives the average depth to the source of the disturbance of the power spectrum, and this can be determined from the slope

Therefore, the power spectrum analysis was applied to the DRTP anomaly map to separate the residual (shallow) from the regional (deep) sources (Fig. 3.11). Depth slice 1 (800-3700 m wavelength) is a shallow mean depth slice that was obtained by applying linear slope correction (Green line) to bring the slope into line with a slope of depth slice 2 (Red line). For intermediate-depth slice 2 (3700-15500 m), linear slope correction is applied to bring slope depths 1 and 3 into line with depth slice 2 while the deep structures, or regional anomalies, represented by depth slice 3 (0-15500 m) were obtained by applying a linear correction to bring slope 1 into line with slope 2 and then the resultant into line with slope 3 (Blue line). The average depth at each slice is calculated in relation to the slope (Table 3.2), which identifies

mean depths for each slice between anomalies. The DRTP anomaly map (Fig. 3.12 a) resulted in three anomaly maps after depth slices were filtered and gridded. The grid of depth slice 1 is dominated by surface and short wavelengths as well as surface noise (Fig. 3.12 b). Depth slice 2 shows the dominance of both short and long wavelengths (Fig. 3.12 c) while the dominance of long wavelengths attributed to deep anomalies and other crustal structures are observable in depth slice 3 (Fig. 3.12 d).

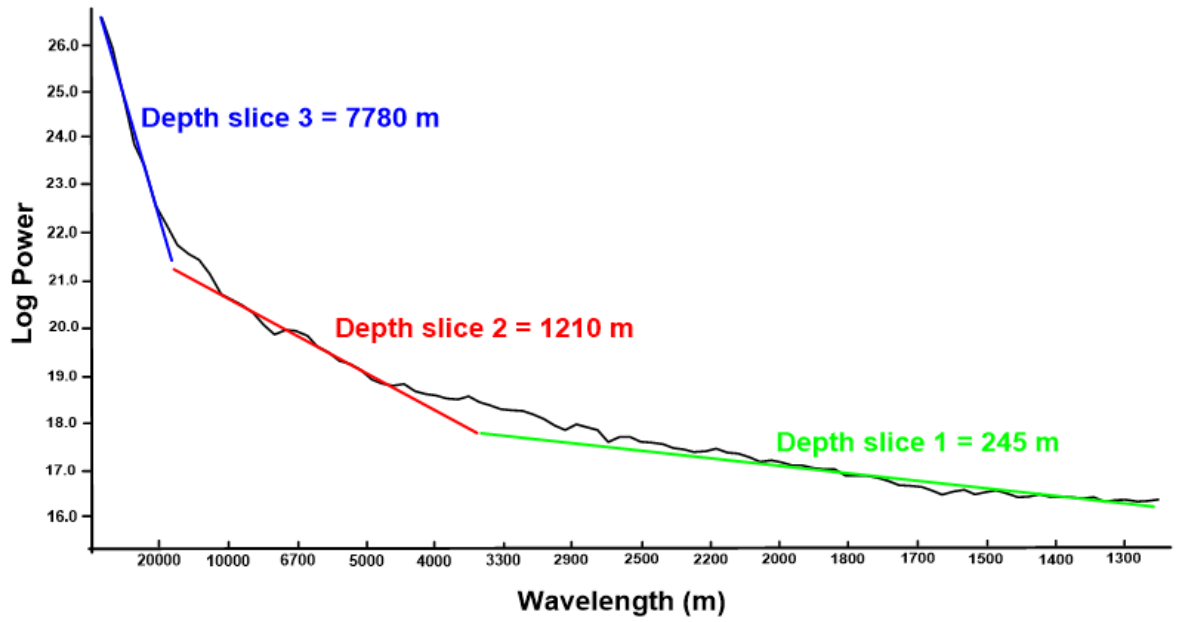

Fig. 3. 11: A power spectrum analyses of DRTP anomaly map matching three distinct pseudo-depth slices. Three (3) average depth slices are mapped due to the processes involved in correcting RTP grids at the equator.

Table 3. 2: Summary of power spectrum analyses

Bandpass wavelength (m)		Mean Depth (m)	Mean Depth below surface (m)-mean height, 80m)	Source Layer	Layer
Minimum	Maximum				
800	3700	245	165	1	Shallow
3700	15500	1210	1130	2	Intermediate
15500	0	7780	7700	3	Deep

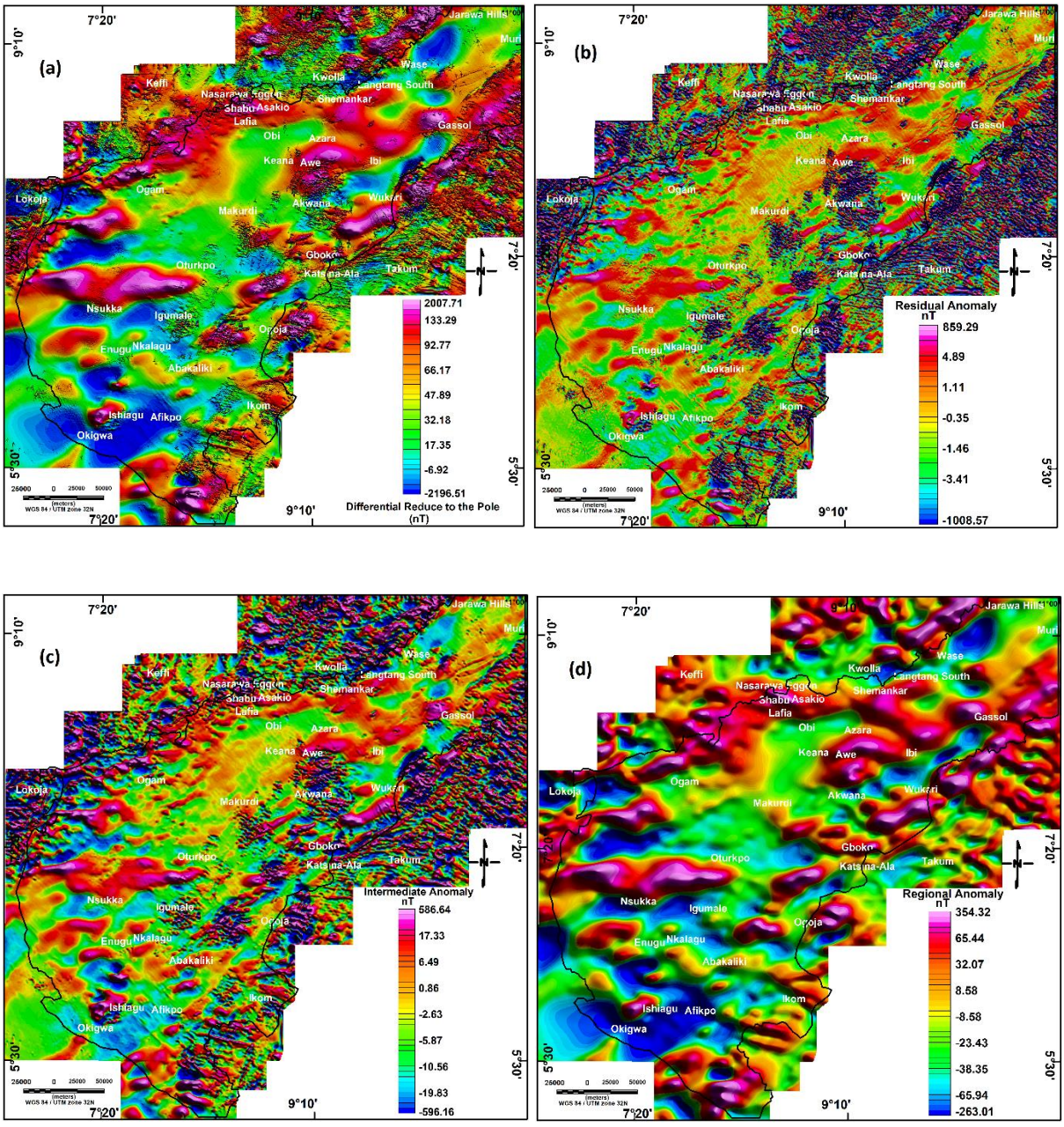

Fig. 3. 12: Aeromagnetic data (a) Differential reduction to the role (DRTP) anomaly map (b) Depth slice 1 corresponding to shallow depth anomalies dominated by surface and cultural noises. (c) Depth slice 2 corresponds to the intermediate wavelengths of the shallow geologic and some cultural features (d) Depth slice 3 corresponds to the deepest equivalent layer at magnetic half space at 7.8 km which could as a result of basement anomaly and other deep crustal geologic features

3.2.3.3 Separating regional-residual azimuthal filtered anomaly using power spectrum analyses.

The separation of regional and residual magnetic fields from an azimuthal filtered anomaly grid was carried out based on power spectrum analyses. The spectrum was plotted using equation 3.18 and three depth slices were obtained (depth slices 1, 2, and 3) to represent shallow, intermediate, and deep anomalies (Fig. 3.13). Table 3.3 shows the summary of the calculations for the various depth slices considering the mean terrain clearance. The average depth of 31 m was estimated from depth slice 1 with a wavelength range of 500 m - 710 m. This can be attributed to shallow (residual) magnetic sources that are dominated by surface features and noise. Depth slice 2 is composed of mostly wavelengths between 710 m and 10,000 m. The average depth of 520 m was estimated and shows less noise from short wavelengths but shows some shallow features more clearly. Regional anomalies signified by depth slice 3 that is related to deep magnetic sources dominated by long-wavelengths greater than 10,000 m have been estimated with an average depth of about 5980 m. Fig. 3.14 (a) is the original azimuthal map that has been depth sliced into the three slices. The results of the three depth slices were gridded and used for delineating surface and near-surface lineaments (Figs. 3.14 b, c, and d).

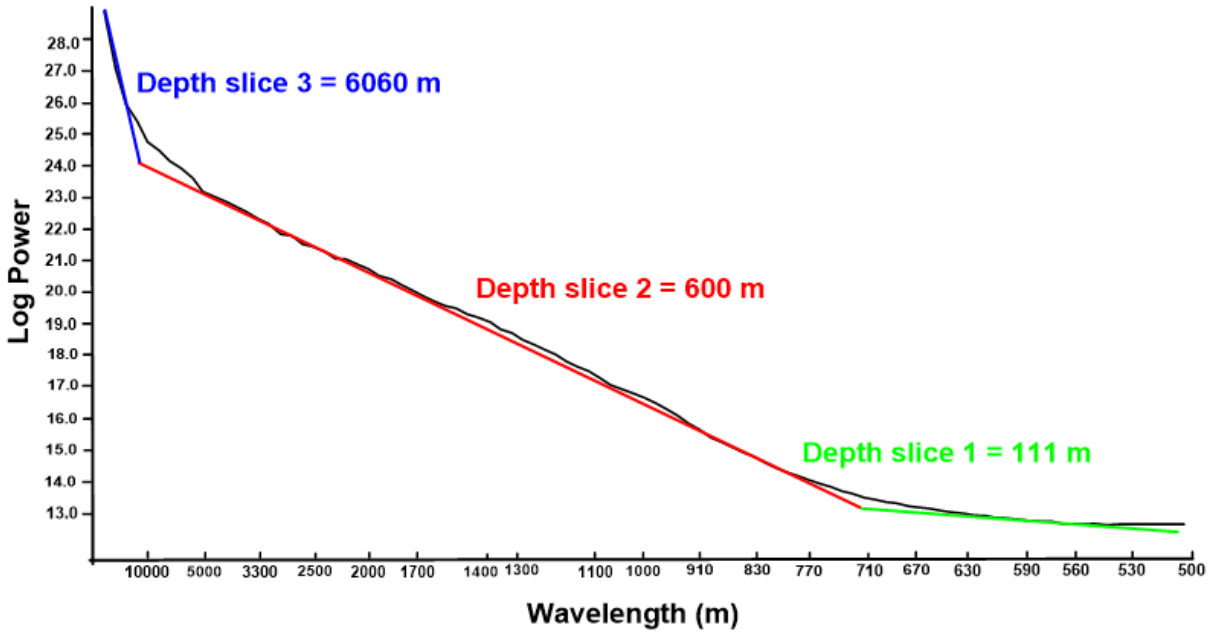

Fig. 3. 13: A power spectrum analyses of azimuthal filtered RTP data sets matching three distinct pseudo-depth slices

Table 3. 3: Summary of power spectrum analyses

Bandpass wavelength (m)		Mean Depth (m)	Mean Depth (m)-mean height, 80m)	Source Layer	Layer
Minimum	Maximum				
500	710	111	31	1	Shallow
710	10 000	600	520	2	Intermediate
10 000	0	6060	5 980	3	Deep

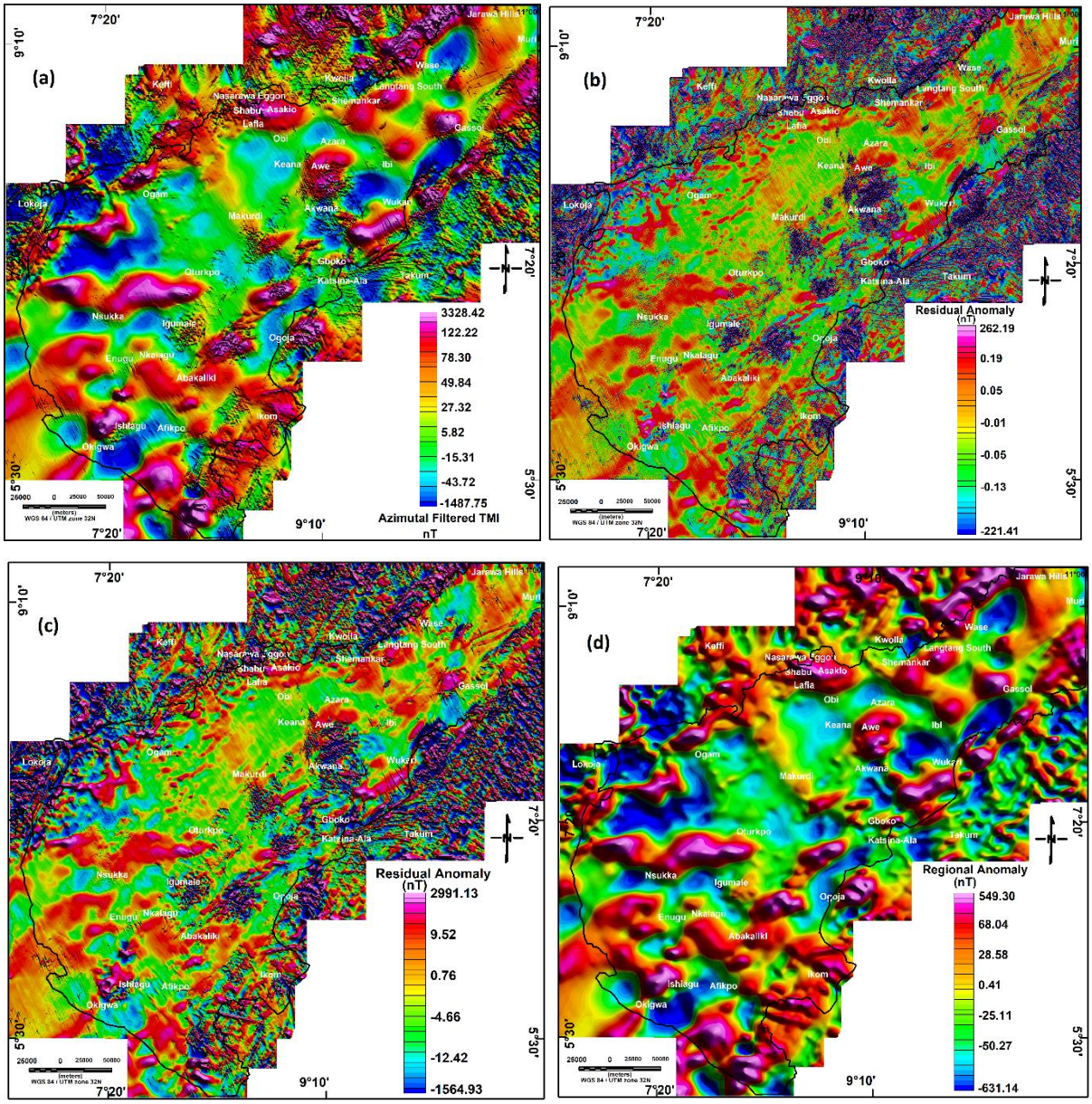

Fig. 3. 14: Aeromagnetic data (a) Azimuthal filtered RTP anomaly map (b) Depth slice 1 corresponding to shallow depth anomalies dominated by surface and cultural noise. (c) Depth slice 2 corresponds to the intermediate wavelengths of the shallow geologic and some cultural features (d) Depth slice 3 corresponds to the deepest equivalent layer - magnetic half space at 7.8 km which could relate to basement anomaly and other deep crustal geologic features

3.3 Gravity data sets processing

3.3.1 Land gravity point dataset

Gravity point data sets were compiled and granted access to by Bureau Gravimétrique International (BGI). These are from databases that were carefully stored and processed for efficient analyses obtained from several surveys over decades of fieldwork (Cratchley and Jones, 1965; Hospers, 1965; Cratchley et al., 1984; Okereke, 1984) (Fig. 3.15). Cratchley and Jones (1965) carried out a gravity survey with a Worldwide N0. 36 gravimeter to interpret the geology and gravity anomalies over the Benue Trough. They used a reduction density of 2.67g/cc with a relative Bouguer anomaly of between +/- 0.5mGal accuracy locally and +/-1 mGal generally. The height accuracy ranges between 1.5 – 3 m. The gravity data obtained from this study cover the northern part of the area. Okereke (1984) employed a Worden Master 1153 gravity meter to measure the gravity field response at 5km intervals. The original reduction density of 2.67 g/cc was used for the calculation. Accuracy of 2 mGal Bouguer anomaly and a 5.3 m height were obtained. The data obtained from this study covered the eastern sector of the trough and the Nigerian basement area. Gravity surveys that cover the southern part of the study area especially the Niger Delta of Nigeria, were obtained from the work of Hosper (1965). These data points were measured at 1-km intervals with a Worden gravimeter (no. 135). Reduction density of 2.67 g/cc and an average sediments density of 2.4 g/cc were used in the estimate.

Several ground data points overlap from the works of the different geophysicists, enabling validation of their results. According to this validation, the north-western part of the study area has not been covered by ground surveys, and this was resolved by combining these data sets with that of the Earth Gravitational Model 2008 (EGM2008) especially the parts that are from ground data.

3.3.2 EGM2008 derived data

The EGM2008 is a spherical harmonic model of the Earth's gravitational potential formed by least squares adjustment estimation technique through the combination of ITG-GRACE03S model and a global 5 arc-minute equiangular grid of area-mean gravity anomalies (Nikolaos K. Pavlis et al., 2012). The ITG-GRACE03S satellite model was estimated at the Institute of Theoretical Geodesy, Germany, based on GRACE Satellite-to-Satellite Tracking mission and is complete spherical to harmonic degree and order 2159 (Pavlis et al., 2012). These anomalies

were developed by merging terrestrial, airborne, and satellite data with altimetry-derived values.

The EGM2008 regional gravity anomaly map of the study area was computed at regional scales obtained using standard densities of 1.03 g/cm3 and 2.67 g/cm3 for water and land density, respectively (Fig. 3.16). Topographic correction was applied out to 167 km using the 1′ ×1′ ETOPO1 Digital Elevation Model (de Castro et al., 2014). The grid was then upward continued to 3 km (0.03 degree) to reduce the effect of high frequencies attributed to short wavelengths and noise and to make it suitable for merging with the point data. The EGM2008 grid resolution is suitable for combination with the terrestrial data points and suitable for regional geological analyses and interpretations (Bomfim et al., 2013). The resolution of the data sets varies depending on the local data quality (Pavlis et al., 2012).

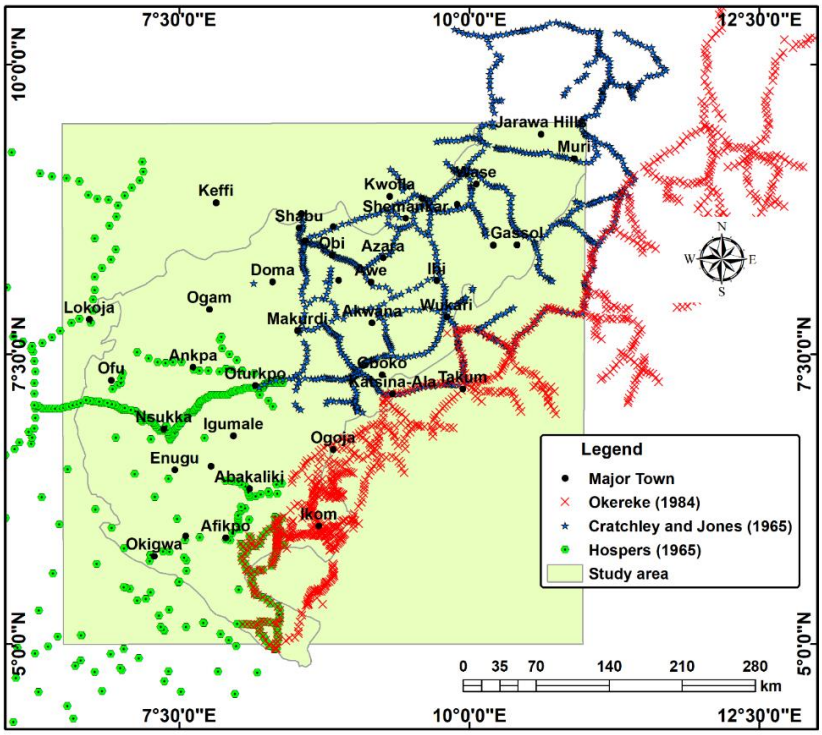

Fig. 3. 15: Gravity point data contributions covering the Lower and Middle Benue Trough

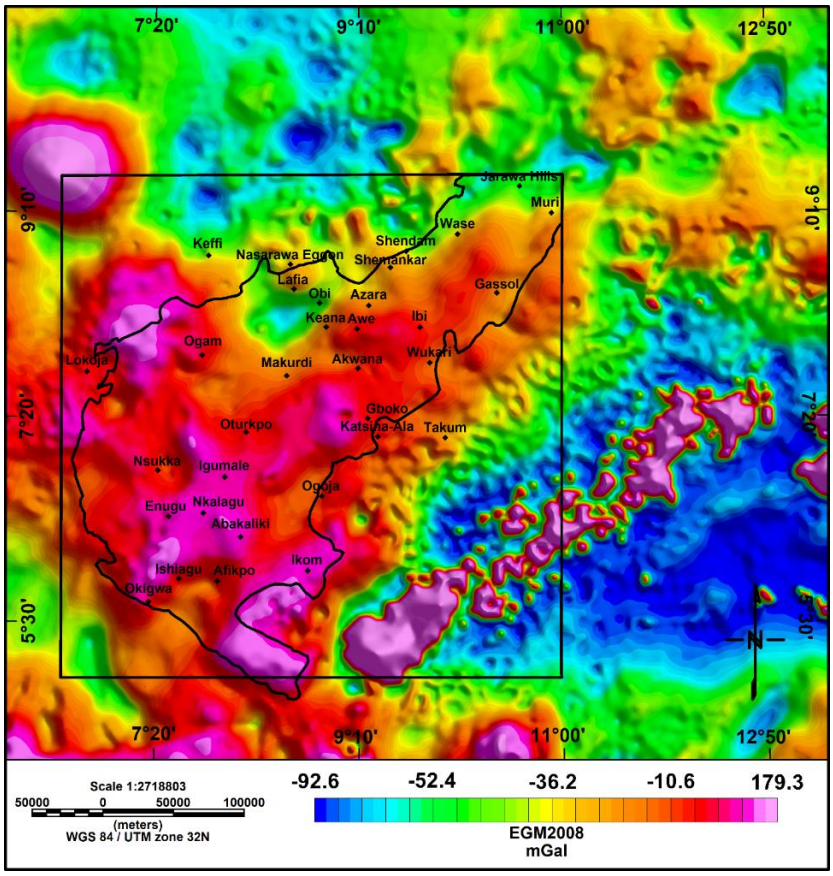

Fig. 3. 16: Colour shaded regional Bouguer anomaly map from EGM2008 spherical harmonic model grids, upward continued to 3km

3.3.3 Gravity data compilation

The gravity dataset was compiled from land gravity point and EGM2008 data. This was achieved by using a polygon to cover the areal extent of the gravity point data in GETgrid software licensed by Getech Plc. and used to mask against the EGM2008 grid such that grid values outside the polygon were retained and converted to points. The newly created points grid data were then combined with the land gravity point data to form the Bouguer anomaly point data of the area. The interpolation of points to form the Bouguer anomaly map of the area was carried out using the continuous curvature splines in tension with Generic Mapping Tools (GMT) software (Smith and Wessel, 1990), as this helps to overcome the difficulties in resolving solutions by the commonly used minimum curvature gridding method. The minimum curvature surfaces usually show big oscillations and implausible inflection points which may be unsuitable for interpretation. Gridding with tension enables the elimination of such extraneous inflection points by fixing or adding tension to create a grid that better mimics the curvature properties of potential field datasets. The smoothest bicubic solution (minimum curvature) is denoted by 0, while 1 gives a harmonic spline solution. Thus, 0.25 or more is good for potential field (smooth) data and 0.5 to 0.75 may be suitable for topography (Smith and Wessel, 1990). In this study, 0.3 tension was used, and the grid was smoothed by a 3 x 3 Hanning filter (Fig. 3.17).

The Bouguer map is composed of a broad positive Bouguer anomaly attributable to thinning of the crust beneath the basin (Fairhead and Green, 1989; Obasi et al., 2018). The highest positive value is 102 mGal, attributed to volcanic emplacement, which trends in a general NE-SW trend. The lowest gravity value within the main rectangular area is -87.6 mGal which could be attributed to sedimentary basin fill. The residual negative anomalies are variable in lateral extent and in amplitude and reflect the spatial distribution of sub-basins or graben structures.

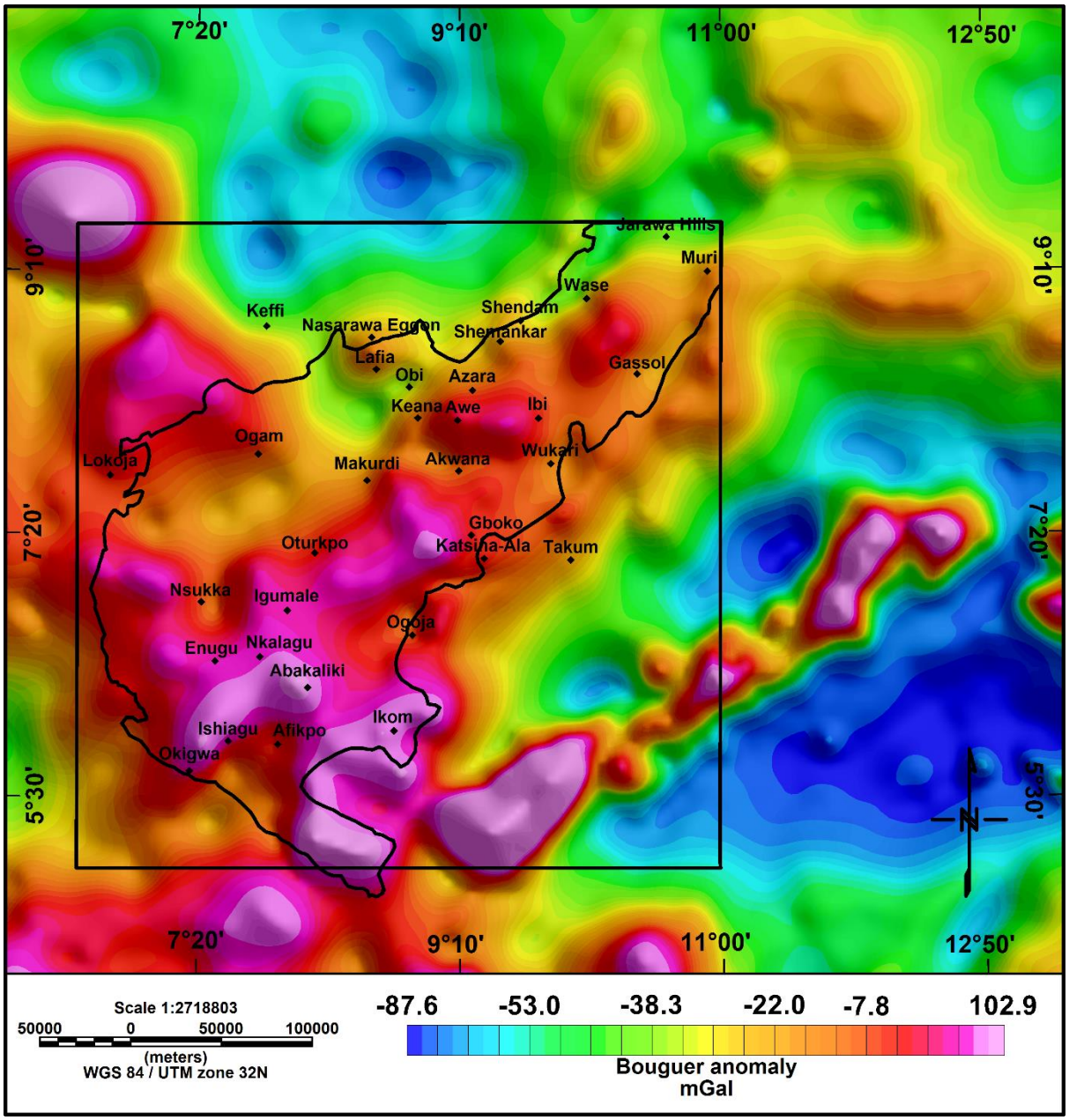

Fig. 3. 17: Combined shaded Bouguer anomaly map of the study area (Gravity point and EGM2008 data). The rectangle shows the study area with positive high at the centre of the trough.

3.3.4 Method for regional-residual anomaly separation using power spectrum analyses

The statistical spectral technique applied on gravity-gridded data can help to estimate the depth to gravity sources through the slope of the logarithmic power spectrum (Spector and Grant, 1970; Jacobsen, 1987; Hinze et al., 2010; Ali et al., 2017). The gravity-gridded data set is usually converted to vertical gradient (VG) making it equivalent to the pseudomagnetic field that is well behaved when the technique is applied to it. This technique was employed for separating regional and residual components of the gridded gravity map. The residual components of the gravity data sets cannot resolve all the shallowest density anomalies due to irregular point spacing and coverage of gravity stations.

A graph of the power spectrum against the wavelengths of source anomalies was plotted based on equation 3.18 and a line of slope across the curve helped in the estimation of the average depth around gravity sources (Fig. 3.18). A summary table of the estimated parameters is shown in Table 3.4. The plot of the Bouguer anomaly map (Fig. 3.19 a) shows three distinct linear segments that correspond to depth slices 1, 2, and 3. Depth slice 1 has a gentle slope and corresponds to the shallower part of the anomaly, with a wavelength less than 16 km and an estimated mean depth of about 3 km (shown as a green line on the plot). It was referred to as the residual component of the gravity anomaly map that has mainly contributions from sedimentary rocks and topographic signals arising from the inability to adequately correct for topography in the Bouguer anomaly (Fig. 3.19 b). The depth slice 2 segment corresponds to the wavelength interval between 16 km and 100 km, with an estimated mean depth of about 15 km (shown as red line on plot). This source is devoid of noise and could result from basement level density contrasts. It also signifies that the basement morphology is irregular i.e., made up of different density sources (Fig. 3.19 c). The steepest part of the graph, referred to as the regional segment, is identified by depth slice 3 (blue line). It is dominated by greater than 100 km wavelength anomalies with a mean depth of about 48 km. This is the deepest source component of the gravity data with most of the shallow parts removed (Fig. 3.19 d). Due to the estimated mean depth and wavelength, this depth slice can be attributed to the middle and lower crust and upper mantle sources. The Moho interface in the region has been estimated both from seismic and gravity data to be shallower than this slice and then contributes to the observed field (Stuart et al., 1985; Fairhead and Okereke, 1987; Akpan et al., 2016).

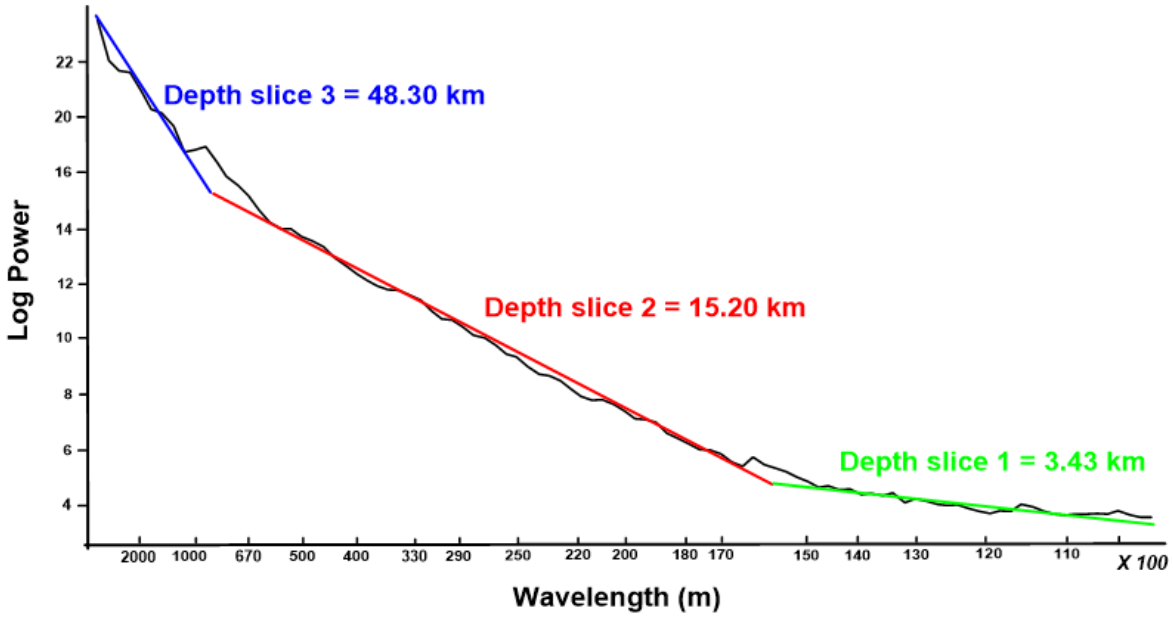

Fig. 3. 18: A power spectrum analysis for Bouguer gravity anomaly compilation. Three different pseudo-depth slice sources; regional, residual, and topographic signals are distinguished, and their average depths are estimated.

Table 3. 4: Summary of power spectrum analyses

Bandpass wavelength (m)		Average Depth (m)	Equivalent source Layer	Layer
Minimum	Maximum			
10 000	16 000	3 430	2	Near surface
16 000	100 000	15 200	3	Shallow
100 000	0	48 300	4	Deep

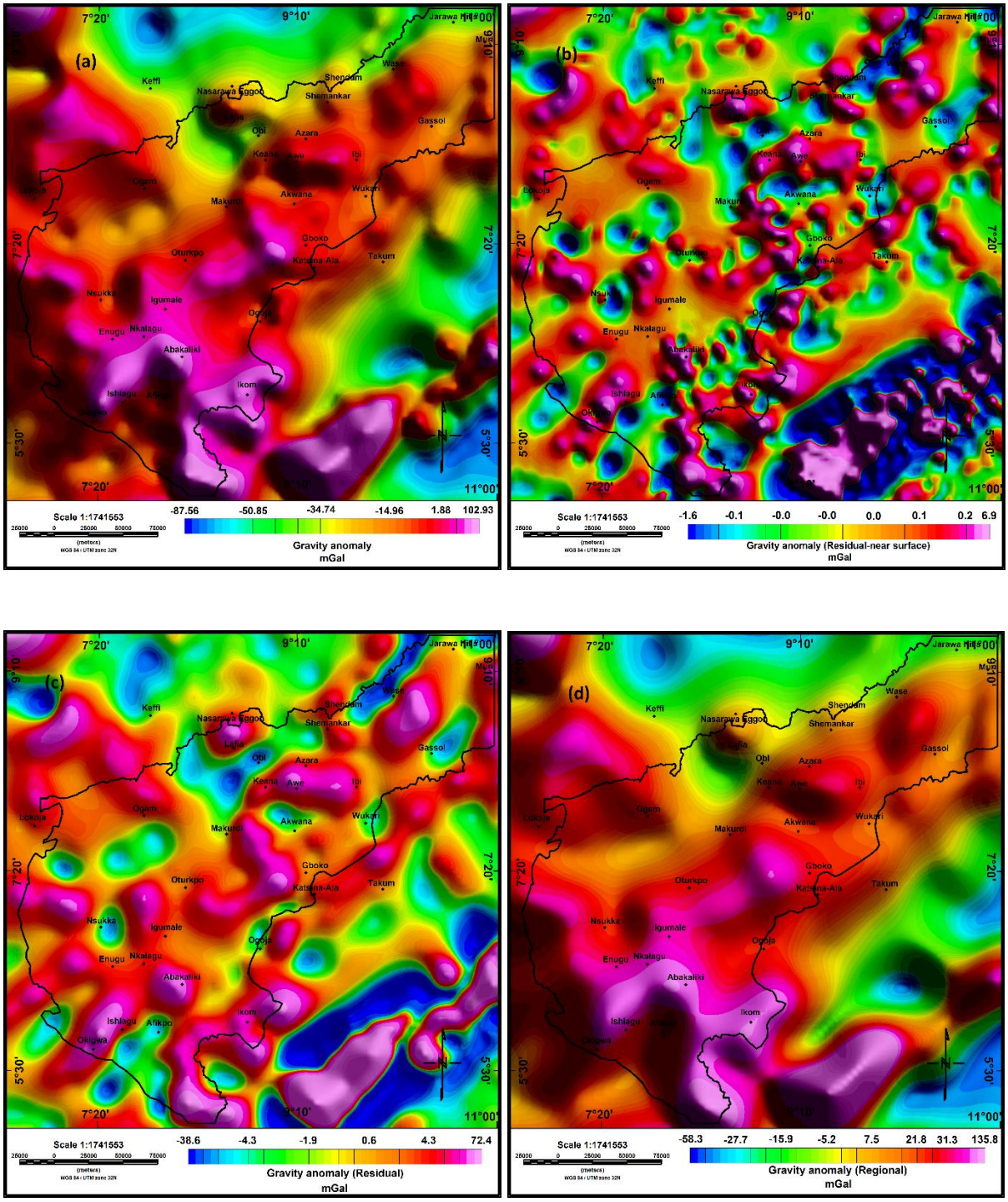

Fig. 3. 19: Gravity data grid (a) Bouguer anomaly (b) Depth slice 1 corresponding to shallow anomalies at an average depth of 3 km (c) Depth slice 2 corresponding to the intermediate wavelengths of the shallow geologic at an average depth of 15 km (d) Depth slice 3 corresponding to the deepest equivalent layer at an average depth of about 48 km.

3.4 Mapping near-surface lineaments from magnetic and gravity datasets

3.4.1 Magnetic and gravity mapping techniques

Magnetic and gravity data can be enhanced by standard derivatives such as total horizontal derivative, vertical derivative, and analytic signal, and other local phase derivatives such as local wavenumber, theta map, and tilt, to help in mapping the edges of structures (Li et al., 2010; Ali et al., 2017). Other techniques such as Goussev filter and Euler Deconvolution can also help to locate magnetic lineaments and other structural discontinuities (Goussev et al., 2003; Cooper, 2004; Abu El-Ata et al., 2013). Mapping tectonic lineaments in this study are critical to understanding the tectonic deformation history of the trough.

3.4.1.2 Total Horizontal Derivative

The total horizontal derivative (THD) or horizontal gradient magnitude or total horizontal gradient is very effective in highlighting the edges of both shallow and deep magnetic and gravity bodies (Grauch and Cordell, 1987; Anudu et al., 2014). It helps in mapping linear and curvilinear geological features/structures such as faults, contacts, and dykes/sills, etc. The main advantage of this method is its low sensitivity to noise since it requires calculations of first-order horizontal derivatives (Phillips, 2000; Fedi and Florio, 2001; Grauch, 2002; Feumoe and Ndougsa-Mbarga, 2012; Abu El-Ata et al., 2013). The horizontal gradient magnitude gives a peak anomaly above gravity contacts but to achieve this with magnetic data, the field must first be reduced to the pole or to the equator before calculating the THD (Li et al., 2010; Ndougsa-Mbarga et al., 2012). The horizontal gradient maxima occur over the steepest parts of anomalies, while the minima occur over the flattest parts. The locations of maxima represent the locations of faults, contacts, steep topographic slopes, or abrupt changes within a rock unit (Abu El-Ata et al., 2013). The horizontal gradient method assumes that the sources are isolated, that vertical contacts separate thick geologic units, and that the magnetization vectors are collinear with the geomagnetic field vector i.e., the induced magnetization is assumed to act in the same direction as the geomagnetic field.

$$\boldsymbol{Horizontal\ Gradient\ Magnitude, THD} = \sqrt{((\boldsymbol{\partial T/\partial x})^2 + (\boldsymbol{\partial T/\partial y})^2)} \quad \textbf{.....(3. 19)}$$

Where T is the observed gravity or total RTP or RTE magnetic field

3.4.1.2 Vertical Derivatives

Vertical derivatives (VD) or vertical gradients enhance the physical expression of shallow causative geological bodies due to the dominance of short-wavelengths while suppressing the effects of long-wavelength anomalies (Phillips, 2000; Anudu et al., 2014). Surface and near-surface/shallow anomalies are dominated by short-wavelengths while deep geological source body anomalies are dominated by long-wavelength anomalies. The zero contour values of VD occur directly over edges of gravity and RTP magnetic source bodies thereby detecting contacts/boundaries of geological bodies more precisely (Cooper and Cowan, 2004; Reynolds, 2011). It can be expressed as.

$$\boldsymbol{First\ Vertical\ Derivative, FVD = (\partial T/\partial z)} \quad \textbf{.....(3. 20)}$$

$$\boldsymbol{Second\ Vertical\ Derivative, SVD = \left(\partial T^2/_{\partial z^2}\right)} \quad \textbf{.....(3. 21)}$$

Where; T = Gravity or total magnetic field

3.4.1.3 Analytic Signal Method

Analytic signal (AS) or total gradient or analytic signal magnitude is expressed as the square root of the squared sum of the vertical and horizontal derivatives of the magnetic and gravity fields. The maxima (ridges or peaks) of the analytic signal occur directly over fault blocks or faults, lithological contacts, shear zones, volcanic plugs, dykes, etc., while some lie over the edges to help in detecting linear structures (Hsu et al., 1996; Pilkington and Keating, 2004; Li et al., 2010; Ndougsa-Mbarga et al., 2012; Abu El-Ata et al., 2013; Anudu et al., 2014). This derivative is applicable at low magnetic latitudes (Baranov, 1957; Roest and Pilkington, 1993) because it involves the use of an amplitude function that is always positive. The AS is independent of the orientation of the magnetizing source but may be a bit noisy especially at low magnetic latitudes where there may be a lot of distortion of anomalies (Nabighian, 1972; MacLeod et al., 1993).

$$\boldsymbol{Analytic\ Signal, AS = \sqrt{((\partial T/\partial x)^2 + (\partial T/\partial y)^2 + (\partial T/\partial z)^2)}} \quad \textbf{.....(3. 22)}$$

T is the observed gravity or total magnetic field

3.4.1.4 Theta Method

The Theta mapping method involves detecting magnetic edges independently of the strike and amplitude of the field. This is very effective in mapping at low-latitude magnetic data after reduction to the equator or to the pole (Wijns et al., 2005). Geologic edges are usually

determined by a plot of cos (θ) patterns in which a maximum bracketed by two minima show the lineaments or tan (θ) pattern where minima bracketed by two maxima represent the lineaments (Cooper and Cowan, 2008). The theta map is equivalent to a map of the zero contours of the tilt angle and presents a better means of picking out structural edges (Ali et al., 2017). Theta mapping can indicate both magnetic and gravity lineaments as well as the direction of dip. The closer the contact is to the surface, the tighter the cos (θ) pattern and vice versa.

$$\boldsymbol{Theta, \theta = cos^{-1}\left(\frac{THD}{AS}\right)} \text{.....(3. 23)}$$

Where total horizontal derivative, THD equation 3.19 and analytic signal, AS equation 3.22.

3.4.1.5 Local Wavenumber

The local wavenumber is the horizontal gradient of the local phase or, simply called, the tilt angle along a 2D profile (Thurston and Smith, 1997; Salem et al., 2014). It usually requires second-order derivatives of the gravity or total magnetic field; and is used to estimate depths to the tops of buried bodies (Li *et al.,* 2010). The maxima are located over isolated contacts and are said to be better than analytic signal method at mapping geology (Nwosu, 2014). The local wavenumber peaks over linear features with maxima directly over the contacts. It is derived from the first and second derivatives of the observed gravity or magnetic field. It is strongly affected by noise (Geosoft Inc. 2007; Abu El-Ata et al., 2013). A simplified local wavenumber estimate formula for a grid is given by.

$$\boldsymbol{Local\ Wavenumber, LW = \frac{\partial}{\partial h}\ tan^{-1}((\partial T/\partial z)/\ (\partial T/\partial h))} \text{.....(3. 24)}$$

Where T is the gravity or magnetic field measured on a horizontal surface and, $\partial T/\partial z$ and $\partial T/\partial h$ are the vertical and horizontal derivatives of the field, respectively.

3.4.1.6 Tilt derivative

The tilt derivative has been used to map the lateral extent of anomalous density or magnetization bodies and their edges (Fairhead et al., 2017). It is slightly different from the local phase since it uses the absolute value of the horizontal derivative or local wavenumber at the denominator (Verduzco et al., 2004). The combination of tilt derivative and the total horizontal derivative is suitable for mapping shallow structures as it produces sharp edges (Verduzco et al., 2004; Geosoft Inc. 2007; Fairhead et al., 2017).

Verduzco et al., (2004) expressed the tilt derivative as :

$$\boldsymbol{Tilt, TDR = \tan^{-1}\left[\frac{VDR}{THD}\right]} \text{..... (3. 25)}$$

Where VDR, equation 3.20 and THD, equation 3.19 are the first vertical and total horizontal derivatives respectively, of the gravity or the total magnetic intensity.

While the tilt to the horizontal derivative, TDR_THD is given as.

$$\boldsymbol{TDR\_THD = \sqrt{\left(\left(\frac{\partial TDR}{\partial x}\right)^2 + \left(\frac{\partial TDR}{\partial y}\right)^2\right)}} \text{.....(3. 26)}$$

Where TDR is the tilt (equation 3.25).

A plot of the zero of tilt marks the edges of lineaments (Salem et al., 2007; Saada, 2015) while the slopes across the zero of tilt contour provide a means of determining the throw direction of faults (Fairhead et al., 2011).

The tilt derivative method is limited when the density or susceptibility contrasts are large i.e., the anomaly will be large if the contrast is large and vice versa (Fairhead, 2017). Mapping magnetic structures at a low latitude with the tilt derivative may not be reliable because of the effects of anisotropy of the magnetic field that results in structures having different strike azimuths (Fairhead et al., 2011). However, it has the advantage of normalizing gravity and can discriminate between signal and noise since the zero crossing of the tilt derivative is close to the edge of the structure.

3.4.1.7 Goussev Filter

The Goussev filter (GF) calculates the scalar difference between the gravity or total magnetic-field total gradient and the total horizontal gradient. This filter enhances shallow and deep magnetic anomalies and is said to be very stable even at low magnetic latitudes (Goussev et al., 2003). The peak of the Goussev filter marks out magnetic lineaments (Armadillo et al., 2007).

$$\boldsymbol{Goussef\ Filter, GF = AS - THD} \text{.....(3. 27)}$$

Where AS and THD as in equations 3.19 and 3.22, respectively.

3.4.1.8 Euler Deconvolution

Euler deconvolution is a semi-automatic inverse method that utilizes the gradients of the potential field data. The method does not need prior knowledge of geology and it interprets gravity and magnetic data in terms of the position, depth, and type of the anomalous source.

Thompson (1982) and Reid et al., (1990) expressed that Euler's homogeneity relationship is applicable to the magnetic and gravity field.

$$(\boldsymbol{x - x_0})\frac{\partial \boldsymbol{T}}{\partial \boldsymbol{x}} + \ (\boldsymbol{y - y_0})\frac{\partial \boldsymbol{T}}{\partial \boldsymbol{y}} + \ (\boldsymbol{z - z_0})\frac{\partial \boldsymbol{T}}{\partial \boldsymbol{z}} = \ \boldsymbol{\eta(b - T)} \ \text{.....(3. 28)}$$

where $\eta, b \ and \ T$ denote the structural index (SI), background value and the gravity anomaly, respectively. $x_0, y_0 \ and \ z_0$ are the positions of x, y, and z observation points, while $\frac{\partial T}{\partial x}, \frac{\partial T}{\partial y}, \frac{\partial T}{\partial z}$ are the gradients of the anomaly with respect to the variables x, y, and z, respectively.

The most important parameter of this technique is the structural index, η which must be known before applying the equation (Thompson, 1982). The value of η is measured as the power governing the rate of change of the gravity and magnetic fields from the source i.e., the rate of fall-off or decay which directly approximate the dimension of the source. Thus, using the appropriate value of structural index to solve the equation is key to a successful result (Reid et al., 2012; Reid et al., 2014).

The Euler deconvolution is calculated based on the least-squares inversion method to solve Euler's equation. It is used to estimate source depths and locations of anomalies (Cooper, 2004; Stavrev and Reid, 2010; Melo and Barbosa, 2018), and thus acts as both a boundary finder and depth estimation tool (Reid et al., 1998; Ndougsa-Mbarga et al., 2012). Euler deconvolution is commonly employed in interpretation because it requires only a little prior knowledge about the gravity or magnetic source geometry (Moghaddam et al., 2016). In practice, it requires a bit of caution due to the need to thin out results for a better interpretation.

3.4.2 Mapping shallow magnetic lineaments and non-linear geologic bodies

3.4.2.1 Residual DRTE magnetic imaging of shallow lineaments/other geologic bodies

Residual imaging of shallow structures was carried out on figs. 3.10 (b) and (c), which show results of a matched bandpass filter over the sedimentary area at average depths of 0.4 km and 2 km, respectively. In mapping the lineaments within the upper 0.4 km (near-surface geologic structures), the second vertical derivative, analytic signal, horizontal gradient, and Goussev

filters are represented by figs. 3.20 a, b, c, and d respectively, were used to map the textural discontinuities in the magnetic fabrics across the whole area. These filters helped in mapping the sedimentary-basement boundary, volcanic rocks, plugs, and sills/dykes (Appendix A5). The magmatic intrusions trend in a general NE-SW direction, but the dykes show two major trends, of NE-SW and NW-SE directions. Horizontal gradient, theta map, local wavenumber, and Goussev filter results are shown in Figs. 3.21 a, b, c, and d respectively, from application to the residual anomaly map with a mean depth of 2 km to enhance lineaments. The volcanic rocks/sills and dykes were however not imaged at this depth signifying that they were emplaced at or near the present-day surface. The maxima of all the derivatives (Horizontal gradient, theta map, local wavenumber, and Goussev filter) represented by the zero contours corresponding to lineaments and the edges of other geologic features were traced and overlaid on the residual TMI grid map (Appendix A6). A common point of intersection of the zero contours among the derivatives marks the best edges of geologic features/structures (Cascone et al., 2017).

A combination of the geologic structures mapped within 0.4 km and 2 km mean depths showed the general shallow structural representation of the area from magnetics (Fig. 3.22). The azimuthal strike orientations of the lineaments were measured and plotted on a rose diagram using FracPaQ software downloaded from GitHub website (Healy and Rizzo, 2017). It shows that the lineaments trend in a major NE–SW with a minor NW–SE trend direction (Fig. 3.23). An average of 80-degree mean strike direction was also determined but the results from this technique normally show bias towards E-W features.

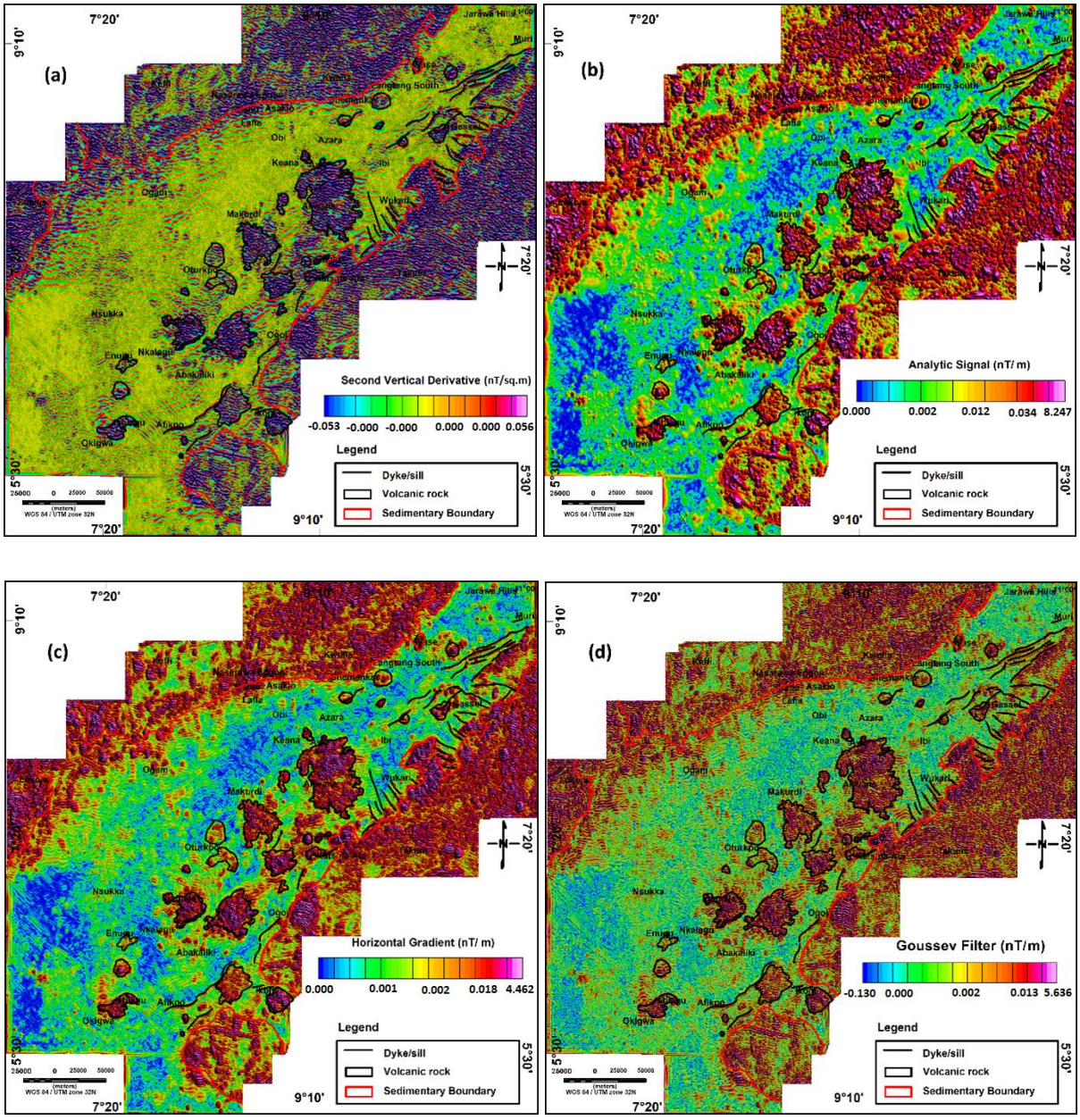

Fig. 3. 20: Residual magnetic map from DRTE processed at 0.4 km mean depth (a) Second vertical derivative (b) Analytic signal (c) Total Horizontal gradient (d) Goussev filter

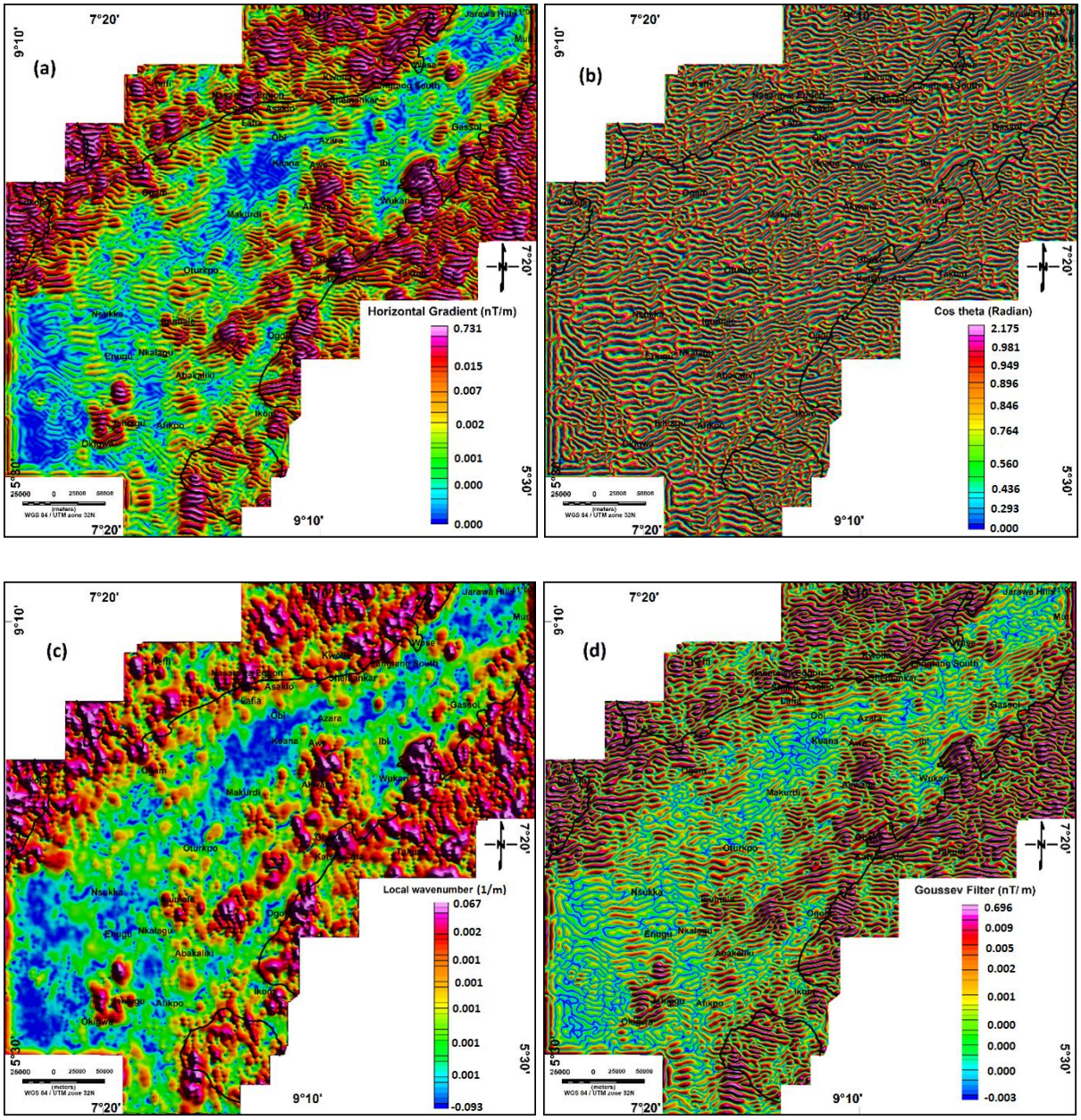

Fig. 3. 21: Residual DRTE magnetic map processed at 2 km mean depth (a) Horizontal Gradient (b) Theta map (c) Local wavenumber (d) Goussev filter

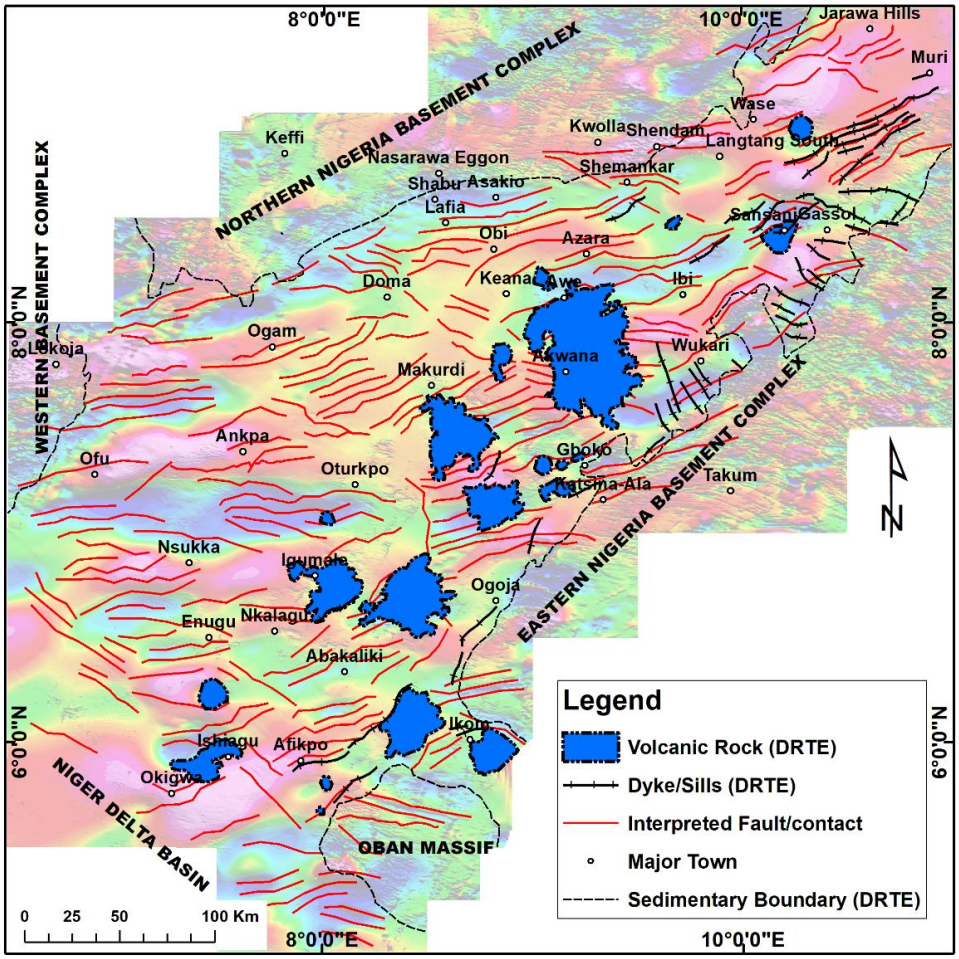

Fig. 3. 22: Geologic structural trends derived from the residual magnetic and draped over the DRTE TMI anomaly map. The outlines of the volcanic rocks might mark centres of magmatic activity.

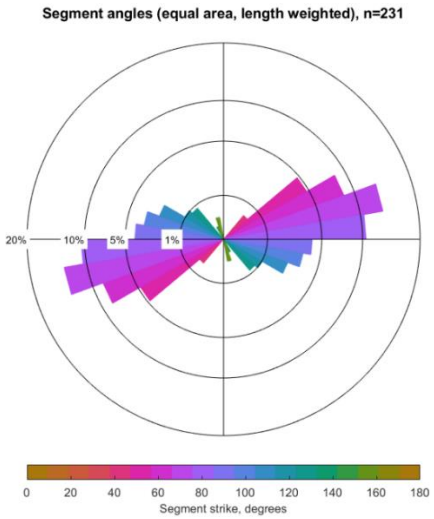

Fig. 3. 23: An equal-area rose diagram colour-coded by segment strike with a major NE-SW and a minor NW-SW trend direction. The mean vector azimuthal direction is 80 degrees of a total of 231 delineated lineaments. The result of the DRTE is biased towards E-W features.

3.4.2.2 Residual DRTP magnetic imaging of shallow lineaments/other geologic bodies

The residual DRTP map of figs. 3.12 (b) and (c), are the results of depth slices 1 and 2 obtained at 165 m and 1130 m mean depth, respectively. They were processed further with the aim of enhancing and mapping shallow geologic lineaments. Vertical derivative and analytic signal enhancements were applied to the residual anomaly at a mean depth of 165 m and the boundaries between the basement and sedimentary, dykes, and volcanic rocks/plugs/sills were delineated (Fig. 3.24 a and b). Mapping lineaments at the mean depth of 1130 m was a little bit difficult due to artifacts in the RTP. However, theta map and horizontal gradient were applied in mapping the lineaments (Figs. 3.24 c and d). There is a general agreement with the structures picked from the DRTE method, but fewer faults were imaged here. The geologic lineaments and other bodies imaged from the two depth slices were combined to represent the structural map from DRTP and draped over the TMI grid (Fig. 3.25).

A rose diagram plot of the lineaments from the DRTP shows a general NE-SW and a minor NW-SE trend direction (Fig. 3.26). A vector mean of 73 degrees has been estimated from the data, and this is about 7 degrees anticlockwise of that estimated from the DRTE. The result is expected since the DRTE tends to highlight more E-W trending structures than those that are aligned to the north. Most of the N-S features have been eliminated during transformation as it corrects for the amplitude of the TMI and prevents N-S structures.

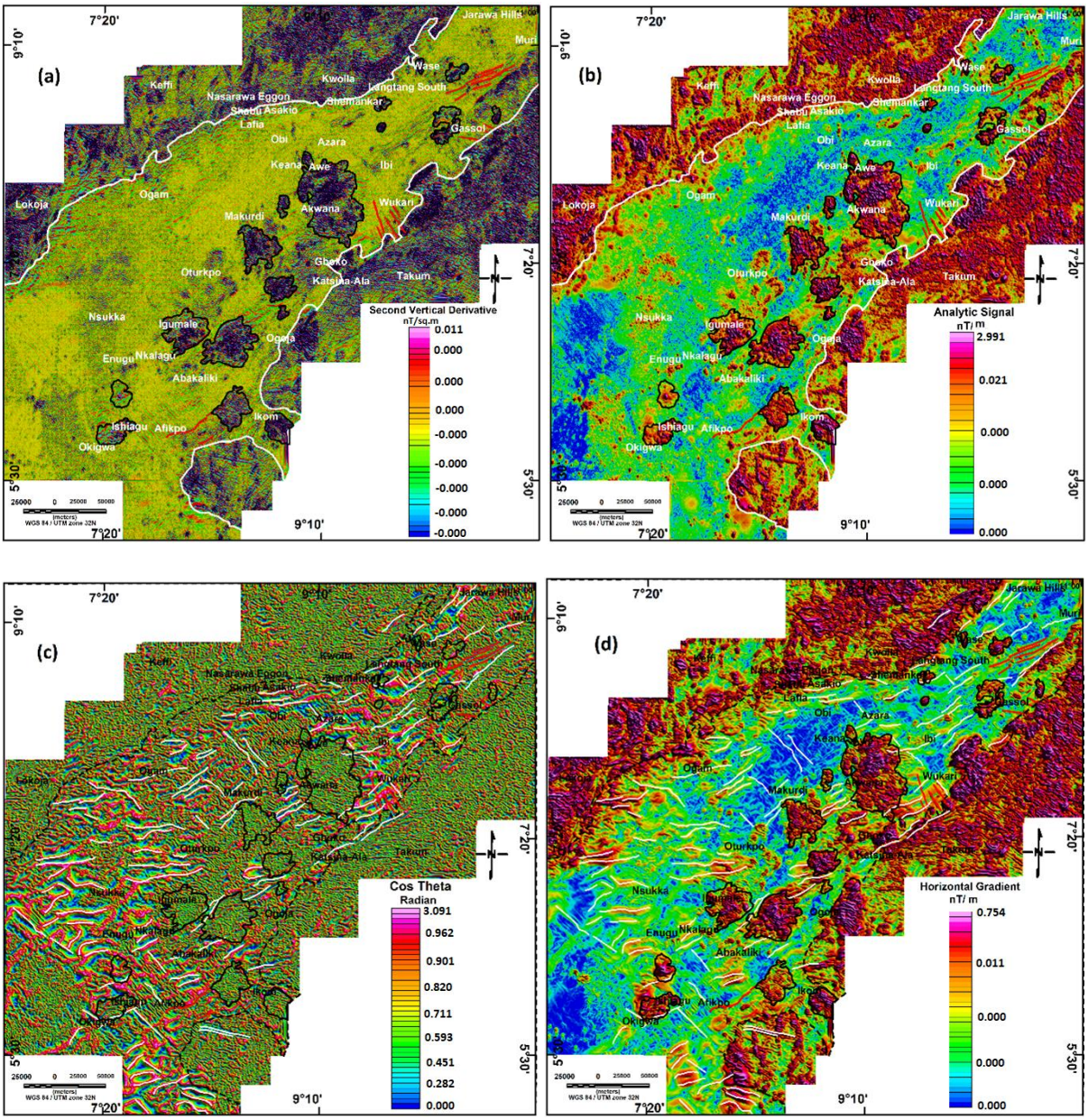

Fig. 3. 24: (a) Vertical derivative and (b) Analytic signal of 0.245 km depth slice 1 in DRTP data sets. The black polygons delineate volcanic rocks, red lines dykes, while the white traces map the boundary between the basin and the basement rocks (c) Theta map and (d) Horizontal Gradient from 1.2 km depth slice 2 where the whites lines are the delineated lineaments, the black dotted polylines marks the basin-basement boundary, the red lines are mapped dykes and the black polygons delineate the volcanic rocks.

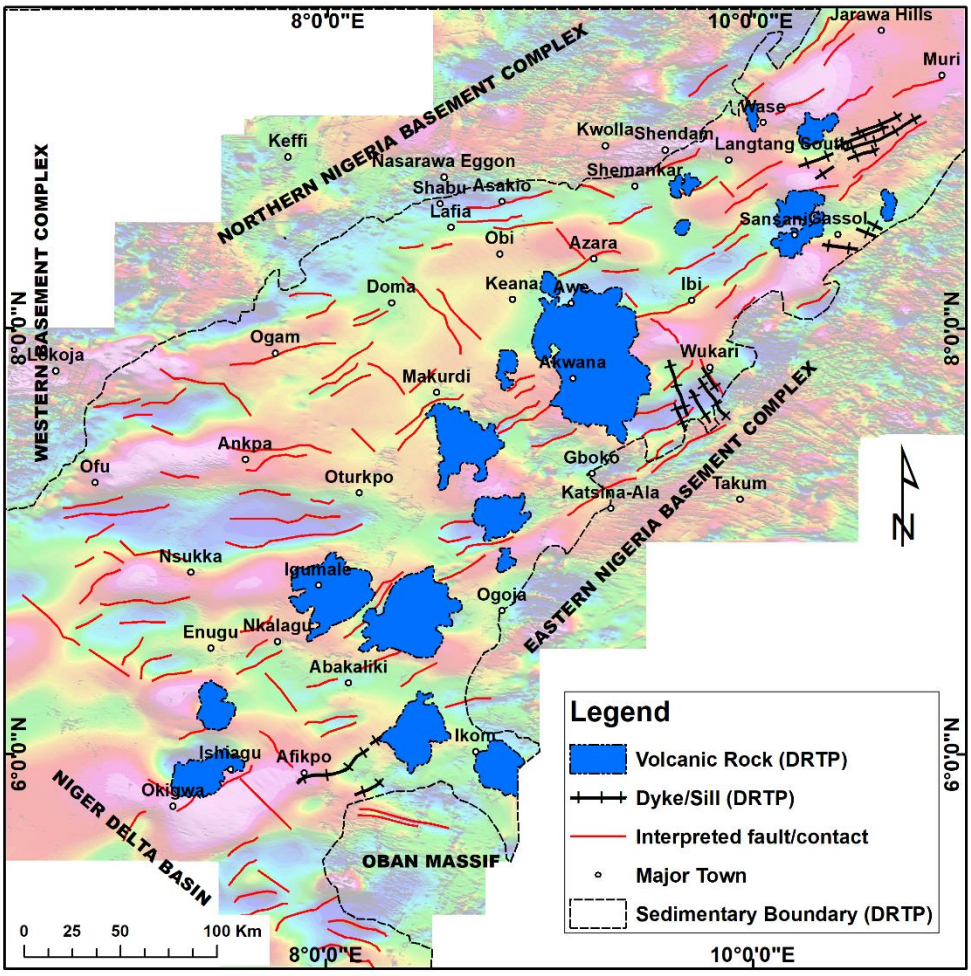

Fig. 3. 25: Delineated geologic structures draped over DRTP TMI anomaly map. The outlines of the volcanic rocks might mark centres of magmatic activity.

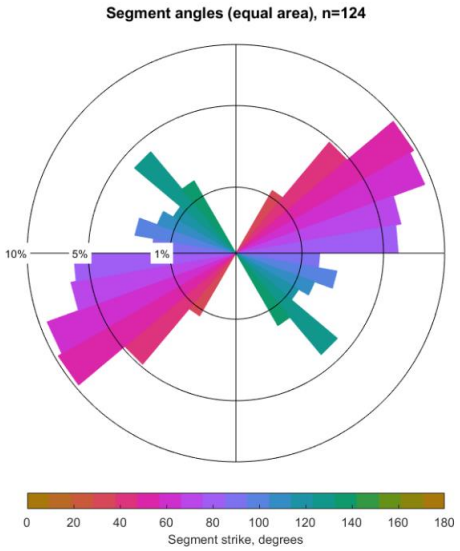

Fig. 3. 26: An equal-area rose diagram colour-coded by segment strike with a major NE-SW and a minor NW-SW trend direction. The mean vector azimuthal direction is 73 degrees with 124 total lineaments delineated.

3.4.2.3 Residual azimuthal filtered magnetic imaging of shallow lineaments/other geologic bodies

The residual azimuthal filtered magnetic data from figs. 3.14 b and c, which were depth sliced at the mean depths of 31 m and 520 m respectively, were enhanced by applying derivative-based filters. Vertical derivative and analytic signal were applied to the 31 m mean depth so that, the sediment-basement boundary, volcanic rocks/plugs/sills, and dykes could be delineated (Figs. 3.27 a and b). The dykes have a similar trend to those obtained from DRTE and DRTP, as they trend in a major NE-SW direction. However, tracking lineaments within depth slice 520 m is difficult due to noise and the limited resolution of the data (Figs. 3.27 c and d). The application of horizontal derivative and theta map techniques on depth slice 2 helped the delineation of a few lineaments. Fig. 3.28 presents the result of a combination of geologic structures obtained from residual magnetic anomaly filtered by the azimuthal method (depth slices 1 and 2). A general clustering of geologic features along the NE-SW trend direction could be interpreted as evidence for an alignment of magmatic structures with possible structural control.

The rose diagram of the strike segment orientations or azimuth directions of the geological lineaments were plotted using FracPaQ software (Healy et al., 2017), and reveals major NE-SW, and minor NW-SE strikes (Fig. 3.29). The lineament directions indicate results expected for geology even though the filter has effectively removed any features close to the N-S direction. This implies that the method of applying RTP and then removing the distorted parts of the spectrum might be adopted as a more robust approach for low latitude areas.

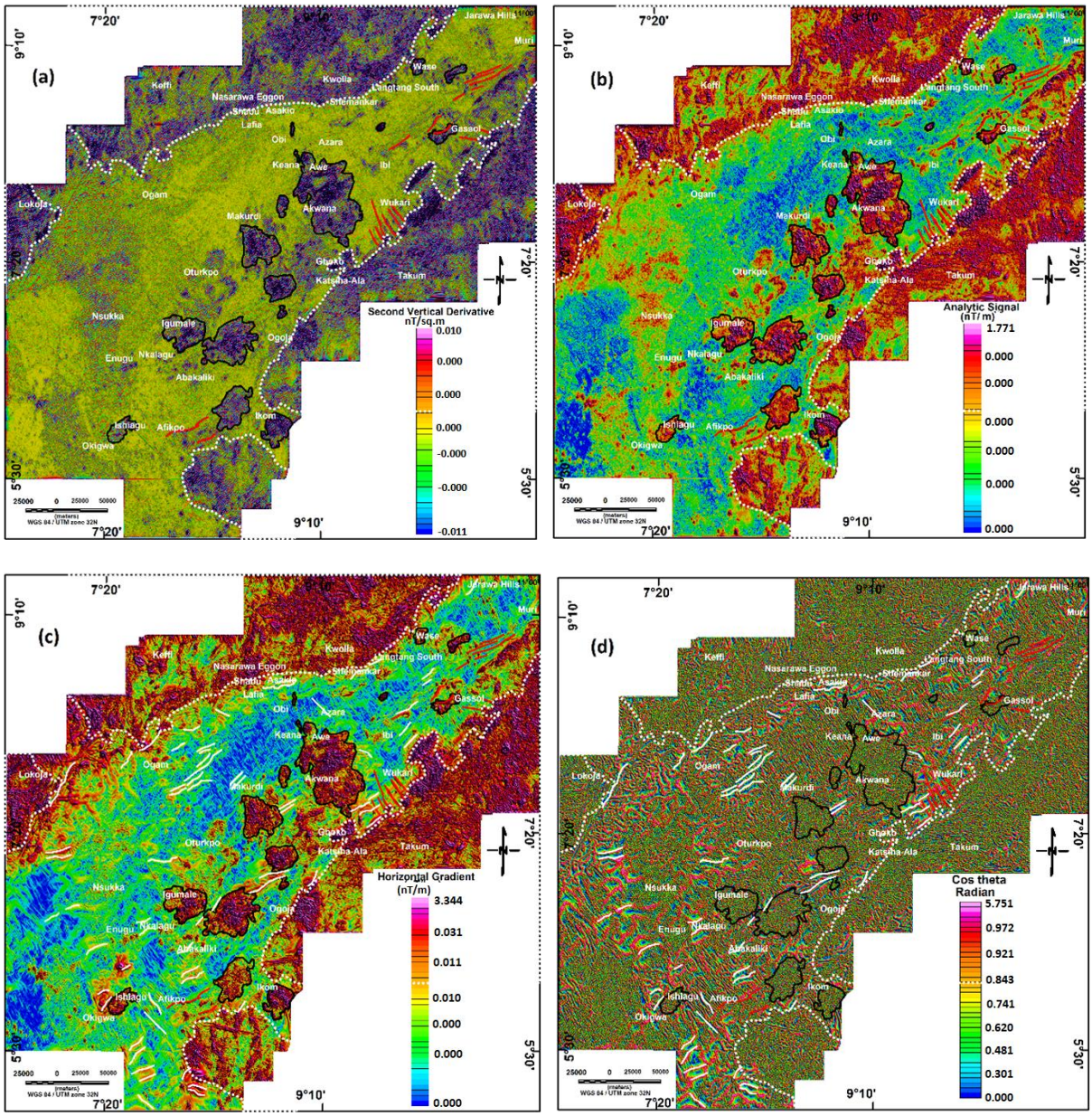

Fig. 3. 27: Second vertical derivative (a) and analytic signal (b) of 31 m depth slice 1. The red lines, white dots, and black polygons are delineated as dykes, basin-basements boundary, and volcanic rocks, respectively. Horizontal gradient (c) and Theta map (d) from the upper 532 m depth slice 2 with the white lines delineating lineaments, the black polygon as volcanic rocks, and the basin-basement boundary represented by the white dots.

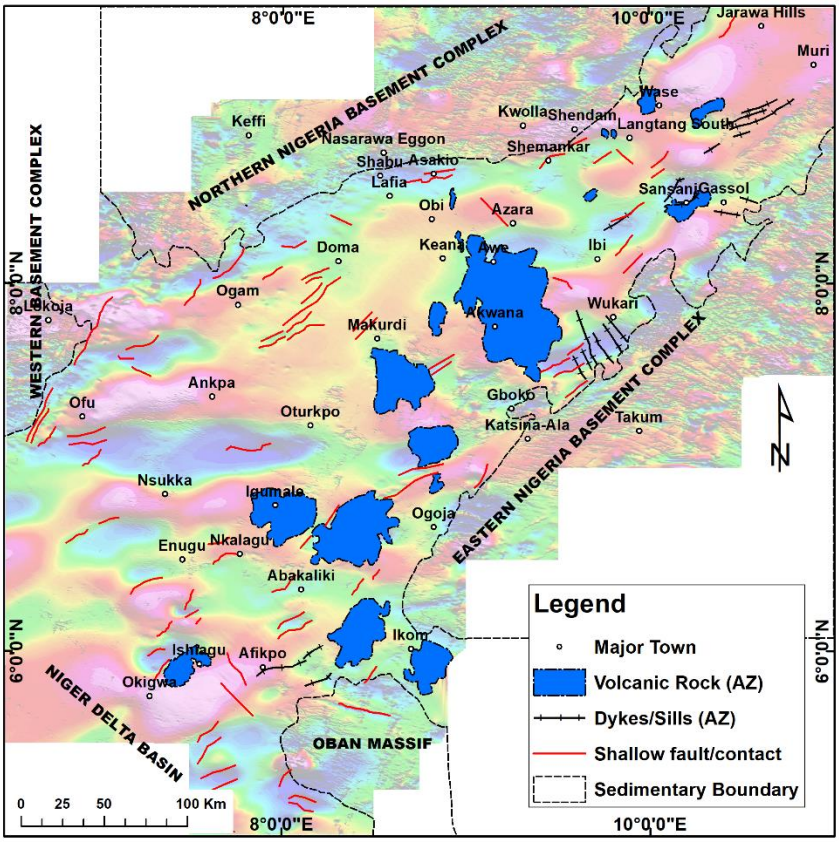

Fig. 3. 28: Geologic structural trends derived from the residual magnetic and draped over the TMI anomaly map. The outlines of the volcanic rocks show the centres of magmatic activity.

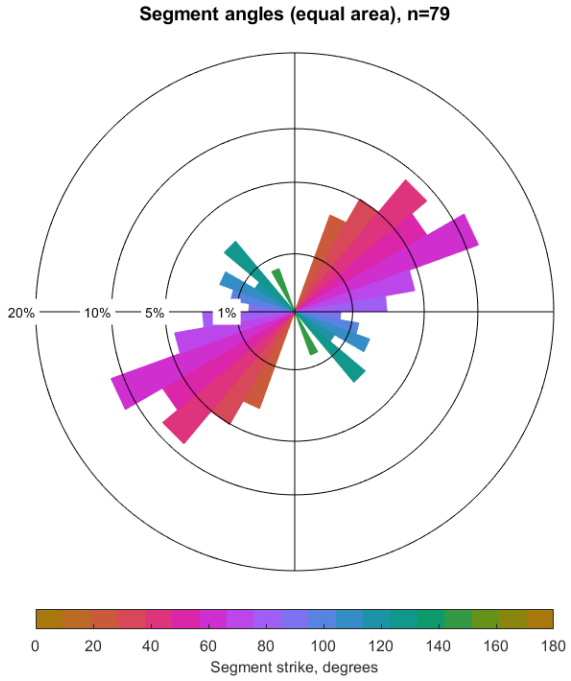

Fig. 3. 29: An equal-area rose diagram colour-coded by segment strike with a major NE-SW and minor NW-SW trend directions. The mean vector azimuthal direction is 59 degrees estimated from 79 total lineaments.

3.4.2.4 Integration of shallow magnetic lineaments/other geologic bodies

The results of geologic structural delineation of the area from DRTE, DRTP, and azimuthal filter methods have been combined (Fig. 3.30). This was achieved by picking lineaments that align with each other from the three methods to be the most reliable and acceptable lineaments (Cascone et al., 2017), and were combined with other geologic bodies to form the final shallow structural magnetic map of the area. The edges of isolated geologic bodies were picked exactly to represent lineaments, volcanic rocks/plugs, and other non-geologic features.

Fig. 3.31 shows two principal lineaments trends over the sedimentary area. The first trend is NE-SW while the second trend is a minor NW-SE. The NE-SW trend grades gradually into some ENE-WSW lineaments. The concentration of the intrusive rocks and their general trend of NE-SW direction indicated that the emplacement of magma could have been structurally controlled by the faults or could have caused faulting. The dykes show a preferred orientation like those of the faults implying that they are related in their evolution i.e., the NE-SW and NW-SE trending dykes align with the NE-SW and NW-SE trending lineaments, respectively, indicating a possible structural relationship.

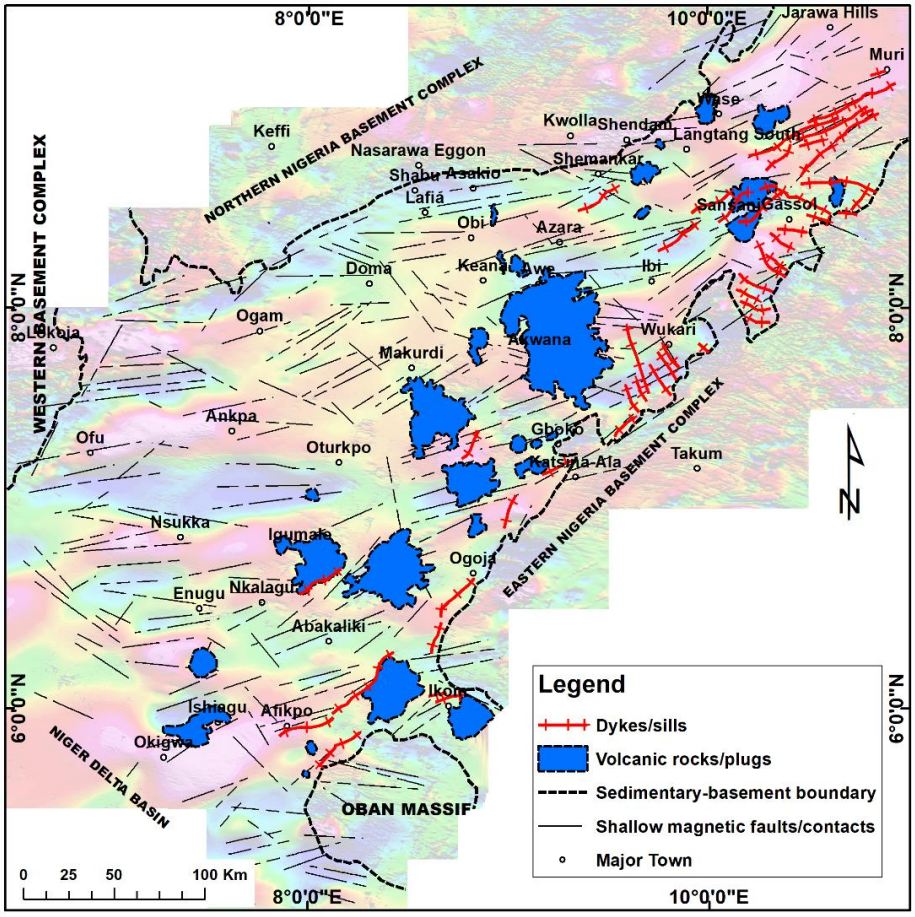

Fig. 3. 30: Integrated map of shallow magnetic lineaments and other geological bodies in the Lower and Middle Benue Trough.

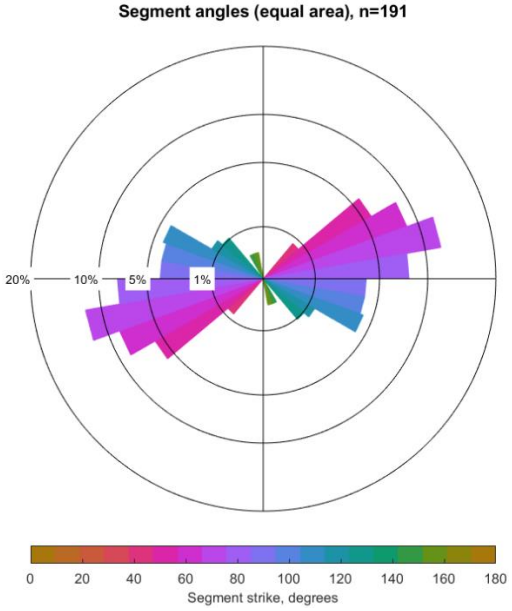

Fig. 3. 31: An equal-area rose diagram colour-coded by segment strike with a major NE-SE and a minor NW-SW trend direction. The mean vector azimuthal direction is 80 degrees of 191 interpreted lineaments

3.4.3 Mapping gravity shallow lineaments

The power spectrum analysis for the gravity data (Fig. 3.18) indicated three layers. Depth slice 1, with a mean depth of 3.43 km, showed the dominance of shallow gravity sources attributed to the contribution of the gravity responses from structures within the sedimentary layer. The residual gravity anomaly result was processed further by applying derivative-based filters and Euler deconvolution to enhance anomalies related to geologic structures. Here, the local extrema signifying points of lineaments in the filtered grid were determined by using a curvature analysis method (Phillips et al., 2007).

The horizontal gradient magnitude was calculated, and its maxima (greater than 0.0001 mGal/m) were marked as lineaments (Fig. 3.32 a). Local wavenumber maxima with values greater than 0.0002 1/m were delineated, and the points overlaid on the map (Figs. 3.32 b). These points traced marked edges of faults and vertical contacts. A tilt angle map was also calculated, and its zero-contour was used to map lineaments (Fig. 3.32 c). The tilt map was used to determine the throw directions of faults. Tilt values less than zero (blue colour) were interpreted as the down-dip throw direction while parts greater than the zero (red colour) represent the up-dip throw direction of the lineament. The estimates from Euler deconvolution solutions showed the location points of anomalous points that signify the edges of the anomalies (Fig. 3.32 d). The most influential parameter used for this calculation is the SI. SIs of 1 and 0 representing the geometries of thin-beds and small step-like faults, respectively, were assumed for the estimation (Reid et al., 2003; Reid and Thurston, 2014). Other parameters used in the calculation are a 10 km x 10 km moving window and a maximum depth of 15 km. Combined point estimated solutions (from SI 1 and 0) have been overlaid on the residual anomaly map to represent lineaments.

Lineaments were carefully mapped out and analysed based on co-located solutions from the derivative-based and Euler deconvolution methods. This provided increased confidence in the reliability of interpreted contacts and faults. The intersection of maxima of horizontal gradient and local wavenumber indicate the most appropriate location for lineament mapping. The horizontal gradient contact locations are continuous, thin, and straight, and to efficiently produce good results, were combined with analytic signal. In locations where the horizontal gradient and the analytic signal contacts are close together, they represent the best available contact location while where the horizontal gradient contacts were parallel to and slightly offset from analytic signal contacts, the analytic signal contact represented the true contact location

and the horizontal gradient contact indicates the down-dip direction (Ndougsa-Mbarga *et al.*, 2012; Cascone *et al.*, 2017). The gravity shallow lineament map of the area was determined by the combination of lineament edges obtained from the horizontal derivative, analytic signal, tilt, and Euler deconvolution analyses (Fig. 3.33).

Fig. 3.34 shows strike orientation rose plot diagram over the sedimentary area from gravity data sets and reveals four main lineament trends: the N-S, NE-SW, ENE-WSW, and the NW-SE orientations. Previous studies have suggested that the presence of these different orientations of lineaments could be a result of several phases of tectonic events that affected the area (Ajakaiye et al., 1991).

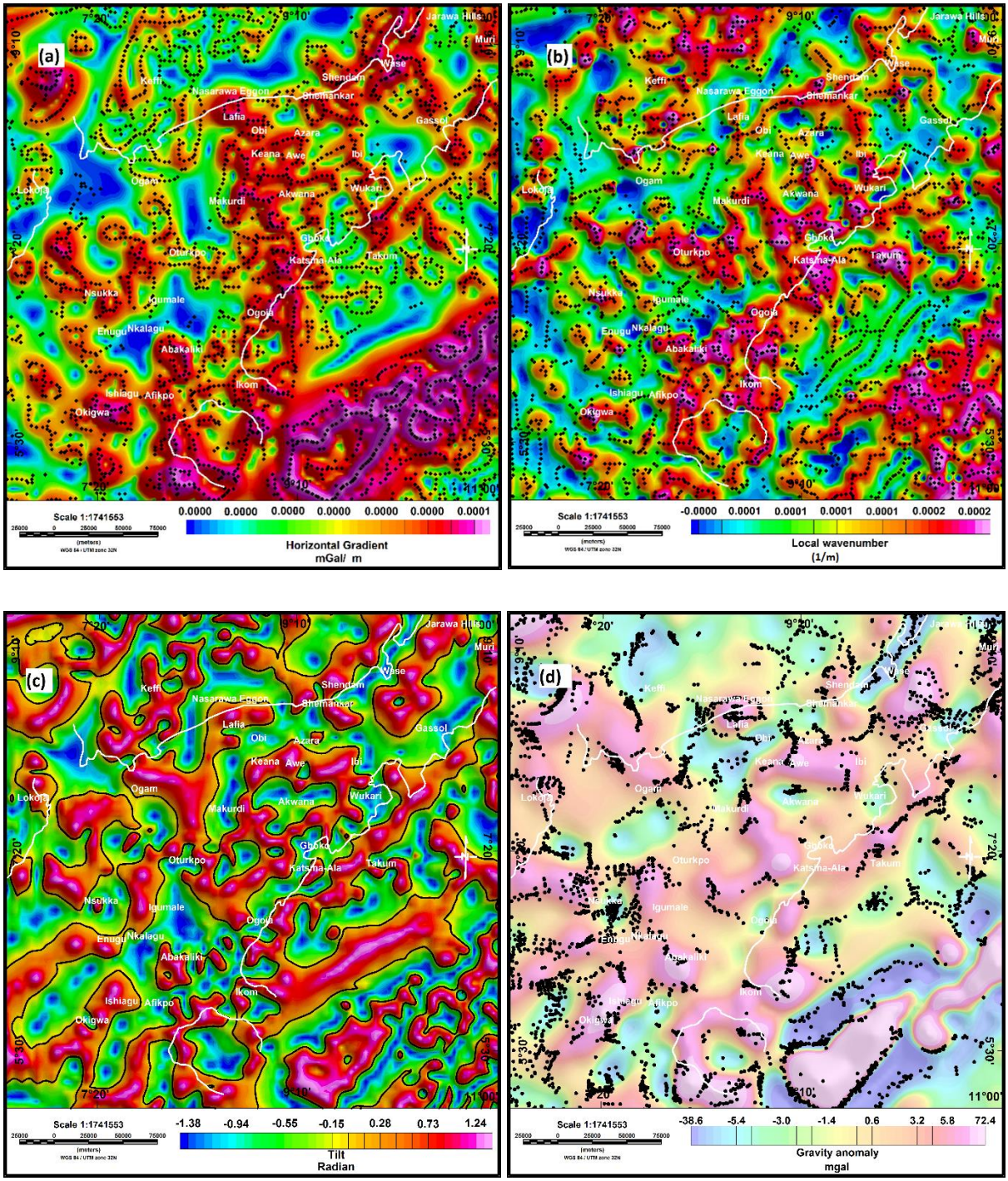

Fig. 3. 32: Residual gravity anomaly at depth slice 1 with mean of 3.43 km (a) Horizontal derivative (b) Local wavenumber (c) Tilt map (d) Euler deconvolution map using the structural indices of 1 and 0. The black dots and line marks edges or contacts forming lineaments.

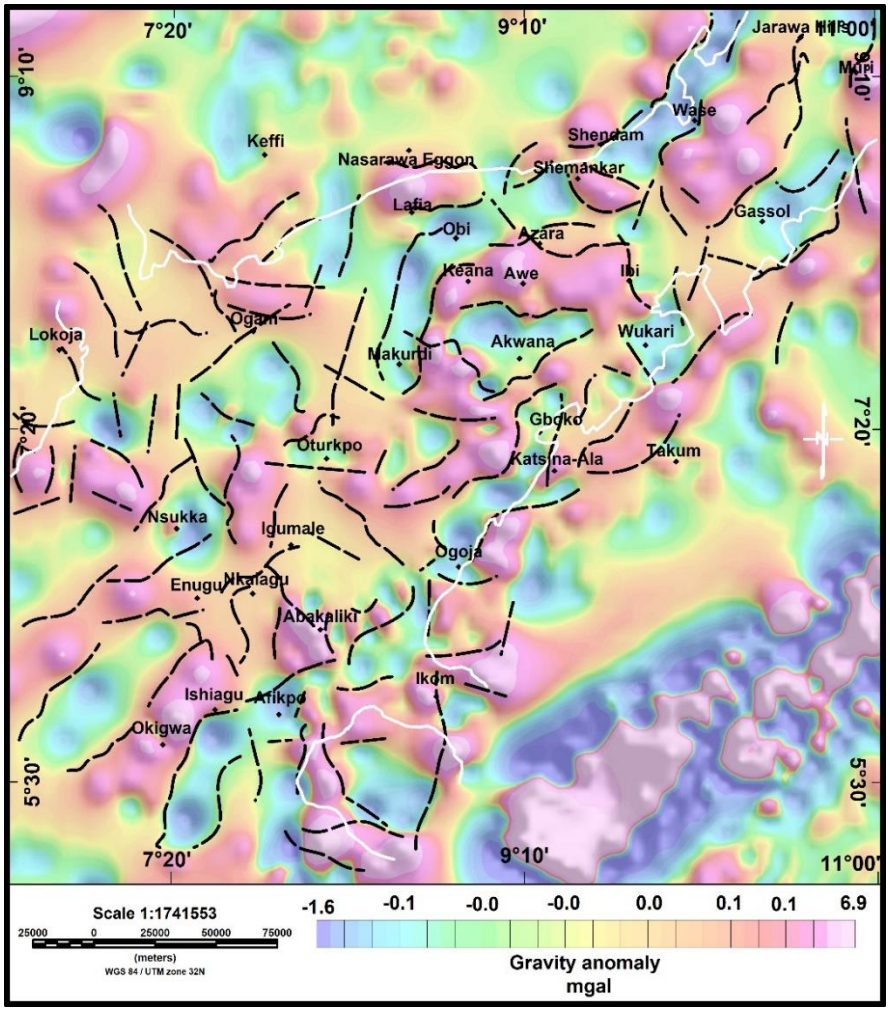

Fig. 3. 33: Lineaments derived from residual gravity and draped over the residual gravity anomaly map.

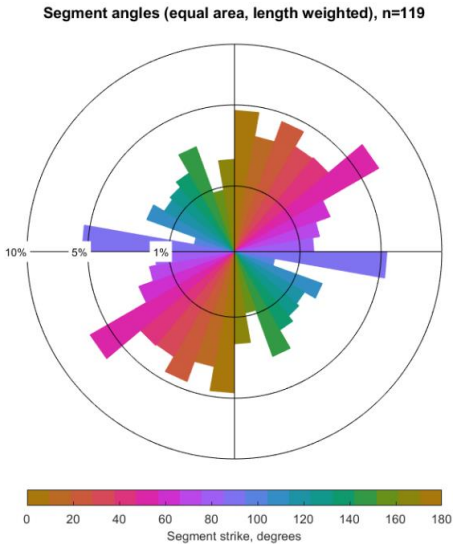

Fig. 3. 34: Rose diagram of lineaments with major NE-SW and ENE-WSW and minor NNE-SSW and NW-SE structural trends with 40-degree vector mean direction.

CHAPTER FOUR

GEOLOGICAL MODELS

4.1 Introduction

This chapter give details of the processes of evaluating the techniques for picking geological lineaments (non-tectonic and tectonic) and non-linear geological bodies over the Benue trough (Middle and Lower) of Nigeria. The main target for this chapter is to construct and update the geology map of the basin from chapters two and three as supporting materials as well as works from literature.

The following processes were involved in the study to achieve the aim:

1. Discussion on the uncertainties associated with the delineation of lineaments and non-linear geological bodies.
2. Separation of geologic-related lineaments from the non-geologic ones by applying the fracture-correlation lineament technique.
3. Estimation of the depth to these geological lineaments and non-linear geological bodies
4. Combining, interpreting, and constructing geological map model for the study area.

4.2 Uncertainties associated with surface/near-surface lineament extraction.

It is very difficult to separate tectonically related structures (faults and shear zones) from the many other lineaments of various types that have been obtained from multispectral images (Landsat and ASTER), shallow gravity, and magnetic data sets. This is because lineaments are any linear or curvilinear patterns on the earth's surface. They include anthropogenic remnants (electric cables, roads, rail lines, runways, plantation patterns, rights-of-way, etc.), topography, erosional features, faults, folds, bedding planes, river channels, dykes, etc. (Abarca, 2006). Methods of mapping lineaments from multispectral images, gravity, and magnetic data are very common and have been applied by several authors (Masoud and Koike, 2006; Taoufik et al., 2016; Abdullahi et al., 2019), but the task of separating them into either geological (dykes, intrusions, lithological contacts, etc) and non-geological lineaments or tectonic and non-tectonic lineaments is the main challenge. The ability to delineate tectonic lineaments from other lineament types for structural analyses may be limited when the source of the data sets have poor resolution and poor scale or are dominated by cultural features, settlements, erosional

features, thick surficial material, data processing noise, vegetation cover, acquisition artefacts or errors (Moore et al., 2002). These factors are commonly associated with uncertainties in results of structural mapping as they make it very difficult to discriminate tectonic lineaments. And yet, reliable maps of tectonic lineaments are essential pre-requisites for paleo stress analyses of an area (Fossen, 2010).

4.3 Nature of surface/near-surface geological lineaments and non-linear geological bodies.

Lineaments are found at all depths and in different sizes. Some are straight, others are curvilinear, and they may trend in different directions. Several methods that include unfiltered analysis, filtered domain-based analysis, and filtered discrete-analysis-based analysis techniques have been used over the years to identify fracture-correlated lineaments that may give results of direct record of tectonic activities (Degnan and Stewart, 2002; Moore et al., 2002; Acharya and Mallik, 2012; Elmahdy and Mohamed, 2016). These methods help in separating geological lineaments from other non-geological lineaments by comparing the lineament trends measured in the field with that obtained by remote sensing or gravity and magnetic data sets i.e., those lineaments trending in the same direction as those observed by field measurements are assumed to be geological lineaments (Moore et al., 2002).

Non-linear structural features present within the trough at the surface and/or near-surface are easily differentiated from the geological lineaments by their unique circular or semi-circular shapes. They may include structures like volcanic rocks, plugs, bosses, sills, etc.

4.3.1 Geological lineaments

Geologic-related lineaments were separated from the non-geologic ones by applying the fracture-correlation lineament technique (Moore et al., 2002; Degnan and Stewart, 2002; Acharya and Mallik, 2012). This involves first comparing the general lineament trends obtained in the area from multispectral data sets (Landsat and ASTER), shallow/residual gravity, and magnetic data sets, with those observed from field data orientations. Those lineaments that align parallel or sub-parallel to the general field observations are interpreted as geological lineaments i.e., fractures, joints, dykes, faults, lithological contacts, shear zones. Tectonic lineaments such as faults/fractures and shear zones were separated from other geological lineaments by overlaying the extracted dykes and those lineaments that align with the dykes are interpreted as non-tectonic lineaments and hence removed. The dykes were located and identified based on their distinct linear short wavelengths and discontinuous

changes in the magnetic fabrics and textures when enhanced by analytic signal. The resulting lineament data sets was still affected by some bedding-related geometries or lithological contacts that are still non-tectonic. These were eliminated by using a geological map to identify linear features that follow the formation geometries and are thus likely to be bedding related. Finally, the remaining lineaments were accepted as the related faults/fractures.

The assumptions and procedures outlined above may reduce the validity of the extracted tectonic lineaments. Some of the assumptions are that any lineaments that do not align with the major field structural trends are non-geological and those that overlay the dykes and lithological contacts are non-tectonic. This may result in the absence from the map of valuable faults that are found on the edges of lithological contacts and dykes. The assumption that the few field lineaments orientation measurements are used to interpret the whole lineament orientation may be insufficient for such analyses as many quadrants in the area can have different lineament orientations.

In this study, however, the unfiltered fracture-correlation technique was used by comparing lineaments extracted from multispectral data sets, gravity, and magnetic data sets with fracture trends obtained from field observations. Table 4.1 shows a summary of the rose plots of the field data orientations of various structures (joints, fractures, veins, dykes, and faults) obtained from observed and measured field data in different parts of the trough by different authors (Anudu et al., 2014; Chukwuebuka et al., 2010; Oha et al., 2017). Dominant NE-SW and NW-SE structural trends, with average mean vectors of 34° and 136° respectively, and minor N-S and ENE-WSW trends, were observed in the field by different authors. These trends were compared with rose plots of the area from the analyses of remote sensing, gravity, and magnetic data sets, and lineaments not aligning with the field data trends were removed and those having a similar trend are assumed to be of geological origin. To achieve this, lineament orientations from remote sensing, gravity, and magnetic data sets that are found to be between 20° and 50°, 120° and 150° (major lineaments) and between 0° and 10°, and 85° and 95° (minor lineaments) are considered to lie within the orientation bounds of published field observations (Anudu et al., 2014; Oha et al., 2017).

A total of 5550 lineaments were obtained from remote sensing data sets (Landsat and SRTM) and used in these analyses to extract geologic-based lineaments as shown in fig. 4.1. The spatial distribution of these lineaments in the southern part of the area showed that the linear features are organized along a N-S axis while those in the northern area are shorter and distributed

without a particular pattern (Fig. 4.1 a). The lineaments do not have a characteristic orientation due to the presence of both geologic and non-geologic lineaments. Fig. 4.1 (b) is a rose plot of the lineaments with no preferred orientation. The fracture-correlated lineaments technique employed here helped in delineating possible geologic related lineaments by removing the non-geologic lineaments (Fig. 4.2 a). Geologic lineaments are assumed to those are greater than 4 km long. A total of 873 geologic lineaments were extracted and presented on a rose diagram indicating four main orientations i.e., NE-SW, NW-SE, ENE-WSW, and N-S trends (Fig. 4.2 b).

The total lineaments derived from both shallow magnetic and gravity data were 229 and 123, respectively (Figs. 4.3 a, and 4.5 a respectively). The magnetic lineaments show general orientations of NE-SW and ENE-WSW directions with minor NW-SE orientation in Fig. 4.3 (b) while gravity lineaments indicate several trends in NE-SW, NW-SE, ENE-WSW, and N-S directions (Fig. 4.5 b). The non-distinct orientations of the gravity lineaments may relate to lateral and vertical changes in the density of the sediments. A fracture-correlation lineament technique was applied to the lineaments derived from magnetic and gravity data (Fig. 4.4 a, and Fig. 4.6 a). Major NE-SW, NW-SE, ENE-WSW, and N-S trends were filtered in both cases to represent the geologic lineament orientations (Fig. 4.4 b and Fig. 4.6 b). This delineated geological lineament data set still retains some non-tectonic lineaments like dykes and lithological contact, and these must be removed.

Table 4. 1: Field observations of the geological structures of the area.

Benue Trough	Terrain	N0. of Data	Rose plots analyses	Trend		Author
				Dominant	Minor	
Middle	Basement	49	Joint, fault, vein, and dyke	NE-SW (mean 40°) & NW-SE (mean 135°)	N-S & ENE-WSW	(Anudu et al., 2014)
	Sedimentary	38		NE-SW (mean 45°) & NW-SW (mean 130°)	NW-SE & N-S	
Lower	Albian Shales	66	Joint	NE-SW (mean 39°) & NW-SE (mean 148°)	N-S	(Oha et al., 2017)
	Dolerite	105	Fractures	NW with vector mean of 140°		(Chukwuebuka et al., 2010)
	Dolerite Dyke	115		NE-SW (mean 45°) & NW-SW (mean 125°)	ENE	

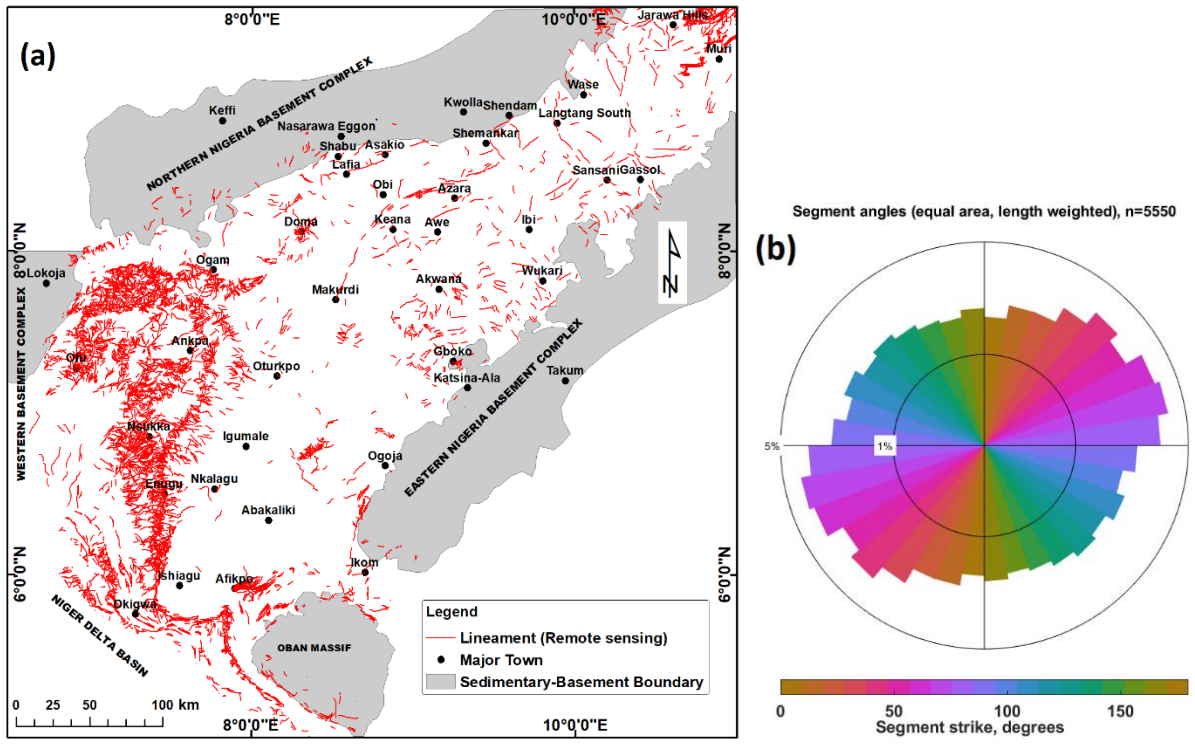

Fig. 4. 1: (a) Lineaments from remote sensing (Landsat and SRTM) (b) Rose diagram showing no distinct lineament orientation due to the presence of geologic and non-geologic lineaments.

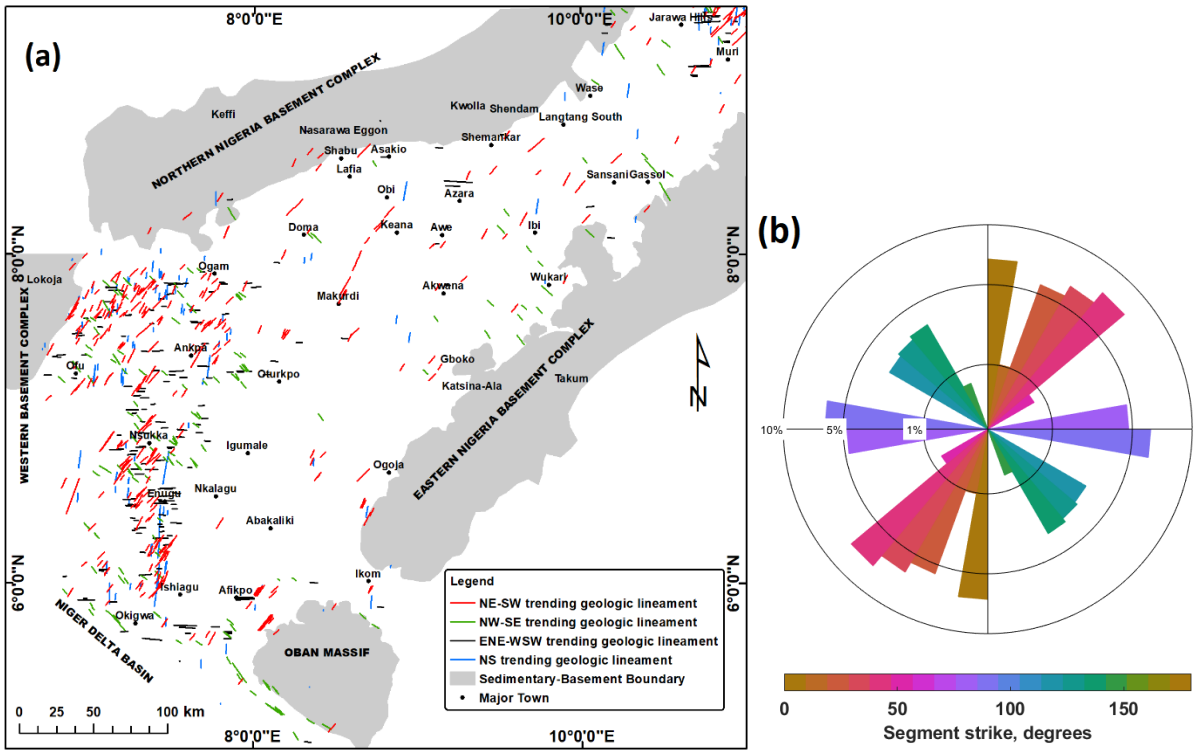

Fig. 4. 2: Interpreted geologic lineaments using the fracture-correlated lineaments technique (a) and the rose plot is presented in (b) with four lineament orientations.

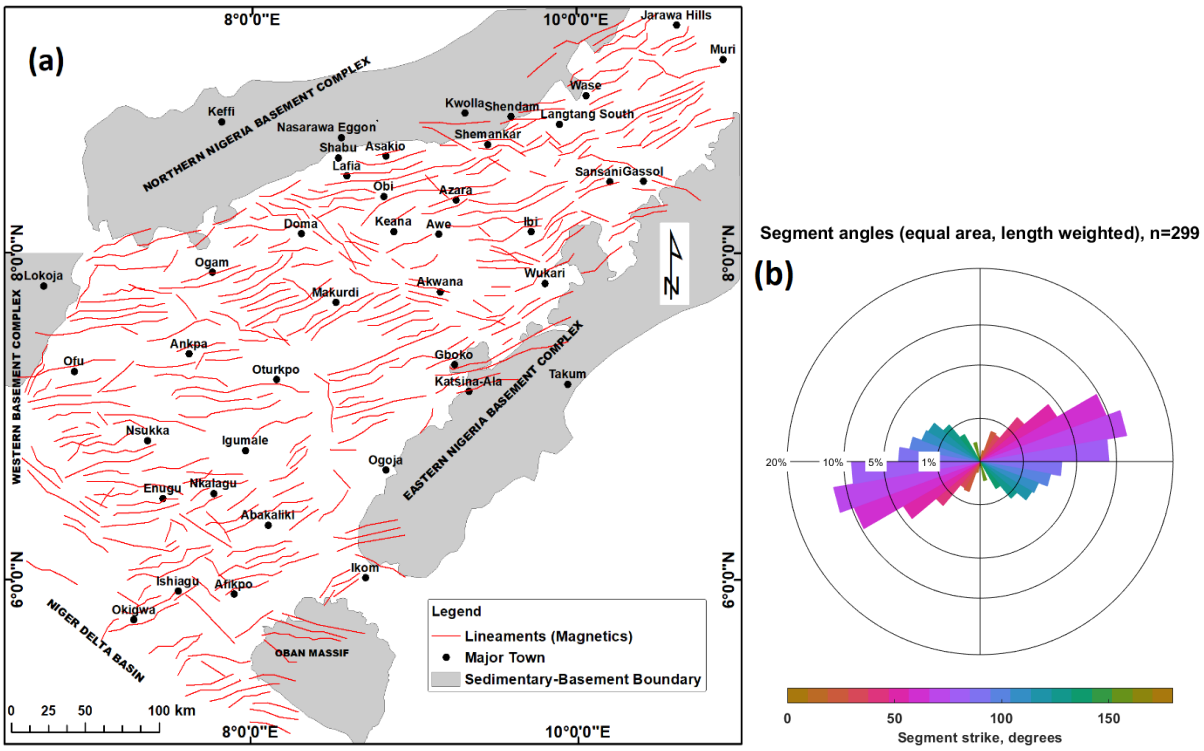

Fig. 4. 3: (a) Shallow lineaments from magnetic data (b) Rose diagram showing major NE-SW and ENE-WSW trends. A minor NW-SE trend was identified.

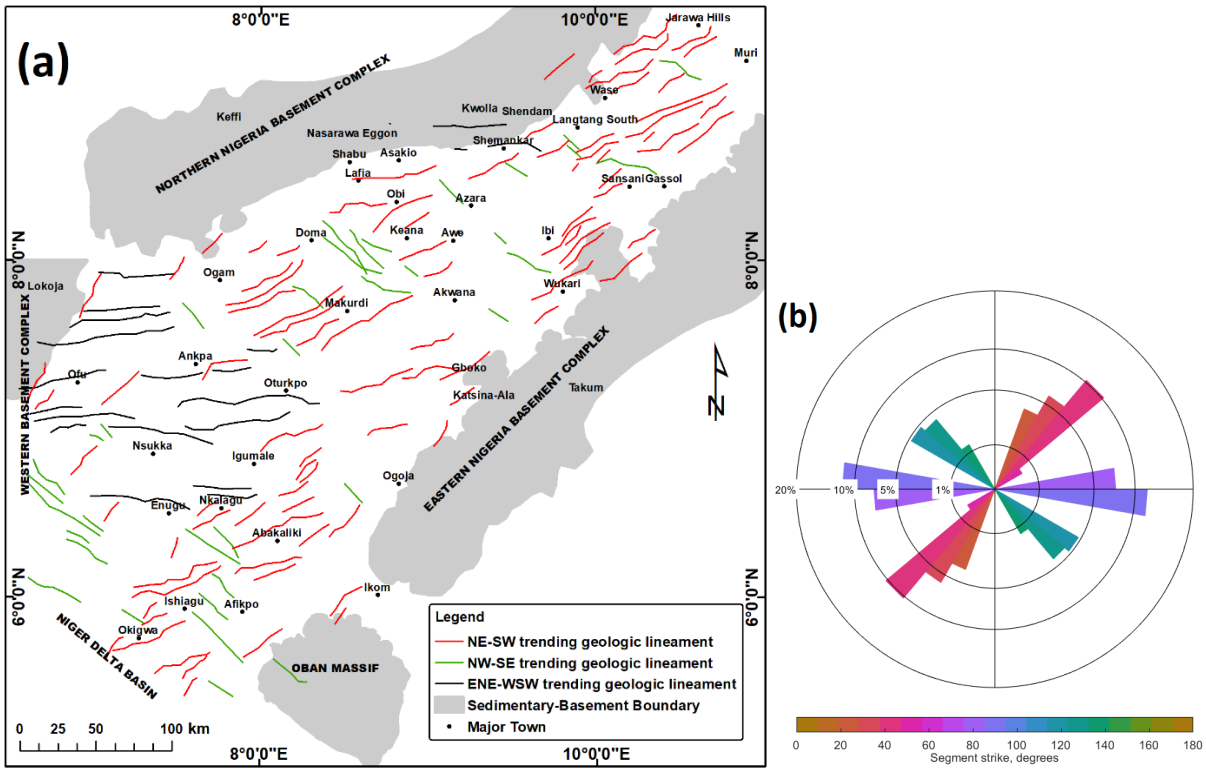

Fig. 4. 4: (a) Interpreted geologic lineaments from shallow magnetic data using the fracture-correlated lineaments technique (b) Rose diagram showing three (3) main filtered trends i.e., NE-SW, NW-SE, and ENE-WSW orientations.

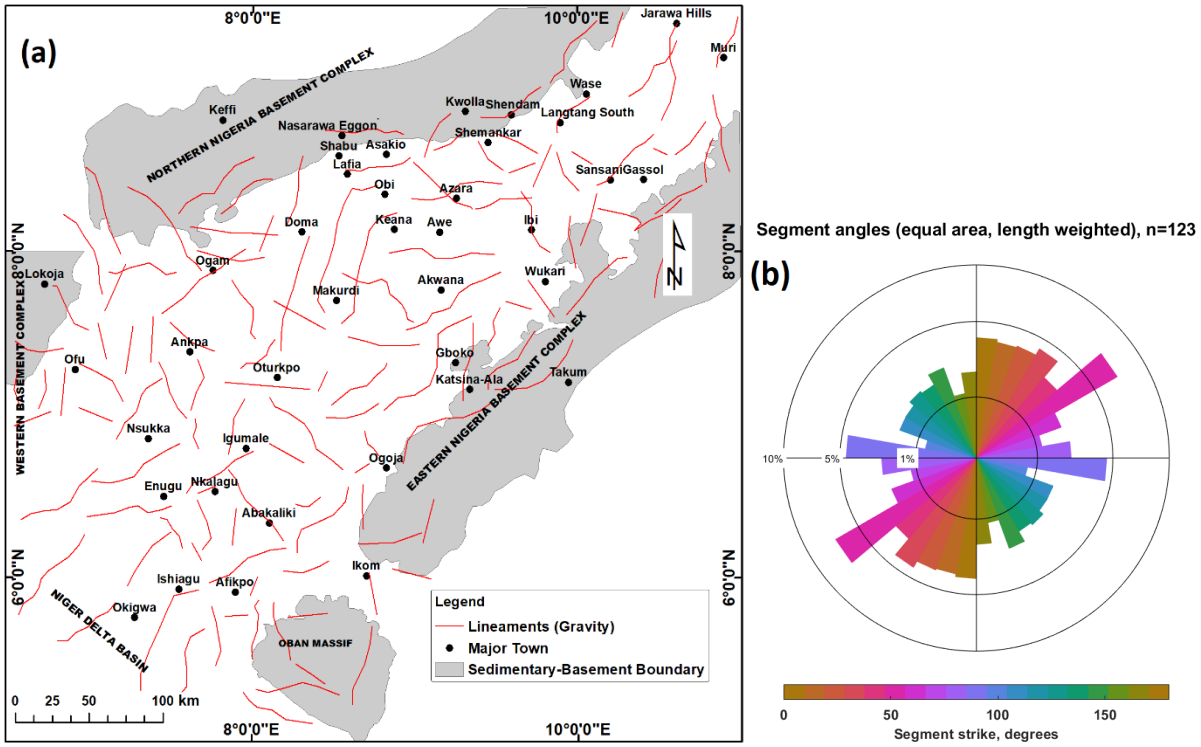

Fig. 4. 5: (a) Shallow lineaments from gravity data (b) Rose diagram showing major NE-SW and ENE-WSW trends.

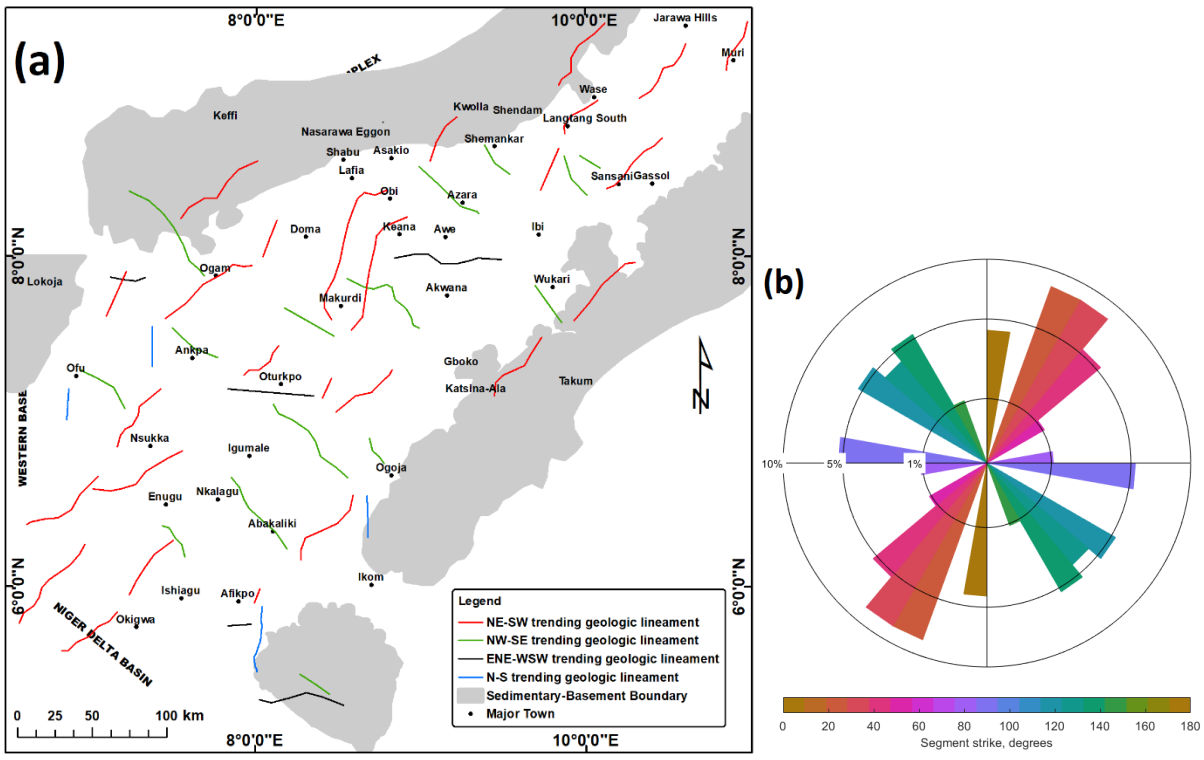

Fig. 4. 6: (a) Interpreted geologic lineament from shallow gravity data sets using the fracture-correlated lineament technique (b) Rose diagram showing four (4) main lineaments trends i.e., NE-SW and NW-SE orientations.

4.3.1.1 The non-tectonic lineaments

The non-tectonic lineaments (Dykes, lithologic contacts), especially the dykes, are easily identified by their unique linear high amplitude dominated by short wavelengths that show abrupt discontinuity in the magnetic fabrics and textures, mostly observed from magnetic data that has been enhanced by methods like the analytic signal, local wavenumber or vertical derivative.

The dykes generally trend in NE-SW and NW-SE directions similar to the general trend directions of the lineaments. Their locations, natures, and depths were estimated in this study using the analytic signal method from magnetic data sets. This method was selected because of its effectiveness in mapping dykes at low geomagnetic latitudes. The method attempts to locate the maximum amplitude and has the advantage of being independent of the direction of the magnetic inclination and declination (MacLeod et al., 1993; Roest and Pilkington, 1993; Hsu *et al.*, 1996; Cooper, 2014). The technique estimates the amplitude ratio between the first order and the second-order analytic signal. Salem and Ravat (2003) gave a simple formula for the analytic signal depth estimate method to locate and calculate depths to dykes as follows.

$$\mathbf{D} = \frac{[(\mathbf{N+1})\ \mathbf{AS_1}]}{\mathbf{AS_2}} \text{..... (4. 1)}$$

Where the 3D analytic signal, AS, is better calculated from the derivatives to reduce noise.

$$\textbf{1st order analytic signal}, AS_1 = \sqrt{\left(\left(\frac{\partial T}{\partial x}\right)^2 + \left(\frac{\partial T}{\partial y}\right)^2 + \left(\frac{\partial T}{\partial z}\right)^2\right)} \text{.....(4. 2)}$$

$$\textbf{2nd order analytic signal}, AS_2 = \sqrt{\left(\frac{\partial^2 T}{\partial x^2}\right)^2 + \left(\frac{\partial^2 T}{\partial y^2}\right)^2 + \left(\frac{\partial^2 T}{\partial z^2}\right)^2} \text{...(4. 3)}$$

Where D is the distance to the source or depth to the top of the anomaly, N is the structural index, which for dykes is 1, while T is the observed total magnetic field at (x, y and z).

Several dykes were obtained in this way and found to trend in two major directions: NE-SW and NW-SE (Fig. 4.7). The dykes are observed to be restricted towards the eastern basement complex stretching NE-SW from the North to the South. Three prominent areas were selected for location and estimation of the depth to the dykes (Fig. 4.8). In all the depths estimated, the mean terrain clearance value (80 m) was subtracted. Fig. 4.9 (a) shows the NE-SW trending dykes 1, 2, and 3 with estimated depths of 0.5 km, 0.6 km, and 0.7 km, respectively. NW-SE trending dykes 1, 2, 3, and 4 were located at the eastern part of the trough with estimated depths

of 0.5 km, 0.6 km, 0.5 km, and 0.7 km, respectively (Fig. 4.9 b). Another NE-SW trending dyke located at the southern part of the trough shows sharp contact with the main sedimentary area and was estimated at a depth of 0.3 km (Fig. 4.9 c). This analysis has located and estimated the depth of the dykes as well as clearly shown the orientation and the geometry of the dykes. The results indicated that the dykes are all quite near the surface i.e., 500 m, 600 m, 500 m, and 700 m for dykes 1, 2, 3, and 4, respectively and are restricted towards the eastern part of the trough. The emplacement of the dykes within the sedimentary rock at shallow depth implies the prior passage of magma through deep-seated basement lineaments.

The delineated dykes were superimposed on the mapped geological lineaments and where the lineaments overlay on each other, the lineament is considered non-tectonic and henceforth removed. This process is also employed for the lithological contacts by using the lithological contacts described in figs. 1.4 and 2.30 to overlay on the geological map and identify lineaments that can be considered non-tectonic and then removed. The remaining lineaments were interpreted as tectonic lineaments.

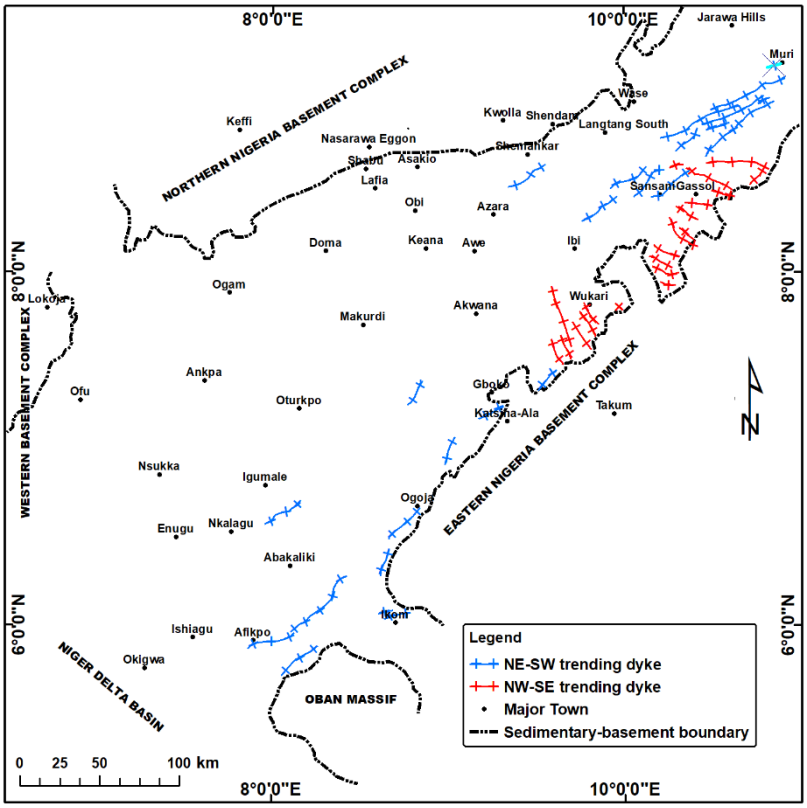

Fig. 4. 7: (a) The spatial distribution of dykes obtained from magnetic data sets constrained to the eastern part of the trough with two major trends.

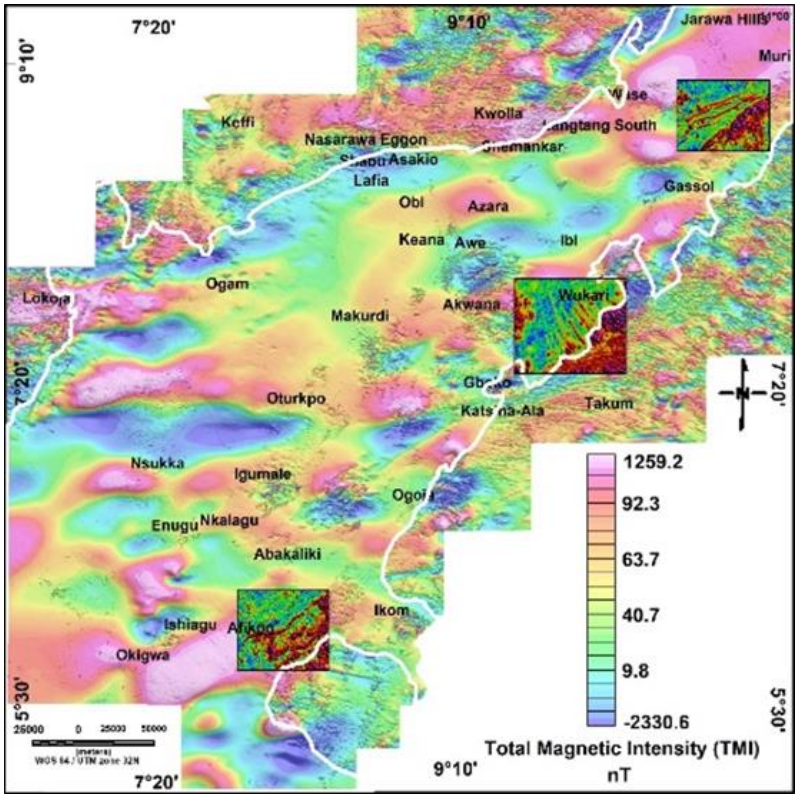

Fig. 4. 8: Location map of dykes showing three windows of dyke dominance overlaid on TMI map.

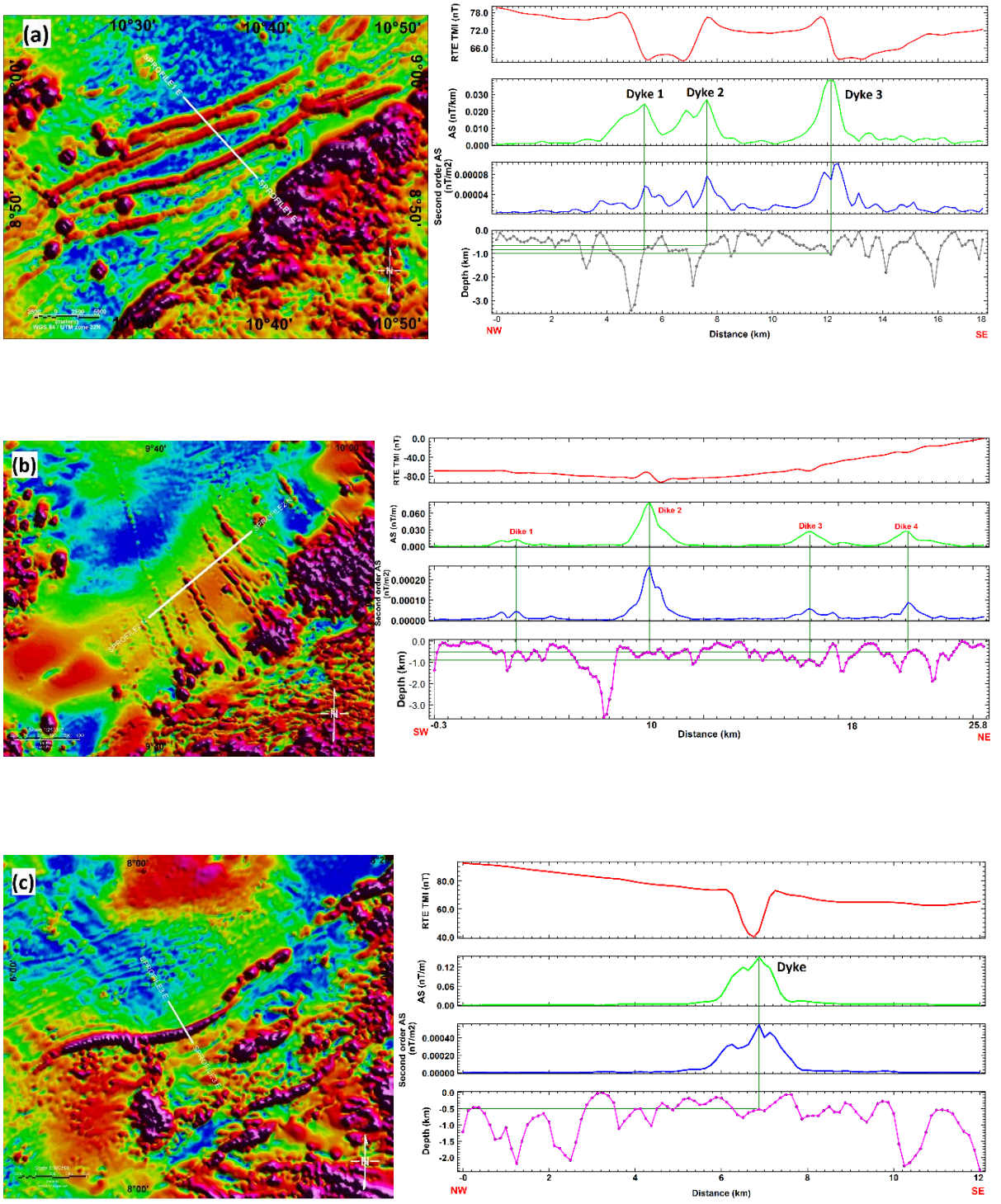

Fig. 4. 9: Analytic signal map showing the location and depth estimation of dykes (a) NE-SW trending dykes located at the northern part of the trough (b) NW-SE trending dykes found towards the eastern part (c) Curvilinear NE-SW trending dyke with sharp contact delineated towards the southern part of the trough.

4.3.1.2 Tectonic lineaments

The tectonic lineaments (faults/shear zones) were obtained by carefully removing non-tectonic lineaments (dykes and lithologic contacts) from the delineated geologic lineament map produced from the fracture-correlation lineament technique. This was done by overlaying the delineated dykes (Fig. 4.7) and the lithological contact maps (Figs. 1.4 and 2.29) on the geologic lineament maps produced by remote sensing (Fig. 4.2), magnetic (Fig. 4.4), and the gravity (Fig. 4.6) such that lineaments/contacts lying on each other are removed and the remaining lineaments are interpreted as the tectonic lineaments (Fig. 4.10). The tectonic lineament map of the area from the shallow data sets is important in building the tectonic model that reveals the evolutionary pattern of the trough.

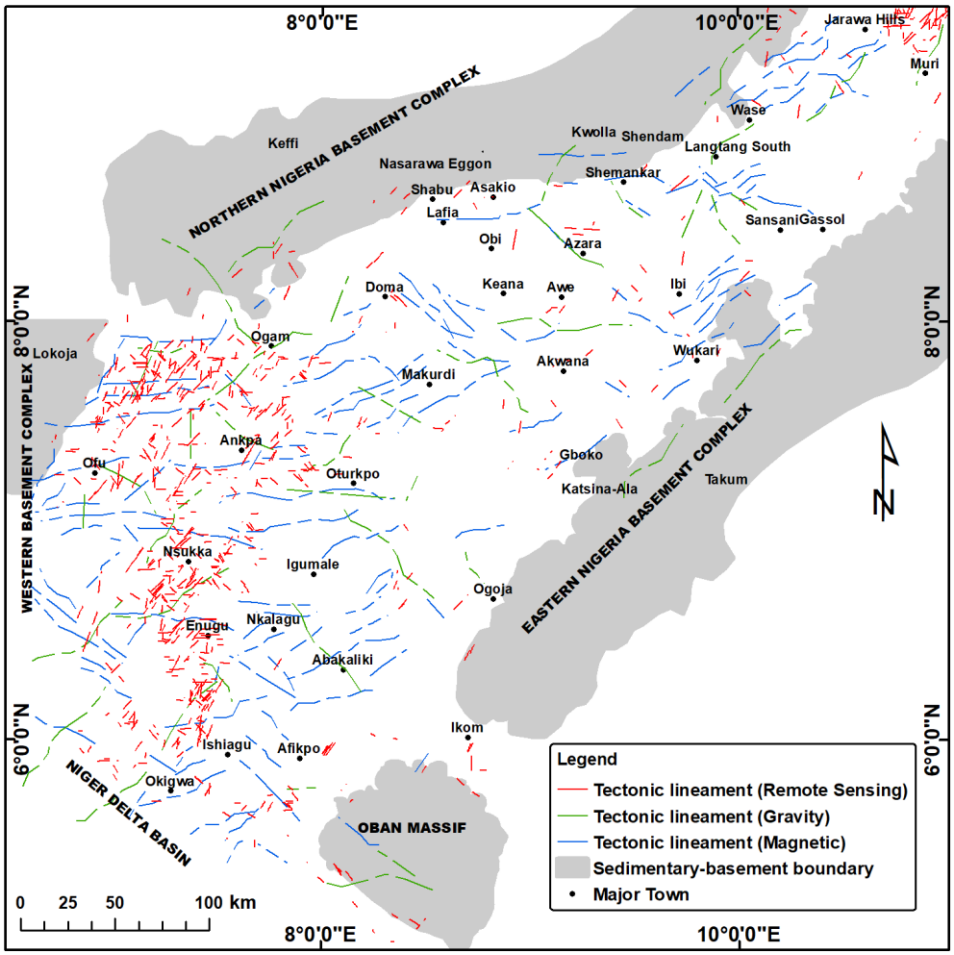

Fig. 4. 10: Combined tectonic map of the area representing the spatial distribution of faults/shear zones that are produced. The non-tectonic geologic lineaments have been removed.

4.3.2 Non-linear geological bodies

The Benue Trough hosts several non-linear shallow geological bodies that have been emplaced within and onto the sediments. They are mainly intrusions/extrusive rocks (volcanic rocks, plugs, bosses, and sills) that occur in different sizes and shapes and are easily differentiated from geological lineaments as they do not have any specific trend and are not linear. It is however very difficult to sub-classify them based on surface observations, but they are easily identified from magnetic data sets by their concentration of very high amplitude short wavelength signals describing a distinct circular or semi-circular shape on enhanced magnetic data.

An attempt to estimate the average depth to the tops of the intrusive/extrusive rocks was made using the infinite local wavenumber method. This method underestimates depth to the top of causative bodies with limited vertical extent (Salem *et al.*, 2014; Ali *et al.*, 2017; Fairhead et al., 2017) but in this case, it was assumed that the depth to the bottom of the geologic feature is the Curie depth or the Moho. The ratio between the depths to the top of magnetic source and that of Moho interface is very large and is assumed to tends towards infinity. The method calculates the maximum of the local wavenumber, k, which lies directly over the anomaly and marks its edges (Salem, Blakely, et al., 2014). It has a simple bell shape that peaks directly over certain simple 2D magnetic sources such as contacts, the tops of thin dykes, and horizontal cylinders. (Thurston and Smith, 1997). Phillips (2000) gave an expression for the 3D local wavenumber which is used here to calculate the peak of local wavenumber and, consequently, the depth to the volcanic rocks.

$$\boldsymbol{k = \frac{1}{\left((t_x{}^2)+(t_y{}^2)+(t_z{}^2)\right)}\left(t_x t_{zx} + t_y t_{zy} + t_z t_{zz}\right)} \text{.....(4. 4)}$$

Where $t_x = {}^{\partial T}/_{\partial x}$, $t_y = {}^{\partial T}/_{\partial y}$ and $t_z = {}^{\partial T}/_{\partial z}$ are the magnetic field gradient in x, y, and z directions respectively while t_{zx} , t_{zy} and t_{zz} are the derivatives of the vertical derivative of the anomalous magnetic field in x, y, and, z directions.

For magnetic sources with infinite depth extent, the local wavenumber at the peak is given by;

$$\boldsymbol{k_{h=0} = \frac{[(N+1)]}{Z_t}} \text{.....(4. 5)}$$

where Z_t is the depth to the top of the body and *N* is a value characterizing source geometry (Salem and Smith, 2005) which is also equivalent to the structural index (Thompson, 1982). In this study, we used 0 for *N* which can be understood in terms of a planar geologic contact.

Areas of dominant intrusive/extrusive rock presence were selected, and their depths were estimated (Fig. 4.11). The rocks are concentrated toward the eastern part of the map in the same areas as the dykes. The depth estimates obtained using this method include a number of spurious values in excess of 2 km. These depths are considered spurious due to the fact that the average estimates for the shallow geologic bodies depths are is 1.8 km, 1.1 km, and 0.5 km from the DRTE, DRTP, and Azimuthal filter methods respectively. An average depth of 0.4 km (400 m), after terrain clearance subtraction was estimated to the tops of the igneous rocks (Figs. 4.12 (a) and (b)). In most parts of the study area where the intrusive/extrusive rocks are located, shallow depth values mark their edges and as such give a fair estimate of geometry.

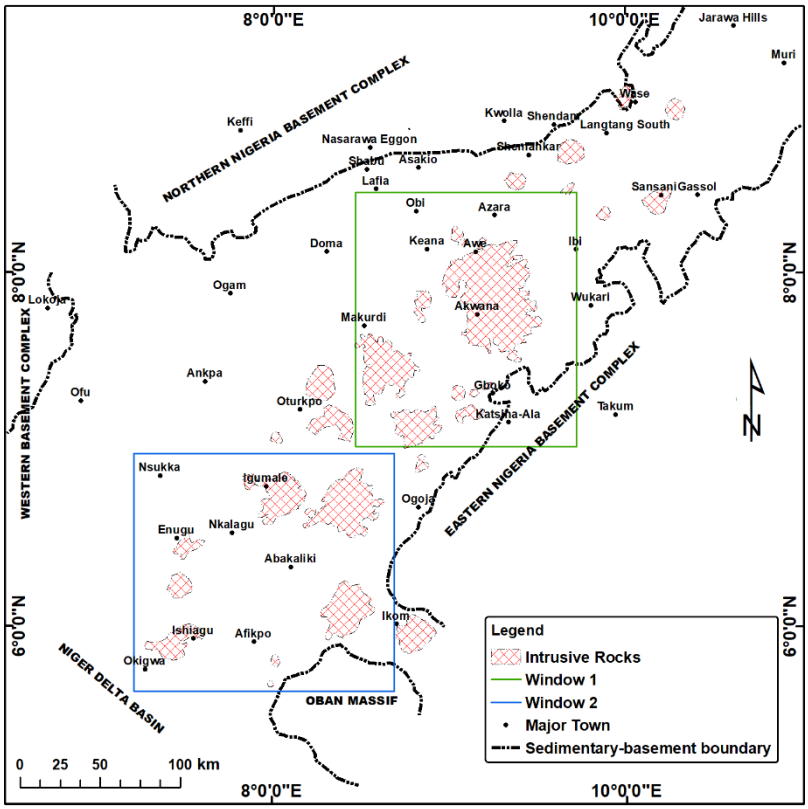

Fig. 4. 11: The spatial distribution of intrusive rocks (volcanic rocks, sills, and plugs) obtained from mapping analytic signal and constrained to the eastern part of the trough. The polygons shapes define areas of intrusive rock emplacement. Window 1 is the topmost box (green) while window 2 is beneath it towards the south (blue).

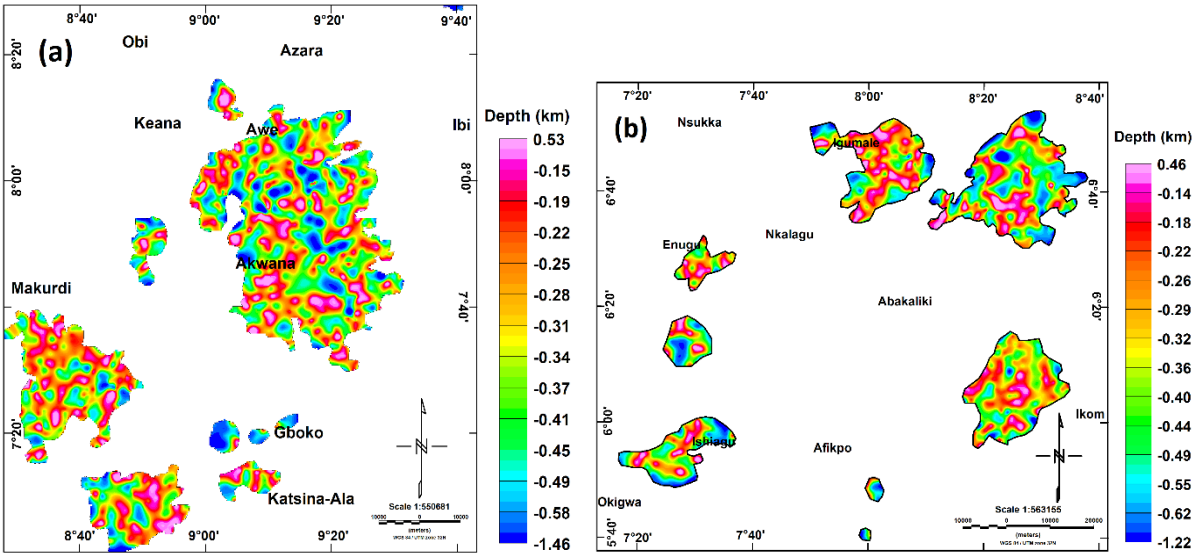

Fig. 4. 12: Depth estimates of major intrusive rock areas presented after terrain clearance subtraction. The outline corresponds to the selected areas where the intrusive rocks are dominant. (a) Window 1 shows intrusive rock depth estimates averaging 0.4 km (400 m) (c) Window 2 shows intrusive rocks depth estimates averaging 0.4 km (400 m).

4.4 Geological interpretation of the area from the analysis of remote sensing, gravity, and magnetic data sets

The combination of remote sensing and magnetic techniques in mapping the geology of the study area has shown the effectiveness of an integrated approach towards the geological mapping of the basin. The techniques were used to map lithological units with their formation names identified from literature with careful analyses of the remote sensing and magnetic data (Fig. 4.13). The stratigraphy includes the Asu-river group, the Bima sandstones, Yolde formation, Awe-Keana formation, Markurdi sandstones, Eze-Aku formation, Pindiga formation, Awgu formation, Lafia Formation, Nkporo formation, Ajali formation, Imo Shale, Ameki formation. The oldest formations that overlie the basement are the Asu-river group in the Middle Benue Trough and the Bima sandstone deposited in the Upper Benue Trough (Benkhelil, 1989; Nwachukwu, 1985). The youngest of all the formations is the Imo shale that is Paleocene to Lower Eocene in age and extends into the Niger Delta basin (Obaje, 2009).

The techniques for structural mapping of the basin involved the use of remote sensing, magnetics, and gravity data sets. Magnetic data effectively delineated the boundary between the sediments and the basement thereby showing the spatial extent of the trough (Section 3.4.2). The distribution of geologic features like the volcanic rocks/plugs, sills, and dykes have been well delineated and shown in this study. These features are found to be concentrated towards the eastern part of the area trending in a major NE-SW direction from the South to the North across the basin. The dykes show two main trends: the NE-SW and the NW-SE trend directions. The areal extent of volcanic rocks/plugs runs from Okigwe (Ishiagu) in the south to Wase (Zurak) in the north. The alignment of the intrusive/volcanic rocks and dykes hints at a spatial control on emplacement of these rocks, for example a deep-seated fault system (Benkhelil, 1989). The emplacement axis of the intra-sedimentary intrusive/extrusive rocks from this study agrees with the NE-SW trend direction of the trough as well as the trend of Cretaceous Pb-Zn and barytes mineralization (Fitton, 1980; Ofoegbu, 1985). A strong relationship exists between magmatic centres and regional fault systems (Wright, 1976; Ofoegbu, 1985). Lineaments observed within the trough indicate a predominance of NE-SW and NW-SE trends with minor N-S and ENE-WSW trends (Fig. 4.13), and these orientations have been observed in the area by many authors (Ofoegbu, 1985; Ajayi and Ajakaiye, 1986; Anudu *et al.*, 2014; Oha *et al.*, 2016; Abdullahi *et al.*, 2019).

The geo-structural map produced from remote sensing, magnetics, and gravity data sets (Fig. 4.13) is similar but more robust than the existing geology map from literature (Fig. 4.14). Most of the lithologies from this study were identified by comparison with the established geology from the literature map. This study mapped fewer lithologies within the basin while existing literature showed more lithologies in the southern part of the basin. However, the lithological boundaries produced from this study show reasonable lithological contacts than those of existing geology. The sedimentary-basement boundary, faults, dykes, and intrusive/volcanic rocks are better defined in this study than on the existing geology map. Synclinal and anticlinal structures have not been imaged by this study but are present in the existing geology map. A combination of the geo-structural map from this study and that of literature has greatly improved and updated the geology map of the area (Fig. 4.14). Generally, the basin widens in the Southern part and tightens towards the northern part to display an asymmetric geometry that hints at possible opening source emanating from the South Atlantic towards the basin. This effect is seen in the southern area, where the basin is deeper than in the northern part making the basin more structurally complicated likely to be associated to the uneven opening of the trough.

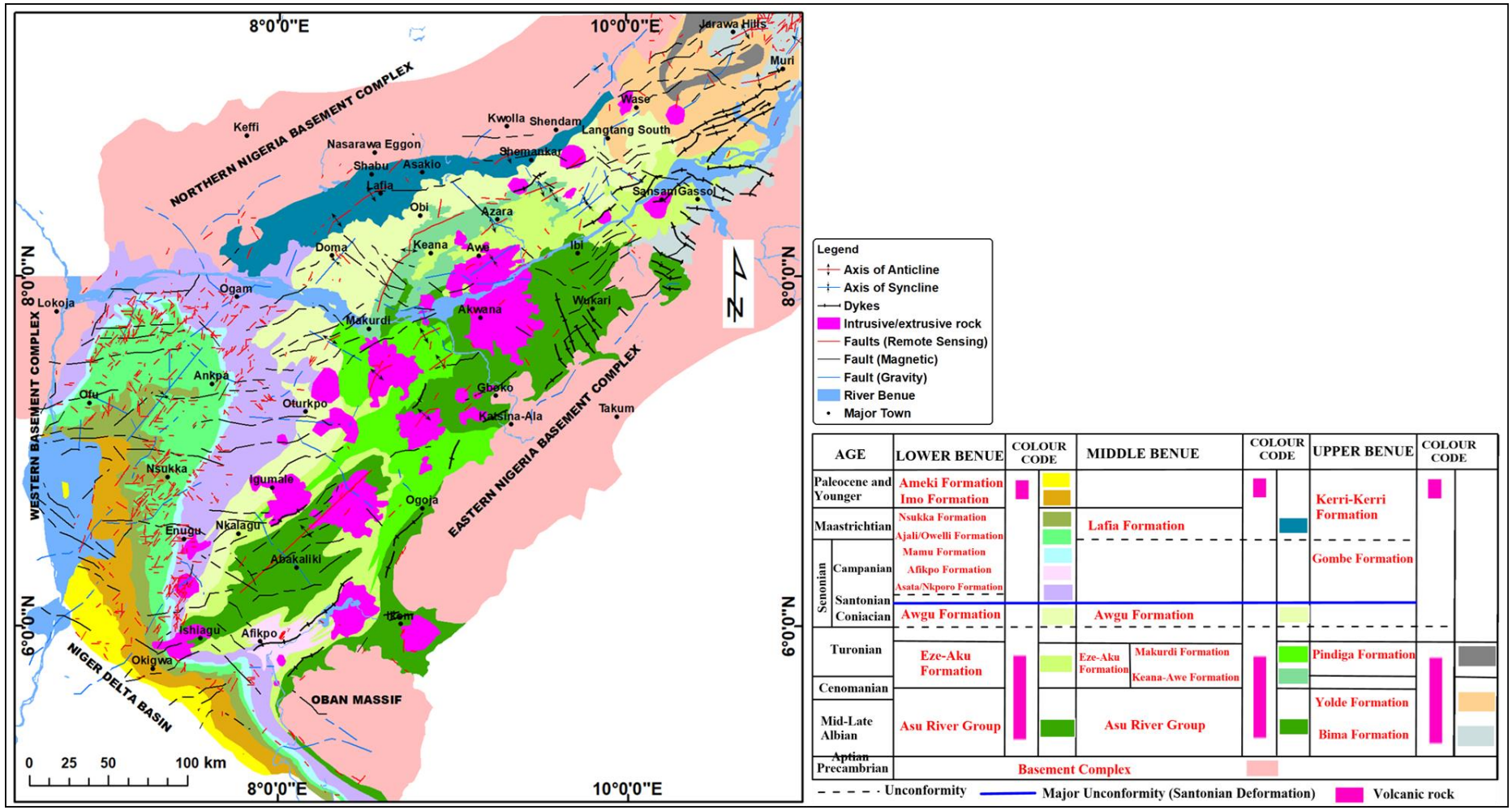

Fig. 4. 13: Updated geo-structural map of Lower and Middle Benue Trough processed from magnetic, gravity, and remote sensing data. Lineaments are interpreted as faults after discrimination from non-tectonic lineaments and thus show different trends than the mapped lithologies. This maps more volcanic rocks than in Fig. 4.13.

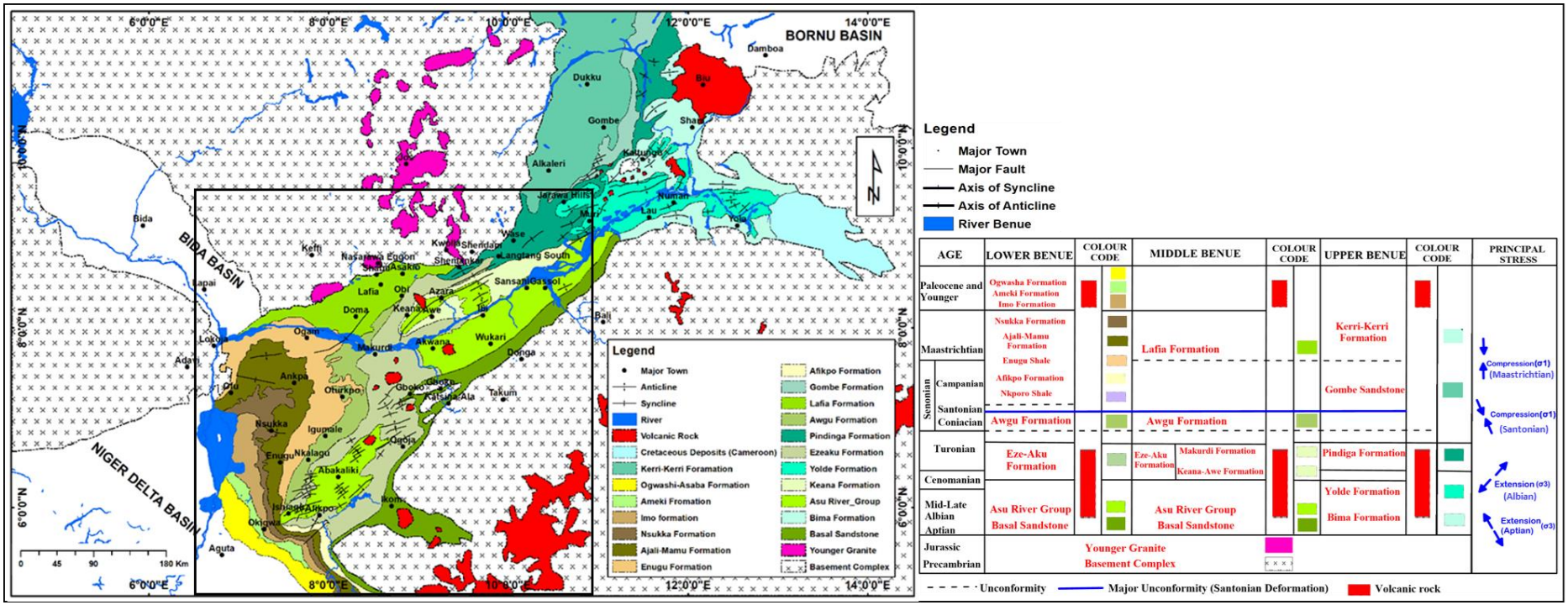

(b)

Fig. 4. 14: A generalized geology of Benue Trough with a simplified stratigraphic succession. The spatial distribution of intrusive rocks (volcanic rocks, dykes, and plugs) is less than those in (a). The four (4) major principal stresses that affected the area over time have been identified.

CHAPTER FIVE

MAPPING AND MODELLING OF DEEP STRUCTURES

5.1 Introduction

This chapter gives detail of the processes of evaluating deeper structures by qualitative and quantitative interpretation of potential field data over parts of the Benue trough (Middle and Lower) of Nigeria. The main targets are to understand in 2- and 3-dimensions the basement structures, morphology, and the crustal architecture, and to understand the related deformational history of the trough. The supporting materials for this study are gravity, magnetics, topography, and well-log data sets (obtained from other tectonically similar basins).

The following processes were involved in the study to achieve the aim:

1. Mapping basement lineaments from regional magnetic and gravity data sets using derivative-based filters (horizontal gradient magnitude, Tilt, theta map, Goussev filters, local wavenumber etc.), Euler Deconvolution, and horizontal gradient magnitude of pseudo gravity.
2. Interpret the nature of the lineaments from magnetic and gravity data sets and isolate tectonically induced lineaments (faults).
3. Estimate the depth to the top of the basement using the finite tilt angle, local wavenumber, and pseudo-gravity inversion depth methods. The finite tilt and local wavenumber methods are limited because they pick depths on edges or contacts of magnetic anomalies. 3D inversion of pseudo-gravity field is applied to give more robust, continuous, and clean depth estimates.
4. Perform 2-dimensional modelling of gravity and magnetic data on selected profiles to understand the depth to basement, crustal structure, and Moho geometry across the trough.
5. Perform 3-dimensional modelling from gravity and magnetic data for the whole basin. Parker-Oldenburg and Li-Oldenburg techniques were used to model the crust and the depth to the Moho interface while total anomaly was used for magnetic inversion to model intrusion into the basement.
6. Estimate the amount of crustal extension using 2D gravity/magnetic models and 3D gravity inversion to interpret the basin and crustal architectures.

The interpretations in this chapter will be used to understand the basin evolutional pattern and the architecture of the crust.

5.2 Deep lineament mapping

Power spectrum analyses and matched bandpass filter techniques discussed in sections 3.2.3 and 3.3.4 of chapter 3, successfully separated magnetic and gravity data into residual and regional contributions. The regional anomalies are those dominated by long-wavelengths and related to deep sedimentary and basement structures (Ali et al., 2017). Mapping of deep lineaments was achieved by applying edge detection filters, the horizontal derivative of pseudo-gravity, and Euler deconvolution techniques, on the regional magnetic and gravity maps. Significant geological features were interpreted (Fedi and Florio, 2001; Li et al., 2010).

5.2.1 Mapping lineaments based on regional magnetic data.

Matched bandpass filter and power spectrum techniques were used to produce regional DRTE, DRTP, and azimuthal filter maps at mean depths of 8.2 km, 7.7 km, and 6.0 km, respectively (Figs. 3.10 d, 3.12 d, and 3.14 d). These regional magnetic maps are suitable to interpret equivalent source layers, those at the basement surface below sediments, and within the basement itself. Derivative-based or edge detection techniques (horizontal gradient magnitude, tilt, theta map, Goussev filter, local wavenumber), Euler deconvolution, and horizontal derivative of pseudo-gravity were used to delineate edges of deep lineaments.

5.2.1.1 Derivative-based Techniques

Horizontal gradient, theta map, and Goussev filter (derivative-based filters) operation were applied to the DRTE regional anomaly map for delineating and interpreting the deep lineaments. The maxima of horizontal gradient and cos theta, and the minima of the Goussev filter were used to mark the edges of anomalous sources and were interpreted to be related to the basement (Figs. 5.1 a, b, and c). Four major structural trends have been identified to characterize the basement lineaments; the NE-SW, NW-SE, N-S, and ENE-WSW trends. The NE-SW and NW-SE structural trends are more dominant than the N-S and ENE-WSW trends (Fig. 5.1 d). The NE-SW and NW-SE lineaments are found in all parts of the study area while the N-S and the ENE-WSW lineaments are observed mostly in the southern parts of the trough. The N-S and ENE-WSW lineaments truncate one another around the town of Ishiagu.

Horizontal gradient magnitude, Tilt angle, and the Goussev filter operation applied to the regional magnetic DRTP to enhance structural edges (lineaments). Figs. 5.2 (a) shows the maxima of horizontal gradient magnitude indicating the presence of basement lineaments. The zero of Tilt angle is marked on the Tilt map to delineate edges of structural features (Fig. 5.2 b). The positive tilt angle (tilt angle > 0.0) across the lineament edges is associated with the magnetic susceptibility, or the upthrown sides of lineaments, while the negative tilt angle value is associated with lower magnetic susceptibility, or the downthrown side (Salem et al., 2010; Fairhead et al., 2011). The minima of the Goussev filter also delineate structural edges in basement (Fig. 5.2 c). A combination of results from mapping structural edges (lineaments) indicated three major trend orientations of NE-SW, NW-SE, and ENE-WSW (Fig. 5.2 d). The analyses of the basement lineaments from DRTP and DRTE show that the NE-SW trend is dominant in the study area. However, the process of correcting the distortion of RTP by DRTP transformation has suppressed the N-S trending structures, hence, these could not be mapped.

Similar edge detection techniques were applied to the regional azimuthal filter map of the area (Fig. 3.14 d) and lineaments were delineated from the maxima of horizontal gradient and cos (theta) map of the area (Figs. 5.3 a and b). Minima of the Goussev filter were mapped too and structural edges (lineaments) were delineated (Fig. 5.3 c) to identify three major structural trends (NE-SW, NW-SE, and E-W trends). As in the case of the DRTP, the azimuthal filter technique was incapable of mapping N-S trending lineaments. Very few N-S trending basement structures were imaged because the process of stabilizing the RTP by the azimuthal filter and DRTP methods has significantly suppressed them.

Lineaments mapped from derivative-based techniques on DRTE, DRTP, and azimuthal filter maps were analysed and those lineaments that aligned across all three methods were picked as the most likely real basement lineaments (Fig. 5.4).

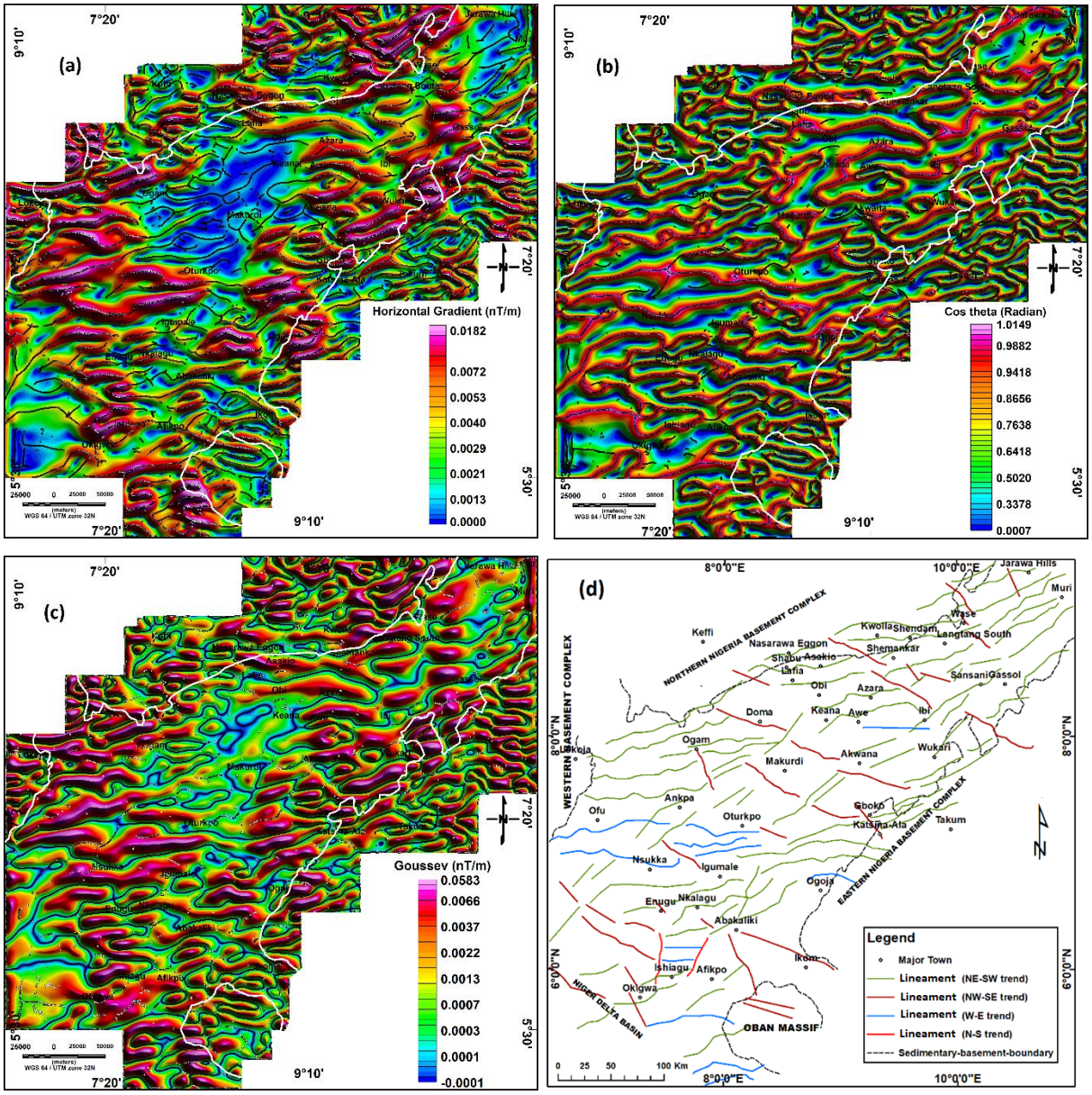

Fig. 5. 1: Basement lineaments extracted from regional DRTE (a) Horizontal gradient map with its maxima marked by black dots (b) Theta map shows maxima points in black dots to delineate lineaments (c) Goussev filter with minima points (blue colour code) indicating lineaments (d) Basement lineaments trending in four major directions.

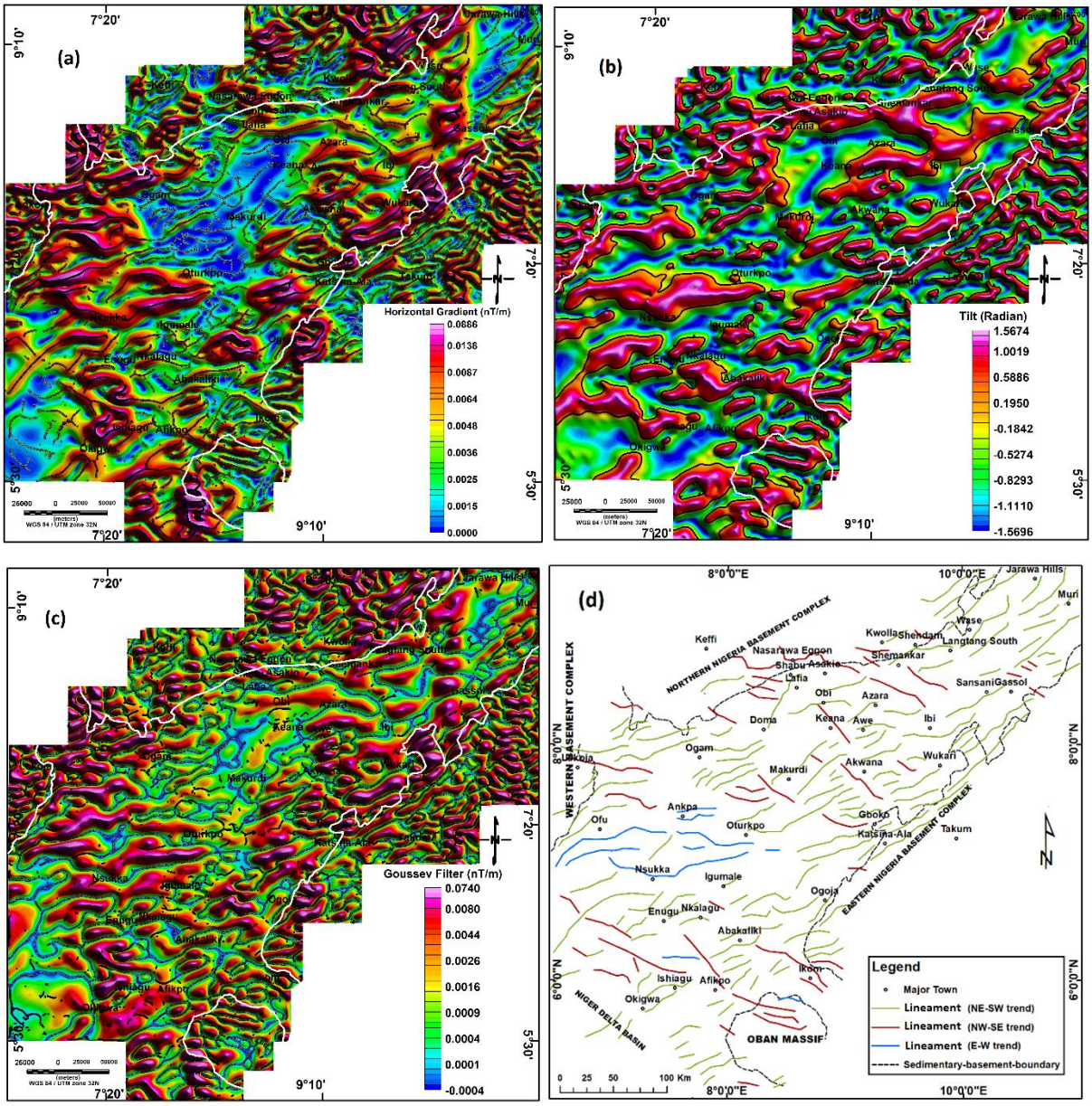

Fig. 5. 2: Basement lineaments extracted from regional DRTP (a) Horizontal gradient with maxima (black dots) overlaid to show the edges of structures (b) Zero of tilt angle marked on tilt angle map (c) Minima of Goussev filter (blue colour code) (d) Basement lineaments map with three main structural trends.

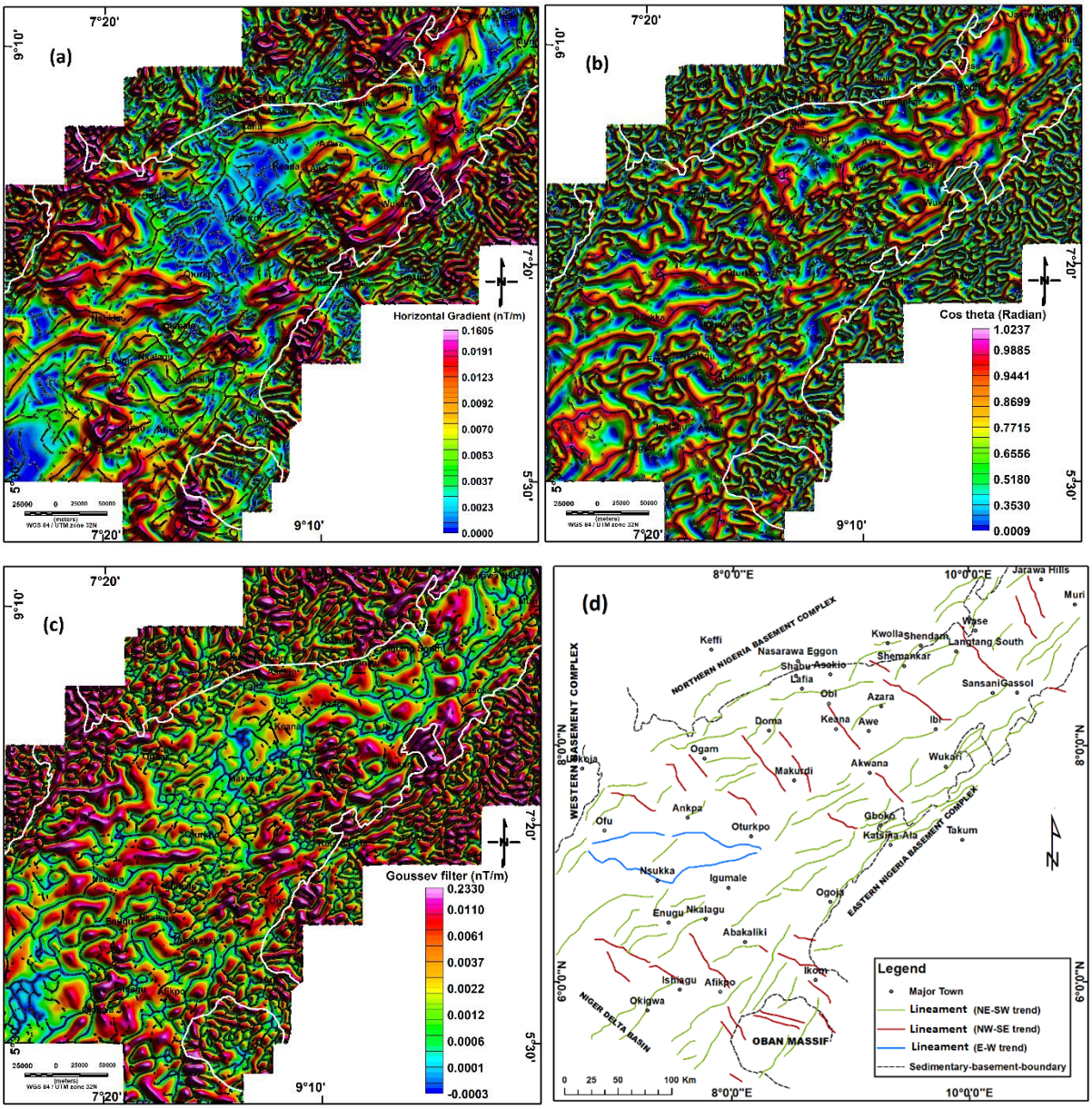

Fig. 5. 3: Basement lineaments extracted from an azimuthal filtered regional map (a) Horizontal gradient with maxima (black dots) overlaid on it (b) theta map with maxima showing lineaments (c) Minima of Goussev filter in blue shows the presence of lineaments (d) Basement lineaments map with three main structural trends.

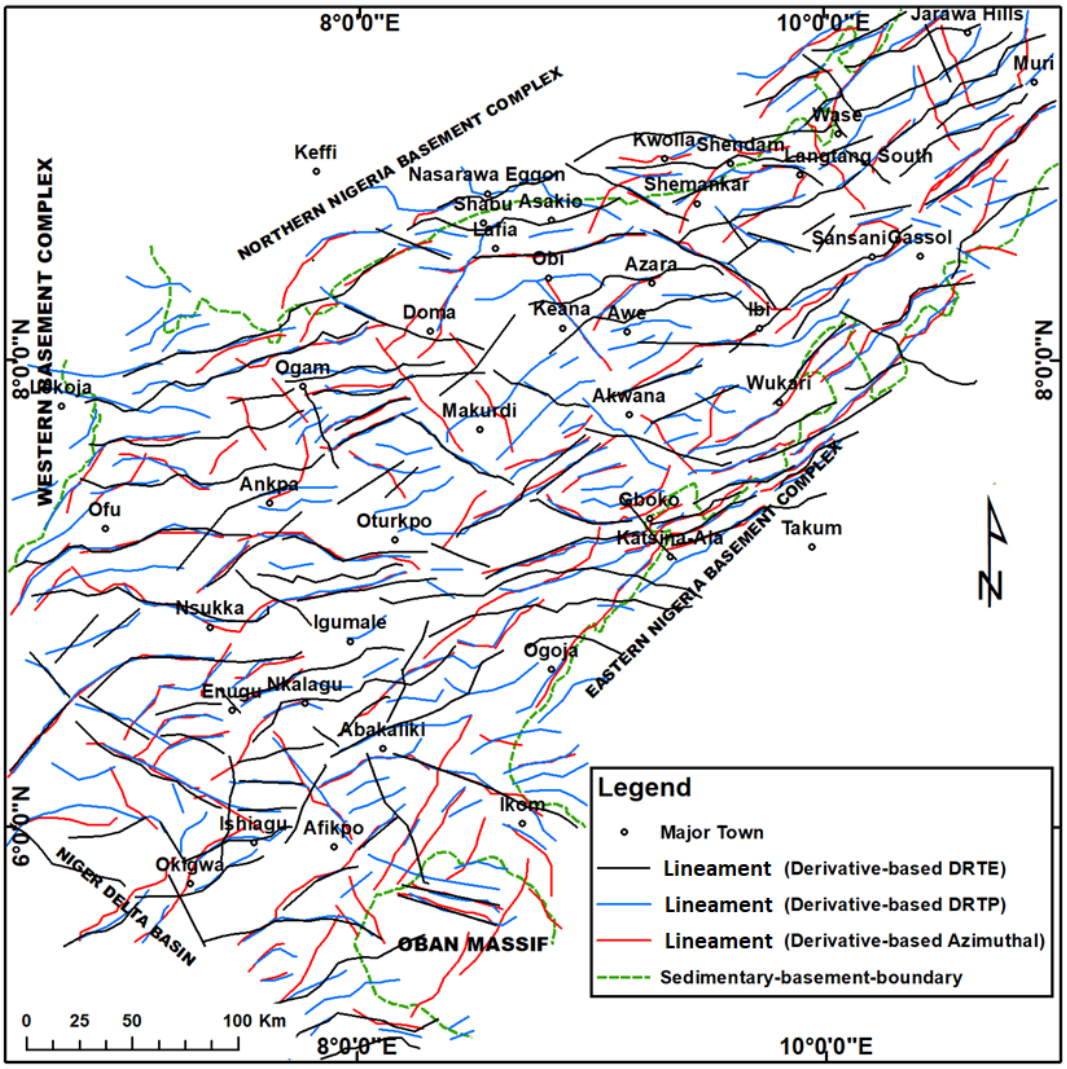

Fig. 5. 4: Combined lineament map from derivative-based techniques on DRTE, DRTP, and azimuthal filter maps. The red, blue, and black polylines represent lineaments obtained from Azimuthal, DRTP, and DRTE techniques.

5.2.1.2 Euler Deconvolution

The 3D Euler deconvolution technique was applied to the DRTE regional magnetic grid (Fig. 3.10 d), and both the locations and the depths of the lineaments were estimated. The calculation was done based on equation 2.28 using a 15 km x 15 km moving window and structural index of 0 which relates to a lineament with an infinite depth extent source geometry (Ndougsa-Mbarga et al., 2012; Reid et al., 2014). Structural indices of 1 and 2 were tested also but the structural index value of 0 is preferred as it relates more to contact of faults. Other essential parameters used for the calculation are 15.0 %, 15 km, and 80 m for maximum percentage error, maximum acceptable depth, and flying height, respectively.

The Euler solutions for source depths range between 0 and 6 km with an average depth of 3.88 km. Most of the Euler solutions within the basin show high depths than the surrounding rock while parts of the basins with shallow depths represent basement highs or uplifts. However, depth solutions were not cleaned since the interest for the estimation is to locate deep lineaments. The depth estimates were gridded into thin strips and the centre of the strips traced and delineated as lineaments (Fig. 5.5 a). Fig. 5.5 (b) shows delineated basement lineament trends in three main orientations of NE-SW, NW-SE, and ENE-WSW directions. The major lineament trend is the NE-SW direction that is observed in all parts of the basin while the least common occurrence is the ENE-WSW structural trend.

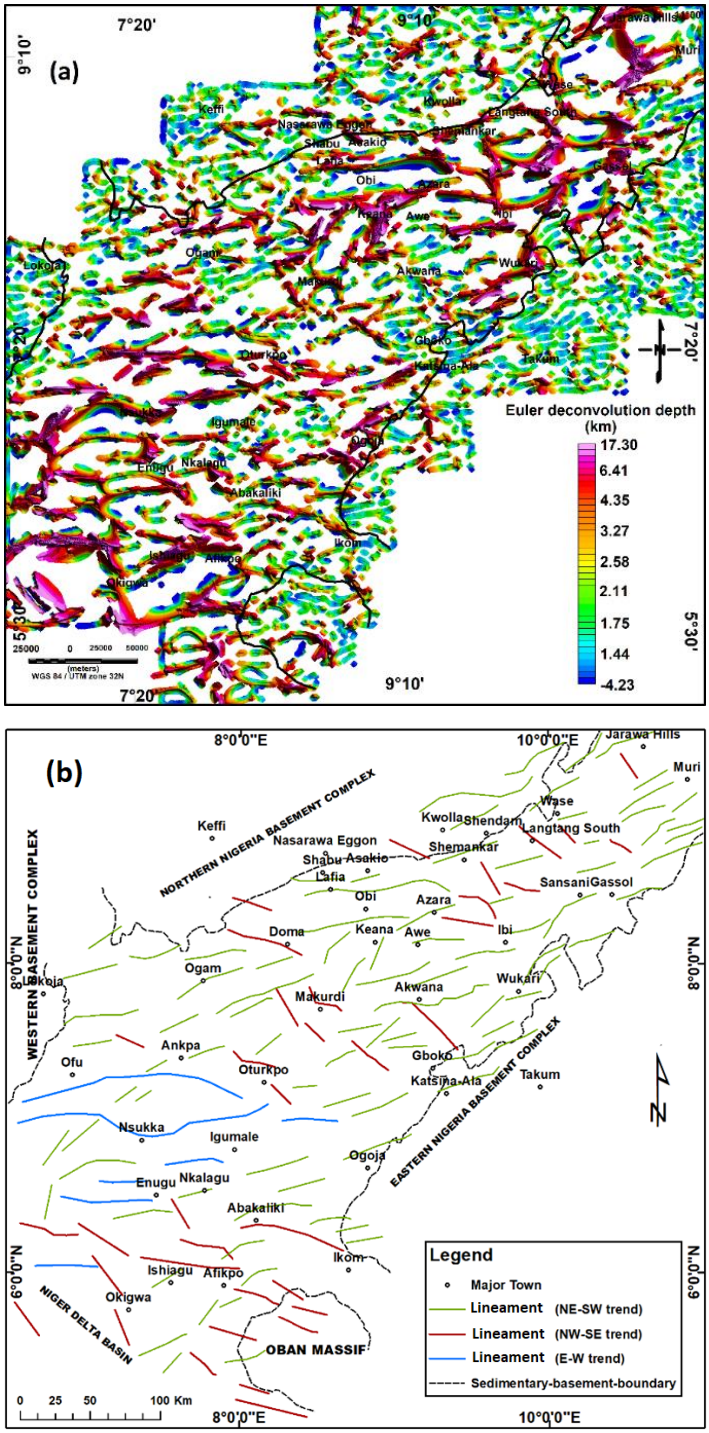

Fig. 5. 5: Results of magnetic 3D EULER Deconvolution (a) Depth solutions gridded to mark edges and locations of lineaments (b) Basement lineaments traced for structural analyses with three interpreted structural trends of NE-SW, NW-SE, and ENE-WSW directions.

5.2.1.3 Horizontal gradient of Pseudo-gravity

Magnetic data can be transformed into so-called pseudo-gravity fields using Fourier techniques for a more robust interpretation of geological features (Keller, 1986; Grauch and Cordell, 1987). The pseudo-gravity transforms magnetic data sets into grids that are assumed to have the similar relationship to magnetic susceptibility that a gravity grid has to density. It reflects the magnetic properties of rocks that are free from distortion caused by inclined magnetic polarization and fields is hence very useful in enhancing regional magnetic anomalies (Hinze et al., 2010; Salem, et al., 2014). Pseudo-gravity can be used to map lineaments especially when the magnetic data sets are reduced to the pole or to the equator (Grauch, 2002). The change of the TMI to RTE before transformation to pseudo-gravity shows some limitations, however, as it enhances the E-W lineaments but largely helps in shifting magnetic anomalies over the centers of magnetic sources. The horizontal gradient of the pseudo-gravity field shows its maximum magnitude directly over lineaments so long as the remanent magnetism is not significant (Phillips, 2000; Grauch, 2002). Remanent magnetism is that which contains information about Earth's magnetic field obtained at the time the rocks and ores were formed (Liu et al., 2018). This technique has been widely used to delineate major basement lineaments (Cordell and Grauch, 1982; Grauch and Cordell, 1987).

Pseudo-gravity was calculated from the DRTE (Fig. 3.3). The transformation has significantly enhanced the magnetic anomalies of deeper magnetic sources (long wavelengths) and reduced the appearance of shallow sources or short wavelengths (Fig. 5.6 a). The horizontal gradient of pseudo gravity was calculated, and its maxima (marked with black dots) were used to delineate basement lineaments (Phillips et al., 2007; Fig. 5.6 b). Pseudo-gravity was also calculated for DRTP data sets (Fig. 3.7), and the result indicates the presence of basement rocks with higher magnetic susceptibility in the northern part of the area than in the south which is dominated by rocks of lower magnetic susceptibility (Fig. 5.7 a). The magnitude of the horizontal gradient of the pseudo gravity was estimated, and its maxima were picked (in black dots) to show basement structural edges (lineaments) (Fig. 5.7 b). Fig. 5.8 (a) shows the calculated pseudo-gravity map from the azimuthal filtered magnetic data (Fig. 3.7) where high values in the basement rocks (red and pink colour codes) could be an indication of basement highs while lows (blue colour codes) could be indicative of deep sub-basins. The maxima of the horizontal gradient of pseudo gravity (marked in black dots) indicate the presence of basement structural edges (lineaments) (Fig. 5.8 b). The inconsistency in magnetic values in the southern part of the basin between

figs. 5.7 and 5.8 are due to the removal of shallow magnetic sources in fig. 5.7 during the process of stabilizing RTP.

The extracted structures from the horizontal gradient magnitude of the pseudo-gravity field generated from DRTE, DRTP, and azimuthal filter methods were combined to interpret the inferred basement lineaments (Fig. 5.9). Three well-defined structural trends in the NE-SW, NW-SE, and E-W directions, have been identified as the best structural edges delineated from all the results. The NE-SW trends are the most dominant. These mapped structures are longer and clearer than those extracted from other methods above.

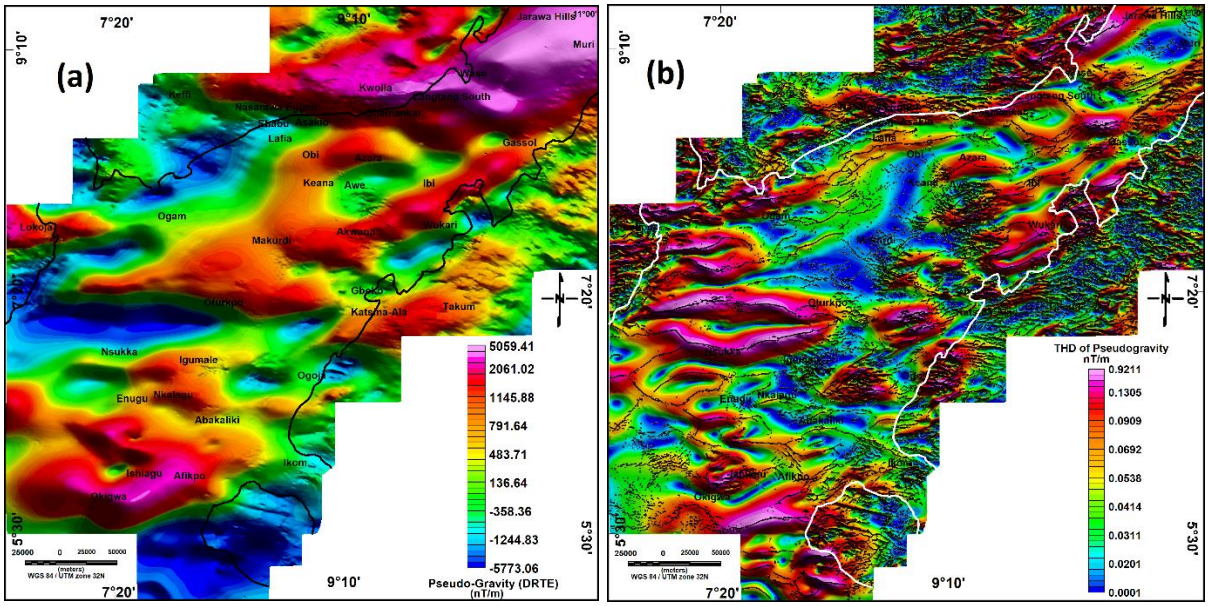

Fig. 5. 6: (a) Calculated pseudo-gravity map on the differential reduction to the equator (DRTE) product (b) Maxima of horizontal gradient magnitude of pseudo-gravity. The peaks are delineated as lineaments in black dots.

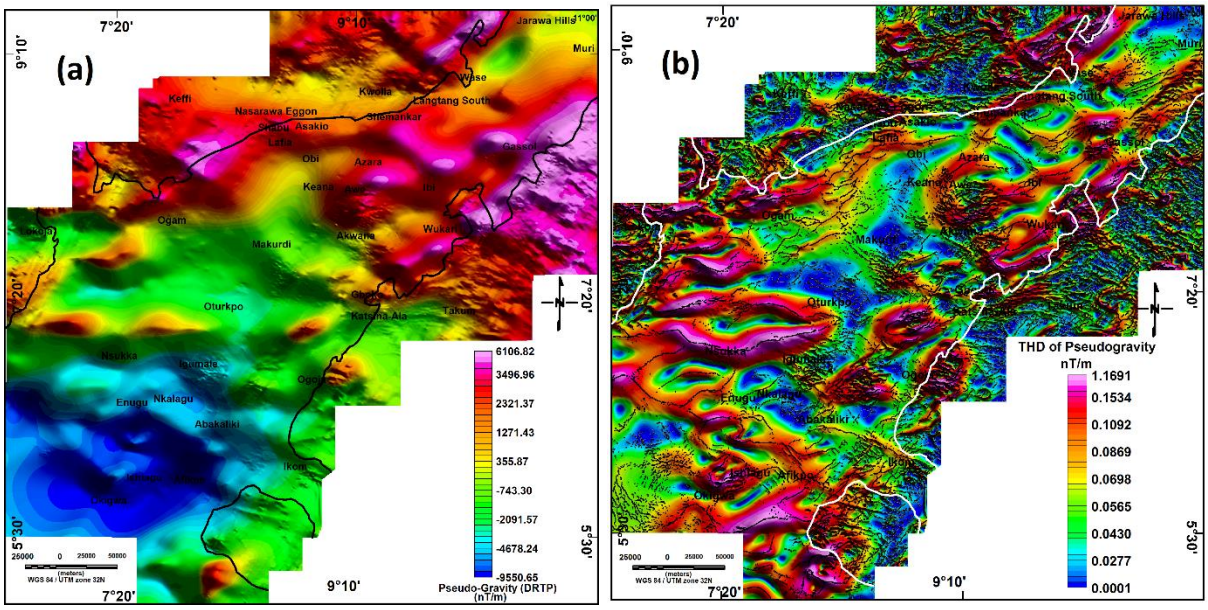

Fig. 5. 7: (a) Calculated Pseudo-gravity on the differential reduction to the pole (DRTP) product (b) Maxima of horizontal gradient magnitude of pseudo-gravity. The peaks are delineated as lineaments in black dots.

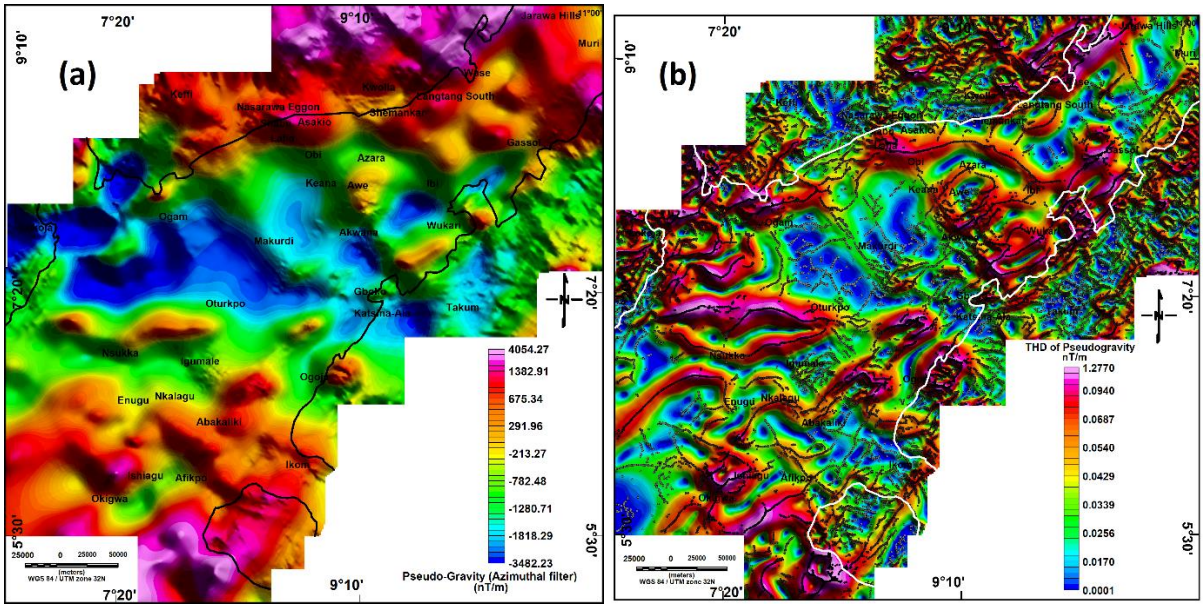

Fig. 5. 8: (a) Calculated pseudo-gravity on the azimuthal filter product (AZ) (b) Maxima of horizontal gradient magnitude of pseudo-gravity marked with black dots to delineate basement structural edges.

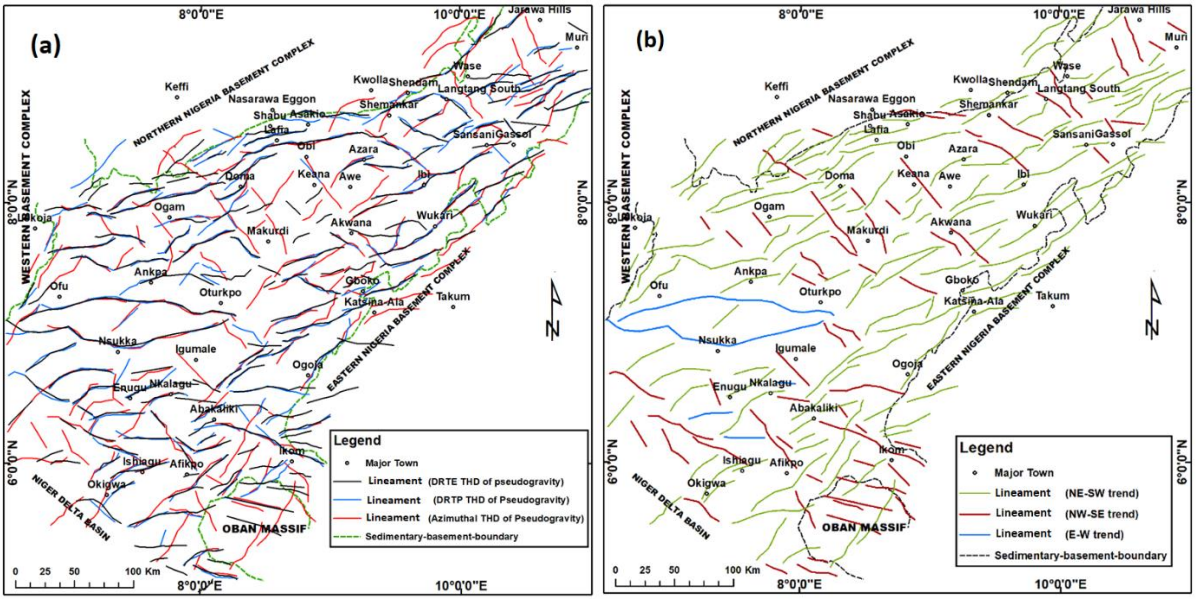

Fig. 5. 9: (a) Combined lineament map from the horizontal gradients of pseudo-gravity on DRTE, DRTP and azimuthal filter products (b) Basement lineaments extracted from the horizontal magnitude gradient of pseudo-gravity of DRTP, DRTE, and AZ with three main structural trends obtained.

5.2.2 Mapping lineaments based on regional gravity data.

A power spectrum was used to identify regional gravity anomaly at an average depth of 15 km (Fig. 3.19 c) which represents the contribution from basement surface and density anomalies within the basement. Horizontal gradient, tilt angle, local wavenumber, and Euler deconvolution techniques were used on this anomaly field to delineate basement lineaments and understand the basin tectonics.

5.2.2.1 Derivative-based technique

Horizontal gradient magnitude was calculated on the regional gravity anomaly map of the study area and its maxima were calculated from the extrema curvature method (Phillips et al., 2007) to indicate the presence of lineaments (Fig. 5.10 a). Fig. 5.10 b shows the result for the zero of tilt angle draped on the tilt angle map. The parts of the tilt angle grid that are greater than the zero contact indicates high basement anomalies with high gravity values and are interpreted as the upthrown walls part of the contacts. The parts that have lower values than the zero of tilt show lower gravity anomalies and are hence interpreted as the downthrown walls of the lineaments. Several low- and high-density contour closures have been identified to represent sedimentary sub-basins and basement uplifts, respectively. The maxima of the local wavenumber are calculated and draped over its grid to delineate faults and lithological boundaries in the basement (Fig. 5.10 c). Fig. 5.10 d shows the intersection of maxima of horizontal gradient and local wavenumber, and zero of tilt angle to map basement lineaments. Four major basement lineament trends have been identified and mapped: The NE-SW, NW-SE, N-S, and E-W structural trends. The basement is dominated by NE-SW trending structures. The regional gravity data set has mapped some of the N-S trending structures that were missed by the regional magnetic data analyses. These are to be found mostly towards the southern part of the basin. The changes in the general structural trends of the area suggest that the basin has been affected by several distinct episodes of deformation, arising from either changing far-field stress directions (plate movements) or from the local stress field (magma plume).

5.2.2.2 Euler deconvolution

The 3D Euler deconvolution technique was applied based on a 10 km × 10 km moving window, maximum depth tolerance of 12 %, and maximum acceptance depth of 20 km. SI of 0 and 1 were used in the calculation in two separate cases that define the geometry of a thin bed or small step fault or a thin sheet edge or horizontal cylinder, respectively (Reid et al., 2003; Reid

et al., 2014). The depth solution estimates for the structural index of 0 are interpretable to show the locations of faults, with an average depth of about 12.4 km. The depth solutions for a structural index of 1-mark linear structures at an average depth of 13.8 km (Figs. 5.11 a and b). The faulting locations of lineaments were mapped, and four structural trends were observed in the NE-SW, NW-SE, N-S, and E-W directions. More E-W and the N-S trending structures have been mapped by the Euler deconvolution method than by the derivative-based technique. However, most of the E-W and N-S lineaments are partly related to station distributions. The sample distribution points of the gravity data sets are not uniform and seem to align with the orientation of the E-W and N-S lineaments when superimposed on each other (Fig. 3.15 and Fig. 5.12).

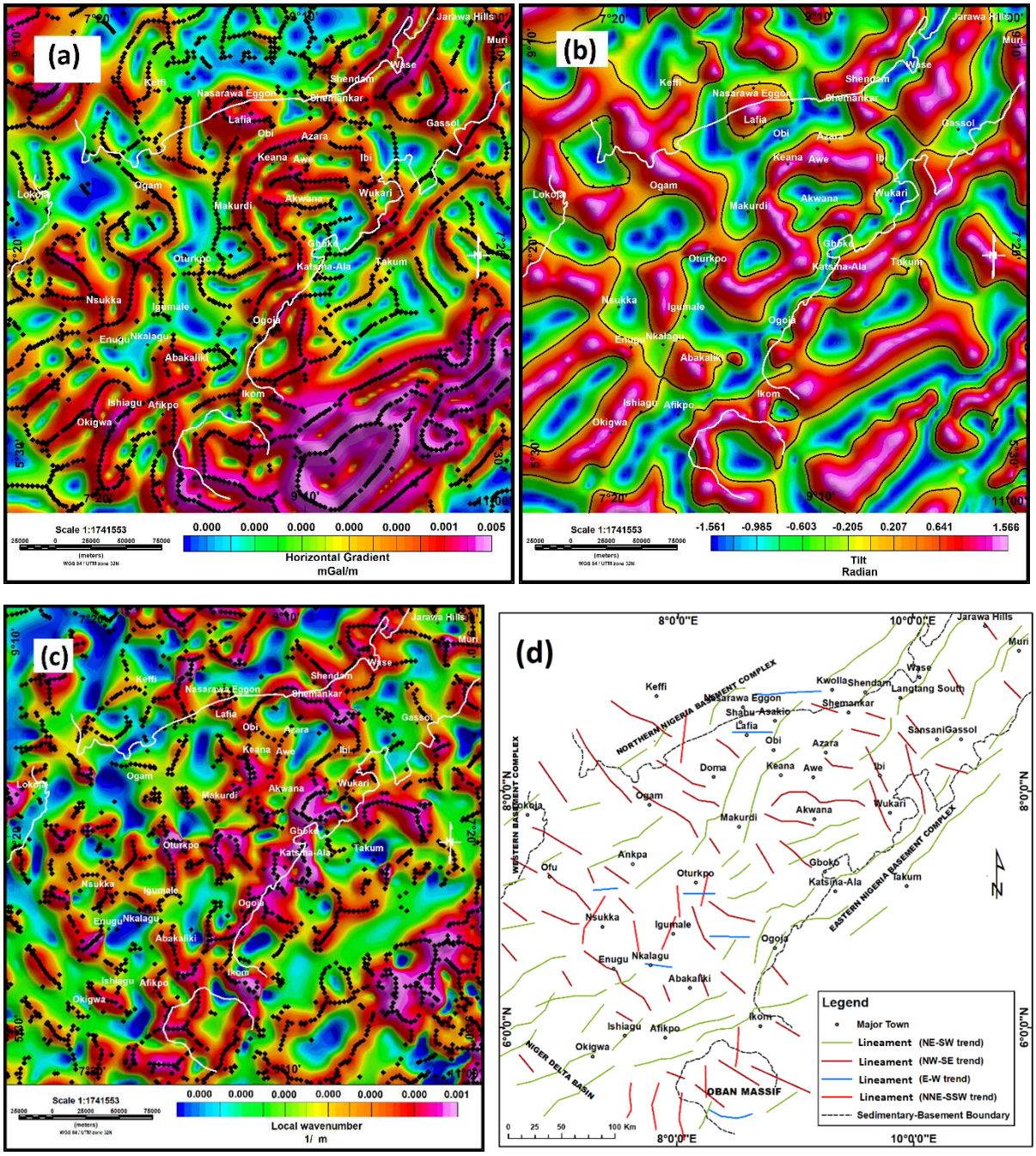

Fig. 5. 10: Regional gravity lineament mapping (a) Maxima of the horizontal gradient indicating lineaments (b) Zero of tilt map showing the edges of the lineaments (c) Maxima of local wavenumber marking the edges of lineaments (d) Basement lineament map extracted from a combination of (a), (b) and (c).

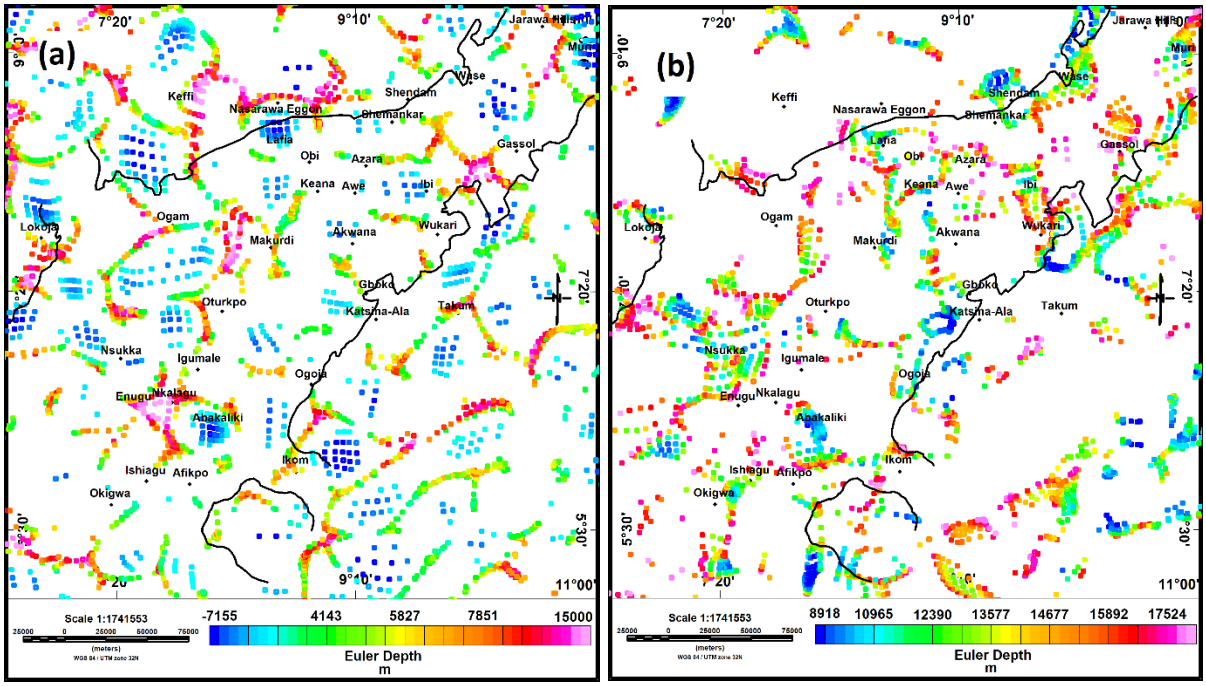

Fig. 5. 11: Gravity 3D Euler deconvolution using a 10 km × 10 km window, maximum depth tolerance of 12 % and maximum acceptance depth of 20 km (a) Depth solutions for a structural index of 0 (b) Depth solutions for a structural index of 1.

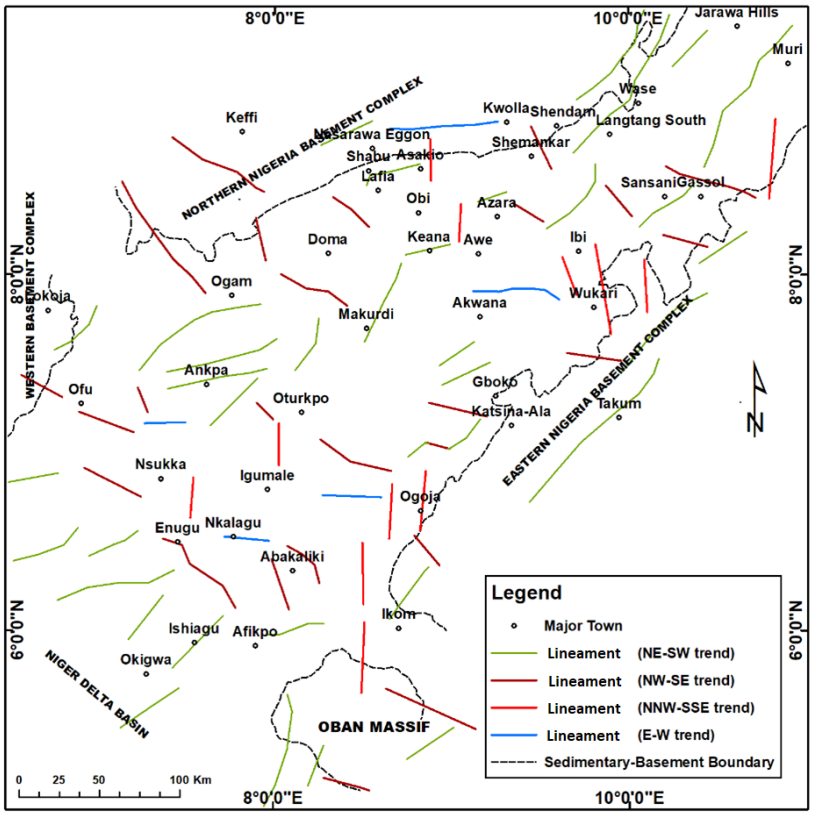

Fig. 5. 12: Delineated basement lineaments traced from gravity Euler deconvolution technique showing four major structural trends.

5.2.3 Deep lineaments obtained from regional magnetic and gravity data

The results of lineament analyses from regional magnetic anomalies were combined to represent the deep lineaments of the basin and displayed overlain on the positive tilt angle (Fig. 5.13). The slope direction of the tilt angle across the edges of the lineaments shown by a bob-head indicates a lower tilt value or low magnetic susceptibility (Fairhead et al., 2011; Ali et al., 2017). The direction of the bob-head pointing towards lower susceptibility can be interpreted as the downthrown-wall of the lineament while the positive tilt angle values as the upthrown wall. Analyses of the lineament trends of the whole area indicated three well-defined basement lineament orientations in NE-SW, ENE-WSW, and NW-SE directions (Fig. 5.14 a and b). The NE-SW trending lineaments are the most dominant basement lineaments and are parallel to the main trend of the trough. They can be associated with normal faulting during the rifting (Fairhead and Green, 1989; Fairhead et al., 2013) and have been observed to be reactivated over time due to shortening and compression forces (Binks and Fairhead, 1992; Guiraud and Bosworth, 1997). The NW-SE trending basement lineaments are fewer and almost perpendicular to the NE-SW lineaments. Most of these NW-SE lineaments are mapped as breaks or offsets in the magnetization boundary continuity of the NE-SW lineaments and are usually associated with later normal faulting (Ajakaiye et al., 1991). The ENE-WSW trending lineaments are sub-parallel to the basin general trend and are interpreted to be associated with a Precambrian mega continental fracture system (Ofoegbu, 1984; Ajakaiye et al., 1991).

The regional gravity anomaly grid has also been analyzed in a similar manner as that done for the regional magnetic data sets. The basement lineament trends from the various techniques were combined and overlaid on a positive tilt angle image. The bob-head mark shows the direction of lower density contrasts representing the downthrow wall while the higher density contrast indicates the upthrown wall of the lineament or basement uplift (Fig. 5.15). The gravity response for the positive tilt angle value with higher density contrast has wider coverage than that of the magnetics. The lineament edges mapped towards the eastern part of the basin correspond to the basement-sedimentary boundary and indicate the presence of a basin-bounding fault. Lineament trend analysis shows four orientations in the NE-SW, NW-SE, NNE-SSW, and E-W directions (Fig. 5.16 a). The trends are the same as those observed from the regional magnetic structures, however, these data reveal the presence of NNE-SSW trending lineaments as well. The absence of NNE-SSW trending structures from the regional magnetic data analyses could be due to suppression of their signals by the RTP transformation. Fig. 5.16 (b) shows a rose plot diagram for the basement lineaments. A pair of lower density

contrast closures (the bob-heads pointing towards each other) could be an indication of a sub-basin or a down warp while a pair of higher density contrast closures with the bob-heads pointing away from each other could be an indication of basement uplift. A set of alternating closures of high and low-density contrasts could be interpretable in terms of a set of horst and graben structures as observed in the structures in the southern part of the map between Ogam-Ankpa-Nsukka-Enugu.

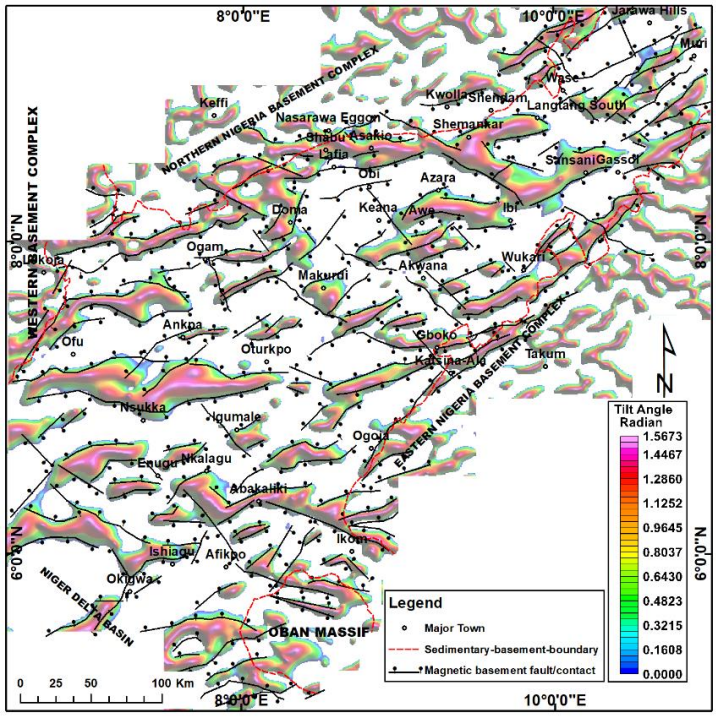

Fig. 5. 13: Basement lineaments overlain on positive tilt angle obtained from the regional DRTP. The bob-heads show the direction of lower magnetic susceptibility (possible downthrown sides of the lineaments) from the delineated structural edges.

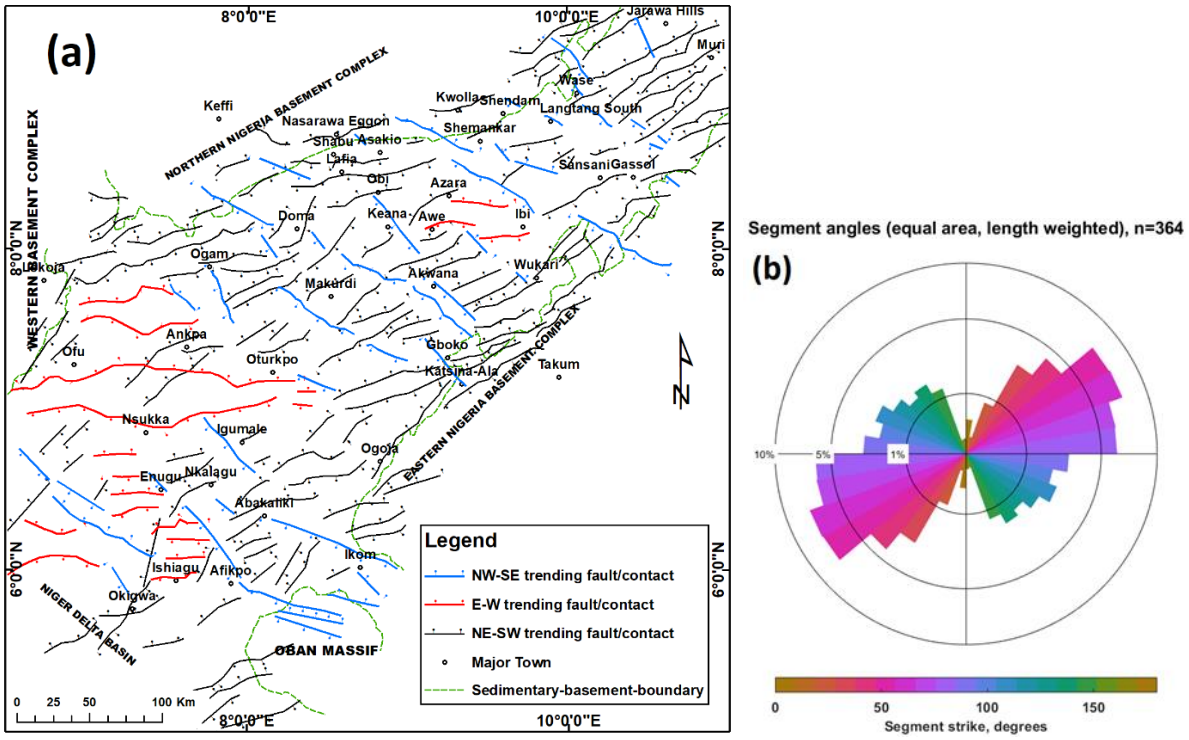

Fig. 5. 14: Basement lineaments from magnetic data sets (a) interpreted lineaments in different colour codes (b) a rose diagram showing the trends of lineaments with major NE-SW, NW-SE, and ENE-WSW orientations.

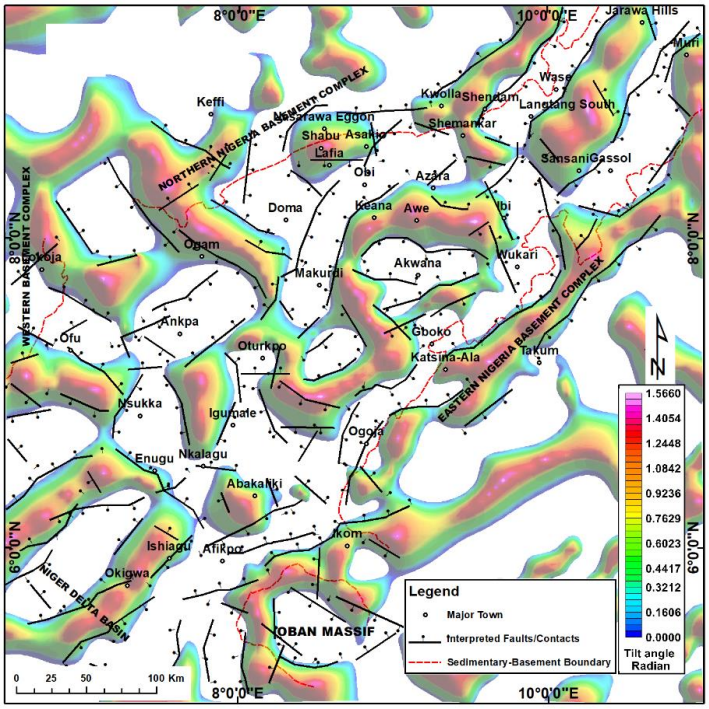

Fig. 5. 15: Basement gravity structures (lineaments) overlain on a positive tilt angle. The bob-heads show the direction of lower density contrasts (possible downthrown sides of the lineaments) from the delineated structural edges.

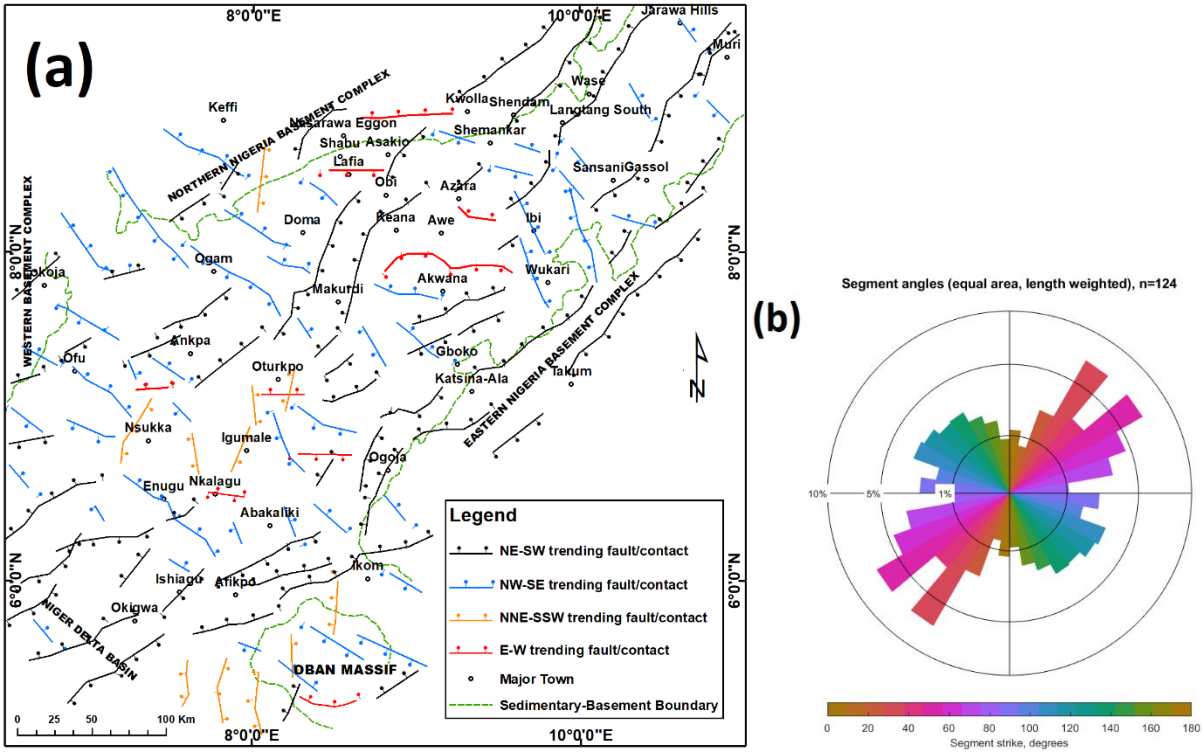

Fig. 5. 16: Basement gravity structures (a) interpreted structures (lineaments) with different colour codes (b) a rose diagram showing the structural trends of lineaments with major NE-SW and minor but significant NW-SE, E-W, and NNE-SSW directions.

5.2.4 Uncertainties associated with deep lineament extraction.

Lineament analyses for deep equivalent layer sources give better discrimination of lineaments than the shallow technique but become more limited in accuracy as the depth of investigation or mapping increases. The better discrimination of deep lineaments in regional data sets is because most of the fabrics that express surface and near-surface non-geologic structures, or non-tectonic lineaments (residual anomalies) are removed using residual-regional separation techniques. Most regional or deep sources are located within the basement, where mapped lineaments are generally expected to be geologic lineaments (faults/contacts/dykes) (Cordell and Grauch, 1982). The uncertainty arising from the deep magnetic anomalies is related to the procedures that aim to correct for the anisotropic nature of magnetic responses, especially at low magnetic latitudes such as in the study area, in particular the difficulty in finding a suitable process to vertically align the directions of magnetization and the measured field. The lateral discontinuity in vertical and horizontal sediment density contrasts, deep sediments with the same density as that of the basement, and heterogenous distributions of station profile points are some of the limitations in mapping geologic lineaments from deep gravity data sets.

5.2.5 Basement fault mapping

Basement tectonic lineaments (faults) are mapped over longer distances than those in the basin fill, and so they were separated from lithological contacts and dykes by a simple discrimination method. The lithological contacts and dykes delineated within the area were overlaid on the geologic lineaments map so that lineaments that overlie each other could be eliminated. The remaining lineaments were interpreted as faults. Interpretation of the trends of basement faults in regional gravity and magnetic anomalies is a good tool for interpreting and understanding basement evolution (Grauch and Hudson, 2007).

In the study, the deep lineaments were filtered by removing the lineaments that are assumed to be related to lithological contacts and dykes. A total of 200 and 111 tectonic lineaments were interpreted as basement faults from magnetic and gravity data sets, respectively (Figs. 5.17 a and b). The faults trend in four main directions; NE-SW, NW-SE, and ENE-WSW trends, and a very few N-S orientations. These faults are assumed to be expressed via the discontinuity in basement fabrics. The regional structural analyses show very similar trends and correlate well with each other and this implies that the regional gravity response due to density contrast on the basement is coherent with those produced by regional magnetic susceptibility (Ali et al., 2017; Fig. 5.18), and thus that the basin could be in a state of isostatic equilibrium.

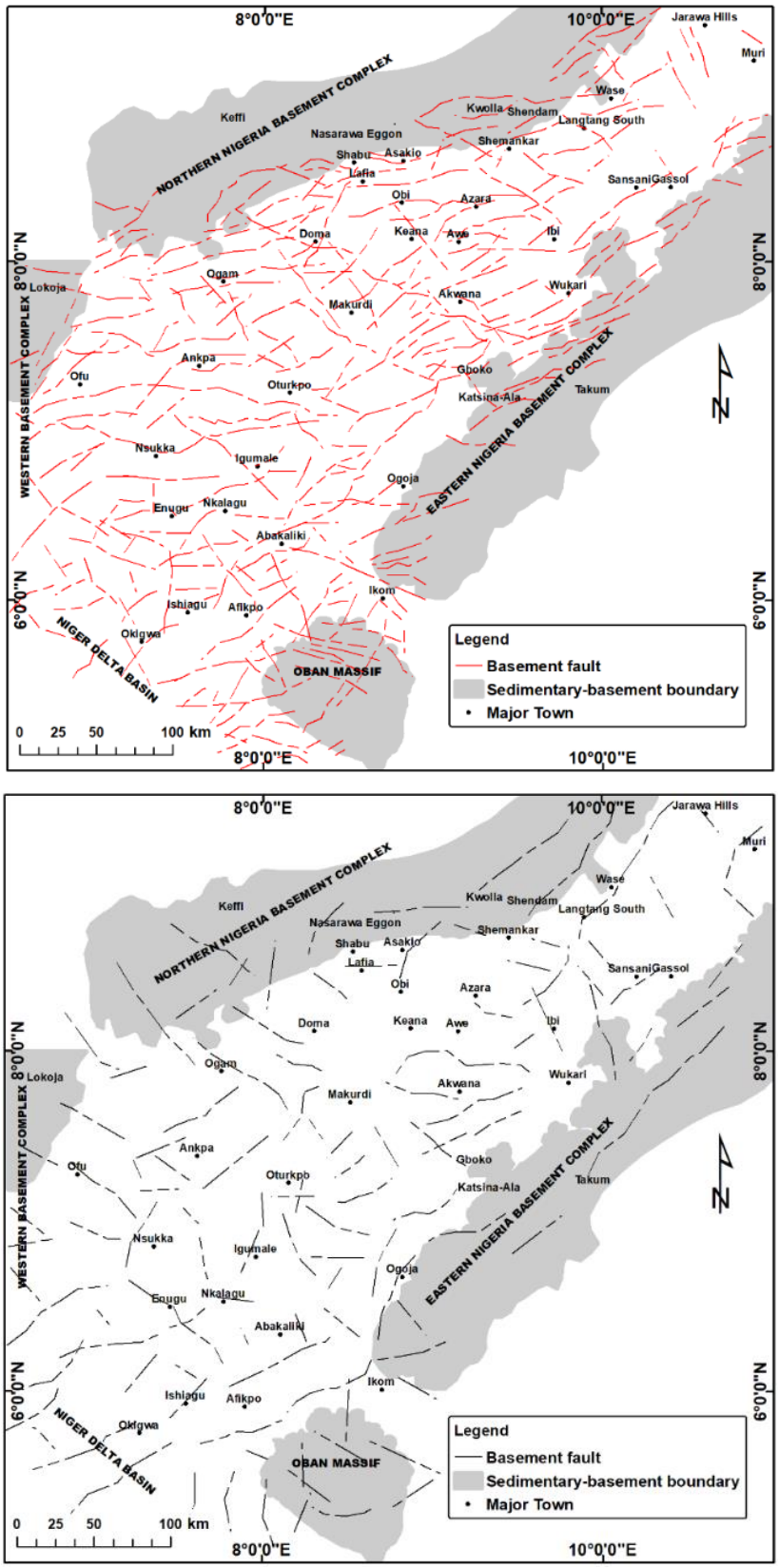

Fig. 5. 17: Basement fault map of the trough after removal of lithological contacts and dykes from (a) deep magnetic data sets (b) deep gravity data sets. These are interpreted to be as a result of tectonic activities induced by plate motion/ far field stress transmission from mantle convection.

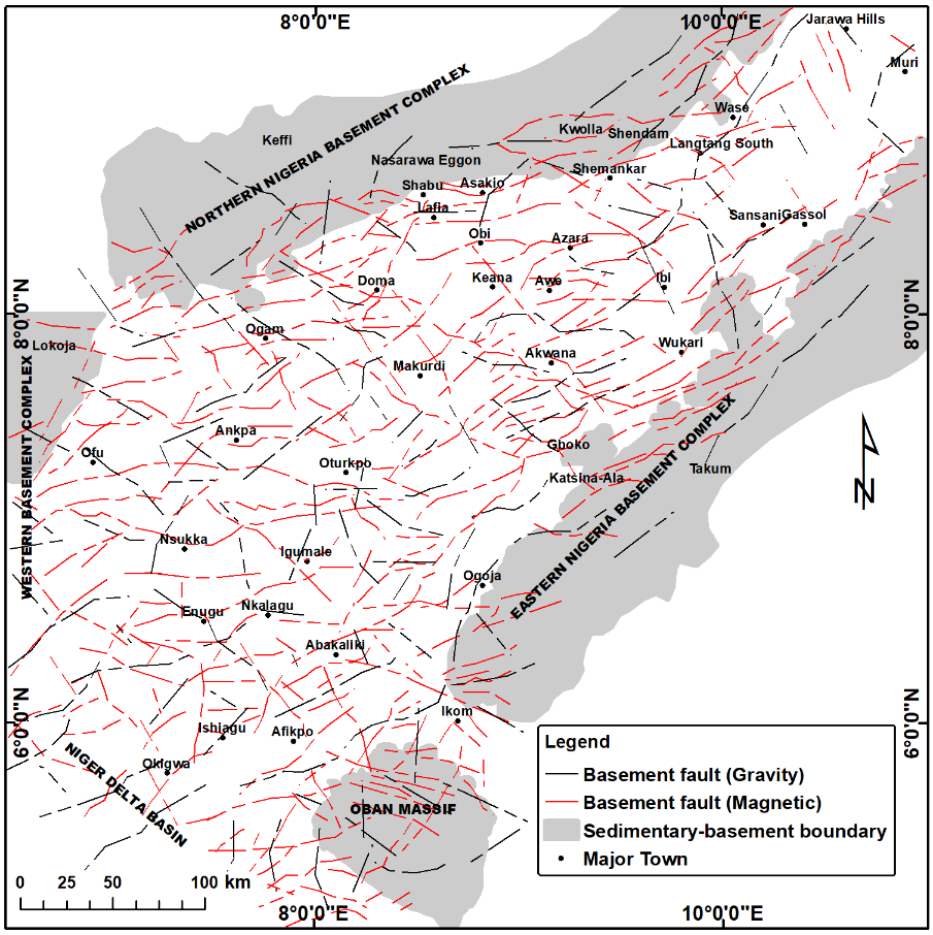

Fig. 5. 18: Combined basement fault map of the area from regional gravity and magnetic anomalies. The results from the two data sets correlate well indicating that the contrasts between basement density and magnetic susceptibility are coherent.

5.3 Basement depth estimation

The estimation of depth technique helps in defining the extents of depo-centres thereby providing boundary conditions for further basin modelling. The depth to the top of the basement from regional magnetic data sets was carefully estimated and used to map the morphology in the basin. Several sub-basin structures were identified to be significant in reconstructing and understanding the nature of the basin. Basement depth estimations are essential in the interpretation of the basement morphology and sediment accumulation of basins (Salem et al., 2013). Finite tilt- and local wavenumber depth estimation methods were applied in this study to estimate depths to the tops of lineaments and to serve as constraints for inversion of pseudo-gravity data in mapping and estimating the depth to top of magnetic basement. The pseudo-gravity depth estimation method serves as a means of solving the limitations inherent in the finite tilt and local wavenumber methods. This result was further used in evaluating and understanding the basement morphology of the study area.

5.3.1 Finite Tilt-depth method

Magnetic tilt angle is in some form a normalizing derivative as it considers the ratio between the vertical and horizontal derivatives of the magnetic field. It can be used to estimate depth if the magnetic data have first been reduced to the pole or the equator (Salem et al., 2007). In this study, the depth calculation was made based on the assumption that the source structures have vertical contacts and are devoid of remanent magnetization (Verduzco et al., 2004; Salem et al., 2007).

The tilt angle is given by.

$$\boldsymbol{\theta = \tan^{-1}\left(\left(\frac{\partial T}{\partial z}\right) \Big/ \left(\frac{\partial T}{\partial h}\right)\right)} \quad \textbf{.....(5. 1)}$$

Where $\frac{\partial T}{\partial z}$ and $\frac{\partial T}{\partial h}$ are the vertical and horizontal derivatives of the magnetic field.

Salem et al. (2007) showed, based on Nabighian (1972), that for an infinite tilt-depth contact model, equation 5.1 can be reduced to.

$$\boldsymbol{\theta = \tan^{-1}\left(Y / Z_t\right)} \quad \textbf{.....(5. 2)}$$

Where Y is the horizontal distance from the contact and Z_t is depth to the top of the magnetic contact.

When tilt, θ = 0°, then Y is 0 and is located over the contact. When the tilt is ±45° then Y is $\pm Z_t$. This implies that the tilt angle can be used to identify both the locations and depths of magnetic contacts. Depth estimation is done by measuring the mean distance between ± tilt angle contours across lineaments, and works on the assumption that the depth to their bottoms is infinite (Salem et al., 2007; Salem et al., 2010; Salem, 2011).

The infinite tilt-depth method has been proven to underestimate the depths of magnetic sources (Fairhead et al., 2017). To address this limitation, Salem et al., (2013) provided an equation that considers suitable approximations for the depth to the bottom of the magnetic source anomalies as either the Curie isotherm or the Moho interface rather than assuming it to be infinite. Based on this, they formulated the finite tilt-depth method for a contact model.

$$\boldsymbol{Z_t = Y\left[\frac{Z_b + Y\tan\theta}{Z_b\tan\theta - Y}\right]}\text{.....(5. 3)}$$

Where $\boldsymbol{Z_t}$ and $\boldsymbol{Z_b}$ are the depths to the top and bottom of the magnetic layer, respectively. θ is the tilt angle and Y is the horizontal distance from the contact where θ = 0.

Fairhead et al. (2011) showed that the tilt-depth method can be applied successfully to both RTP and RTE magnetic data sets. In the Benue Trough, the regional DRTE magnetic map of the area was used because it is cleaner and more stable than the other regional magnetic data sets. Getech Plc's Geosoft Executable (GX) downloaded from Sequent website was applied to the grid with θ ranging between -45° and +45° assuming that the depth to the bottom of the source layer is infinite (Esuene, 2012) for the infinite tilt-depth method. The Moho depth grid (crust 1.0 model) was substituted for Y, in equation (5.3) for finite-tilt depth estimation (Fig. 5.19 a and b). Depth to the basement was calculated and constrained to a maximum of 15 km and shown in strip colour codes to represent the depth to basement magnetic contact of the study area (Fig. 5.20). The results show estimates of depth to the lineaments without providing depth estimates to other smooth surfaces of the basement. Simple gridding of the depth estimates to cover the whole area could lead to erroneous and misleading interpretations due to the non-existence of depth estimates in many parts of the basement.

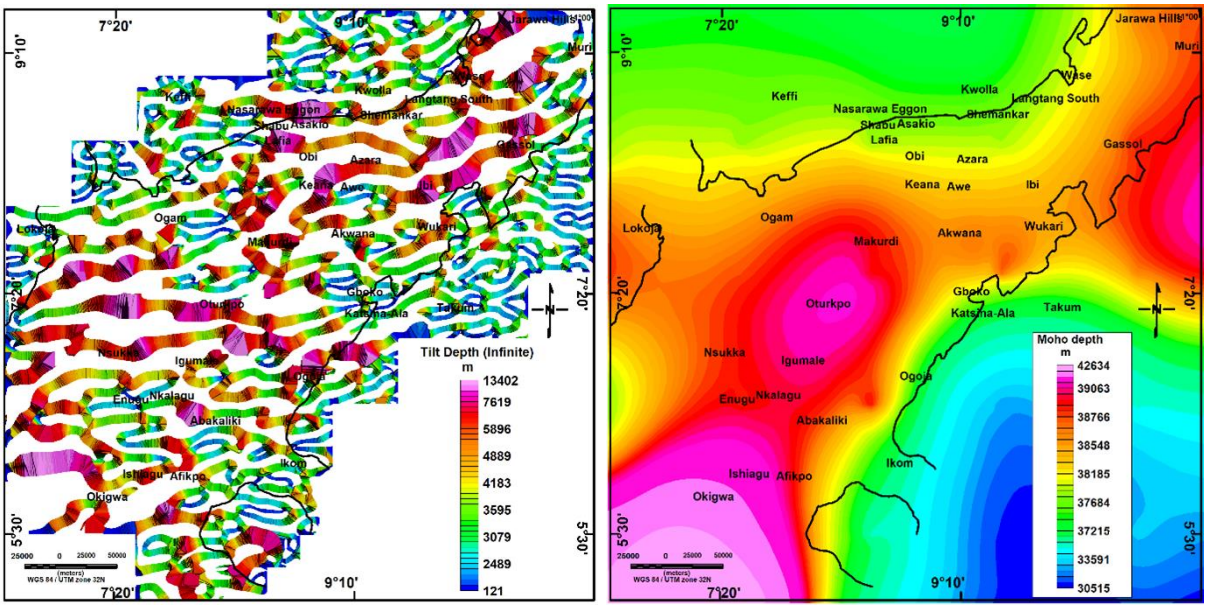

Fig. 5. 19: (a) Infinite tilt depth map showing strips of basement depth estimates constrained to a 15 km bottom depth (b) Moho depth interface from the Crust 1.0 model as a proxy for the depth to the magnetic bottom since the depth of the Curie isotherm could not be directly determined for the area.

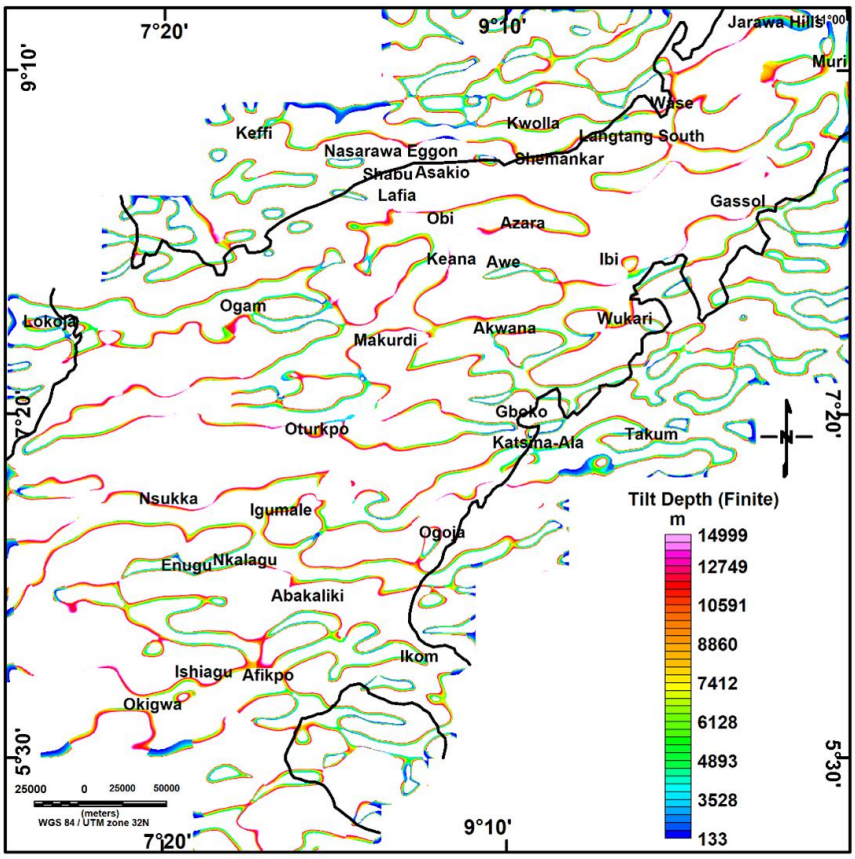

Fig. 5. 20: Finite tilt-depth map from regional DRTE magnetic anomaly map showing cleaned and processed depths to a maximum depth of 15 km. These are the Z_t estimates from equation 5.3.

5.3.2 Finite Local Wavenumber

Depth estimation by local wavenumber is done by analyzing the spectral content of the anomaly associated with a single magnetic contact, assuming that the depth to the base of the source is infinite (Salem, et al., 2014). The local wavenumber may be considered as the horizontal gradient of the local phase (Thurston and Smith, 1997; Smith et al., 1998). It can be approximated from the total horizontal derivative of tilt (Verduzco, et al., 2004), and calculated for a profile over a 2-D source.

$$\boldsymbol{lw = \frac{\partial}{\partial h}\tan^{-1}\left(\frac{\frac{\partial T}{\partial z}}{\frac{\partial T}{\partial h}}\right)}\text{.....(5. 4)}$$

Where T is the magnetic field and $\frac{\partial T}{\partial z}$ and $\frac{\partial T}{\partial h}$ are the vertical and horizontal derivatives, respectively.

Phillips (2000) gave an equivalent local wavenumber expression for 3D grids as.

$$\boldsymbol{lw = \frac{1}{\left((t_x{}^2)+(t_y{}^2)+(t_z{}^2)\right)}\left(t_x t_{zx} + t_y t_{zy} + t_z t_{zz}\right)}\text{.....(5. 5)}$$

Where $t_x = {}^{\partial T}/_{\partial x}$, $t_y = {}^{\partial T}/_{\partial y}$ and $t_z = {}^{\partial T}/_{\partial Z}$ are the magnetic field gradients in the x, y, and z directions respectively while t_{zx} , t_{zy} and t_{zz} are the derivatives of the vertical derivative of the anomalous magnetic field in the x, y, and, z directions.

Therefore, for a 2D magnetic source with an infinite depth extent, the local wavenumber at the peak is given by.

$$\boldsymbol{lw_{max} = \frac{\eta+1}{z_t}}\text{.....(5. 6)}$$

Where the η is the structural index, characterizing the source geometry, and Z_t is the depth to the top of the anomalous body. This method of depth estimation often leads to an underestimation of basement depth because it assumes an infinite magnetic layer bottom (Salem, et al., 2014).

Salem et al. (2014) gave the finite depth model for a contact and showed that the maximum of the local wavenumber lies directly over the contact by

$$\boldsymbol{lw_{max} = \frac{1}{z_t} + \frac{1}{z_b}}\text{.....(5. 7)}$$

The depth to the bottom of the contact model, Z_b is usually defined by either the Curie isotherm or the Moho depth interface.

The regional DRTE was also used here to estimate the depths to the tops of basement contacts. The Moho depth estimate from the Crust 1.0 model (Fig. 5.19 b) was used as a proxy for the depth to the bottom of basement contact, Z_b while the maxima of the local wavenumber, lw_{max}, were obtained from the calculated local wavenumber grid. The depths to the top of the basement contacts, Z_t, were estimated using equation 5.7. The depths were cleaned, gridded, and constrained to a maximum depth of 15 km (Fig. 5.21).

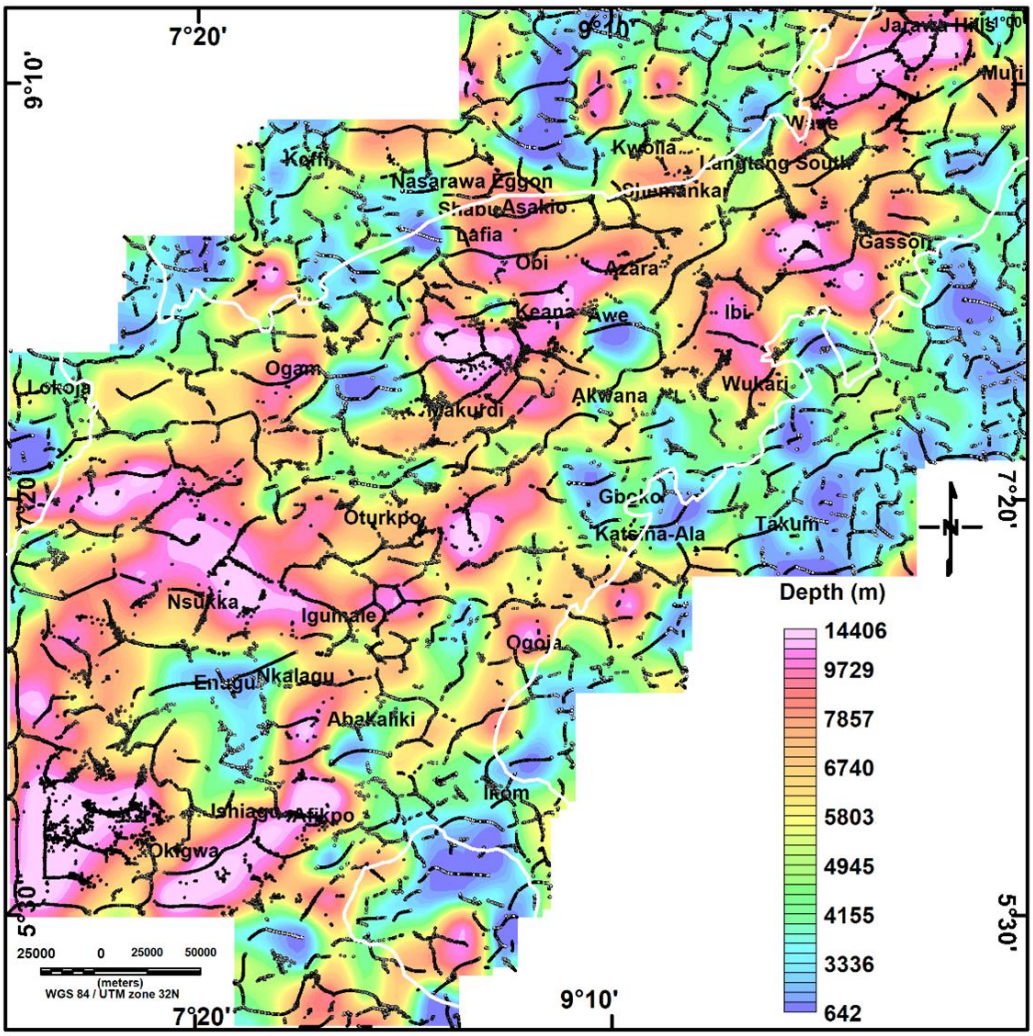

Fig. 5. 21: Finite local wavenumber method depth estimates by minimum curvature gridding to cover the whole of the study area with black dots representing the maxima of the local wavenumber grid for the points at which the depth was initially estimated and superimposed on the local wavenumber.

5.3.3 Pseudo-gravity inversion method

The finite depth estimates (tilt and local wavenumber) discussed above are limited in mapping the basement morphology because they generate basement depth estimates at lineament points and interpolating between these depths may lead to spurious depths in regional grid (Salem et al., 2012). The methods consider magnetic anomaly sources to be confined to the top edges of basement lineaments, and thus exhibit strong bias towards shallower depths, while deeper parts of the basement lack sufficient constraining values for proper and continuous gridding (Salem et al., 2012; Salem, et al., 2014). Simple gridding of estimates of depth to the anomaly edges gives shallower depth across the basin and unrealistic basement morphology arising from underestimation around the deeper basin or close to and on the down-thrown sides of faults (Fairhead et al., 2011; Salem et al., 2014). This problem has been addressed effectively by applying the 3D inversion technique to map depth to the basement using the pseudo-gravity field, which is not limited to identifying particular structural features, or by variations in sediment compaction and basin inversion, etc. (Fairhead et al., 2011; Salem et al., 2012; Salem et al., 2014).

This study applied the 3D inversion method on the pseudo-gravity field obtained from the DRTP magnetic anomaly map (Figs. 5.22 a) to estimate the basement depth. The following steps were involved in the depth estimation process.

- DRTP magnetic anomaly map was transformed into a pseudo-gravity field according to equation 5.8 (Salem et al., 2014). This makes it possible to invert the pseudo-gravity as though it was gravity data.

$$\textbf{Pseudogravity}, \mathbf{PSG} = \mathbf{VI}/(\mathbf{149.8F}) \quad \textbf{(5. 8)}$$

  Where; VI is the vertical integration or vertical derivative to order -1 and, F is the ambient field. The constant factor, 149.8 is applied the inverse of gravitation constant involved in the calculation so that the inversion for susceptibility using gravity software will be suitable (Salem et al., 2014).

  The vertical integration was calculated from the MAGMAP filter menu (Geosoft Inc., 2015), and an ambient value, F of 33269.4 nT was derived from the average total field of the area. The pseudo-gravity generated enhanced deep magnetic anomalies (long wavelengths) and reduces the presence of shallow magnetic sources (short wavelengths) (Fig. 5.22 b).

- To estimate the susceptibility contrast of the area, a cross plot of the pseudo-gravity data against control point depths picked from the local wavenumber depth estimates was used from the 1D assumption in equation 5.9. The assumption was based on the Bouguer slab formula where the pseudo gravity effect is like that of an infinite slab. Twenty-six depth control points overlaid on the pseudo-gravity depth map were picked on the edges of lineaments to represent the thickness of the slab (Fig. 5.22 b). The susceptibility contrast, Δk, was estimated from the slope of a graph of pseudo-gravity against depth (Fig. 5.23).

$$PSG_{slab} = 2\pi G\gamma h = 0.04193\gamma h \quad \text{(5. 9)}$$

The best line of fit from the plot (blue dotted line) in fig. 5.23 was used to calculate the slope and an intercept value of 0.0002 and 0.1193 nT.m, respectively. The susceptibility contrast of 0.004770 (Slope/0.04193) was estimated from the slope.

- To ensure that the pseudo-gravity grid is suitable for inversion, the grid was reduced and made to be less than or equal to zero which enables each of the selected control points valid. This makes it easier to relate pseudo-gravity fields with shallower depths. This was achieved by using a smooth surface to match the control depth points (equation 5.10) to calculate the pseudo-gravity. The observed pseudo-gravity is adjusted by finding the difference between it and the calculated pseudo-gravity data (Appendix C1)
- The intercept value of 0.1193 from the plot is the effective constant of integration in the pseudo-gravity calculation and was subtracted from the adjusted pseudo-gravity data (Fig. 5.24). This is the pseudo-gravity data used for the 3D inversion.
- A MATLAB source code 3DINVER.M, which is based on the Parker–Oldenburg equation (Gómez-Ortiz and Agarwal, 2005) was employed for the depth estimates:

$$F[h(x)] = -\frac{F[\Delta g(x)]e^{(-kz0)}}{2\pi G\gamma} - \sum_{n=2}^{\infty}\frac{k^{n-1}}{n!}F[h^n(x)] \quad \text{(5. 10)}$$

where F [] is the Fourier transform, G is the universal gravitational constant, γ is the magnetic susceptibility contrast across the interface, k is the wavenumber, h(x) is the depth to the interface (positive downwards) and z0 is the mean depth of the horizontal interface.

- Equation 5.10 was then applied to the adjusted pseudo-gravity data by substituting the mean depth of 5.5 km obtained from the average depth value from the finite local

wavenumber method and susceptibility contrast value of 0.004770. The inversion produced a basement depth estimate and relief with an average depth of 6.54 km and an RMS value of 0.0017 with 2 iterations (Fig. 5.25).

The 3D inversion of the pseudo-gravity field of the area has provided a more robust estimate of the depth to the top of the basement. This helped in understanding the basement morphology of the basin as well as provided a suitable resource to infer sediment thickness. Fig. 5.25 shows significant basement uplift in the Northern part (Middle Benue Trough) of the study area particularly around Awe-Azara and Gassol towns. A major NW-SE trending basement uplift between Shemankar and Ibi and a NE-SW trending ridge-like feature is observed between Gboko and Wukari. Basin subsidence (sub-basins) is observed around Wase-Jarawa Hills, Lafia-Asakio-Keana, Akwana-Ibi-Wukari, and Makurdi axes. Further basement uplifts occur in the southern part of the area (Lower Benue Trough), including along the Ogoja-Katsina-Ala, Ishiagu-Okigwa, and Nsukka-Oga axes while the Afikpo-Enugu-Okigwa, and Nkalagu-Igumale-Oturkpo, Lokoja axes show the occurrence of subsidence. The Middle Benue Trough is expected to have thin sedimentary cover while the Lower Benue Trough has a thick sedimentary cover.

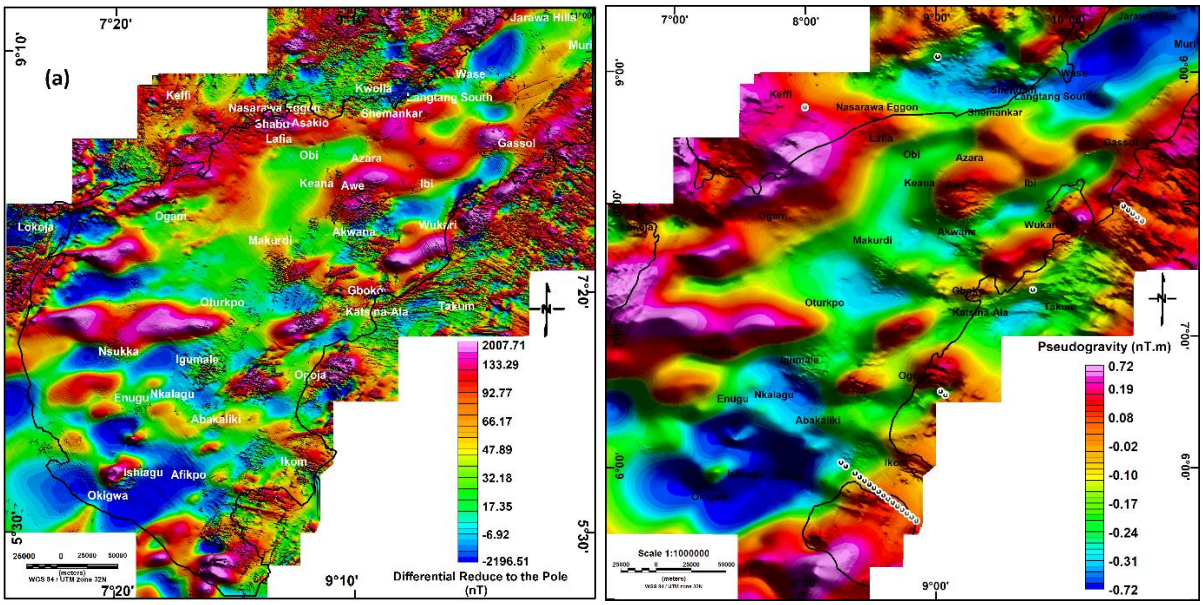

Fig. 5. 22: (a) DRTP magnetic anomaly map produced from TMI transformation (b) Pseudo-gravity map derived from the DRTP with the control point depth overlaid for the estimation of susceptibility contrast of the area for 3D inversion. The circles are carefully picked from the local wavenumber depth estimates. The picks are made outside the basin (on the basement) as such depths easily relate to the true closest value of susceptibility.

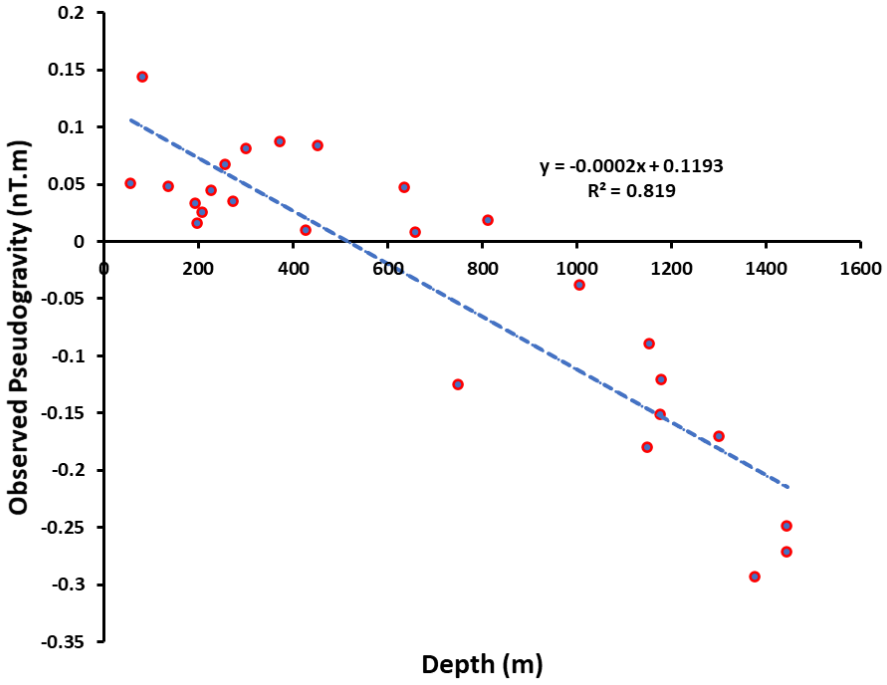

Fig. 5. 23: Plot showing the relation between the control point depths from finite local wavenumber estimate and the pseudo gravity data. The slope of the plot is 0.0002 and the intercept is 0.01193 which is subtracted from the data before inversion (arising from the vertical integral constant). The R square value is high showing a strong correlation of the plotted parameters.

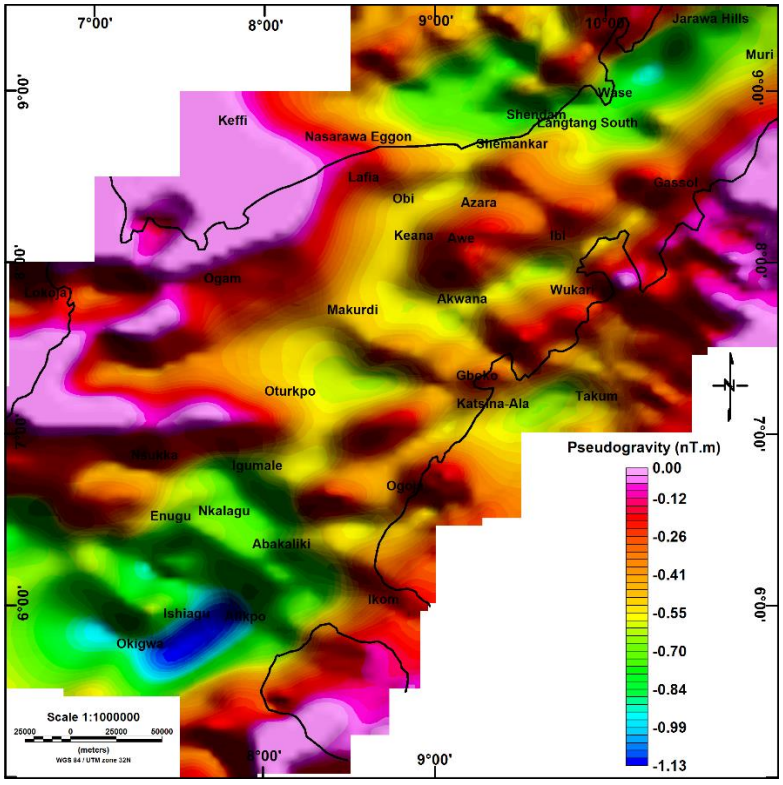

Fig. 5. 24: Adjusted pseudo gravity grid used for the 3D basement depth inversion after the grid values have been modified so that all values are less than or equal to zero.

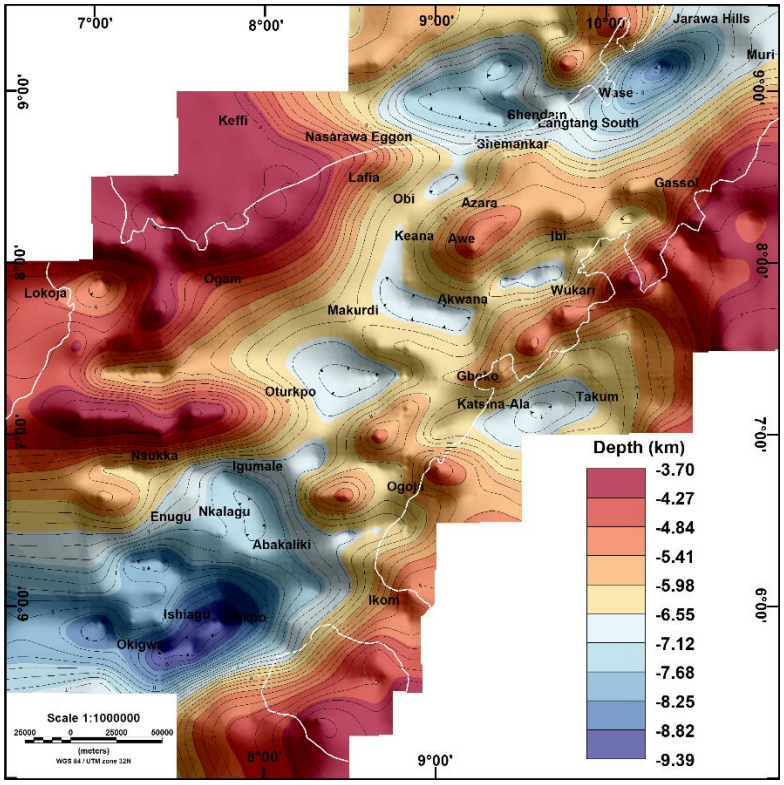

Fig. 5. 25: Depth to the basement of Middle and Lower Benue Trough from 3D inversion of pseudo-gravity data. Mean terrain clearance of 80 m has been removed.

5.3.4 Basement morphology of the trough

The basement morphology was obtained by mapping the depth to basement from 3D inversion of pseudo gravity data (Fig. 5.26). The maximum depth estimated is about 9 km while the minimum is about 4 km. The basement relief shows that there are areas of basement uplift and subsidence in different parts of the trough. The basement geometry is a good proxy for the production of sedimentary thickness maps because areas of shallow basement can be expected to have thin sedimentary cover while areas of deep basement have thick sedimentary cover. Basement troughs or sub-basins are suitable centres for the deposition and accumulation of sediments (depocentres). Some of the areas where the basement shallows have been found to be associated with high magnetic susceptibility values, while areas where the basement deepens are associated with low magnetic susceptibility (Fig. 5.24). The high susceptibilities are probably due to magmatic intrusions (Fairhead, 2015) within or on the basement. Examples of areas of basement uplift with high magnetic susceptibility are to be found around the Awe-Ibi and Ishiagu-Abakaliki towns. The lineament analysis shows the areas of basement blocks and basins to be fault-bounded. Four main fault types have been interpreted to define the basement; NE-SW, NW-SE, ENE-WSW, and N-S normal directions. These faults trends agree to a great extent with the structural trends reported by many authors (Anudu, et al., 2014, Oha et al., 2016; Abdullahi et al., 2019). The NE-SW trend is parallel to the structural trend of the Neoproterozoic-Early Paleozoic ductile shear zones associated with deep-seated basement tectonic structures, and offshore the Chain and Charcot Fracture Zones (Benkhelil, 1989; Anudu et al., 2014). These fault types also control the geometry and activities of the basin and aside from these controls, are also responsible for restricting the emplacement of magmatic material towards the eastern part of the trough.

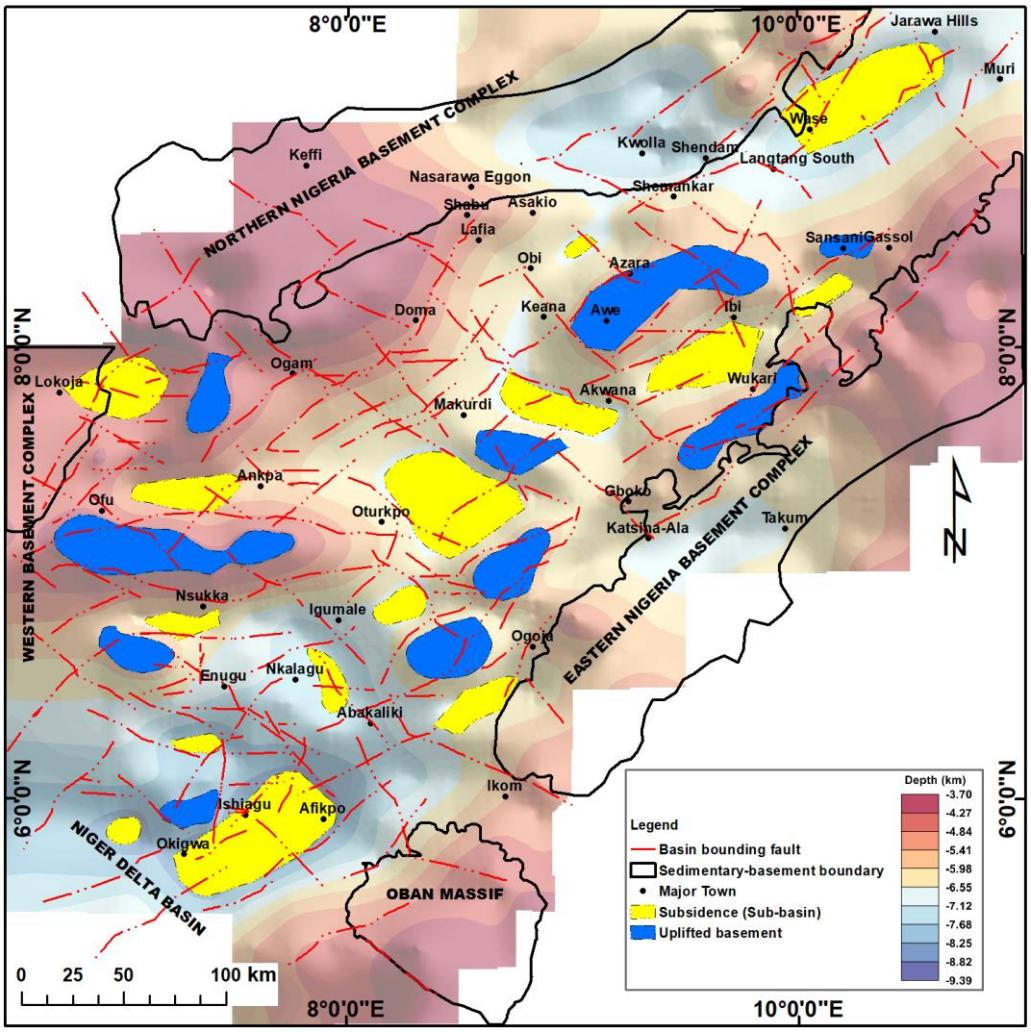

Fig. 5. 26: Basement morphology map showing basement faults, highs (uplift), and lows (subsidence). The basement highs (uplifts), and lows (sub-basins) are fault-bounded. The sub-basins are suitable centres for the deposition and accumulation of sediments (depocentres) while the basement highs exhibit high magnetic susceptibility from 3D magnetic inversion (this study). The sub-basins are bounded by two opposite down-throw direction faults and the basement highs are sand-witched by two opposite upthrown direction faults.

5.4 Modelling of the basin

5.4.1 Two-dimensional gravity and magnetic modelling

Two-dimensional gravity and magnetic modelling techniques have been applied in several environments to appreciate the presence of structures and geological features both within sediments and the basement (Vargas et al., 2015; Ghazala et al., 2018). Modelling and interpretation of gravity and magnetic data sets are usually non-unique i.e., the response from gravity and magnetic to associated geologic features may give different and varied results depending on available constraints, geological and structural knowledge of the area, and the expertise of an interpreter (Tulyatid, 1997; Tulyatid and Fairhead, 1996; Geosoft Inc., 2009; Aboud et al., 2015). In this study, the level of ambiguity was reduced by modelling both gravity and magnetic data sets along the same profiles, applying the results derived from the updated geological map and emplaced intrusive rocks (chapter four), basement morphology and lineaments (this chapter), Moho depth from the Crust 1.0 model (Laske et al., 2013), relevant literature, etc. as suitable constraint for the approach.

The 2D gravity and magnetic modelling were performed using GM-SYS^{TM} version 9.8 downloaded from Sequent website for both Bouguer anomaly and differential reduction to the equator magnetic data sets. The gravity/magnetic response of the model was estimated and compared with the observed profiles and then the model was modified to fit the response between the calculated and the observed values. Four cross-sectional profiles were drawn across the trough (MBT1N, MBT2N, MBT3N, MBT4N) in the NW-SE trend direction, perpendicular to the NE-SW main structural trend direction (Mazur et al., 2015) (Figs. 5.27 and 5.28). Profiles MBT1N and MBT2N are located in the Middle Benue Trough (northern part) while MBT3N and MBT4N are in the Lower Benue Trough (Southern part). Bouguer, magnetic and topographic (ETOPO1) data were used in the modelling process. Since there are no available seismic or exploratory well data to constrain the modelling technique better, the basement depth estimate and the intrusive rocks map produced from this study were used to constrain the geologic model.

Profile MBT1N shows 2-D gravity/magnetic modelling results from a geologic model cross-section with a 350 km NW-SE trending profile (Fig. 5.29). The calculated and the observed gravity anomalies fit better than the magnetic anomalies. The high gravity anomaly amplitude has been attributed to the Moho uplift. Shallow basement undulations could be modelled based on observed magnetic variation. The geologic model shows three basic components: sediments,

crust, and upper mantle. The sediments were subdivided into four layers and assumed to vary with depth but not laterally. The sediments were also assumed to be non-magnetic (SI=0) aid to have lower density values than the basement rocks. The topmost layer is believed to have the lowest density contributing to shorter wavelengths while the lowest layer is ascribed to the highest density and contribute to long wavelengths like the top of the basement. The deepest sediments are modelled to lie at 4.30 km, thus marking the depth to the basement top (basin depth). The crust is divided into magnetic and non-magnetic layers. The two layers are divided by the Curie depth interface (depth of about 580 ^{0}C) below which materials cease to be magnetically susceptible. Generally, the section shows uplift of the mantle to an average depth of 18.78 km and crustal subsidence indicating the presence of extension or stretching of the crust during rifting. This geometry of the crust may be due to pure shear at depth with the action of normal faults in the upper crust. The undulating geometry of the Moho lies almost parallel to the Curie depth interface which confirms that the basin rifting process is purely continental since the mantle materials are not serpentinized.

In cross-section MBT2N, the total length of the profile is 560 km (Fig. 5.30). The gravity anomalies show high positive values at the centre and in the far SE of the area. These anomalies could be attributed to mantle uplift and the presence of volcanic rocks. The geologic model cross-section identified three major components (sediments, crust, and the upper mantle). The sedimentary basin shows emplacement of intrusive rocks within layers, thereby, increasing the gravity anomaly amplitude within the trough. An average basement depth of 7.62 km was estimated over the basin. There are variations in the magnetic blocks across the profile with a major volcanic plug at the end of the profile. The magnetic and non-magnetic layers form the crustal fabric of the area. The relatively flat Curie depth interface could be attributable to the cooling of the crust over time. The geologic section indicates that the crust has been well stretched, thinned, and extended under the basin. The mantle, with its high density, is uplifted to a depth of about 17.30 km towards the centre of the basin. The crust is extensively and symmetrically stretched implying pure shear mode of extension.

2D gravity/magnetic modelling was completed for the 626 km MBT3N profile on the Lower Benue Trough (South) (Fig. 5.31). The trough is wider at this cross-section and more complex than the Middle Benue Trough. This complexity could be because of the presence of the Bida basin at the far left of the profile and the scissors style opening geometry of the southern part of the trough. Supracrustal volcanic rock emplacement is observed towards the SE end of the

profile. A mean depth of 7.10 km has been estimated to the top of the basement. The magnetic crust shows areas of large volcanic complex emplacement, which are indicated by two peaks of high gravity anomalies. The model indicates that the Curie depth is shallower than the Moho interface signifying the absence of oceanic materials for serpentinization (Welford et al., 2010). The mantle is slightly uplifted under the basin with a depth of about 17.08 km; thus, the crust is slightly thinned under the trough but thicker towards the basement. A double gravity anomaly peak is observed towards the right of the profile. This is because a gravity low is between the two gravity highs attributed to a volcanic pipe and crater probably of low density. This is not being studied and investigated further as it is not the focus of the thesis.

Profile MBT4N is 436 km long and located across the Lower Benue Trough. It has low magnetic anomalies towards the NW compared to the centre and the SE where the magnetic anomalies strongly fluctuate (Fig. 5.32). The sediments have been modelled to have been deposited over the basin in layers whose density increases with depth. The maximum depth of the trough along this profile is estimated at an average of 9.65 km observed towards the SW end of the basin. A gently sloping crust bounds the basin to SW left which could be a dipping fault. Volcanic rocks have been emplaced towards the NW edge of the basin while the Curie and Moho have been effectively mapped to separate the magnetic and non-magnetic crusts, and the crust and upper mantle, respectively. The mantle is raised to a maximum depth of 19.02 km accompanied by subsidence of the basin due to stretching of the crust.

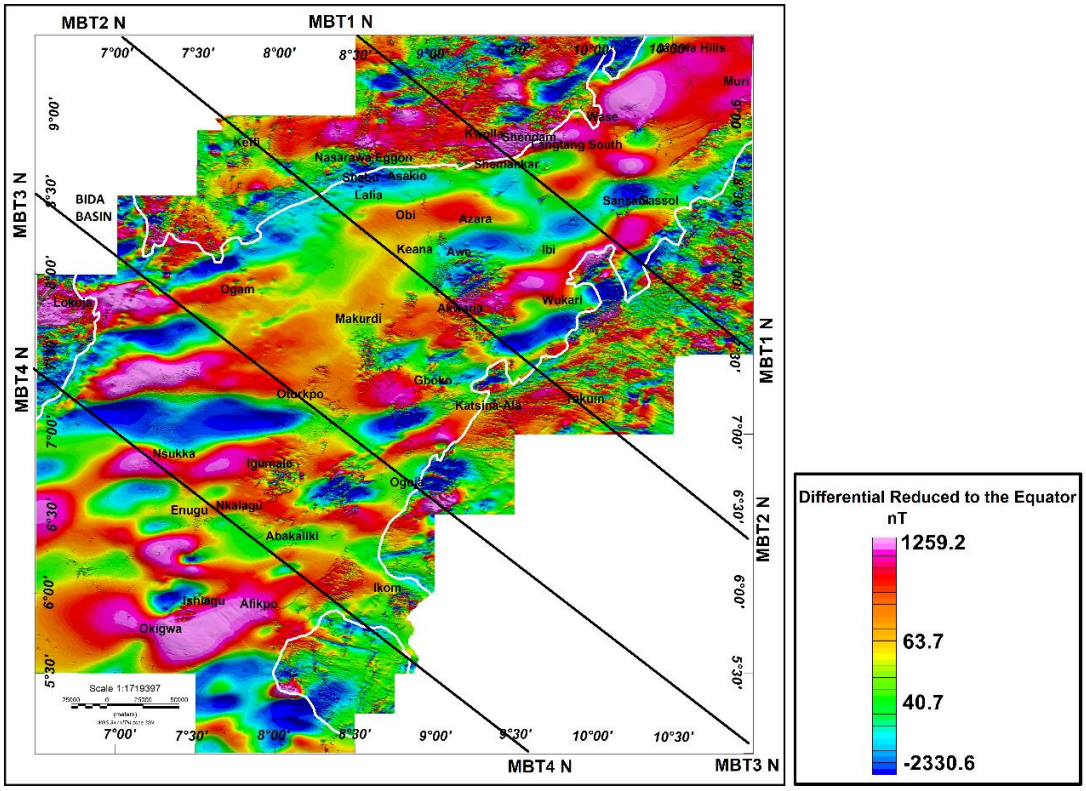

Fig. 5. 27: DRTE magnetic profile lines perpendicular to the general strike of the trough.

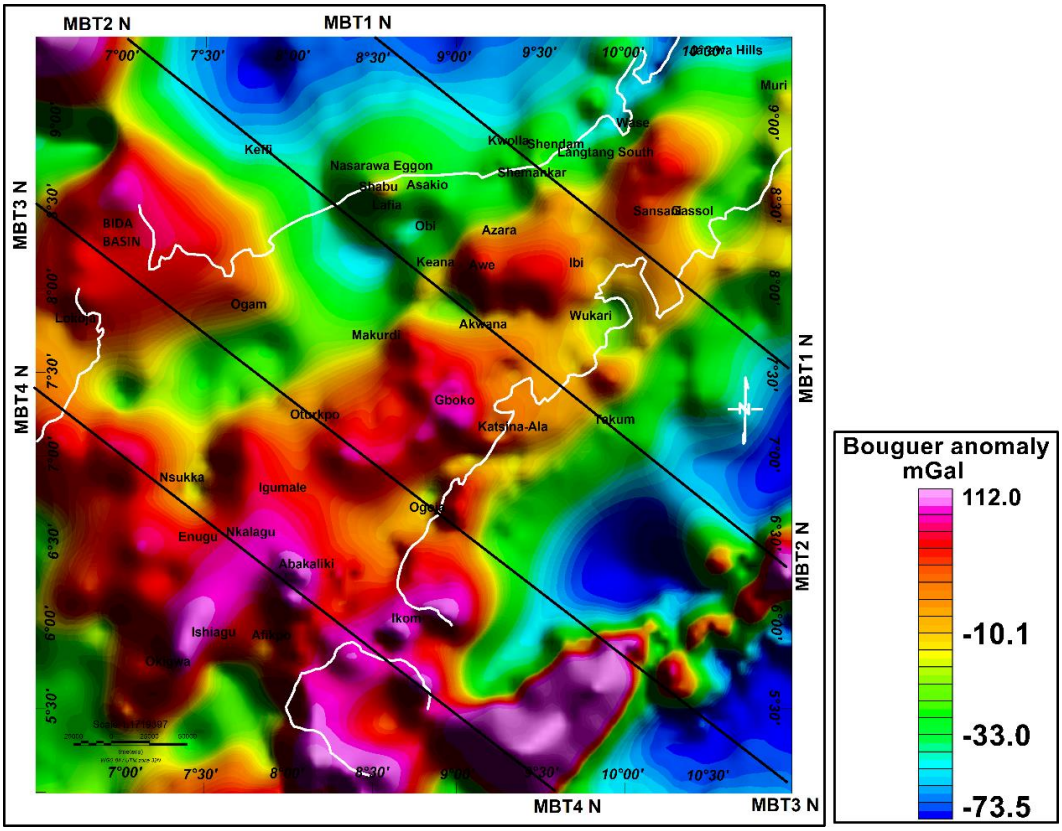

Fig. 5. 28: Bouguer anomaly (Gravity) profile lines perpendicular to the general strike of the trough.

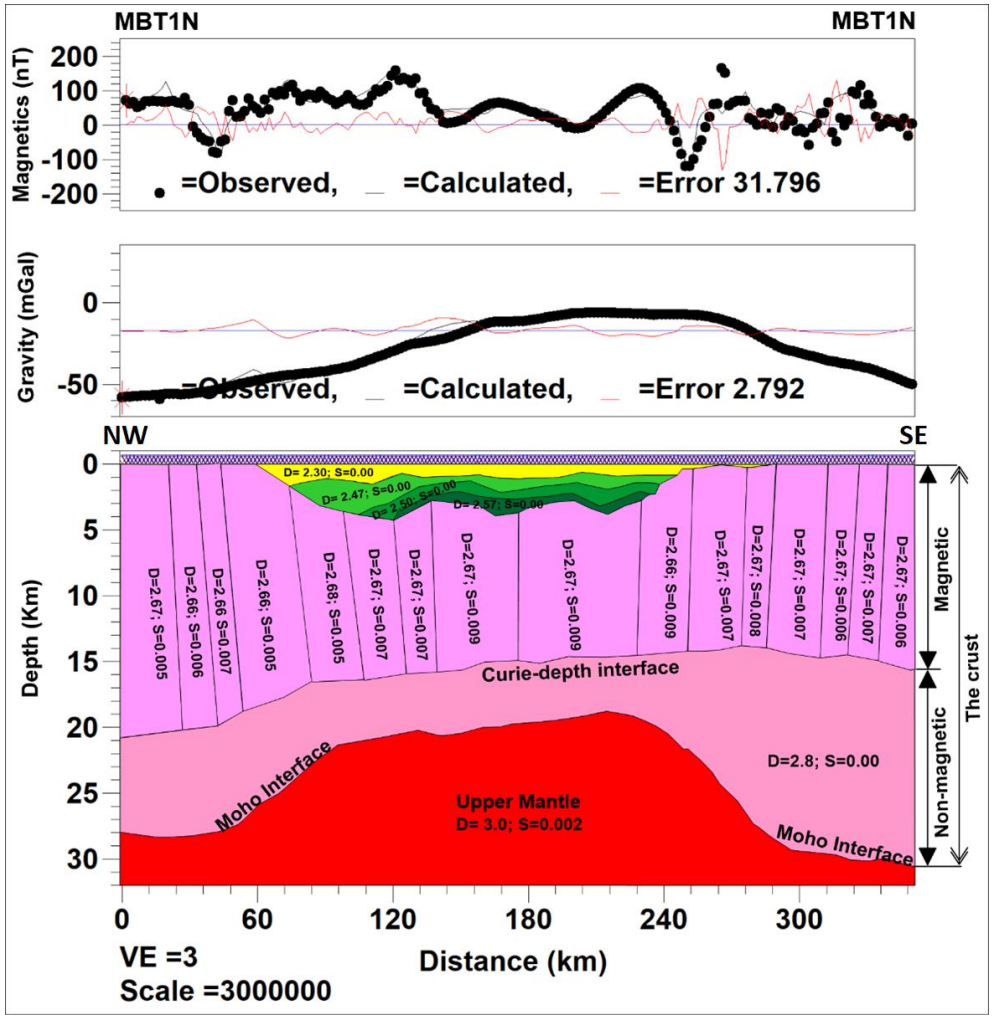

Fig. 5. 29: 2D gravity and magnetic modelling cross-section MBT1N of total profile length of 350 km. The top section shows observed and calculated magnetic and gravity anomalies from the geologic section model located at the bottom. D is density in g/cc and S is the susceptibility in SI. VE represents the vertical scale exaggeration.

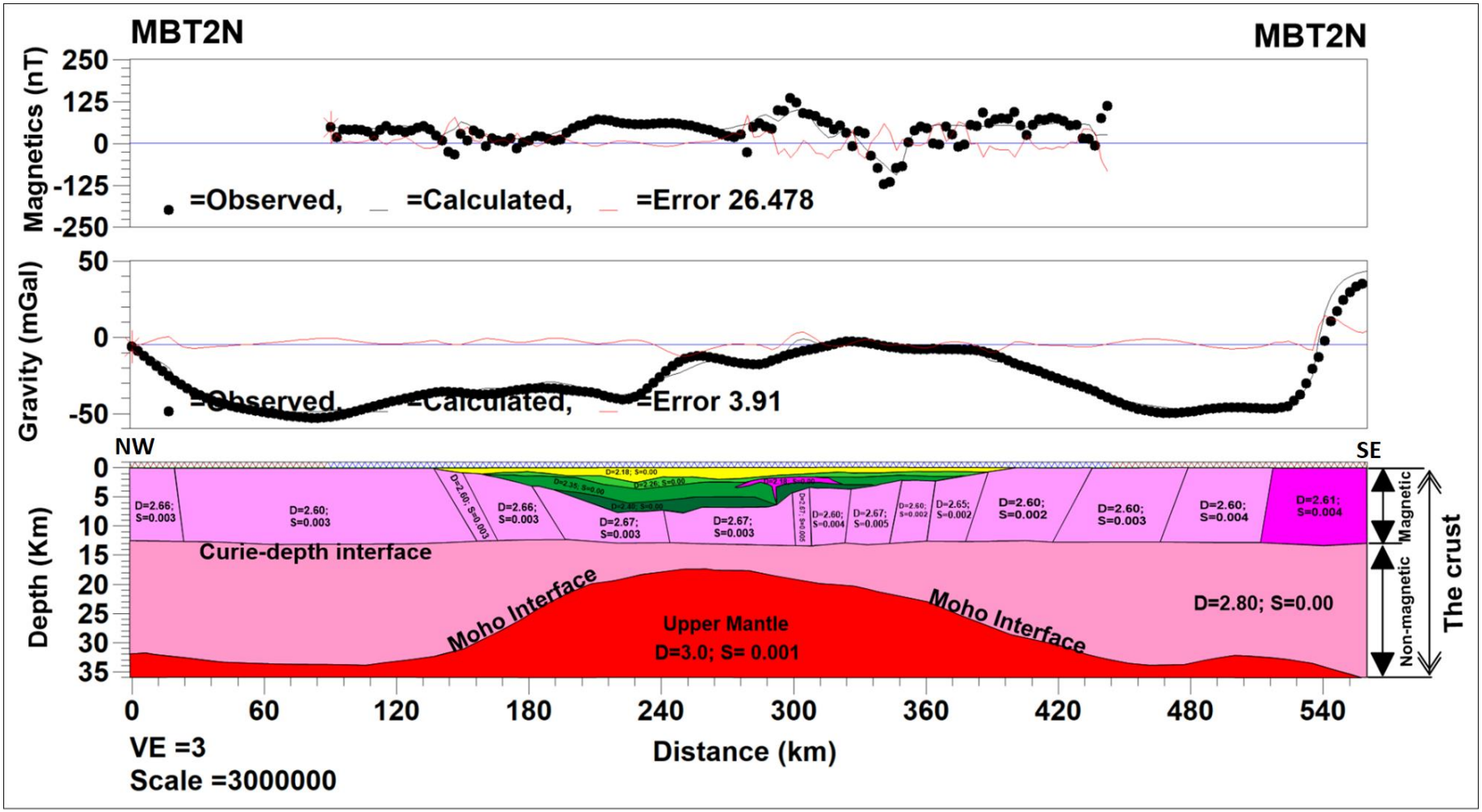

Fig. 5. 30: 2D gravity and magnetic modelling cross-section MBT2N of profile length of 560 km. The top, middle and bottom sections show observed and calculated magnetic and gravity anomalies, and the geologic model, respectively. D, S and VE are density (g/cc), susceptibility (SI), and vertical exaggeration, respectively.

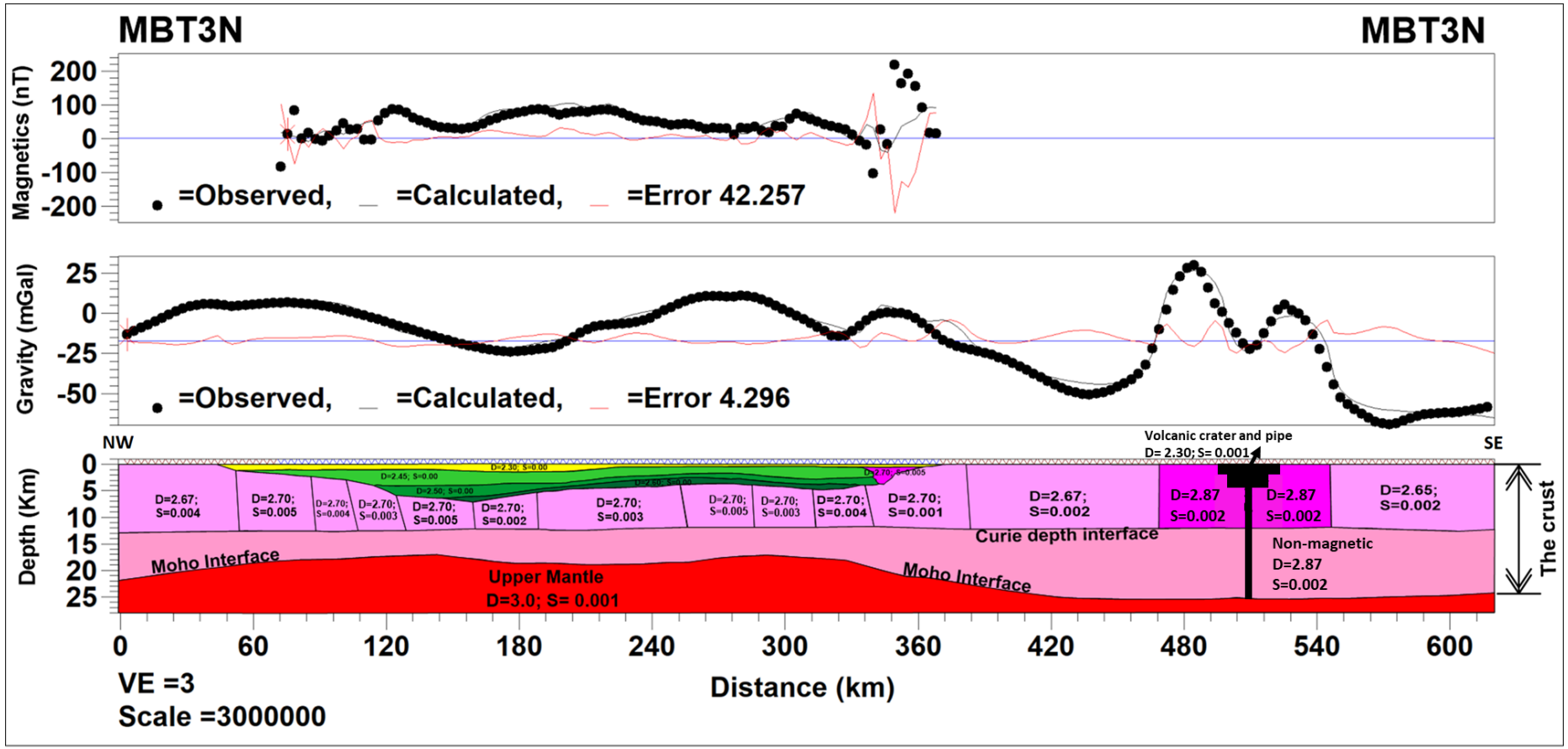

Fig. 5. 31: 2D gravity and magnetic modelling cross-section MBT3N of profile length of 626 km. The top, middle, and bottom sections are magnetic and gravity anomalies, and the geologic model, respectively while D, S, and VE are density (g/cc), susceptibility (SI), and vertical exaggeration, respectively. The double peak at the right side of the profile is due to a volcanic pipe and crater with lower density materials (volcaniclastics and local sediments) acting as a conduit through which magmatic materials are emplaced. The magma chamber (black polygon) may be empty or contains volcanic ash that is relatively lower in density than its surrounding volcanic rocks.

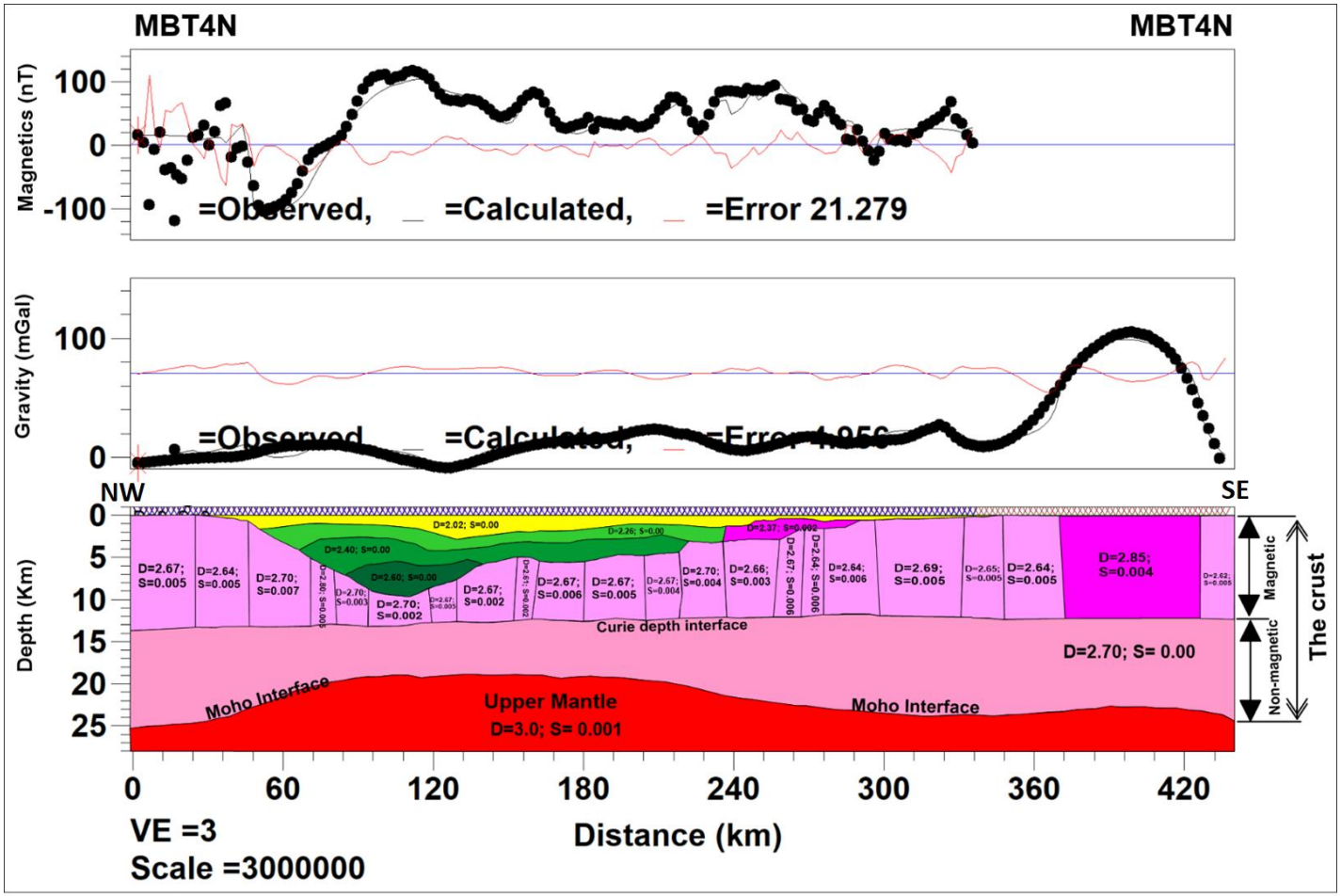

Fig. 5. 32: 2D gravity and magnetic modelling cross-section for MBT4N of profile length 436 km. The top, middle and bottom sections show observed and calculated magnetic and gravity anomalies, and the geologic model, respectively. D, S and VE are density (g/cc), susceptibility (SI), and vertical exaggeration, respectively. Basement depth, Crustal thickness variation, Moho geometry, Curie depth and sub-basin mapped. The profile has been constrained by the basement depth estimate, the intrusive rocks and basement fault maps produced from this study.

5.4.2 Three-dimensional gravity and magnetic modelling

3-D models have been effectively used to map the variations in density and susceptibility contrasts of a basin from both gravity and magnetic data (Dressel et al., 2018). Gravity and magnetic data can be inverted to map deeper three-dimensional structures such as crustal thickness and Moho interface.

5.4.2.1 Gravity 3-D modelling

3-D gravity modelling helps in mapping density variation within sediments, the crust, and the upper mantle (Welford and Hall, 2007). This may reveal lateral changes in density and give important information about the crustal structure and the presence of tectonic structures. Density models were produced by inversion of gravity data. Parker-Oldenburg and Li-Oldenburg inversion techniques (Parker, 1972; Li and Oldenburg, 1998; Gómez-Ortiz and Agarwal, 2005) were used in this study to map the Moho interface and the variation in density below the basement surface. The Parker-Oldenburg method was used to map the Moho interface and then combined with basement depth estimates from magnetics to interpret the crust while the Li-Oldenburg method involves providing 3-D density variation blocks where the Moho and crustal structures were directly studied.

(A) Gravity models from Parker-Oldenburg inversion technique

The Bouguer anomaly map of the area reflects inhomogeneous gravity effect contributions from different sources. These sources are made up of shallow or residual anomalies dominated by short-wavelengths considered as located in the sedimentary basin fill, while other sources are deep and produce long-wavelength anomalies attributed to basement, crustal and mantle anomalies. The main challenge here is to separate these two sources for further regional structural mapping. Thus, to separate the gravity effects corresponding to sediments from those corresponding to the basement and effectively remove the effects of dense and long-wavelength sediments mixed with the basement, the gravity stripping approach was used (Hammer, 1963; Cordell and Henderson, 1968; Cordell, 1973; Simeoni and Brückl, 2009; Miroslav et al., 2013; Chakravarthi et al., 2013). This involved the removal of the gravity effect of sediments within the basin by considering evidence for their density contrasts (constrained by well log density data) and magnetic depth to the top of basement estimate (a proxy for sediments thickness map), thereby allowing for a determination of gravity effects corresponding to basement/mantle sources only (Mazur et al., 2012).

Here, the gravity effect of a sedimentary basin fill with an exponential density-depth relationship can be estimated using the formula below (Parker, 1972 and Granser, 1987; Pham et al., 2018);

$$\Delta g = F^{-1}\left[2\pi G\Delta\rho o\frac{1}{|K|+\lambda}\left(F\left[1-e^{-\lambda h}\right]-\sum_{n=1}^{\infty}\frac{(-|K|^{n})}{n!}F\left[e^{-\lambda h}h^{n}\right]\right)\right]\ldots\ldots\ldots\ldots \textbf{(5. 11)}$$

The function $F[\ ]$ is the Fourier transform, F^{-1} is its inverse G is the universal gravitational constant, $|K|$ is the wavenumber and h is the depth to an undulating interface, which in this case is the depth to the basement from magnetic data. $\Delta\rho o$ and λ are the density contrast observed at the ground surface (mGal) and λ is a reciprocal length (decay constant) in km^{-1}, respectively. $\Delta\rho o$ and λ are estimated by relating the exponential decrease in density to the contrast in a sedimentary basin with depth (Hammer, 1963; Cordell and Henderson, 1968; Cordell, 1973; Granser, 1987; Chakravarthi et al., 2013; Miroslav et al., 2013; Pham et al., 2018);

For this study, the density contrast values, $\Delta\rho$ and the reciprocal length decay constant, λ, were estimated from the average densities of the various strata as obtained from several well-logs of different basins with comparable tectonic origin; the Niger delta, the Bornu-Chad basin, and the East Niger rift basins (Table 5.1) using the equation. These are Cretaceous rift basins that have similar stratigraphy and structural characteristics. The Niger Delta, the Benue Trough, and the Bornu basin fall within the third and the failed arm of the triple junction rift system. The Benue Trough trend in a major NE-SW direction while the Eastern Niger basin trends in a major NW-SE trend (Fairhead and Binks, 1991; Okosun, 1995; Isyaku et al., 2016).

$$\textbf{Density contrast, } \Delta\rho = \Delta\rho o\left(e^{-\lambda z}\right)\ldots\ldots\ldots\ldots\ldots\ldots\ldots\ldots\ldots\ldots\ldots\ldots\ldots\ldots\textbf{(5. 12)}$$

where $\Delta\rho_o$ defines the density contrast observed at the ground surface (mGal), z is depth (positive downward), λ is a reciprocal length (decay constant) in km^{-1}. These unknowns were easily calculated by fitting the curve of $\Delta\rho$ and λ.

A graph of density contrast against depth was plotted and the best line of fit for the curve gave estimates of the average density contrast, Δρo, and decay constant, λ, of 0.7501 and 0.44, respectively (Fig. 5.33). The average exponential density contrast-depth model from well logs of sediments and the depth to basement constraints were then substituted into equation 5.11, and the gravity anomaly due to sedimentary rocks within the trough was then determined (Fig. 5.34). This modelled gravity effect was then subtracted from the Bouguer anomaly to produce

a map of anomalies whose sources lie in the crust and mantle (Fig. 5.35 a). This stripped gravity anomaly map was upward continued to a height of 18 km (Jacobsen, 1987). This step is important in removing some of the short-wavelength and low-amplitude anomalies from small structures that are not accounted for in the stripped off map (Mazur et al., 2012). The upward continued stripped gravity map shows a major gravity anomaly towards the southern part of the area (Fig. 5.35 b). This can be attributed to the uplift of the mantle and magma emplacement, and action of a possible mantle plume.

The depth to Moho was calculated from the upward continued map by using the modified version of equation 5.10 to compute for the depth of an anomalous surface (Moho depth) from the gravity anomaly through the iterative inversion procedure (Hinze et al., 2010). The susceptibility contrast across the interface, γ, in the equation was substituted with the density contrast, ρ, associated with the crust-mantle interface.

This expression in equation 5.11 gives the Parker–Oldenburg inversion algorithm that allows the determination of the topography of a density interface by means of an iterative inversion procedure. Gómez-Ortiz and Agarwal (2005) implemented the equation in MATLAB to compute the 3D geometry of a horizontal density interface at Moho depth from a gridded gravity anomaly. The code works on the principle of relating the Fourier transform of the gravity anomaly to the sum of the Fourier transform of the interface topography. This code was used for calculating Moho topography using a mean Moho depth of 23 km chosen based on the analyses from seismic refraction and receiver function analyses in the study area (Stuart et al., 1985; Akpan et al., 2016). Density contrast values between the crust and the upper mantle of 0.17 g/cc and 0.5 g/cc were previously used for crustal structure analyses of the area (Fairhead and Okereke, 1987, 1990; Fairhead et al., 1991; Mukaila et al., 2019) and hence used in this study. Values of 0.3 g/cc and 0.4 g/cc were also tested to determine the most credible three-dimensional geometry of the Moho interface. Other parameters that remained constant during the inversion were smaller and greater cut-off frequency filters of 0.022 and 0.12 respectively as well as a convergence criterion of 0.02 km and 0.1 truncation window size.

In all the inversions, the iterative process terminated at 2 iterations with root mean square (RMS) error values of 1.7058e-05, 5.4775e-05, 3.0811e-05, and 1.9719e-05 for the density contrasts values of 0.17, 0.3, 0.4 and 0.5, respectively (Appendices C2, C3 and C4). The inversion result from the density contrast 0.17 is preferred in this study because it shows a wider range of Moho depth values than the others, and provides available estimates that fit

closely to the true values of the interface based on the low rms values-1.7058e-05 (Fig. 5.36). This result gave a very good correlation with the stripped upward continued gravity input map and an insignificant residual range of 0.40 to 0.42 mGal. The maximum and minimum gravity anomaly values from the stripped upward continued map are 4.493 mGal and 98.909 mGal while the calculated gravity anomaly from the Moho contrast ranges from 4.080 mGal to 98.500 mGal (Fig. 5.37). The inversion method has to a large extent predicted the Bouguer anomaly. However, the four density contrast values gave essentially similar Moho topography and any of them can be used in further study.

Table 5. 1: Average density-depth estimates from well-logs of different basins with a similar tectonic history of the study area.

Depth (m)	Bornu-Basin Δρ (g/cc)	East Africa Δρ (g/cc)	Niger Delta Δρ (g/cc)	Average Δρ (g/cc)
0	0.77	0.59	1.04	0.80
200	0.77	-	0.83	0.80
250	-	0.55	-	0.55
400	0.67	-	0.79	0.73
500	-	0.57	-	0.57
600	0.62	-	0.56	0.59
750	-	0.5	-	0.50
800	0.47	-	0.49	0.48
1000	0.465	0.48	0.42	0.46
1200	0.45	-	0.36	0.41
1250	-	0.44	-	0.44
1400	0.45	-	0.33	0.39
1500	-	0.43	-	0.43
1600	0.45	-	0.31	0.38
1750	-	0.36	-	0.36
1800	0.44	-	0.28	0.36
2000	0.37	0.3	0.26	0.31
2200	0.32	-	0.24	0.28
2250	-	0.28	-	0.28
2400	0.32	-	0.23	0.27
2500	-	0.22	-	0.22
2600	0.32	-	0.21	0.27
2750	-	0.21	-	0.21
2800	0.22	-	0.20	0.21
3000	0.22	0.23	0.18	0.21

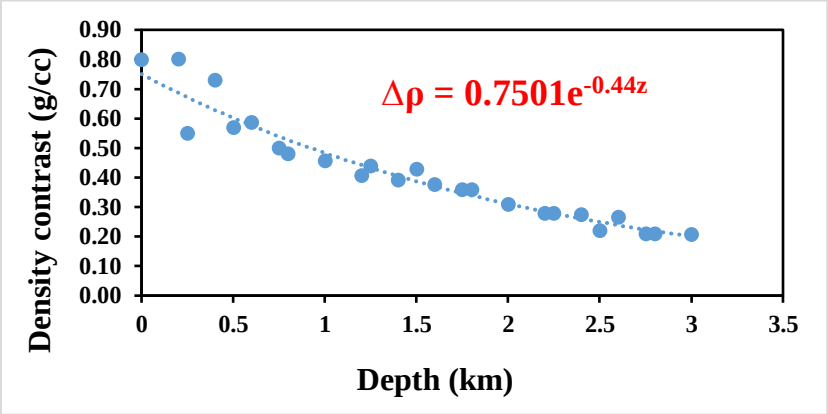

Fig. 5. 33: Average density measured in deep drilled wells (exponential density-depth models) from the Bornu-Chad basin, East Niger rift Basin, and Niger Delta. Density contrast is assumed based on the assumption that the country rock density is 2.67 g/cm^3 ($\Delta\rho_o$ = 0.7501 and λ=0.44).

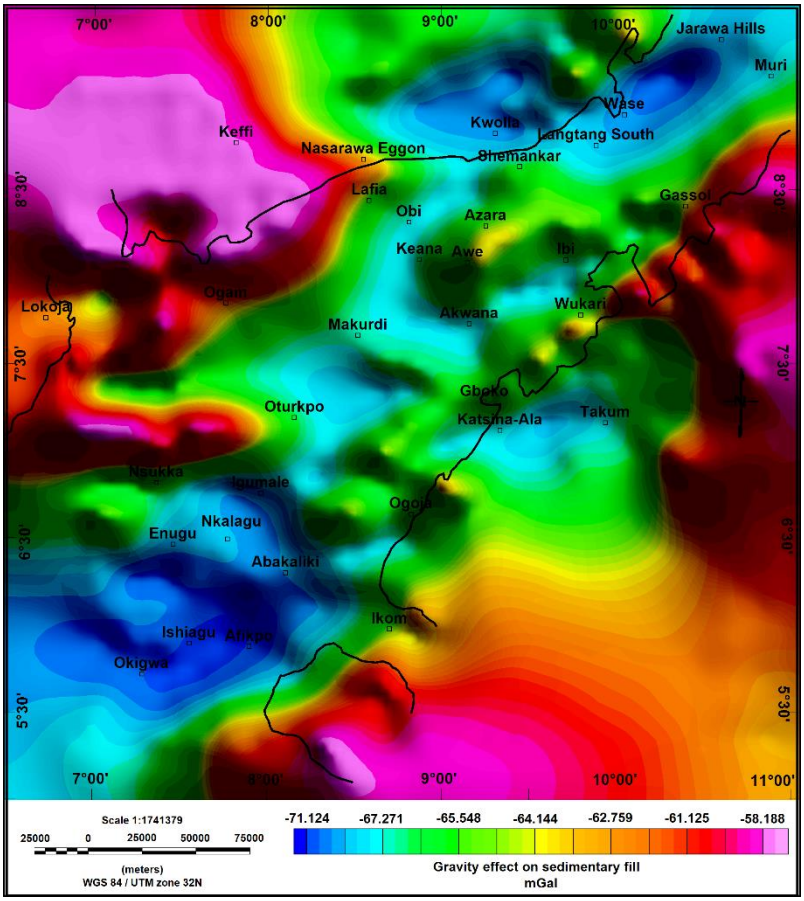

Fig. 5. 34: Sedimentary gravity effect model constrained by the basement depth estimate obtained from this study via the pseudo gravity anomaly map

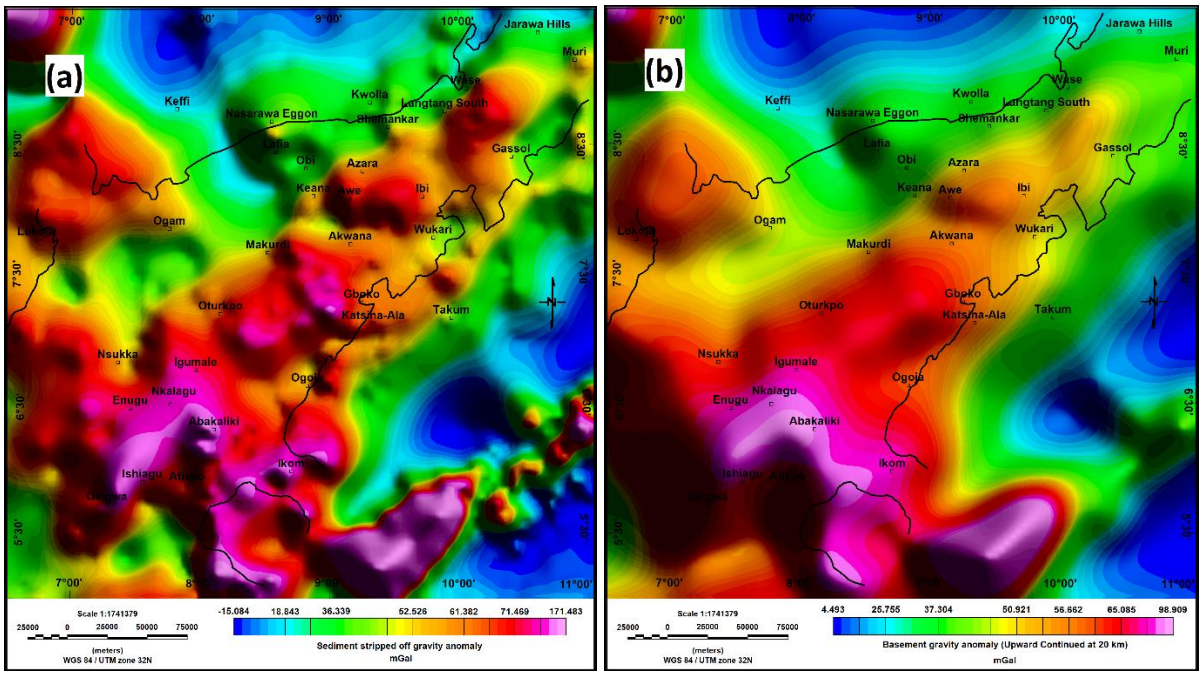

Fig. 5. 35: Sedimentary stripped gravity anomaly map (a) representing top of basement gravity anomaly response (b) upward continued by 18 km to remove mostly supracrustal intrusive effects of the area.

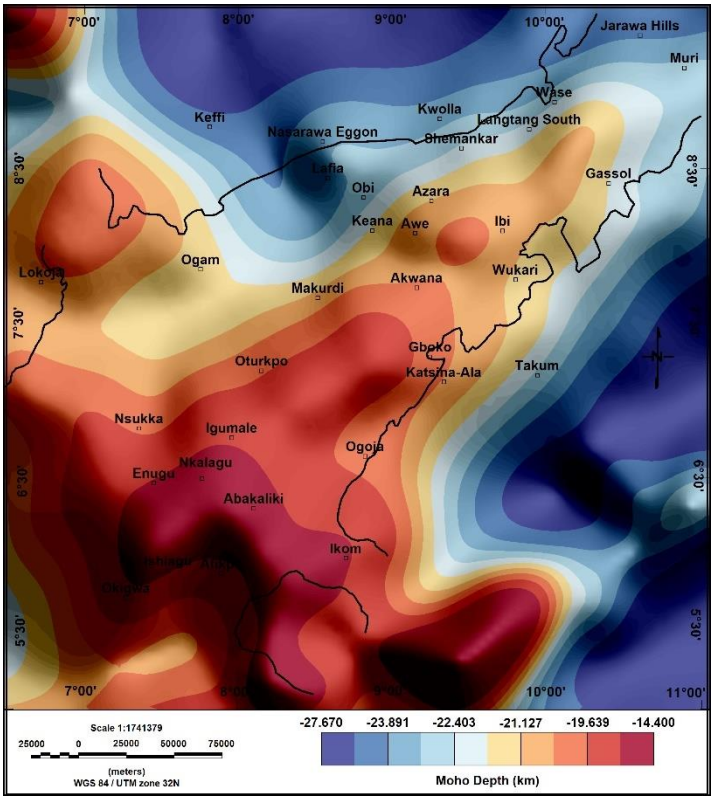

Fig. 5. 36: Moho depth interface showing the topographic variation from the 3D inversion after filtering and considering the density contrast of 0.17.

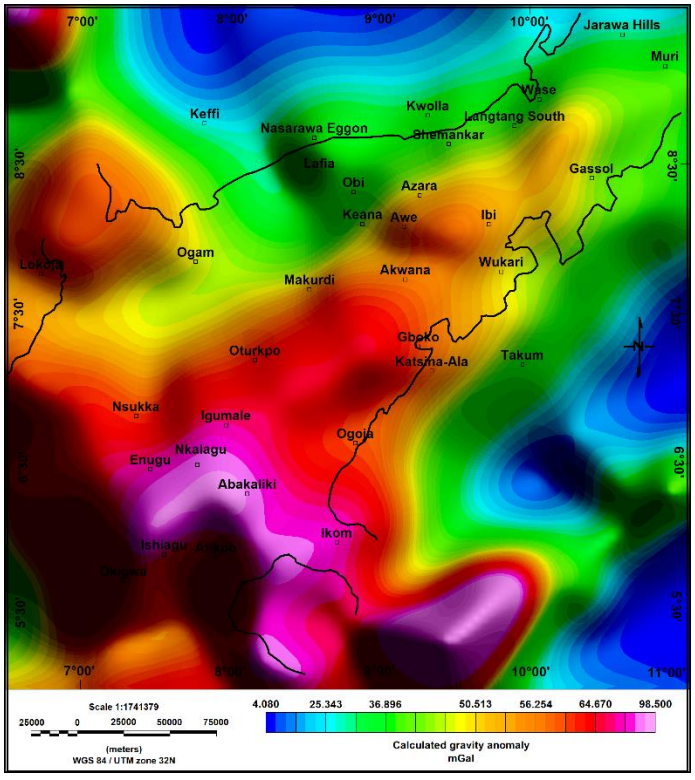

Fig. 5. 37: Calculated gravity map forward model from the estimated Moho depth interface. The difference between the input gravity map and the one due to the calculated interface ranges between 0.40 and 0.42 mGal.

(B) Gravity models from the Li-Oldenberg inversion technique

Gravity inversion of Bouguer anomalies can be employed to generate a 3-D density anomaly model which serves as a platform for understanding the Moho interface, crustal density structure, and the geodynamics of rifted basins (Welford and Hall, 2007) with or without the application of constraints. This technique is usually applied to the observed Bouguer anomaly to track deep structures such as the Moho interface and is employed in understanding the crustal structure of the basin.

The Li-Oldenberg technique involves the use of the GRAV 3D inversion algorithm which is a robust 3-D gravity inversion software that allows the incorporation of a priori model information to produce a targeted result (Li and Oldenburg, 1996 and 1998; Welford and Hall, 2007). This algorithm inverts gravity observations at the Earth's surface (Bouguer anomalies) to obtain a subsurface 3-D density anomaly below the observation point relative to background density.

The GRAV 3D algorithm is very flexible and can be modified for more robust results. Therefore, before the inversion, the following were constructed and calculated.

- For the inversion process, a mesh of flattened cubes was constructed with lateral extent corresponding to the study area and dimensions of 10 km X 10 km containing 50 cells in both the easting and northing directions. Welford and Hall (2007) cautioned on the need to use an appropriate vertical extent for the mesh during inversion as it affects the result. This was achieved by testing several vertical depth extents (25 km, 30 km, 35 km, and 40 km) with the smallest cube depth of 100 m (Appendix C5). The vertical depth of 35 km gave the preferred result for the Moho interface as it seems to evenly and reasonably distributes density values across the whole area with depth (Fig. 5.38).
- To produce a more acceptable density anomaly model, a reference density model that holds a priori geophysical information was designed and incorporated into the Grav3D software (Welford and Hall, 2007, Welford et al., 2010; Deng et al., 2014). The development of a reference model for inversion of the Moho and crustal structure of the study area was achieved by assigning sedimentary densities into the model using average density well logs based on an exponential density-depth function (Fig. 5.33) and imposing the depth to the basement (Fig. 5.25). The inversion algorithm for the sediments was modified such that the density anomaly within a given prism was designed to only vary within a set range of values based on the density-depth function

and controlled by the depth to the basement. This has ensured that features of known density from the density logs are incorporated directly into the reference density anomaly model and the remaining cubes below the basement are unaffected during the inversion. Hence, all the remaining mesh prisms were given a starting 0 kgm^{-3} density anomaly conforming to the background density anomaly in which during the inversion, the density anomaly in each of these prisms could vary between -1000 kgm^{-3} and 1000 kgm^{-3} density contrast for the whole area i.e., the density ranges between 1600 kgm^{-3} and 3600 kgm^{-3} (average host rock density 2600 kgm^{-3}). This allowed for great freedom in assigning density anomalies below the sediments during the inversion to reproduce the observed gravity effect as no constraints were placed on the prisms (Fig. 5.39).

- Also, owing to the fact that gravity data sets have no inherent depth resolution, which may lead to the concentration of structural anomalies near the surface (Li and Oldenburg, 1998), a depth weight function was constructed and applied so that all cubes at all depths were considered during the inversion (Welford and Hall, 2007). The depth weighting function is given by.

$$\boldsymbol{w(z) = \frac{1}{\left((z+z_0)^{\beta/2}\right)}} \quad \textbf{.....(5. 13)}$$

where z, z_0 and β are observation height, the cell size of the model of discretization, and a constant measuring the field decay of the source, respectively (Li and Oldenburg, 1996; Li and Oldenburg, 1998). The value, β could also be substituted for a structural index, η, if known (Cella and Fedi, 2012). Here, a β value of 2 was applied since a cube is a reasonable approximation to a spherical dipole.

The observed gravity anomaly map (Bouguer anomaly) of the study area was used directly for the Grav3D software inversion to produce a 3-D density structure of the area. Several inversion parameters were tested for different vertical depths (25 km, 30 km, 35 km, and 40 km). Parameters input from the 35 km vertical depth trials gave the preferred result (Appendix C 5). The best result for the inversion modelled effectively the 3-D density structure of the basin with density contrasts ranging between 0.247 g/cc and -0.76 g/cc (Fig. 5.40). The density structure model showed two blocks (the crust and upper mantle blocks) below the basement surface. Four profiles were examined in 2-D cross-sectional depth slices to map the crust and the Moho interface i.e. L1-L2, L3-L4, L5-L6, and L7-L8 (Fig. 5.40).

Figs. 5.41 and 5.42 show 2D depth slices along profiles L1-L2 and L3-L4 with the interpreted crust, Moho interface, and the upper mantle shown. The Moho interface is uplifted underneath the basin where there is high gravity response. The high gravity anomaly could be attributed to the injection and emplacement of magma materials within and on the basement rocks or the crust. These models indicate that crustal stretching led to thinning and upwelling of the mantle with associated block faulting and subsidence (McKenzie, 1978). Figs. 5.43 and 5.44 are 2D depth slices along profiles L5-L6 and L7-L8 which show the crust, Moho, and upper mantle. Moho elevation is not prominent but very gentle and subtle. This could be attributed to the development and opening of the Bida basin towards L5 and L6 in the southern end of the area. The SE ends of these profiles indicate an increase in crustal thickness due to the presence of magmatic materials. Generally, all the depth slices showed and effectively differentiated the crust and the mantle, even though there is no distinct boundary between the two. The fit between the observed and predicted or calculated gravity anomaly is very good, thereby, validating the 3D block model and the technique. This is because the density contrast distribution with depth seems to diferentiate appropriately between two depths of density contrast, i.e., high density contrast (sedimentary layers) and low density contrast (basement and mantle). A 3D Moho interface and depth model were produced by removing the gravity cell responses from sedimentary and crustal materials (Fig. 5.45). The Moho depth surface was picked at a density contrast around 0.135 g/cc. This was used to create the Moho depth map of the area (Fig. 5.46 a). A good fit was also observed from the predicted gravity response obtained from the estimated Moho depth of the basin (Fig. 5.46 b).

A cross-plot between Moho depth estimates from Parker-Oldenburg and Li-Oldenburg inversion methods was made to validate the estimates (Fig. 5.47). The result shows a high correlation between the two depth estimates. The correlation is straight between 20 km and 38 km, showing that the two methods best interpret the Moho interface within these depths.

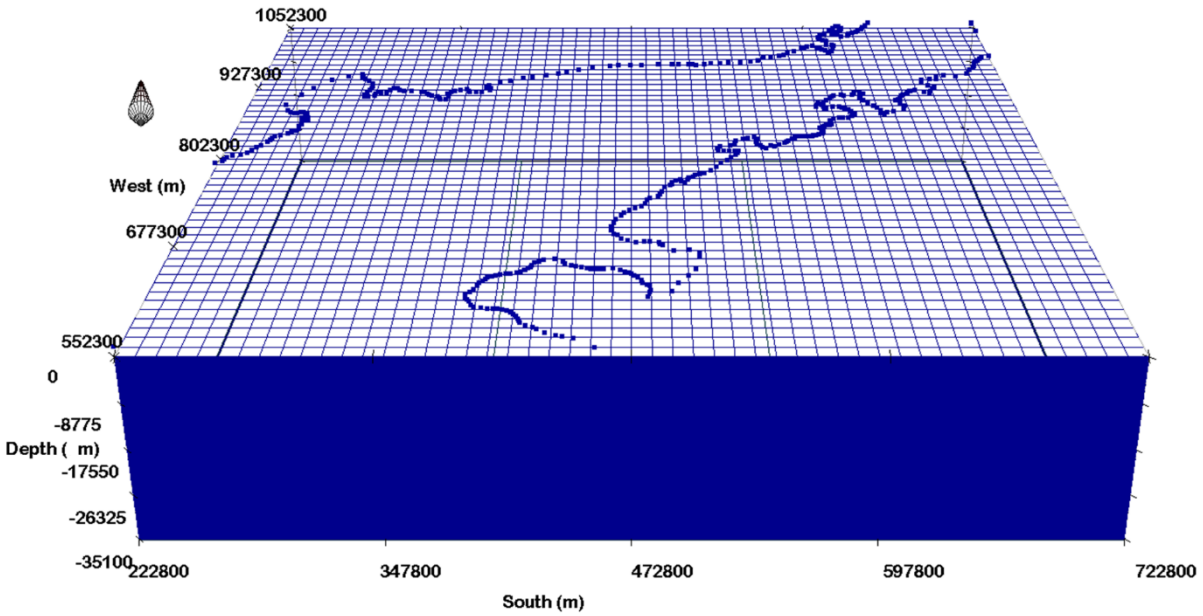

Fig. 5. 38: Mesh constructed in cubes with each cube or cell measuring 10 km x 10 km x 0.1 km. The total number of cells is 50 x 50 x 351 with a total mesh dimension of 500 km x 500 km x 35.1 km. The blue dotted points on the mesh show the basement sedimentary boundary of the area.

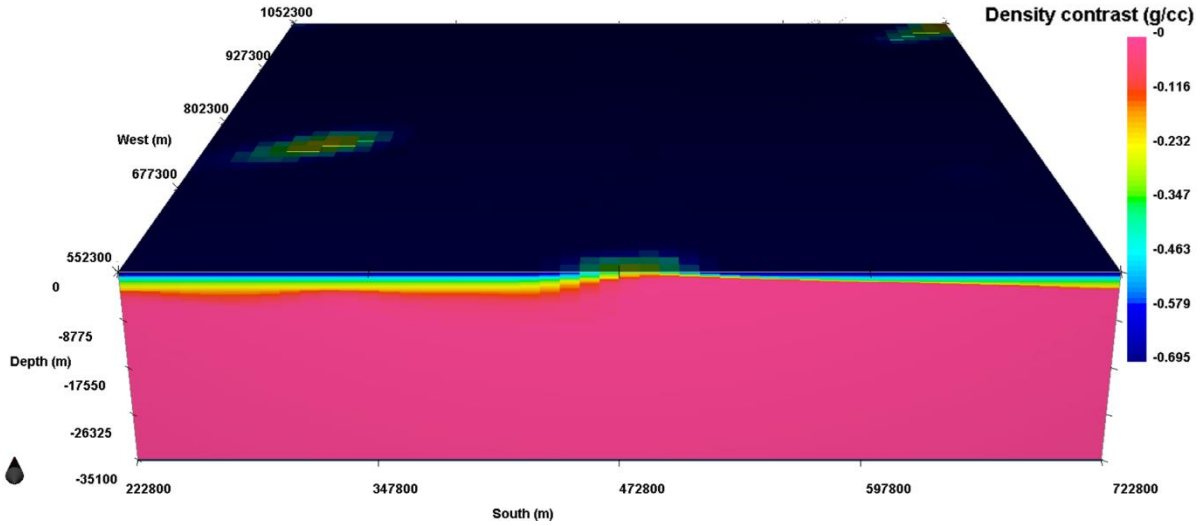

Fig. 5. 39: The reference density anomaly model showing imposed starting 0 g/cc density contrast below the top of the basement to allow for an inversion of the Moho interface.

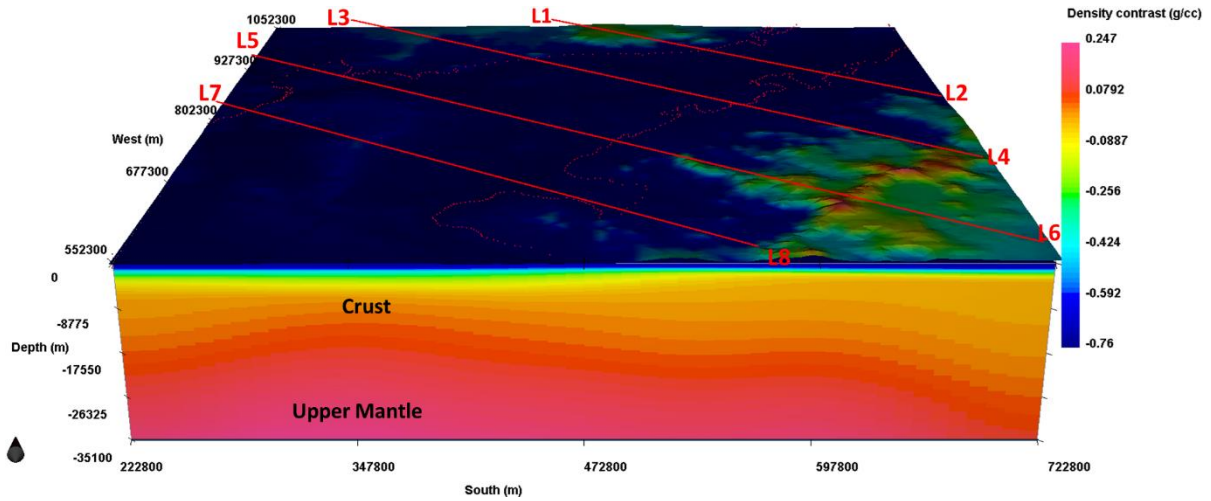

Fig. 5. 40: 3D inverted density structural model block for Moho depth mapping showing four profiles across the major structural trend of the basin. The inversion of the density structure is from Grav3D software indicating the presence of the crust and the upper mantle.

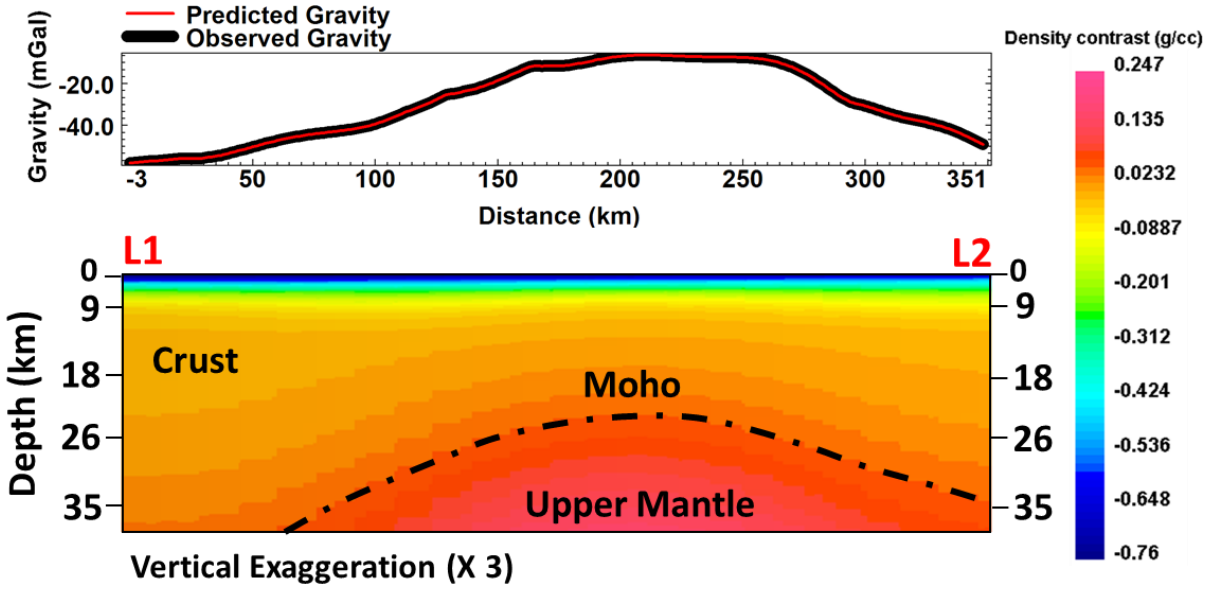

Fig. 5. 41: 2D depth slice along profile L1-L2 showing the crust, Moho interface, and the upper mantle. The Moho interface is uplifted within the basin.

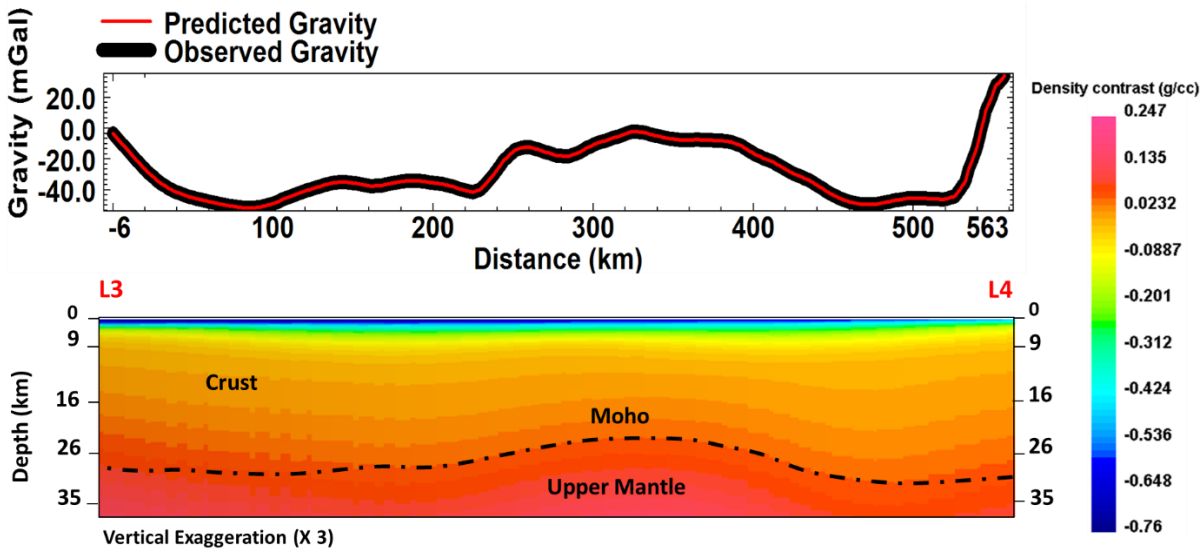

Fig. 5. 42: 2D depth slice along profile L3-L4 showing slight uplift of Moho under the basin with gentle Moho slope at both ends of the basin.

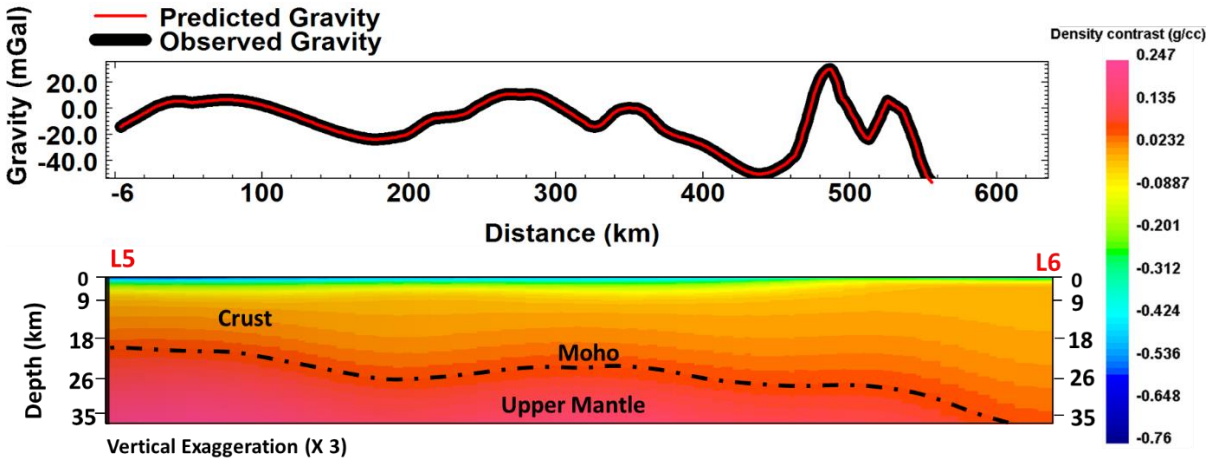

Fig. 5. 43: 2D depth slice along profile L5-L6 showing the crust, Moho, and the upper mantle. The Moho is not well elevated with the basin because of the opening of the Bida basin towards L5.

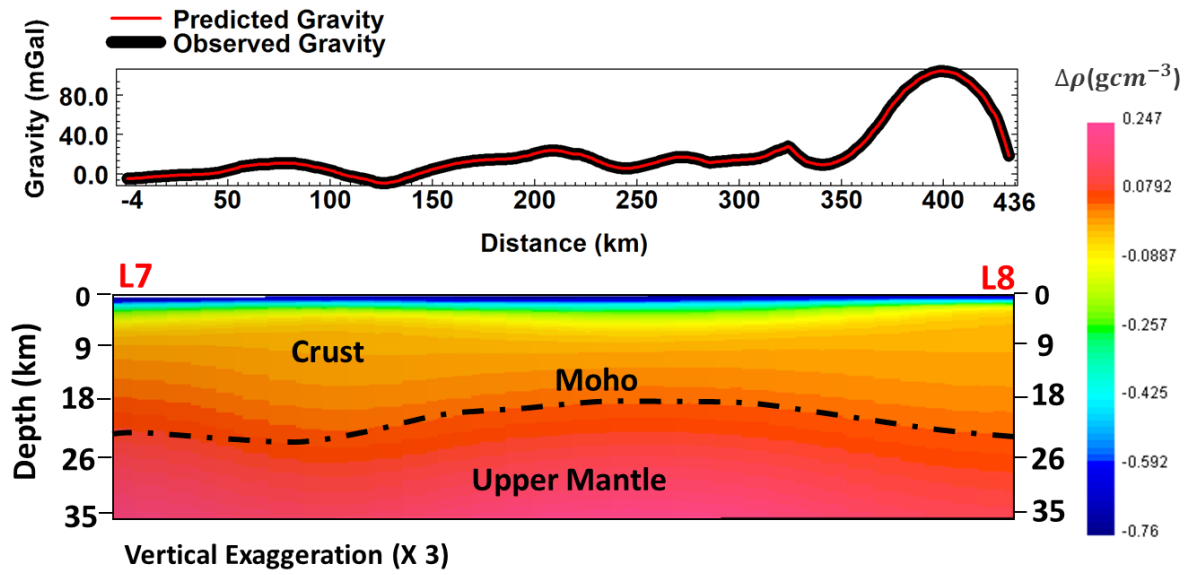

Fig. 5. 44: 2D depth slice along profile L7-L8 with slight uplift of the Moho interface over the Lower Benue Trough.

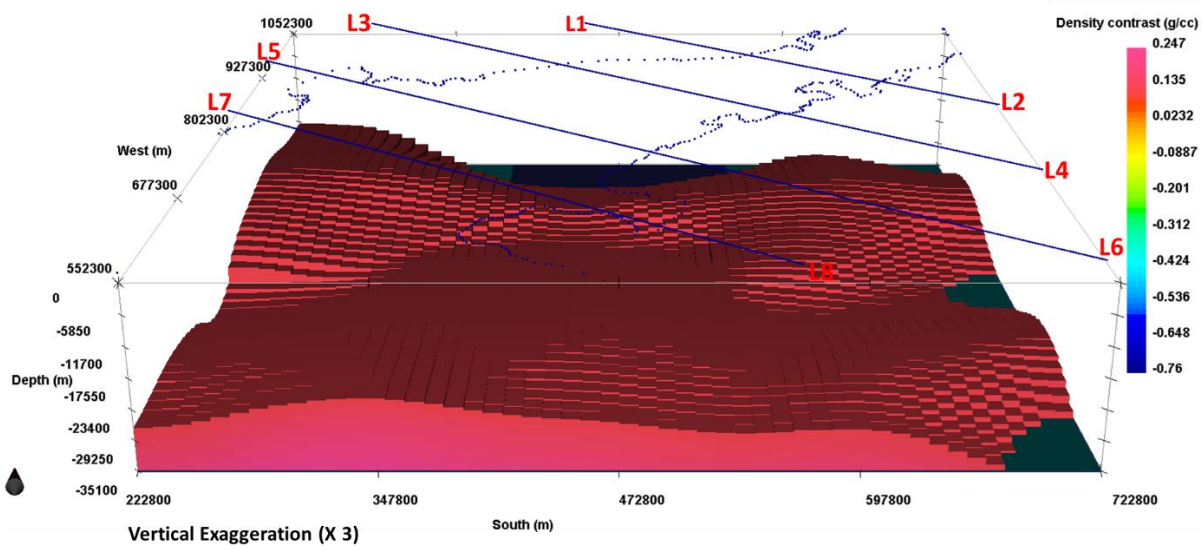

Fig. 5. 45: 3D density anomaly model block for Moho depth mapping with the crust and sedimentary effect removed (Density contrast of 0.135 g/cc).

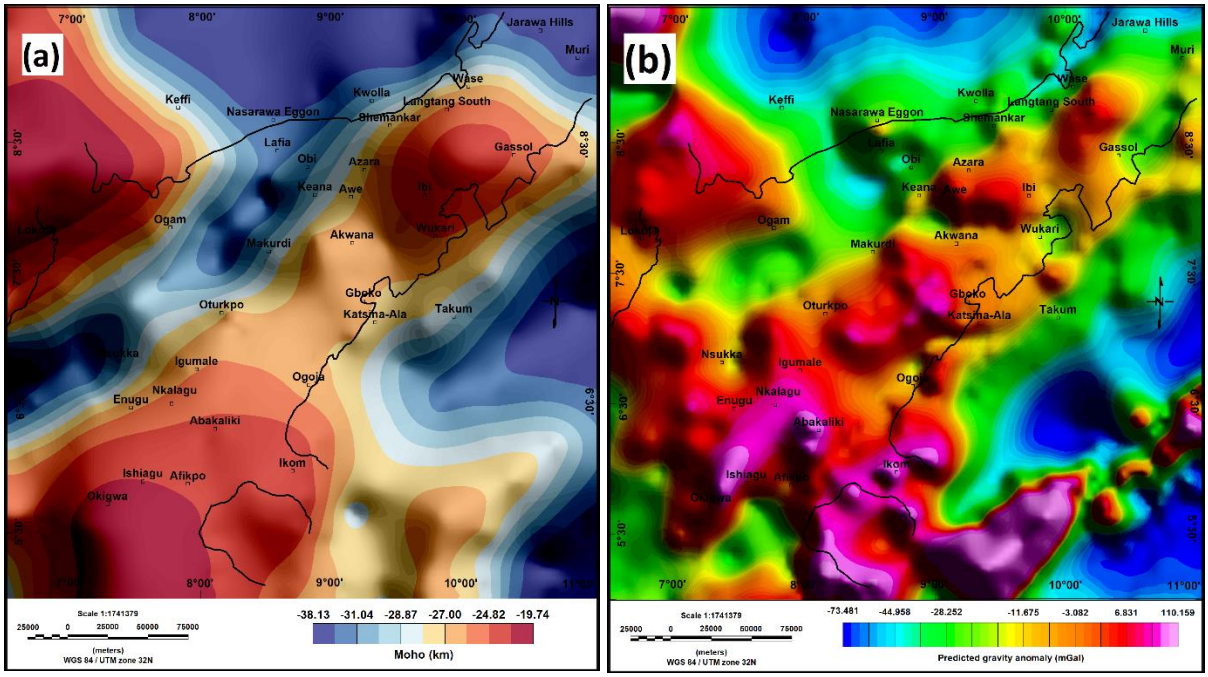

Fig. 5. 46: (a) Plan view of Moho depth surface showing the topography variation obtained from 3D block inversion of the Bouguer anomaly (b) Predicted gravity anomaly map obtained from the estimated Moho depth interface.

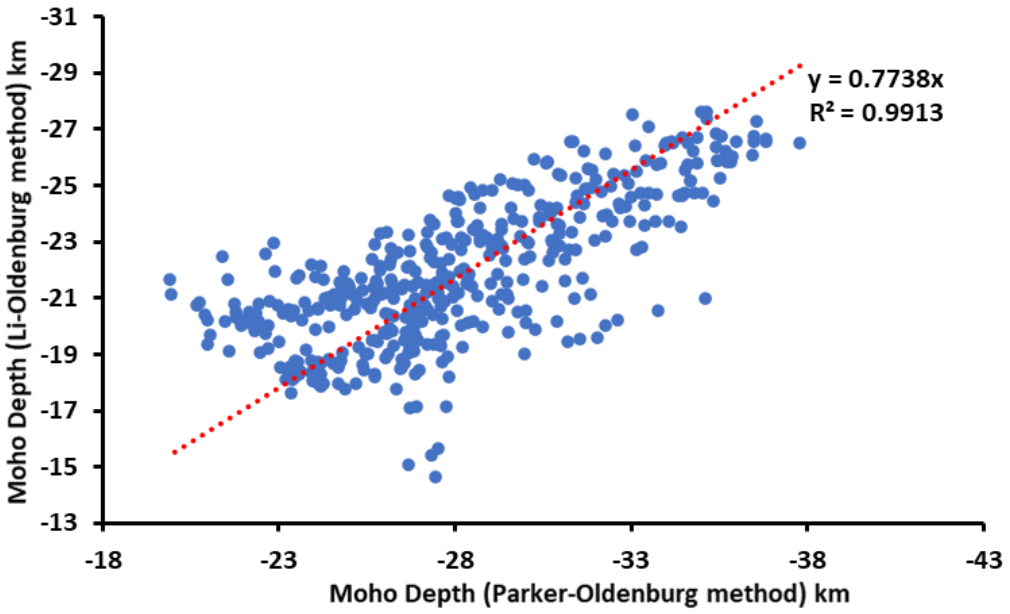

Fig. 5. 47: A Cross-plot of Moho depth (Parker-Oldenburg inversion) against Moho depth (Li-Oldenburg inversion). The two depth estimates show a high correlation with about 99% R-squared value observed between 20 km and 38 km (Mark in red dotted points).

5.4.2.2 Magnetic 3-D modelling

Magnetic susceptibility inversion can model the subsurface basement susceptibility distribution in 3D so that intrusions into or on the basement can be mapped. The magnetic amplitude approach was used for the 3D modelling of the magnetic susceptibility of the basement. This approach is robust and insensitive to variations in the magnetization direction and the presence of remanent magnetization, as well as performing well for complex and multiple magnetic anomalies (Li and Oldenburg, 1996; Shearer, 2005). It involves the calculation of magnetic amplitude from TMI data sets before carrying out the inversion.

The magnetic amplitude inversion approach avoids the determination of the magnetic direction and inverts for quantities that are not sensitive to magnetic directions or remanent magnetization (Gerovska and Stavrev, 2006; Cella and Fedi, 2012). The amplitude of the magnetic anomaly field or the total anomaly, TA, has a weak dependence on the magnetization direction and the remanent magnetization (Stavrev and Gerovska, 2000). It can be determined by the equation

$$\boldsymbol{TA = \ (X_a^2 + \ Y_a^2 + Z_a^2)^{1/2}} \text{.....(5. 14)}$$

where the subscript a stands for anomalous, and X_a, Y_a, and Z_a are the anomalous magnetic field components in the north, east, and vertically down directions, respectively.

The TA can be obtained by transforming the TMI into its three directional components based on equation 5.14. This transformation produces a high centricity over the anomalous body with a weak dependence on the magnetization and geomagnetic field directions (Stavrev and Gerovska, 2000; Gerovska and Araúzo-bravo, 2006; Gerovska and Stavrev, 2006; Gerovska et al., 2009; Cheyney et al., 2016). This transformation process has the advantage of being easy since no knowledge of the inclination and declination of the geomagnetic field is required and it gives a stable result at low magnetic latitude (Gerovska and Stavrev, 2006).

The total amplitude inversion approach was carried out using VPmg software downloaded from Mira Geoscience website through the following processes.

- The TMI data for the study area (Fig. 5.48 a) are converted to TA by calculating the X_a, Y_a, and Z_a components in Magmap extension of Geosoft software sourced from Sequent website and then applying equation 5.14. The TA shows non-negative values, a reduced

number of extrema, and has low sensitivity to the source magnetization direction (Gerovska and Araúzo-bravo, 2006) (Fig. 5.48 b).

- A magnetic model was created in VPutility which is a menu in VPmg helps in creating and modifying suitable models or meshes used for inversion. This is done by discretizing and laterally dividing the study area into equal vertical prisms (VP), which are then sub-divided in depth to correspond to the undulating topographic and geologic layers. Two VPmodels are important in making the meshes, the regional and the local models. The local model is the size of the study area while the regional model has a larger size and encloses the local model. This is done normally to reduce edge effects and the effect of half-space. A VPmodel for the whole area was constructed such that each cell for the local model measures 25 km X 25 km while the regional model cell measures 29 km x 29 km. The number of prisms in the active model area is 1156 with the depth to top basement measuring -13 km and bottom elevation -25 km (Fig. 5.49).
- The TA was inverted by VPmg software using the VP model created above and a magnetic susceptibility 3D block was obtained for the area (Fig. 5.50 a) and the area indicated by magnetic susceptibility values greater than 0.0103 SI. The 3D block magnetic susceptibility was clipped at values greater than 0.0103 SI (Fig. 5.50 b). Strongly magnetic materials are shown to be distributed around the basement.
- The area was further divided into window subsets containing strong magnetic anomalies, and their susceptibility values were determined (Fig. 5.51). A 3D magnetic inversion was inverted for window 1 and the source of the anomaly, body A, was estimated to have a magnetic susceptibility greater than 0.0125 SI (Figs. 5.52 a and b). There is a broad magnetic anomaly record in window 2 and inverting it in VPmg showed the location of the main source, B of the anomaly exactly to be towards the right of the anomaly with a magnetic susceptibility value greater than 0.01826 SI (Fig. 5.53 a and b). Windows 1 and 2 then contain possible evidence of magmatic intrusion into the basement, or the presence of block faulting. For window 3, the source of the anomaly, C, is shown to be attached to the surrounding basement rock. It has a magnetic susceptibility value greater than 0.0168 SI (Figs. 5.54 a and b). Figs. 5.55 a and b, show there are two ridge-like structures located with magnetic susceptibility values greater than 0.0168 SI over the window 4 magnetic anomaly. Window 5 located and indicated several sources of magnetic anomalies around E and with magnetic susceptibility values greater than 0.0145 SI (Fig. 5.56 a and b). There are two main sources of anomalies

trending in NE-SW and NW-SE directions. The NW-SE trending block appears to be attached to the surrounding rock.

The 3D magnetic inversion results show that there are rifted blocks or intrusions into the basement or its contact with sediments, and some of the intrusive blocks are attached to the surrounding rocks or their parent rock on the basin margin. The fragments within the basin and some that are attached to the surrounding rocks show evidence of extensional rifting with block faulting. The main disadvantage of this method is that the phase component, necessary for inverting for a dip and other structures encoded in the magnetic anomaly has been significantly reduced and/or lost and, as such, it may not be good for showing the dipping directions of geology bodies (Li and Oldenburg, 1996). However, the method is very efficient in locating the source and estimating its magnetic susceptibility. The geologic model from this inversion shows that several intrusions are present on or in the basement as well as the sedimentary rocks (Fig. 5.57). Therefore, the basement has been intruded in all parts of the trough and this has significantly affected the morphology of the basin.

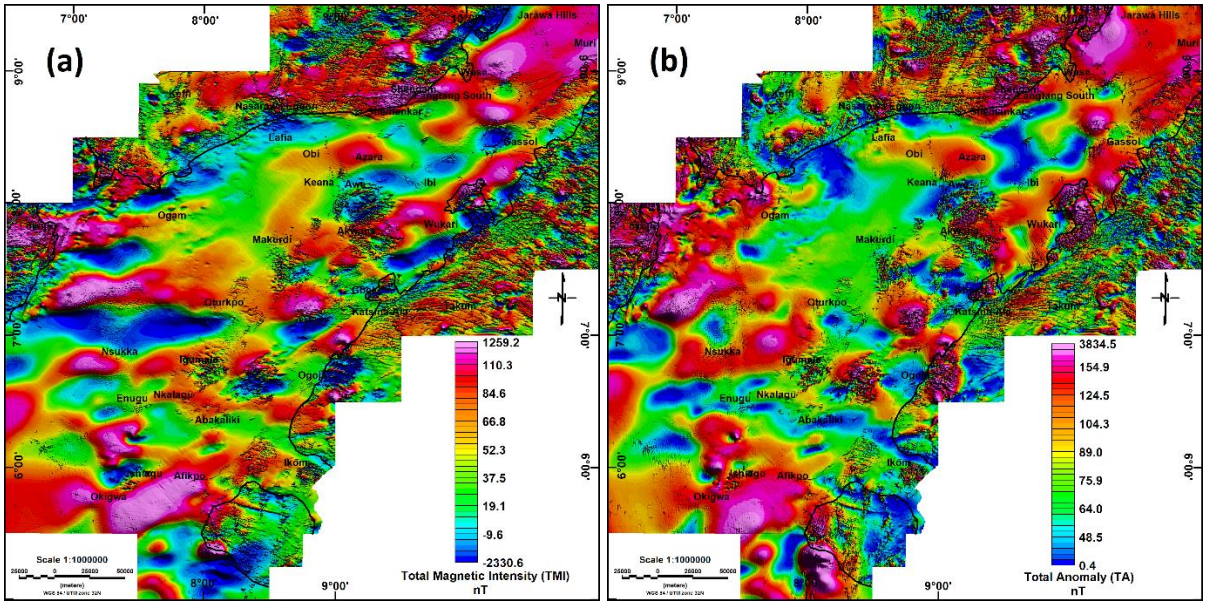

Fig. 5. 48: Magnetic data (a) TMI map (b) Total amplitude (TA) map showing reduced extrema and enhancing non-negative magnetic values.

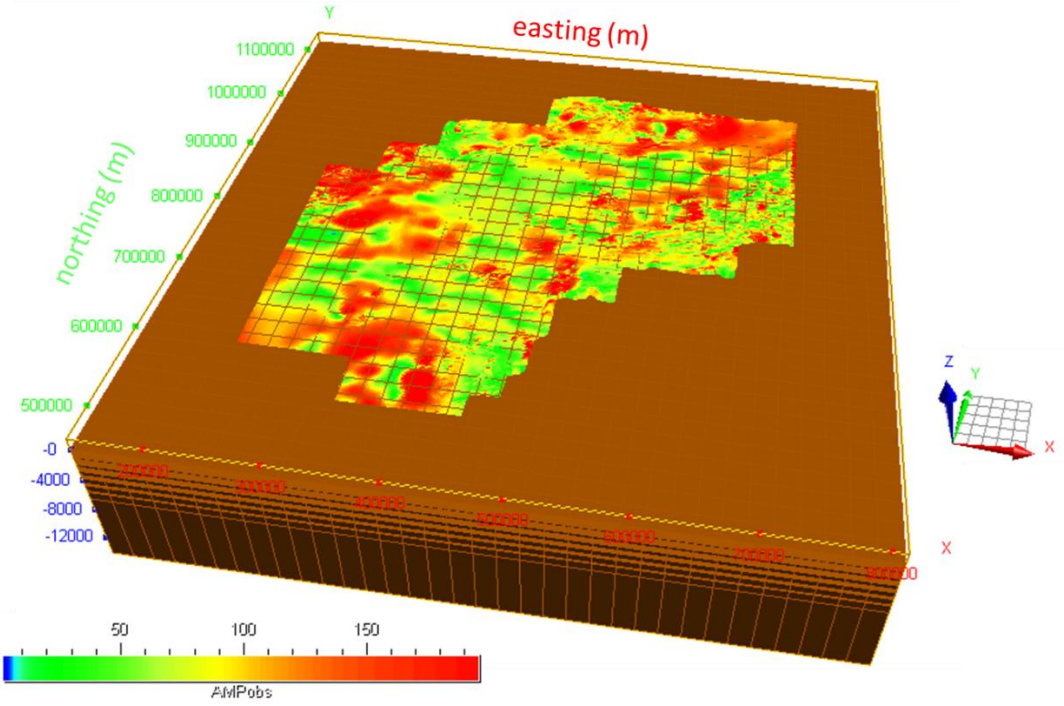

Fig. 5. 49: VP model showing the study area hosted within the regional model prior to inversion. The model cell size measures 25 km x 25 km X 13 km in depth. The depth is half-spaced to 6.5 km i.e., the total model depth is 13 km, but available depth involved in the inversion is 6.5 km and heterogenous divided into 1 km each. The sedimentary component is assumed to be non-magnetic.

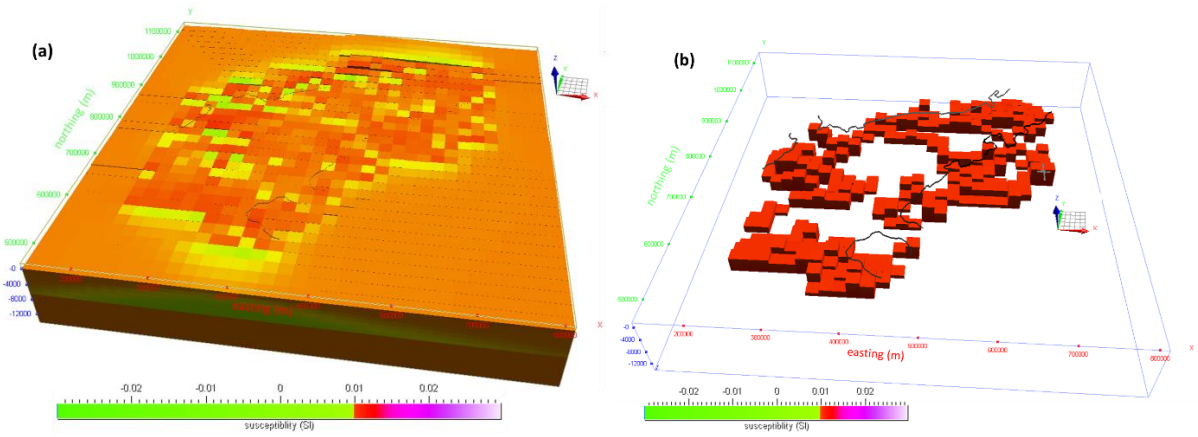

Fig. 5. 50: (a) 3D magnetic susceptibility block inverted from TA (b) Magnetic susceptibility of crustal materials of the area clip at greater than 0.0103 SI values

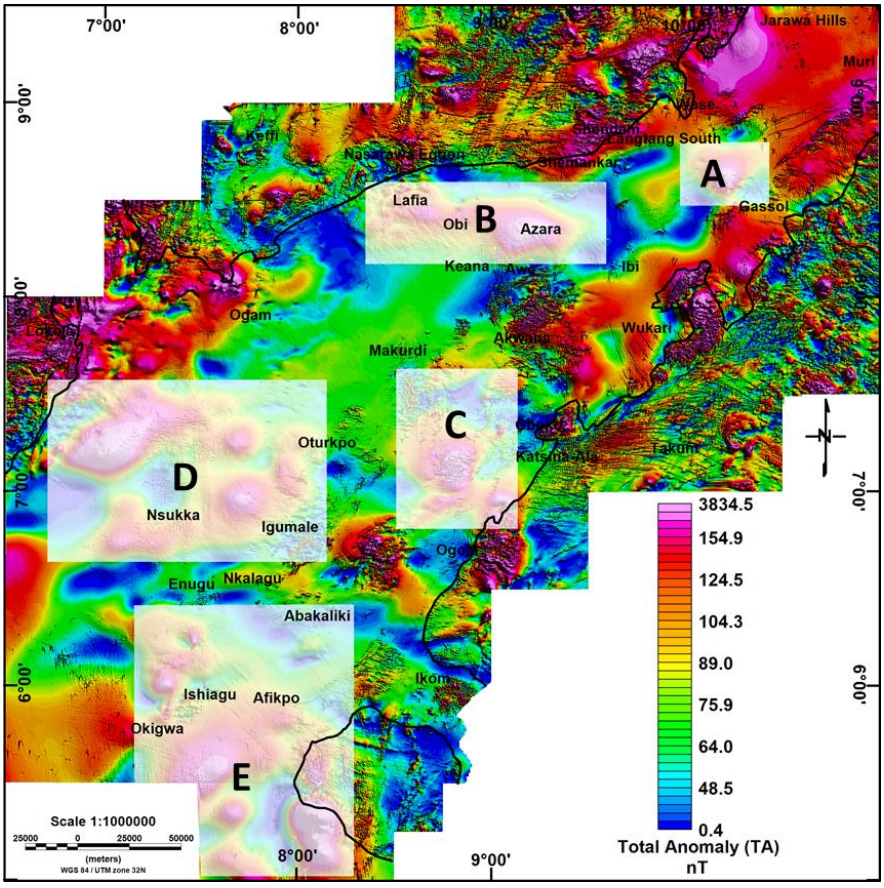

Fig. 5. 51: Five sub-set windows A, B, C, D, and E with high total anomaly values within the area to be inverted for calculating the magnetic susceptibility of the basement.

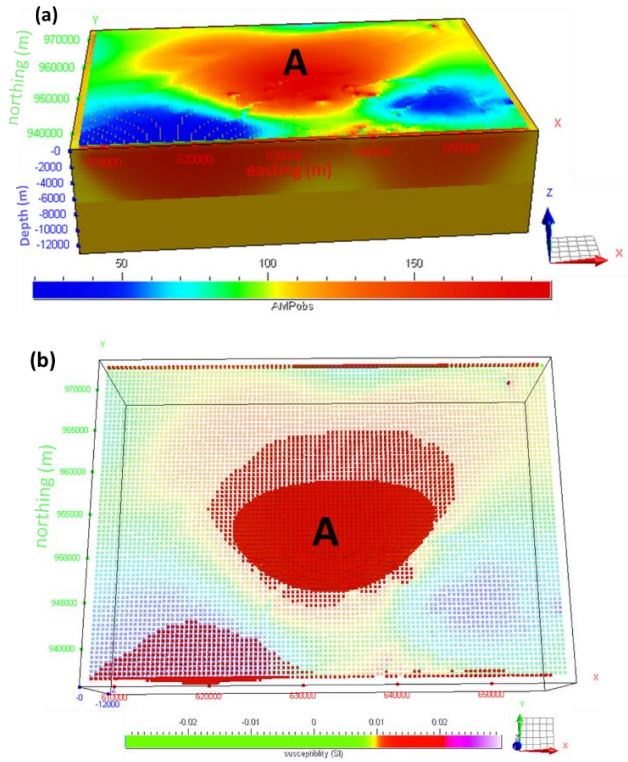

Fig. 5. 52: 3D magnetic inversion (a) Inverted total anomaly source body A (b) Located anomalous magnetic body A with magnetic susceptibility greater than 0.0125 SI at a depth of 2.7 km from the earth surface.

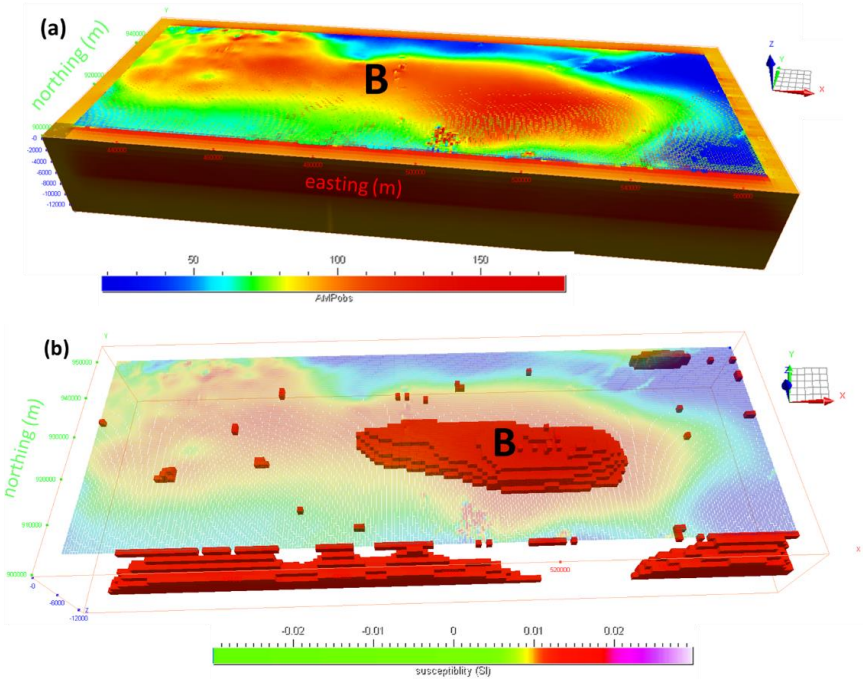

Fig. 5. 53: 3D magnetic inversion (a) total anomaly overlaid on the inverted block of source body B (b) Located anomalous magnetic body B with magnetic susceptibility value greater than 0.0183 SI and interpreted as an intrusive rock. The main source of the anomaly is towards the right side and located 4 km below the surface.

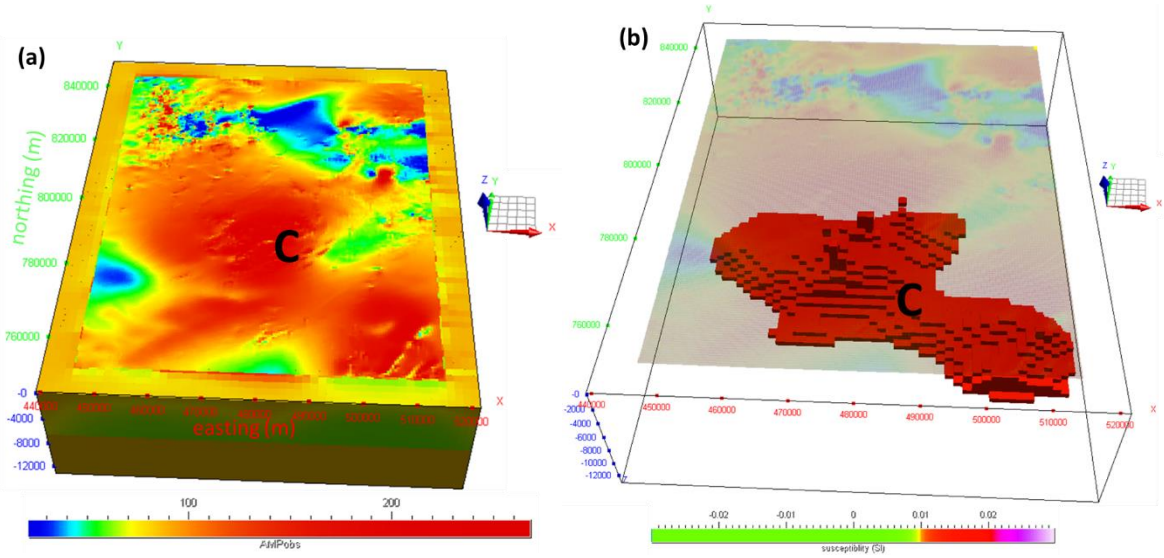

Fig. 5. 54: 3D magnetic inversion (a) total anomaly overlaid on the inverted block of source body C (b) Located anomalous magnetic body C with magnetic susceptibility values greater than 0.0168 SI. The source of the anomaly could be an intrusive rock at 2.9 km below the surface that spans from the basin material to the adjacent basement interface.

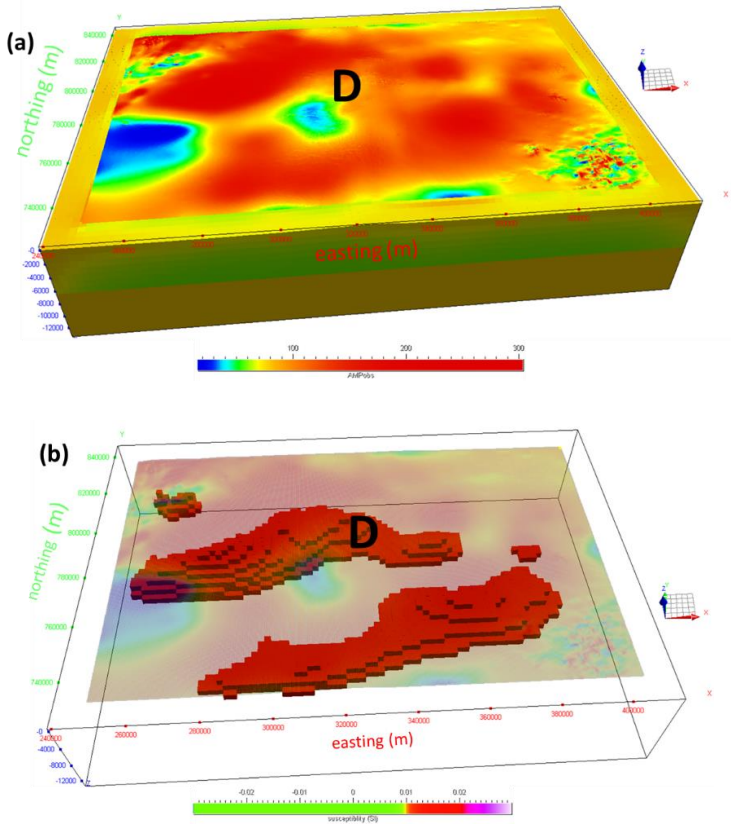

Fig. 5. 55: 3D magnetic inversion (a) total anomaly overlaid on the inverted block of source body D (b) Two located anomalous magnetic bodies, D, with magnetic susceptibility value greater than 0.0133 SI. The source body north of D is 1.8 km and that south of D is 3.8 km below the surface.

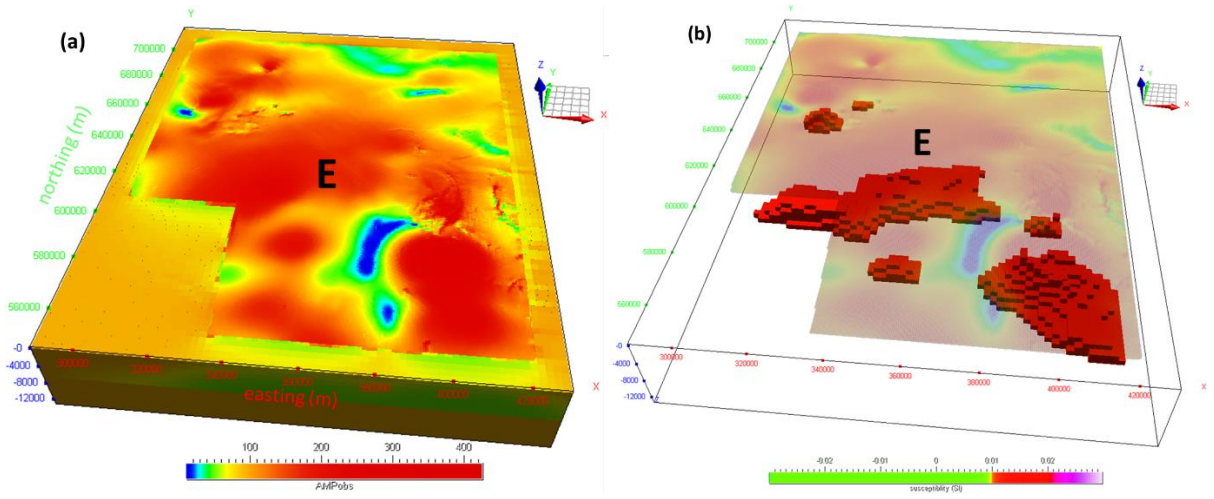

Fig. 5. 56: 3D magnetic inversion (a) total anomaly overlaid on the inverted block of source body E (b) Located anomalous magnetic bodies within window E with two major magnetic anomalies that have susceptibility values greater than 0.0145 SI. The anomaly running NE-SW is 2.9 km and the one running NW-SE crops out on the surface. These geological bodies are not observed on the geological maps since they are located in the subsurface.

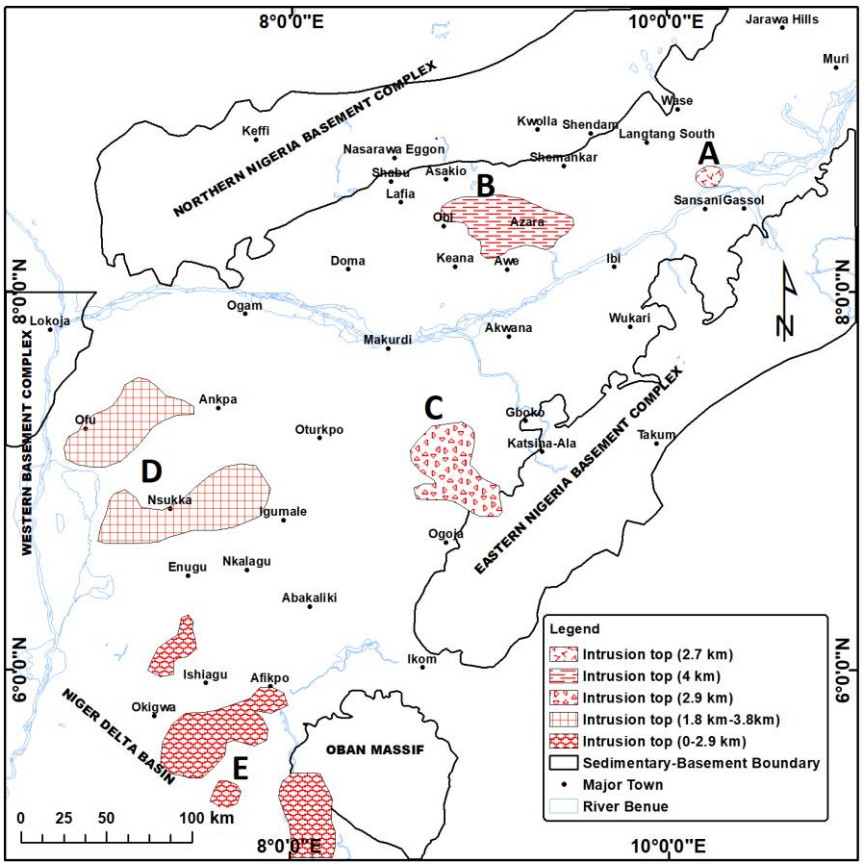

Fig. 5. 57: High magnetic susceptibility points interpreted as intra-basement and intra-sedimentary intrusives. The 3D magnetic models show the penetration depth of intrusive rocks from the surface to the basement rocks.

5.5 Crustal extension and rift architecture

The amount of crustal extension can help in understanding major tectonic events that occurred during the basin evolution process (McKenzie, 1978) and expose its architecture. The amount of crustal stretching can be used in determining the amount of extension generated and its variation along rift systems (Mazur et al., 2012; Mazur et al., 2015). Stretching can be estimated using the simple lithospheric extension model formula (Mazur et al., 2012). This method of extension calculation does not assume constant stretching of the crust as proposed by McKenzie (1978).

$$e = X - \left(A/T\right) \text{.....(5. 15)}$$

Where *X, A and, T* are the distance between the rift flanks, crustal cross-sectional area, and the initial thickness of the unstretched continental crust (Fig. 5.58).

Two approaches relevant to this study were used for the estimation of crustal extension using gravity and magnetic data sets; the 2D gravity/magnetic models and the 3D gravity inversion approaches (Mazur et al., 2012). The 2D model approach assumes that the rift is oriented perpendicular to the direction of extension.

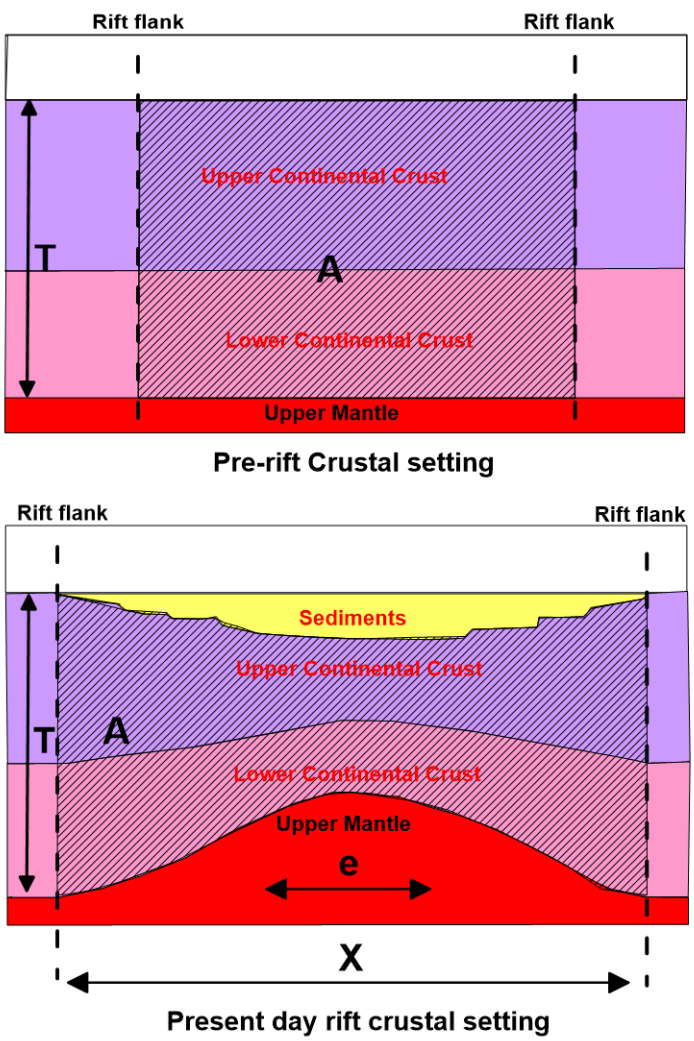

Fig. 5. 58: Demonstration of crustal extension calculation method (Modified after Mazur et al., 2012). It is assumed that there is no lateral variation in the composition of the crust.

5.5.1 Estimation of crustal extension in two-dimension

The 2D gravity/magnetic models constructed earlier (section 5.4.1) were used to estimate the amount of crustal extension beneath the trough. The profiles helped in constraining the limit of the unstretched crust, crustal thickness, and the cross-sectional area of the deformed continental crust. Four profiles were used in estimating the crustal extension of the trough. The 2-D models were also located to measure the amount of extension by displacement along the rift i.e., perpendicular to the major structural trend of the area.

The first profile, MBT1N, runs in the NW-SE direction in the northern part of the trough (Fig. 5.29). The length of the stretched crust (X) along the profile was measured to be 228 km between the NW (60 km) and the SE (288 km) basin flanks. The NW rift flank shows a more stable crustal thickness, T, of about 29 km while the cross-sectional area, A under the rifted basin was estimated to be 3, 780 km squared. Applying equation 5.15, the crustal extension value, e, of 93 km for the cross-section was estimated.

The second 2D model is along the profile MBT2N (Fig. 5.30). This model has a more consistent crustal thickness on its NW flank and as it reaches the basin boundary, the crust thins and then thickens again towards the SE side. The crustal thickness, T, of 33 km was estimated from the NW stable crustal part of the cross-section to represent the unstretched crust while the stretched cross-sectional area, A, of 5, 017 km squared was estimated between the left and the right flanks of the basin. The distance between the NW and SE flanks of the trough, X, is estimated to be 228 km picked between 132 km and 396 km. A crustal extensional value, e, of 111 km was thus estimated along the profile.

The third estimate of the crustal extension was done along 2D model MBT3N (Fig. 5.31). Unstretched crustal thickness, T, of 25 km was located from the SE flank where it is relatively stable. The distance between the left and right flanks of the stretched crust, X, was measured to be 312 km (picked between 48 km and 360 km) while the cross-sectional area, A, was estimated to be approximately 4, 326 km squared. Crustal extension value, e, of 139 km was estimated for the area between the rift flanks across the model.

The fourth 2D model profile, MBT4N, was used in this case (Fig. 5.32). The left and the right flanks of the basin were picked at approximately 24 km and 336 km along profile respectively with the estimate of the width of stretched crust, X, of 312 km. The average unstretched crustal thickness, T, was picked from the right-hand crust which is relatively stable and found to be

approximately 25 km. Hence, a crustal extension value, e, of 142 km was estimated for this model.

The crustal extension across the basin showed an increase in crustal stretching from the north to the south while alluding to the 'scissors style' extensional opening of the trough.

5.5.2 Estimation of crustal extension in three-dimensions

Crustal extension, in this case, was studied using the grid from depth to Moho (section 5.4.2.1 and Fig. 5.36), the depth to the top of the basement grid map (section 5.3.3 and Fig. 5.25), crust 1.0 model and the 2D gravity/magnetic model along the profile MBT4N (section 5.4.1 and Fig. 5.32) of this study. The crustal extension factor, β was computed from the above data sets showing the amount of extension.

The extension factor can be estimated using (Welford et al., 2020);

$$\boldsymbol{\beta = \frac{r_0}{r_1}} \text{.....(5. 16)}$$

Where r_0 and r_1 are unstretched crustal thickness and the extended crustal thickness, respectively.

The value of r_0 (unstretched crustal thickness) is picked as 42 km referenced from P-wave receiver functions and the continental and global models (i.e., Crust 1.0 model), assuming that the basement complex is unstretched (Laske et al., 2013; Akpan et al., 2016). The value of unstretched crustal thickness from the 2D gravity/magnetic model along the profile MBT4N was compared with that of the Crust 1.0 model and observed that the crust along the profile might have been affected by the magmatic intrusion and therefore possibly stretched after intrusion. The stretched crustal thickness is estimated by subtracting the depth to the basement grid (Fig. 5.59 a) from the Moho depth grid (Fig. 5.59 b) to produce the crustal thickness map of the basin (Fig. 5.59 c). The crustal thickness map indicated thickening towards the northern part of the area with a value of about 34 km and gradual thinning towards the southern part of the area by approximately 10 km. The southern continental crust is strongly stretched with very low crustal thickness while the north is thicker. The crustal thickness grid map and the value of the unstretched crust (42 km) were substituted in equation 5.16 and the extension factor was estimated (Fig. 5.59 c). An extension factor value greater than 2, as typified across the Lower Benue Trough, is indicative of polyphase faulting and the point at which the entire crust could

break up to expose mantle rocks leading to the development of crustal-scale faults that may let fluids travel down the upper mantle to cause serpentinization (Welford et al., 2020). The extension factor values decrease from the north to the south showing two main tectonic domains and architecture; crust that is moderately stretched (North) and that which is extremely extended almost to break up (South). Based on the above, the study implies that the Middle and the Lower Benue Troughs can be differentiated based on the crustal thickness and extension factor. Clearly, the rift architecture is simpler in the northern or Middle Benue trough which is tied to usual extensional rifting while it becomes more complex in the south where there is evidence for polyphase faulting, the opening of the Bida and Memfe basins as well as its closeness to the Niger Delta forming a more local triple-triple-triple rift system.

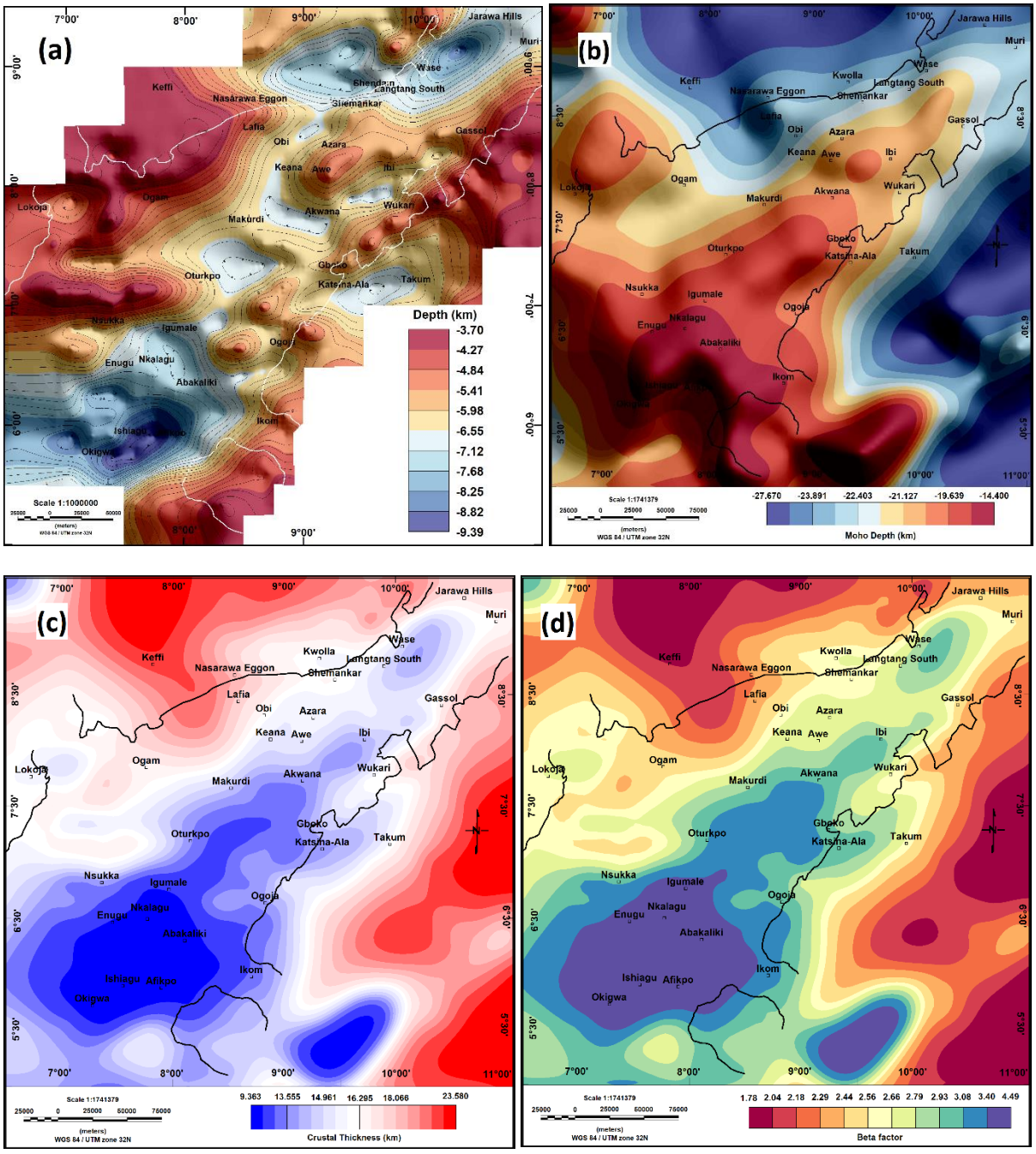

Fig. 5. 59: (a) Depth to the basement of Middle and Lower Benue Trough from 3D inversion of Pseudo-gravity data (b) Moho depth interface showing the topographic variation from the 3D inversion after filtering and considering the density contrast of 0.17 (c) Crustal thickness of the area (d) The calculated extension or stretching factor map for the crustal thickness with minimum and maximum values of 0.178 and 4.49 respectively.

CHAPTER SIX

REGIONAL GEOLOGY AND TECTONICS – ISOSTASY, ELASTIC THICKNESS AND CURIE DEPTH

6.1 Introduction

The long-term strength of the lithosphere is investigated in this chapter using spectral modelling techniques. Understanding the behaviour of the lithosphere (the crust and the upper mantle) is key in modelling the tectonic processes that led to the evolution and development of the Benue Trough. The thermal state of the lithosphere has significant influence on its strength and the *Te* is controlled largely by the thermal structure (Jiménez-Díaz et al., 2014). To a very large extent, the thermal structure obtained before, during or after rifting and deformed from either the Curie depth or the stretching factor methods have some relationships with *Te*, and may give interesting ideas of the structural features expected for the Middle and Lower Benue Trough.

Therefore, the main aim of this chapter is to understand the various processes that affect lithospheric strength and relate it to the thermal structure and architecture of the trough. Supporting data sets for the study are magnetic, topography, free-air and Bouguer anomaly grids.

The following steps were applied in the study:

1. The strength of the lithosphere was estimated using spectral modelling techniques. The spectral method involves determining the effective elastic thickness of the lithosphere, which is a proxy for the lithosphere rigidity and strength obtained from admittance and coherence methods carried out in the wavenumber domain for correlation between topography and free-air and/or Bouguer anomalies.
2. The magnetic dataset was used to predict the thermal structure, which influences the long-term strength of the lithosphere. Power spectrum and three-dimensional magnetic inversion techniques were used to estimate the Curie depth interface. This was then used to map the spatial distributions of geothermal gradient and heat flow in the basin.

6.2 Isostasy

Isostasy defines the condition in which the Earth's crust and mantle are in a state of buoyancy equilibrium. The state is maintained by adjusting to changing geological loads on and within the earth's lithosphere (freezing and melting of ice, sedimentation, and volcanism, etc) (Watts, 2001). This isostatic state can be analyzed by the use of gravity and topography data sets. Broadly, there are two classes of basic models used to explain the state of isostasy in nature; the local (Airy and Pratt) and the regional (flexural) isostasy models.

6.2.1 Local (Airy and Pratt models)

The local models affect a small spatial area and are categorized into the Airy and the Pratt models. These models help in explaining complex rift geometry as it relates to the behaviour of the lithosphere under various loads applied (Fairhead and Green, 1989). Airy isostasy model suggested that the load represented by an elevated region would be compensated by underlying lateral changes in the thickness of a uniform density crust (Watts, 2001). The Pratt model in contrast implies that elevated regions are underlain directly by low-density rocks whereas depressed regions were underlain by high-density rocks (Galán and Casallas, 2010). Fig. 6.1a shows a simple illustration of the Airy model where a topographic low is compensated for by an anti-root achieved by crustal thinning and mantle upwarp. The Airy model assumes that isostatic compensation is uniform where the compensating layer is located directly below the load and reaches a depth where equilibrium prevails. In the Pratt case, topography is compensated for by lateral changes in the density of the crust and the mantle. The density of the crust above topography compensation is the same as that below it and varies laterally while the depth of compensation is everywhere equal (Fig. 6.1 b).

6.2.2 Regional Isostasy (Flexural Model)

The flexural model is similar to both the Airy and the Pratt models. The main difference is that topography is compensated in the Airy and Pratt models in the form of crustal thickening or density variation immediately and only break the load while the flexure model involves compensation distribution over a wide geologic region (Figs. 6.2). Flexure is the general case because the lithosphere always has some strength. The flexural rigidity of the lithosphere can be estimated by comparing the calculated linear transfer functions (admittance and coherence) between gravity anomalies and topography using observational gravity and topography data sets (Forsyth, 1985).

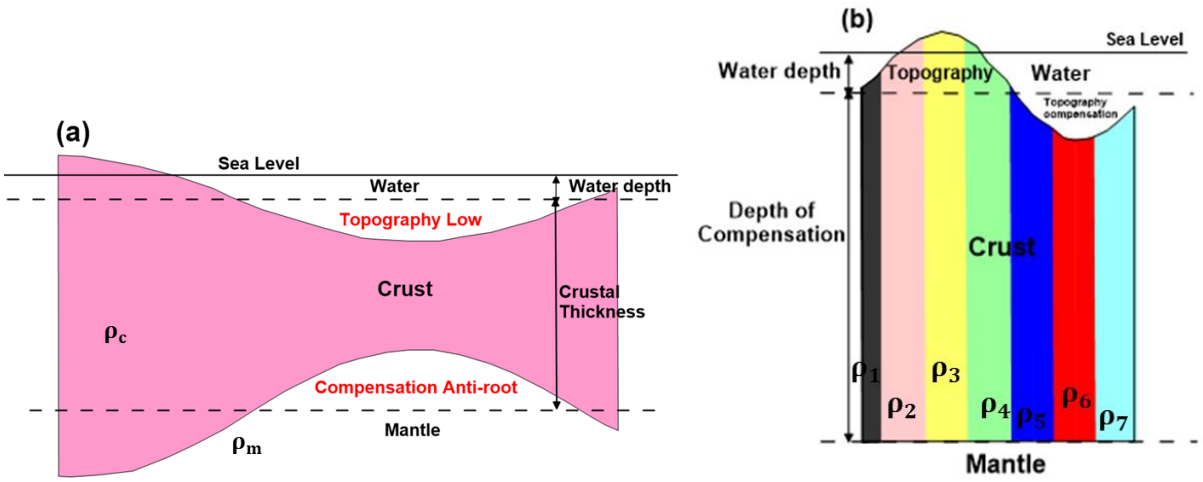

Fig. 6. 1: Simplified model of isostatic compensation (a) Airy model (b) Pratt model (After Watts, 2001). ρ_c and ρ_m are crustal and mantle densities, respectively, while ρ_1, $\rho_2, \rho_3, \rho_4, \rho_5, \rho_6,$ and ρ_7 are densities from seven different crustal bodies.

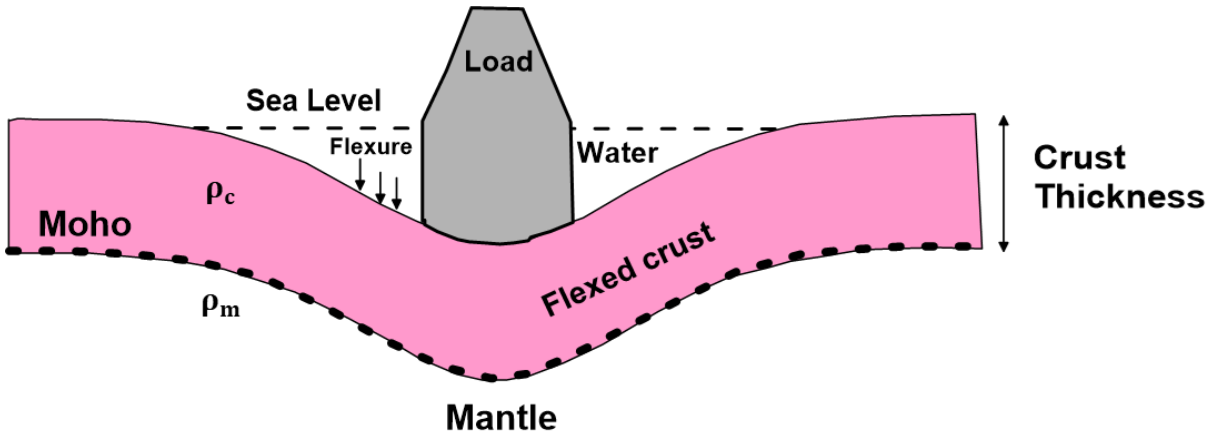

Fig. 6. 2: Simplified elastic plate or flexure model of isostatic compensation considering an Airy model (After Watts, 2001).

6.3 Estimating the Effective Elastic Thickness (Te) of the Lithosphere

The study of the lateral variation of the lithosphere enables on understanding of how surface deformations are formed and how they relate to very deep crustal activities (Pérez-Gussinyé et al., 2009), and this can be achieved by understanding the relationship between gravity and topography data sets. The long term strength of the continental lithosphere is believed to be confined to the crust as the mantle may be weak i.e., crème-brûlée model, or reside in the crust and the mantle i.e., jelly sandwich model (Burov and Watts, 2006; Petit et al., 2008). Therefore, the lithosphere is strong and capable of withstanding both surface and subsurface loads over a long period of time. The strength of the lithosphere can be determined by estimating its equivalent elastic thickness (T*e*) which acts as a proxy for understanding how the strength of the lithosphere effects elastic deformation and at the same time is affected by other processes such as rifting and sediment loading (McKenzie and Fairhead, 1997). The T*e* expressed as the response to loading by topography and subsurface loads depends largely on the crustal age and crustal thickness via temperature/heat (McKenzie and Fairhead, 1997). Gravity has been used to explain the lithospheric strength of a basin and reveal a lot about features observed on the surface and in the subsurface (Watts, 2001; McKenzie et. al., 2015).

In this study, the effective or equivalent elastic thickness, T*e*, was estimated by using the spectral (admittance and coherence) method which employs gravity and topography data sets to estimate T*e* directly by calculating the transfer function as a function of wavelength (Burov and Watts, 2006; McKenzie et al., 2015).

6.3.1 Spectral Approach

The presence of a load on the surface of the lithosphere may cause its downward flexure or deflection and so produces a change in the surface topography and internal surfaces. The flexure can be approximated to that of an elastic plate (Luis and Neves, 2006). There thus exists a relationship between the gravity anomaly and topography over the surface load as a function of the wavelength and, since the wavelength of the flexure is controlled by the flexural strength or effective elastic thickness of the lithosphere, T*e,* it is then possible to calculate the isostatic response function using the spectral approach (Watts, 2001, Pérez-Gussinyé et al., 2004, Fairhead, 2015). Based on this, the spectral approach is applied in analysing the frequency content of the observed gravity and the topography over such a load region and comparing its spectral content with the predicted model of both local and regional isostasy. Simply, the spectral approach involves calculating the average coherence and/or admittance between the Bouguer anomaly and the surface topography (Bouguer coherence), or between free-air anomaly and topography (Free-air admittance) (Pérez-Gussinyé et al., 2004). The theoretical coherence and admittance are also calculated for an elastic plate model for several values of T*e* and the best fit is determined as the one that minimizes the difference between observed and calculated gravity anomalies (Burov and Watts, 2006). Therefore, results were interpreted based on the assumption that the estimated T*e* defines the lithospheric strength. A low T*e* value is an indication of a weak lithosphere while a high value is interpreted as a strong lithosphere.

The topography, Bouguer, and free-air anomaly data sets were regridded with a 5 km grid size interval in the GMT version 6.3 program interface from guthub website using a spline with continuous tension of 0.3 (Smith and Wessel, 1990) (Fig. 6.3 a, b, and c). Based on the proposed division of structural tectonics of the basin in chapter five, the area was divided into two tectonic settings; the Lower (crosshatches) and Middle (vertical hatches) tectonic settings (Fig. 6.3 d). The idea to calculate separate T*e* values for those two tectonic provinces is intended to reduce the possibility of achieving inappropriate admittance and coherence averages (Luis and Neves, 2006). GMT gravfft module was used to calculate observed coherence and admittance, and compare them with the theoretical value(s) of T*e* considering that loading could be from the top of the crust and also from below or within the lithosphere. The topography or surface load (top) modelled are the sediments and/or the topography within the basin with expected compensation at Moho. It is assumed that there is downwards deflection in response to surface topographic loads and the topography is in response to loading within the interior or beneath the elastic plate.

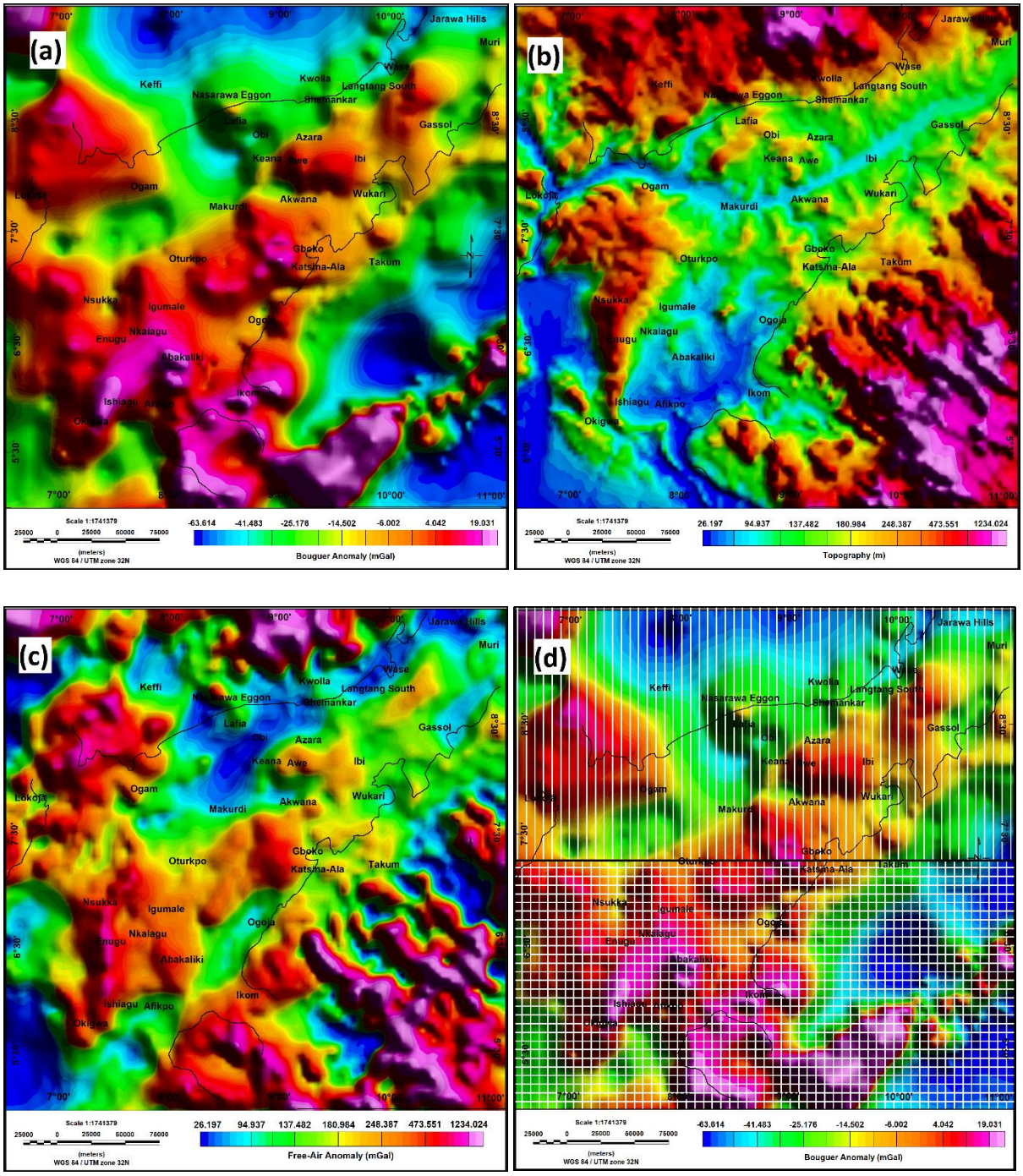

Fig. 6. 3: (a) Bouguer anomaly (b) topography (c) free-air anomaly (d) The Bouguer anomaly map was separated into the Middle Benue Trough (vertical hatches) and Lower Benue Trough (Cross hatches).

6.3.1.1 Admittance Method

Admittance is defined as the wavenumber parameter that modifies the topography to produce a gravity anomaly effect (Watts, 2001; Galán and Casallas, 2010). Admittance is very sensitive to the distribution of surface loading on the lithosphere (Hartley et al., 1996). The method is such that the observed admittance curve is calculated and compared with several values of the theoretical admittance curves with varying values of effective elastic thickness. The T*e* obtained is that with the best fit after comparison between the observed admittance curve and each of the theoretical curves.

The observed admittance function, $Z(k)$ is given by Watts (2001) as

$$\boldsymbol{Z(k)_{obs} = \frac{\Delta g(k)}{H(k)}} \quad \textbf{.....(6. 1)}$$

where $\boldsymbol{\Delta g(k)}$ and $\boldsymbol{H(k)}$ are Fourier transforms of gravity and topography, respectively.

Theoretical admittance is defined as:

$$\boldsymbol{Z(k)_{theo} = 2\pi G\rho_c \left(\frac{1-\exp(-kT_c)}{\emptyset_e(k)}\right)} \quad \textbf{.....(6. 2)}$$

where $\emptyset_e(k)$, the flexural response function, is given by

$$\boldsymbol{\emptyset_e(k) = \left[\frac{Dk^4}{(\rho_m-\rho_c)g} + 1\right]^{-1}} \quad \textbf{.....(6. 3)}$$

The flexural rigidity, D is given by:

$$\boldsymbol{D = \left[\frac{ET_e^3}{12(1-\sigma^2)}\right]} \quad \textbf{.....(6. 4)}$$

Where $E, \sigma, g, \rho_m, \rho_c,$ and T_e are Young's modulus, Poisson's ratio, the average acceleration due to gravity, mantle density, crustal density, and the effective elastic thickness, respectively. T$_e$ approximates the strength of the lithosphere and $k = \sqrt{k_x^2 + k_y^2}$. Table 6.1 defines other important parameters. This means that a large elastic thickness corresponds to strong lithosphere which supports loads by flexing over a wide area while the small elastic thickness can support little elastic stress (Pérez-Gussinyé et al., 2004). When the T_e value is 0, it is an Airy Isostasy being the end member of this range.

The computation of admittance was done for sub-region of the rift in the Middle and Lower Benue Trough tectonic provinces under the expectation that the long-term strength of the

lithosphere might differ significantly between them (Forsyth, 1985; Luis and Neves, 2006; Section 5.5.2 of the study). Free-air anomaly (Fig. 6.3b) and topographic grids (Fig. 6.3c) were used to estimate observed admittance based on equation (6.1) using the GMT gravfft module for the Middle and Lower Benue Trough. In each case, loading on the surface and subsurface of the lithosphere was considered and it was assumed that the loadings are statistically uncorrelated (Forsyth, 1985). Subsurface loads are usually attributed to mafic intrusions, accreted lower crustal materials, variations in thermal state and composition, while surface loading is due to the presence of topography, mountains, and sedimentary basins (Jiménez-Díaz et al., 2014).

Fig. 6.4 shows the observed admittance curve of the Middle Benue Trough. At very short wavelengths, the admittance is dominated by surface noise but with the noise increase to peak at about 50 km (wavenumber of $0.02\ \mathrm{km}^{-1}$) before decreasing through to about 100 km wavelength (wavenumber of $0.01\ \mathrm{km}^{-1}$). The admittance then gradually increases again and peaks at 150 km wavelength (wavenumber of $0.0067\ \mathrm{km}^{-1}$), an indication of the presence of crustal materials and structures. The correlation between surface topography and crustal loads then decreases at longer wavelengths to a minimum at about 300 km (wavenumber of $0.003\ \mathrm{km}^{-1}$), after which admittance increases again. This implies that the regional gravity effect has a strong influence on surface deformation at wavelengths beyond 300 km (wavenumber of $0.003\ \mathrm{km}^{-1}$) i.e., that loading from below is evidenced (Luis and Neves, 2006). The theoretical admittance was computed using equations 6.2, 6.3, and 6.4, and the parameters in table 6.1. Several values of T_e (between 0 and 40 km) were used in the computation and the theoretical admittance was then compared with the observed gravity anomaly based on the assumption that loading is from the surface or top (Forsyth, 1985; Tiwari and Mishra, 1999; Fig. 6.5 a). T_e values varying between 5 km and 10 km were found to explain the admittance to a wavelength of up to 320 km (wavenumber of $0.003\ \mathrm{km}^{-1}$) well. For longer wavelengths (greater than than 320 km), the calculated admittance could not recognise the effects of very deep crustal sources, but the gradual increase in the admittance shows that loading from within the crust has an influence on the deformation of surface features (Forsyth, 1982). Loading from the bottom also has a good fit for crustal anomalies at short and long wavelengths but regional anomalies or very long wavelengths (> 320 km) are not modelled (Fig. 6.5 b). At this very long wavelength, the admittance increase is an indication that the topography loading is fully compensated by Moho deflections (Gómez-Ortiz et al., 2005).

The observed admittance between the free-air anomaly and topography for the Lower Benue Trough indicates an increase in correlation at short and medium wavelengths. The admittance at longer wavelengths decreases, indicating that the formation of the topography of the area (sediments) is mainly controlled by structures on the surface and within the crust (Watts, 2001; Fig. 6.6). Thus, the theoretical admittance transfer function of both "load on top" and "load from below" models was used in predicting the best T_e as proposed by Forsyth, 1985. The elastic model considering loading from the top predicted both short and long wavelengths and estimated the best fit T_e to vary between 5 km and 10 km (Fig. 6.7 a). The best fit, in this case, is assessed from a calculated root-mean-square (rms) error especially i.e., the closest of the predicted curves to the centre error of the envelope (Hartley et al., 1996). When subsurface loading was considered, T_e values of between 5 km and 15 km gave the best fit for short and medium wavelengths (Fig. 6.7 b). The best-fit T_e estimate is the one that gives the minimum root-mean-square error between the observed and the theoretical admittance for the medium range wavelength (Gómez-Ortiz et al., 2005). This is restricted to between 50 km and 300 km wavelengths due to the fact that they characterize the crust and the upper mantle mainly describing the lithosphere. Both assumptions of loading of the elastic plate model from above and within predicted the effective elastic thickness, T_e, to vary between 5 and 15 km but loading from above fitted the observation better than loading from within. This model further allows an interpretation that sedimentary loading in the Lower Benue Trough is thick and contributes strongly to flexing the lithosphere i.e., that the lithosphere is weak.

The analyses above indicated that the topography of the Middle and Lower Benue Trough is controlled by both surface processes (short-wavelength dominance) and crustal structures (medium-wavelength dominance). Generally, the T_e maximum of 15 km estimated for the whole basin (Middle and Lower Benue Trough) implies that the long-term strength of the lithosphere might have been weakened. Hartley et al., (1996) observed that the African continent has less than 10 km effective elastic thickness values for Mesozoic/Tertiary rift systems. Therefore, the lithosphere might have been weakened or/and prone to easy flexing due to loading at the top, within, and below the lithosphere. The weak lithosphere could also be attributed to the heating of the lithosphere from mantle upwelling or radiogenic materials (Pérez-Gussinyé et al., 2004).

Table 6. 1: Parameters assumed in the flexure model calculations.

Parameter	**Value**
Poisson ratio, σ	0.25
Young's modulus, E	0.7×10^{10} N/m^2
Crustal density, ρ_c	2700 kg/m^3
Mantle density, ρ_m	3300 kg/m^3
Air density, ρ_a	1.225 kg/m^3
Water density, ρ_w	1030 kg/m3
Sediment density, ρ_s	2400 kg/m^3 and 2500 kg/m^3 for Middle and Lower Benue Trough
Average Crustal thickness, T_c	23 km
Universal gravity constant, G	6.67×10^{-11}N
Gravity acceleration, g	9.81 m^2/s

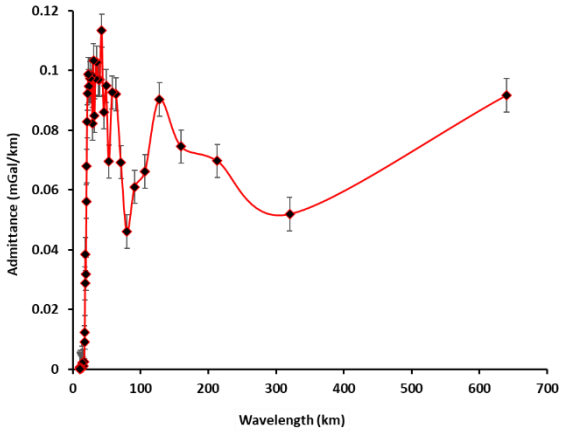

Fig. 6. 4: Observed admittance between free-air anomaly and the topography of Middle Benue Trough.

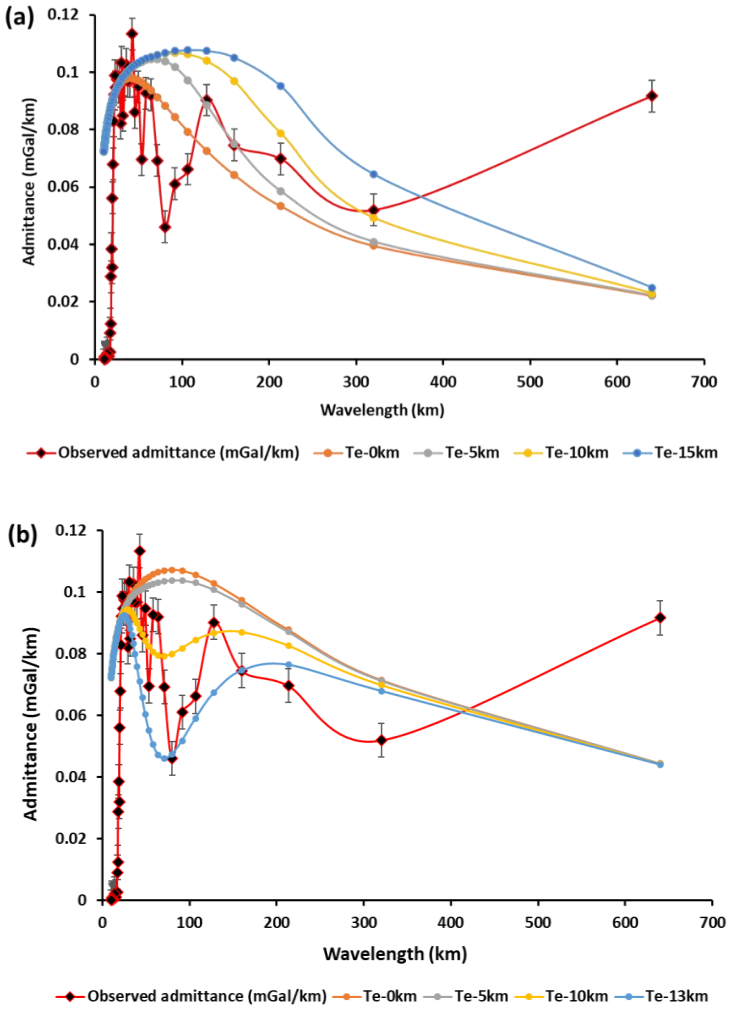

Fig. 6. 5: Observed admittance compared with theoretical admittance of the Middle Benue Trough (a) Loading from above with the best T*e* values between 5 km and 15 km. (b) Loading from within with best T*e* values between 5 and 13 km. The observed admittance (Red line) is shown with error bars representing ±1 σ with the best average T*e* about 15 km.

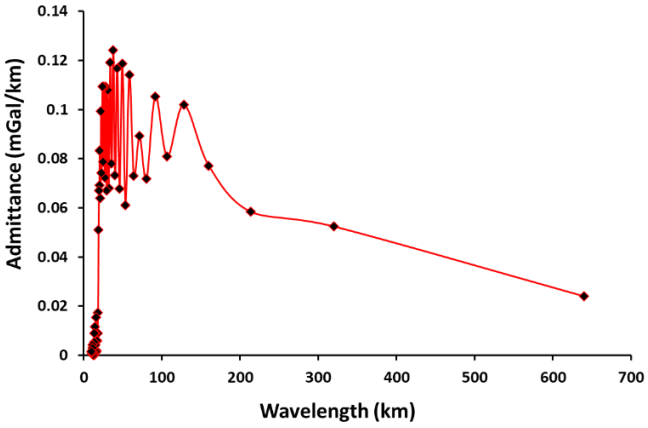

Fig. 6. 6: Observed admittance between free-air anomaly and the topography of Lower Benue Trough.

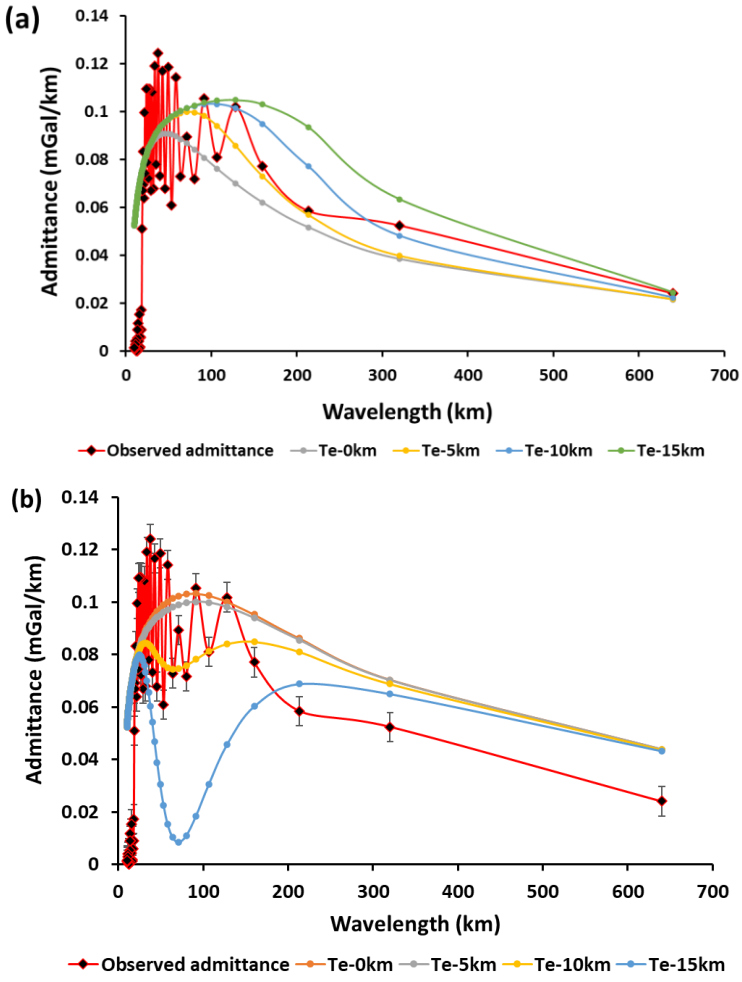

Fig. 6. 7: Observed admittance compared with theoretical admittance for Lower Benue Trough (a) Surface loading of materials. The T*e* values vary between 5 and 15 km (b) Loading from within with the best fit of T*e* values varying between 5 km and 15 km. The T*e* modelled deep crustal bodies i.e, there is loading at the subsurface. The observed admittance (Red line) is shown with error bars representing ±1 σ with the best average T*e* about 10 km .

6.3.1.2 Coherence Method

The coherence method is essentially a wavenumber correlation between the topography and the Bouguer anomaly. This is not sensitive to the ratio of surface to subsurface loading (Hartley et al., 1996; Gómez-Ortiz et al., 2005).

The coherence is defined as.

$$\boldsymbol{\gamma^2(k) = \frac{C(k)\, C^*(k)}{E_G(k)\, E_H(k)}} \text{ .....(6. 5)}$$

where $C(k)$ is the cross-spectrum of topography and Bouguer gravity, and $E_G(k)$ and $E_H(k)$ are the power spectra of gravity and topography, respectively.

The theoretical coherence, $\gamma^2(k)_{theo}$,

$$\boldsymbol{\gamma^2(k)_{theo} = \frac{\left(1+(f/\xi(k)\varphi(k))^2\right)^2}{\left(1+(f/\varphi(k))^2\right)(1+f^2\xi(k)^2)}} \text{ .....(6. 6)}$$

f is the ratio of the amplitude of loads at the subsurface to the surface of the area. $\xi(k)$ is the flexural response, as in equation 6.3, but here considering the density contrast between the crust, ρ_c and air, ρ_a.

The assumption that there must be coherence between the observed free air and the topography before calculating the T_e (Forsyth, 1985; McKenzie and Fairhead, 1997) has been established at short-wavelength in Fig. 6.4.

The admittance method is weak in accounting for loading of great depths (very long-wavelengths).The coherence method can be employed to examine the effects of such loads better when estimating T_e (Sreejith et al., 2019). Very deep-seated (long-wavelength) anomalies due to variation of the geoid can easily be determined using the MBA, providing the ability to estimate deep subsurface loading (Tiwari and Mishra, 1999; Luis and Neves, 2006). The Bouguer anomaly (Fig. 6.3 a) was analysed to produce the mantle Bouguer anomaly. Observed coherence was then estimated from the relationship between MBA and topography (Luis and Neves, 2006; Sreejith et al., 2019). The MBA was derived by subtracting the gravity effects of the sediment/crust and crust/mantle interfaces from the Bouguer anomaly assumed that the crust has a constant thickness (Luis and Neves, 2006; Sreejith et al., 2019). This technique works on the assumption that the long-term strength of the lithosphere is sourced within the crust (Burov and Watts, 2006; Petit et al., 2008). The gravity effects of the interfaces

were calculated using the method of Parker (1972) where the density contrasts for sediment/crust and the crust/mantle are 300 and 600 kg/m^3, respectively (Luis and Neves, 2006; Sreejith et al., 2019). The MBA was then upward continued to 10 km to reduce the effects of surface noise (Fig. 6.8). The observed coherence between MBA and the topography as a function of wavelength was calculated based on equation (6.5) and the result shows that the coherence values are close to zero at very short wavelengths while the value increases until a medium wavelength of about 35 km, and then drops again at about 100 km (Fig. 6.9 a). The short wavelengths are dominated by the presence of noise (<35 km) and show no coherence, suggesting that the topography is supported by the flexural rigidity of the lithosphere and that there is no deflection from the surface sediments (Lowry and Smith, 1994; Gómez-Ortiz et al., 2005). The low coherence at short wavelengths shows also that there is no correlation between the MBA and the topography, as is to be expected because the gravity effects from the topography have been effectively removed in calculating the MBA (Luis and Neves, 2006). Beyond 35 km, there is a slight increase in the coherence which peaks at about 50 km and the gradually declines to a wavelength of about 250 km. This slight increase in the coherence at relatively short wavelength could be due to loads in the upper crust, perhaps magmatic centres (Gómez-Ortiz et al., 2005). The coherence gradually increases from about 250 km wavelength to about 420 km wavelength. This is the transition from low to high coherence is interpretable in terms of the flexural rigidity of the lithosphere i.e., relatively stores mantle materials at greater depth (Luis and Neves, 2006). At a very long wavelength (> 420 km), the coherence tend towards 0.5 indicating a high degree of flexure and isostasy to a point where coherence is 1 and T_e is 0 (Pérez-Gussinyé et al., 2004). This also implies that the topography is fully compensated by the deflection of Moho (Gómez-Ortiz et al., 2005).

The theoretical coherence between the MBA and topography was estimated based on equation 6.6 assuming that surface and subsurface loading are statistically unrelated (Forsyth, 1985). The value of f = 0.8, and other values for the flexural response in table 6.1, were used for the calculation. The theoretical coherence was calculated using elastic models with various T_e values of between 0 and 40 km. The observed and theoretical coherence curves were compared and elastic models representing T_e= 5 km and T_e= 7 km were found to be the best fit after physical examination (Fig. 6.9 b). The T_e value of 7 km has been accepted as the highest value that best fits the two curves. Therefore, the T_e value of 7 km showed a weak lithospheric strength concentrated within the crust (probably the upper crust). The upper crust is observed to be the major contributor in surface loading while mantle materials contribute to subsurface

loading, and they both control the basin architecture of the area. This analysis did not take into consideration the thermal effects of the lithosphere since such data were not available for the study. The calculated MBA values have components of thermal effects attributed to lithospheric cooling and age-dependent subsidence (Sreejith et al., 2019). Thus, the gravity effects of lithosphere cooling and age-dependent subsidence should have been removed but this estimation is still valid as it might have given the maximum T_e which in this case will still be lower than that estimated.

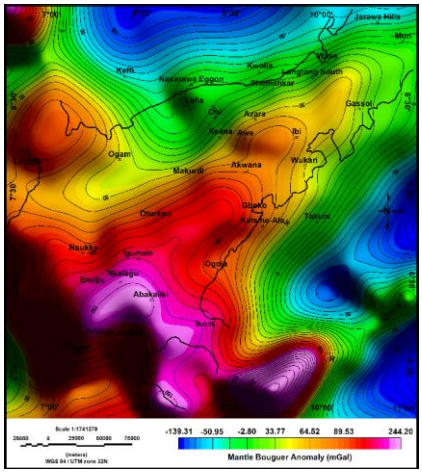

Fig. 6. 8: Mantle Bouguer anomaly derived from the subtraction of the gravity effects of the sediments/crust and crust/mantle density contrasts from the Bouguer anomaly, upward continued to 10 km.

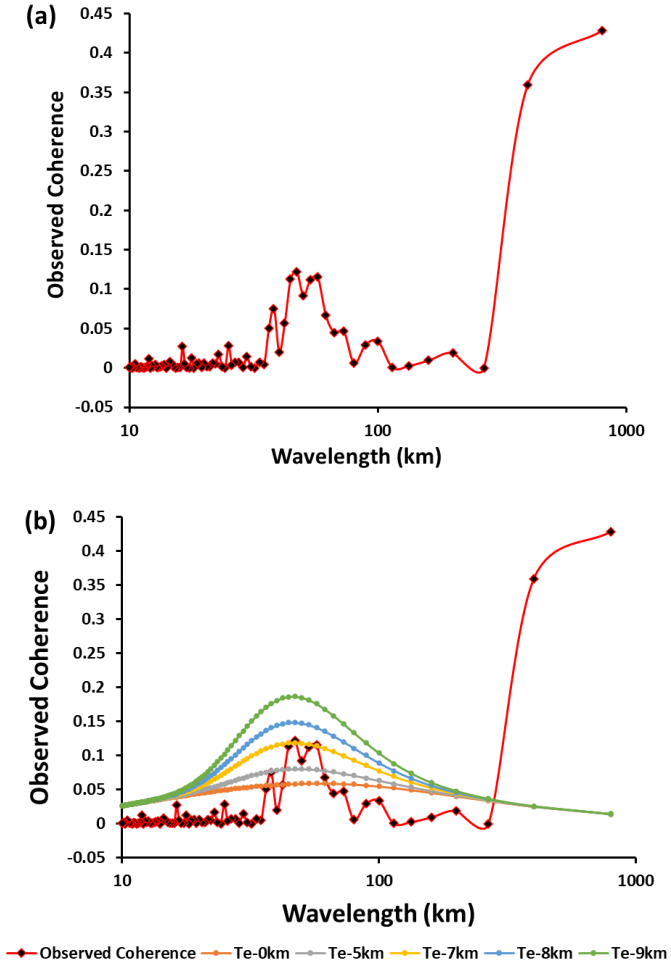

Fig. 6. 9: (a) Coherence of Mantle Bouguer Anomaly (MBA) to the topography as a function of wavelength for the trough (b) MBA compared with theoretical coherence. Curves show the coherence prediction for elastic models with combined loading (f = 0.8) and the preferred fits of 5 km and 7 km considering loading at the surface and at the Moho.

6.4 Curie Depth Estimate

The thermal structure of the crust is key in controlling geodynamic processes that affect it as well as contributing to the understanding of the long-term strength of the lithosphere. It can be obtained by analyses of Curie depth points. Direct crustal temperature measurements are not feasible for regional studies and, as such, geophysical processes have become the major tool in estimating thermal structures (Nwankwo and Sunday, 2017). The 2D power spectrum method and 3D inversion of magnetic data sets were used to determine the Curie depth point which was applied in mapping the thermal structure of the trough.

6.4.1 Power spectrum method

The power spectrum method is a statistical technique that employs the shape of the spectrum of magnetic anomalies to determine the depth of the magnetic source by transforming the spatial data to the frequency domain (Tanaka et al., 1999).

The average radial power-density spectra of a total field anomaly, $\phi_{\Delta T}$ is given by (Okubo et al., 1989; Tanaka et al., 1999).

$$\ln\left[\boldsymbol{\phi}_{\Delta T}(|\boldsymbol{k}|)^{1/2}\right] = \ln \boldsymbol{B} - |\boldsymbol{k}|\boldsymbol{Z}_{\boldsymbol{t}} \quad \text{.....(6. 7)}$$

Where B, k and, Z_t are a constant, the wavenumber and the depth to the top of the magnetic sources, respectively. This method assumes that the thickness of the magnetic source is large compared to its depth.

On the other hand, the depth to the centroid of an anomalous source, Z_0 can be estimated by using a modified form of equation (6.7), so that calculation is made around the long wavelengths (Tanaka et al., 1999).

$$\ln\left\{\left[\boldsymbol{\phi}_{\Delta T}(|\boldsymbol{k}|)^{1/2}\right]/|\boldsymbol{k}|\right\} = \ln \mathrm{B} - |\boldsymbol{k}|\boldsymbol{Z}_{\mathbf{0}} \quad \text{.....(6. 8)}$$

The center of the magnetic layer or centroid can be estimated by fitting a straight line through low-wavenumber parts of the radially averaged spectrum to obtain the slope and subsequently the depth to the center of the anomaly.

The depths to the top of the magnetic layer, $Z_{t,}$ and that of the centroid, Z_0, are related by equation (6.9), to enable estimation of the basal depth of the magnetic source, Z_c. This depth is the depth to the bottom of the magnetic source and is generally assumed to be the Curie point

depth (Maus et al., 1997; Kasidi and Nur, 2014; Hsieh et al., 2014; Nwankwo, 2015; BİLİM, 2017). However, not all depths to the bottom of magnetic sources are Curie depths as lithology contrasts could also be present (Mickus and Hussein, 2016; Nwankwo and Sunday, 2017).

The depth to the bottom of the magnetic source (Z_c) can be obtained from the relation (Okubo et al., 1989; Tanaka et al., 1999).

$$\boldsymbol{Z_c = 2Z_0 - Z_t} \quad \textbf{.....(6. 9)}$$

The Curie depth of the study area was estimated on 16 selected overlapping windows measuring 200 km x 200 km each (Fig. 6.10). The window size is appropriate for this study since it is assumed that magnetic anomalies with basal depths greater than window length/ 2π may not be properly resolved (Shuey et al., 1977; Nwankwo and Sunday, 2017). Examples of plots for power spectrum analyses within the trough representing an estimation of depths to the tops and bottom of magnetic sources are shown in figs. 6.11 (a) and (b), 6.12 (a) and (b), and 6.13 (a) and (b). Table 6.2 summarizes the results for the estimation of Curie depth, the geothermal gradient, and heat flow from analyses of the power spectrum.

Generally, the average depth to the top of the magnetic layer is estimated to be 1.18 km while the centroid is about 11.09 km, and the estimated Curie depth is 21 km with estimates corrected at sea level. In obtaining the Curie depth map, the spectral depth to the top of the magnetic layers was replaced with the depth to the basement from the pseudo-gravity inversion method, which gives a more robust estimate for the depth to the top of the magnetic body and spatially covers the whole trough. For example, basement depth estimates from the power spectrum method for window 7 is about 2 km while that from pseudo gravity is about 6 km. Generally, the depth point estimates from the power spectrum are shallower than the pseudo-gravity depth estimates (Table 6.3) since the power spectrum assumes an average depth estimate with infinite depth and length. This might have led to underestimation of the depth to the top of the magnetic layer from different blocks. The depth from the pseudo-gravity method filters shallow anomalies, which are not considered in the other methods. The Curie depth point estimates were gridded to cover the area forming the Curie isotherm (Fig. 6.14). The isotherm shows two major and significant areas with varying Curie depth points; the deep Curie depth points around the western (black rectangle) and shallow Curie depth point around the eastern parts of the Benue Trough (green rectangle). The deep Curie isotherm window (black rectangle) shows average depths to the top, bottom and Curie point to be 2.84 km, 24.86 km, and 22.02 km,

respectively (Figs. 6.15 a and b) while the shallow isotherm window (green rectangle) estimated average depths to the top, bottom and Curie point of 0.80 km, 17.20 km 16.40 km, respectively (Figs. 6.16 a and b). The shallower Curie point depths window is located around the magmatic activity zone where hydrothermal fluids are present and basement fracturing is dominant. This may act as a suitable zone for focussing the process of extension within the trough (Mickus and Hussein, 2016).

The geothermal gradient, δG, was obtained from the calculated Curie depth point (depth to the bottom of magnetic sources, Z_c) by using equation (6.10) (Tanaka et al., 1999; Nwankwo and Sunday, 2017). δG was further employed to calculate the spatial variation of heat flow within the trough (Salem et al., 2014; Nwankwo, 2015; BİLİM, 2017; Nwankwo and Sunday, 2017; Salazar et al., 2017; Mono et al., 2018) using equation (6.11). The heat flow, Q_z is given in the 1D vertical approximation assuming that the temperature variation is vertical, no radiogenic heat production, and a constant temperature gradient (Salem et al., 2014; Tanaka et al., 1999) according to

$$\boldsymbol{\delta G = \frac{\theta_c}{Z_c}} \text{ ……..(6. 10)}$$

$$\boldsymbol{Q_z = \sigma \frac{\theta_c}{Z_c}} \text{ ..... (6. 11)}$$

where σ is the thermal conductivity and averages to 2.5 $Wm^{-1}{}^{o}C^{-1}$, θ_c is the temperature variation of the earth between the surface temperature (0℃) and the Curie temperature (580℃) and Z_c is the Curie point depth (Oghuma et al., 2015; BİLİM, 2017).

The Curie depth point was further used to estimate the geothermal gradient and heat flow pattern of the trough. The geothermal gradient ranges between 19 °C/km and 50 °C/km (Fig. 6.17). The areas of high geothermal gradient correspond to areas of shallow Curie point depths where intra-crustal heat sources such as thick radiogenic sediments might be expected. Fig. 6.18 shows the heat flow isotherm map with values ranging between 41 mW/m^2 and 122 mW/m^2. High heat flow and geothermal gradient values are observed to be high at areas where the basement is influenced by magmatic activity (emplaced volcanic rocks) and shallow Curie point depths, whereas low heat flow and geothermal values are observed in areas where the Curie point depths are deep with significant thick sediments. The negative correlation between Curie depth points and heat flow gives an understanding of the thermal structure of the basin, which may have a significant indication on the long-term strength of the lithosphere.

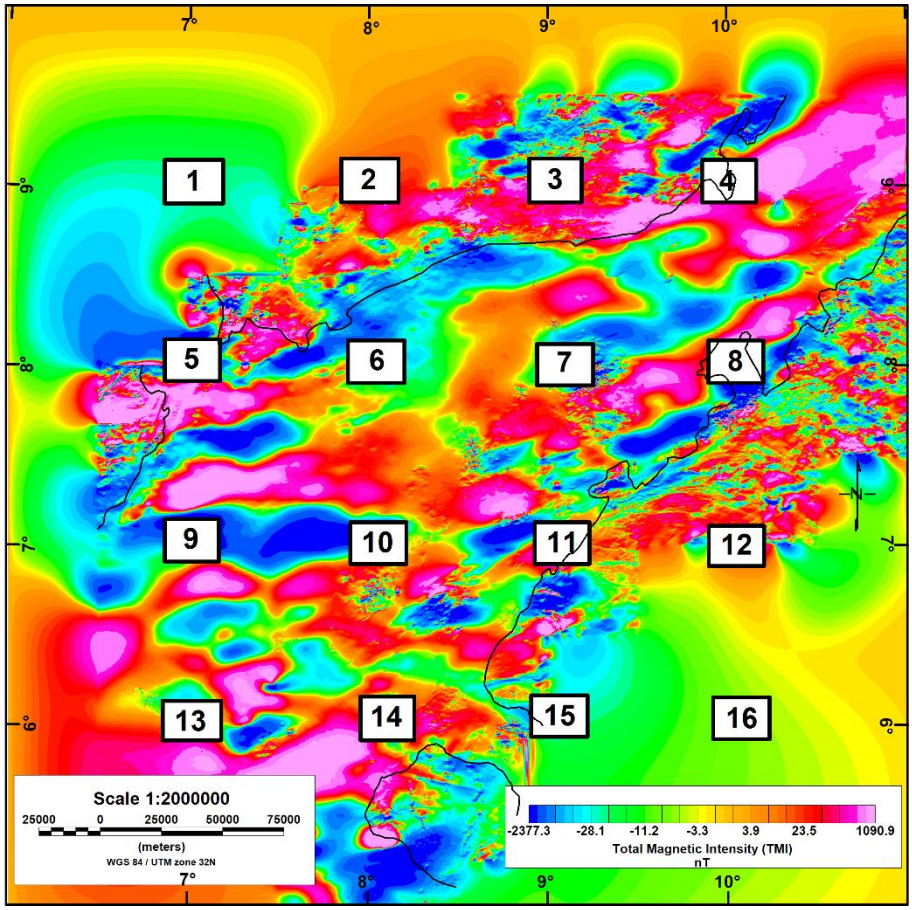

Fig. 6. 10: Total magnetic intensity showing 16 selected window centres. The box with numbers represents the centre of the overlapping windows. The TMI signals in boxes 1 and 16 are boundary signals for complete gridding.

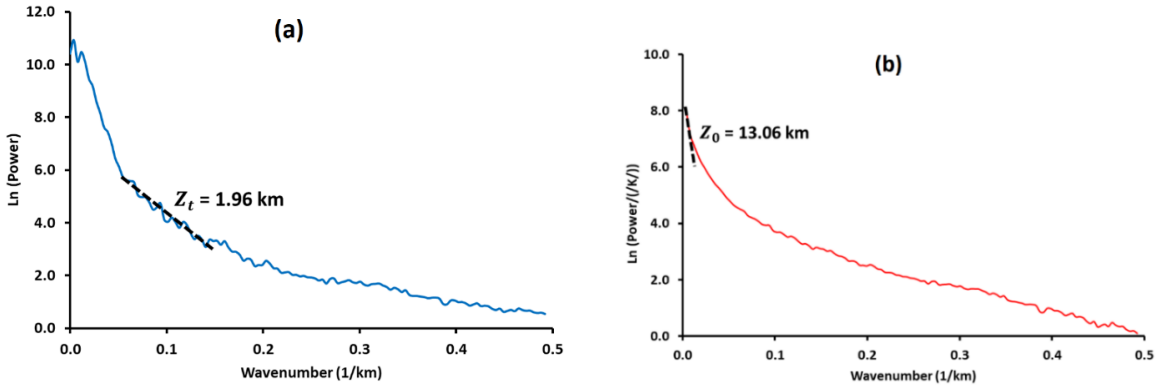

Fig. 6. 11: Examples of power spectrum plots for window 7 (a) Depth to top of the magnetic anomaly at approximately 1.96 km estmated by fitting a straight line through the slope of high wavenumber (b) Depth to centroid at 13.06 km. The window block centred at 9.00º E and 8.00º N is dominated by mostly low magnetic anomalies. This is by fitting a straight line through low wavenumber part.

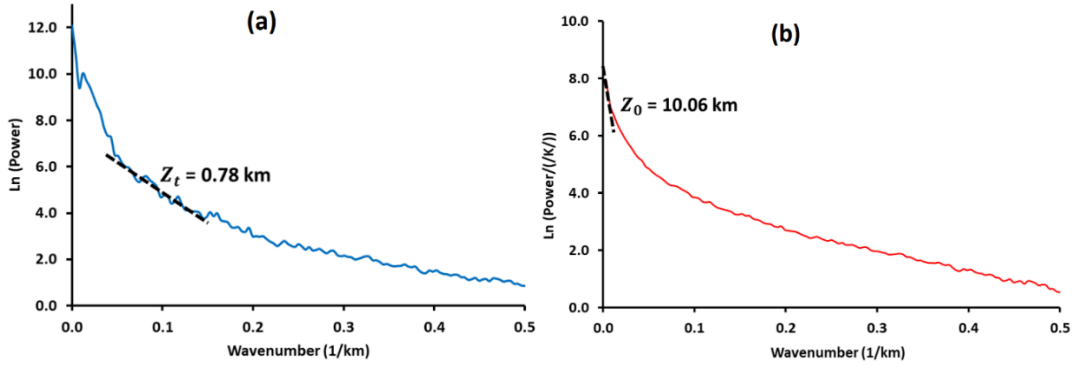

Fig. 6. 12: Example of power spectrum for window 8 (a) Depth to top boundary of the magnetic anomaly at approximately 0.78 km. Depth is estmated by fitting a straight line through the slope of high wavenumber. (b) Depth to centroid at 10.06 km obtained by fitting a straight line through low wavenumber part. The window block is centred at 10.00º E and 8.00º N.

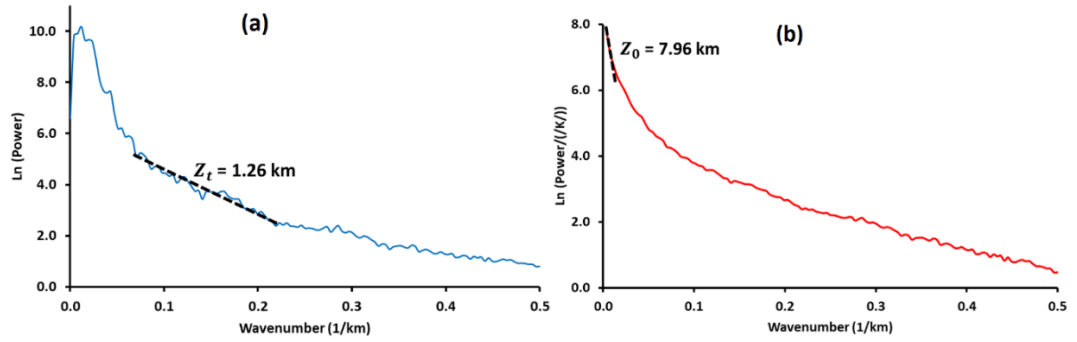

Fig. 6. 13: Example of power spectrum plots for window 11 (a) Depth to the top boundary of the magnetic anomaly at approximately 1.26 km obtained by fitting a straight line through the slope of high wavenumber (b) Depth to centroid at 7.96 km obtained fitting a straight line through the slope of low wavenumber part. The window block is centred on 9.00º E and 7.00º N with the dominance of short-wavelength anomalies.

Table 6. 2: Summary of the results of power spectrum analyses for the estimation of Curie depth, the geothermal gradient, and heat flow.

Block	Long. (degree)	Lat. (degree)	Depth to Top, Z_t (km)	Centroid Depth, Z_0 (km)	Depth to Bottom, Z_c (km)	Corrected Z_c (Z_c-80 m)	Geothermal Gradient (°c/km)	Heat Flow (mW/m^2)
1	7	9	2.65	8.75	14.85	14.84	39.08	97.70
2	8	9	2.39	7.58	12.77	12.76	45.45	113.62
3	9	9	1.39	9.86	18.33	18.32	31.66	79.14
4	10	9	0.08	7.42	14.76	14.75	39.32	98.29
5	7	8	1.91	13.26	24.61	24.60	23.58	58.94
6	8	8	1.59	14.32	27.05	27.04	21.45	53.62
7	9	8	1.96	13.06	24.16	24.15	24.01	60.04
8	10	8	0.78	10.06	19.34	19.33	30.00	75.01
9	7	7	0.58	9.95	19.32	19.31	30.03	75.08
10	8	7	0.60	8.95	17.30	17.29	33.54	83.85
11	9	7	1.26	7.95	14.64	14.63	39.64	99.10
12	10	7	0.99	10.61	20.23	20.22	28.68	71.70
13	7	6	0.72	15.91	31.10	31.09	18.65	46.64
14	8	6	0.72	13.26	25.80	25.79	22.49	56.22
15	9	6	0.60	11.94	23.28	23.27	24.92	62.31
16	10	6	0.66	14.59	28.52	28.51	20.34	50.86
Average			**1.18**	**11.09**	**21.00**	**21.00**	**27.62**	**69.06**

Table 6. 3: Comparison of the depth to the top of the magnetic layer using power spectrum and Pseudo-gravity methods.

Block	Power Spectrum	Pseudo-gravity
	Depth to Top, Z_t (km)	
1	2.65	3.8
2	2.39	4.6
3	1.39	7.4
4	0.08	7.4
5	1.91	4.42
6	1.59	4.42
7	1.96	5.88
8	0.78	5.47
9	0.58	4.18
10	0.6	5.72
11	1.26	6.44
12	0.99	6.29
13	0.72	7.99
14	0.72	8.09
15	0.60	4.96
16	0.66	4.88
Average	**1.18**	**5.74625**

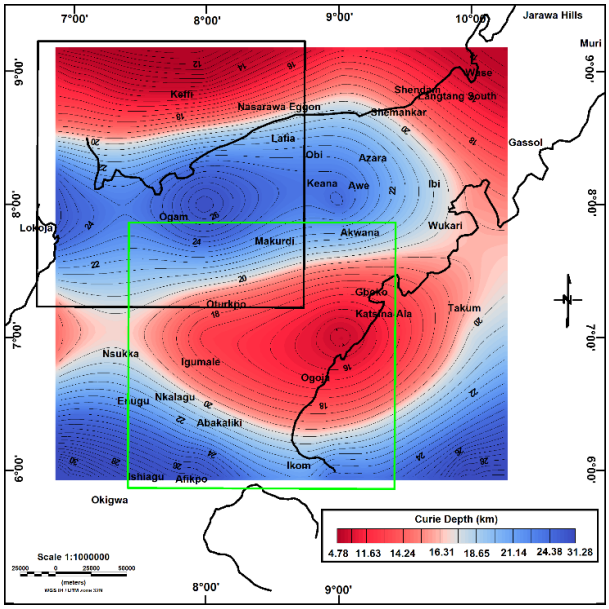

Fig. 6. 14: Curie point depth estimates for the study area. The black and green rectangles are drawn on areas indicating deep and shallow Curie depth estimates, respectively.

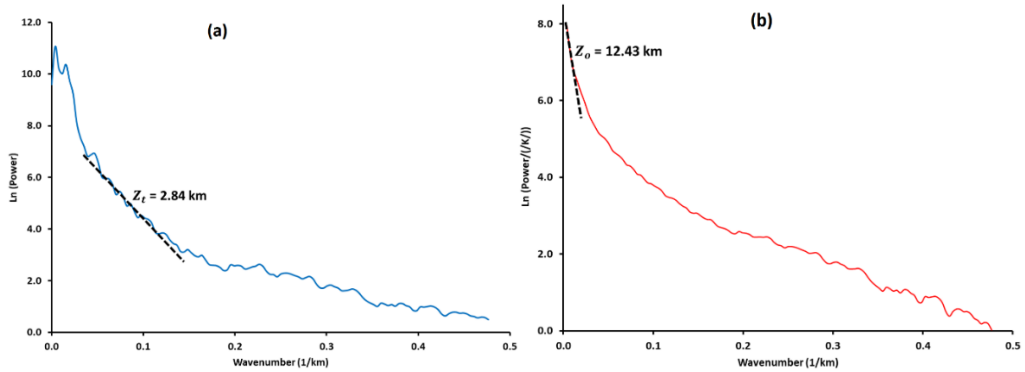

Fig. 6. 15: Power spectrum plots within black rectangle window (a) representing the depth to the top of the anomaly of 2.84 km (b) representing the depth to the magnetic centroid 12.43 km deep. The average depth to the Curie isotherm for this window is 22.02 km.

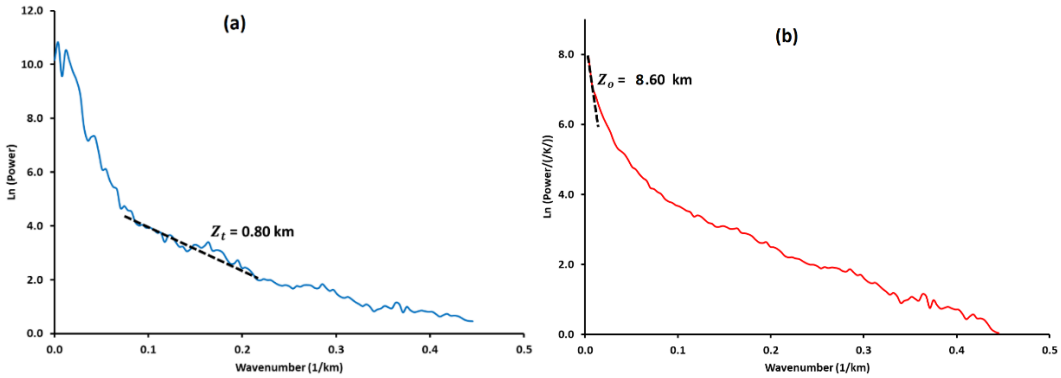

Fig. 6. 16: Power spectrum plots within green rectangle window (a) representing the depth top of the anomaly of 0.80 km (b) representing the depth to the magnetic centroid 8.60 km deep. The average depth to the Curie isotherm for this window is 16.40 km.

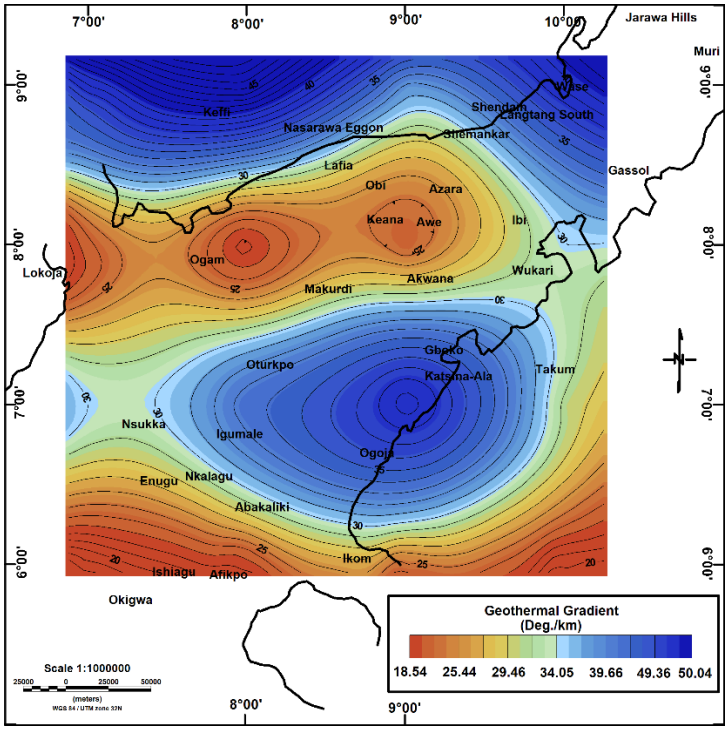

Fig. 6. 17: Geothermal gradient map of the trough. A significant increase in geothermal gradient was observed with a major ENE-WSW trending direction where the Curie depth points are shallow.

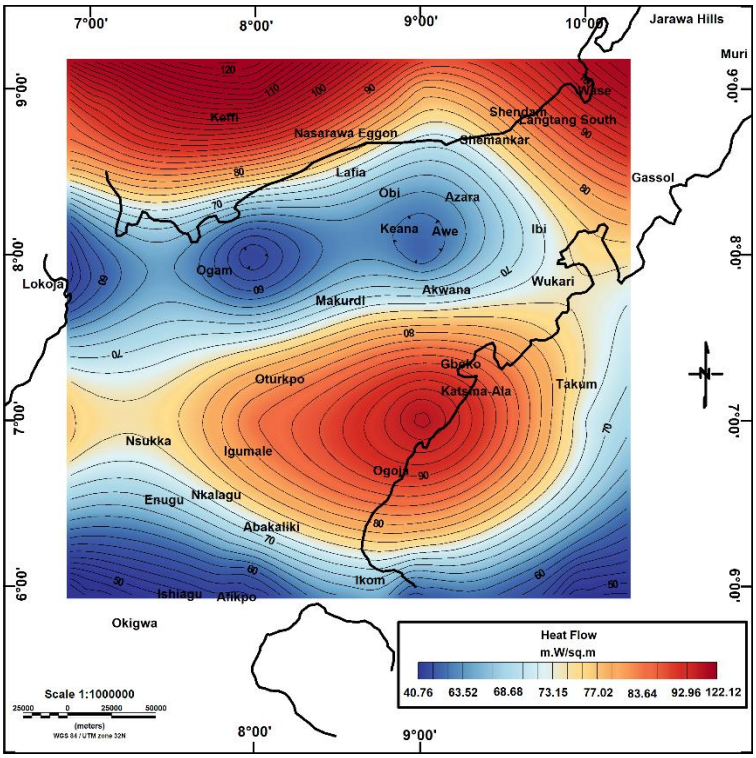

Fig. 6. 18: Heat flow map. A significant increase in heat flow is seen to trend in a major NE-SW direction where the Curie depth points are shallow. This is a proxy for the thermal structure of the area.

6.4.2 Three dimensional magnetic inversion

This method involves modelling the magnetic susceptibilities of isolated magnetic bodies using the inversion technique to assist in the mapping of the subsurface basement and to determine the depths to the bottoms of magnetic sources (Mickus and Hussein, 2016; Kolawole et al., 2017). The 3D magnetic inversion approach requires estimating the magnetization direction before inverting for magnetic susceptibility and determining the depth to the bottom of the magnetic bodies (their Curie point depths). The approach assumes that the anomalous magnetization direction is the same as that of the inducing earth's field (Li and Oldenburg, 1996; Macleod and Ellis, 2013). The magnetization direction was estimated from cross-correlation and Helbig's integral methods before inversion with the assumption that the remanent magnetization is negligible for the whole area (Arkani-Hamed, 1988; MAG3D, 2017). The cross-correlation method calculates the correlation coefficient between the vertical gradient and total gradient of the RTP field and estimates the inclination and declination (Dannemiller and Li, 2004) while Helbig's integral method uses the integral relations between the moments of magnetic anomalies (Phillips, 2005).

The estimated average inclination and declination for the study region were -26.5° and -32.2° for the cross-correlation method and, -26.08° and 27.64° for Helbig's integral method. Helbig's magnetization direction estimate was preferred because the inclination is quite stable, and it has less ambiguity in estimating the declination and inclination. The inversion was carried out by discretizing the area using mesh-sized cubes with lateral extent corresponding to the study area and dimensions of 50 km X 50 km containing 50 cells in both the easting and northing directions and a fixed vertical depth of 50 km measuring 1 km for 50 cells. The TMI dataset was directly inverted using Mag 3D inversion software version 6.0 from UBC website (Li and Oldenburg, 1996) and a 3D magnetic susceptibility contrast block was modelled (Fig. 6.19). This shows the distribution of magnetic susceptibilities across the basin in depth. An isosurface plot of the inverted magnetic susceptibility contrast was obtained by removing lower values and keeping magnetic values greater than $0.3e^{-6}$ SI (Fig. 6.20). The result shows basement magnetic intrusions/bodies around Awe and Ishaigu areas while a ridge-like basement magnetic intrusion/body runs from Lokoja-Igumale-Ogoja along an E-W trend. These anomalies are probably associated with the induced magnetization of the volcanic and intrusive rocks (Arkani-Hamed, 1988). A plan view depth slice through the 3D block at depths of 920 m, 6920 m, 14920 m, and 20920 m below the surface as shown in Fig. 6.21. Fig. 6.21 (d) shows the plan view depth slice at 21 km that indicates decreased magnetic susceptibility in many

parts of the area i.e., marks the bottom of isolated magnetic sources or the Curie depth interface signifying higher temperature gradients and gradual loss of magnetism due to increased heating from mantle materials.

The 3D magnetic susceptibility distribution block is depth sliced across four profiles that show various components of magnetic bodies within and without the trough and give an estimate of the depth of the magnetic bottom i.e., the Curie depth points (Fig. 6.22). The depth slice across profile L1-L2 indicated three main magnetic bodies identified as A, B, and C with estimated average Curie point depths of 16.58 km, 16.50 km, and 17.48 km, respectively (Fig. 6.23 a). Profile L3-LT4 depth slice shows four main isolated magnetic anomalous sources A, B, C, and D with estimated CPD of 11.11 km, 17.14 km, 16.89 km, and 18.02 km, respectively (Fig. 6.23 b). Fig. 6.23 c shows the depth slice across profile L5-L6 where the average CPD of the magnetic body A is 17.12 km while that of magnetic body B is 18.51 km. Models across profile L7-L8 indicated magnetic bodies A and B with CPDs of 18.25 km and 16.54 km, respectively (Fig. 6.23 d). In each of the depth slices, the Curie depth interface was identified and interfaces beyond this point are assumed to be non-magnetic (beyond Curie temperature 580 °C) (Hsieh et al., 2014; Speranza et al., 2016).

A comparison of CPD estimate from the 3-D inversion with those of the power spectral method indicated similar results. The two methods show vertical and lateral variations in the distribution of magnetic susceptibilities and limits to the bottom of magnetic sources, or the Curie depth points, in the subsurface across the trough. The results for the inversion method across profile L1-L2 show an average Curie point depth (CPD) of about 16.85 km while the power spectrum gives about 15.5 km. Profile L3-L4 shows an average of 15.79 km CPD estimate for the inversion method while 18.0 km is observed for the spectral method within the trough. An average CPD of 17.82 km is estimated from the inversion technique while an average of 16.70 km is estimated for the spectral method across profile L5-L6. Profile L7-L8 estimated an average CPD of 17.40 km and 16.90 km for the inversion and the spectral methods, respectively.

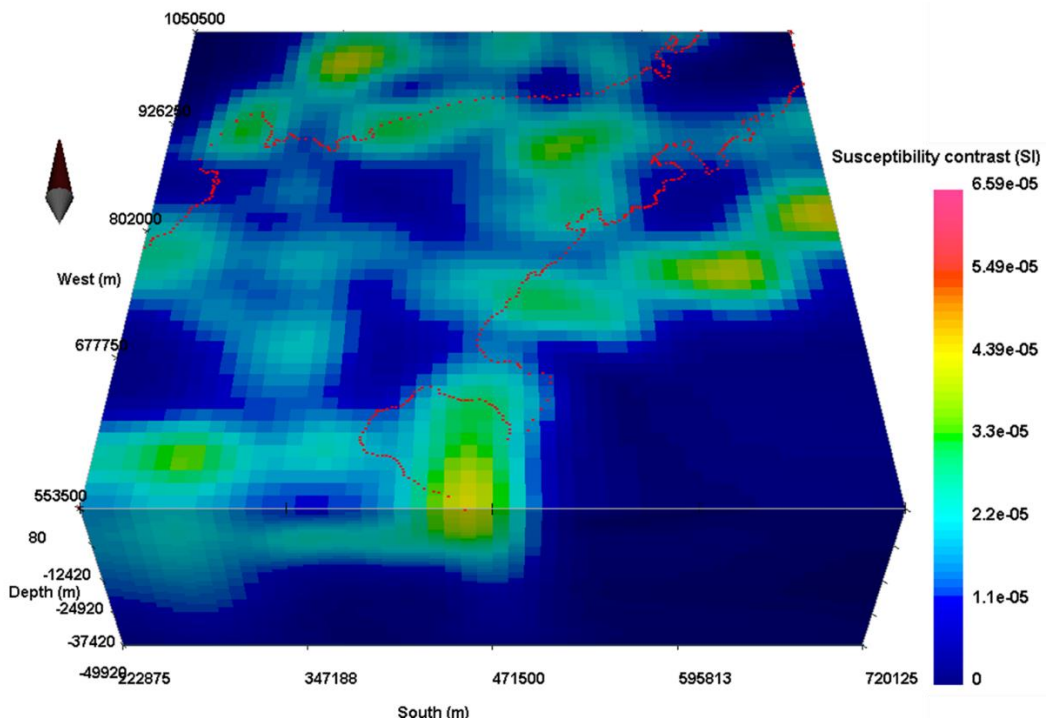

Fig. 6. 19: 3D magnetic susceptibility contrast block distribution. The top view is modelled at 80 m terrain clearance and the vertical exaggeration is x 3.

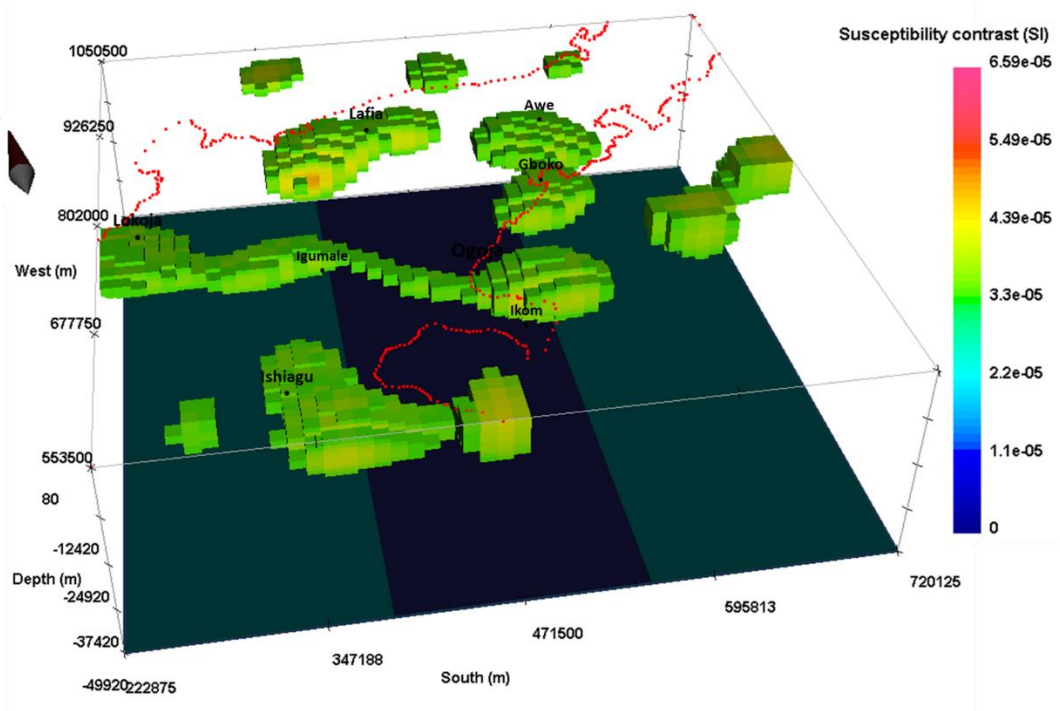

Fig. 6. 20: Isosurface plots of the inverted magnetic susceptibility (> 0.3e^{-6} SI). The magnetic distribution shows magnetic susceptibilities with the lower values removed. The compacted bodies are interpreted as igneous intrusions within the basement and the sedimentary rocks.

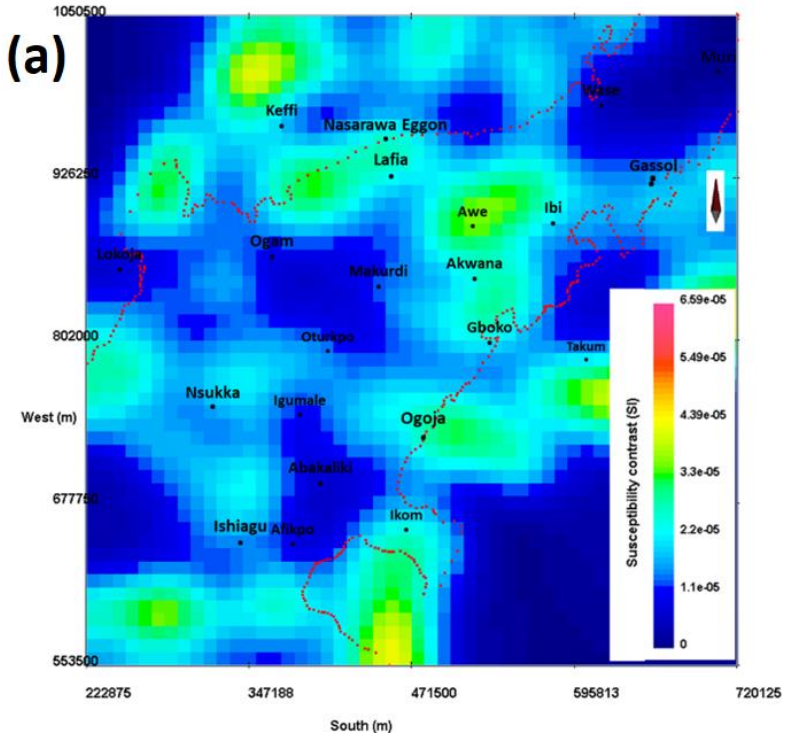
(a)
1050500
926250
802000
677750
553500
West (m)
222875
347188
471500
595813
720125
South (m)
Keffi
Nasarawa Eggon
Lafia
Gassol
Awe
Ibi
Ogam
Lokoja
Makurdi
Akwana
Gboko
Oturkpo
Takum
Nsukka
Igumale
Ogoja
Abakaliki
Ishiagu
Afikpo
Ikom
Wase
Susceptibility contrast (SI)
6.59e-05
5.49e-05
4.39e-05
3.3e-05
2.2e-05
1.1e-05
0

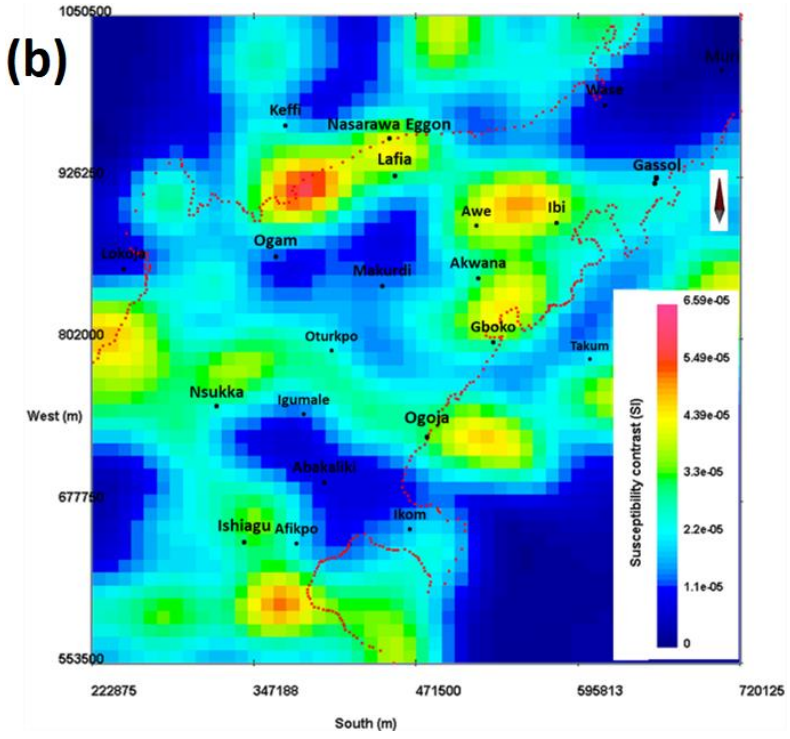
(b)
1050500
926250
802000
677750
553500
West (m)
222875
347188
471500
595813
720125
South (m)
Keffi
Nasarawa Eggon
Lafia
Gassol
Awe
Ibi
Ogam
Lokoja
Makurdi
Akwana
Gboko
Oturkpo
Takum
Nsukka
Igumale
Ogoja
Abakaliki
Ishiagu
Afikpo
Ikom
Wase
Susceptibility contrast (SI)
6.59e-05
5.49e-05
4.39e-05
3.3e-05
2.2e-05
1.1e-05
0

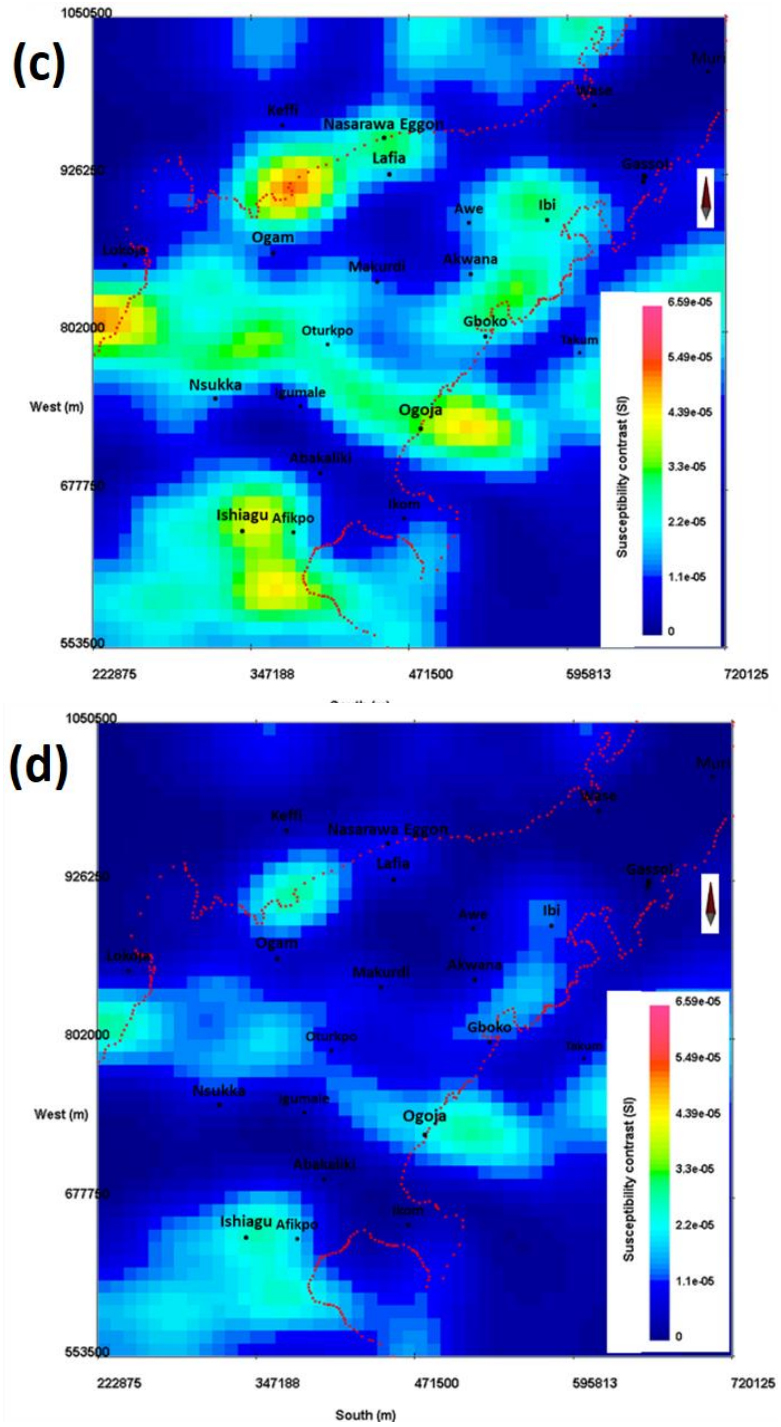

Fig. 6. 21: Plan view depth slice of 3D block magnetic susceptibilities (a) depth slice at 920 m below the surface. High magnetic susceptibilities observed within the basin around Awe-Akwana-Ibi-Gboko and Nsukka-Igumale-Ishiagu towns (b) depth slice at 6920 m below the surface indicating an increase in magnetic susceptibility of materials and generally interpretable as the centroid of magnetic body (c) depth slice at 14920 m indicating relative decrease in magnetic susceptibility i.e., reduction in susceptibility due to possible increase in temperature and loss of magnetic properties of the interpreted igneous rocks or isolated relics of basement (d) depth slice at 20920 m below the surface. Decreased magnetic susceptibility in many parts of the area indicates higher temperature gradients and Curie depth interface.

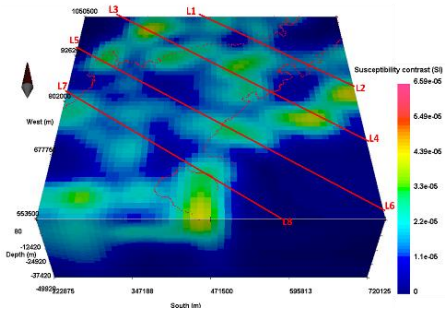

Fig. 6. 22: 3D magnetic susceptibility block showing four profiles across the basin.

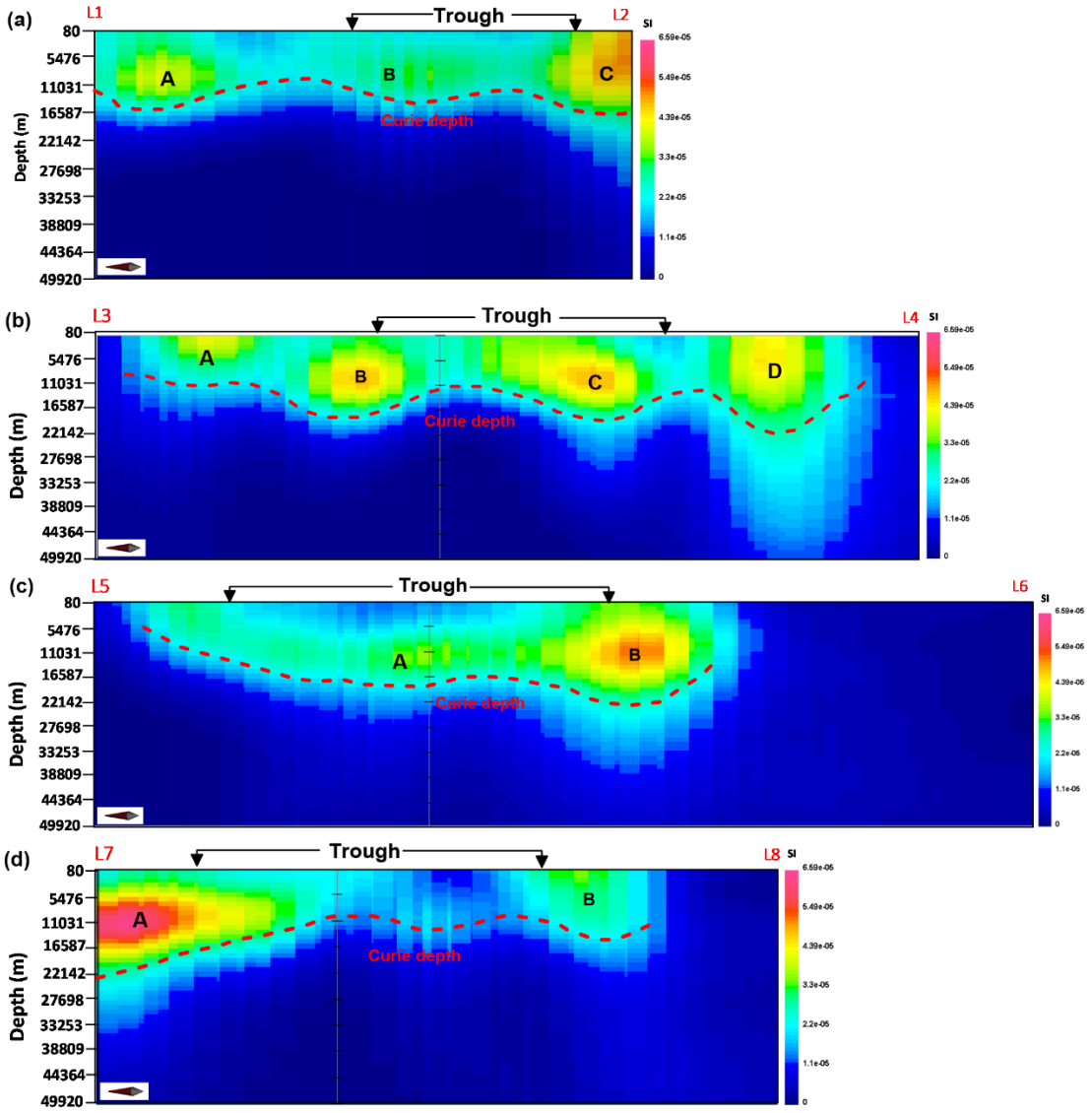

Fig. 6. 23: 3D magnetic susceptibility depth slices (a) across profile L1-L2. A and C are from basin shoulders while B is within the basin with lesser magnetic susceptibility (b) across profile L3-LT4 with body C found within the basin. (c) across profile L5-L6 where body A is found within the basin while body B is part of the surrounding rocks. (d) across profile L7-L8. Bodies A and B are found at the boundary of the basin. No significant magnetic body with the basin. All depth slices have their vertical scale exaggeration (VE) of X 3.

6.5 Relationship between the effective elastic thickness, T_e, CPD, and the heat flow of the area.

Lithospheric strength depends to some extent on heat contact which implies that $T_{e,}$ is directly related to CPD but show an inverse relationship with heat flow (Deng. et al., 2014; Jiménez-Díaz et al., 2014; Ji et al., 2017). This relationship may be complex in continental areas due to local variations in crustal structures and composition (Watts and Burov, 2003). In its simplest sense, this however means that higher heat flow and lithospheric temperatures imply lower or weaker lithospheric strength. The amount of heat flow can be estimated from the Curie depth point analyses (Tanaka et al., 1999) or by understanding and calculating the stretching factor within a rift-type basin (Watts, 2001; Wyer and Watts, 2006). High heat flow denotes a low value of Curie depth point and a low T_e value.

This study generally indicated lower T_e values of 10 km which signifies low or weak lithospheric strength. The Lower Benue Trough showed lower T_e values of between 5-10 km while the Middle Benue Trough gave T_e values of between 5-15 km. This low T_e is attributed to the thermal age of the rifted lithosphere (Cretaceous), thinning and heating at the time of rifting, and post-rift sediment loading (Watts and Burov, 2003). Heat flow estimated for the trough ranges between 41 mW/m^2 and 122 mW/m^2 (Fig. 6.18) while the CPD is estimated to range between 5 and 31 km, with lower values corresponding to areas of high heat flow and higher values to areas of low heat flow. Generally, there is relatively high heat flow (average of 69 mW/m^2) within the area with some local variations occurring in areas with very high heat flow as observed towards the eastern part of the map where evidence for magmatic activities is prominent. Even though there is no spatial distribution map of T_e values for the area, the generally low T_e values agree favourably with the high average heat flow. The heat flow estimates are associated with relatively high uncertainties since they are derived from a 1D model, however, there is a relatively good inverse correlation between surface heat flow and the T_e of the area. It can also be deduced further that areas of strong lithospheric heating are identified by high stretching factor and thinning, which may be associated with observed/modelled low T_e values (Pérez-Gussinyé et al., 2009) and low CPDs (Fig. 6.14). Detailed correlation between the heat flow and the T_e without using their spatial distribution may suggest that the thermal structure of the lithosphere has a strong influence on its strength.

6.6 Uncertainties in estimating T_e and its relationship with heat flow

The accuracy of T_e estimated using the spectral technique strongly depend on the size of the selected window for analyses (Daly et al., 2004; Pérez-Gussinyé et al., 2004). The variance of T_e estimates increase with decreasing window size and to obtain a more accurate T_e estimate, several window sizes are usually analysed. However, the areal extent of the study is small and only a single-sized window was analysed without overlapping different tectonic settings. This may result to introduction of errors and recovery of inaccurate T_e . The fact that the study area is part of the continent posed a challenge in the T_e values estimate as several errors are added in the calculation due to noise inclusion from variation in internal composition of the continent (Burov and Diament, 1995; She et al., 2016). McKenzie and Fairhead (1997) and Kirby and Swain (2009) gave that the value of T_e using free air and Bouguer anomalies over the continents are upper bounds and not estimates because the short-wavelength topography has been removed by erosion. Since the T_e estimation technique gives an upper bound for the continents, Burov and Diament (1995) questioned its physical meaning and significance for continents since the continental lithosphere estimation of T_e bear little relation to specific geological or physical boundaries. Again, the calculation for T_e using the elastic plate models are self-unreliable in that they can predict intraplate stresses high enough to lead to inelastic (brittle or ductile) deformation which in itself may not account for the variation in the composition of the lithosphere as well as its strength (Burov and Diament, 1995; Burov and Watts, 2006; Petit et al., 2008). These really contribute strongly to the uncertainities experience in the methods for estimating T_e .

The method for estimating the heat flow of the study area assumed that a vertical temperature variation at a point is significant enough in understanding both crustal geothermal gradient and mantle convection (Deng et al., 2014; Tanaka et al., 1999). However, this assumption may possess some uncertainties about the relationship between surface heat flow and T_e since the temperature at depth can be large and vary spatially (Deng et al., 2014; Jiménez-Díaz et al., 2014). The high values of T_e can only partly explain present day geothermal gradients (Burov and Diament, 1995). In building and interpreting the relationship between the T_e and the heat flow for the area, a negative correlation is discovered to exist (Deng. et al., 2014; Jiménez-Díaz et al., 2014; Ji et al., 2017). This assumption may be inappropriate and may introduce errors because a spatial distribution of heat flow estimated from 1D point model may not have an easy relationship with the T_e that is a representation of average values believed to be at best the upper end limits (Forsyth, 1985; McKenzie and Fairhead, 1997).

CHAPTER SEVEN

GEOLOGICAL AND TECTONIC INTERPRETATION OF THE GEOPHYSICAL DATA AND MODELS

7.1 Introduction

The Lower and Middle Benue Trough are parts of the Benue Trough megastructure, which is a rifted basin that trends in a general NE-SW direction. This regional trend evolved from movements between African subplates (Fairhead et al., 2013), or magma plumes (Olade, 1975), or a combination of both (Ofoegbu, 1984a). The formation of the rift has led to the development of local structures that characterize the geometry and provide ideas about the evolutionary history of the trough. This chapter, therefore, focuses on describing and interpreting the tectonic significance of the basin by analysing geologic formations and bodies as well as tectonic and non-tectonic lineaments involved in the formation of the basin. Results obtained from the analyses in chapters 2, 3, 4, 5 and 6 were used and combined with some literature studies to support the chapter. It also briefly summarises the hydrocarbon potentials of the trough based on its structural framework and basement morphology.

The following steps were applied in the study:

1. Employ the relationship between faults and stress fields in understanding and modelling the evolutionary pattern of the basin.
2. Interpret the local paleo-stress field from the analyses of dykes and model the sources of magmatic intrusions.
3. Employ the results of the crustal structure obtained from 3D Moho and basement depth estimates to estimate stretching factors, and together with the time span of rifting, model the temperature needed to cause melting for subsequent emplacement.
4. Establish the basin tectonic model based on fault kinematics and relate it to magmatic emplacement concepts.
5. Carry out geological and tectonic interpretation of the trough based on results from 2- and 3D models and the fault kinematics with a view to developing a holistic and better understanding of the surface and the subsurface structures.

7.1.1 Geodynamic fundamentals and processes

The principles and processes of geodynamics are usually linked with continental margin type, basin position, and crustal structural geometry to understand sedimentary basins in a tectonic setting (Klein, 1990; Ju et al., 2022). In the plate interiors, cratonic basins are formed by mechanical extension, thermal subsidence and possibly flexure while in passive margin, rift basins form by extension and thermal subsidence (Pérez-Diaz and Eagles, 2014). Some of these processes are discussed below.

Rifting: The break apart of crustal and mantle materials separated through faulting caused by plate tectonics is referred to as rifting. Rift may result to basins that occur at the interior or edge of a passive margin and possibly defines the boundary of the passive margin (Klein, 1991).

Stretching: Stretching involves increase in the size of rocks under stress. When elastic rock material resists a change in shape but strains as more stress is applied. After stretching, it may return to its original shape once the applied stress (force) is removed. This elastic strain is recoverable because it involves stretching rather than breaking atomic bonds (Fossen, 2010). Stretching factors are normally calculated for rifts and extensional basins.

Flexure: Flexure basins mostly evolved by load flexure along the plate margin. The flexure basins at the passive margins form in response to sediment loading on the continental crust (Klein, 1991). Subsidence occurs due to loading being spread laterally away from the point load of sediment accumulation. Intercontinental flexural basin forms within the continent by contraction and buckling of continental lithosphere (Ju et al., 2022).

Compression: The process of negative extension is referred to as compression initiated by stress (Fossen, 2010). This results to decrease in size of rock and possible folding.

Extensional basins: Extensional basins are formed under an extension setting as a result of stretching and subsidence of the crust or the continent (Cunningham and Mann, 2007; Ju et al., 2022). When the basin forms under an extension setting in a craton or continent where no oceanic crust forms or accompanied by initial breakup of a continent and the formation of a new oceanic crust, it produces an intracontinental extensional basin, and they include intracontinental rift basins and aulacogens. However, when the oceanic basin continues to grow with the spreading of the oceanic crust, an oceanic extensional basin is formed (Capponi et al., 2018).

Thermal subsidence: Thermal subsidence indicates subsidence where conductive cooling in the mantle thickens the lithosphere causing elevation decrease (Klein, 1990; Klein, 1991). This is because of loading by sediments, tectonic activities, and thermal contraction during the cooling of the crust. Tectonic and thermal processes are involved in sedimentary basins formation (Fossen, 2010; Cunningham and Mann, 2007). Lithospheric cooling leads to thermal contraction as it responds to isostatic equilibrium resulting in thermal subsidence. Thermal subsidence becomes the main basin forming process after tectonic subsidence has ceased (Capponi, Festa and Rebay, 2018).

Aulacogen: Aulacogens are basin types that extend from the edges of passive margins towards the continents and may be oriented perpendicular to the margin of the continent (Klein, 1991). They are formed by extension, stretching, and thermal subsidence which may signify failed arm of a triple-junction rift system.

7.1.2 Andersonian model

Faults are simply the expression of localized mechanical failure of the material of the Earth's crust (Scheidegger, 1982). The purpose of this interpretation is to understand the relationship between faulting and stress field and interpret the origin of the trough using the faults derived from remote sensing, gravity, and magnetic data sets. This interpretation was achieved by considering the Andersonian model that gives an idea for classifying tectonic stress regimes based on oberved fault pattern (Fossen, 2010, Fig. 7.1). This model classified the tectonic stresses into normal, thrust, and strike-slip regimes in which one of the principal stresses has to be vertical and the other two will have to be horizontal. For the normal-fault regime, σ_1 is vertical while the strike-slip and the thrust faults regimes, σ_2 and σ_3 are vertical, respectively.

A normal fault occurs when the a non-vertical fault separates the hanging wall from the underlying footwall and the hanging wall is downthrown relative to the footwall (Fig. 7.1). When the opposite case occurs, then the hanging wall is upthrown relative to the footwall, and this is reverse fault. When the movement is in the horizontal plane, then the fault is a strike-slip fault. A left-lateral strike-slip fault is also called a sinistral strike-slip while it is called a dextral strike slip fault when the movement is in right-lateral direction (Fossen, 2010).

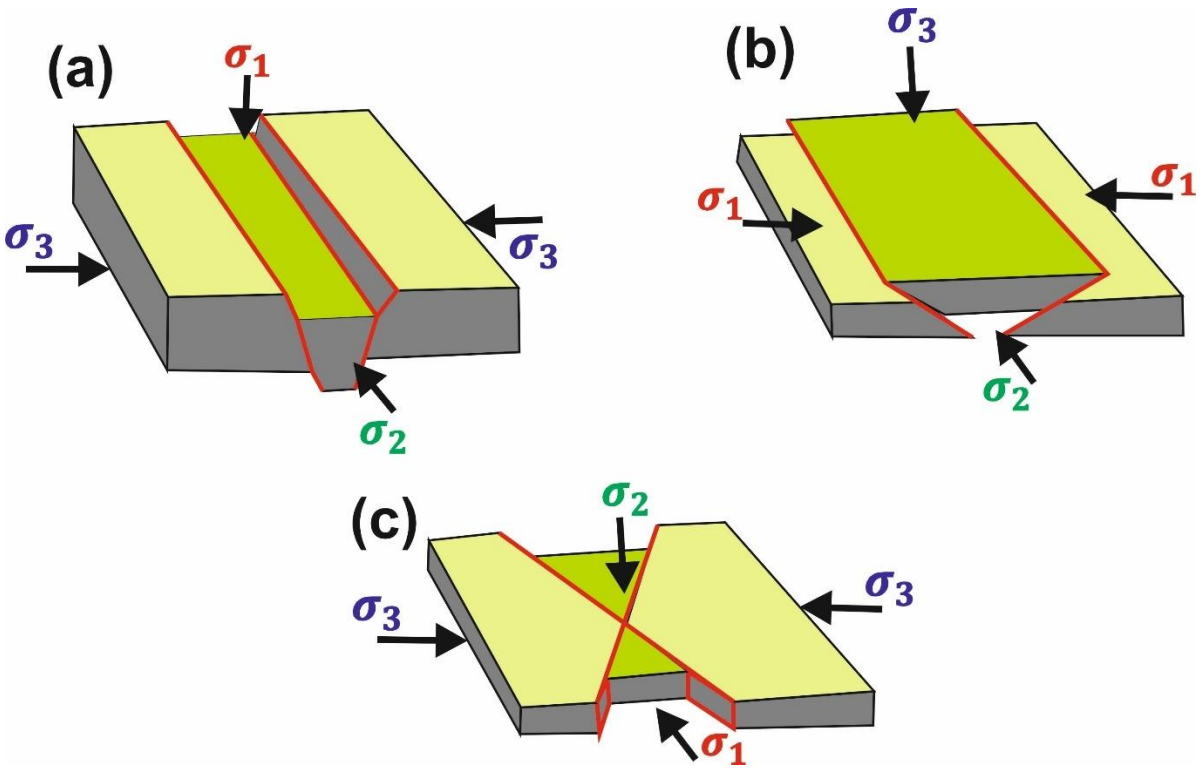

Fig. 7. 1: The relationship between the orientation of the principal stresses and faults (a) Normal fault regimes (b) Thrust-fault regime (c) Strike-slip regime (Fossen, 2010). σ_1, σ_2, and σ_3 are the maximum, intermediate, and minimum principal stress axes, respectively.

7.1.3 Fundamentals in petroleum geoscience

7.1.3.1 Processes of petroleum systems

The generation of the hydrocarbons depends on the presence of rich organic matter, adequate temperature, sufficient time, pressure, and the presence of bacteria (Charpentier and Ahlbrandt, 2004). When hydrocarbons are generated, they migrate from the source to the reservoir rocks. This movement from their source into reservoir rocks is known as migration. It could be primary when the movement of the generated hydrocarbon is out of the source rock while it is natural when the movement is into the reservoir rock (Guerriero et al., 2010). Migration could be from one formation to another or within the formations themselves. The moved hydrocarbon accumulates in the reservoir rock where they remain trapped until extracted (Hallett, 2002).

7.1.3.2 Elements of Petroleum systems

Petroleum system consists of a mature source rock, migration pathway, reservoir rock, trap and seal while its elements include source, reservoir, seal and traps. These are important exploration elements that when found complete gives idea of suitable presence of oil and gas.

Source rock: This is a subsurface sedimentary rock unit(s) made up of organic-rich rock of shale or limestone filled with kerogen and bitumen subjected to high temperature and pressure for a long time (Akande et al., 2012).

Reservoir rock: These are subsurface or surface rocks that have sufficient porosity and permeability to store and transmit hydrocarbons from one point to another (Hallett, 2002). Examples are sedimentary rocks, highly fractured and interconnected igneous and metamorphic rocks.

Seal or cap rock: They are impermeable rock bodies that act as hindrances to the migration of hydrocarbons within the reservoir and/or source rocks or through faults. They include shale, mudstone, anhydrite, and salt (Guerriero et al., 2010; Guerriero et al., 2011).

Trap: A suitable rock for containing hydrocarbons and sealed by an impermeable rock formation preventing the easy migration of hydrocarbons is known as a trap (Guerriero et al., 2011). This can either be a structural or a stratigraphic trap. A structural trap is a geologic structure such as folds and faults that prevent the flow of hydrocarbons while a stratigraphic

trap is one that results from changes in rock types due to pinch-out of rocks, unconformities, and reef build-ups.

7.2 Fault and paleo-stress field interpretation

7.2.1 Faults

The general tectonic map of the trough defines and delineates surface and near-surface faults from multispectral, gravity, and magnetic data sets (Fig. 7.2 a) and deep faults from regional gravity and magnetic data sets (Fig 7.2 b). The combined tectonic map has been interpreted to show different fault orientations that reveal the presence of different stress fields acting within the trough (Fig. 7.3). The faults appear correlated or clustered between different crustal levels and within the sediments and therefore are likely to define areas of deep-seated fault zones.

A closer observation of the spatial spread of the faults shows that most of the faults align with or are close to other faults. Deep faults that link with both shallow and surface faults were assumed to be the best locations for the deep-seated faults and were picked and cleaned for a more robust interpretation of the fault system (Fig. 7.3). The fault system is dominated by NE-SW and NW-SE trends with minor ENE-WSW and N-S trends. The NE-SW, NW-SE, and the ENE-WSW trending faults were interpreted to be related and dominated by the extensional deformation event (i.e., to be rift-related) while the N-S trending faults were related to an ENE-WSW compressional deformational event (Fig. 7.3). The NE-SW trending faults are the most dominant and form en-echelon sets that run parallel to the main trend of the trough. The NE-SW faults correspond to the orientation of the basin-bounding faults associated with the Aptian rifting, and combined with the regional sinistral setting show some sinistral kinematic components (Guiraud and Maurin, 1992). The NW-SE striking faults are interpreted to have initially formed during rifting in the Albian (Fairhead et al., 2013). The NW-SE trending faults are perpendicular to the NE-SW trends and act as breaks or offsets to the NE-SW trends across the area. The ENE-WSW and the N-S trending faults are found mainly in the southwestern part and seem to control major tectonic activities (uplift and down-warping) and the scissors-style opening geometry of the Lower Benue Trough. The ENE-WSW faults correspond to further change in the stress field orientation of the regional trend experiencing a wrench or pull-apart motion due to relative sub-plate movements from NE-SW to this current position (Fairhead et al., 2013). The N-S trending faults are approximately perpendicular to the ENE-WSW faults and correspond to compressional stresses in the later stage of the basin development due to the strike slip faults attributed to WCARS.

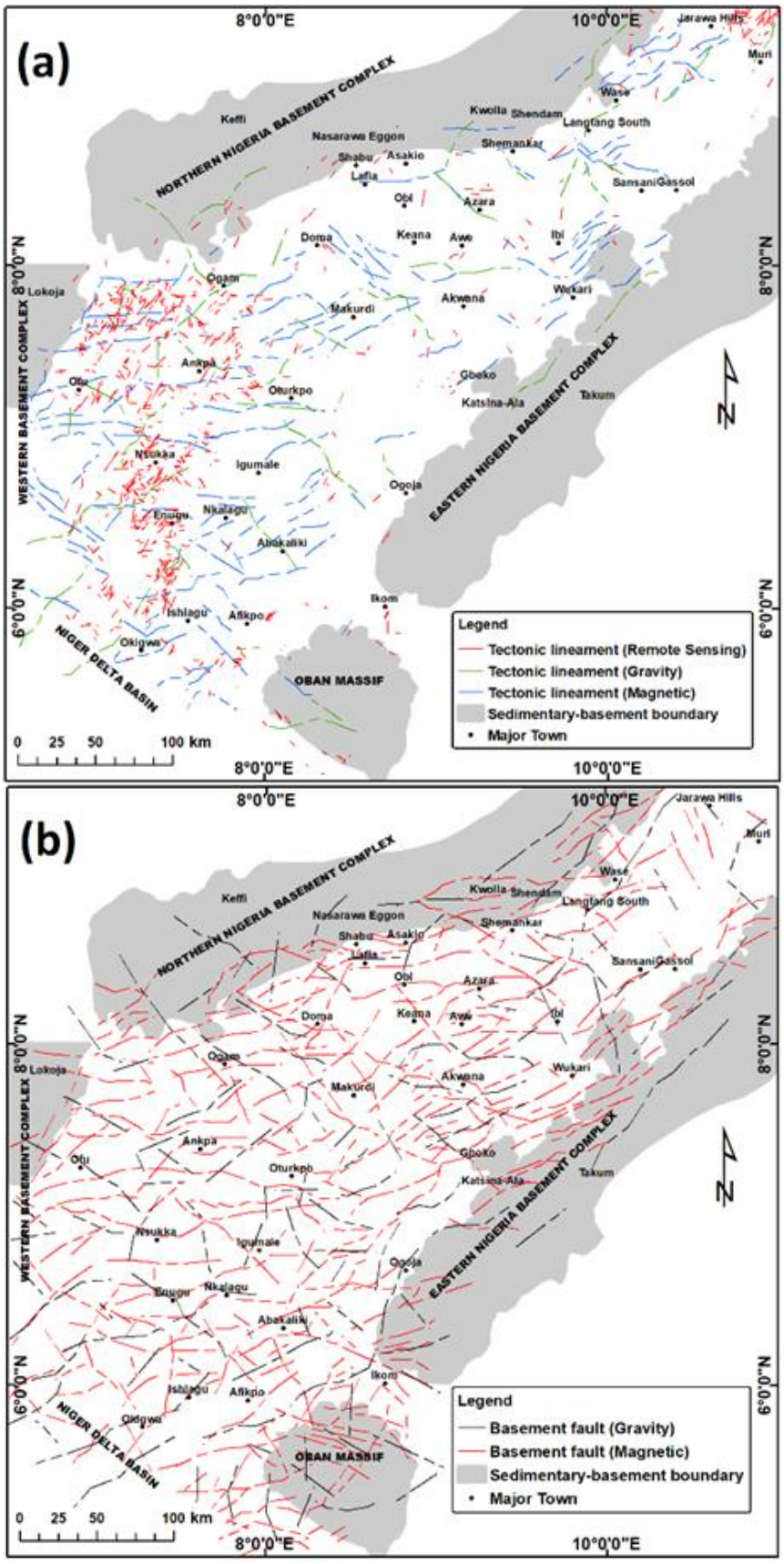

Fig. 7. 2: The tectonic map representing interpreted faults derived from the surface, shallow and deep data sets (remote sensing, gravity, and magnetic) (a) Surface/near-surface/shallow faults (b) deep faults.

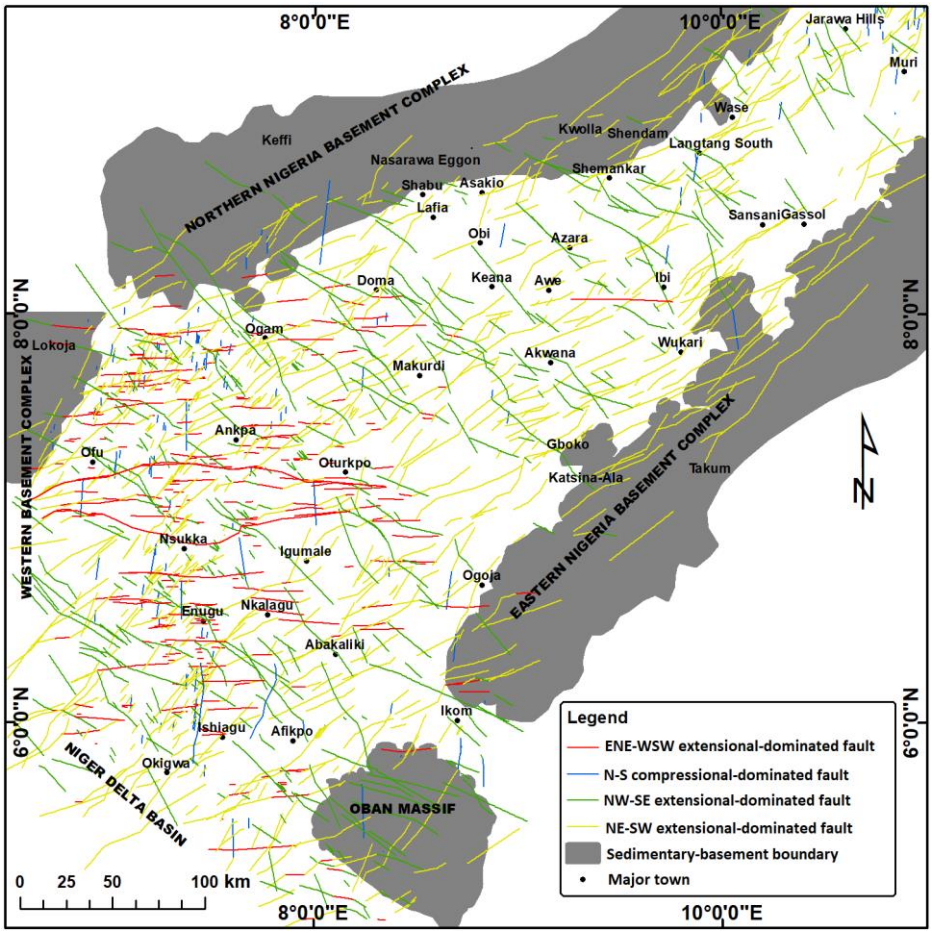

Fig. 7. 3: Interpreted tectonics map of the troughbased on combined analyses of multispectral, gravity, and magnetic data. The map shows fault trends in NE-SW, NW-SE, ENE-WSW, and N-S directions from all depths.

7.2.2 Fault kinematics and paleo-stress field interpretation

Rifting started in the Early Cretaceous (Aptian; 142-120 Ma) where the regional maximum extensional stress was approximately NNW-SSE (Guiraud and Maurin, 1992; Fairhead et al., 2013). This created NE-SW trending extension-dominated normal faults with some strike-slip components known as 'NE-SW normal faults' located in different parts of the basin (Fig. 7.4 a). The σ_3 is assumed to act horizontally while the σ_1 is vertical (Fig. 7.4 b). The regional maximum extensional stress (NNW-SSE direction) also enabled the development of the ENE-WSW trending normal faults in the late Aptian (Ajakaiye et al., 1991; Guiraud and Maurin, 1992; Fig. 7.4 a). They are fewer with similar fault kinematics as above, found mostly around the southern part of the study area, and are believed to be reflections of wrench faulting during the Aptian tectonic regime. During the Albian (119-101 Ma), regional sinistral strike-slip movements associated with the Central African Rift System (CARS) continued the opening of the trough as evidenced by the NE-SW extension in most of the basins in Africa (Fairhead and Green, 1989; Guiraud and Maurin, 1992; Fairhead et al., 2013). This extension is related to the NW-SE fault orientation of the trough when a normal faulting regime is considered (Fig. 7.5 a). The NW-SE normal fault kinematic is such that both the intermediate and the minimum stress axes are horizontal with the principal extensional stress axes acting parallel to the regional sinistral strike-slip direction i.e., NE-SW direction and the maximum stress axis acting vertically (Fairhead and Binks, 1991, Fig. 7.5 b). This indicates that there is a change in the orientation of the principal extensional stress axis from NNW-SSE to NE-SW i.e., giving it a dextral sense of movement but showing a form of sinistral kinematics along the NW-SE faults. The NE-SW trending faults are more dominant than the NW-SE faults and seem to accommodate most of the crustal extension during rifting.

Rifting continued until during the Late Santonian (84 Ma), there was shortening and compression with the maximum compressive principal stress orientated NNW-SSE i.e., a reversal of the stress pattern from the extensional stress field to the compressive stress field (Fig. 7.6 a). Here, the least compressive stress axis acts vertically (Guiraud and Maurin, 1992, Mamah et al., 2005, Fig. 7.6 b). This reversal in stress fields led to basin inversion and deformation of pre-existing sedimentary rocks through the reactivation of already formed fault networks (Binks and Fairhead, 1992; Fairhead et al., 2013). The NE-SW and the NW-SE normal faults were possibly selectively reactivated during this period since fault reactivation requires less energy than nucleation and localization of the orientation of the existing faults is appropriate, as in this case (i.e., the angle of these faults are assumed not to be too high nor too

low with respect to σ_1 (Fairhead and Binks, 1991; Lowell, 1995; Mamah et al., 2005; Guiraud and Bosworth, 1997). The Santonian event led to the compression of some of the deposited sediments resulting in the creation of folds and uplift of basement blocks, thereby creating anticlinal and synclinal structures with NE-SW striking axial traces e.g., the Keana and Abakaliki anticlines and, Afikpo synclinal structures. (Fairhead and Green, 1989; Guiraud and Bosworth, 1997; Fairhead et al., 2013). The inversion of this basin could have occurred with or without the presence of border faults as basin inversion can still occur within basement lows (Lowell, 1995) but here, basement uplifts and sub-basins are bounded by faults, and those areas where faults correlate with observed or interpreted anticlinal and synclinal structures are the most probable sites of inversion (Ajakaiye et al., 1991). Even though the interpreted faults around the basement blocks (horst-graben-like structures) can be reactivated, these data sets do not allow the determination of reactivation for any specific individual fault. Therefore, some of the faults with the potential to be reactivated were picked by correlating the faults with the observed and interpreted anticlinal structures from the field.

At the end of the Cretaceous around the Maastrichtian (65 Ma), another shortening event occurred due to the maximum compressive stress field slightly shifting to approximately N-S direction leading to folding, uplift, and faulting (Fairhead et al., 2013, Fig. 7.7 a). This event can be expected to have reactivated certain structural orientations with specific kinematics, evidenced in the E-W folds or the NE-SW and the NW-SE faults in a strike-slip sense, without producing significant folding. Here, both orientations must be regarded as equally optimal for reactivation during compression. σ_3 is expected to be vertical while σ_3 and σ_2 are horizontal (Fig. 7.7 b). Structures relating to this event have been observed in the the Upper Benue Trough (Guiraud et al., 1989; Benkhelil et al., 1998) but none have been identified in the southern part due to the presence of thick younger sedimentary cover. However, this study used high-resolution data sets which mapped deeper faults that are covered by sediments. The alternation of basement block uplift and down-warping during this period might have caused the formation of horst- and graben-like structures (Fairhead and Green, 1989; Fairhead et al., 2013).

A summary of the interpreted fault paleo-stress field orientations during the extensional phase of rifting (the Albian and Aptian times), and the compressional phase of the basin evolution (the Santonian and the End of Cretaceous) have been effective in fault kinematics study in Africa. In both cases, a sinistral fault and dextral extension movements were identified to be responsible for developing faults and basin geometry.

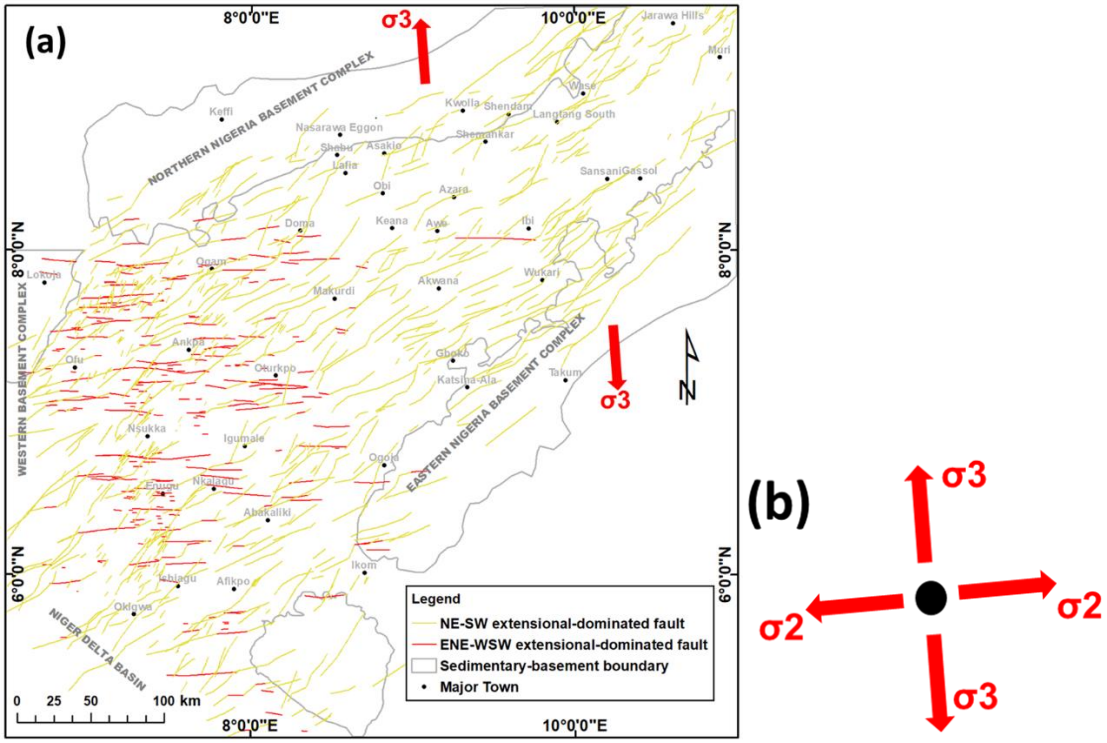

Fig. 7. 4: (a) NE-SW and ENE-WSW trending faults corresponding to normal faulting with some components of strike-slip faults. The maximum extensional stress axis is in approximately NNW-SSE direction during the Aptian (b) Interpreted fault paleo-stress field orientation during the extensional phase of rifting (Aptian).

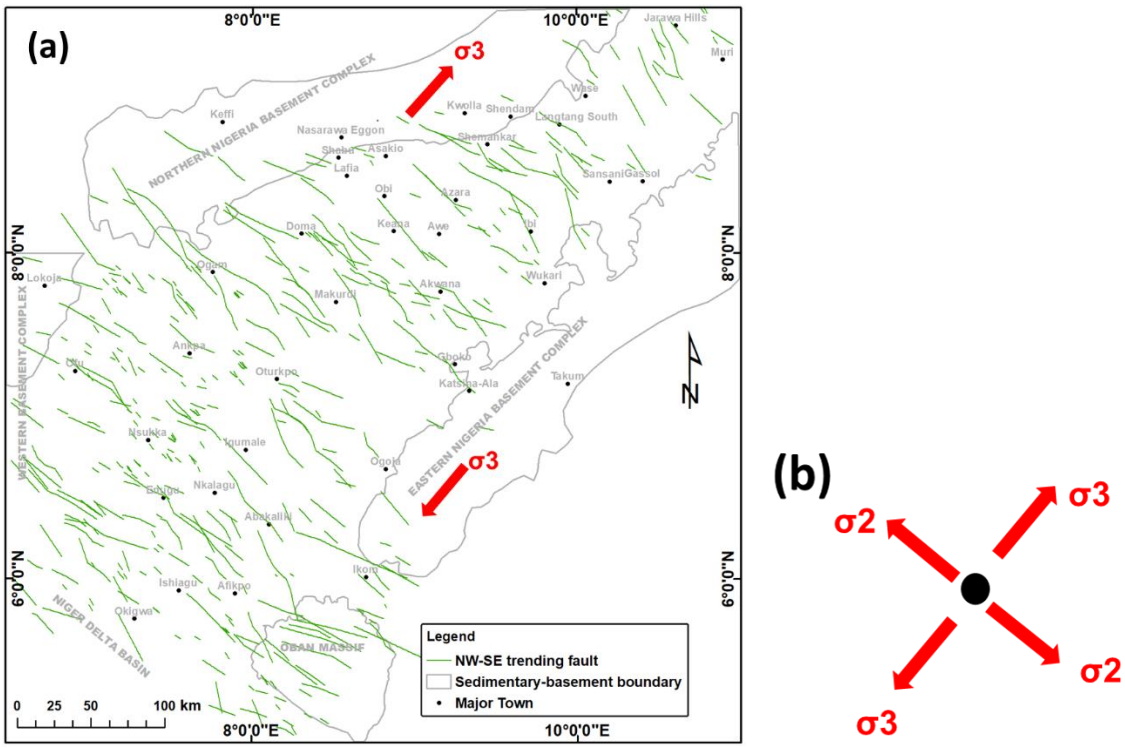

Fig. 7. 5: (a) NW-SE trending faults (Albian) with changes in stress fields due to advanced stage plate separation. (b) Albian fault kinematics where the tectonic model indicates sinistral fault kinematics and a general dextral extensional movement.

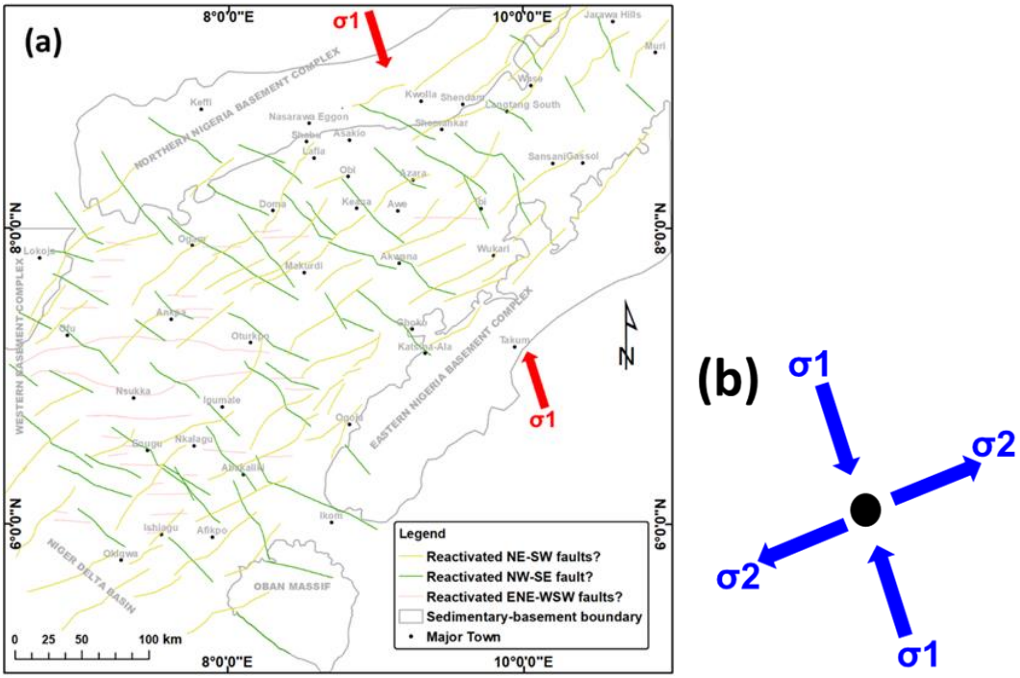

Fig. 7. 6: (a) Basin inversion during the compressional regime (Late Santonian 84 Ma) showing existing normal faults with high probability to be reactivated for inversion (showing reversed faulting). These interpreted faults were the NW-SE faults show a significant dextral strike-slip component makes it easy for basin inversion to cause the folding of pre-existing sediments. (b) Interpreted fault paleo-stress field orientation during the compressional regime (Santonian).

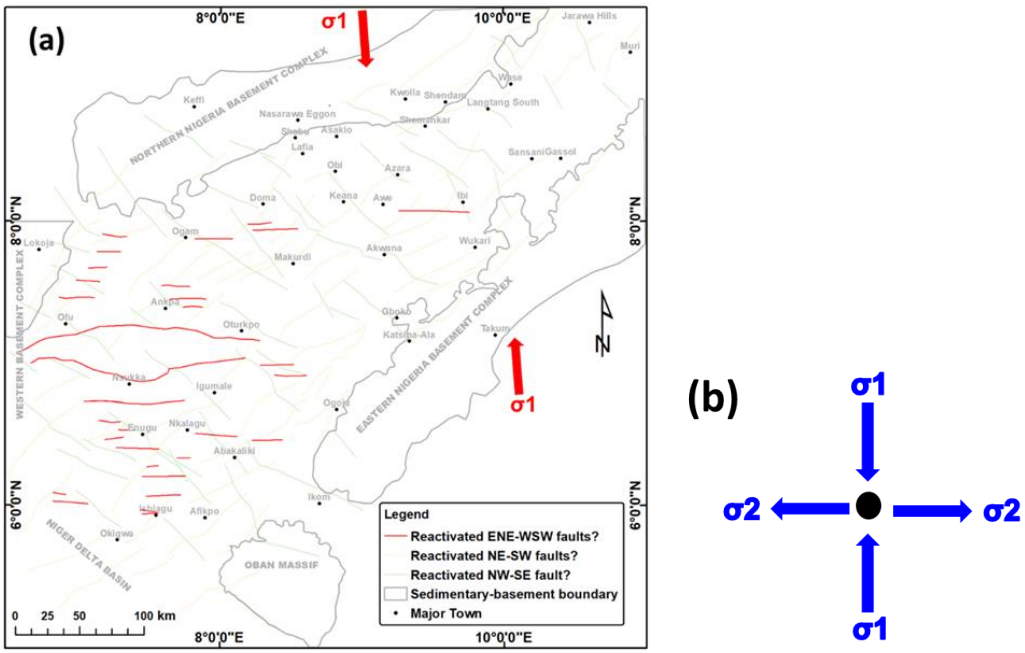

Fig. 7. 7: (a) End Cretaceous tectonics (65 Ma) with strong compressional event and reactivation of ENE-WSW trending faults leading to basement uplift/down-warping, folding, and faulting. (b) End Cretaceous fault kinematics. The tectonic model of the stress field indicates general fault movements over time and the compressional regimes allow reverse faulting and folding with σ_3 vertical.

7.3 Magmatic belts and paleo-stress field interpretation from dykes

7.3.1 Magmatic belts

Mapping the intrusive/extrusive rocks (volcanic rocks/sills and dykes) from shallow magnetic data and comparing them with the Moho interface mapped from 3D gravity inversion is significant in revealing and predicting the source, migration pathways, and emplacement patterns of the intrusive rocks. These rocks probably account for the major positive density anomaly observed in the middle part of the area (Fig. 4.13, Ofoegbu, 1984a). The dykes have two main orientations of NE-SW and NW-SE and are valuable in paleo-stress fault analyses. The intrusive/extrusive rocks are concentrated towards the eastern part of the trough along a general NE-SW trend direction, and similarly, the Moho interface is observed to have been uplifted directly under the intrusive/extrusive rocks in a major NE-SW trend (Fig. 7. 8). This obviously suggests that the source of the volcanic rocks, other intrusive rocks, and dykes is mainly from the mantle (Coulon et al., 1996), and their distribution is controlled by the presence of the faults as they align along a specific direction. The alignment within a zone of a general NE-SW trend shows restricted magmatism where most of the NE-SW faults are located. Also, this restricted zone of magmatism is an indication of extensional tectonic activity accompanied by magmatic emplacement (Ofoegbu, 1982; Ajayi and Ajakaiye, 1986) and indicating the zone where lithospheric extension is accommodated to give an asymmetrical shape. The depth to the top of the intrusive rocks/sills is estimated to be between 0.3 and 0.7 km while the shallowest depth to the Moho interface is 14 km (highest point of uplift). This implies that much energy is required for magmatic materials to migrate within or through a 13 km thick crust, and so many have exploited on existing fault system. Therefore, it can be interpreted that the migration pathways could probably be via existing NE-SW and NW-SE extensional trending faults since this will require less energy. This study has revealed that the eastern part of the trough documented the main magmatic event i.e., the magmatic centre of the trough.

Generally, igneous rocks were emplaced within the trough during the Early to Middle Cretaceous (147-106 Ma), Late Cretaceous (97-81 Ma), and Palaeocene-Eocene (68-49 Ma) (Ofoegbu, 1985; Coulon et al., 1996). The Upper Benue Trough has older emplaced igneous rocks than the Lower Benue Trough i.e., the emplaced rocks become younger from NE to SW. However, at larger scale within the Lower and the Middle Benue Trough, their ages vary less systematically. The sills and the volcanic rocks around Makurdi, Afikpo, and Oturkpo are 49

Ma, 55 Ma, and 60 Ma, respectively, and can be associated with the N-S compressional fault kinematic regime while the sills and volcanic rocks in areas like Gboko, Wanaka Hills, and Okigwe are dated to between 81 and 97 Ma (Coulon et al., 1996), and are associated with the compressional phase of the basin inversion with the reactivation of several faults. Magmatic activities also occurred around Gboko at 113 Ma, and so may correlate with the NW-SE paleo-stress field kinematics while the oldest recorded magmatic emplacement is around Abakaliki, which is Upper Albian in age and closely followed the NE-SW and ENE-WSW paleo-stress field kinematics (Coulon et al., 1996).

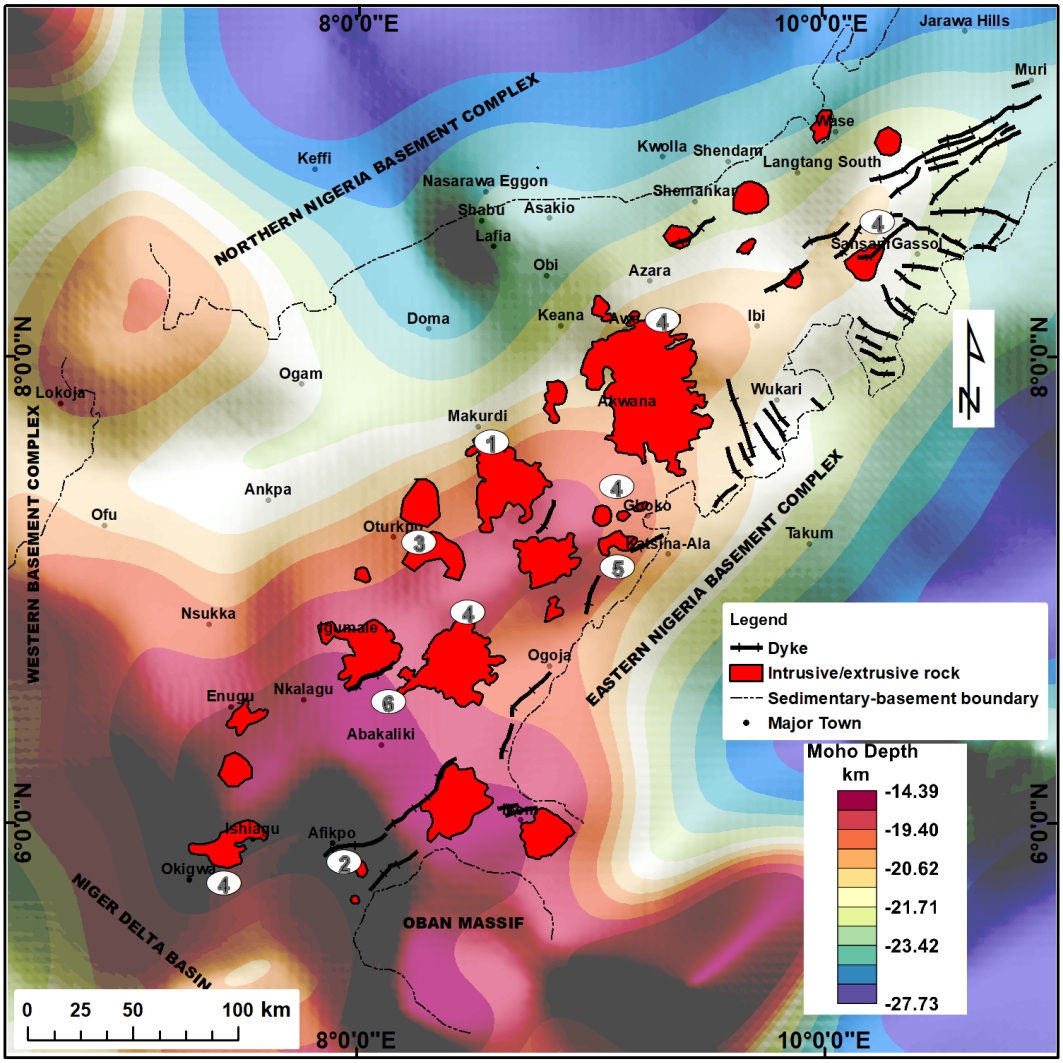

Fig. 7. 8: Magmatic zones constrained in a major NE-SW trend. The intrusive rocks (volcanic rock and the dykes) lie directly over the areas of the uplifted mantle (shallow Moho interface) indicating a possible mantle source. The circled numbers are sample locations for ages of the magmatic rocks. 1 = Markudi (49 Ma), 2 = Afikpo (55 Ma), 3 = Oturkpo (60 Ma), 4 = Gboko, Wanaka Hills and Okigwa (97-81 Ma), 5 = Gboko (113 Ma), 6 = Abakaliki (130 Ma).

7.3.2 Paleo-stress field interpretation from dykes

The geometries of dyke swarms can be used to approximate the regional or local stress states of an area during their emplacement (Walker et al., 2017; Stephens et al., 2017). The emplacement of dykes into extensional fractures helps to preserve the stress-strain relationships and sometimes gives an idea of paleo-stress regimes (Fossen, 2010). The strike direction of a dyke is usually normal to the direction of least compressive stress acting at the point of intrusion (Delaney and Gartner, 1997; Delaney and Pollard, 1982). When dykes infill extensional fractures, they are formed at a high angle to the least principal stress, σ3 (Titus et al., 2002; Fossen, 2010). Thus, the least principal stress is perpendicular to a dyke's strike direction (Fig. 7.9). The orientations of σ_3 can also be determined using offset i.e., a break in a long trending dyke showing displacement (Fossen, 2010) and help in determining the local stress of the area. The spatial distributions of the dykes within the area shows two main trends: NE-SW and NW-SE trends.

The paleo-stress regime associated with dyke intrusion can be determined by analysing the NE-SW trending dyke swarms and comparing them with existing regional tectonics. The minimum principal stress direction, σ_3, can be approximated by passing a straight line across the offset, perpendicular to the dykes in the area (red circles) in fig. 7.10 a (Fossen, 2010). The orientation of σ_3 perpendicular to the NE-SW trending faults signifies that the kinematics appropriately describe the geometry of dykes that might have infilled existing or created extensional faults. The paleo-stress kinematic model is interpreted to be that the maximum principal stress axis, σ_1, acts vertically while the intermediate principal stress axis is parallel to the NE-SW trending faults, if the intrusion of the dykes occurred during the rifting stage (Albian-Aptian) (Fig. 7.10 b). Also, it can be deduced that the NE-SW trending dykes might have been emplaced after the formation of the normal faults (NE-SW extensional normal faults) since magmatic activities have been recognized to have occurred from the Late Aptian to Eocene (Coulon et al., 1996). Therefore, it is probable that the NE-SW trending dykes are the oldest within the trough since the NE-SW faulting is believed to have occurred before Aptian time. The NE-SW dykes remain perpendicular to the NW-SE direction of extension but parallel to the faulting trend, hence, confirming the fault kinematic history of the area.

The paleo-stresses in the case of the NW-SE trending dykes can best be explained if they are assumed to have been emplaced during the tectonic extensional regime. This implies that the maximum extensional principal stress axis, σ_3, has changed its orientation, and acted

perpendicular to the dykes with NE-SW extension causing structural dilation suitable for magma emplacement (Walker et al., 2017; Stephens et al., 2017). The maximum principal stress axis, σ_1, is assumed to also act vertically but the intermediate principal stress axis is parallel to the strike direction of the dykes (Fig. 7.11 a). This paleo-stress field and dyke orientation agree significantly with the NE-SW extension caused by the sinistral strike-slip movement that affected the WCARS during the Albian (Fairhead et al., 2013) and contemporaneous with the emplacement of magma within the basin (Coulon et al., 1996) i.e., the NW-SE trending dykes could be younger than the NE-SW trending dykes. Hence, the paleo-stress regime can be constructed such that the intermediate and minimum principal stress axes are all horizontal and perpendicular to each other while the maximum principal stress is vertical (Fig. 7.11 b).

Therefore, the NE-SW dykes were emplaced possibly during the Aptian (about 145 Ma) and are probably older than the NW-SE dykes. Other igneous intrusions could be associated with this paleo-stress orientation such as the magmatic bodies around Abakaliki (130 Ma) while the NW-SE dykes could have been emplaced later, during the Albian (about 113 Ma). The NW-SE dykes and the paleo-stress field kinematics are believed to be associated with emplacements of magmatic activities around Gboko (113 Ma) (Coulon et al., 1996).

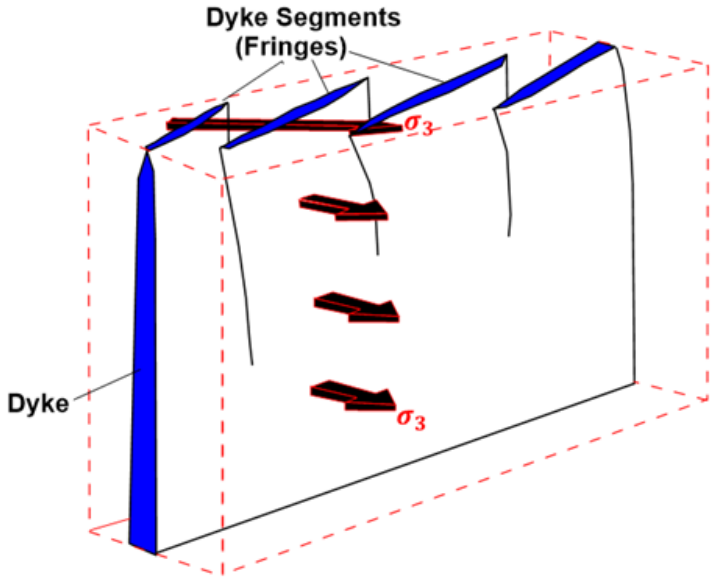

Fig. 7. 9: The en-echelon dike systems that are interconnected at depth during magma intrusion with described extensional forces (Fossen, 2010).

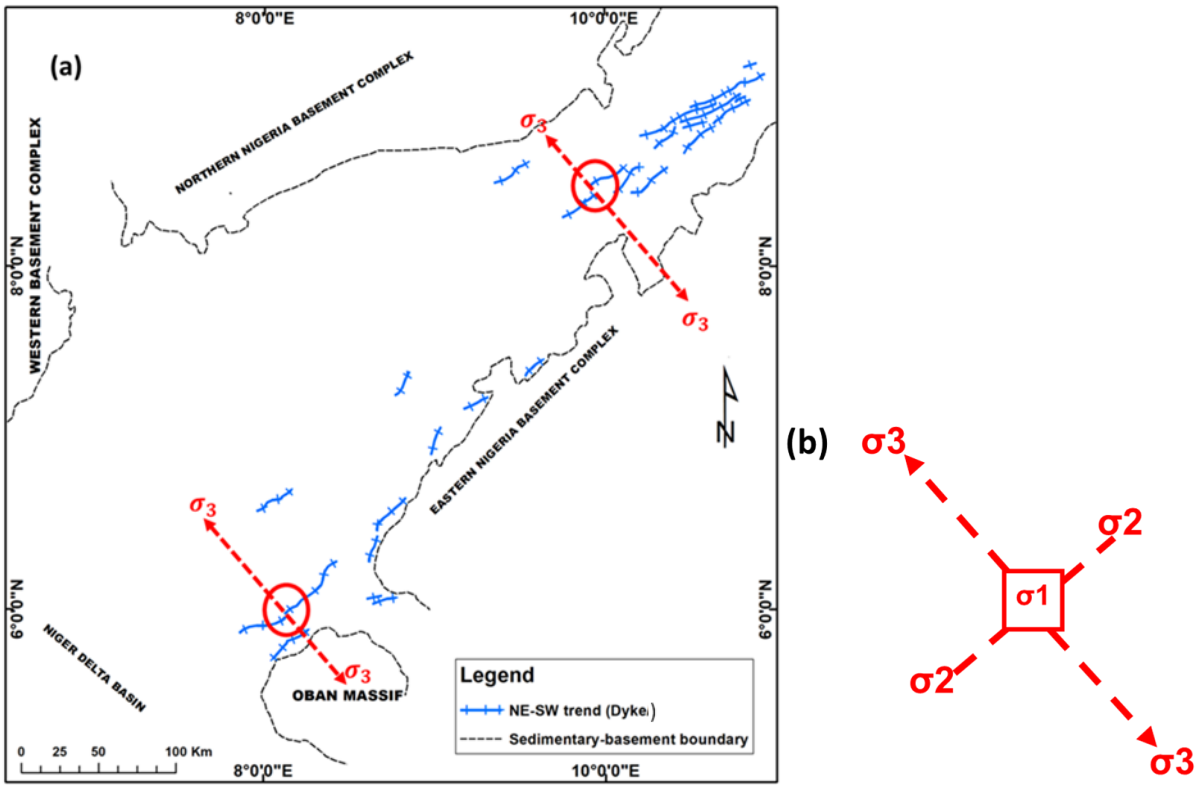

Fig. 7. 10: Distribution of NE-SW trending dyke swarms (a) Dyke offset indicating the direction of minimum principal stress (b) Interpreted paleo-stress orientation from dyke offset. σ_1, σ_2, and σ_3 are maximum, intermediate, and minimum principal stress axes, respectively.

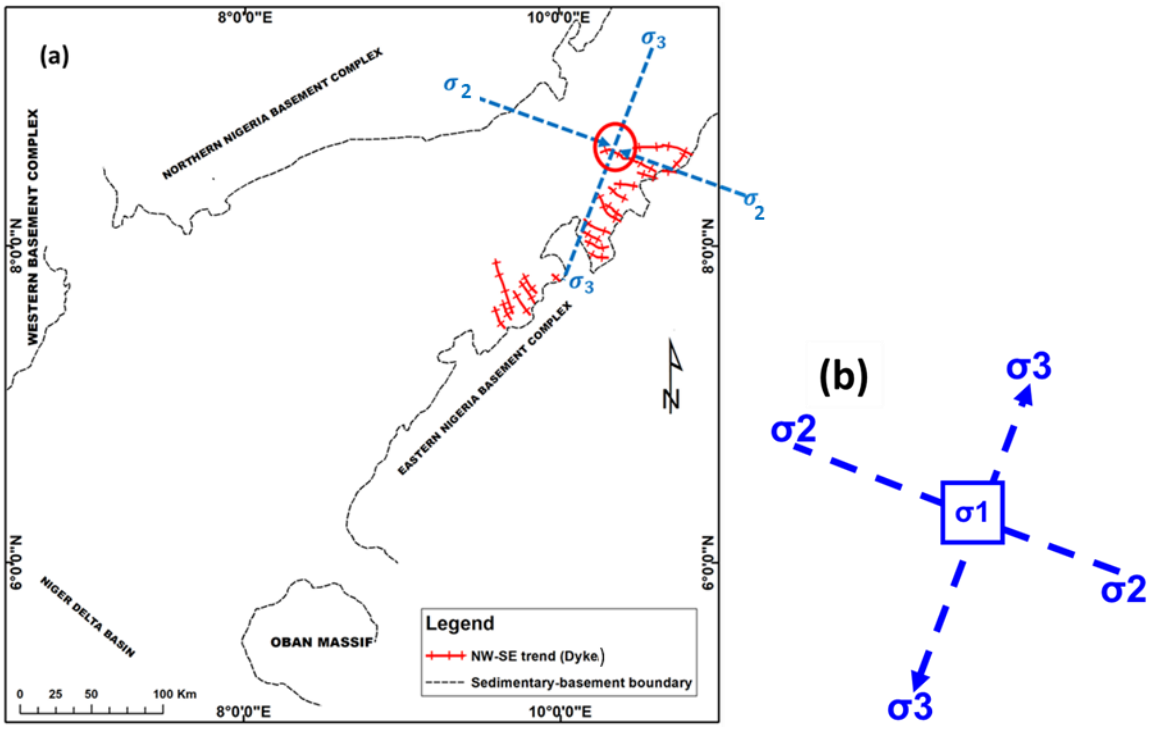

Fig. 7. 11: Spatial distribution of dyke swarms trending in major NW-SE directions (a) Dyke offset indicating the direction of minimum principal stress (b) Modelled paleo-stress orientations from dyke offset. σ_1, σ_2, and σ_3 are maximum, intermediate, and minimum principal stress axes, respectively assuming that the NE-SW and NW-SE dykes resulted from conjugate extensional faults.

7.4 Crustal structure of the basin

The crustal structure was obtained from 3D basement depth and 3D Moho estimates (Figs. 5.25 and 5.36, respectively). The crust is observed to be stretched and thinned across the trough and the amount of stretching increases from north to south i.e., from 93 km in the north to 142 km in the south, which gives a scissor-like style geometry in plan view (section 4.4). Crustal stretching and extension combined with Moho uplifts are believed to have caused crustal thinning observed directly beneath the centre of the trough. The southern part of the trough has a thinner crust than the northern part with the smallest crustal thickness of about 9 km in the south compared to 13 km in the north. The southern part of the area with the largest stretching distance relates well to the high value for the stretching factor here. The area showed crustal thinning at the centre of the trough with a stretching factor greater than 2 during extension (Fig. 7.12 a, section 5.5.2). The stretching factor increases from 2.79 in the north to 4.49 in the south along the centre of the trough. Mckenzie and Bickle (1988) observed that extension of continental lithosphere generates melts of alkali basalts and tholeiites when the beta or stretching factor and mantle potential temperature are greater than 2 and 1380℃, respectively. It has been implied earlier from this study that the source of the magma emplaced within the trough is from mantle materials as areas of shallow Moho correspond to the zone of magmatic activities. In the same way, areas of crustal thinning with higher stretching factors correspond to the areas of magma intrusion (Fig. 7.12 b).

The value of β and the duration of rifting can be used to help understand and model the amount of heating i.e., mantle temperature and predict the amount of melt expected from the mantle to cause the emplacement of magmatic materials within the trough (Watts, 2001). The main duration of rifting for the area lasted for a period of about 25 Ma i.e., rifting commenced during the Early Aptian (125 Ma) and ended around Upper Albian (100 Ma), giving way to thermal relaxation and subsidence in the Cenomanian (Fairhead et al., 2013). The stretching factor developed through time changes from 1.78 to 4.49 (hatched rectangle in Fig. 7.12 c). Factors of between 2.5 and 4.5 (within green shade) indicate that the mantle temperature to cause some significant melt is 1400℃ (Fig. 7.12 c). This melt is predicted to be formed for a period of 25 Ma after the initiation of rifting observed from the main rifting phase (the green line). Thus, in order to produce a melt for such duration recorded for the main rifting from literature requires a stretching factor greater than 2 (Calvès et al., 2012). A long rifting period of 25 Myr is usually expected whenever estimation of mantle melts is done using β factor within the continent (Mckenzie and Bickle, 1988).

Stretching factors in relation to the dykes/sills/volcanic rocks at the eastern part of the study area indicated values ranging between 2.5 and 4.5 (Fig. 7.13 a). The thickness of the melt produced for the stretching factors of between 2 and 5 and a mantle temperature of 1400 ℃ is about 9 km (green arrowheads in Fig. 7.13 b). The areas that show high mantle temperature (1400 ℃) and stretching factor (between 2.5 – > 4.5) correspond to areas of shallow Moho or Moho uplift which implies that the lithosphere has been stretched and hot material has been brought to shallower depth thereby increasing the temperature of the surrounding host rock. Therefore, the melt thickness of about 9 km has demonstrated that the amount of stretching calculated and the duration of rifting is compatible with the large amount of magmatism that occurred during Aptian-Albian (Fig. 7.13 b). The amount of emplaced magma within the trough is shown to be smaller than the amount calculated. A large amount of the generated magma is believed to have been emplaced along the Cameroon volcanic line in the eastern part and along the Jos volcanic line in the North-western part of the area (Ajakaiye and Burke, 1973; Deplaen et al., 2014). These areas of shallowing Moho also correspond to the areas of crustal thinning and shallow Curie depth. The shallow Curie depth is mainly towards the eastern part of the trough where the magmatic intrusion is prominent and can connote low $T_{e,}$ i.e., implying that the lithosphere has been weakened by heating and by being intruded to some extent over time (Jiménez-Díaz et al., 2014).

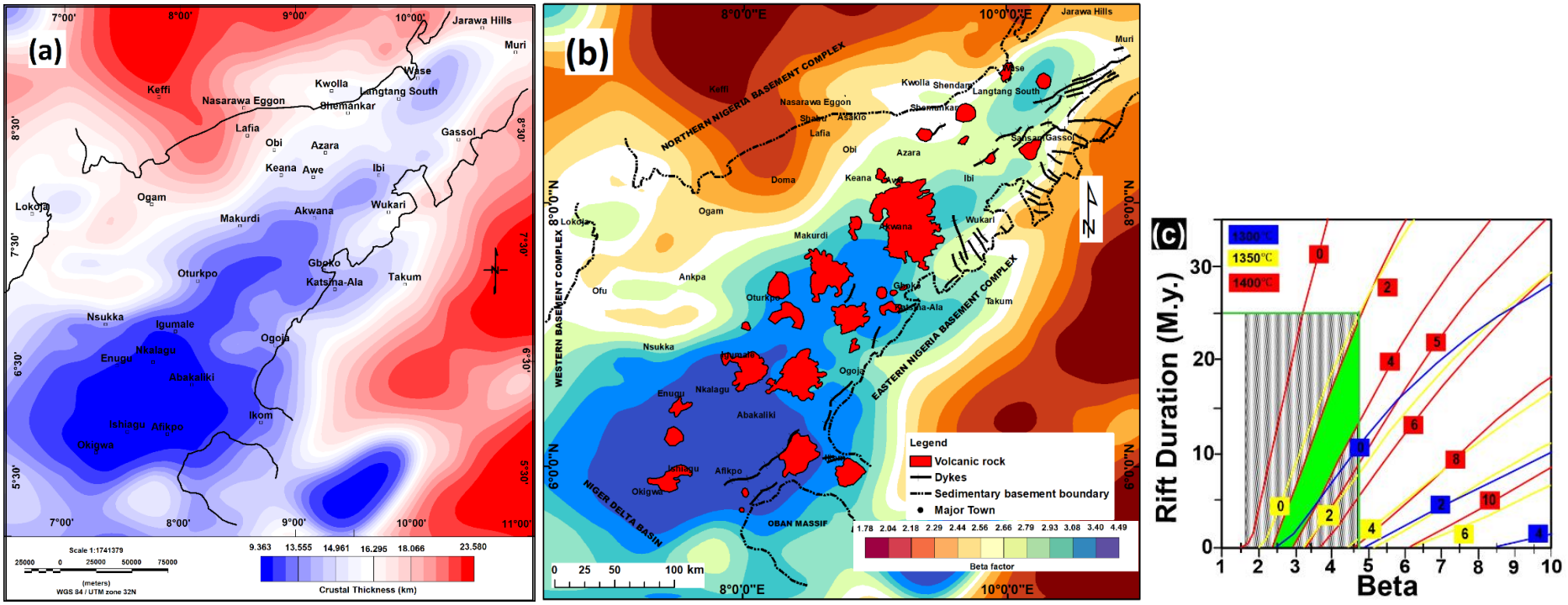

Fig. 7. 12: (a) Crustal thickness map of the area with the crust thinned towards the centre due to stretching and mantle uplift (b) stretching factors with intrusive rocks overlaid on it. Areas of high stretching factor correspond to zones of magmatic activity (intrusive rocks) (c) Plot to predict the control of stretching factor during rifting and the rift duration on melt production (modified after Calvès et al., 2012). The grey hatched rectangle represents stretching factor 1.78-4.49 for a rifting duration of 25 Myr (Calvès et al., 2012) while the green block indicates a stretching factor of 2.5-4.5 that models a rifting duration of 25 Myr from this study at 1400℃.

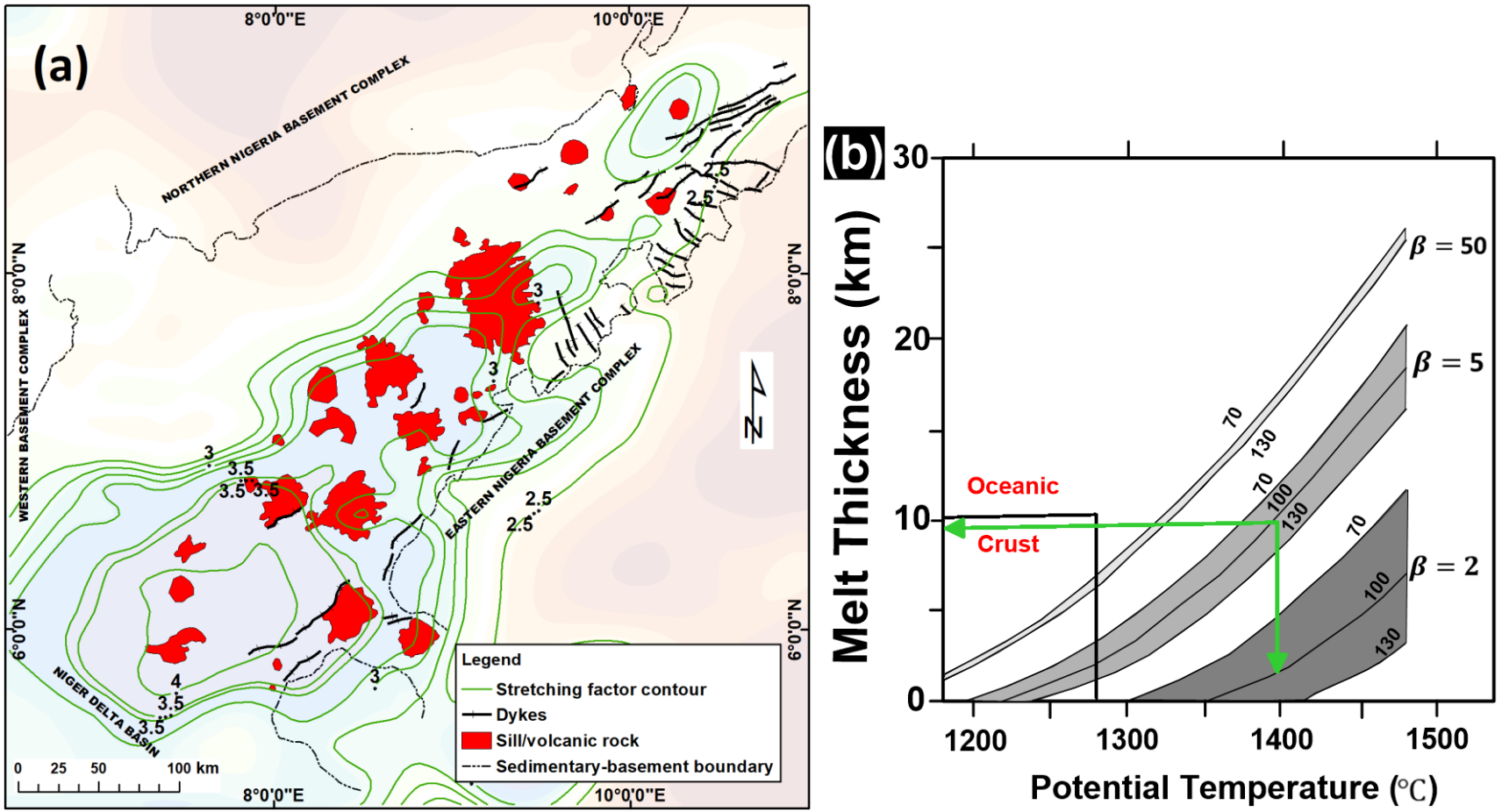

Fig. 7. 13: (a) The relationship between stretching factors (Stretching factors) and dykes/sills/volcanic rock (b) Predictive melt thicknesses obtained from adiabatic decompression of mantle for several temperatures (modified after Calvès et al., 2012). Diagram from the literature that has been added data from this study to predict melt thicknesses.

7.5 Tectonic evolution model of the Lower and Middle Benue Trough

The interpretation of remote sensing, gravity, and magnetic results from this study indicated crustal stretching and thinning during rifting of the trough with the development of normal faults trending in different directions of NE-SW, NW-SE, ENE-WSW, and N-S. These faults are spatially distributed across the whole area and bound the trough at both flanks as well as the sub-basin and the uplifted basement blocks. Results of interpretation also indicated that the faults are deep-seated and show sinistral-type movement during the main deformation regimes i.e., the extensional and compressional deformation periods. The extensional phase is believed to be the time where most of the faults were formed but when the stress field direction late reversed during the compressional phase, many of the faults were reactivated (i.e., a period of basin inversion saw several features such as horsts-like, grabens-like, sub-basins, and uplifted basement blocks develop). This study also showed that Moho shallowed right beneath the trough with the injection of mantle materials through the faults and possible heating of the crust. The emplacement and geometry of the intrusive/extrusive rocks (volcanic rocks, plugs, sills, dykes, etc.) in a specific location indicated that they are fault-controlled as observed by their concentration towards the eastern part of the trough which is believed to be zones that accommodated the major effect of the crustal stretching.

Based on all the information and interpretation of results obtained from this study and relevant works of literature, a more robust tectonic evolution of the basin is suggested below;

- Early Aptian time (142-120 Ma) marks the beginning of the development of the Lower and Middle Benue Trough. Rifting was initiated during this time along the line of the proto-South Atlantic as a result of the separation of South America and Africa plates (Binks and Fairhead, 1992). The regional maximum extensional stress acted in an NNW-SSE direction (Fairhead et al., 2013). Fault kinematic analyses and interpretation from this study indicated that the NE-SW trending faults were developed as extensional normal faults during this period. The extensional regime also showed that the faults created pathways for the emplacement of mantle materials on the basement and within the trough. Moho was uplifted beneath the trough a decompressing and melting to provide magmatic materials that are evident today as the basin's igneous rocks. Among these, the NE-SW trending dykes are interpreted to have been emplaced during this time. Some of the volcanic rocks/sills dated over the area show that magmatic bodies around Abakaliki are as old as 130 Ma, and so are interpreted to have been emplaced

during this period too (Fig. 7.14 a). During the Upper Aptian, there was a shift in σ_3 to N-S, leading to the development of ENE-WSW trending faults. Results from this study indicated that the faults are mainly located in the southwestern part of the basin (Fig. 7.14 b).

- During the Albian (119-101 Ma), the rift continued to develop in the area. However, this phase is characterized by a change in the orientation of the principal extensional stress axis from a NNW-SSE orientation to NE-SW. This is due to the regional sinistral transcurrent movements associated with the Central African Rift System (CARS) attributed to the advanced differential opening of the Central and South Atlantic Oceans (Fairhead and Green, 1989; Guiraud and Maurin, 1992; Fairhead et al., 2013). The results of this study indicate that the NW-SE faults fit into the regional NE-SW extensional regime (Fig. 7.14 c). This implies that the maximum principal stress field is vertical, to enable the formation of NW-SE normal faults. Again, these NW-SE trending normal faults may be suitable pathways for the emplacement of NW-SE trending dykes i.e., the dykes have infilled the NW-SE normal faults as a result of shallowing Moho leading to melting and emplacement of magma within the faults. Sills were emplaced around Gboko in 113 Ma which correspond to the period of rifting. Rifting and the emplacement of magmatic materials continued into the period between Cenomanian (100 Ma) and Early Turonian (85 Ma) but thermal relaxation or subsidence took prominence at these times (Fairhead et al., 2013).
- During the Late Santonian (84 Ma), there was a reversal in stress orientation leading to the extensional phase to give way to a compressional phase leading to basin inversion, fault reactivation, shortening, and the deformation of pre-existing sediments (Mamah et al., 2005; Guiraud and Bosworth, 1997). The maximum compressive principal stress was orientated NNW-SSE, leading to the reactivation of most of the basins, sub-basins, and uplifted block bounded faults (Guiraud and Bosworth, 1997). This study interpreted that the NE-SW and NW-SE normal faults, especially the bounding faults, were reactivated during basin inversion (Fig. 7.15 a). This event resulted in the folding and produced basement uplifts and basins such as the Wase, Wukari, Afikpo, Makurdi, Abakaliki, Ogam, Nsukka, Keana sub-basin/uplift, and Ishiagu uplift. Again, during this period, volcanic rocks/sills mapped around Gboko, Wanaka Hills, and Okigwe, etc. estimated to be 87-91 Ma in age correlates with this tectonic event (Coulon et al., 1996).

- The compressional phase continued right to the end of the Cretaceous around the Maastrichtian (65 Ma). This period is marked by a compressional phase with further shortening. The maximum compressive stress field slightly shifted to approximately N-S direction leading to strong folding, uplift of basement blocks, and faulting (Fairhead et al., 2013) of mainly the ENE-WSW trending faults. The ENE-WSW trending faults are deep-seated continental faults were easily reactivated in the N-S compressive stress field (Guiraud et al., 1989; Benkhelil et al., 1998; Ajakaiye, 1975). These faults are located mainly in the southern part of the basin and, based on the regional compressive regime, the results indicated that the least maximum stress axis is vertical leading to the uplift of the southern part of the basin (Fig. 7.15 b). Horst-like and graben-like structures were developed as a result of fault reactivation bounding the uplifted and subsided basement (Fairhead and Green, 1989; Fairhead et al., 2013). This event is marked by the associated emplacement of the Palaeocene-Eocene (68-49 Ma) igneous rocks (Coulon et al., 1996).

In summary, the findings of this study showed two main tectonic regimes; the extensional and the compressional regimes. The tectonic development model of the area, in general, supports the idea that doming of the mantle occurred due to rifting without specific heating. The outcomes from this study are fundamentally in agreement with the proposed plate tectonic model responsible for the evolution of the basin (McKenzie 1978; Fairhead and Green 1989; Fairhead et al. 2013) as discussed in Chapter one. Also, it showed that the deep-seated faults control the boundaries of the main basin, the sub-basin, and the uplifted basement blocks as well as the emplacement of magmatic materials. Therefore, the tectonic model involves rifting, crustal stretching, and thinning as well as Moho uplift or doming and magma emplacement within the basin. These may henceforth indicate the characteristics of an aulacogen development (Klein, 1990; Klein, 1991).

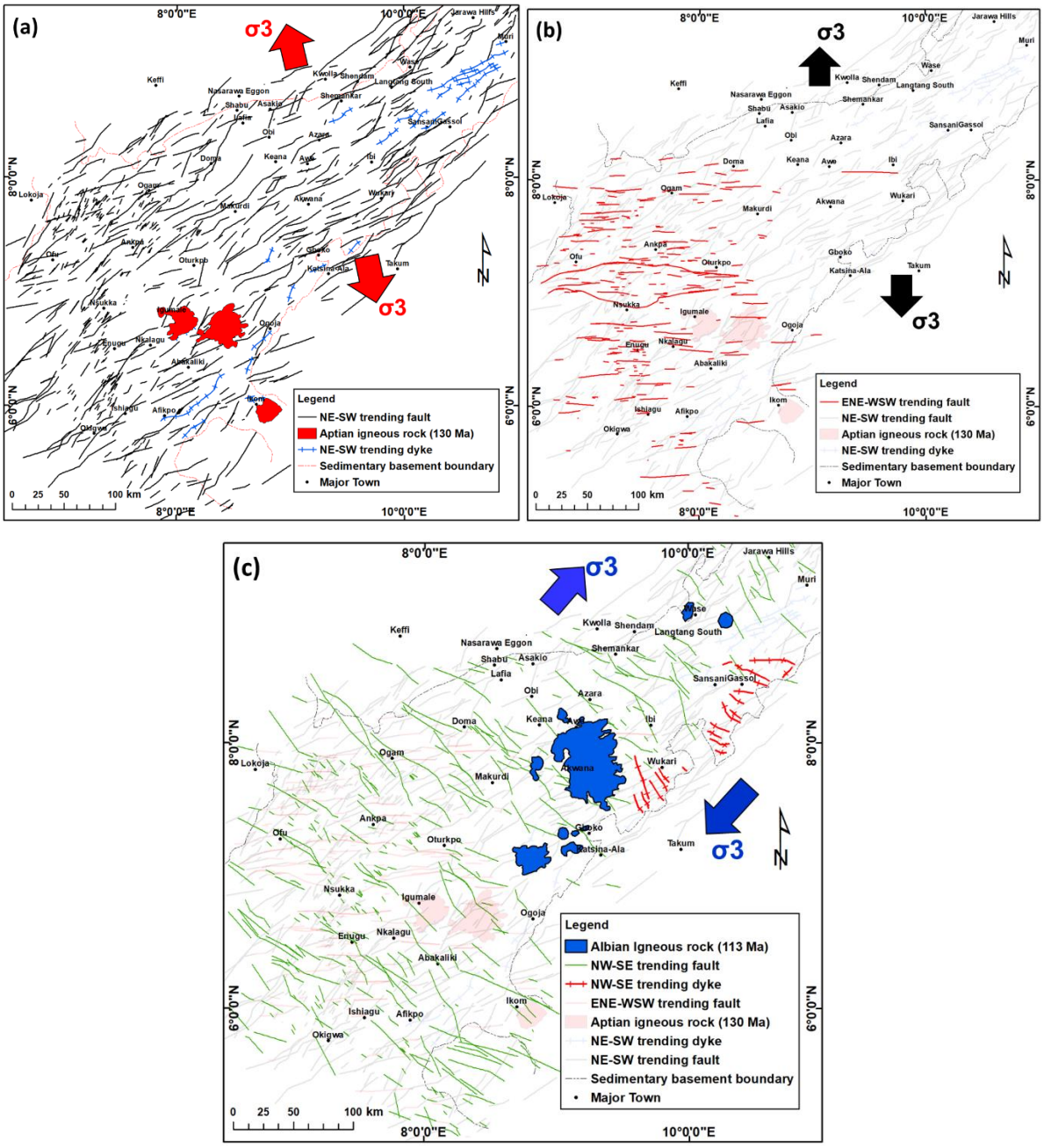

Fig. 7. 14: Extensional tectonic regime (a) NE-SW trending normal faults where the maximum extensional stress axis is NNW-SSE and occurred during the Aptian. (b) ENE-WSW trending normal faults with the maximum extensional stress axis shifting slightly to the right to an N-S direction. (c) NW-SE trending normal faults (Albian 119-101 Ma) with changes in stress fields due to advanced stage plate separation. This event assumes that σ_1 is vertical.

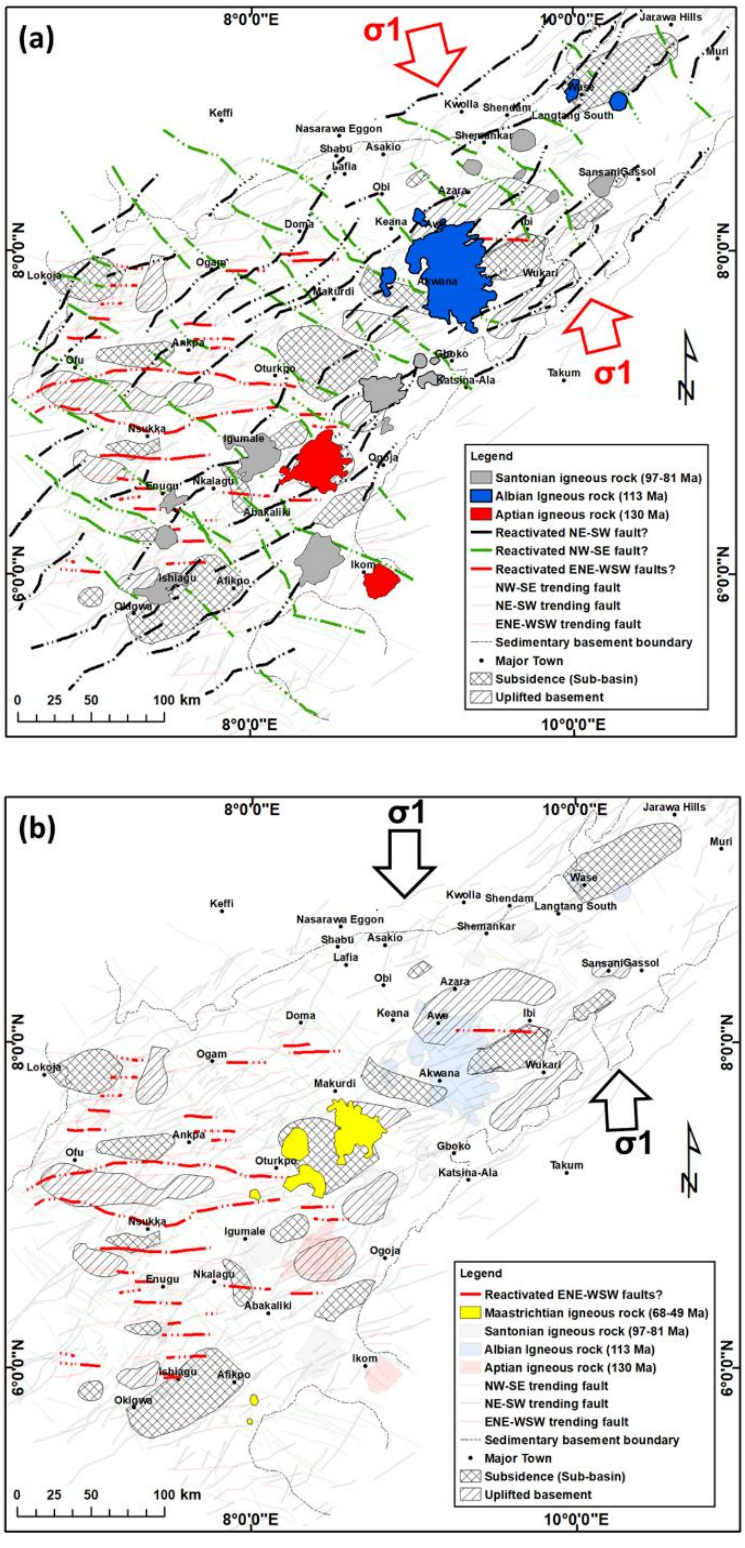

Fig. 7. 15: Compressional tectonic regime showing reversal in stress field axes from extensional to compressional (a) Basin inversion of the compressional event (Late Santonian 84 Ma) showing existing NE-SW, NW-SE, and ENE-WSW normal fault reactivated inversion. (b) Basin reactivation of the ENE-WSW trending faults and emplacement of igneous rock (intrusions identified during the Maastrichtian). The maximum compressional stress field is in the N-S direction with the least compressional stress field acting vertically.

7.6 The geological and tectonic interpretation from the 2D and 3D models

The updated geological map of the Lower and Middle Benue Trough indicated that the faults penetrated deeply through the sediments and into the basement and thus are evidence of the response to external regional movements. The basement faults are deeply seated and trend in NE-SW, NW-SE, ENE-WSW, and N-S directions. These faults, with the emplaced magmatic intrusive/extrusive rocks (volcanic, plugs, sills, and dykes), were combined with the 2D magnetic profile models, the 3D gravity, and magnetic depth map to provide a more robust understanding of the trough in the subsurface. Four profiles perpendicular to the major basin trend were selected (Fig. 7.16).

Results from the combination of faults and, 2D and 3D gravity and magnetic models were integrated to construct a tectonic model of the area and presented in 2D sections. Fig. 7.17 (a) indicates several major faults flanking the ends of basement uplift or subsidence and within the basin. These faults are interpreted as high-angle normal faults believed to control the geometry of the trough along the profile by showing areas of basement uplift and subsidence. They also act as suitable pathways for the migration of mantle materials evident by the presence of volcanic rocks/sills and dykes i.e., the magma movement through the crust indicates the presence of very deep-seated fault(s) that possibly penetrate all the way to the mantle where the melts are sourced. Here, Moho and the Curie depth are shallow, indicating the rise of mantle materials and a high amount of heat flow. The crust has been stretched and thinned over time and eventually, the Moho shallowed with the emplacement of mantle materials. At the middle part of the trough where profile P3-P4 was picked, the faults are interpreted as normal faults and describe general basement subsidence with basin bounding faults observed (Fig. 7.17 b). The maximum sediment thickness along this profile is 6.7 km. The presence of a large block of igneous intrusion within the sediments, bounded by high angle faults is an indication of the magmatic emplacement within the trough. Significant features such as Keana and Lafia anticlines have been identified towards the left side of the profile where there is thick sedimentation probably formed during the compressional phase tectonics. The Moho interface shallows beneath the basin while the Curie depth is down warped due to cooling or emplacement of the igneous body i.e., the emplacement of the igneous body increases the temperature as the Curie depth shallows but after time, the igneous material cools as the high temperature and initial temperature are not replaced by radiogenic heat. Again, the heat flow is high across the profile which makes it interesting for geothermal resource exploration. The crust indicated that it has been stretched during extensional rifting also. Fig. 7.18 (a) represents

profile P5-P6 and indicates the emplacement of a large mass of volcanic rocks/sills within and on the crust. The profile shows a wider basin with a maximum sedimentary thickness of 6.6 km. Horst-like and graben-like structures have been mapped along the profile, where areas that show shallowed basement are accompanied by deep basement, Curie point depth, and Moho interfaces. Fig. 7.18 (b) represents profile P7-P8 cutting across significant structural features such as the Abakaliki anticlinorium and Anambra sub-basin. Most of the faults are interpreted as normal faults based on their assumed direction of movement and seem to bound the major structural features along the profile. The maximum sedimentary thickness across the profile is about 7.5 km which is deeper than all the other profiles. Crustal extension, thinning and dyke intrusions are identified under the basin with shallowing of Curie and Moho depths.

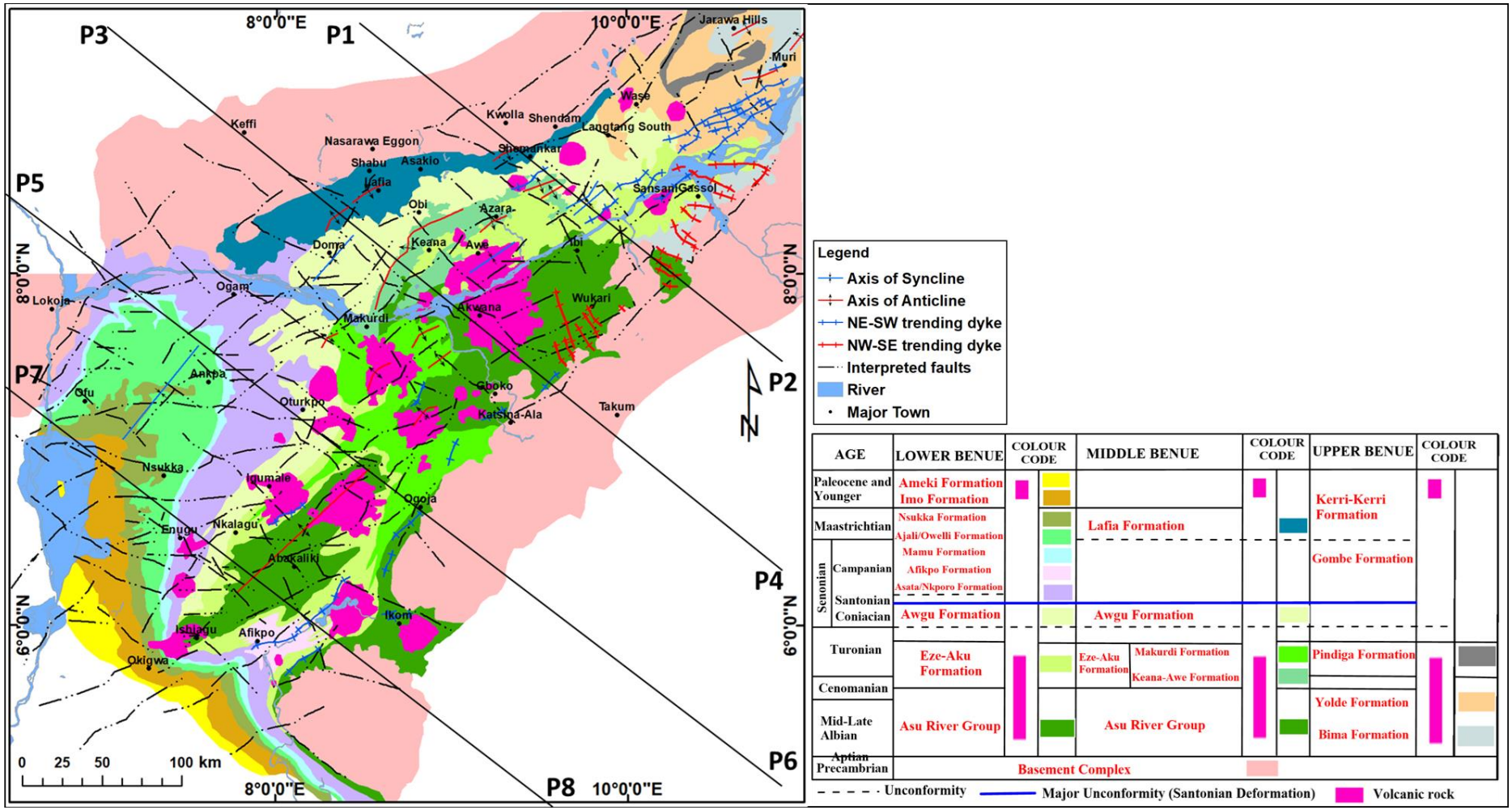

Fig. 7. 16: Interpreted and updated geo-structural map showing the fault framework of the Lower and Middle Benue Trough from remote sensing, gravity, and magnetic data sets. Four profiles (P1-P2, P3-P4, P5-P6, P7-P8) were drawn perpendicular to the major NE-SW structural trend.

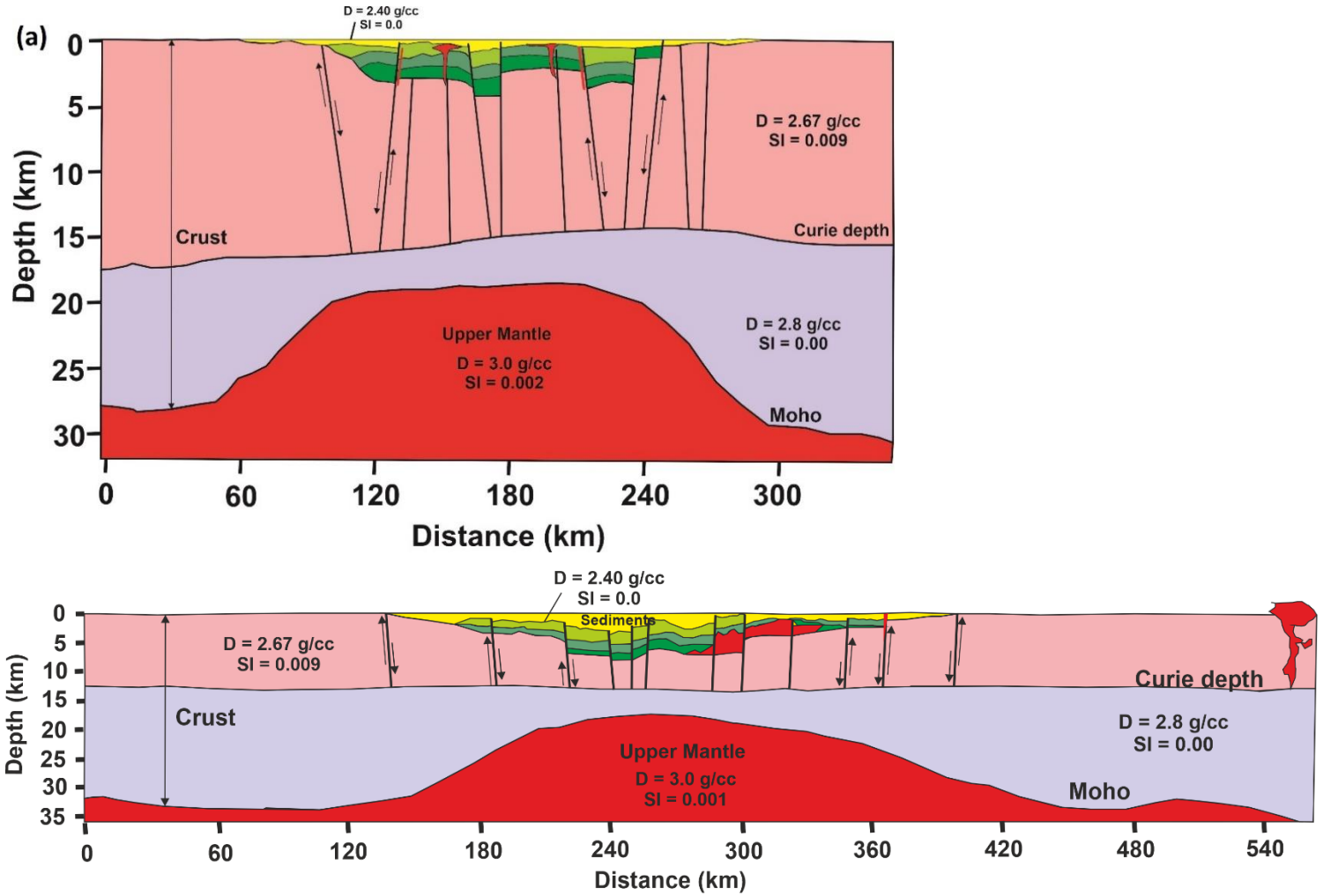

Fig. 7. 17: 2D sections of interpreted tectonic model showing three basic interfaces; the basement depth, the Curie, and the Moho interfaces (a) Along profile P1-P2 (left-right). (b) Along profile P3-P4 (left-right). Faults are represented by thick lines with black arrows indicating the direction of movement. Intrusive rocks and the dykes are indicated by red polygons and red thin-lines respectively. Crustal thinning and injection of magmatic materials are observed along the profile. Vertical scale exaggeration is X3.

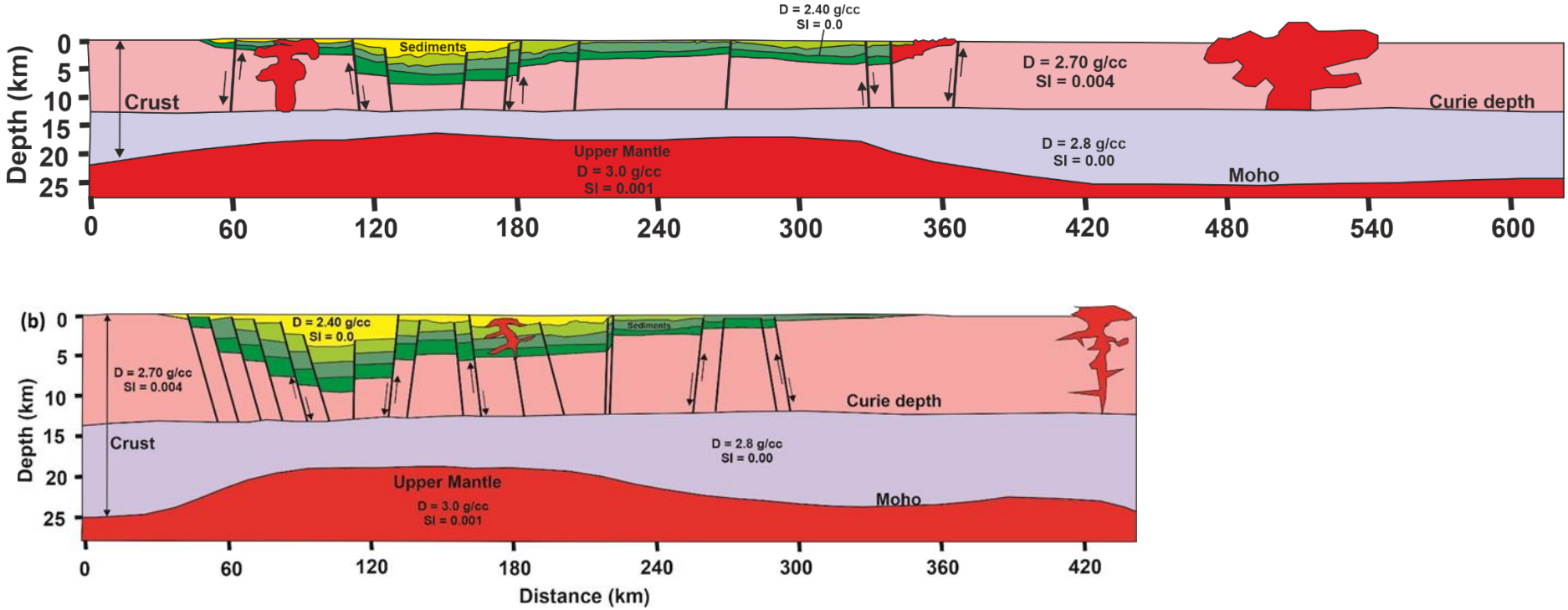

Fig. 7. 18: 2D sections of interpreted tectonic model showing three (3) basic interfaces; the basement depth, the Curie, and the Moho interfaces (a) Along profile P5-P6 (left-right). (b) Along profile P7-P8 (left-right). Faults are represented by thick lines with black arrows indicating the direction of movement. Intrusive rocks and the dykes are indicated by black polygons and red thin-lines respectively. Crustal thinning and injection of magmatic materials are observed along the profile within and outside the basin. Vertical scale exaggeration is X3.

7.7 Hydrocarbon exploration potential and prospectivity

The Benue Trough has similar structural and tectonic events as that of the Muglad basin in Sudan and the Termit basin of Chad and Niger where commercial hydrocarbons have been discovered (Obaje et al., 2006; Abubakar, 2014). Hydrocarbon exploration within the trough has been carried out in the Upper Benue Trough at Kolmani River-1, Kuzari-1, and Nasara-1 exploratory wells with total depth estimates of 3 km, 1.5 km, and 2 km respectively (Obaje et al., 2004; Obaje, 2009; Habib and Xie, 2012) while recent exploration for oil and gas was carried out in the Anambra basin of the Lower Benue Trough (Habib and Xie, 2012).

This study indicated areas of basement subsidence forming good depocentres for the deposition and accumulation of sedimentary rocks maximum of about 9 km thick, and basement uplifted blocks over which the sedimentary thickness is about 4 km thick (Fig. 5.25). Most of the sub-basins and the uplifted blocks form graben and horst structures and are observed to be bounded by deep-seated faults. The depocentres (grabens) are also presumed to be sites of synclinally folded marine Cretaceous sediments and are shown to have a high geothermal gradient and heat flow. Deep-seated faults have been shown to be good pathways for the migration of fluid, and may form components of traps for hydrocarbons accummulation (Zbořil et al., 1986; Tulyatid, 1997; Cunningham and Mann, 2007). In the Upper Benue Trough and the Bornu basin, drilled exploratory wells on basement horsts (uplift) have been observed to host hydrocarbons (Obaje et al., 2004; Esuene, 2012).

Basin inversion can complicate the hydrocarbon play in an area while the presence of intrusive rocks can either benefit or complicate hydrocarbon exploration (Esuene, 2012). Basin inversion has been observed in the southeastern part of the area where there is overturn of stratigraphy with the oldest layer on the surface (Guiraud and Bosworth, 1997) . The occurrence of intrusive rocks in the eastern part of the basin can be positive where they may play the role of serving as igneous reservoirs (micro-spaces and high number of fractures) and as cap rocks (when not fractured) as well as providing thermal effects that may be sufficient to mature source rocks or over-mature source rocks as well (Holford et al., 2013; Ren et al., 2020) while a negative effect of intrusive rocks is seen when they occur as sheet-like intrusions and are interconnected with low-permeability in surrounding sedimentary rocks as well (Holford et al., 2013). This study has shown that intrusive rocks are observed at shallow depth, but are believed to be deep-rooted. Therefore, areas of magmatic intrusions are assumed to have a positive influence on the potential of hydrocarbon. None of the samples of the intrusive rocks analysed in the

literature have produced overcooked facies but are highly fractured and emplaced at shallow depth (Obaje et al., 2006).

Therefore, five areas within the trough show the most favourable potential for hydrocarbon exploration based on some or all of the criteria above; Wase, Keana, Makurdi, Anambra, and the Afikpo basins (Fig. 7.19). The Asu River group and the Bima sandstones crop out in certain areas that are exempted from potential zoning since they are not covered by younger lithologies that may act as a suitable reservoir, source, and seal rocks. Rectangular block 1 located at the northern part of the area between Wase and Jarawa Hills is estimated to have a maximum depth of 9 km with the stratigraphy intact and fault-bounded, high heat flow and geothermal gradient, and absence of a large scale magmatic intrusion. It is interpreted to have high hydrocarbon potential. Block two has faults bounding established synclinal and anticlinal structures with high heat flow and geothermal gradient. The stratigraphy is well maintained, with sediment thickness between 5 km and 6 km, without basin inversion or magmatic intrusions affecting the sub-basin. This indicates the possibility of storing hydrocarbon. Several basement uplifts and subsidences interpreted as horsts and grabens respectively are observed within block 3. The graben delineated around Ofu and Ankpa corresponded with that picked from literature. The presence of horst and graben here are fault-bounded and make the prospects for hydrocarbon exploration very high as the deepest depth is about 6 km and the shallowest has been up to 3 km. In the Niger Republic, hydrocarbons have been observed in sedimentary sequences in the East Niger Graben (Obaje, 2009). Blocks 4 and 5 indicated that the basic structural features (horst and graben) are fault-bounded and are affected by magmatic intrusions. Heat flow and geothermal gradient are moderate but have a very deep basement depth of between 6 km and 9 km.

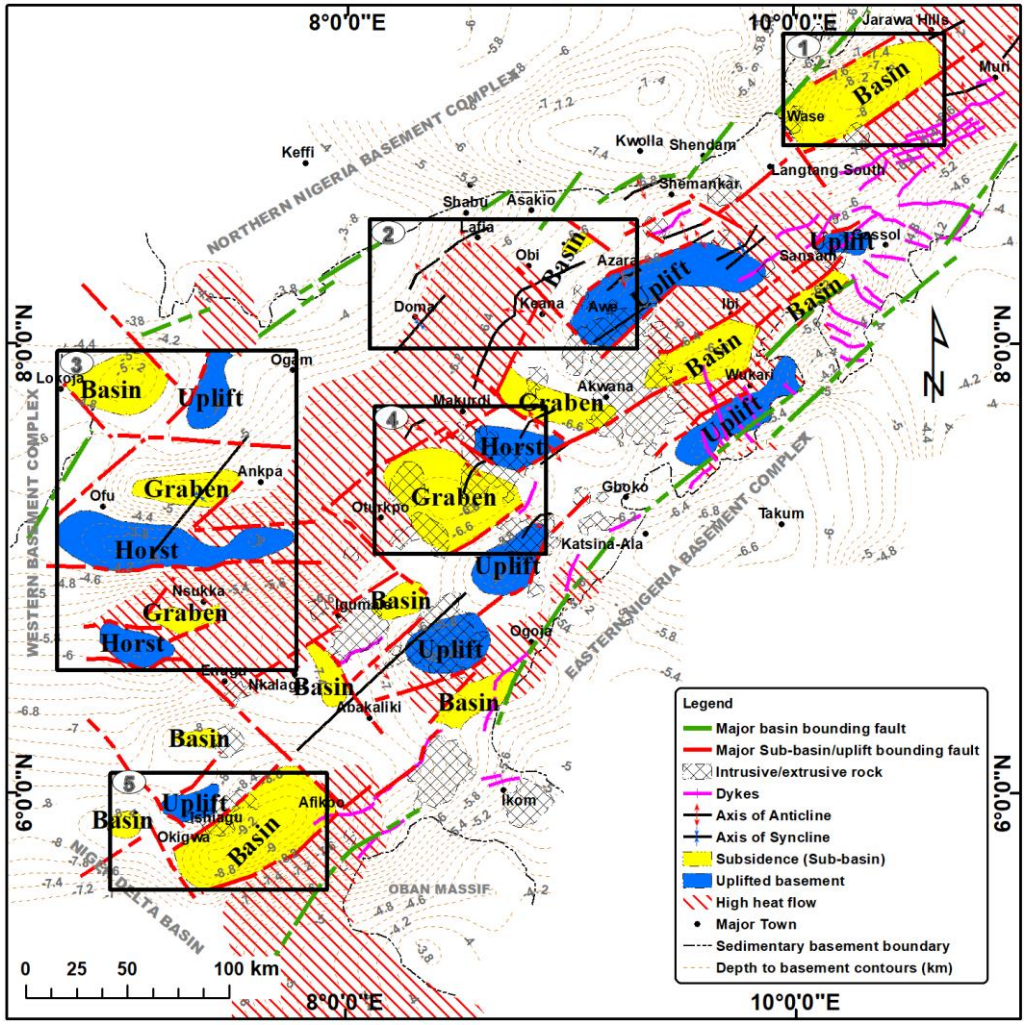

Fig. 7. 19: Hydrocarbon potential map of the Lower and Middle Benue Trough showing areas of high prospects for further exploration. The black rectangle blocks represent; 1: Wase basin, 2: Keana basin, 3: Anambra Basin, 4: Makurdi Basin, 5: Afikpo Basin.

CHAPTER EIGHT

SUMMARY AND CONCLUSION

8.1 Introduction

The integration and interpretation of the results from remote sensing, gravity, and magnetic data covering the Lower and Middle Benue trough based on modelling approach have given more robust insights into the structural evolution at the surface and the subsurface. This chapter summarizes the results and interpretations obtained from the previous chapters and presents the conclusions of the study. Remote sensing (multispectral) data sets provided information on lithology, boundary, and surface structures whereas the aeromagnetic data focus on shallow lineaments, geological bodies (dykes and volcanic rocks), basement structures, and the Curie depth. Gravity and magnetic data sets offered valuable information on the shallow and basement lineaments, Moho depth, and estimates of the present state the strength of the lithosphere based on a steady-state assumption. Integration of these results and interpretations gave valuable information about the extent and geometry of the basin, crustal structure, and the extension rate of the trough. The chapter ends by presenting the main conclusions derived from the study and recommendations suggested for future work.

8.2 Summary

The area of study comprising the Lower and Middle Benue Trough proved to be a continental rifted basin with interesting structural occurrences. The study employed remote sensing data sets (Landsat and ASTER) to map the lithology of the area and combined with existing maps from literature to propose a new geological map. Surface geological lineaments were extracted from Landsat and SRTM while shallow or near-surface geological lineaments (dykes, faults, shear zones, lithological contacts, etc) and non-linear geological bodies (Volcanic rocks, sills, plugs, bosses, etc.) were delineated from residual gravity and magnetic data sets. The fracture-correlation lineament technique was used to delineate geologic lineaments and isolate the tectonic-related lineaments (faults/shear zones) from the non-tectonic lineaments (dykes/lithological contacts). The surface/shallow/near-surface geologic lineaments and the non-linear geologic lineaments were superimposed on the new geology map to produce a new geo-structural map of the area.

The study further mapped deeper lineaments, interpreted as basement lineaments, from regional gravity and magnetic data sets and applied the regional magnetic data to estimate the depth to the top of the basement with the aim of mapping basement morphology to understand areas of basement uplift and subsidence within the trough. 2D gravity and magnetic models were produced across the area along four profiles to study the geological structures at the surface, near surface, and sub-surface. Also, 3D gravity block models were built using Parker-Oldenburg and Li-Oldenburg inversion techniques to map the density structure of the sub-surface, crustal architecture, and the depth to the Moho aiming at understanding the deformational history of the trough. A 3D magnetic amplitude inversion approach was also performed to map areas of magnetic susceptibility and delineate areas of magmatic intrusions. The study then estimated the distance of extension, crustal thickness, and the amount of crustal extension/stretching of the trough. This study further examined the long-term strength of the lithosphere under the basin by estimating the value of elastic thickness, *Te*, as a proxy for determining the lithospheric strength using spectral modelling methods. The long-time strength of the lithosphere is strongly influenced by heating over time, and this was revealed from the thermal structure estimated from power spectrum and three-dimensional magnetic inversion techniques. The thermal structure was established from the approximation of Curie depth interface, geothermal energy gradient, and heat flow.

The evolutionary pattern of the basin was then proposed based on the relationship between fault kinematics and regional stress fields. The presence of magmatic intrusions as part of the evolutionary geo-history of the basin was also investigated as well as the relationship that existed between dyke trends, local paleo-stress field, and the regional stress field in African. A tectonic model based on fault kinematics and the magmatic intrusion was constructed and discussed with the understanding that two phases are extensional and are compressional, affected the area. 2D slices were obtained for geological and tectonic interpretation based on the results of faults kinematic analyses, and 2D and 3D models, and interpreted to understand the subsurface tectonics. The study finally looks at the importance of these structural models proposed in understanding the hydrocarbon potentials of the basin.

8.3 Conclusions

The following conclusions were made for the study.

- This study successfully employed multispectral data sets (Landsat and ASTER) to enhance areas of diagnostic minerals and give a reasonable classification of lithologies and their boundaries to update the geological map of the area. This dataset also helped in delineating surface lineaments that are derived from textural discontinuity in the pattern of the images. Residual gravity and magnetic data sets revealed hidden near-surface geological features such as dykes, volcanic rocks, plugs, etc., and lineaments as well as demarcating the basement-sedimentary boundary. This research established that the area hosts several types of magmatic intrusions within the sediments located at different depths and specifically concentrated towards the eastern part of the trough. This has not been mapped before in the area and this finding has significantly improved the understanding of the geology and structural features.
- Regional gravity and magnetic anomaly interpretations clearly confirm the existence of four well-defined basement lineament population in NE-SW, NW-SE, NNE-SSW, and ENE-WSW orientations. The NE-SW and the NW-SE trending lineaments are interpreted as normal faults formed in response to tectonic events of different times. The N-S and the ENE-WSW sets are believed to be relics of the Precambrian basement fabrics. This study found that these lineaments were formed as results of regional plate movements at different times during the evolution of the basin.
- The fracture-correlation lineament technique helped in differentiating tectonically induced lineaments (faults/shear zones) from the non-tectonic lineaments (dykes/lithological contacts) by comparison with lineaments from field observations. The uplifted basement blocks and sub-basins are identified to be fault-bounded with four main fault types; the NE-SW, NW-SE, N-S, and ENE-WSW trending normal faults. They control the geometry and the emplacement of magmatic materials located and restricted towards the eastern part of the area and this has improved the basis for the tectonic evolution theory for the formation of the trough.
- Interpretation of results from fault kinematics and dyke swarm orientations indicated that the trough evolved through two main tectonic phases; the extensional phase that involves the Albian and the Aptian fault/dyke kinematic regimes, and the compressional phase involving the Santonian and the End of Cretaceous fault

reactivations/kinematics. The fault kinematics generally gave a sinistral fault movement over time.

- Finite tilt- and local wavenumber depth estimation methods proved effective in this study in constraining and estimating the depth to the top of the basement by inversion of pseudo-gravity data. Basement depth of 9 km is interpreted in the deepest part of the trough, found near its southern end, while the shallowest part of 3 km is at the northern end. This estimate helped in interpreting the basement morphology and sedimentary thickness map by defining basement subsidence/sub-basin (depo-centers) and uplifted basement blocks. This study has indicated the presence of undulating basement morphology beneath the relatively flat surface topography due to the deposition of thick sediments and the effects of erosion.
- 2D gravity and magnetic modelling show variations in density and susceptibility across and within the basin and the crust. This provided valuable information about the maximum thickness of the sediments that filled the basin (4.3 km - 9.65 km) and validates the depth estimation obtained by gravity inversion. Results also indicated that the crust is thinned directly under the basin which is attributed to extensional rifting of the lithosphere and Moho doming leading to the emplacement of intrusive rocks. This has shown that rifting was accompanied by Moho uplift.
- Parker-Oldenburg and Li-Oldenburg inversion techniques proved effective in understanding the 3-D crustal and Moho structures of the trough from the gravity dataset. Both techniques showed a significant rise in Moho directly under the trough which is still tied to rifting of the lithosphere.
- 3-D magnetic models of the study area from the magnetic amplitude inversion approach indicated areas of high magnetic susceptibility interpretable as remnants of rifted Pan-African and Precambrian basement rock as well as intra-sedimentary/basement intrusive rocks.
- The amount of crustal extension increases from the north with 93 km, through the centre with 111 km and 139 km, to the southern part with 142 km. This indicated that the crust is more widely stretched in the south than in the north giving the trough a ‘scissors-like style’ of extensional opening. The crust is thinner in the south than in the north. This has added constraints to the plate tectonic theory which argues that the trough was formed due to continental rifting emanating from the Atlantic ocean, with the south of the study area having greater extension.

- Areas of thinner crust correspond to areas with intrusive rocks emplacement (volcanic rocks and dykes). Thicker crusts have indications of lower beta values. It has been shown that a mantle temperature of 1400 ℃ is required to melt about 9 km thick of the crust to cause crustal thinning. This indicated that rifting and magma emplacement within the trough could have occurred between the Aptian and the Albian times (125-100 Ma i.e., 25 Ma).
- The long-term strength of the lithosphere under the Lower and the Middle Benue trough has been established by the admittance and coherence methods to be weak and in isostatic equilibrium. These methods showed that there is loading from the top by sediments and from the bottom i.e., from mantle materials. This study found that the lithosphere within the trough is generally weak but also that the southern lithosphere is weaker than the northern lithosphere.
- The thermal structure of the crust is a viable indicator that heat is of one of the contributory factors to the long-term strength of the lithosphere. Power spectrum analyses and 3D magnetic inversion indicated a major NE-SW structural thermal trend with a deep Curie depth interface occuring side by side with shallow Curie depth interface, and the high heat flow by low heat flow. The deep Curie depth interface aligns with areas of magmatic emplacement that imply a thermal heat region towards the eastern part of the trough.
- Finally, this study showed that the tectonic architecture of the trough is in agreement with the plate tectonic model (section 1.5.2), which suggests it should be characterized by crustal rifting and extension, faulting, Moho shallowing due to crustal thinning, magma emplacement, and thermal subsidence or relaxation. Though the amount of magma estimated within the area seems large, it was attributed to the different parameter values used during calculations. However, this also does not justify the plume model as having been responsible for the production of the various deformational structures within the basin. There is strong possibility that the excess magma was emplaced on surrounding basement rocks e.g., the large presence of volcanic rocks along the Cameroon and the Jos-plateau volcanic lines.

8.4 Recommendations for future work in the area

- This study provided valuable baseline results for basin analysis but the addition of seismic reflection data sets through the acquisition of a new 2- or 3-D seimic data sets in the future will help develop and control the model better. This will undoubtedly improve and confirm or modify the findings of the study. The results of seismic reflection profiling in particular will help provide high-resolution information about the lithology facies, stratigraphy, fault angles, deep crust, etc.
- Further fieldwork especially biogeochemical survey can be done to verify the findings in this study and predict targets for drilling. This will help provide valuable and cheaper records for confirmation or exploration of hydrocarbons. Drilling of exploratory wells in the trough especially within the Wase, Keana basin, Anambra Basin, Makurdi Basin, Afikpo Basin based on this study is strongly recommended
- It will be interesting to repeat the strategies applied in this study to the Niger Delta region and the Bornu-Chad basin where there are many seismic reflection data sets for more detailed analyses. Also, applying the methods from this study to the Upper Benue Trough will help provide a complete holistic structural framework model of the Benue Trough.
- Detailed thermal tectonic subsidence analyses of the trough are recommended to be carried out in the future as this will help give details of the syn-rift and post-rift subsidence history of the trough. This can be achieved by considering the stretching factor and sedimentary thickness map, compaction, variation in depositional water depth through time, absolute fluctuations of sea level.
- More work is recommended using existing radiometric data sets and shallow coring could also help to validate and explore the geology and stratigraphy of the trough better and possibly constrain and reveal the resources associated with the magmatic intrusions of the area.

REFERENCES

Abarca, M.A.A. 2006. Lineament Extraction from Digital Terrain Models. Case Study San Antonio del Sur Area , South-Eastern Cuba. . (March), p.86.

Abbass, A.A. and Mallam, A. 2013. Estimating the Thickness of Sedimentation within Lower Benue Basin and Upper Anambra Basin , Nigeria , Using Both Spectral Depth Determination and Source Parameter Imaging. *ISRN Geophysics*. **2013**(1 to 10), p.10.

Abdullah, A., Akhir, J.M. and Abdullah, I. 2010. Automatic mapping of lineaments using shaded relief images derived from digital elevation model (DEMs) in the Maran - Sungi Lembing area, Malaysia. *Electronic Journal of Geotechnical Engineering*. **15 J**, pp.1–9.

Abdullahi, M., Kumar, R. and Singh, U. 2019. Magnetic basement depth from high-resolution aeromagnetic data of parts of lower and middle Benue Trough (Nigeria) using scaling spectral method. *Journal of African Earth Sciences*. **150**(October 2018), pp.337–345.

Abdullahi, M., Singh, U.K. and Roshan, R. 2019. Mapping magnetic lineaments and subsurface basement beneath parts of Lower Benue Trough (LBT), Nigeria: Insights from integrating gravity, magnetic and geologic data. *Journal of Earth System Science*. **128**(1), pp.1–17.

Aboud, E., El-Masry, N., Qaddah, A., Alqahtani, F. and Moufti, M.R.H. 2015. Magnetic and gravity data analysis of Rahat Volcanic Field, El-Madinah city, Saudi Arabia. *NRIAG Journal of Astronomy and Geophysics*. **4**(1), pp.154–162.

Abrams, M. and Hook, S. 2002. ASTER User Handbook Version 2. *Jet Propulsion*. **2003**(23/09/2003), p.135.

Abu El-Ata, A.S., EI-Khafeef, A.A., Ghoneimi, A.E., Abd Alnabi, S.H. and Al-Badani, M.A. 2013. Applications of aeromagnetic data to detect the Basement Tectonics of Eastern Yemen region. *Egyptian Journal of Petroleum*. **22**(2), pp.277–292.

Abubakar, A.J., Hashim, M. and Pour, A.B. 2018. Identification of hydrothermal alteration minerals associated with geothermal system using ASTER and Hyperion satellite data: a case study from Yankari Park, NE Nigeria. *Geocarto International*. **6049**(December), pp.1–29.

Abubakar, M.B. 2014. Petroleum Potentials of the Nigerian Benue Trough and Anambra Basin : A Regional Synthesis. *Natural Resources*. **2014**(5), pp.25–58.

Acharya, T. and Mallik, S.B. 2012. Analysis of lineament swarms in a Precambrian metamorphic rocks in India. *Journal of Earth System Science*. **121**(2), pp.453–462.

Adighije, C.I. 1981a. A gravity interpretation of the Benue Trough, Nigeria. *Tectonophysics*. **79**, pp.109–128.

Adighije, C.I. 1981b. Gravity study of Lower Benue Trough, Nigeria. *Geol. Mag.* **118**(1976), pp.59–67.

Adighije, C.I. 1978. Studies of the gravity field of the Benue Trough of Nigeria. *Ph.D. Thesis, Univ. Ibadan, Ibadan (unpubl.)*.

Agagu, O.K. and Adighije, C.I. 1983. Tectonic and sedimentation framework of the lower Benue Trough, southeastern Nigeria. *Journal of African Earth Sciences (1983)*. **1**(3–4), pp.267–274.

Ajakaiye, D.E. 1975. A gravity survey over the Nigeria Younger Granite Province. *In: CA. Kogbe (Editor), GeoIogy of Nigeria. Elizabethan Publ. Co., Lagos*., pp.207–224.

Ajakaiye, D.E. and Burke, K. 1973. A Bouguer gravity map of nigeria. *Tectonophysics*. **16**(1–2).

Ajakaiye, D.E., Hall, D.H., Ashiekaa, J.A. and Udensi, E.E. 1991. Magnetic anomalies in the Nigerian continental mass based on aeromagnetic surveys. *Tectonophysics*. **192**(1–2), pp.211–230.

Ajayi, C.O. 1979. A Detailed Gravity Survey of the Middle Benue, Nigeria. *Unpublished Ph.D. thesis, Ahmadu Bello University*.

Ajayi, C.O. and Ajakaiye, D.E. 1986. Structures deduced from gravity data in the Middle Benue, Nigeria. *Journal of African Earth Sciences*. **5**(4), pp.359–369.

Ajayi, C.O. and Ajakaiye, D.E. 1981. The Origin and Peculiarities of the Nigerian Benue Trough: Another look from Recent Gravity Data obtained from the Middle Benue. *Tectonophysics*. **80**, pp.285–303.

Akande, S.O., Egenhoff, S.O., Obaje, N.G., Ojo, O.J., Adekeye, O.A. and Erdtmann, B.D. 2012. Hydrocarbon potential of Cretaceous sediments in the Lower and Middle Benue Trough, Nigeria: Insights from new source rock facies evaluation. *Journal of African Earth Sciences*. **64**, pp.34–47.

Akpan, O., Nyblade, A., Okereke, C., Oden, M., Emry, E. and Julià, J. 2016. Crustal structure of Nigeria and Southern Ghana, West Africa from P-wave receiver functions. *Tectonophysics*. **676**, pp.250–260.

Ali, M.Y., Fairhead, J.D., Green, C.M. and Noufal, A. 2017. Basement structure of the United Arab Emirates derived from an analysis of regional gravity and aeromagnetic database. *Tectonophysics*. **712**–**713**, pp.503–522.

Anudu, G.K., Stephenson, R.A. and Macdonald, D.I.M. 2014. Using high-resolution aeromagnetic data to recognise and map intra-sedimentary volcanic rocks and geological structures across the Cretaceous middle Benue Trough, Nigeria. *Journal of African Earth Sciences*. **99**, pp.625–636.

Anudu, G.K., Stephenson, R.A., Ofoegbu, C.O. and Obrike, S.E. 2020. Basement morphology of the middle Benue Trough, Nigeria, revealed from analysis of high-resolution aeromagnetic data using grid-based operator methods. *Journal of African Earth Sciences*. **162**(July 2019), p.103724.

Arkani-Hamed, J. 1988. Differential reduction-to-the-pole of regional magnetic anomalies.

Geophysics. **53**(12), pp.1592–1600.

Arkani-Hamed, J. 2007. Differential reduction to the pole: Revisited. *Geophysics*. **72**(1).

Armadillo, E., Bozzo, E., Ferraccioli, F., Gambetta, M., Raymond, C.E., Talarico, F., Zangani, M. and Zunino, a 2007. A high-resolution aeromagnetic survey over the Cape Roberts rift basin; correlations with seismic reflection and magnetic susceptibility log data. *Open-File Report - U. S. Geological Survey*. **1**(Figure 2), Extended Abstract 076.

Azizi, M. and Saibi, H. 2015. Integrating Gravity Data With Remotely Sensed Data for Structural Investigation of the Aynak-Logar Valley, Eastern Afghanistan, and the Surrounding Area. . **8**(2), pp.1–9.

Bakker, W.H., Grabmaier, K.A., Huurneman, G.C., Meer, F.D. van der, Prakash, A., Tempfli, K., Gieske, A.S.M., Hecker, C.A., Janssen, L.L.F., Parodi, G.N., Reeves, C. V., C.Weir, M.J., Gorte, B.G.H., Horn, J.A., Kerle, N., Pohl, C., Ruitenbeek, F.J. van and Woldai, T. 2004. Principles of Remote Sensing. , p.250.

Baranov, V. 1957. A new method for interpretation maps: pseudo-gravimetric. *Geophysics*. **22**(2), pp.359–382.

Beard, L.P. 2000. Detection and identification of north-south trending magnetic structures near the magnetic equator. *Geophysical Prospecting*. **48**(4), pp.745–761.

Beiranvand Pour, A. and Hashim, M. 2015. Integration of PALSAR and ASTER Satellite data for geological mapping in tropics. *ISPRS Annals of the Photogrammetry, Remote Sensing and Spatial Information Sciences*. **2**(2W2), pp.105–109.

Benkhelil, J. 1989. The origin and evolution of the Cretaceous Benue Trough (Nigeria). *Journal of African Earth Sciences*. **8**(2–4), pp.251–282.

Benkhelil, J., Mascle, J. and Guiraud, M. 1998. Sedimentary and Structural Characteristics of the Cretaceous Along the Côte D'Ivoire-Ghana Transform Margin and in the Benue Trough: a Comparison 1. . **159**, pp.93–99.

Bhagat, S.N. and Verma, E.K. 2006. Relation between lineaments and tectonics in parts of the Vindhyan basin, Madhya Pradesh. *Journal of the Indian Society of Remote Sensing*. **34**(2), pp.203–207.

BİLİM, F. 2017. Investigating Moho depth, Curie Point, and heat flow variations of the Yozgat Batholith and its surrounding area, north central Anatolia,Turkey, using gravity and magnetic anomalies. *Turkish Journal of Earth Sciences*. **26**, pp.410–420.

Binks, R.M. and Fairhead, J.D. 1992. A plate tectonic setting for Mesozoic rifts of West and Central Africa. *Tectonophysics*. **213**(1–2), pp.141–151.

Blakely, R.J. 1996. Potential Theory in Gravity and Magnetic Applications. *Cambridge University Press, Cambridge, UK.*, p.461.

Bomfim, E.P., Braitenberg, C. and Molina, E.C. 2013. Mutual evaluation of global gravity models (EGM2008 and GOCE) and terrestrial data in Amazon Basin, Brazil.

Geophysical Journal International. **195**(2), pp.870–882.

Bosworth, W., Guiraud, R. and Kessler, L.G. 1999. Late Cretaceous (ca. 84 Ma) compressive deformation of the stable platform of northeast Africa (Egypt): Far-field stress effects of the 'Santonian event' and origin of the Syrian arc deformation belt. *Geology*. **27**(7), pp.633–636.

Boud, a 1987. Potential Application of Remote-Sensing Systems to the African Rift System. *Journal of Geodynamics*. **7**(3–4), pp.373–394.

Bourgeois, O., Dauteuil, O. and Hallot, E. 2005. Rifting above a mantle plume: Structure and development of the Iceland Plateau. *Geodinamica Acta*. **18**(1), pp.59–80.

Brune, S. and Autin, J. 2013. The rift to break-up evolution of the Gulf of Aden: Insights from 3D numerical lithospheric-scale modelling. *Tectonophysics*. **607**, pp.65–79.

Burov, E.. and Watts, A.B. 2006. The long-term strength of continental lithosphere: "jelly sandwich" or "crème brûlée"? *GSA Today*. **16**(3), pp.4–11.

Burov, E.B. and Diament, M. 1995. The effective elastic thickness (Te) of continental lithosphere: what does it really mean? *Journal of Geophysical Research*. **100**(B3), pp.3905–3927.

Calvès, G., Torvela, T., Huuse, M. and Dinkleman, M.G. 2012. New evidence for the origin of the Porcupine Median Volcanic Ridge: Early Cretaceous volcanism in the Porcupine Basin, Atlantic margin of Ireland. *Geochemistry, Geophysics, Geosystems*. **13**(6), pp.1–18.

Capponi, G., Festa, A. and Rebay, G. 2018. Birth and death of oceanic basins: Geodynamic processes from rifting to continental collision in Mediterranean and circum-Mediterranean orogens. *Geological Magazine*. **155**(2), pp.229–232.

Cascone, L., Green, C., Campbell, S., Salem, A. and Fairhead, D. 2017. ACLAS — A method to define geologically significant lineaments from potential-field data. *Geophysics*. **82**(4), pp.G87–G100.

de Castro, D.L., Fuck, R.A., Phillips, J.D., Vidotti, R.M., Bezerra, F.H.R. and Dantas, E.L. 2014. Crustal structure beneath the Paleozoic Parnaíba Basin revealed by airborne gravity and magnetic data, Brazil. *Tectonophysics*. **614**, pp.128–145.

Cella, F. and Fedi, M. 2012. Inversion of potential field data using the structural index as weighting function rate decay. *Geophysical Prospecting*. **60**(2), pp.313–336.

Chakravarthi, V., Ramamma, B. and Venkat Reddy, T. 2013. Gravity anomaly modeling of sedimentary basins by means of multiple structures and exponential density contrast-depth variations: A space domain approach. *Journal of the Geological Society of India*. **82**(5), pp.561–569.

Charpentier, R.R. and Ahlbrandt, T.S. 2004. Petroleum (Oil and gas) Geology and Resources. *GEOLOGY*. **Vol. V** – **P**.

Chavez, P.S., Berlin, G.L. and Sowers, L.B. 1982. Statistical Method for Selecting Landsat Mss Ratios. *Journal of applied photographic engineering*. **8**(1), pp.23–30.

Cheyney, S., Green, C.M., Campbell, S.J. and De Lerma, D. 2016. Applying magnetic magnitude transforms to aid structural mapping in areas where the RTP calculation is unreliable. *78th EAGE Conference and Exhibition 2016: Efficient Use of Technology - Unlocking Potential*. (June).

Chowdari, S., Singh, B., Rao, B.N., Nageswara Rao, B., Kumar, N., Singh, A.P. and Chandrasekhar, D. V. 2017. Structural mapping based on potential field and remote sensing data , South Rewa Gondwana Basin , India. *Journal of Earth System Science*. **126**(6), pp.1–27.

Chukwu-Ike, I.N. 1977. Regional Photogeological Interpretation of the Tectonic Features of the Central Nigerian Basement Complex: A Satellite Imagery Based Study. *Ph.D. Thesis, Imperial College, London (unpubl.).* **7**(1), pp.541–559.

Chukwuebuka, C.K., Egesi, N. and Beka, F.T. 2010. Structural Geology of the Lower Benue Trough: A Case Study of the Ishiagu Area of Ebonyi State, Nigeria. *AAPG Search and Discovery Article #90115©2010 AAPG Africa Region Annual Conference*. (November), p.90115.

Cooper, G.R.J. 2004. Euler Deconvolution applied to Potential Field Gradients. . **35**(3), pp.165–170.

Cooper, G.R.J. 2014. The Automatic Determination of the Location and Depth of Contacts and Dykes from Aeromagnetic Data. *Pure and Applied Geophysics*. **171**(9), pp.2417–2423.

Cooper, G.R.J. and Cowan, D.R. 2005. Differential reduction to the pole. *67th European Association of Geoscientists and Engineers, EAGE Conference and Exhibition, incorporating SPE EUROPE2005 - Extended Abstracts*. **67th Europ**, pp.1707–1710.

Cooper, G.R.J. and Cowan, D.R. 2008. Edge enhancement of potential-field data using normalized statistics. *Geophysics*. **73**(3), pp.H1–H4.

Cordell, L. 1973. Gravity analysis using an exponential density-depth function-San Jacinto Graben, California. *Journal of Geophysics*. **38**(4), pp.684–690.

Cordell, L. and Grauch, V. 1982. Mapping Basement Magnetitation Zones from Aeromagnetic Data in the San Juan Basin , New Mexico. *Society of Exploration Geophysicists*. (Paper presented at the 1982 SEG Annual Meeting, Dallas, Texas, October 1982.), pp.181–197.

Cordell, L. and Henderson, R.. 1968. Iterative Three-Dimensional Solution of Gravity Anomaly Data Using a Digital Computer. *Journal of Geophysics*. **33**, pp.596–601.

Coulon, C., Vidal, P., Dupuy, C., Baudin, P., Popoff, M., Maluski, H. and Hermitte, D. 1996. The mesozoic to early cenozoic magmatism of the Benue Trough (Nigeria); geochemical evidence for the involvement of the St Helena Plume. *Journal of Petrology*. **37**(6), pp.1341–1358.

Cratchley, C.R. and Jones, G.P.G.P. 1965. An Interpretation of the Geology and Gravity Anomalies of the Benue Valley, Nigeria. *Geophys. Pap. Overseas geol. Surv*. **1**(3), p.413.

Crippen, R.E. and Blom, R.G. 2001. Unveiling the Lithology of Vegetated Terrains in Remotely Sensed Imagery. *American Society for Photogrammetry and Remote Sensing Proceedings*. **91109**(August), pp.935–943.

Cŕosta, A.P., De Souza Filho, C.R., Azevedo, F. and Brodie, C. 2003. Targeting key alteration minerals in epithermal deposits in Patagonia, Argentina, using ASTER imagery and principal component analysis. *International Journal of Remote Sensing*. **24**(21), pp.4233–4240.

Cunningham, W.D. and Mann, P. (eds) 2007. *Tectonics of Strike-Slip Restraining and Releasing Bends.* Geological Society, London, Special Publications 290, 143-168.

Daly, E., Brown, C., Stark, C.P. and Ebinger, C.J. 2004. Wavelet and multitaper coherence methods for assessing the elastic thickness of the Irish Atlantic margin. *Geophysical Journal International*. **159**(2), pp.445–459.

Dannemiller, N. and Li, Y. 2004. A new method for determination of magnetization direction. *Geophysics*. **71**(6), pp.L69–L73.

Darros de Matos, R.M. 2021. Magmatism and hotspot trails during and after continental break-up in the South Atlantic. *Marine and Petroleum Geology*. **129**(April), p.105077.

Degnan, J.R. and Stewart, C.F. 2002. Fracture-Correlated Lineaments at Great Bay , Southeastern New Hampshire. *U.S. Geological Survey Open-File Report.*, pp.02–13.

Deng., Y., Zhang., Z., Fan., W. and Pérez-Gussinyé., M. 2014. Multitaper spectral method to estimate the elastic thickness of South China: Implications for intracontinental deformation. *Geoscience Frontiers*. **5**(2), pp.193–203.

Deng, Y., Zhang, Z., Badal, J. and Fan, W. 2014. Tectonophysics 3-D density structure under South China constrained by seismic velocity and gravity data. . **627**, pp.159–170.

Deplaen, R.S.M., Bastow, I.D., Chambers, E.L., Keir, D., Gallacher, R.J. and Keane, J. 2014. The development of magmatism along the Cameroon Volcanic Line: Evidence from seismicity and seismic anisotropy. *Journal of Geophysical Research: Solid Earth*. **119**(5), pp.4233–4252.

Dressel, I., Barckhausen, U. and Heyde, I. 2018. A 3D gravity and magnetic model for the Entenschnabel area (German North Sea). *International Journal of Earth Sciences*. **107**(1), pp.177–190.

Ducart, D.F., Silva, A.M., Toledo, C.L.B. and Assis, L.M. de 2016. Mapping iron oxides with Landsat-8/OLI and EO-1/Hyperion imagery from the Serra Norte iron deposits in the Carajás Mineral Province, Brazil. *Brazilian Journal of Geology*. **46**(3), pp.331–349.

Ekwueme, B.N. 1994. Basaltic magmatism related to the early stages of rifting along the Benue Trough: The Obudu dolerites of south-east Nigeria. *Geological Journal*. **29**(3),

pp.269–276.

Elmahdy, S.I. and Mohamed, M.M. 2016. Mapping of tecto-lineaments and investigate their association with earthquakes in Egypt: a hybrid approach using remote sensing data. *Geomatics, Natural Hazards and Risk*. **7**(2), pp.600–619.

Esuene, S.M.. 2012. A critical evaluation of the " Tilt-Depth " method of magnetic data interpretation : Application to aeromagnetic data from NorthEastern by The University of Leeds. *Unpublished Ph.D. thesis, University of Leeds*.

Fairhead, J.D. 2015. Advances in Gravity and Magnetic Processing and Interpretation. . (EAGE Publications.).

Fairhead, J.D. 1988. Mesozoic plate tectonic reconstructions of the central South Atlantic Ocean: The role of the West and Central African rift system. *Tectonophysics*. **155**(1–4), pp.181–191.

Fairhead, J.D. and Binks, R.M. 1991. Differential opening of the Central and South Atlantic Oceans and the opening of the West African rift system. *Tectonophysics*. **187**, pp.191–203.

Fairhead, J.D., Cooper, G.R.J. and Sander, S. 2017. Advances in Airborne Gravity and Magnetics. *Proceedings of Exploration 17: Sixth Decennial International Conference on Mineral Exploration*., pp.113–127.

Fairhead, J.D. and Green, C.M. 1989. Controls on rifting in Africa and the regional tectonic model for the Nigeria and East Niger rift basins. *Journal of African Earth Sciences*. **8**(2–4), pp.231–249.

Fairhead, J.D., Green, C.M., Masterton, S.M. and Guiraud, R. 2013. The role that plate tectonics, inferred stress changes and stratigraphic unconformities have on the evolution of the West and Central African Rift System and the Atlantic continental margins. *Tectonophysics*. **594**, pp.118–127.

Fairhead, J.D., Misener, J.D., Green, M.C., Bainbridge, G. and Redford, S.W. 1997. Large Scale Compilation of Magnetic , Gravity , Radiometric and Electromagnetic Data : The New Exploration Strategy for the 90s. *Applications of regional geophysics and geochemistry*. **103**, pp.805–816.

Fairhead, J.D. and Okereke, C.S. 1987. A regional gravity study of the West African rift system in Nigeria and Cameroon and its tectonic interpretation. *Tectonophysics*. **143**(1–3), pp.141–159.

Fairhead, J.D. and Okereke, C.S. 1990. Crustal thinning and extension beneath the Benue Trough based on gravity studies. *Journal of African Earth Sciences*. **11**(3–4), pp.329–335.

Fairhead, J.D., Okereke, C.S. and Nnange, J.M. 1991. Crustal structure of the Mamfe basin, West Africa, based on gravity data. *Tectonophysics*. **186**(3–4), pp.351–358.

Fairhead, J.D., Salem, A., Cascone, L., Hammill, M., Masterton, S. and Samson, E. 2011.

New developments of the magnetic tilt-depth method to improve structural mapping of sedimentary basins. *Geophysical Prospecting*. **59**(6), pp.1072–1086.

Fatoye, F.B. and Gideon, Y.B. 2013. Geology and mineral resources of the Northern Territory. . **4**(June), pp.21–28.

Fedi, M. and Florio, G. 2001. Detection of potential fields source boundaries by enhanced horizontal derivative method. *Geophysical Prospecting*. **49**(1), pp.40–58.

Feumoe, A.N.S. and Ndougsa-Mbarga, T. 2012. Delineation of tectonic lineaments using aeromagnetic data for the south-east Cameroon area. *Geofizika*. **29**, pp.1–18.

Finlay, C.C., Maus, S., Beggan, C.D., Bondar, T.N., Chambodut, A., Chernova, T.A., Chulliat, A., Golovkov, V.P., Hamilton, B., Hamoudi, M., Holme, R., Hulot, G., Kuang, W., Langlais, B., Lesur, V., Lowes, F.J., Lühr, H., Macmillan, S., Mandea, M., McLean, S., Manoj, C., Menvielle, M., Michaelis, I., Olsen, N., Rauberg, J., Rother, M., Sabaka, T.J., Tangborn, A., Tøffner-Clausen, L., Thébault, E., Thomson, A.W.P., Wardinski, I., Wei, Z. and Zvereva, T.I. 2010. International Geomagnetic Reference Field: The eleventh generation. *Geophysical Journal International*. **183**(3), pp.1216–1230.

Fitton, J.G. 1980. The Benue trough and cameroon line - A migrating rift system in West Africa. *Earth and Planetary Science Letters*. **51**(1), pp.132–138.

Forsy, D.W. 1982. Kane fracture zone from topography and gravity. , pp.125–150.

Forsyth, D.W. 1985. Subsurface loading and estimates of the flexural rigidity of continental lithosphere. *Journal of Geophysical Research*. **90**(B14).

Foss, C. 2011. *Magnetic Data Enhancements and Depth Estimation* [Online]. In: Gupta H.K. (eds) Encyclopedia of Solid Earth Geophysics. Encyclopedia of Earth Sciences Series. Springer, Dordrecht. Available from: http://link.springer.com/10.1007/978-90-481-8702-7.

Fossen, H. 2010. *Structural Geology* [Online]. Available from: http://library1.nida.ac.th/termpaper6/sd/2554/19755.pdf.

Gad, S. and Kusky, T. 2006. Lithological mapping in the Eastern Desert of Egypt, the Barramiya area, using Landsat thematic mapper (TM). *Journal of African Earth Sciences*. **44**(2), pp.196–202.

Galán, R.A. and Casallas, I.F. 2010. Determination of effective elastic thickness of the Colombian Andes using satellite-derived gravity data. *Earth Sciences Research Journal*. **14**(1), pp.7–16.

Geosoft 2004. Topics in Gridding. *Technical Workshop*.

Geosoft Inc. 2015. Defining and applying filters and inverse FFT in MAGMAP. *Www.Geosoft.Com.*, pp.1–27.

Gerovska, D. and Araúzo-bravo, M.J. 2006. Calculation of magnitude magnetic transforms with high centricity and low dependence on the magnetization vector direction.

Geophysics. **71**(5).

Gerovska, D., Araúzo-Bravo, M.J. and Stavrev, P. 2009. Estimating the magnetization direction of sources from southeast Bulgaria through correlation between reduced-to-the-pole and total magnitude anomalies. *Geophysical Prospecting*. **57**(4), pp.491–505.

Gerovska, D. and Stavrev, P. 2006. Magnetic data analysis at low latitudes using magnitude transforms. *Geophysical Prospecting*. **54**(1), pp.89–98.

Ghazala, H.H., Ibraheem, I.M., Lamees, M. and Haggag, M. 2018. Structural study using 2D modeling of the potential field data and GIS technique in Sohag Governorate and its surroundings, Upper Egypt. *NRIAG Journal of Astronomy and Geophysics*. **7**(2), pp.334–346.

Gómez-Ortiz, D. and Agarwal, B.N.P. 2005. 3DINVER.M: A MATLAB program to invert the gravity anomaly over a 3D horizontal density interface by Parker-Oldenburg's algorithm. *Computers and Geosciences*. **31**(4), pp.513–520.

Gómez-Ortiz, D., Tejero, R., Ruiz, J., Babín-Vich, R. and González-Casado, J.M. 2005. Estimating the effective elastic thickness of the lithosphere of the Iberian peninsula based on multitaper spectral analysis. *Geophysical Journal International*. **160**(2), pp.729–735.

Goussev, S.A., Charters, R.A., Peirce, J.W. and Glenn, W.E. 2003. Jackpine Creek magnetic anomaly: Identification of a buried meteorite impact structure. *The Leading Edge*. **22**(8), pp.740–741.

Granser, H. 1987. Three-Dimension Interpretation of Gravity Data from Sedimentary Basins Using an Exponential Density-Depth Function. *Journal of Geophysical Prospecting*. **35**(June 1986), pp.1030–1041.

Grauch, V.J.S. 2002. High-Resolution Aeromagnetic Survey to Image Shallow Faults, Dixie Valley Geothermal Field, Nevada. . (July), p.14.

Grauch, V.J.S. and Cordell, L. 1987. Limitations of determining density or magnetic boundaries from the horizontal gradient of gravity or pseudogravity data. *Geophysics*. **52**(1), pp.118–121.

Grauch, V.J.S. and Hudson, M.R. 2007. Guides to understanding the aeromagnetic expression of faults in sedimentary basins: Lessons learned from the central Rio Grande rift, New Mexico. *Geosphere*. **3**(6), pp.596–623.

Grebby, S., Cunningham, D., Tansey, K. and Naden, J. 2014. The impact of vegetation on lithological mapping using airborne multispectral data: A case study for the north Troodos region, Cyprus. *Remote Sensing*. **6**(11), pp.10860–10887.

Guerriero, V., Iannace, A., Mazzoli, S., Parente, M., Vitale, S. and Giorgioni, M. 2010. Quantifying uncertainties in multi-scale studies of fractured reservoir analogues: Implemented statistical analysis of scan line data from carbonate rocks. *Journal of Structural Geology*. **32**(9), pp.1271–1278.

Guerriero, V., Vitale, S., Ciarcia, S. and Mazzoli, S. 2011. Improved statistical multi-scale analysis of fractured reservoir analogues. *Tectonophysics*. **504**(1–4), pp.14–24.

Guiraud, M., Ajakaiye, D.E. and Ugodulunwa, F.X.O. 1989. Characterisation of late Cretaceous NE-SW sinistral wrench faults in the Upper Benue Trough (Nigeria) using microtectonic and aeromagnetic data. *Journal of African Earth Sciences*. **9**(1), pp.9–21.

Guiraud, R. and Bosworth, W. 1997. Senonian basin inversion and rejuvenation of rifting in Africa and Arabia: Synthesis and implications to plate-scale tectonics. *Tectonophysics*. **282**(1–4), pp.39–82.

Guiraud, R. and Maurin, J.C. 1992. Early Cretaceous rifts of Western and Central Africa: an overview. *Tectonophysics*. **213**(1–2), pp.153–168.

Habib, M. and Xie, C. 2012. Nigeria's inland basins : Investment opportunities and environment. *Petroleum and Gas Exploration Research*. **2**(11), pp.202–211.

Hallett, D. 2002. Chapter 8 - Petroleum Systems. *Editor(s): Don Hallett, Petroleum Geology of Libya, Elsevier.*, Pages 355-416.

Hammer, S. 1963. Deep gravity interpretation by stripping. *Geophysics*. **28**(3), pp.369–378.

Haralick, R.M., Sternberg, S.R. and Zhuang, X. 1987. Image Analysis Using Mathematical Morphology. *IEEE Transactions on Pattern Analysis and Machine Intelligence*. **9**(4), pp.532–550.

Hartley, R., Watts, A.B. and Fairhead, J.D. 1996. Isostasy of Africa. *Earth and Planetary Science Letters*. **137**(1–4), pp.1–18.

Healy, D. and Rizzo, R. 2017. Fracture Pattern Quantification User Guide. . (Version 2.6), pp.1–33.

Healy, D., Rizzo, R.E., Cornwell, D.G., Farrell, N.J.C., Watkins, H., Timms, N.E., Gomez-Rivas, E. and Smith, M. 2017. FracPaQ: A MATLAB™ toolbox for the quantification of fracture patterns. *Journal of Structural Geology*. **95**, pp.1–16.

Hewson, R., Robson, D., Mauger, A., Cudahy, T., Thomas, M. and Jones, S. 2015. Using the Geoscience Australia-CSIRO ASTER maps and airborne geophysics to explore Australian geoscience. *Journal of Spatial Science*. **60**(2), pp.207–231.

Hinze, W.J., Von Frese, R.R.B. and Saad, A.H. 2010. *Gravity and magnetic exploration: Principles, practices, and applications*.

Holford, S.P., Schofield, N., Jackson, C.A.-L., Magee, C., G., Green, P.F. and Duddy, I.R. 2013. Impacts of Igneous Intrusions on Source and Reservoir Potential in Prospective Sedimentary Basins Along the Western Australian Continental Margin. *West Australian Basins Symposium*. (August), pp.18–21.

Hoyer, P.A., Haase, K.M., Regelous, M., O'Connor, J.M., Homrighausen, S., Geissler, W.H. and Jokat, W. 2022. Mantle plume and rift-related volcanism during the evolution of the Rio Grande Rise. *Communications Earth & Environment*. **3**(1).

Hsieh, H.H., Chen, C.H., Lin, P.Y. and Yen, H.Y. 2014. Curie point depth from spectral analysis of magnetic data in Taiwan. *Journal of Asian Earth Sciences*. **90**, pp.26–33.

Hsu, S.-K., Sibuet, J.-C. and Shyu, C.-T. 1996. High-resolution detection of geologic boundaries from potential-field anomalies: An enhanced analytic signal technique. *Geophysics*. **61**(2), pp.373–386.

Hung, L.Q., Batelaan, O. and De Smedt, F. 2005. Lineament extraction and analysis, comparison of LANDSAT ETM and ASTER imagery. Case study: Suoimuoi tropical karst catchment, Vietnam. . **5983**, p.59830T.

Hunt, G.R. 1977. Spectral Signatures of Particulate Minerals in the Visible and Near Infrared. *Geophysics*. **42**(3), pp.501–513.

Jacobsen, B.H. 1987. A case for upward continuation as a standard separation filter for potential-field maps. *Geophysics*. **52**(8), pp.1138–1148.

Jain, N., Vinod Kumar, K., Singh, R., Martha, T.R., Chauhan, P. and Roy, P. 2018. Mapping of hydrothermally altered zones in Aravalli Supergroup of rocks around Dungarpur and Udaipur, India, using Landsat-8 OLI and spectroscopy. *Arabian Journal of Geosciences*. **11**(16).

Jiménez-Díaz, A., Ruiz, J., Pérez-Gussinyé, M., Kirby, J.F., Álvarez-Gómez, J.A., Tejero, R. and Capote, R. 2014. Spatial variations of effective elastic thickness of the lithosphere in Central America and surrounding regions. *Earth and Planetary Science Letters*. **391**, pp.55–66.

Ju, Y., Wang, G., Li, S., Sun, Y., Suo, Y., Somerville, I., Li, W., He, B., Zheng, M. and Yu, K. 2022. Geodynamic mechanism and classification of basins in the Earth system. *Gondwana Research*. **102**, pp.200–228.

Kalinowski, A. and Oliver, A. 2004. ASTER Mineral Index Processing. *Remote Sensing Application Geoscience Australia*. (October).

Kasidi, S. and Nur, A. 2014. Estimation of Curie Point Depth, Heat Flow and Geothermal Gradient Infered from Aeromagnetic Data over Jalingo and Environs North–Eastern Nigeria. *International Journal of Science & …*, pp.294–301.

Kaufmann, H. 1988. Mineral exploration along the aqaba-levant structure by use of tm- data concepts, processing and results. *International Journal of Remote Sensing*. **9**(10–11), pp.1639–1658.

Keller, G. V. 1986. *An Introduction to Geophysical Exploration* [Online]. Available from: http://doi.wiley.com/10.1029/EO067i011p00132-01.

Khaleghi, M., Ranjbar, H., Shahabpour, J. and Honarmand, M. 2014. Spectral angle mapping, spectral information divergence, and principal component analysis of the ASTER SWIR data for exploration of porphyry copper mineralization in the Sarduiyeh area, Kerman province, Iran. *Applied Geomatics*. **6**(1), pp.49–58.

Khidir, S.O. El and Babikir, I.A.A. 2013. Digital image processing and geospatial analysis of

landsat 7 ETM+ for mineral exploration, Abidiya area, North Sudan. *International Journal of Geomatics and Geosciences*. **3**(3), pp.645–658.

Kirby, J.F. and Swain, C.J. 2009. A reassessment of spectral Te estimation in continental interiors: the case of North America. *Zootaxa*. **68**, pp.58–68.

Klein, G. 1990. Maturation-based geodynamic / geochemical classification of sedimentary basins. . **69**, pp.1–6.

Klein, G.D. V. 1991. Geodynamic and geochemical aspects of sedimentary basin classification. *Journal of African Earth Sciences*. **13**(1), pp.1–11.

Kolawole, F., Atekwana, E.A., Malloy, S., Stamps, D.S., Grandin, R., Abdelsalam, M.G., Leseane, K. and Shemang, E.M. 2017. Aeromagnetic, gravity, and Differential Interferometric Synthetic Aperture Radar analyses reveal the causative fault of the 3 April 2017 Mw6.5 Moiyabana, Botswana, earthquake. *Geophysical Research Letters*. **44**(17), pp.8837–8846.

Koumetio, F., Njomo, D., Tatchum Noutchogwe, C., Ndoh Ndikum, E., Nguiya, S. and Kamga Tokam, A.-P. 2019. Choice of suitable regional and residual gravity maps, the case of the South-West Cameroon zone. *Earth and Planetary Physics*. **3**(1), pp.26–32.

Laske, G., Masters, G., Ma, Z. and Pasyanos, M. 2013. Update on CRUST1.0---A 1-degree global model of Earth's crust. *EGU General Assembly 2013*. **15**, p.2658.

Li, X. 2008. Magnetic reduction-to-the-pole at low latitudes: Observations and considerations. *Leading Edge (Tulsa, OK)*. **27**(8), pp.990–1002.

Li, Y. and Oldenburg, D.W. 1998. 3-D inversion of gravity data. *Geophysics*. **63**(1), pp.109–119.

Li, Y. and Oldenburg, D.W. 1996. 3-D inversion of magnetic data. *Geophysics*. **61**(3), pp.394–408.

Li, Y., Yang, Y. and Liu, T. 2010. Derivative-based techniques for geological contact mapping from gravity data. *Journal of Earth Science*. **21**(3), pp.358–364.

Liu, S., Fedi, M., Hu, X., Baniamerian, J., Wei, B., Zhang, D. and Zhu, R. 2018. Extracting Induced and Remanent Magnetizations From Magnetic Data Modeling. *Journal of Geophysical Research: Solid Earth*. **123**(11), pp.9290–9309.

Loughlin, W.P. 1991. Principal component analysis for alteration mapping. *Photogrammetric Engineering & Remote Sensing*. **57**(9), pp.1163–1169.

Lowell, J.D. 1995. Mechanics of basin inversion from worldwide examples. *Geological Society Special Publication*. **88**(88), pp.39–57.

Lowry, A.R. and Smith, R.B. 1994. Flexural rigidity of the Basin and Range-Colorado Plateau-Rocky Mountain transition from coherence analysis of gravity and topography. *Journal of Geophysical Research*. **99**(B10).

Luis, J.F. and Neves, M.C. 2006. The isostatic compensation of the Azores Plateau: A 3D admittance and coherence analysis. *Journal of Volcanology and Geothermal Research*. **156**(1–2), pp.10–22.

Macleod, I. and Ellis, R. 2013. Magnetic Vector Inversion, a simple approach to the challenge of varying direction of rock magnetization. *23rd International Geophysical Conference and Exhibition*. (August), pp.1–6.

MacLeod, I.N., Jones, K. and Dai, T.F. 1993. 3-D analytic signal in the interpretation of total magnetic field data at low magnetic latitudes. *Exploration Geophysics*. **24**(4), pp.679–688.

MAG3D 2017. A Program Library for Forward Modelling and Inversion of Magnetic Data over 3D Structures, version 6.

Mamah, L.., Okogbue, C.. and Onuoha, K.. 2005. Inversion Tectonics of Benue Trough. , pp.163–167.

Marghany, M. and Hashim, M. 2010. Lineament mapping using multispectral remote sensing satellite data. *International Journal of the Physical Sciences*. **5**(10), pp.1501–1507.

Masoud, A. and Koike, K. 2006. Tectonic architecture through Landsat-7 ETM+/SRTM DEM-derived lineaments and relationship to the hydrogeologic setting in Siwa region, NW Egypt. *Journal of African Earth Sciences*. **45**(4–5), pp.467–477.

Masoud, A.A. and Koike, K. 2011. Auto-detection and integration of tectonically significant lineaments from SRTM DEM and remotely-sensed geophysical data. *ISPRS Journal of Photogrammetry and Remote Sensing*. **66**(6), pp.818–832.

Maus, S., Gordon, D. and Fairhead, D. 1997. Curie-temperature depth estimation using a self-similar magnetization model. *Geophysical Journal International*. **129**(1), pp.163–168.

Maus, S., Sazonova, T., Hemant, K., Fairhead, J.D. and Ravat, D. 2007. National geophysical data center candidate for the world digital magnetic anomaly map. *Geochemistry, Geophysics, Geosystems*. **8**(6), pp.1–10.

Mazur, S., Campbell, S., Green, C. and Bouatmani, R. 2015. Extension across the Laptev Sea continental rifts constrained by gravity modeling. *Tectonics*. **34**(3), pp.435–448.

Mazur, S., Green, C., Bouatmani, R., Whittaker, J.M., Stewart, M.G. and Williams, S. 2012. Displacement along the Red River Fault constrained by extension estimates and plate reconstructions. *Tectonics*. **31**(5), pp.1–22.

McKenzie, D. 1978. Some remarks on the development of sedimentary basins. *Earth and Planetary Science Letters*. **40**(1), pp.25–32.

Mckenzie, D. and Bickle, M.J. 1988. The volume and composition of melt generated by extension of the lithosphere. *Journal of Petrology*. **29**(3), pp.625–679.

McKenzie, D. and Fairhead, D. 1997. Estimates of the effective elastic thickness of the continental lithosphere from Bouguer and free air gravity anomalies. *GEOPHYSICAL*

RESEARCH. **102**(B12), pp.523–27.

McKenzie, D., Yi, W. and Rummel, R. 2015. Estimates of Te for Continental Regions using GOCE gravity. *Earth and Planetary Science Letters*. **428**(Watts 2001), pp.97–107.

Melo, F.F. and Barbosa, V.C.F. 2018. Correct structural index in Euler deconvolution via base-level estimates. *Geophysics*. **83**(6), pp.J87–J98.

Mickus, K. and Hussein, M. 2016. Curie Depth Analysis of the Salton Sea Region, Southern California. *Pure and Applied Geophysics*. **173**(2), pp.537–554.

Min, G. and Hou, G. 2019. Mechanism of the Mesozoic African rift system: Paleostress field modeling. *Journal of Geodynamics*. **132**(April).

Miroslav, B., Michael, R. and Michael, L. 2013. Tutorial: The gravity-stripping process as applied to gravity interpretation in the eastern Mediterranean. *Leading Edge*. **32**(4), pp.410–416.

Moghaddam, M.M., Sabseparvar, M., Mirzaei, S. and Heydarian, N. 2016. Interpretation of Aeromagnetic Data to Locate Buried Faults in North of Zanjan Province, Iran. *Journal of Remote Sensing & GIS*. **4**(2).

Mohriak, W.U., Lira Rabelo, J., De Matos, R.D. and De Barros, M.C. 1995. Deep seismic reflection profiling of sedimentary basins offshore Brazil: Geological objectives and preliminary results in the Sergipe Basin. *Journal of Geodynamics*. **20**(4), pp.515–539.

Mokhtari, Z., Boomeri, M. and Bagheri, S. 2015. Digital Image Processing and Analysis Techniques for Detection of Hydrothermal Alteration Zones: A Case Study in Siah-Jangal Area, North of Taftan Volcano, Southeastern Iran. *Journal of the Indian Society of Remote Sensing*. **43**(2), pp.363–377.

Moore, R.B., Schwarz, G.E., Clark, S.F., Walsh, G.J. and Degnan, J.R. 2002. *Factors related to well yield in the fractured-bedrock aquifer of New Hampshire*.

Mukaila, A., Upendra, K.S. and Umar, M.M. 2019. Crustal structure of southern Benue Trough, Nigeria from 3D inversion of gravity data. *Journal of Geology and Mining Research*. **11**(4), pp.39–47.

Nabighian, M.N. 1972. The Analytic Signal of Two-Dimentional Magnetic Bodies with Polygonal Cross-section: Its Properties and Use for automated Anomaly Interpretation. *Geophysics*. **37**(3).

Najime, T. 2011. Depositional framework and Cretaceous stratigraphy of the Gboko Area Lower Benue Trough , Nigeria Introduction Cretaceous tectonic evolution and sedimentation along the Benue Trough was not uniform . This has led to the conventional sub-division of the tr. *Journal of Mining and Geology*. **47**(2), pp.147–165.

Ndougsa-Mbarga, T., Feumoe, A.N.S., Manguelle-Dicoum, E. and Fairhead, J.D. 2012. Aeromagnetic Data Interpretation to Locate Buried Faults in South- East Cameroon. *Scientific Research and Essays*. **7**(22), pp.49–63.

Ninomiya, Y. 2004. Lithologic mapping with multispectral ASTER TIR and SWIR data. *Sensors, Systems, and Next-Generation Satellites VII*. **5234**(February 2004), p.180.

Ninomiya, Y. 2003. Mapping quartz, carbonate minerals, and mafic-ultramafic rocks using remotely sensed multispectral thermal infrared ASTER data. *Thermosense XXIV*. **4710**(March 2002), pp.191–202.

Ninomiya, Y. and Fu, B. 2016. Regional Lithological Mapping Using ASTER-TIR Data: Case Study for the Tibetan Plateau and the Surrounding Area. *Geosciences*. **6**(3), p.39.

Ninomiya, Y., Fu, B. and Cudahy, T.J. 2005. Detecting lithology with Advanced Spaceborne Thermal Emission and Reflection Radiometer (ASTER) multispectral thermal infrared 'radiance-at-sensor' data. *Remote Sensing of Environment*. **99**(1–2), pp.127–139.

Nkono, C., Féménias, O. and Demaiffe, D. 2009. Geodynamic framework of large volcanic fields highlighted by SRTM DEMs: Method evaluation and perspectives exampled on three areas from the Cameroon Volcanic Line. *Journal of Volcanology and Geothermal Research*. **187**(1–2), pp.13–25.

Nwachukwu, J.I. 1985. Petroleum Prospects of Benue Trough, Nigeria. *American Association of Petroleum Geologists Bulletin*. **69**(4), pp.601–609.

Nwachukwu, S.O. 1972. The tectonic evolution of the the southern portion of the Benue Trough, Nigeria. *Geological Magazine*. **109**(5), pp.411–419.

Nwankwo, L.I. 2015. Geothermics Estimation of depths to the bottom of magnetic sources and ensuing geothermal parameters from aeromagnetic data of Upper Sokoto. *Geothermics*. **54**, pp.76–81.

Nwankwo, L.I. and Sunday, A.J. 2017. Regional estimation of Curie-point depths and succeeding geothermal parameters from recently acquired high-resolution aeromagnetic data of the entire Bida Basin, north-central Nigeria. *Geothermal Energy Science*. **5**(1), pp.1–9.

Nwosu, O.B. 2014. Determination Of Magnetic Basement Depth Over Parts Of Middle Benue Trough By Source Parameter Imaging (SPI) Technique Using HRAM. . **3**(1), pp.262–271.

Obaje, N.G. 2009. *Geology and Mineral Resources of Nigeria* [Online]. Available from: http://www.springerlink.com/index/10.1007/978-3-540-92685-6.

Obaje, N.G., Attah, D.O., Opeloye, S.A. and Moumouni, A. 2006. Geochemical evaluation of the hydrocarbon prospects of sedimentary basins in Northern Nigeria. *Geochemical Journal*. **40**(3), pp.227–243.

Obaje, N.G., Wehner, H., Scheeder, G., Abubakar, M.B. and Jauro, A. 2004. Hydrocarbon prospectivity of Nigeria's inland basins: from the viewpoint of organic geochemistry and organic petrology. *American Association of Petroleum Geologists Bulletin*. **Vol. 88**(No. 3), pp.325-353.

Obasi, A.I., Selemo, A.O.I. and Nomeh, J.S. 2018. Gravity models as tool for basin boundary

demarcation: A case study of Anambra Basin, Southeastern Nigeria. *Journal of Applied Geophysics*. **156**, pp.31–43.

Ofoegbu, C.O. 1984a. A model for the tectonic evolution of the Benue Trough of Nigeria. *Geologische Rundschau*. **73**(3), pp.1007–1018.

Ofoegbu, C.O. 1985a. A review of the geology of the Benue Trough, Nigeria. *Journal of African Earth Sciences*. **3**(3), pp.283–291.

Ofoegbu, C.O. 1984b. Interpretation of aeromagnetic anomalies over the Lower and Middle Benue Trough of Nigeria. *Geophys. J. R. astr. SOC*. (March), pp.813–823.

Ofoegbu, C.O. 1985b. Interpretation of an aeromagnetic profile across the Benue Trough of Nigeria. *African Earth Earth Sciences*. **3**(3), pp.293–296.

Ofoegbu, C.O. 1982. Methods of interpreting magnetic anomalies with application to the Minch dyke and magnetic anomalies over the lower and middle Benue trough of Nigeria. *Unpublished Ph.D. thesis, Durham University*.

Ofoegbu, C.O. 1986. Preliminary results from a pseudogravity study of the Benue Trough, Nigeria. *Journal of African Earth Sciences*. **5**(2), pp.187–192.

Ofoegbu, C.O. and Onuoha, K.M. 1991. Analysis of magnetic data over the Abakaliki Anticlinorium of the Lower Benue Trough, Nigeria. *Marine and Petroleum Geology*. **8**(2), pp.174–183.

Oghuma, A.., Obiadi, I.. and Obiadi, C.. 2015. 2-D Spectral Analysis of Aeromagnetic Anomalies over Parts of Monguno and Environs, Northeastern Nigeria. *Journal of Earth Science & Climatic Change*. **06**(08), pp.6–11.

Ogunmola, J.K., Ayolabi, E.A. and Olobaniyi, S.B. 2014. Lineament extraction from spot 5 and Nigeriasat-X imagery of the Upper Benue Trough, Nigeria. *International Archives of the Photogrammetry, Remote Sensing and Spatial Information Sciences - ISPRS Archives*. **40**(1), pp.323–330.

Ogunmola, J.K., Ayolabi, E.A. and Olobaniyi, S.B. 2016. Structural-depth analysis of the Yola Arm of the Upper Benue Trough of Nigeria using high resolution aeromagnetic data. *Journal of African Earth Sciences*. **124**, pp.32–43.

Oha, I.A., Onuoha, K.M. and Dada, S.S. 2017. Contrasting styles of lead-zinc-barium mineralization in the Lower Benue Trough, Southeastern Nigeria. . **21**(1), pp.7–16.

Oha, I.A., Onuoha, K.M., Nwegbu, A.N. and Abba, A.U. 2016. Interpretation of high resolution aeromagnetic data over southern benue trough, Southeastern Nigeria. *Journal of Earth System Science*. **125**(2), pp.369–385.

Okereke, C.S. 1984. A gravity survey of the eastern sector of the Nigerian Basement Complex and studies of the gravity field of the West African Rift System. *Ph.D. Thesis, University of Leeds, Leeds (unpubl.).*, p.272.

Okereke, C.S. 1988. Contrasting modes of rifting: the Benue Trough and Cameroon volcanic

line, West Africa. *Tectonics*. **7**(4), pp.775–784.

Okiwelu, a a, Ph, D., Okwueze, E.E. and Akpabio, I.O. 2009. The Bouguer Gravity Anomaly Map of the Calabar Flank , Southeastern , Nigeria . . **10**(1), pp.656–662.

Okubo, Y., Tsu, H. and Ogawa, K. 1989. Estimation of Curie point temperature and geothermal structure of island arcs of Japan. *Tectonophysics*. **159**(3–4), pp.279–290.

Olade, M.A. 1975. Evolution of Nigeria's Benue Trough (Aulacogen): A tectonic model. *Geological Magazine*. **112**(6), pp.575–583.

Omo-Irabor, O., Ogala, J., Osokpor, J., Asadu, A., Ovarare, B. and Ogagarue, D. 2014. Geologic Mapping of Parts of the Benue Trough, Nigeria, Using Remotely Sensed Satellite Data. . (October), pp.417–512.

Onuoha, K.M. 1999. Structural features of Nigeria's coastal margin: An assessment based on age data from wells. *Journal of African Earth Sciences*. **29**(3), pp.485–499.

Onwuemesi, A.G. and Egboka, B.C.E. 1989. Gravity and vertical magnetic gradient investigations of a localised area of the Benue Trough, Nigeria. *Journal of African Earth Sciences*. **9**(3–4), pp.525–529.

Osinowo, O.O. and Taiwo, T.O. 2020. Analysis of high-resolution aeromagnetic (HRAM) data of Lower Benue Trough , Southeastern Nigeria , for hydrocarbon potential evaluation. *NRIAG Journal of Astronomy and Geophysics*. **9**(1), pp.350–361.

Oyewole M.A, Ukaegbu, V.. 2017. A GEOLOGIC FIELD REPORT ON THE GEOLOGY OF AFIKPO BASIN , LOWER BENUE TROUGH , SOUTH EASTERN NIGERIA. . **1**(1), pp.50–72.

Papliński, A.P. 1998. Directional filtering in edge detection. *IEEE Transactions on Image Processing*. **7**(4), pp.611–615.

Paranhos Filho, A.C., Nummer, A.R., Albrez, E.A., Ribeiro, A.A. and Machado, R. 2013. A study of structural lineaments in Pantanal (Brazil) using remote sensing data. *Anais da Academia Brasileira de Ciencias*. **85**(3), pp.913–922.

Parker, R.L. 1972. The rapid calculation of potential anomalies. *Geophys. J. R. Astron. Soc.* **31**(4), pp.447–455.

Pavlis, N. K., Holmes, S.A., Kenyon, S.C. and Factor, J.K. 2012. The development and evaluation of the Earth Gravitational Model 2008 (EGM2008). *Journal of Geophysical Research*. **117**(5), p.2633.

Pavlis, Nikolaos K., National Geospatial-Intelligence Agency Springfield, V.U.S.A., Holmes, S.A., SGT Incorporated, G.M.U.S.A., Kenyon, S.C., National Geospatial-Intelligence Agency Arnold, M.U.S.A., Factor, J.K. and National Geospatial-Intelligence Agency Arnold, M.U.S.A. 2012. The development and evaluation of the Earth Gravitational Model 2008 (EGM2008). *Journal of Geophysical Research*. **117**(5), p.2633.

Pérez-Diaz, L. and Eagles, G. 2014. Constraining South Atlantic growth with seafloor

spreading data. *Tectonics*. **33**(9), pp.1848–1873.

Pérez-Gussinyé, M., Lowry, A.R., Watts, A.B. and Velicogna, I. 2004. On the recovery of effective elastic thickness using spectral methods: Examples from synthetic data and from the Fennoscandian Shield. *Journal of Geophysical Research: Solid Earth*. **109**(10).

Pérez-Gussinyé, M., Metois, M., Fernández, M., Vergés, J., Fullea, J. and Lowry, A.R. 2009. Effective elastic thickness of Africa and its relationship to other proxies for lithospheric structure and surface tectonics. *Earth and Planetary Science Letters*. **287**(1–2), pp.152–167.

Petit, C., Burov, E. and Tiberi, C. 2008. Strength of the lithosphere and strain localisation in the Baikal rift. *Earth and Planetary Science Letters*. **269**(3–4), pp.523–529.

Pham, L.T., Oksum, E. and Do, T.D. 2018. GCH_gravinv: A MATLAB-based program for inverting gravity anomalies over sedimentary basins. *Computers and Geosciences*. **120**(February), pp.40–47.

Phillips, J.D. 2005. Can we estimate total magnetization directions from aeromagnetic data using Helbig ' s integrals ? . **0**(1), pp.681–689.

Phillips, J.D. 2001. Designing matched bandpass and azimuthal filters for the separation of potential-field anomalies by source region and source type. *ASEG 15th Geophysical Conference and Exhibition, August 2001, Brisbane.* (August).

Phillips, J.D. 2000. Locating magnetic contacts : a comparison of the horizontal gradient , analytic signal , and local wavenumber methods. . (1).

Phillips, J.D. 1997. Potential-Field Geophysical Software for the PC , version 2.2. *U S GeologicalS urvey,*.

Phillips, J.D., Hansen, R.O. and Blakely, R.J. 2007. The use of curvature in potential-field interpretation. *Exploration Geophysics*. **38**(2), pp.111–119.

Pilkington, M. and Keating, P. 2004. Contact mapping from gridded magnetic data ? a comparison of techniques. *Exploration Geophysics*. **35**(4), pp.306–311.

Pour, A.B., Hashim, M., Hong, J.K. and Park, Y. 2017. Lithological and alteration mineral mapping in poorly exposed lithologies using Landsat-8 and ASTER satellite data: North-eastern Graham Land, Antarctic Peninsula. *Ore Geology Reviews*. (July), pp.0–1.

Rajendran, S., al-Khirbash, S., Pracejus, B., Nasir, S., Al-Abri, A.H., Kusky, T.M. and Ghulam, A. 2012. ASTER detection of chromite bearing mineralized zones in Semail Ophiolite Massifs of the northern Oman Mountains: Exploration strategy. *Ore Geology Reviews*. **44**, pp.121–135.

Reford, S.W., Misener, D.J., Ugalde, H.A., Mcmaster, U., Gana, J.S. and Oladele, O. 2010. Nigeria ' s Nationwide High -resolution Airborne Geophysical Surveys Nigeria ' s Nationwide High -resolution Airborne Geophysical Surveys. , pp.1835–1839.

Reid, A., FitzGerald, D. and McInerny, P. 2003. Euler deconvolution of gravity data. *SEG*

Technical Program Expanded Abstracts. **22**(1), pp.580–583.

Reid, A.B., Allsop, J.., Granser, H., Millett, A.J. and Somerton, I.. 1990. Magnetic Interpretation in three dimensions using Euler Deconvolution. *Geophysics*. **8**(1), pp.80–91.

Reid, A.B., Allsop, J.M., Granser, H., Millett, A.J. and Somerton, I.W. 1998. Magnetic interpretation in 3-D using euler deconvolution. *1988 SEG Annual Meeting*. **55**(I), pp.364–366.

Reid, A.B., Ebbing, J. and Webb, S.J. 2014. Avoidable Euler Errors - the use and abuse of Euler deconvolution applied to potential fields. *Geophysical Prospecting*. **62**(5), pp.1162–1168.

Reid, A.B. and Thurston, J.B. 2014. The structural index in gravity and magnetic interpretation: Errors, uses, and abuses. *Geophysics*. **79**(4), pp.J61–J66.

Ren, K., Zhao, Junfeng, Liu, Q. and Zhao, Jian 2020. Hydrocarbons in igneous rock of Brazil: A review. *Petroleum Research*. **5**(3), pp.265–275.

Renne, P.R., Ernesto, M., Pacca, I.G., Coe, R.S., Glen, J.M., Prévot, M. and Perrin, M. 1992. The age of Paraná flood volcanism, rifting of Gondwanaland, and the Jurassic-Cretaceous boundary. *Science*. **258**(5084), pp.975–979.

Richards, J.A. and Jia, X. 2006. *Remote Sensing Digital Image Analysis*.

Rodríguez, E., Morris, C.S. and Belz, J.E. 2013. A global assessment of the SRTM performance. *Photogrammetric Engineering & Remote Sensing*. **72**(3), pp.249–260.

Roest, W.R. and Pilkington, M. 1993. Identifying remanent magnetization effects in magnetic data. *Geophysics*. **58**(5), pp.653–659.

Rowan, L.C., Mars, J.C. and Simpson, C.J. 2005. Lithologic mapping of the Mordor, NT, Australia ultramafic complex by using the Advanced Spaceborne Thermal Emission and Reflection Radiometer (ASTER). *Remote Sensing of Environment*. **99**(1–2), pp.105–126.

Saada, S.A. 2015. Edge Detectionand Depth Estimation from Magnetic DataofWadi Araba,Eastern Desert-Egypt. *IOSR Journal of Applied Geology and Geophysics Ver. I.* **3**(6), pp.2321–990.

Saadi, N.M., Watanabe, K., Imai, A. and Saibi, H. 2008. Integrating potential fields with remote sensing data for geological investigations in the Eljufra area of Libya. *Earth, Planets and Space*. **60**(6), pp.539–547.

Sabins, F.F. 1999. Remote sensing for mineral exploration. *Ore Geology Reviews*. **14**(3–4), pp.157–183.

Salem, A. 2011. Interpretation of magnetic data over tilted basement blocks: An example from the northern North Sea. *Geophysical Prospecting*. **59**(6), pp.1013–1020.

Salem, A., Blakely, R., Green, C., Fairhead, D. and Ravat, D. 2014. Estimation of depth to top of magnetic sources using the local-wavenumber approach in an area of shallow Moho and Curie depth — The Red Sea. *Interpretation*. **2**(4), pp.SJ1–SJ8.

Salem, A., Campbell, S., Moorhead, L. and Fairhead, D. 2013. An enhanced tilt depth method for interpreting magnetic data over vertical contacts of finite extent. *75th European Association of Geoscientists and Engineers Conference and Exhibition 2013 Incorporating SPE EUROPEC 2013: Changing Frontiers*. (June 2013), pp.365–369.

Salem, A., Green, C., Cheyney, S., Fairhead, J.D., Aboud, E. and Campbell, S. 2014. Mapping the depth to magnetic basement using inversion of pseudogravity: Application to the Bishop model and the Stord Basin , northern North Sea. *Interpretation*. **2**(2), pp.69–78.

Salem, A., Green, C., Fairhead, D. and Aboud, E. 2012. Mapping basement relief of Abu Gharadig Basin, Western Desert of Egypt using 3D inversion of pseudo-gravity data. *ASEG Extended Abstracts*. **2012**(1), pp.1–4.

Salem, A., Green, C., Ravat, D., Singh, K.H., East, P., Fairhead, J.D., Mogren, S. and Biegert, E. 2014. Depth to Curie temperature across the central Red Sea from magnetic data using the de-fractal method. *Tectonophysics*. **624**–**625**, pp.75–86.

Salem, A. and Ravat, D. 2003. A combined analytic signal and Euler method (AN-EUL) for automatic interpretation of magnetic data. *Geophysics*. **68**(6), pp.1952–1961.

Salem, A., Williams, S., Fairhead, J.D., Ravat, D. and Smith, R. 2007. Tilt-depth method: A simple depth estimation method using first-order magnetic derivatives. *The Leading Edge*. **26**(12), pp.1502–1505.

Salem, A., Williams, S., Samson, E., Fairhead, D., Ravat, D. and Blakely, R.J. 2010. Sedimentary basins reconnaissance using the magnetic Tilt-Depth method. *Exploration Geophysics*. **41**(3), pp.198–209.

Scheidegger, A.E. 1982. Principles of Geodynamics.

Scheidegger, A.E. and Ajakaiye, D.E. 1985. Geodynamics of Nigerian shield areas. *Journal of African Earth Sciences*. **3**(4), pp.461–470.

Shearer, S.. 2005. Three-dimensional remanent magnetization in the presence of inversion of magnetic data. *Colorado School of Mines, Unpublished M.Sc. thesis*., p.148.

Shemang, E.M., Ajayi, C.O. and Jacoby, W.R. 2001. A magmatic failed rift beneath the Gongola arm of the upper Benue trough, Nigeria? *Journal of Geodynamics*. **32**(3), pp.355–371.

Shuey, R.T., Schellinger, D.K., Tripp, A.C. and Al, L.B. 1977. Curie depth determination from aeromagnetic spectra. *Geophysical Journal of the Royal Astronomical Society*. **50**(1), pp.75–101.

Simeoni, O. and Brückl, E. 2009. The effect of gravity stripping on the resolution of deep crustal structures in the eastern alps and surrounding regions. *Austrian Journal of Earth*

Sciences. **102**(2), pp.157–169.

Sleep, N.H. 1990. Hotspots and mantle plumes: some phenomenology. *Journal of Geophysical Research*. **95**(B5), pp.6715–6736.

Smith, R.S., Thurston, J.B., Dai, T.F. and MacLeod, I.N. 1998. iSPI^{TM} - The improved source parameter imaging method. *Geophysical Prospecting*. **46**(2), pp.141–151.

Smith, W.H.F. and Wessel, P. 1990. Gridding with continuous curvature splines in tension. *Geophysics*. **55**(3), pp.293–305.

Solomon, S. and Ghebreab, W. 2006. Lineament characterization and their tectonic significance using Landsat TM data and field studies in the central highlands of Eritrea. *Journal of African Earth Sciences*. **46**(4), pp.371–378.

Spector, A. and Grant, F.. S. 1970. Statistical models for interpreting aeromagnetic data. *Geophysics*. **35**(2), pp.293–302.

Speranza, F., Minelli, L., Pignatelli, A. and Gilardi, M. 2016. Curie temperature depths in the Alps and the Po Plain (northern Italy): Comparison with heat flow and seismic tomography data. *Journal of Geodynamics*. **98**, pp.19–30.

Sreejith, K.M., Unnikrishnan, P. and Radhakrishna, M. 2019. Isostasy and crustal structure of the Chagos–Laccadive Ridge, Western Indian Ocean: Geodynamic implications. *Journal of Earth System Science*. **128**(6).

Stanton, N., Manatschal, G., Autin, J., Sauter, D., Maia, M. and Viana, A. 2016. Geophysical fingerprints of hyper-extended, exhumed and embryonic oceanic domains: the example from the Iberia–Newfoundland rifted margins. *Marine Geophysical Research*. **37**(3), pp.185–205.

Stavrev, P. and Gerovska, D. 2000. Magnetic field transforms with low sensitivity to the direction of source magnetization and high centricity. *Geophysical Prospecting*. **48**(2), pp.317–340.

Stephens, T.L., Walker, R.J., Healy, D., Bubeck, A., England, R.W. and McCaffrey, K.J.W. 2017. Igneous sills record far-field and near-field stress interactions during volcano construction: Isle of Mull, Scotland. *Earth and Planetary Science Letters*. **478**, pp.159–174.

Stuart, G.W., Fairhead, J.D., Dorbath, L. and Dorbath, C. 1985. A seismic refraction study of the crustal structure associated with the Adamawa Plateau and Garoua Rift, Cameroon, West Africa. *Geophysical Journal of the Royal Astronomical Society*. **81**(1), pp.1–12.

Sultan, M., Arvidson, R.E., Sturchio, N.C. and Guinness, E.A. 1987. Lithologic mapping in arid regions with Landsat thematic mapper data: Meatiq dome, Egypt. *Geological Society of America Bulletin*. **99**(6), pp.748–762.

Swain, C.J. 2000. Reduction-to-the-pole of regional magnetic data with variable field direction, and its stabilisation at low inclinations. *Exploration Geophysics*. **31**(2), pp.78–83.

Tanaka, A., Okubo, Y. and Matsubayashi, O. 1999. Curie point depth based on spectrum analysis of the magnetic anomaly data in East and Southeast Asia. *Tectonophysics*. **306**(3–4), pp.461–470.

Taoufik, M., Baghdad, B. and Hadi, H. El 2016. Structural Interpretation of Lineaments by Remote Sensing and GIS using Landsat 8 Data : A Case Study of Akreuch Area (Morocco). *European Journal of Scientific Research*. **138**(May), pp.216–224.

Testa, F.J., Villanueva, C., Cooke, D.R. and Zhang, L. 2018. Lithological and hydrothermal alteration mapping of epithermal, porphyry and tourmaline breccia districts in the argentine andes using ASTER imagery. *Remote Sensing*. **10**(2), pp.1–45.

Thompson, D.T. 1982. EULDPH: A new technique for making computer-assisted depth estimates from magnetic data. *Geophysics*. **47**(1), p.31.

Thurston, J.B. and Smith, R.S. 1997. Automatic conversion of magnetic data to depth, dip, and susceptibility contrast using the SPI (TM) method. *Geophysics*. **62**(3), p.807.

Tiwari, V.M. and Mishra, D.C. 1999. Estimation of effective elastic thickness from gravity and topography data under the Deccan Volcanic Province, India. *Earth and Planetary Science Letters*. **171**(2), pp.289–299.

Tulyatid, J. and Fairhead, J.D. 1996. Application of combined aeromagnetic and radiometric mapping of geological structure in Central Thailand. *Paper presented at the 1996 SEG Annual Meeting, Denver, Colorado, November 1996.*, pp.1391–1394.

U.S Geological Survey, U.S. 2015. Advanced Spaceborne Thermal Emission and Reflection Radiometer Level 1 Precision Terrain Corrected Registered At-Sensor Radiance (AST_L1T) Product, AST_L1T Product User's Guide. *Open-File Report*. **1**, pp.1–68.

Ugbor, D.. and Okeke, F.N. 2010. Geophysical investigation in the Lower Benue trough of Nigeria using gravity method. *Int. J. Phys. Sci.* **5**(11), pp.1757–1769.

Vargas, R., Sainz-Maza Aparicio, S., Muñoz-Martín, A., Granja Bruña, J.L. and Sentre Domingo, M.A. 2015. Gravity modeling of the lithosphere in the Calatrava Volcanic Province (Spain): geodynamic implications. *Journal of Iberian Geology*. **41**(2), pp.233–252.

Verduzco, B., Fairhead, J.D., Green, C.M. and MacKenzie, C. 2004. New insights into magnetic derivatives for structural mapping. *The Leading Edge*. **23**(2), pp.116–119.

Volesky, J.C., Stern, R.J. and Johnson, P.R. 2003. Geological control of massive sulfide mineralization in the Neoproterozoic Wadi Bidah shear zone, southwestern Saudi Arabia, inferences from orbital remote sensing and field studies. *Precambrian Research*. **123**(2–4), pp.235–247.

Walker, R.J., Healy, D., Kawanzaruwa, T.M., Wright, K.A., England, R.W., McCaffrey, K.J.W., Bubeck, A.A., Stephens, T.L., Farrell, N.J.C. and Blenkinsop, T.G. 2017. Igneous sills as a record of horizontal shortening: The San Rafael subvolcanic field, Utah. *Bulletin of the Geological Society of America*. **129**(9–10), pp.1052–1070.

Watts, A.B. 2001. Isostasy and Flexure of the Lithosphere. *Cambridge: Cambridge University Press.*

Watts, A.B. and Burov, E.B. 2003. Lithospheric strength and its relationship to the elastic and seismogenic layer thickness. *Earth and Planetary Science Letters*. **213**(1–2), pp.113–131.

Welford, J.K., Dehler, S.A. and Funck, T. 2020. Crustal velocity structure across the Orphan Basin and Orphan Knoll to the continent ocean transition, offshore Newfoundland, Canada. *Geophysical Journal International*. **221**(1), pp.37–59.

Welford, J.K. and Hall, J. 2007. Crustal structure of the Newfoundland rifted continental margin from constrained 3-D gravity inversion. *Geophysical Journal International*. **171**(2), pp.890–908.

Welford, J.K., Shannon, P.M., O'Reilly, B.M. and Hall, J. 2010. Lithospheric density variations and Moho structure of the Irish Atlantic continental margin from constrained 3-D gravity inversion. *Geophysical Journal International*. **183**(1), pp.79–95.

Wijns, C., Perez, C. and Kowalczyk, P. 2005. Theta map: Edge detection in magnetic data. *Geophysics*. **70**(4), pp.L39–L43.

Wilson, M. 1992. Magmatism and continental rifting during the opening of the South Atlantic Ocean: a consequence of Lower Cretaceous superplume activity? *In: Storey, B.C., Alabaster, T., Pankhurst, R.J. (Eds.), Magmatism and the Causes of Continental Break-up. Geological Society of London, Special Publication No. 68, pp. 241–255*. (68), p.1992.

Wright, J. 1968. South Atlantic continental drift and the Benue Trough. *Tectonophysics*. **6**(4), pp.301–310.

Wright, J.B. 1976. Fracture systems in Nigeria and initiation of fracture zones in the South Atlantic Figure 1 represents the convergence of two quite different lines of evidence which together make a compelling case for proposing that initiation of the Romanche and Chain f. . **34**, pp.43–47.

Wright, J.B. 1985. The Benue Trough and coastal basins. *Geology and Mineral Resources of West Africa*. **120**, pp.57–68.

Wu, J.E., McClay, K. and Frankowicz, E. 2015. Niger Delta gravity-driven deformation above the relict Chain and Charcot oceanic fracture zones, Gulf of Guinea: Insights from analogue models. *Marine and Petroleum Geology*. **65**, pp.43–62.

Wyer, P. and Watts, A.B. 2006. Gravity anomalies and segmentation at the East Coast, USA continental margin. *Geophysical Journal International*. **166**(3), pp.1015–1038.

Yamaguchi, Y. and Naito, C. 2003. Spectrail indices for lithologic discrimination and mapping by using the ASTER SWIR bands. *International Journal of Remote Sensing*. **24**(22), pp.4311–4323.

Yao, K., Pradhan, B. and Idrees, M.O. 2017. Identification of Rocks and Their Quartz

Content in Gua Musang Goldfield Using Advanced Spaceborne Thermal Emission and Reflection Radiometer Imagery. *Journal of Sensors*. **2017**.

Yu, L., Porwal, A., Holden, E. and Charles, M. 2011. Suppression of vegetation in multispectral remote sensing images. *International Journal of Remote Sensing*. (November), pp.37–41.

Zbořil, L., Bodnár, J., Orlický, O. and Šefara, J. 1986. Geophysical investigation of deep-seated oil-bearing structures in the central part of the African continent. *Journal of African Earth Sciences*. **5**(2), pp.155–162.

Zhang, H., Marangoni, Y.R., Hu, X. and Zuo, R. 2014. NTRTP: A new reduction to the pole method at low latitudes via a nonlinear thresholding. *Journal of Applied Geophysics*. **111**, pp.220–227.

Zhang, Q., Zhang, Y.T., Yin, G. and Li, Z.N. 2018. An improved frequency-domain algorithm for stable reduction to the pole at low latitudes. *Journal of Geophysics and Engineering*. **15**(4), pp.1767–1782.

Zhang, T., Yi, G., Li, H., Wang, Z., Tang, J., Zhong, K., Li, Y., Wang, Q. and Bie, X. 2016. Integrating data of ASTER and Landsat-8 OLI (AO) for hydrothermal alteration mineral mapping in duolong porphyry cu-au deposit, Tibetan Plateau, China. *Remote Sensing*. **8**(11).

APPENDICES

APPENDIX A: Surface mapping and structure

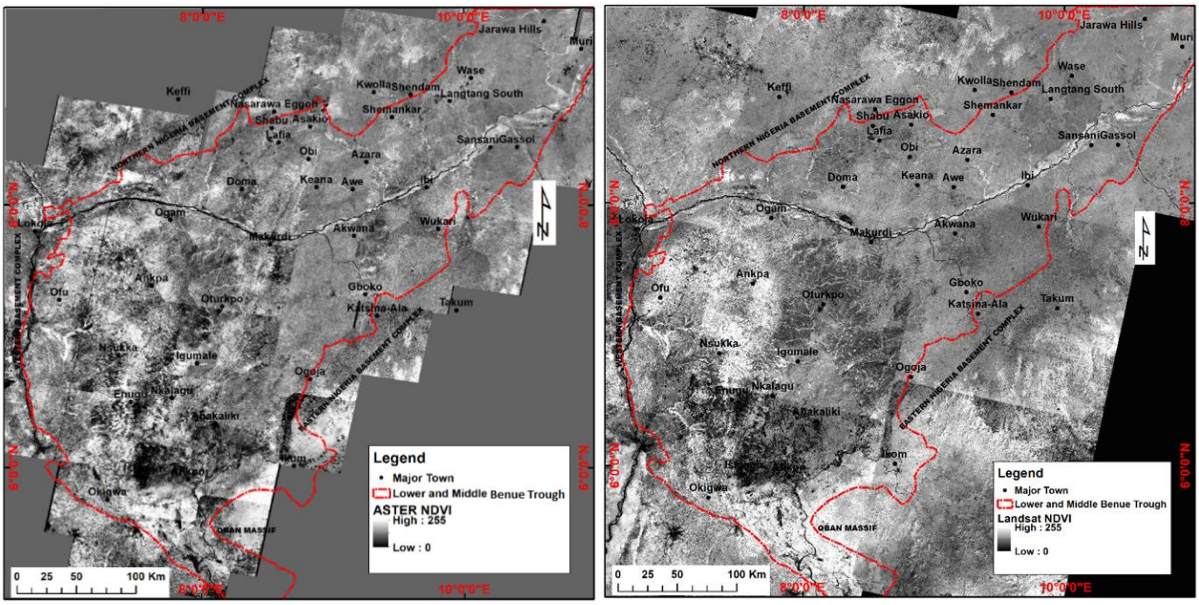

(a) **(b)**

Appendix A 1: (a) NDVI of ASTER (b) NDVI of Landsat

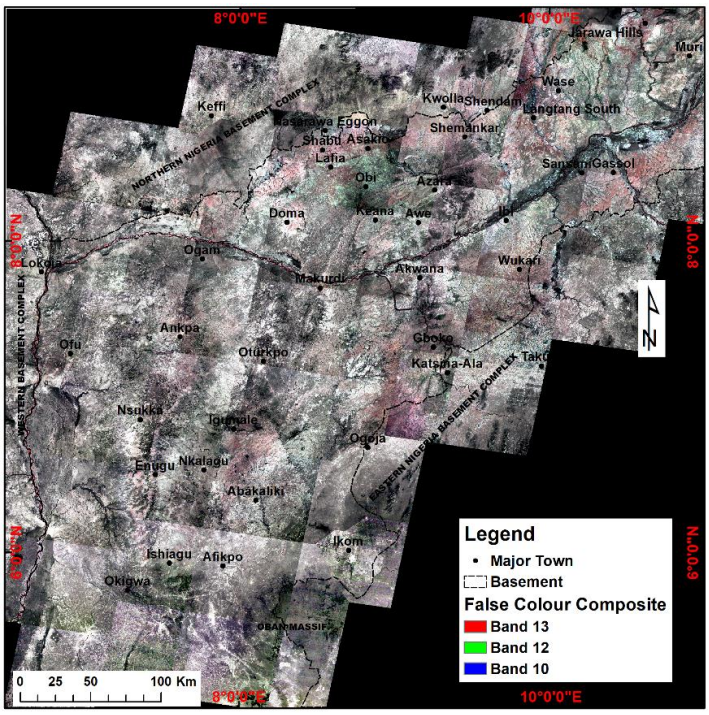

Appendix A 2: ASTER TIR false colour composite from bands 13, 12, 10 in RGB. The combination is highly correlated and so the need for decorrelation stretch.

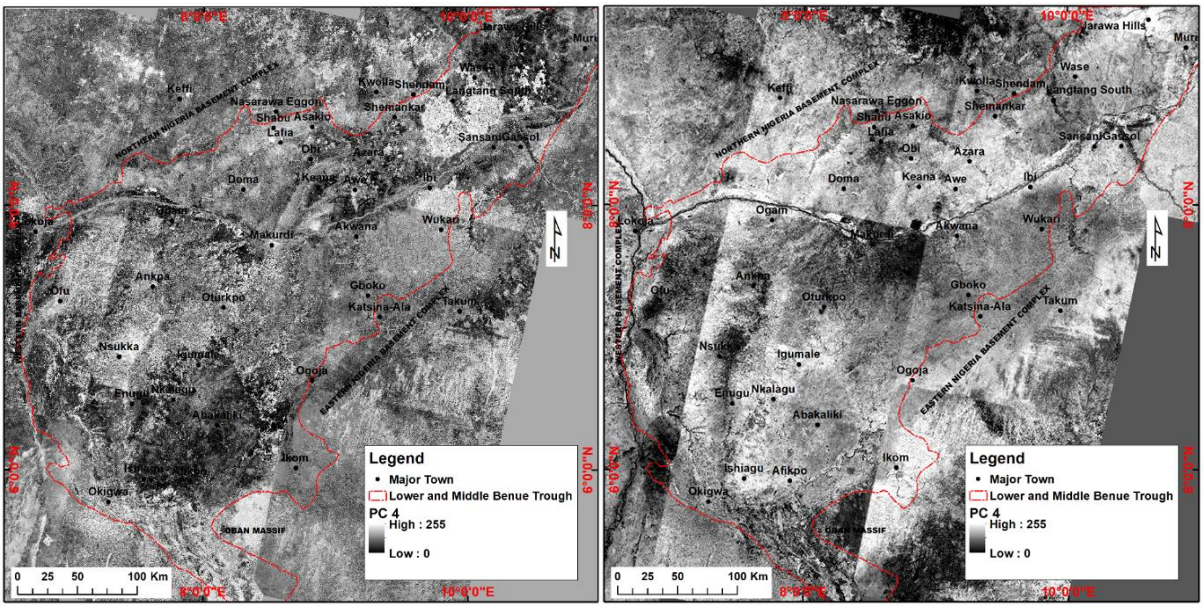

(a) **(b)**

Appendix A 3: (a) Principal component 4 for bands 2, 5, 6 and 7 (Hydroxyl image) (b) Principal component 4 for bands 2, 4, 5, and 6 (Iron-oxide image).

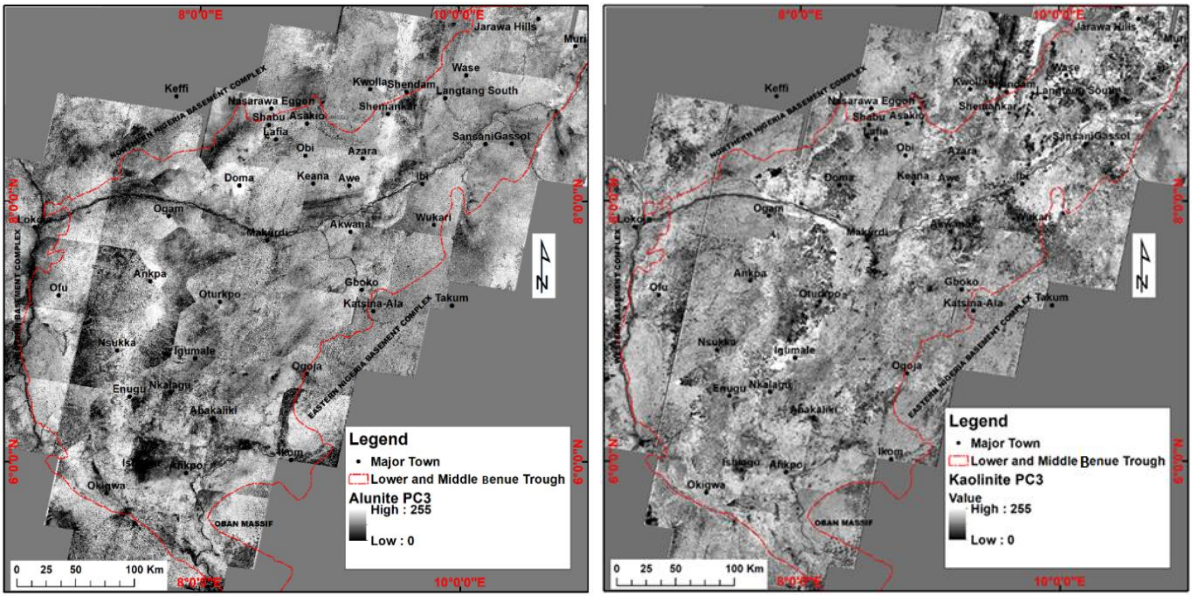

(a) **(b)**

Appendix A 4: (a) Alunite mineral abundance from ASTER bands 1, 3, 5, 7 in dark pixels (b) Kaolinite mineral stains from ASTER bands 1, 4, 6, 7 where the dark pixels indicate the presence kaolinite.

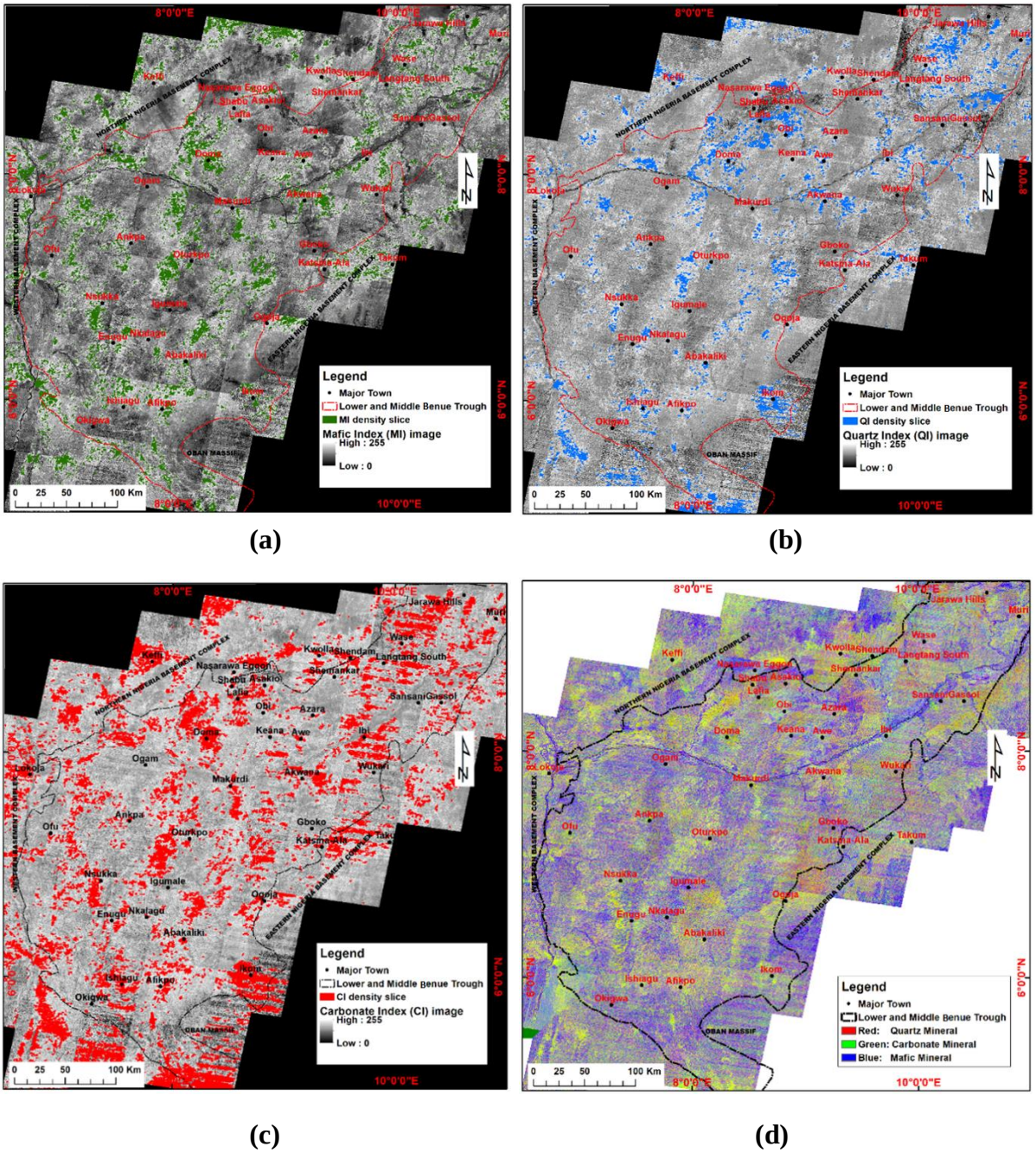

Appendix A 5: **(a) Mafic index image (b) Quartz index image (c) Carbonates index image (d) Composite mineral indices for ASTER image where QI (Quartz index), CI (Carbonate Index) and MI (Mafic Index) are represented as red, green, and blue, respectively.**

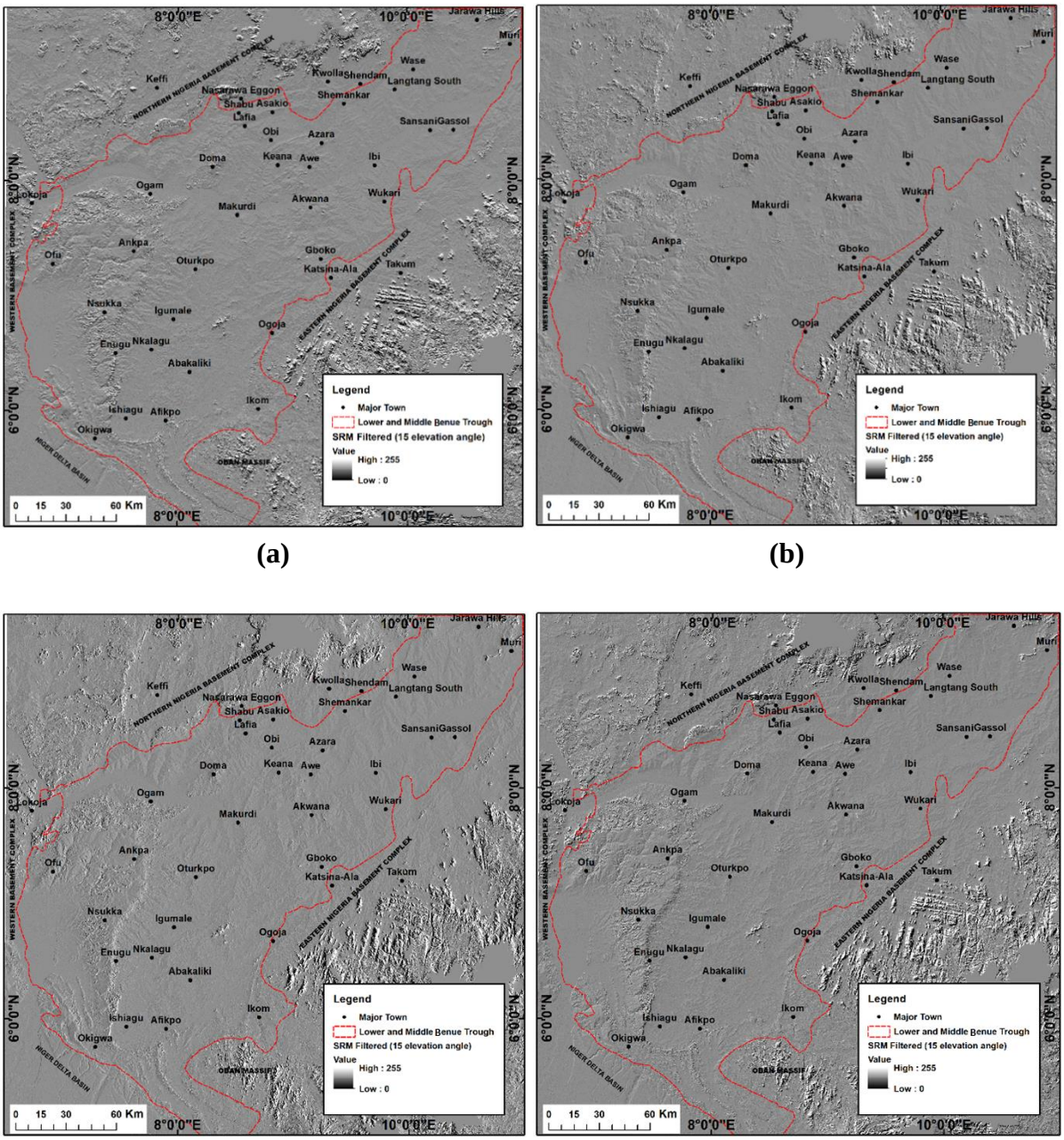

(a) **(b)**

(c) **(d)**

Appendix A 6: SRTM shaded relief model filtered at 15° sun tilt angle with azimuthal angle (a) 0° (b) 45° (c) 90° (d) 135°

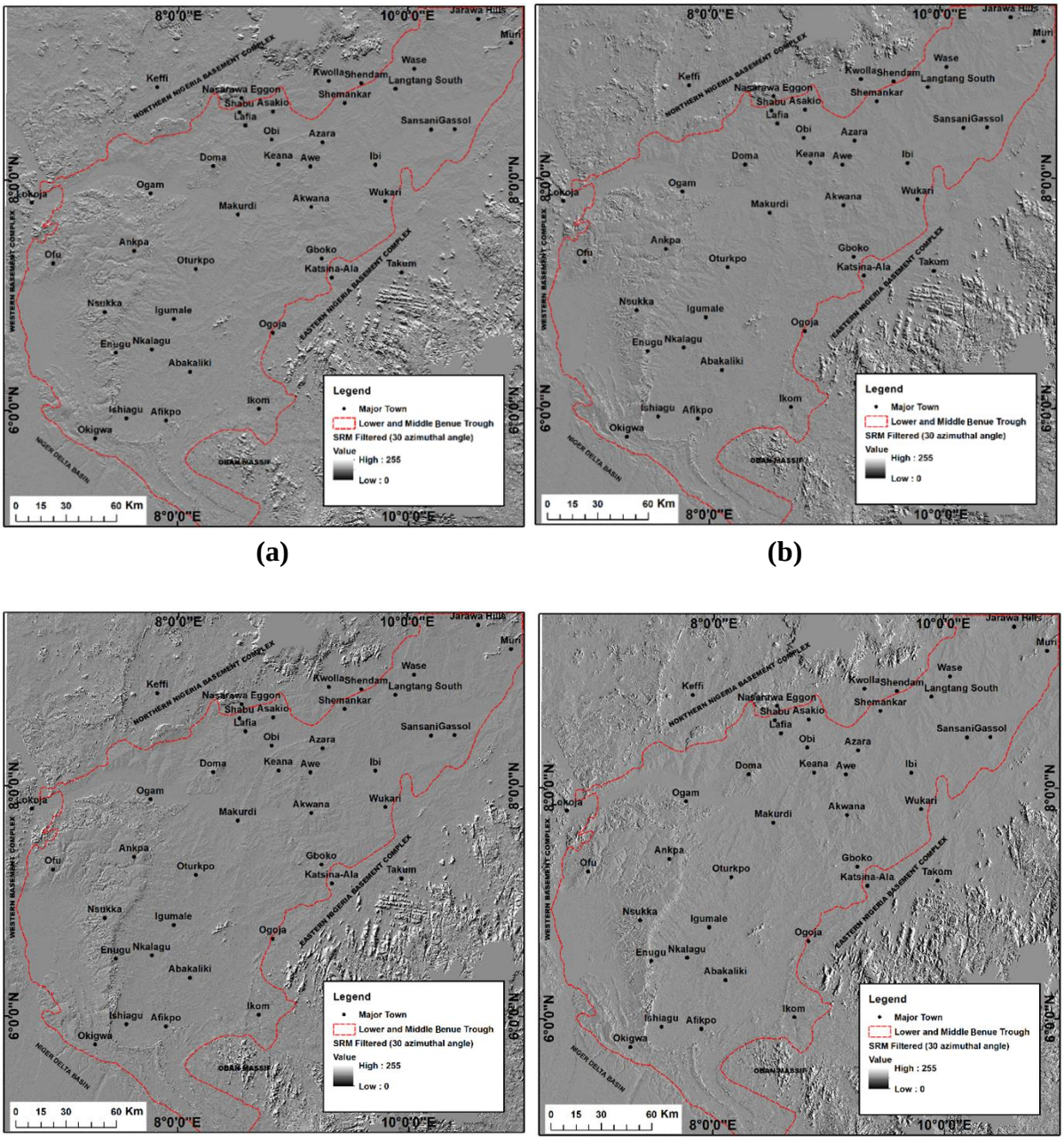

(a) **(b)**

(c) **(d)**

Appendix A 7: SRTM Shaded Relief Model Filtered at 30° Sun tilt angle with Azimuthal angle (a) 0° (b) 45° (c) 90° (d) 135°

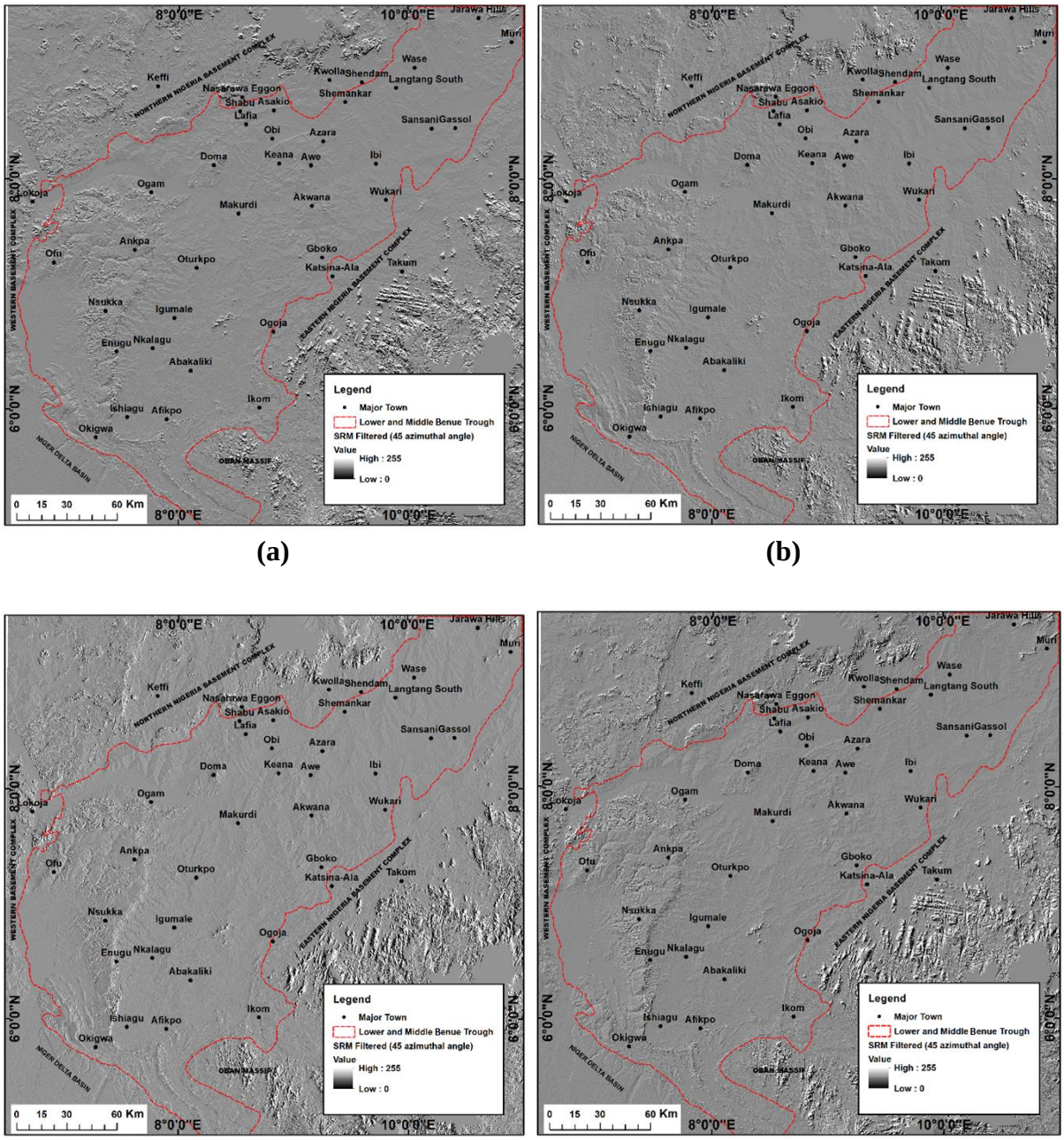

(a) **(b)**

(c) **(d)**

Appendix A 8: SRTM Shaded Relief Model Filtered at 45° Sun tilt angle with Azimuthal angle (a) 0° (b) 45° (c) 90° (d) 135°

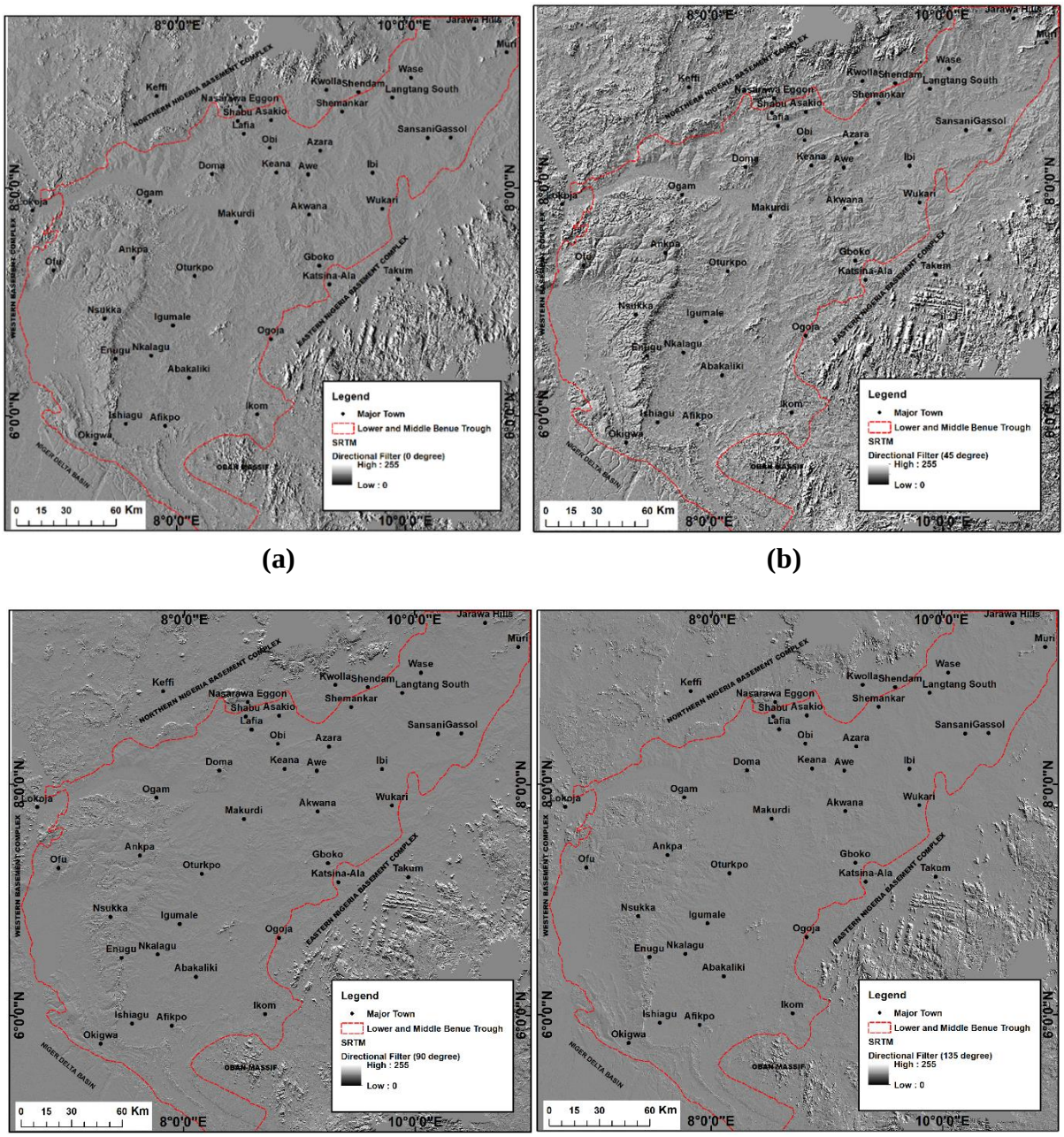

(a) **(b)**

(c) **(d)**

Appendix A 9: SRTM Directional Filter (a) 0° (b) 45° (c) 90° (d) 135°

APPENDIX B: Magnetic and gravity data sets and methods

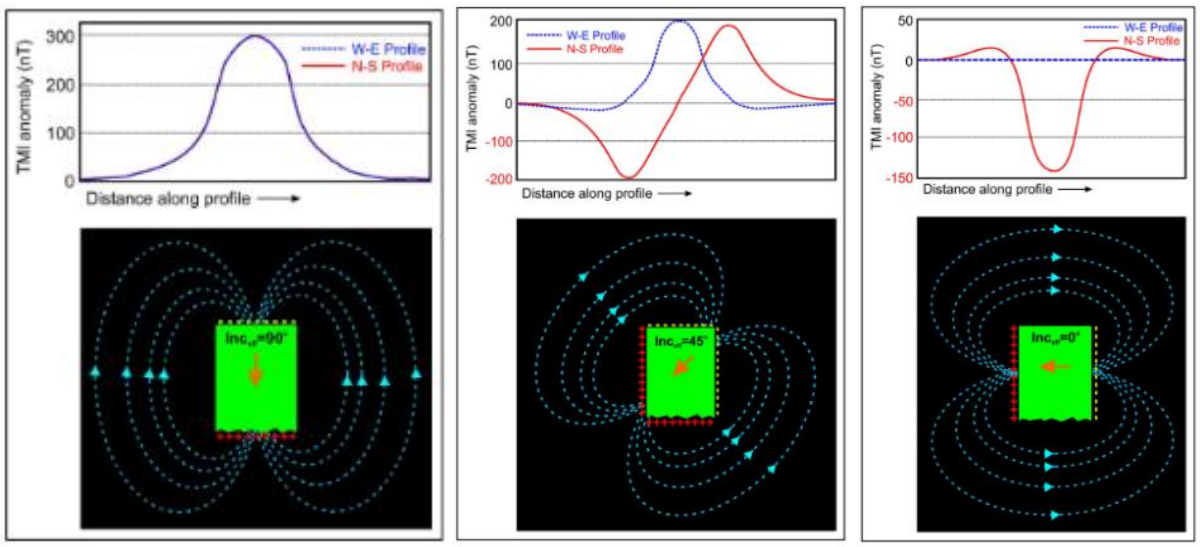

Inclination = 90° (RTP) **Inclination = 45°** **Inclination = 0° (RTE)**

Appendix B 1: Diagram showing North-South model (Red-coloured) and East-West, E-W (Blue-coloured) profiles across North-South (N-S) cross sections of magnetic anomaly. The green-coloured structure and its magnetic 2D contacts strike perpendicularly into the page (Esuene, 2012). The body has an anisotropic structure with inclination of 45° but RTP (inclination = 90°) transforms the anomaly such that it peaks vertically over the body while RTE (Inclination = 0°) transforms the anomaly over the body but in this case its trough over the anomaly with a negative anomaly.

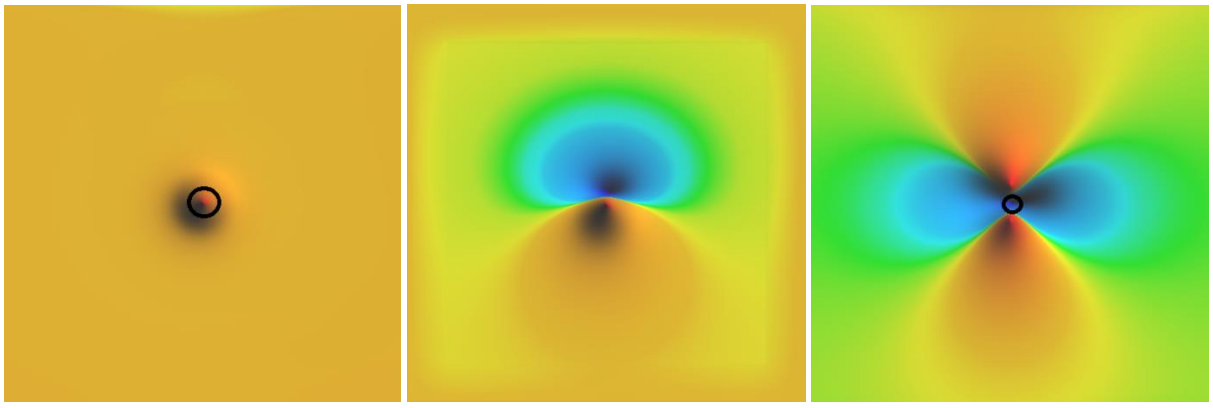

Inclination = 90° (RTP) **Inclination = 60°** **Inclination = 0° (RTE)**

Appendix B 2: Plan view of a vertical pipe dipole model with inclination of 60°. RTP (Inclination = 90°) centres the anomaly in both directions over the causative body. The RTE also centres the anomaly over the causative body, but it has a negative anomaly (trough) and then causes E-W anomaly body.

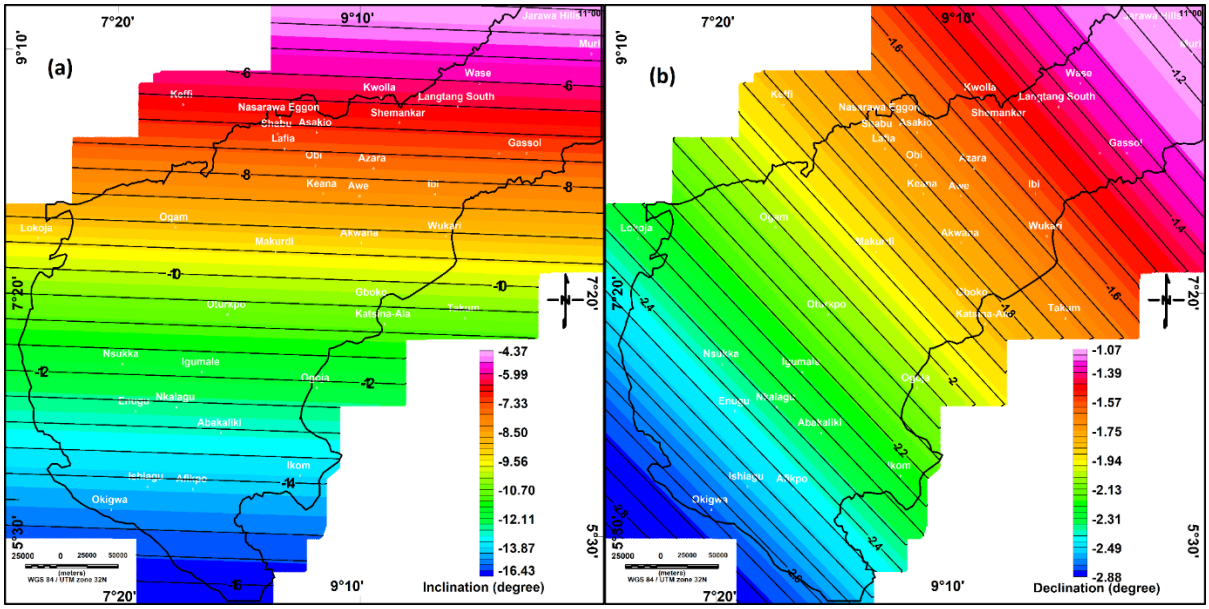

Appendix B 3: (a) Variation in inclination of geomagnetic field (b) Variation in geomagnetic field declination across the area (Geosoft Inc., 2015).

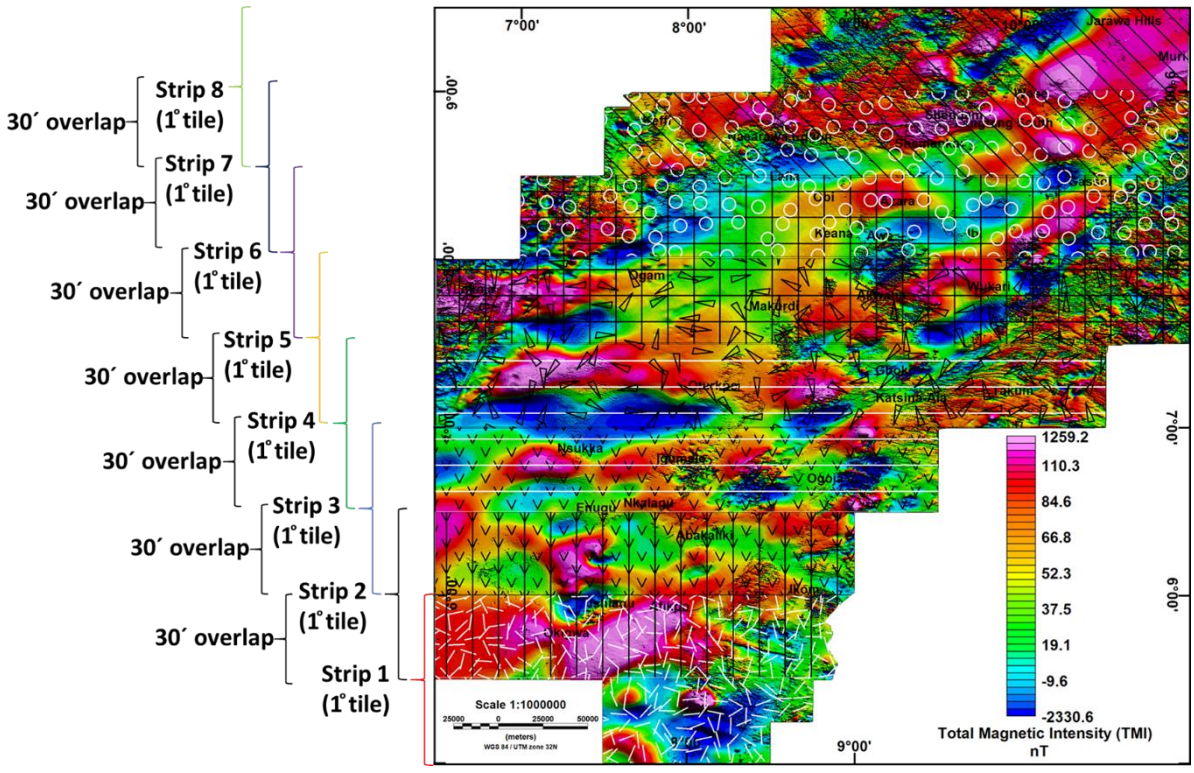

Appendix B 4: An index to aeromagnetic data strips overlain on the total magnetic intensity (TMI) map. The mean inclinations and declinations for strip 1 are -16.4° and -13.7°; Strip 2 are -5.9° and -2.5°; Strip 3 are 12.5° and -2.3°; Strip 4 are -11.1° and -2.1°; Strips 5 are -9.8° and -1.9°; Strip 6 are -8.6° and -1.8°; Strip 7 are -7.2° and -1.6°; and Strip 8 are -5.9° and -1.9° respectively.

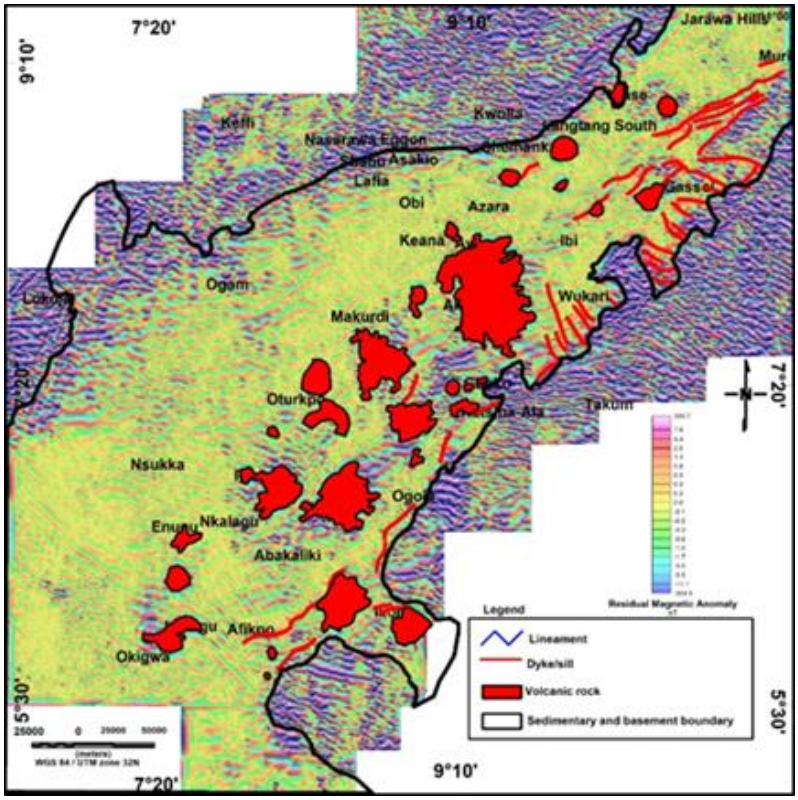

Appendix B 5: Residual DRTE magnetic shallow structures at 400 m mean depth

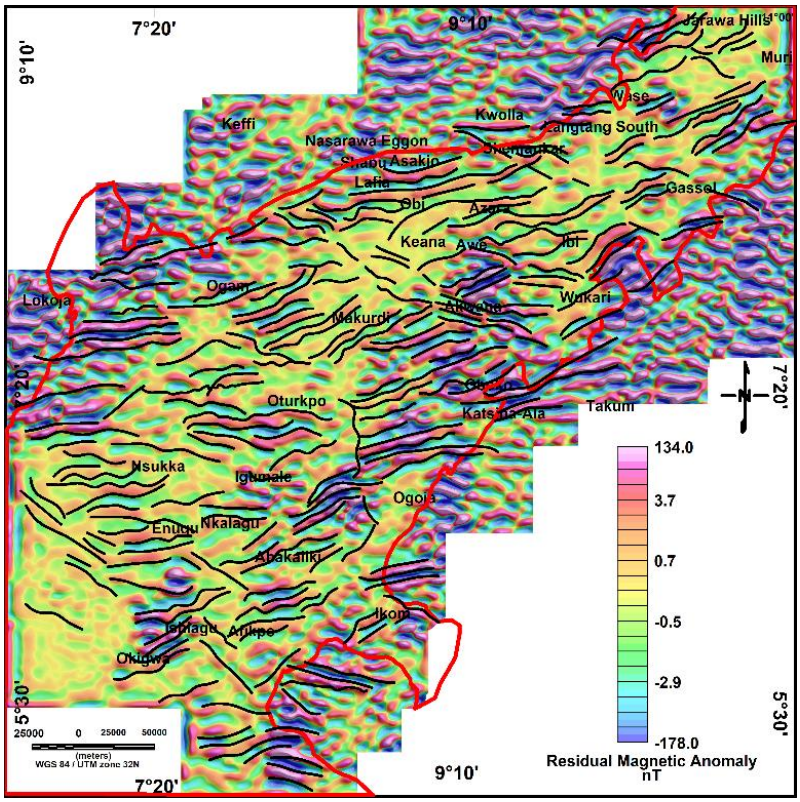

Appendix B 6: Residual DRTE magnetic imaging of shallow structures at 2 km mean depth.

APPENDIX C: Modelling of the basin

X (m)	Y (m)	Depth (m)	Observed Pseudogravity (nT.m)	Calculated Pseudogravity (nT.m)
389952.86	965855.23	81.91	0.1435	0.0164
459769.91	637455.01	372.38	0.0869	0.0745
455812.71	640511.24	451.92	0.0840	0.0904
463727.11	634398.78	301.70	0.0814	0.0603
467684.31	631342.55	258.26	0.0667	0.0517
672942.33	870412.02	58.04	0.0506	0.0116
669044.94	873544.16	137.85	0.0481	0.0276
451855.51	643567.48	635.86	0.0467	0.1272
471641.51	628286.32	228.80	0.0440	0.0458
665147.55	876676.31	274.43	0.0349	0.0549
483513.12	619117.62	193.71	0.0327	0.0387
475598.72	625230.09	208.29	0.0255	0.0417
447898.30	646623.71	812.93	0.0181	0.1626
479555.92	622173.85	199.25	0.0156	0.0399
661250.17	879808.46	427.81	0.0093	0.0856
657352.78	882940.61	659.68	0.0076	0.1319
443941.10	649679.94	1006.44	-0.0382	0.2013
439983.90	652736.17	1153.60	-0.0896	0.2307
436026.70	655792.40	1179.34	-0.1210	0.2359
507880.74	724487.90	748.80	-0.1250	0.1498
503909.25	727525.54	1175.92	-0.1514	0.2352
432069.50	658848.64	1301.03	-0.1709	0.2602
581220.31	812748.20	1148.62	-0.1799	0.2297
501457.20	1008226.56	1444.95	-0.2494	0.2890
424155.09	664961.10	1444.96	-0.2716	0.2890
420197.89	668017.33	1377.63	-0.2933	0.2755

Appendix C 1: Depth control points showing estimates of observed and calculated pseudo-gravity data.

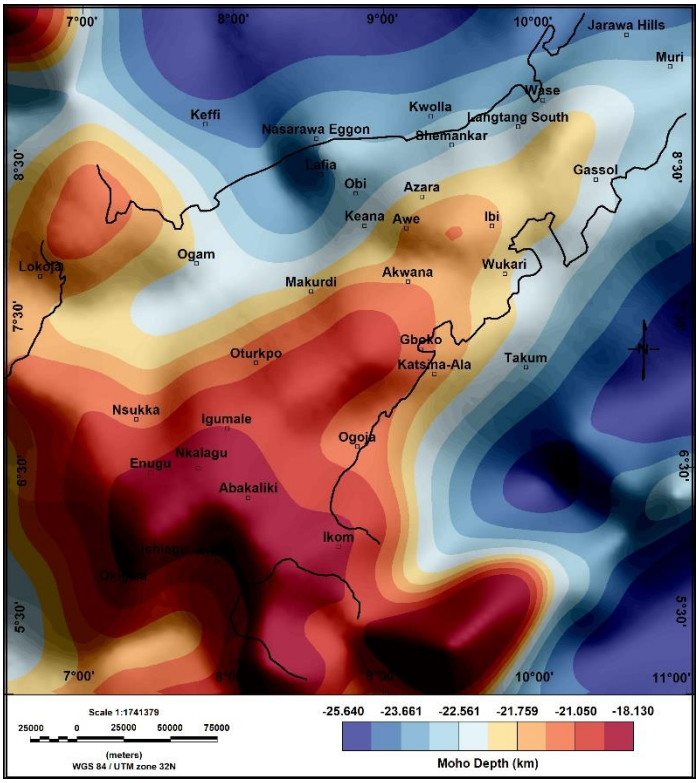

Appendix C 2: Moho depth interface showing the topography variation from the 3D inversion after filtering and considering a density contrast of 0.3.

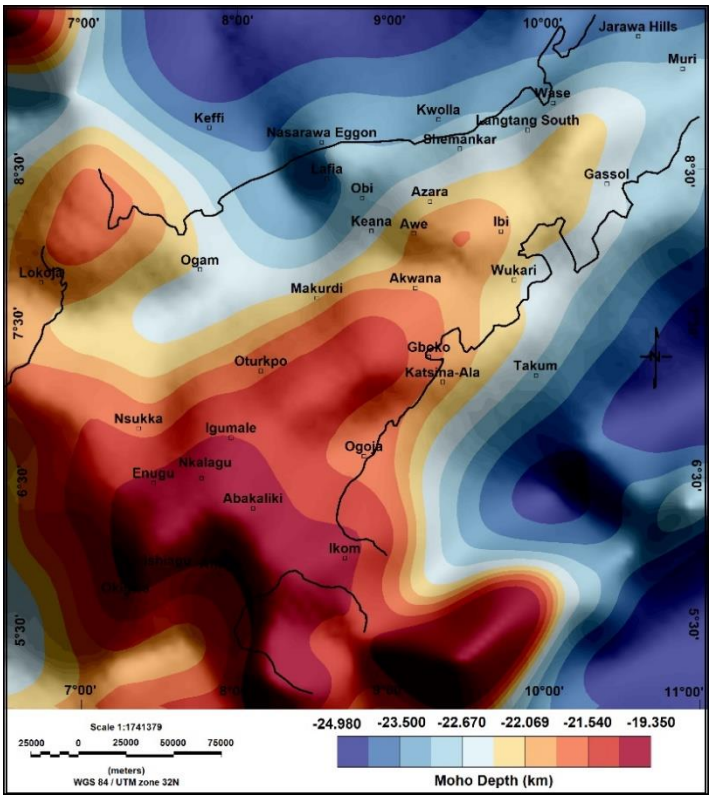

Appendix C 3: Moho depth interface showing the topography variation from the 3D inversion after filtering and considering a density contrast of 0.4.

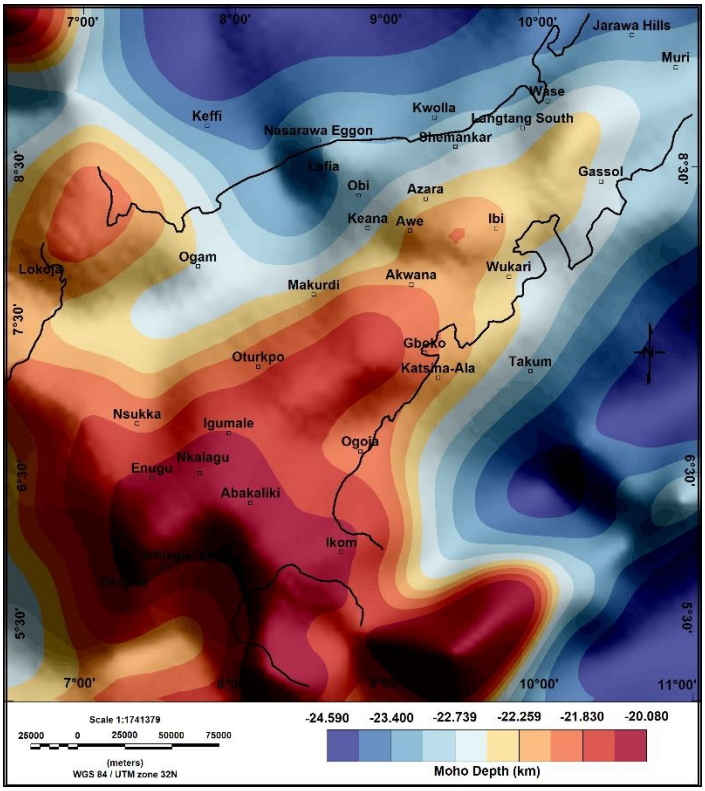

Appendix C 4: Moho depth interface showing the topography variation from the 3D inversion after filtering and considering a density contrast of 0.5.

Inversion File	Mesh (Size)			Reference model constraints		Depth Weight		Bounds		Length, S			Vertical Depth (km)	Preferred inversion	Remark
	x	y	z	Density	decay constant	beta	znot	Upper	Lower	Le	Ln	Lz			
2	50, 10000	50, 10000	251, 100	0.7501	0.44	2	0	1	-1	0	0	0	25	None	
22	50, 10000	50, 10000	251, 100	0.7501	0.44	2	0	1	-1	20000	20000	200	25	9	
2_inverse	50, 10000	50, 10000	251, 100	-0.7501	0.44	2	0	0.7501	-0.7501	20000	20000	200	25	4	
22_inverse	50, 10000	50, 10000	251, 100	-0.7501	0.44	2	0	1	-1	20000	20000	200	25	9	
222_inverse	50, 10000	50, 10000	251, 100	-0.7501	0.44	2	0	0.63	-0.7501	20000	20000	1000	25	3	
2222_inverse	50, 10000	50, 10000	251, 100	-0.7501	0.44	2	0	0.63	-0.7501	20000	20000	200	25	3	
22222_inverse	**50, 10000**	**50, 10000**	**251, 100**	**-0.7501**	**0.44**	**2**	**0**	**0.63**	**-0.7501**	**0**	**0**	**0**	**25**	**9**	**best**
Test_0.3	50, 10000	50, 10000	251, 100	-0.7501	0.44	2	0	0.3	-0.7501	0	0	0	25	9	
Ref1_2_0	50, 10000	50, 10000	301, 100	0.7501	0.44	2	0	1	0.7501	0	0	0	30	12	
22	50, 10000	50, 10000	301, 100	0.7501	0.44	2	0	1	-1	20000	20000	200	30	5	
2_inverse	50, 10000	50, 10000	301, 100	-0.7501	0.44	2	0	1	-1	20000	20000	200	30	4	
22_inverse	50, 10000	50, 10000	301, 100	-0.7501	0.44	2	0	1	-1	20000	20000	200	30	8	
222_inverse	50, 10000	50, 10000	301, 100	-0.7501	0.44	2	0	0.63	-0.7501	20000	20000	1000	30	2	
2222_inverse	50, 10000	50, 10000	301, 100	-0.7501	0.44	2	0	0.63	-0.7501	20000	20000	200	30	2	
22222_inverse	**50, 10000**	**50, 10000**	301, 100	**-0.7501**	**0.44**	**2**	**0**	**0.63**	**-0.7501**	**0**	**0**	**0**	30	**8**	**best**
Test_0.3	50, 10000	50, 10000	301, 100	-0.7501	0.44	2	0	0.3	-0.7501	0	0	0	30	10	
2	50, 10000	50, 10000	351, 100	0.7501	0.44	2	0	1	-1	0	0	0	35	10	
22	50, 10000	50, 10000	351, 100	0.7501	0.44	2	0	1	-1	20000	20000	200	35	6	
2_inverse	50, 10000	50, 10000	351, 100	-0.7501	0.44	2	0	1	-1	20000	20000	200	35	4	
22_inverse	50, 10000	50, 10000	351, 100	-0.7501	0.44	2	0	1	-1	20000	20000	200	35	10	
222_inverse	50, 10000	50, 10000	351, 100	-0.7501	0.44	2	0	0.63	-0.7501	20000	20000	1000	35	2	
2222_inverse	**50, 10000**	**50, 10000**	**351, 100**	**-0.7501**	**0.44**	**2**	**0**	**0.63**	**-0.7501**	**20000**	**20000**	**200**	**35**	**1**	best
22222_inverse	50, 10000	50, 10000	351, 100	-0.7501	0.44	2	0	0.63	-0.7501	0	0	0	35	9	
Test_0.3	50, 10000	50, 10000	351, 100	-0.7501	0.44	2	0	0.3	-0.7501	0	0	0	35	8	
2	50, 10000	50, 10000	401, 100	0.7501	0.44	2	0	1	-1	0	0	0	40	13, 15	
22	50, 10000	50, 10000	401, 100	0.7501	0.44	2	0	1	-1	20000	20000	200	40	6	
2_inverse	50, 10000	50, 10000	401, 100	-0.7501	0.44	2	0	1	-1	20000	20000	200	40	2,1	
22_inverse	50, 10000	50, 10000	401, 100	-0.7501	0.44	2	0	1	-1	20000	20000	200	40	5	
222_inverse	50, 10000	50, 10000	401, 100	-0.7501	0.44	2	0	0.63	-0.7501	20000	20000	1000	40	2	
2222_inverse	50, 10000	50, 10000	401, 100	-0.7501	0.44	2	0	0.63	-0.7501	20000	20000	200	40	3	
22222_inverse	**50, 10000**	**50, 10000**	401, 100	**-0.7501**	**0.44**	**2**	**0**	**0.63**	**-0.7501**	**0**	**0**	**0**	40	**8**	**best**
Test_0.3	50, 10000	50, 10000	401, 100	-0.7501	0.44	2	0	0.3	-0.7501	0	0	0	40	9	

Appendix C 5: Fundamental inversion parameters and input files used for magnetic directional inversion trials. File 2222_inversion for 35 km vertical depth gave the most appropriate estimate for Moho surface. The highlighted parameters and result in red gave the result used for the study.